Measurement, analysis and modeling at the microscale of printed dots to improve the printed anti-counterfeiting solutions

Louis Vallat-Evrard

Communauté
UNIVERSITÉ Grenoble Alpes

THÈSE

Pour obtenir le grade de

DOCTEUR DE LA COMMUNAUTE UNIVERSITE GRENOBLE ALPES

Spécialité : **Matériaux, Mécanique, Génie Civil, Électrochimie**

Arrêté ministériel : 25 mai 2016

Présentée par

Louis VALLAT-EVRARD

Thèse dirigée par **Nadège REVERDY-BRUAS,** Maître de Conférences, HDR, Grenoble INP-Pagora/LGP2,
Codirigée par **Lionel CHAGAS**

préparée au sein du **Laboratoire Génie des Procédés Papetiers, LGP2**
dans **l'École doctorale Ingénierie - Matériaux, Mécanique, Environnement, Energétique, Procédés, Production**

Mesure, analyse et modélisation à l'échelle microscopique de points imprimés pour améliorer les solutions de lutte anti-contrefaçon

Thèse soutenue publiquement le **21 juin 2019**,
devant le jury composé de :

M. Naceur Belgacem
Professeur Grenoble INP, Grenoble INP-Pagora (Président)
M. Patrick Bas
Directeur de recherche CNRS, Ecole Centrale de Lille (Rapporteur)
M. Mathieu Hébert
Maitre de conférences HDR, Université Jean Monnet Saint Etienne (Rapporteur)
M. Edgar Dörsam
Professeur, Université de technologie de Darmstadt (Membre)
M^{me} Nadège Reverdy-Bruas
Maitre de conférences HDR, Grenoble INP-Pagora (Directrice de thèse)
M. Lionel Chagas
Ingénieur de recherche, Grenoble INP-Pagora (Co-encadrant de thèse)

Acknowledgment

I would like to thank my supervisors, Nadège Reverdy-Bruas and Lionel Chagas, for your confidence in me, for the guidance and the support that you provided.

I would also like to thank the members of the jury including Naceur Belgacem, Patrick Bas, Mathieu Hébert and Edgar Dörsam for the evaluation of my work, for your feedback, interesting discussions and questions.

Thank you to the Lycée Argouges and especially to Daniel Naud for printing the offset samples, for your time and expertise.

I would like to express my gratitude to the members of LGP2 and especially to the microscopy team: Raphaël Passas and Bertine Khelifi. Thank you, Anne Blayo for coaching my teaching experience. Thanks as well to all the members of the technical service of the lab for all the projects we achieved.

A PhD adventure would be different without the passionate discussions and interactions with the PhD students and the Post Docs. Thank you especially to my desk mates: Vincent, Fanny, Miriam and Gioia.

Last but not least, I would like to thank my family for their unconditional support, thank you dear Victoria, Elisabeth, Clémentine, Bernard, François, Tatiana, Irina and of course Avrora ;) It is a blessing to have you all! Thank you also “les Ollivier”, “les Luango” and to my friends, Xavier, Mitch, Céline, Samuel, Dominique, Natalie, Rémy, Cyrille, Colombe, Aurélien, Fanny, “et tous les autres”; I was very happy to see you at my defense at to receive your beautiful messages!

“

La perfection est atteinte, non pas lorsqu'il n'y a plus rien à ajouter,
mais lorsqu'il n'y a plus rien à retirer.

“

Antoine De Saint-Exupéry

Artiste, Aviateur, écrivain (1900 - 1944)

Contents

Notations and acronyms

Notation	Denomination
$\mathbf{R}(\boldsymbol{\lambda})$	Spectral reflectance
$\mathbf{I_r}(\boldsymbol{\lambda})$	Reflected spectral irradiance
$\mathbf{I_0}(\boldsymbol{\lambda})$	Incident spectral irradiance
$\mathbf{I}(\mathbf{x},\mathbf{y})$	Pseudo spatial irradiance
$\mathbf{R_a}(\mathbf{x},\mathbf{y})$	Halftone spatial reflectance
$\mathbf{R_a}$	Halftone reflectance
$\mathbf{R_{aw}}$	Halftone reflectance without optical dot gain
$\mathbf{R_p}\,(\mathbf{x},\mathbf{y})$	Paper spatial reflectance in halftone
$\mathbf{R_p}$	Paper reflectance in halftone
$\mathbf{R_{ps}}$	Bare paper reflectance
$\mathbf{R_i}\,(\mathbf{x},\mathbf{y})$	Ink spatial reflectance in halftone
$\mathbf{R_i}$	Ink reflectance in halftone
$\mathbf{R_{is}}$	Solid print ink reflectance
$\mathbf{T_i}(\mathbf{x},\mathbf{y})$	Ink spatial transmittance
$\mathbf{T_i}$	Ink transmittance
$\Delta\mathbf{a_{tot}}$	Total dot gain
$\Delta\mathbf{a_{opt}}$	Optical dot gain
$\Delta\mathbf{a_{phy}}$	Physical dot gain
$\mathbf{a_a}$	Apparent ink coverage
$\mathbf{a_e}$	Effective ink coverage
$\mathbf{a_n}$	Nominal ink coverage
$\mathbf{H}(\mathbf{x},\mathbf{y})$	Paper point spread function - 2D
$\circledast$	Convolution operator
$\mathbf{h}(\mathbf{i})$	Histogram
$\mathbf{IM}(\mathbf{x},\mathbf{y})$	Image (i: name of image)
$\mathbf{px_i}(\mathbf{x},\mathbf{y})$	Pixel value frame i
$\mathbf{K}$	Threshold value
$\mathbf{A}$, $\mathbf{A_c}$	Area, Convex area
$\mathbf{P}$, $\mathbf{P_c}$	Perimeter, Convex perimeter
$\mathbf{D_{F_{min,max}}}$	Feret diameters
$\mathbf{BP_e}$	Histogram similarity index
$\mathbf{CS_p}$	Profile similarity index
$\mathbf{ICD}$	Ink coverage difference
$\mathbf{Q_r}$	Relative mean index difference
$\mathbf{FD_b}$	Binary fidelity index
$\mathbf{FD_g}$	Grayscale Fidelity index
$\mathbf{O}(\mathbf{x},\mathbf{y})$	Over inked region
$\mathbf{U}(\mathbf{x},\mathbf{y})$	Under inked region

Acronym	Denomination
AM	Amplitude Modulated halftone
CCD	Charge Couple Device
CMOS	Complementary Metal Oxide Semiconductor
dpi	Dot Per Inch
EIC	Effective Ink Coverage
GTI	Ground Truth Image
FM	Frequency Modulated halftone
IC	Ink Coverage
ICD	Ink Coverage Difference
lpi	Line Per Inch
MCI	Microscope Captured Image
NIC	Nominal Ink Coverage
AIC	Apparent Ink Coverage
PSF	Paper Point Spread Function
SHI	Simulated Halftone Image
SMI	Simulated Microscope Image
XOR	Exclusive disjunction logical operation

List of publications

- Vallat-Evrard, L., Chagas, L., Passas, P. & Reverdy-Bruas, N. Microscale halftone dots analysis: A spatial threshold evaluation method. in Proceedings of the 43rd International Iarigai Conference in Toronto (2016).

- Vallat-Evrard, L., Chagas, L., Passas, P. & Reverdy-Bruas, N. Microscale halftone analysis: Measurement framework and convolution strategy to differentiate physical and optical dot gain. in Proceedings of the 44rd International Iarigai Conference in Fribourg (2017).

- Vallat-Evrard, L., Chagas, L., Passas, P. & Reverdy-Bruas, N. "High dynamic range capture and sensor calibration to improve microscale halftone ink and paper surface quantification." Review of Scientific Instruments 90.8 p.083706 (2019).

Chapter 1 Introduction

1.1 General context

Information is amongst the most important tools driving our society. Information is everywhere allowing communicating, educating and building common knowledges required to live as a responsible free citizen. Mechanical printing was reinvented by J. Gutenberg in the 15th century in Strasbourg, the capital of Europe. For years, printing was the main support of information and thus, printing was among the most important inventions of mankind. With the invention of the halftoning method by William Henry Fox Talbot in 1852, the reproduction of illustrations and photography shifted from manual craftsmanship art to industrial technique. This led scientists and industrials to study the relations between print properties and stimuli produced on the human eye [1].

Murray and Davies were among the first scientists to investigate the relations between the printed dot morphology at the microscale and the measured optical density [2]. In their work, the authors proposed the well-known Murray-Davies model linking the optical density to the ink coverage of halftones. Their approach was based on a microscale study of the print. Then, with the development of fast and portable optical densitometers and spectrophotometers, researchers focused on a macroscopic quantitative characterization of the print, progressively becoming the standard characterization in the graphic industry. Multiple models have been developed to predict the reflectance of a halftone, such as for example the Yule-Nielsen model, the Clapper-Yule or the probability model [3,4]. These models were progressively modified to account for different optical and physical phenomena such as the internal reflections, the ink spreading, the ink penetration, spectral reflection, non-uniform ink thickness, etc. [4]. These models were also extended to account for color printing, assessing the problems of ink superposition and colorant mixing. Models such as the Neugebauer model, the cellular or ink spreading models were proposed [4]. These models relied on the surface coverage of the colorants on paper [5–7]. The ink coverage can be considered to be an integrated measurement since the geometric and morphologic properties of the ink are not taken into account. However, a macroscopic characterization of a microscopic system results in a loss of information. Therefore these models only allow an observation – deduction study of the effects of the print parameters on the reflectance.

A more phenomenological approach was proposed and relied on a spatial description of the ink layer on the surface of paper [8–16]. Instead of having an integrated ink coverage, the ink coverage is discretized on the paper surface allowing a prediction of the spatial description of the halftone reflectance. The characterization of the halftone print can then be performed for different regions of the print and reflectance distributions can be obtained. The model is called model of the light diffusion on halftones and was also extended to color prints [13,17]. Ultimately, the integrated reflectance or the integrated ink coverage can be computed from the spatial description of these quantities. The model of the light diffusion on halftones benefits from the advantage that it only requires to be optimized as a function of the paper type (light diffusion characteristics). Nevertheless, this model was less studied than the integrated models, most certainly because obtaining the spatial description of the ink transmittance and of the paper point spread function required advanced tools and image processing treatments. Recent studies developed approaches to measure precisely the dots characteristics at the microscale, facilitating the implementation of the model [17,18,10,19,20]. Moreover, microscale measurements retrieve further significant indexes such as print quality, optical dot gain, physical dot gain, ink penetration, etc. [21,22].

In the last 30 years, printing helped fight against counterfeiting, a plea threatening citizen safety and impacting the financial health of our industries. Counterfeits are copies of a genuine product, infringing intellectual properties, being produced without control and being marketed to trick the consumer into buying a fake genuine-like branded product. According to the European union intellectual property office, the global counterfeit trade reached USD 461 billion representing 2.5% of the world trade in 2013 [23]. Europe was highly impacted with USD 116 billion of imported counterfeit goods. A tradeoff has to be adopted between the cost of the authenticating solution and the level of security delivered. Printed anti-counterfeiting solutions, such as 2D micro-barcodes, are an interesting alternative providing solutions with high security at low cost, Figure 1.1. 2D micro-barcodes are composed of dots printed with conventional or digital print processes at high resolution. The security comes from the printer limitations to print dots accurately yielding to a deformation of the printed dots. A part of these deformations are reproductible and contains the printer signature. Another part of the deformations are random and make the code difficult to reproduce. The codes can be read with a smartphone, providing a magnifying optic. Development of printed anti-counterfeit solutions depends then highly on the capacity to control the print process and on the ability to measure the print accurately [24–26]. Fulfilling the goal of developing printed solutions to fight against counterfeits, the Estampille project was founded by the national agency for research in 2010 and yielded to several original results. Nguyen proposed a statistical model to simulate the shape of the ink dot at microscopic scale, [24,26,27].

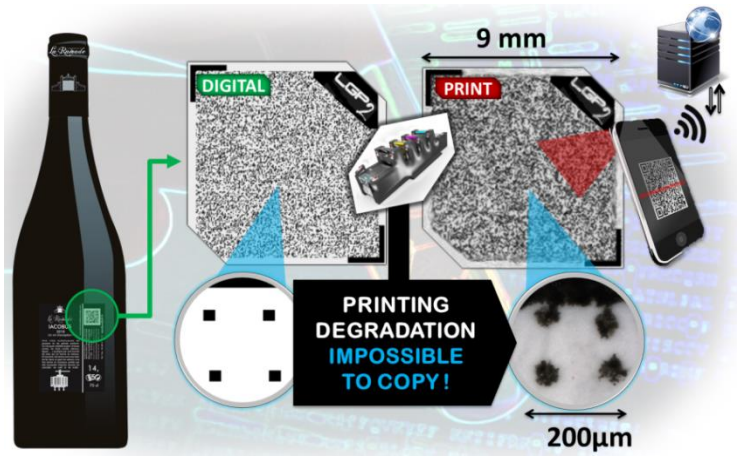

Figure 1.1: Printed anti-counterfeiting principle and authentication.

1.2 Objectives

A paper-ink boundary measured with an optical microscope and a scanning electron microscope is presented in Figure 1.2. Optical microscopy is fast, the geometrical deformations are controlled and the sample does not require a metal coating. Optical microscopy yields to the ink surface morphology as well as the ink reflectance distribution. However, compared to the image obtained with scanning electron microscopy, numerous limitations appear: the ink-paper boundaries are blurry and not well defined, un-inked area of the ink region are hardly visible, the ink reflectance is not homogeneous, etc. The optical dot gain is the consequence of the interactions between light, ink and paper and generates shifts of ink and paper reflectances [17–19,28,29]. The shifts are spatially dependent and thus mixed regions appear. The mixed regions are regions where the limits between the ink and the paper are not clearly defined. Moreover, the amount of optical dot gain depends on the ink coverage as well as on the halftone cell size, dot resolution, halftoning method, etc.

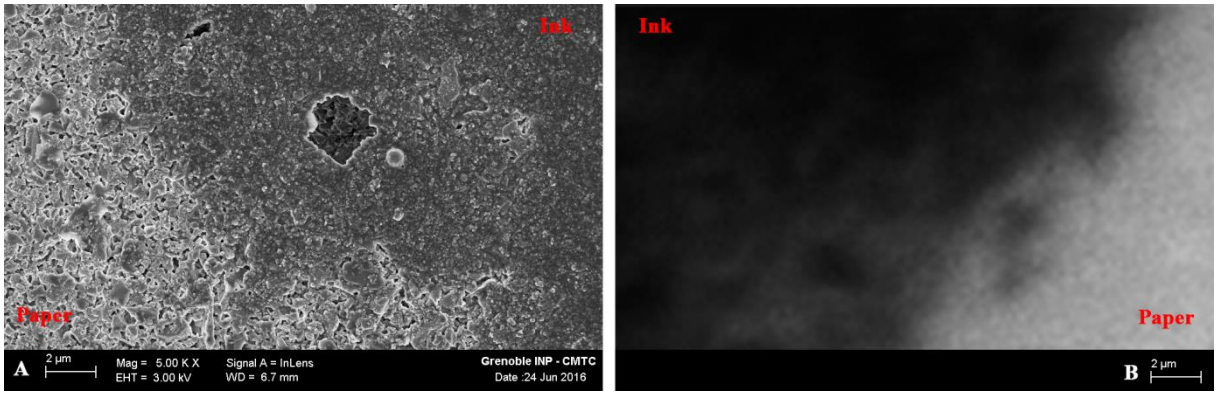

Figure 1.2: (A) Field emission gun scanning electron microscope image and (B) Optical microscope image (with numerical enlargement, bicubic interpolation) of an offset print on glossy coated paper.

The main objective of this thesis is to develop experimental methods and image treatments improving the microscale measurements and the ink-paper separation of halftone dots, Figure 1.3. Improved measurements of the halftone dots at the microscale and separations of the ink region from the paper are keys to develop. Indeed they allow implementing and improving the model of light diffusion on halftones as well as improving the security and authentication of printed anti-counterfeiting devices with improved characterization and models of the printed dots shapes. Multiple challenges are associated with the measurement and the modelling of printed halftone at the microscale:

- Several apparatuses have been developed in literature and performed print measurements at various scales with multiple geometries and strategies. This shows that the research community has not agreed yet on the characteristics required to measure halftone dots at the microscale.
- The halftone dots present morphologies and reflectance properties at the microscale associated with large variations. Thus, a large number of dots should be measured and measurement automations can facilitate the process. However, automation algorithms developed for microscopy applications are not specifically designed for halftone dots.
- Solutions to separate optical dot gain from physical dot gain have been proposed in literature, [17–19,22,28,30–32]. The strategies to perform this separation either rely on image analysis with thresholding and segmentation or rely on combined measurements using reflected and transmitted images. The impact of optical dot gain on transmitted images remains a subject of controversy and is still being studied [33,34]. The threshold and segmentation methods to separate optical and physical dot gain present an interesting alternative solution. Multiple algorithms have been employed. However, their performances and accuracy are not known.
- The ink and paper mean reflectances in a halftone depend on the optical dot gain and on the ink coverage. Therefore, Arney and coworkers proposed an expanded Murray-Davies model taking into input the effective ink and paper reflectances [5]. However, the measurements conducted relied on non-evaluated threshold algorithms or on manual histogram analyses [5,19,27,28,35–38]. Automated characterization of the ink and paper peaks on the histogram can help improve the understanding of the optical dot gain effects on halftones.
- Modrić suggested that the paper point spread function depends on the paper properties but also on the ink properties [12]. Reasons for this dependency exposed by the author are the multiple photons scattering in paper and ink and the internal reflections at the border between ink-paper and air. The most known effect of optical dot gain suggests a shadowing around the halftone dots. Nevertheless, a global darkening of the paper regions and a global brightening of the ink regions occur simultaneously, suggesting more complex interactions between ink, light and paper.

Moreover, dependencies of the halftone properties such as for example the distance between the printed dots, the dot size or perimeter, in relation with the optical dot gain effects, are not fully understood.

- When printing a halftone image, deformations of the printed dots induce the physical dot gain. The physical dot gain can then be used as a signature authenticating a printed anti-counterfeiting code. Moreover, understanding the deformations dependencies induced by the printer allows increasing the security level. An improved knowledge of the dot deformations also allows an improvement of the printed color reproduction. Nevertheless, studying the dot deformations is difficult: it requires first to be separated from optical dot gain, several measurements are required to obtain an average and the halftone dots deformations depend on the interactions between several adjacent nominal dots (a halftone dot is printed by juxtaposition of multiple nominal dots).

1.3 Content

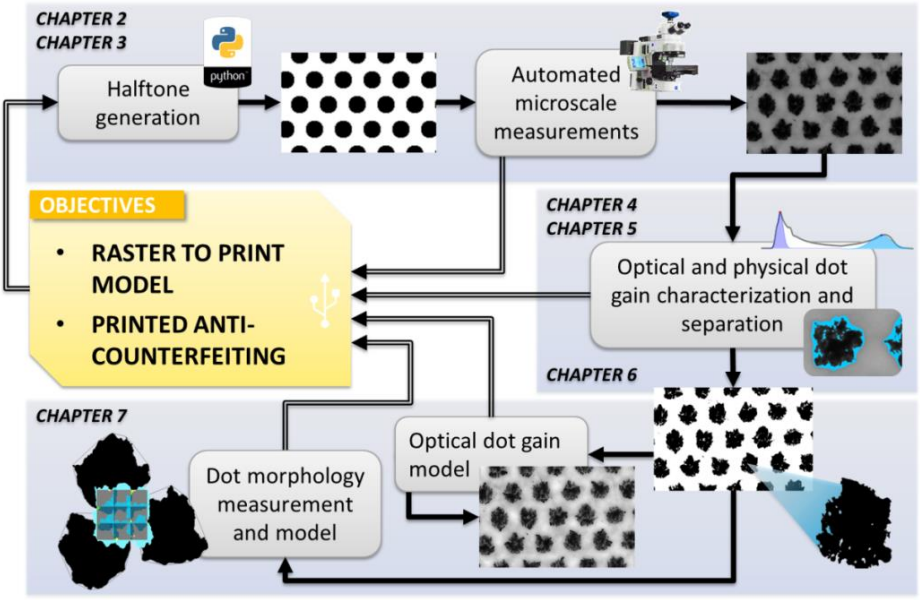

Figure 1.3: Chapters organization, relationships between chapters and objectives.

The chapters organization, relationships between chapters and objectives are illustrated in Figure 1.3. The research effort has been focused on developing tools and methods to measure and characterize halftone dots at the microscale (chapter 2). Multiple approaches were proposed to separate and characterize the ink regions from the paper regions on printed halftones (chapters 3, 4, 5). Furthermore, the physical and optical dot gains were characterized and modeled (chapter 6).

Chapter 1) State of art: halftone printing, measuring and modelling are presented. Two main focuses are proposed: the first one, on the experimental methods developed to measure and separate the ink and paper regions of printed halftones at the microscale; the second one, over the measured effects of optical dot gain. Models developed to predict the ink reflectance and applied to dot gain characterization are presented. A selection of anti-counterfeiting printed solutions is also summarized, focusing on approaches adopted and on researches conducted previously at the LGP2.

Chapter 2) Materials and methods: an important research effort has been directed toward the development of measurement methods and apparatus to characterize halftone dot at the microscale. A polarized reflection optical microscope has been adapted with a commercial digital camera in order to control the measurements. The microscope stage, the camera, photometer and thermometer were

controlled directly in a Python graphic user interface specifically developed. The Bayer matrix was removed from the sensor surface of the camera and raw images were retrieved to insure a complete control over the measurements. Test forms and experiments with different halftone dot configurations were specifically designed. An automated measurement method was developed allowing measuring automatically a large number of halftone dots at the microscale. Finally, a high dynamic range capture method was proposed and tuned specifically for halftone dots.

Chapter 3) Gaussian fit to measure automatically ink and paper reflectances on histogram: impacted by the optical dot gain effect, the ink and paper reflectances become dependent on the ink coverage. A Gaussian fitting of the ink and paper histogram peaks to measure automatically the ink and paper reflectances was then proposed. A double optimization was used in order to fit the width of the Gaussian and the position of the center of the Gaussian. The performance of the method was then analyzed and applied to optical dot gain determination.

Chapter 4) Convolution strategy to differentiate physical and optical dot gain: two convolution strategies to differentiate physical and optical dot gain were then proposed based on the model of the light diffusion on halftones developed by Callahan, Yule and Lehmbeck. The first strategy is developed by approximating the spatial description of the ink transmittance by the square root of the ink reflectance. The optical dot gain can then be removed from the halftone image by subtracting with the spatial description of the ink transmittance convolved with the paper point spread function. The second strategy focuses on the approximation that the spatial description of the ink transmittance can be obtained from the thresholded halftone image. Optical dot gain separations were evaluated.

Chapter 5) Supervised evaluation of threshold algorithms and novel threshold algorithms: an objective threshold evaluation method was developed in order to define the best threshold method as a function of the printing processes, the halftone types, the halftone resolutions, the paper point spread functions, etc. The method is based on a generation of ground truth images. A simulation of the optical dot gain effects and of the microscope distortions are performed to obtain test images that have similar characteristics than the images measured on the microscope. The test images are then thresholded by the different algorithms and their performances are evaluated by comparison with the ground truth. Two novel threshold algorithms based on the properties of printed halftones and developed specifically for halftone dots were proposed. The first threshold algorithm proposed is based on determining the amount of ink peak shift, yielding to compress the ink reflectance distributions to match the distribution of the solid ink. The second threshold algorithm proposed is based on a pre-treatment of the images by applying the convolution strategy to differentiate physical and optical dot gain (chapter 4). The performances of the two proposed threshold algorithms are then compared to threshold algorithms from literature.

Chapter 6) Raster to print halftone models: two models were proposed in order to predict the halftone reflectance. The first model is based on the measurements of single dot morphologies and on the measurements of dot-dot interactions. An automated microscope capture of a large number of single dot configurations is performed, allowing a quantification of the dot morphologies, area increase and dependencies with the printer parameters. Dot-dot interactions are then characterized and modelled. The second model reproduces the interactions between ink light and paper. A divergence of the model of the light diffusion on halftones with the experiments was observed near the borders of the halftone dots. A new model is then proposed based on a double convolution with two different paper point spread functions. The first convolution reproduces the main effects of light diffusion with a global reflectance increase of the ink regions and a global reflectance decrease of the paper region. The second convolution reproduced the reflectance increases and decreases observed near the edges of the dots. The model performance was then analyzed for multiple halftone configurations. The effects of the distance between the halftone dots, the size, shape and edges morphologies of the halftone dots were investigated for 3 printing processes: electrophotography, inkjet and offset.

Chapter 2 Halftone printing, measuring and modelling: A review

Louis Vallat-Evrard, Lionel Chagas, Raphaël Passas, Nadège Reverdy-Bruas
Univ. Grenoble Alpes, CNRS, Grenoble INP*, LGP2, F-38000 Grenoble, France
Agefpi, LGP2, F-38000 Grenoble, France

2.1 Introduction

In the last 30 years, printing helped to fight against counterfeiting, a plea threatening our safety and impacting the financial health of our companies. Development of printed counterfeit solutions depends highly on the capacity to control and measure the print. With the improvement of modern digital measurement instruments, accurate measurement of printed dots at the microscale is becoming easier and easier. However recent improvements in the field of microscopy widened the measurement possibility, opening the door to new challenges:

- What is the best strategy to measure the print at the microscale? (resolution, magnification, microscopy methods, high dynamic range, etc.)
- What automation should be adopted? (autofocus, automatic placement, stack of images on the focus axis, etc.)
- What image processing treatment should be performed? (how to separate ink from paper, how to measure ink attributes, how to account for ink thickness variation, etc.)
- How does the optical dot gain affect the measurements? And how can the optical dot gain effect be measured?

The state of the art is focused on researches conducted to solve these challenges. It starts with an overview on counterfeiting demonstrating the needs of controlling the print process and the need of accurate measurement of printed dots at the microscale. In a second part, print processes are introduced. In a third part digital optical microscopy and image processing are presented. In a fourth part the paper, ink and light interactions and associated measurement methodologies are surveyed. In the fourth part the effects of optical dot gain and the parameters impacting optical dot gain are discussed. The fifth and last part is focused on presenting a selection of the print reflectance models used to obtain a measurement of dot gain.

2.2 Counterfeiting

2.2.1 A global threat

Counterfeits are copies of a genuine product, infringing intellectual properties, being produced without control (material and process) and being marketed to trick the consumer into buying a fake genuine-like branded product. First traces of counterfeiting were already found during the Roman empire with counterfeited jars containing wine. The counterfeit was used during wars as a weapon with counterfeit money disturbing the opponent's economy. More recently, starting in the eighties, counterfeits became a global society issue with the globalization of trades and exchanges. However

countries and companies counteract only slowly since identifying and authenticating the counterfeits are difficult. Europe responded by creating the Office for Harmonization in the Internal Market (OHIM) in 1994. The OHIM was reorganized and renamed the European Union Intellectual Property Office (EUIPO) in 2006. Outside Europe the Counterfeiting Intelligence Bureau (CIB) of the International Chamber of Commerce (ICC) performs similar tasks. The European Union office organizes the patent, design and brand registrations, monitors the counterfeits, dispenses training and communicates on the dangers of counterfeits. Nevertheless the counterfeits persist in world trades and the public health and security is involved, as sadly demonstrated by few cases in the last decade [39–41]. Multiple studies have been conducted to measure the effect of counterfeiting in relation with the consumer behavior [23,42–44]. According to the EUIPO, the global trade in counterfeit reached USD 461 billion representing 2.5% of the world trade in 2013. Europe was highly impacted with USD 116 billion of imported counterfeiting goods representing 5% of the imports. According to the Organization for Economic Co-operation and Development (OECD), the European companies produce mostly intellectual properties and counterfeit impact their economy directly leading to less employment. France is the third country impacted with 12% of the world seizures infringing the intellectual property rights of French companies in the 2011 to 2013 period. The first country is the United States with a 20% impact. According to the Anti-counterfeiting intelligence supporting tool (ACIST), more than 87% of the counterfeits seized were coming from China and Hong Kong in 2013. Turkey, Malaysia, Morocco, Greece and India export counterfeits as well. According to EUIPO, most goods seized are footwear and clothes (76%), followed by electronics and household electricals (10%). Toys, tabaco, spirits and drugs were seized as well. Counterfeiters are now starting to produce counterfeited food and beverages [23]. Authenticating a counterfeit is difficult as copies are more and more accurate, Figure 2.1. A few design differences are visible on the counterfeit cartridge but an expertise is necessary to identify these differences. To solve that problem and to allow the consumer to detect counterfeits, multiple solutions authenticating the products have been developed.

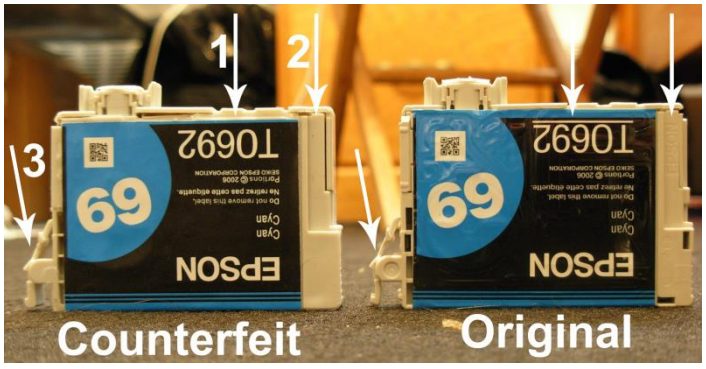

Figure 2.1: Counterfeited inkjet cartridge, 1, 2 and 3 visible design differences, reproduced [45].

2.2.2 Product authentication solutions

Multiple solutions for product authentication have been developed to fight against counterfeit. The authentication solutions can be visible or hidden:

- Overt: overt authenticating solutions are directly visible and are usually known from the consumer (holograms, optically variable inks, watermarks, special inks, tamper evident, etc.)
- Covert: covert authenticating solutions are invisible to the naked eye and require a tool to be revealed (UV inks, microprint, digital watermarks, spectral signature, hidden fibers, etc.)
- Forensic: forensic authenticating solutions require the analysis of the laboratory to statute on its authenticity (fiber arrangement of paper, nano-particle, magnetic particle, chemical composition, ink formulation, biological markers, DNA markers, etc.)

A tradeoff has to be adopted between the cost of the authenticating solution and the level of security delivered. Overt solutions are usually less expensive than cover solutions that are themselves less expensive than forensic solutions. The flexibility for the product authentication depends also on the level of security, higher security methods requiring complex tools to perform the authentication. In this context, smartphones are a game changer, as most consumers possess a smartphone and considering that software applications can be easily added on the device. Smartphones present multiple sensors that can be used and tuned for product authentication. The smartphone camera sensor is actively considered in studies for product authentication [46–53]. Multiple technologies have been developed to fight counterfeits. A selection of these technologies, potentially authenticable with a smartphone is presented in Table 2.1.

Table 2.1: Selected main innovative authenticating solutions for products.

Cryptoglyph Alp Vision [54]

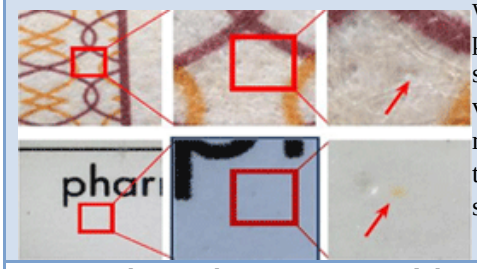

Digital invisible marking printed on paper cardboard and polymers with conventional inks or varnishes. The printed image contains pseudo-random patterns of dots (10 to 20 µm). A second layer of security can be achieved by placing microholes (40 to 80 µm non-varnished regions) in the varnish layer of the print. The pseudo-random printed dots and microholes contain encrypted information that can be read with a simple smartphone or with a desktop scanner. Decoding requires the encryption a 128 bit encryption key.

Bubble Tag Novatec [55]

Novatec, known by its commercial brand Prooftag, has developed multiple technologies to perform product authentication. Bubble Tag is a three-dimensional code (surface of 1 cm²) produced by a random generation of air bubbles in a transparent thin polymer (200 to 500 µm). The Bubble generation is random and thus each code features (bubble size, shape and position) has unique properties. Ramdot presents a random dispersion of optically variable particles. FiberTag presents a random dispersion of visible and non-visible fibers in the paper structure (addition in the paper pulp during the paper making process). These unique features can be measured with a smartphone, a scanner, a microscope or directly visually (comparison with database).

Bokode Massachusetts institute of technology (MIT) [56]

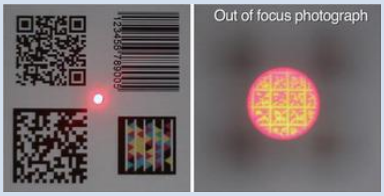

The bokode is a visual datatag of 3 mm diameter readable from a distance (up to a few meters) by placing the camera out of focus. A lens deposited on the surface of the code allows its readability. The bokode offers the advantage of being almost visually invisible but contains rich information when imaged with a camera (directly readable by smartphone). Given the dimension of the code, a reproduction is difficult since acquiring the micro pattern is difficult. A drawback is the cost associated with the technology estimated today at USD 5 dollars.

Seal vector, Advance track and trace [57]

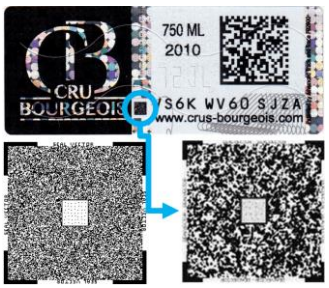

The Seal vector is a 2D barcode composed of dots printed on paper or polymers with conventional and numeric print processes. The security comes from printers limitations to print dots accurately. A deformation of the input is then induced. A part of these deformations are reproductible and contains the printer signature. Another part of the deformations are random and make the code impossible to reproduce. The codes can be read with a smartphone, providing a magnifying optic. The original code cannot be obtained from a microscale analysis since printing induced deformations. Thus, printing a counterfeit code without the original one would result in a different code. Even if the counterfeiter possesses the original code, similar deformations could not be obtained since they are randomly induced.

3DShining Popims code [58]

3DShining is produced by printing variable optical flakes. The unique authentication technology comes from a dual capture with and without flash. The numerical subtraction gives the signature of the optical variable flakes. Extended authentication can be adopted by the use of infrared and ultraviolet illuminant. Smartphone can be used to verify the authenticity of the product. Additional technology can be used such as 3DShiningNature, a micro-sandblasting of the surface creating a random unique topographical signature. 3DShiningFrost uses a dual layer of varnish to produce unique 3D structures allowing for a high level security.

Pelta Pagemark technology [59]

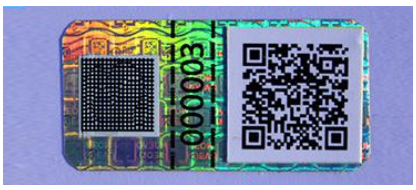

The Pelta codes are classical Quick response barcodes (QR codes) embedding a secondary layer of encrypted information. For this technology only the encryption technology and the algorithm embedding hidden information to the tag participate to the security features. A code can be copied, however the code cannot be tuned to include for example a serial number that should be identical to the non-encrypted serial code and displayed on the label. Authentication can be easily performed with a smartphone.

Digimarc [60]

Digimarc is a code hidden in the printed halftone (digital watermarking). The embedding of the code uses steganography and visual cryptography techniques. Since the code is embedded in the halftone organization, copying it requires to reconstruct the original binary images for all print layers, making it difficult for the counterfeiter. The reading of Digimarc code can be achieved directly with a smartphone, a scanner or with dedicated devices.

2.2.3 Project ESTAMPILLE, National Agency for Research (ANR)

The Estampille project has been founded by the national agency for research and gathered four university laboratories: CERDI University Paris XI, GIPSA National center for research, LAGIS National center for research, LGP2 Polytechnic institute of Grenoble and two private companies: Advance track and trace and Michel Lata S.A. The project started in 2010 and was founded for 46 months. The aim of the project was to develop printed solutions to fight against counterfeits. The project was then split in three parts: generation of a secure printed code design, measurement of the printed code and verification of the robustness of authenticating solution. The technology proposed to secure the product relies on Advanced Track and Trace patented micro code called seal-vector. Printing the code induces deformations that are recorded in a database. A measure with a smartphone for example computes an index (based on the printed micro-dots registrations and shapes) that can be compared to the index stored in the database. When the code is copied a different deformation of the dots at the microscale is induced by the second print. The deformations do not match the original and the counterfeit is detected. Five technological or scientific limitations had been identified:

- Analysis and modelling of the printing process with physical and signal processing models (influence of the micro dot shape as a function of the resolution, the ink, the paper and the process)
- Development of methods and tools to quantify and analyze the difference between the original non-printed code, the printed authentic code and a counterfeited code
- Generation of microcodes with optimized characteristics as a function of the printing process to maximize the security robustness
- Listing the counterfeiting scenarios leading to a breach of security
- Building of the required juridical proofs to insure the compliance with the law

The work conducted at the LGP2 included three master thesis and one PhD thesis (based in LAGIS). The main results of these studies are the starting point of this work:

- Lanneau [61] studied the effects of the print parameters (dot sizes, etc.) and the printing process (offset, inkjet and electrophotography) on the histogram of the image of dots captured at the microscale with a reflection darkfield optical microscope. Results showed that the histogram presented a peak for the ink and a peak for the paper. These peaks were fitted by two Gaussian functions. The kurtosis and skewness of the fitted Gaussian in relation to the histogram were used to distinguished original printed codes from counterfeited codes. Lanneau compared also three acquisition methods: an USB portable microscope, a darkfield reflection optical microscope with 5x objective and a desktop scanner. Results showed that the USB portable microscope presented geometrical distortion and color aberration in the field of view. The scanner presented a spatial resolution too small compared to the size of the printed dots. Darkfield reflected microscopy delivered accurate measurements.

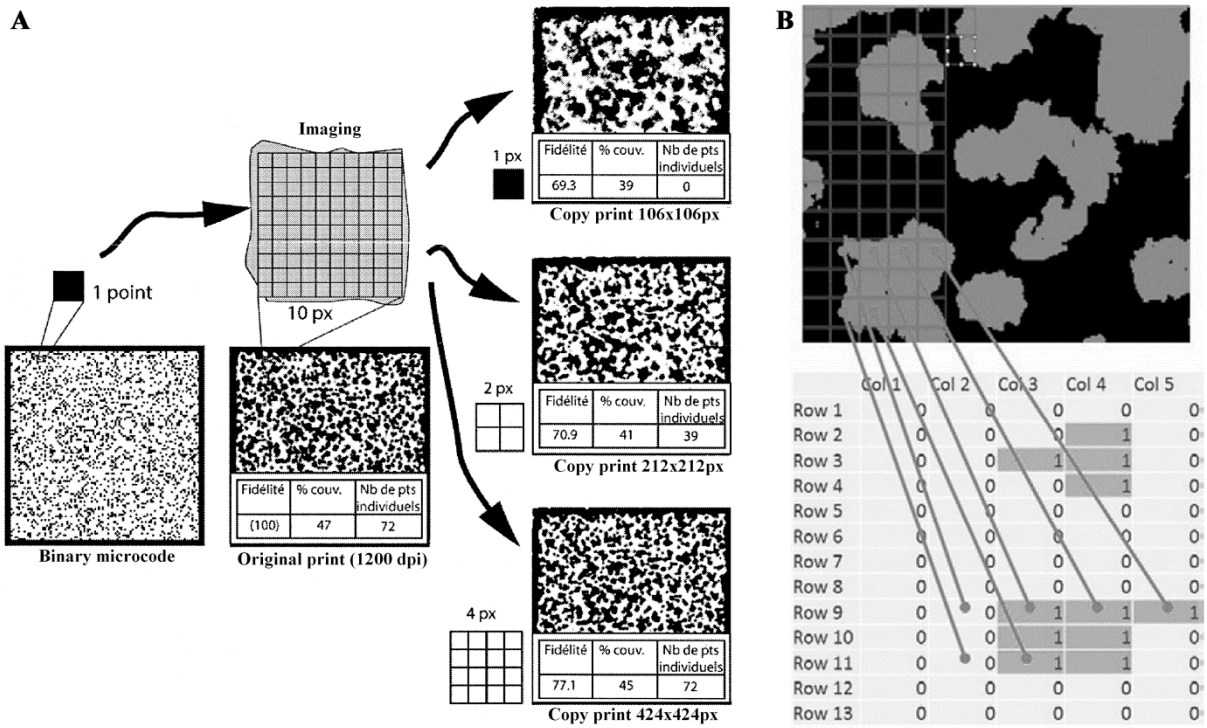

Figure 2.2: (A) Counterfeit strategy and impact on the fidelity ratio, adapted [62], (B) Resampling strategy to counterfeit a microcode reproduced [25].

- Pflimlin [62] proposed a novel threshold algorithm based on a fidelity index computed by comparison with the non-printed binary microcode. The fidelity ratio is the ratio of similar pixels from the printed code and the non-printed original code. The threshold method is based on an iterative search for all threshold values to maximize the fidelity ratio index. Only the blue channel of the image acquisition is used as it was observed to output sharper measurements. Effects of ink coverage (20%, 40% and 70%), of the print process (conventional offset and waterless offset), of the dot size (2400, 1200, 800 and 600 dot per inch) and of the type of paper (coated and uncoated) on the fidelity ratio were analyzed. Results showed that small dot sizes were associated with a small fidelity ratio due to physical and optical dot gain effects. Coated paper was associated with less variation of the fidelity ratio (1% variation) as opposed to uncoated paper (5% variation). Small ink coverage lead to improved fidelity ratios, as well as waterless offset compared to conventional offset. Counterfeiting attempts demonstrated that the fidelity ratio was not sensitive enough, with counterfeits showing large visual differences despite similar fidelity ratios, Figure

2.2 (A). The dot shape was studied using image processing shape descriptors. Results were impacted by noise and no clear conclusion could be drawn. Nevertheless a model was developed to model the dot shape. This model approximates the dot to a super-ellipse. Applying the model to the original binary image allowed to simulate the print. Image registration was the largest limitation encountered by comparing the model with measured printed dots.

- Poletti [63] proposed a classification of the dots and sub-dots sizes on the microscale captured image as a mean to identify the print process. Coated and uncoated paper printed with conventional and waterless offset at 2400, 1200, 800 and 600 dpi were analyzed and showed classification differences. Results showed a large difference between coated and uncoated paper. Other parameters greatly influenced the size distribution. Distribution recognition was developed as a mean to authenticate an original printed code. Results showed similar tendencies between the digital non-printed code and the original printed code. Poletti proposed also a resampling method in order to counterfeit the microcode, Figure 2.2 (B). He obtained improved results with enhanced fidelity ratios for the counterfeits. Three threshold algorithms were tested (Li method, Otsu method and moment method). Otsu threshold method was found the best method.

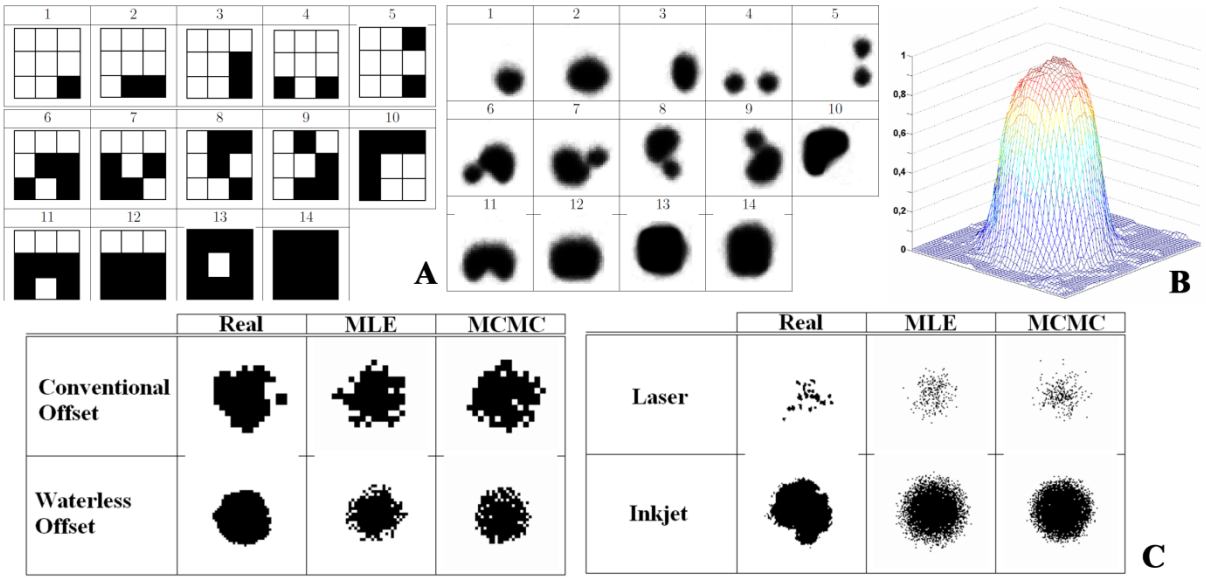

Figure 2.3: (A) 14 studied dot-dot patterns and statistical average over 100 microscale capture of the printed patterns, (B) ink reflectance of a single dot (average of 100 measurements) and (C) dots estimation with maximum likelihood estimator (MLE) and the Markov chain Monte Carlo estimator (MCMC) as compared to measurements (Real). Adapted [27].

- Nguyen [24,26,27] worked on the development of a statistical model to simulate the shape of the ink dot at microscopic scale. Dots were analyzed and parameters determined through maximum likelihood estimation and with Bayesian interference. The effect of the dot clustering on the dot shape was studied, analyzing more than 100 samples of 14 dot-dot patterns, Figure 2.3 (A). Analyzing single printed dots, Nguyen showed that the average of the dot surface became stable after 20 measurements, Figure 2.3 (B). The ratio of experimental area to theoretical area was analyzed for the 14 patterns for coated and uncoated paper. This ratio was found to fluctuate as a function of the pattern for both papers, demonstrating the dots-dots interactions during printing. The relations between area, perimeter and compactness were investigated for the 14 patterns and results showed a dependency on the print resolution as well as on the type of paper selected. Nguyen introduced then a microscopic printing probabilistic model reconstructing ink and paper distribution using a Log-normal distribution for the paper and a Beta distribution for the ink. Calculating the Kolmogorov-Smirnov distance, an optimization of the distribution parameters could be established for paper and ink. A second model was developed by Nguyen to predict the dot morphology as a function of the process. Two estimators were developed, the maximum likelihood estimator and the Markov chain Monte Carlo estimator. Results of these two estimators

showed that the measurements presented more fragmented perimeter and less miss-inking in their surfaces Figure 2.3 (C). The model was improved by introducing a third estimator: the Markov spatial model taking into account the effect of the vicinity of pixels.

Finally, a thesis conducted outside of the scope of the Estampille project was highly related to print counterfeiting solutions. Tkachenko [64] worked on print and scan relations in order to incorporate in a QR code a second layer of security, Figure 2.4. Tkachenko proposed a novel thresholding algorithm to determine if a module of the second security layer of the QR code was either white or black. This threshold algorithm is based on the weighted means square error measurement, placing more importance on pixels at the center of the modules, since they are less subjected to print and scan deformations. Moreover, patterns were proposed in order to code the second security layer QR codes. The robustness of the patterns to counterfeiting was evaluated and compared to the readability. A study of the deformation and noise generated during printing and scanning was performed.

Figure 2.4: Standard QR code and second security layer QR code, reproduced [64].

2.3 Printing

2.3.1 From the early stages to nowadays: 150 years of improvements

First pictorial representations have been traced at the mist of mankind. These representations were and remain nowadays the most simple and universal form of communication. From product marketing, advertising, road and safety signs, art and many other fields, these pictorial representations are everywhere in our daily life. Papazian [65] estimated 600 to 625 potential exposures to advertisement per day noticed or not. A part of these pictorial reorientations is produced by printing. Printing was first invented in China during the Han Dynasty, from 206 BC to 220 AD. The printing invention did not reach Europe immediately and a similar process was re-invented by Johannes Gutenberg starting 1434 in Strasbourg. Gutenberg printing process, called the typography, uses mechanical movable metal type, a wooden screw press and oil based inks. This invention was the starting point of the modern printing industry. At this early stage, only text and full tone graphical illustrations could be printed. These illustrations were produced by the perseverant work of artists engraving metal plates as shown on Figure 2.5 (different tones were produced by leaving more or less metal on the plate).

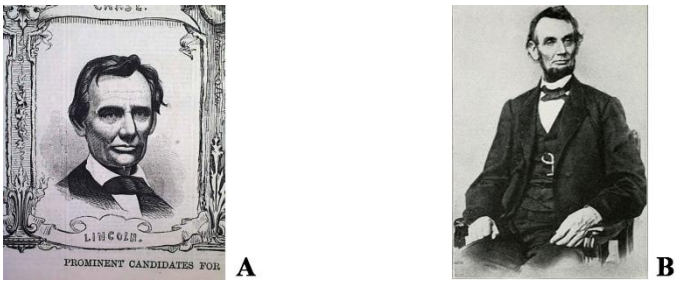

Figure 2.5: The invention of halftoning: (A) Printed illustration that was manually engraved before invention of halftoning, HARPER'S WEEKLY, New York, May 12, 1860, (B) Printed halftone.

The invention of the halftoning by William Henry Fox Talbot, in 1852, allowed to produce, for the first time, accurate pictorial representations without manual engraving and started a new era of printing. Indeed, with the halftoning method, print editors were able to photo-chemically engrave a printing plate, first translating the continuous tones of a photograph into a series of dots (i.e. halftones dots), then insolating these dots on the photosensitive coating of a printing plate and finally etching the plate with acids, producing the printing and non-printing areas. Producing pictorial representations introduced the questions of the fidelity and quality of the print reproduction. In fact, the perception of the printed image differs from the original photograph, affected by the halftoning method, by the spreading of the ink during printing and by optical phenomena. Parts of these alterations are commonly called dot gain as a reference to the increase of the halftone dot surface area, impacting the perception of the print. Thus, color management was introduced and focused on putting in relation inputs and outputs of the printer, in order to print a specified and controlled color. Since 1852, printing processes, associated with halftone methods and color management evolved continuously and although the printing throughput chain is mostly controlled today, phenomena affecting the print perception continue to be investigated in order to simplify, improve and understand the relations between printing and visual perception. Dot gain phenomena research in this field was very active in the 20th century and continues to be widely investigated nowadays. Changes in the approaches to study dot gain phenomena were observed from the last quarter of the 20th century to today, with a decrease of the scale of observation (from macroscopic to microscopic) and with the development of numerical simulation enabling the study the print at the scale of the photon (Monte Carlo light diffusion simulations).

2.3.2 Halftoning

The colors on pictorial representations, painted or photographed, are obtained by different concentration or layer thickness of pigments or dyes. However, to print the same pictorial representation a major limitation has to be overcome: printers are not capable of varying locally the ink thickness deposited or capable of mixing locally inks to obtain the different tints. Thus printing processes are said “binary” (depositing constant ink thickness or no ink) and can be seen as on/off ink deposition systems. As discussed by Ruckdeschel and Hauser [13] attempts to print continuous tones in electrophotography have been investigated but showed poorer reproduction qualities due to limitations in the process. The invention of halftoning allowed to overcome this process limitation and introduces a method to obtain continuous tone from a binary tone print. Halftoning methods consist in printing separately small dots of primary inks (i.e. halftone) over a small area. Relying on the property of the human visual system (i.e. averaging the light received under its resolution limit), a halftone printed area is perceived as a continuous tone [66]. Studies have been conducted to determine the visual threshold of halftone dots at standard viewing distance and results showed that halftone dots are becoming visible below 200 line per inch [67]. Multiple halftoning methods allow converting continuous tones to halftones and their main differences lay in the size, shape and organization of the halftone dots over the print area. These methods can be mainly classified into two categories: Amplitude Modulated (AM) and Frequency Modulated (FM) halftones. The binary image sent to the printer is called bitmap since it only contains 0 and 1 commanding the on/off deposition of the printer [1,66,68].

For AM halftones, the print area is divided into smaller areas having constant dimensions and called halftone cells. To produce various tints, these halftone cells are more or less filled with ink as shown on Figure 2.6 (A). Since the number of addressable print areas (i.e. addressable dots) inside the halftone cells is fixed, the numbers of different tints that can be produced are fixed. Metrics have been developed to describe these different dimensions. The first metric is the line per inch (lpi) which describes the width of the halftone cells (only one dimension is given because they are designed as squares). A classical value used by the printing industry is 150 lpi, and corresponds to a halftone cell width of 170 µm. The resolution of the printing machine (i.e. the number of individual dots

addressable by the machine) is given in dot per inch (dpi). Offset printing processes classically achieve resolution around 2400 dpi, corresponding to an elementary dot width of 10.58 µm (considered theoretically also as a square). Thus, in the example given, 256 dots are addressable per halftone cells, allowing a production of 257 tint levels. In the case of electrophotography, printer resolution is classically around 1200 dpi. Therefore, printing at 150 lpi leads to 64 addressable dots per halftone cells, producing then only 65 tint levels. Decreasing the size of the halftone cells (increasing the lpi) will increase the spatial resolution but decrease the tonal resolution with less tint levels addressable. Optimizations of spatial and tonal resolution are performed depending on the print process and on the content printed, however AM halftoning methods are limited in the details reproducible.

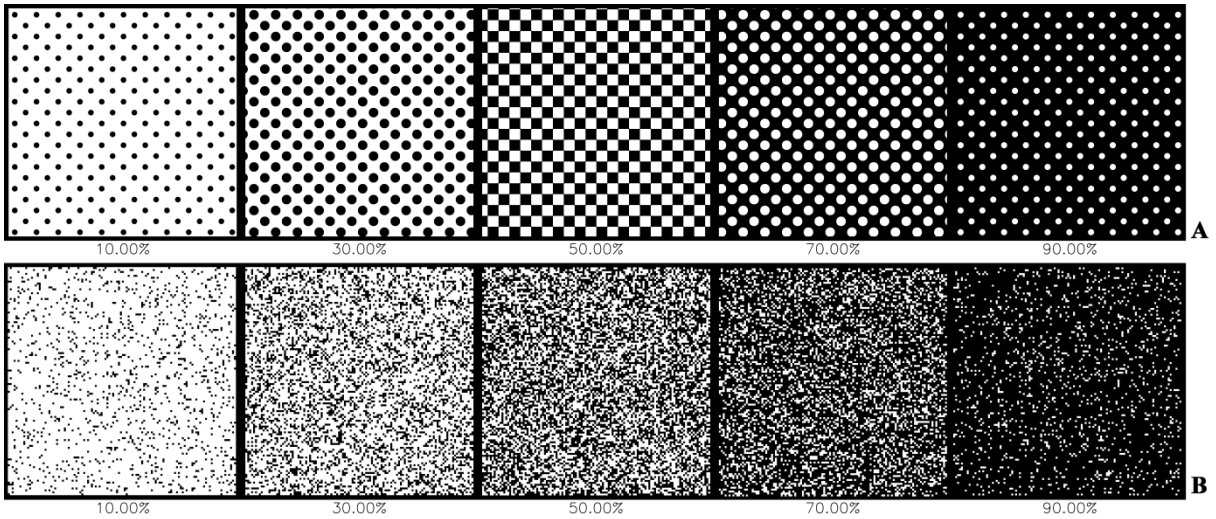

Figure 2.6: Grayscale levels obtained with (A) amplitude modulated halftoning (B) frequency modulated halftoning (random dither), enlarged to visualize the halftone cells.

For FM halftones, the different tints are produced by variating the number of printed dots per unit area, Figure 2.6 (B). Generally the dot width is fixed and usually corresponds to the smallest dot width addressable by the printer. Metrics for FM halftones are less developed since no apparent dot organization is found and thus only the size of the elementary dot is controlled and referred to in dpi. FM halftoning presents great benefits when printing graphics with large elementary dot size (small dpi), such as for newspaper print or with low resolution electrophotography or inkjet printers. These methods allows reproducing thinner details, however they present large visible variations (noisy effect) when printing large surfaces where the tones vary slowly. The printed image quality relies on the printer ability to print small isolated dots and for this reason it is mostly used with inkjet printers.

Numerous digital halftoning algorithms have been successively developed such as the supercell method [69], the dispersed dot method [70,71], the white noise method [72], the blue noise method [73], the green noise method, the error diffusion method [74], the direct binary search method [75], the human visual model method, etc. It interesting to note that the performance of a halftone method relies on the ability of the printer to print accurately the binary images generated. Following this idea, Pappas and Neuhoff developed a halftoning model taking into account the printed dot deformation of the printer. The halftone dots are modelled as rounded dots instead of square pixels [76]. To optimize the performance of halftoning for different processes, hybrid AM-FM halftone methods were introduced lately and benefits from the advantages of both methods. Printed dots are clustered and vary both in size and spacing. Thus, print patterns are less visible and the printability is improved [77–82].

Color halftoning requires splitting the color image into three or more color channels corresponding to the inks on the printer, usually cyan, magenta, yellow and black. Each channel layer is halftoned separately. However additional considerations have to be taken into consideration such as the superposition or non-superposition of each layer and the rotation of each layer. An optical

interference, called the Moiré effect, can be generated when the spacing between printed dots follows a specific pattern. To prevent these visible artifacts, halftone screens can be oriented with specific angles of 75°, 15°, 0° and 45° for respectively the cyan, magenta, yellow and black layers [83]. The choices of these angles produce the well-known rosette pattern. Misregistration of a layer or of printed dots can have significant effects on the reproduced color. For this reason a printer profile is often measured, allowing correcting the printer constant errors. In the case of FM halftoning, each layer are halftoned independently and given the smaller size of the printed dots and the randomness of the dot placement less Moiré artifacts appear. A grainy appearance can sometime become visible reducing the print quality. Specific color halftone algorithms [84–86] introduce layer dependent FM color halftoning to improve the print quality.

2.3.3 Print processes and inks

Print processes to obtain a colored image are based the same principle: applying a layer of material absorbing specific wavelengths on a reflective substrate. Colorants are formed by superposition or juxtaposition of inks deposited on the substrate. The colorant terminology is used in the context of color models and refers to a mixing of the local reflectances of the different materials illuminated. Printing two inks on paper will result in a generation of 4 different colorants: the colorant generated by the first ink, the colorant generated by the second ink, the colorant generated by the superposition of the two inks and the colorant generated by paper. Printing processes consist then in depositing a controlled amount of a specific ink at a specific location. Multiple printing processes were developed and include letterpress, flexography, gravure, intaglio, offset, screen printing, electrophotography and inkjet, Figure 2.7. The conventional printing is based either on a raised print form (relief), a flat print form, and a sunken print form (hollow) and requires a preparation of the print form before printing. The continuous variable printing (digital printing) is based either contact or contactless printing. For the purpose of this dissertation, offset, electrophotography and inkjet will be detailed. Extended information on printing processes can be found in the Handbook of print media: technologies and production methods [87].

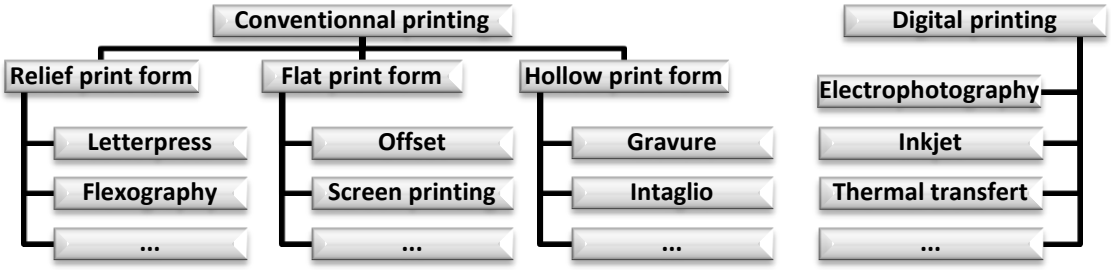

Figure 2.7: Printing processes classification (non-exhaustive).

2.3.3.1 Offset

Offset process is the most used technology in the printing industry nowadays. It allows a production flexibility, high quality print as well as fast print runs. For these reasons, offset is used to print books, magazines, newspaper, catalogues, packaging, etc. Offset process can either print sheet by sheet or continuous rolls. In the latter, the printing press is called web-fed offset. The offset designation comes from the transfer of the ink from the test form to a rubber cylinder called the blanket cylinder before the transfer to paper. This double transfer allows reducing the wear of the print form caused by friction with the paper. The offset process is divided into 4 parts, Figure 2.8 (A). First, the printing form composed of an aluminum sheet, covered on certain regions with a layer of polymer, is wetted with a dampening solution (water, alcohol and additives) by the dampening unit (water rollers). The hydrophilic regions of the plate (non-image area, aluminum regions) link with water leaving a homogeneous film. On the contrary, the hydrophobic regions of the plate (image area,

polymer regions) reject the water. It has to be noted that alternatively dry and waterless offset print processes have been developed. The second stage consists in inking the plate. Ink is deposited only onto hydrophobic area of the plate, the film of water protecting the non-printing area. Then in a third stage the ink and a part of the water are transferred to the blanket cylinder. The blanket cylinder is a soft cylinder made of polymer allowing preserving the plate surface. In the fourth part, ink and part of the water film are then transferred onto paper by contact between the plate cylinder and the impression cylinder. Extremely thin ink films are deposited on paper (0.5 to 1.5 µm). Multiple key parameters impact the print quality:

- Chemical composition of the dampening solution (water hardness, additives, surface tension, pH, emulsion behavior, rheological behavior).
- Quality of the printing plate (surface tension, surface roughness, capillarity, microstructure, production method of the test form).
- Influence of the inking cylinders and of the blanket cylinders (surface roughness, surface tension, viscoelasticity of the polymer, defects, temperature).
- Physicochemical properties of the ink (viscosity, tack, surface tension, emulsification, temperature, drying behavior).
- Influence of the substrate (printability, wettability, absorption, roughness, pH, tension, cohesion).
- Influence of the print press (mechanical vibrations, components control, temperature control, alignment and registration control, ink feeding system).

Offset inks are especially developed for the process and require to be oil based. Offset inks are highly viscous (dynamic viscosity from 40 to 100 Pa.s), compatible with the dampening solution and must not dry in the inking system of the press. Offset inks are composed of a vehicle also called binding agents (resins and vegetable oils, 70 to 75%), pigments (coloring particles, 15 to 20%) and additives (to control drying and rheological properties, 10%). Inks can be cured by an oxido-polymerization or with an exposition to specific electromagnetic waves or to electron particles [87–91].

2.3.3.2 Electrophotography

Electrophotography is a digital print process allowing a different print on each sheet. Electrophotography is based on the charge interactions of the photoconductor cylinder with toner particles. The print occurs in five stages: imaging, inking, toner transfer, toner fixing and cleaning, Figure 2.8 (B). Imaging consists in a preparation of the photoconductor cylinder with a corona, placing homogeneous charges on the surface of the cylinder. A laser or a led array, removes specific charges on the photoconductor cylinder corresponding to non-image areas. Then, in a second stage, toner particles are laid on the photoconductor cylinder and interact with the latent electrostatic image. Toner particles will only hold above a charged zone of the photoconductor cylinder. The third stage consists in the transfer of the toner particles from the photoconductor cylinder to the substrate (paper or filmic materials). To perform this transfer, toner particles are electrically attracted by a corona lying under the substrate. In some cases charges can be transferred first to an intermediate cylinder or belt in order to protect the photoconductor cylinder from direct contacts with the substrate. The fourth stage consists in fixing the toner permanently on the substrate. This is achieved by heating and pressing the substrate to melt and anchor the toner particles on the substrate surface. The fifth and last stage is devoted to cleaning remaining particles of toner on the photoconductor cylinder by mechanical brushing and suction. A charge cleaning of the photoconductor cylinder is also performed by insolation with led or laser. The process can then be repeated to produce a new latent image and a new print. This process presents the advantages addressing new markets such as print on demand, book on demand or even on continuous personalization prints. However a drawback observed is a greater variability from sheets to sheets when printing a similar page. A difference of the print speed is observed compared to offset, however improvement of the technology tends to reduce the gap. The printing process is affected by:

- Quality of the photoconductor cylinder in conjunction with the illuminant and source driver.
- Precision and stability of the ink transfer (spreading, dusts, etc.).
- Stability of the ink transfer to paper and of the ink setting.
- Cleaning of the toner particles on the photoconductor drum (often in multicolor print, toner particles are left and deposit on non-printed regions).
- Embedded printer signature depositing particles of toner in non-printed area to authenticate the print (defect voluntary induced by the manufacturer but not controlled by the operator).

The toner can be either solid or liquid and consists for both cases of electrostatic or magnetic colored particles. In the case of a solid toner, particles are obtained by a melting-grinding process (irregular shapes) or with a chemical direct synthesis (regular shapes) and present a diameter of 6 to 20 µm associated with a small size distribution [4]. The thickness of the toner layer obtained on paper is in the 6 to 15 µm range. Solid toner particles are composed of thermoplastic polymers (playing the role of binders), pigments and additives. In the case of liquid tonners, particles are smaller, 1 to 2 µm and are dispersed in a liquid (vehicle, 5% concentration). The viscosity of the toner reaches $15x10^{-3}$ Pa.s. Liquid tonner contains polymers to set the particles and pigments to the substrate allowing thinner ink layers and higher spatial resolution [4,87,92–94]. The thickness of the layer obtained on paper is in the 1 to 2 µm range.

2.3.3.3 Inkjet

Inkjet is the second widely available digital printing process. Inkjet technology is based on a controlled deposition of ink droplets on the substrate. The inkjet printer can be classified into two main categories: the continuous inkjet and the drop on demand inkjet. For continuous inkjet, droplets are generated continuously by the oscillation of the piezo crystal in the print head cavity. This oscillation creates a pressure wave. This pressure wave pushes ink through the nozzle forming a continuous stream of droplets. Droplets are then charged or not based on the image signal. Droplets pass through a high voltage field deflecting droplets that should not be printed to a gutter. The substrate moves perpendicular to the print head and droplets exiting the print head drop on its surface. In the case of on demand printing, the ejection of droplets is triggered only based on the digital image signal. Multiple technologies have been developed to perform droplets ejection, Figure 2.8 (C). Piezo electric inkjet works with the deformation of a piezo crystal inside the print head chamber creating a pressure wave. Ink is pushed through the head nozzle. In case of thermal inkjet, the pressure wave is caused by the formation of a bubble of gas, generated by a rapid heating of a localized portion of the ink. The print head contains a large number of chambers and nozzles that are either put in series to cover the print width or put in movement in the print width direction. Advantages and drawbacks of the inkjet process are similar to electrophotography with a print on demand customizable, however suffering from a lower speed than conventional print processes. Inkjet printing usually requires a paper with surface characteristics allowing absorbing the ink droplets rapidly while limiting the ink diffusion into paper. Print quality depends on the print heads (clogging of the nozzles, droplets ejection defects, registration), as well as on the physicochemical interactions between the ink and the substrate (deformation of the substrate due to high water content of the ink, droplets superposition, penetration into paper and spreading). Very thin printed layers, inferior to 0.5 µm, are obtained. Inkjet inks have a low viscosity ($1x10^{-3}$ to $30x10^{-3}$ Pa.s) and are mostly water based (90 to 95%). Dyes and pigments are traditionally used. UV inks have been developed to improve the print quality [4,87,95–98].

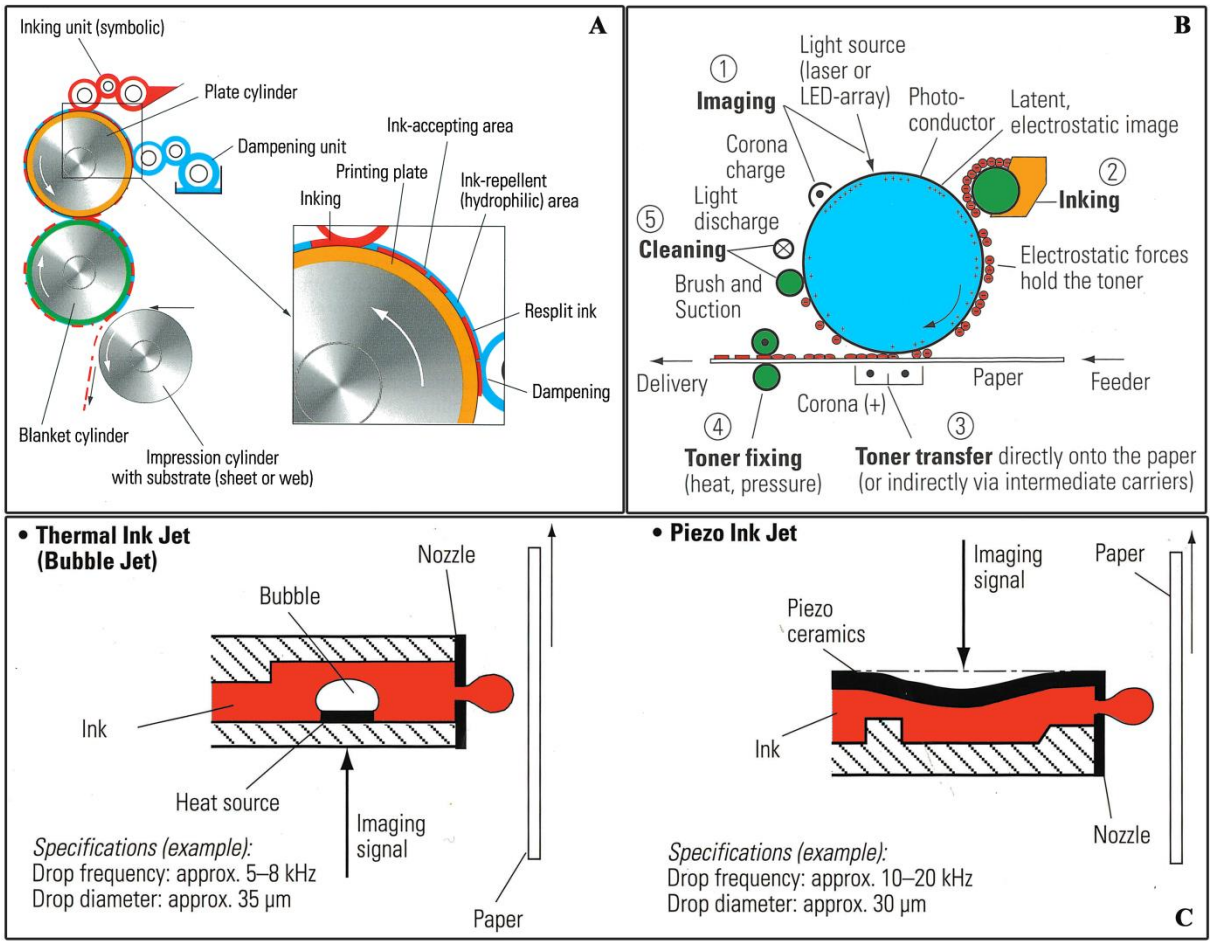

Figure 2.8: (A) Offset printing, (B) Electrophotography and (C) Inkjet principles reproduced [87].

2.3.4 Paper as a print substrate

Paper was invented in Anno Domini 105 in China and was used as a mean of communication and for administrative organization. Paper is composed of stacks of cellulose fibers extracted from wood and annual plants. A paper machine is used to produce paper from cellulose pulp, Figure 2.9. Paper pulp is produced, either mechanically (grinding, disk de-fibering, chemo-thermo-mechanical treatments or extruding) or chemically (alkaline sulfate, soda anthraquinone or acid bisulfite), by a destructuring of the wood to extract the cellulose fibers. Wood essences are mainly composed of 40% of cellulose fibers, 30% of lignin and 30% of hemicelluloses [99]. Thus, the pulping process aims for separating the three wood components and retrieving the cellulose fibers. The cellulose pulp is more or less pure depending on the process and can be bleached to increase the paper whiteness. Recycled paper can be also used as a source of cellulose fibers. The cellulose pulp can then be processed prior to introduction on the paper machine by refining treatments producing a fibrillation of the cellulose fibers, hydration of the fibers and a reduction of the fibers lengths. Parameters of the refining impact greatly the physical characteristics (mechanical properties, surface roughness, etc.) and the optical properties of the paper. Fillers such as kaolin or calcium carbonate can be added to improve the printability and the whiteness. Additives can also be added to improve the control of the process and improve the paper properties. Cellulose pulp is then introduced in the head box of the paper machine with a concentration of 10 g.L-1. The function of the head box is to distribute homogeneously, with a specified orientation, the paper fibers on the drainage table [100]. The next stages of the process, consisting in the wire section, the press section and the dryer section, aim at reducing the water content of the fiber mattress. The water content at the introduction of the cellulose pulp is 99% and should reach 5 to 10% at the end of the machine [101]. When water is removed hydroxyls bounds form

between the cellulose fibers giving a mechanical strength to the paper. Additional operations can be performed to improve the paper surface characteristics, such as:

- Calendering: Mechanical smoothening of the surface by contact and pressing with hot cylinders.
- Coating: A layer of mineral particles or pigments and binders is applied on the surface.
- Sizing: Impregnation with chemicals to control water absorption and other characteristics.

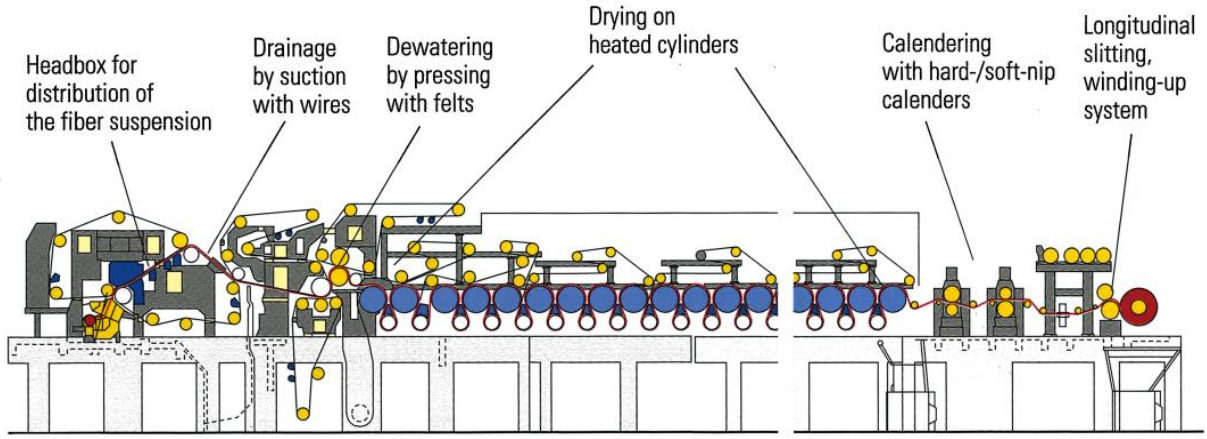

Figure 2.9: Paper machine diagram, adapted [87].

The paper printability is usually expressed in terms of ink acceptance, gloss, glaze, surface roughness, ashes analysis, compressibility, light fastness, absorption capacity, mottling sensitivity, tear resistance, moisture expansion, moisture content, breaking load, real tightness, blistering, mechanical stretching, ink drying, picking resistance, cut quality, creasing, dusts, holes and sheet formation [87,102–107]. The multiple grades of papers for the printing industry are detailed in the standard ISO 12647-2.

2.4 Digital optical microscopy and image processing

Optic instruments have been used for centuries to characterize what our eyes cannot detect. Consequently, measurements devices such as densitometry or spectrophotometry based on an optical apparatus were developed and allowed to characterize the print. Murray and Davies proposed the first model linking the ink layout on paper to the optical density, based on microscopy observations. Nowadays the improved digital optical microscopy is a major tool to characterize the print at the microscale and compared to non-optical methods is fast, reliable and accurate.

2.4.1 Digital optical microscopy

The microscope was invented more than 400 years ago and tremendous research has been conducted to improve the optical resolution and reduce chromatic and spatial aberrations. Moreover, the more recent development of digital imaging sensors offers an advanced tool to image the matter at the microscale. Adding band-pass filters to the microscope allows extending conventional 2D image measurements to multispectral 2D imaging, enabling a characterization of the spectrum of the sample independently for each location on its surface. In this section, a description of key components of multiple microscopy techniques is proposed [108–119]. Microscopy basics can be found in Wu, Merchant and Castleman [108].

2.4.1.1 Microscopy techniques

Transmission and reflection microscopy

Transmission and reflection microscopy differ from the geometry of the measurement. In transmission microscopy, incident illuminant passes through the sample. On the contrary in reflection microscopy, incident light passes through the objective and is reflected on the sample. For reflection microscopy a beam splitter is required to separate incident and reflected light, Figure 2.10 (A).

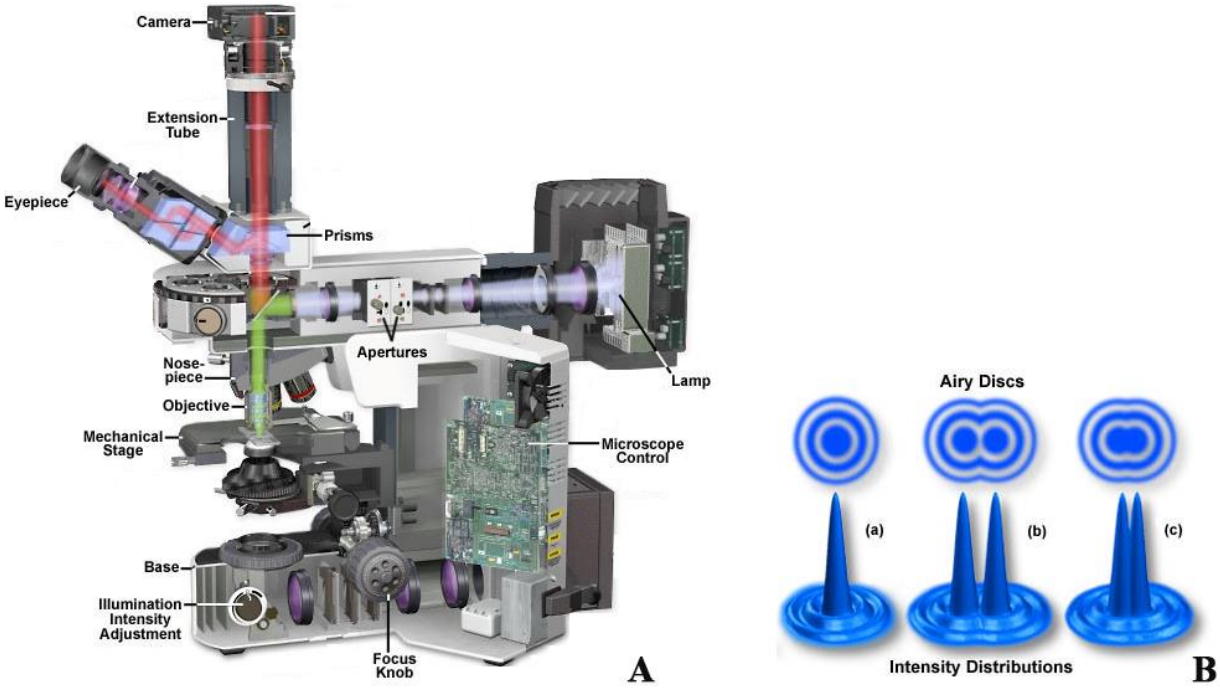

Figure 2.10: (A) Light source, optical microscope and image sensor, (B) Airy discs, adapted [109].

Brightfield and darkfield microscopy

In brightfield microscopy, the illuminant is on the axis normal to the image plane. Thus, for transmission the contrast is produced by different absorption of the sample over the field of view. For reflection microscopy the contrast comes from the reflection of the sample and includes the specular reflection (gloss) and the diffuse reflection. In darkfield microscopy the illuminant is moved from the center of the objective, illuminating the sample with a low angle. In this configuration almost no specular reflection is generated on the axis normal to the image plane and only the diffuse component is measured. Due to the illumination geometry, darkfield microscopy is associated with reduced image irradiances, requiring more sensitive cameras.

Polarized microscopy

Polarized microscopy is mostly based on the brightfield geometrical configuration. A set of a polarizer and an analyzer are placed in the light path, with a polarization of the light prior to the sample and an analyzer after the sample. The analyzer is composed of a polarizer and can be rotated in order to select the direction of the polarization filtered. Using cross polarizer – analyzer removes the specular reflection from the measurement. The illuminant is polarized at 0° and arrives on the sample. The part of this illuminant directly reflected (specular reflection) conserves the polarization orientation. The analyzer placed at 90° allows only the light polarized at 90° to pass through and thus specular reflection is blocked. The light diffusing and interacting with the sample will lose its polarization and can pass through the analyzer. Polarized microscopy beneficiate from higher image irradiance levels compared to darkfield microscopy.

Fluorescence, phase contrast and differential interference contrast microscopy

Fluorescence microscopy uses the florescent properties of the sample or of markers on the sample (absorption of a specific wavelength and re-emission of a different wavelength). A specific illuminant irradiates the sample. Reflection on the sample contains the illuminant light and the re-emitted light. Pass band filters allow obtaining only the re-emitted light forming the image. Phase contrast microscopy allows imaging samples that only absorb a really small portion of the light (transparent samples). A combination of direct and diffracted light from all azimuths allow obtaining a high contrast since the samples generate a shift in the phase of the diffracted light. In differential interference contrast microscopy the incident illuminant is split in two beams very close from each other (distance is smaller than the resolving power of the objective) but not interacting. The beams pass through the sample and interact differently with the sample since they are not located at the same point of space. The two beams are recombined and interact, generating differences in color and intensity on the image plane.

Confocal microscopy

Confocal microscopy allows imaging only the focused region of the sample in the field of view. This is achieved by spatial filtering techniques. By imaging at different focused planes, a 3D reconstruction of the sample is obtained with high resolution.

2.4.1.2 High resolution microscale images

Illuminants and Köhler illumination

Multiple light sources can be used for optical microscopy with differences in their spectra. They have to be tuned precisely to obtain high quality microscope measurements. Incandescent lamps such as tungsten filament lamps are commonly used and are associated with a large spectrum, pronounced in the high wavelength part of the visible light and in the infrared. A blue filter is usually used to correct the spectrum. Illuminant irradiance is tuned through the lamp voltage (inducing also a change in the spectrum), by density filters in the light path or by closing the field diaphragm. Led lamps are emerging to replace the incandescent lamps and are associated with improved irradiance stability. Arc lamps (mercury or xenon) are another source of illuminant allowing for high power with more discrete spectrum peaks (used for fluorescence mostly). Laser illuminants are also used and are associated with a monochromatic emission (single peak spectrum). These sources are extremely useful for confocal microscopy. Köhler illumination is a technique allowing a precise tuning of each element of the microscope in order to obtain the best illumination of the sample and thus the best image.

Numerical aperture and resolution

The numerical aperture of an objective gives its ability to gather light and thus to produce images with high resolution. The numerical aperture is given by the angular aperture and the refractive index between the sample and the objective (usually air or oil). The resolution of a microscope is given by the Abbe distance or alternatively by the Rayleigh distance (for circular aperture). According to the Rayleigh criterion, the ability of the microscope to resolve fine details is given by the distance at which two point objects can be separated in the image plane. That distance is called the Airy distance. Airy discs are diffraction patterns induced that blurs the objects details in the image plane. This phenomena is caused by the diffraction and scattering of light in the optics of the microscope. On Figure 2.10 (B) airy disc patterns are visible with (a) a single point object, (b) two points at the Airy distance (minimum resolving distance) and (c) two points at distance smaller than the Airy distance.

Magnification and field of view

Magnification depends on the objective used as well as on the second magnification often used to adapt the camera sensor size to the image plane. Only the magnification archived with the objective has a resolving power, secondary magnifications are said empty, increasing the size of the field of

view without adding object resolution. The field of view is the size of the region projected on the image plane. The magnification will dictate the resolution obtained on the camera in terms of pixel as a function of the physical dimensions.

Errors of measurements

Optical aberrations can reduce the accuracy of the measurement. The spherical aberration is a deformation and blurring of the point objects depending on the distance with the center of the field of view. Chromatic aberrations are produced by the dependency of the refractive index of the microscope lenses with the wavelength and place the focal point for each wavelength on different planes. Imaging on a plane will result in a portion of the image blurred depending on the "colors" (wavelengths sampled). The geometric distortion aberration deforms the object plane to a non-flat surface. The image plane presents then distorted spatial dimensions. Most of these deformations are corrected with especially designed objectives called plan, achromat, fluorite, and apochromat, depending on the correction level.

2.4.1.3 Modern digital microscope features for multi-data measurements

Autofocus

Autofocus is an important feature allowing improving the speed of measurement, improving its objectivity and is required to perform automated measurements. The autofocus aim is to put the sample in the best focal plane and thus to produce high quality images. The focal plane of the sample is changed by a translation of the stage along the objective axis (Z-axis). Multiple autofocus algorithms have been developed and a trade-off between speed and precision is usually required. Autofocus algorithms acquire images of the sample at multiple stage heights and compute an index usually evaluating the image sharpness. Autofocus algorithms have been reviewed in literature and continued to be developed [120–122].

High dynamic range (HDR)

High dynamic range is a method consisting in acquiring multiple images of the sample without changing the stage position. Each capture is performed at a different exposure time, allowing extending artificially the dynamic range of the sensor. Fusion of the images is then performed to obtain an HDR image. Multiple fusing algorithms have been developed [123–125].

Tiles acquisition

Tiles acquisition allows extending the field of view represented on the image. This is performed by capturing an image and then by moving the microscope stage on the x-y axis to reach a field of view directly adjacent. Stitching of the captured images allows reconstructing a single image with an extended field of view. Stitching algorithms usually requires a superposition of the captured images [126].

Multiple focal planes acquisition

Multiple focal planes acquisition, also called z-stack, allows obtaining focused images of samples exhibiting rough topography. In microscopy, the focus depth is limited by the objective and only the objects near the focal plane can be imaged. Multiple images at different focal planes are captured. The regions of the image in focus are extracted and an image with all regions in focus is reconstructed. The reconstruction generates 3D images consisting in the 2D description of the irradiances plus the height description of the sample (obtained by recording the stage position when the region is in focus) [127,128].

Multispectral imaging

Multispectral imaging can be used on microscopes to obtain not only the light intensity but also the wavelength distribution for each point of the sample. Multispectral imaging requires to filter the incident, reflected or transmitted light with band pass filters (blocking photons with higher or lower wavelength than the band pass wavelengths). Physical filters can be used as well as moving grating filters and liquid crystal tunable filters. Multiple research fields are now focusing on multispectral acquisition systems to obtain richer information from the measurements [19,129–133,133–135].

2.4.2 Imaging sensors

Imaging sensors are composed of a semiconductor capable of converting radiative energy (electro-magnetic waves) into an electrical signal by absorption of the electromagnetic waves. Thus sensors have been designed in order to measure each type of electromagnetic waves ranging from the gamma rays (wavelength of 10^{-12} m) to the infrareds (wavelength of 10^{-5} m). For this purpose, two strategies can be adopted: a direct conversion of the photons to electrons (quantum detectors) or an indirect detection of secondary effects produced by the absorption of the electromagnetic waves (thermal detection). The function of quantum optical image sensors is to convert spatially distributed photons (electromagnetic waves between $400x10^{-9}$ m and $800x10^{-9}$ m) to a numeric array of digital levels representing a quantization of the amount of photons received during a time t. Basic operation of an optical image sensor can be split in 5 stages [136].

1) Conversion: The incident spatially varying radiative energy is converted into electric charges (electrons) at each photosites of the sensor (array) [137]. For this conversion the size of the photosites is finite and defines the spatial resolution of the sensor. With large photosites surfaces the sensitivity of the sensor is increased since there are more photon to electron conversions on a single photosite. However, the spatial resolution is reduced. It is then important to choose a sensor with photosites size fitting the application. An electronic shutter controls the time allowed for the photon to electron conversion (integration).

2) Storage: The electric charges generated have to be stored during the integration time and during the time preceding the read out. This storage capacity is finite and when reaching the maximum capacity, no more photons can be measured (the sensor is saturated). The storage is submitted to noises impacting the measurements when only a small number of electrons are stored.

3) Read-out: Following directly the integration time (conversion and storage), the read-out process transfers the electrical charges stored to a signal processing line conditioning the signal. That step rearranges the array of electric charges into a sequential flow of electric charges (each photosite is read sequentially and sent to the signal processing line).

4) Signal processing: The electric charges are amplified. The level of amplification is set to match the input requirement of the analog to digital converter. The level of amplification is called gain and is controlled. The gain applied is constant for each electric charge of each photosites, in order to preserve the linearity of the measurement.

5) Analog to digital conversion: The analog signal is then converted to a digital signal in order to be stored. The digitalization is essential since at this stage the image is composed of an array of analog currents. The digitalization determines bins of currents and attributes each measured current to the corresponding bin. The numerical signal is then defined as the bin number. Typically sensors can have digitalization processors of 8, 10, 12 or 16 bits corresponding respectively to 256, 1024, 4096 and 65536 levels (number of bins).

Two different optical imaging sensor technologies co-exist: the Charge Couple Device (CCD) and the Complementary Metal Oxide Semiconductor (CMOS). CCD were developed in the early seventies and were a breakthrough for digital imaging. CCD are produced from silicon based circuits

and integrate a large array of photodiodes, potential wells and transfer controls. Electrons are generated from the interactions with a doped silicon junction (photodiode) and are stored in a potential well surrounded by controllable potential barriers and drains, Figure 2.11 (A). Each photodiode is isolated electrically from its neighbors. The read out of each electron collected in the potential well is conducted serially, column by column, Figure 2.11 (B). All electrons stored in the potential well are then shifted to the right. The rightmost column is consequently placed in the serial register column. This column is then shifted down line by line, reaching sequentially the amplifier. When all lines have been read, the columns of the array are again shifted to the right and the line by line shifting and amplifying occurs. That process is repeated to read all the electrons lying in the potential wells of all photodiodes. The column and line shifting is controlled by a series of tunable potential barriers called gates [138]. By controlling the sensor temperature, only a few electrons are lost during the transfer. This architecture is called full-frame CCD. Sensors with alternative architecture such as frame-transfer CCD and interline transfer CCD have been conjointly developed. Frame-transfer CCDs have separate cells where the integrated electrons are stored during the readout process [139]. It allows capturing the next image as the readout process of the previous capture image is running. Similarly interline transfer CCD also beneficiate from separate storing cells, however these cells are located individually next to the photodiodes and potential wells (instead of being grouped at one side of the array) [140]. An advantage of this architecture is the ability to operate without a mechanical shutter, increasing the frame rate and the ability to reduce image smearing. The drawback is mostly a decrease of the photosensitive surface yielding to a decrease of sensitivity and an increase of blooming [141].

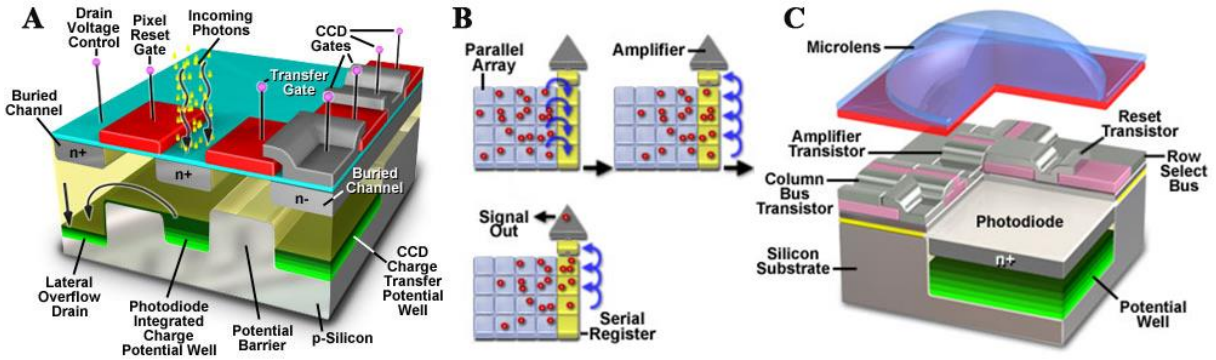

Figure 2.11: (A) Diagram of a CCD, reproduced [109], (B) diagram of the CCD read out, reproduced [142], (C) diagram of a CMOS, reproduced [109].

The CMOS are a logic evolution of the CCD technology. For CMOS sensors the amplification of the electrons generated by the photodiode and stored in the potential well is conducted in an amplifier circuit located on each photosite, Figure 2.11 (C). All photosites have then their dedicated electron amplifier and only a transfer of the amplified current is conducted. The readout is simplified, reducing the noise associated [143]. A bias is however introduced from the difference of amplification from amplifier to amplifier (called fixed pattern noise). The bias can be corrected by the analog signal processing embedded on the chip or by a dark frame subtraction. One major advantage of the CMOS technology is a lower electrical consumption reducing the sensor heating. A major drawback is a reduced surface available for the photodiode yielding to lower sensitivity as well as photons reflection and scattering yielding to vignetting, pixel crosstalk or light diffusion. A micro lens array (single micro lens visible on Figure 2.11 (C)) is deposited on the sensor allowing a focus of the photons over the photodiode and yielding to an increase of the sensitivity. A filter, blocking photons with short wavelengths (<400 nm), limits the reflection and scattering on the electronics of the photosites. Each photosite on the CMOS sensor can be triggered and read independently and have a reset transistor allowing an independent control of the photons integration time (exposure time) [144–146].

Researchers have worked to improve the sensors to obtain a high spatial resolution (small photosites) while preserving the performances of the measurements [147]. The performance of CCD and CMOS sensors depends on multiple characteristics of their architecture [148–152]:

Responsivity: The responsivity gives the ratio between the incident irradiance and the resulting digital signal.

Quantum efficiency: Quantum efficiency describes the ability of the photodiodes to convert photons into electrons. The quantum efficiency depends on the photon wavelength and on the design of the sensor. Photons can be either reflected by the sensor, transmitted or absorbed. When they are absorbed, they can generate a charge that is not collected. The quantum efficiency represents the amount of photons that are absorbed with their charge collected.

Source of noise: Multiple sources of noise impact the measurements on CMOS or CCD sensors. Dark current is the generation of electric charges without photodiode exposition to photons. Charges are generated by thermal effects yielding a background signal fluctuating from pixel to pixel. Photon noise describes the variations induced by the fluctuation of photons arrival on a photodiode from pixel to pixel corresponding to the square root of the signal (shot noise). Read noise is associated to the loss of photons and to variations during the conversion from charges to current and from current to digital signal [153,154].

Saturation: potential wells have limited storing space and limit the capability of the sensor to measure incoming photons. Saturation occurs when the potential well is totally filled with electron, photons arriving on the photodiode becoming non measureable.

Dynamic range: Dynamic range is the ratio between the maximum output signal and the dark current noise. Dynamic range gives an indication on the sensor performance to measure simultaneously bright and dark signals on different region of its surface.

Signal to noise ratio: Signal to noise ratio is an index giving the effective measurement range of the sensor. Signal to noise ratio allows distinguishing sensors with high responsivity and high noise to sensors with medium responsivity but low noise, the latter having potentially a higher signal to noise ratio.

Exposure time: Exposure time defines the duration for photon to electron conversion on the photodiodes. The challenge of choosing the right exposure time is to prevent photosites to saturate while at the same time capturing enough photons giving a signal higher than the noise [155].

Electronic shutter: Electronic shutter is a continuous draining of the electric charges generated by the photodiodes. Once the exposure starts, the draining is stopped, charges accumulate in the potential well and are moved to a storing well. The draining of the charges is then reactivated.

Sensor linearity: Sensor linearity is the ability of the sensor to output a digital signal that is linear with the level of irradiance illuminating the sensor. Sensor linearity measurements are commonly performed illuminating the sensor with an integrating sphere (diffuse light) and by varying the irradiance. Two limits appear for the CMOS and CCD sensors: a non-linearity in the low irradiance levels attributed to the influence of noises and a non-linearity in the high irradiance levels due to saturation.

2.4.3 Image processing

The goal of image processing is to determine the geometry, photometry and spatial structure of objects captured and digitalized by an imaging apparatus. Multiple image processing treatments have been developed in order to transform the information contained in the digital image. The processing chain as well as the parameters of each function has to be precisely tuned to extract the correct information from images. Multiple image processing handbooks have been written and the aim of that section is to introduce briefly the main concepts and methods. A digital image is a spatial and intensity discretization of the continuous irradiances. The spatial discretization is induced from the photosite arrangement of the sensor. The representation of a photosite on a digital image is a pixel. The intensity

discretization is induced from the analog to digital convertor of the sensor. The number of bits used to store the measured irradiance is called the bit depth. The digital image size corresponds to the number of pixels in the X and Y directions. Pixels have physical dimensions expressed in µm. The pixel size is often called the digital resolution, even if the term resolution in imaging refers to the ability of a system to reproduce the contrast of objects. The sampling theory developed by Nyquist states that 2 pixels at least are necessary in order to resolve a point object of an image. The image processing can be presented in five categories as proposed by Glasbey and Horgan [156].

Image visualization

Image visualization is the first step of image processing and allows an evaluation of the data. In some cases, especially for automatic quality control for the industry, the image processing is fully automated. However to insure constant results, imaging conditions (illuminant, magnification, geometry, etc.) have to be kept constant. Images are then often displayed allowing the operator to perform a fast visual inspection. Images are usually visualized on a digital display and tools can help adapting the data contained in the image to make it more relevant for the human eye, Figure 2.12. These treatments can be an optimization of the brightness, contrast, gamma, hue, chroma, luminance, look up table (LUT) pixel value switch, mathematical transformations (derivative, integrals, logarithm, exponential, square root, etc.). Geometrical transformations can also be performed: enlargement, translation, rotation, scaling, distortions and non-linear transformations, [156].

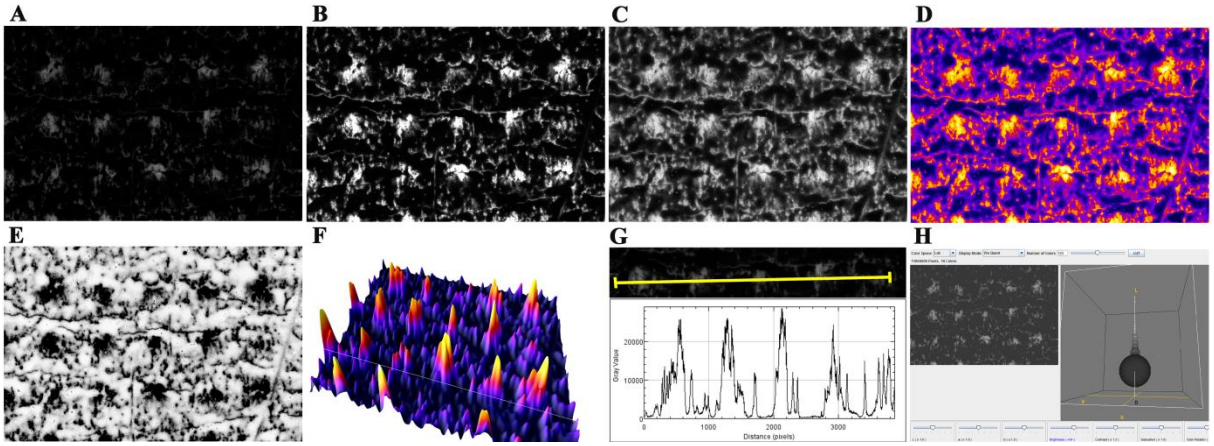

Figure 2.12: Offset halftone dots imaged at the microscale with an optical microscope. Multiple data visualization can be adopted to help the experimenter interpret data: (A) Original image, (B) Brightness and contrast enhancement, (C) Gamma 0.4 transformation, (D) Fire look up table (LUT) application, (E) Grayscale inversion, (F) 3D visualization (pixel value represented by height) combined with a fire LUT, (G) Plot of the pixel value as a function of the position along the yellow line, (H) Color quantization (Wu quantization) in the L,a*,b* color space.*

Filtering

Filtering applies spatial and frequency treatments in order to reduce the noise contained in the image or to amplify regions of the image such as the edges of objects for example. The differences of the transformations performed for filtering compared to the transformations performed for visualization are that they do not present an identical transformation for all pixels are tuned for each pixel depending on the neighbor pixels. Filters can be classified into linear filters and nonlinear filters and in a second level into spatial domain or into frequency domain. Linear filters are well controlled: the order of application of successive linear filters does not change the results. Nonlinear filters are more difficult to control however they can produce improved results (for example to reduce the image noise without reducing the spatial resolution). Spatial filters are mostly based on the convolution with a kernel. The discretized convolution is a mathematical operation corresponding to the sum of the products of the kernel with defined neighbor pixels. Kernels are usually normalized, in such way that they do not modify the average mean pixel value. The size of the kernel has a strong impact on the

result of the filtering. The box filter, called also blur filter, replaces the pixels by the average of the neighbor pixels in the kernel. Gaussian smoothening applies a similar average; however neighbor pixels are multiplied by a scalar decreasing from the kernel center and following a Gaussian distribution. First derivative kernels are usually used for edge detection. Second derivative kernels also called Laplacian transforms also allow emphasizing the edges. Other kernel allows sharpening the image. Multiple variations of these filters can be adopted, such as anisotropic filters, non-normalized filters, etc. Median blur is a non-linear filter computing the median of the neighbor pixels. The filter yields to a reduction of salt and pepper noise. The bilateral filter allows a noise reduction while conserving sharp edges. The filter works as a combination of a convolution with a Gaussian kernel in conjunction with an analysis of the pixel values in order to maintain the edges. Other kernels are based on the variance of the neighbor pixels. Filtering treatments can also be performed in the frequency domain by performing a fast Fourier transform of the image. Working in the frequency domain allows processing the image similarly to waves processing, applying high frequency pass, band pass and low pass filters and thus reducing specific frequencies of the image. The Wiener filter can be applied for image restauration and Sobel and Canny edge filters for edge detection, [156].

Segmentation

Image segmentation is an image processing aiming at separating digitally different region of the image (objects and background). Image segmentation is essential in order to measure objects. Human vision constantly decomposes the images to find objects and background. However for image processing, images are simply large tables of pixel values. Multiple methods have been developed and can be classified as thresholding methods, edge based methods and region based methods. Thresholding methods consider only the pixel values of the image. Multiple thresholding algorithms have been developed and consist in defining a threshold value corresponding to a pixel value. All pixel values inferior or equal to this threshold value will classified as objects and pixels values superior will correspond to the background (object and background can be alternatively switched). Global threshold methods mostly work based on the frequency distribution of the pixel value. Local threshold methods work similarly as global thresholds, however the image is subdivided into smaller regions and the threshold is adapted depending on the region properties. The spatial component is, in that case, partially considered. Multiple global and local threshold algorithms have been developed and were reviewed [157–160,160–175]. Depending on the application and on the image, a threshold algorithm can give better results than others. For that reason an evaluation of the threshold algorithms have been developed [176–184]. Edge-based segmentation methods perform edges detection and classify the pixels inside the borders of close edges to the objects and the pixels outside as background. Usually the experimenter has to check and modify the obtained boundaries in order to improve the results. Semi-automatically drawing helps to perform that task. Edge based segmentations rely mainly on the ability to detect accurately the edges and multiple methods were developed: the Laplacian of Gaussian filter, Prewitt algorithm, Roberts and Canny edge detection. The pixel grouping is then usually performed using connected component algorithms. Finally, region-based segmentation methods operate interactively from the center of the object and group neighbor pixels with similar pixel values. Groups of pixels with different pixel values are then split and registered as objects. In that case one of the objects corresponds to the background. The centers of the objects are called seeds and are the starting point of the method. The seeds can be defined manually or automatically finding for example the local minimum after a variance filtering (watershed algorithm). Other algorithms have been developed such as the Fuzzy C-mean, the k-mean clustering, the support vector machine, the pulse coupled neural network, etc.

Mathematical morphology

Mathematical morphology in image processing is based on the set theory. Most morphology algorithms require a binary image (image with only two pixel levels: 1 for the objects and one for the background). Nevertheless the mathematical morphology algorithms can be adapted for grayscale

images. Morphology algorithms transform the image in order to correct the objects and perform more accurate measurements. For example noise or errors in the segmentation can generate holes in the objects and fuzzy edges. Morphology aim, in that case, would be to fill the holes (closing operation) and clean the fuzzy pixels on the edges (erosion operation). Classical morphology algorithms developed are: structuring elements, erosion, dilatation, opening, closing, distance transform, thinning and skeleton.

Measurements

The final step of image processing consists in the quantification of different properties of the objects. The number of objects is counted (size or shape conditions can be applied to filter the considered objects). Areas (object area, convex hull area, circular equivalent area, ellipse fit area) of the objects can be measured. Perimeters (circular equivalent perimeter, Ferret diameters, ellipse fit perimeter, boundary perimeter, convex hull perimeter) of the objects can be also measured. Shape characterization (length and width, ellipse fit major and minor axis) of the objects can also be measured. Distances between the objects and positions in the image can also be obtained. Centers of gravity of the objects can be determined as well as second-order moments (for example inertia). Bounding box, ellipse fitting are also indexes of importance to measure and classify objects. From these measurements indexes such as the aspect ratio, circularity, convexity and solidity can be determined. Olson investigated the evolution of the indexes as a function of the object geometry [185–188].

2.5 Paper, ink and light interactions

Light is a set of electromagnetic radiations visible to the human eye (i.e. photons). The human eye is mainly sensitive in the spectrum of wavelengths from 400 nm to 700 nm. A photon is associated with an energy which corresponds to wavelength noted λ and is said "monochromatic". Optic is the field of study of light and its interactions with matter. Radiometry is the science of measuring the light energy. Color science differs from radiometry as color is not a physical quantity but a physiological sensation (visual perception) resulting from the light entering the retina. Photometry differs from radiometry by adapting the energy measurements of light to conform with a human observer: the energy measurement at each wavelength is weighted by a visual sensitivity function, making the measure homogeneous with the human perception. The illuminant is the light sent from a source to an object. The reflectance is the ratio of light reflected by the substrate compared to the incident light. Transmittance is the ratio of light transmitted by the substrate compared to the incident light. The irradiance is the density flux per unit area that is incident on a specified surface expressed in W/m^2. Illuminance is the equivalent photometric quantity and is expressed in lux. Detail information on optic and radiometry fundamentals for color reproduction can be found in [189].

To control printing, colors reproduction and apply authentication, prints have to be measured. Multiple measurements have been developed such as densitometric measurements, spectrophotometric measurements or microscale imaging. These measurements either retrieve the mean irradiance of the print or retrieve the irradiance distribution over the wavelengths or over the surface. The aim of these measurements is either to obtain reflectance information (optical density), to obtain colorimetric information of the print (X, Y, Z or L*, a*, b*) or to obtain the Ink coverage (IC) on paper. The IC can be obtained through fitting models with reflectance measurements or through direct measurements. In the case of direct measurements, specific image treatments have to be performed to differentiate of the ink from the paper. This differentiation can be difficult due to the light, ink and paper interactions: light scattering on paper induces multiple optical phenomena generating artifacts impacting the measurements called dot gain. Dot gain in printing is an artifact associated with a change of the ink coverage from the image sent to printer to the printed result. Two different types of dot gain can occur:

a physical dot gain and an optical dot gain. The physical dot gain is generated from the ink spreading and setting during the printing. The optical dot gain is generated from light interactions with ink and paper during viewing and measuring.

In literature, the ink coverage can refer to different quantities. The following notation of literature will be used in this work [19]. The Nominal Ink Coverage (NIC) refers to the ink coverage sent to the printer. The Effective Ink Coverage (EIC) refers to the ink coverage obtained after printing, including physical dot gain but excluding the optical dot gain. The Apparent Ink Coverage (AIC) refers to the total ink coverage, including the physical dot gain and the optical dot gain.

2.5.1 Print process by-product effect: the physical dot gain

The physical dot gain, referred also as mechanical dot gain, is the increase or decrease in ink coverage after printing due to the multiple ink transfers, the ink setting, the ink spreading and the ink drying. According to the process the mechanical mechanisms generating the physical dot gain can differ. For offset ink transferring is achieved by multiple pressure transfers: ink is pressed from the inking cylinder onto the printing plate. The ink is then pressed onto the blanket cylinder and from the blanket onto the paper. The ink spreads at each stage of the transfer. Ink film separation in the transfer is another source of printed dot deformation and can generate a contraction of the ink spread. For electrophotography, the physical dot gain can be generated by the melting and pressing of toner particles. Toner particle size distribution as well as defects of the electrostatic imaging or cleaning generates a cloud of toner particles around the printed dot causing a type of physical dot gain. For inkjet physical dot gain is generated by process variations such as variations of the print head (nozzle size, ejection speed, ejection volume, etc.) or by variations of the substrate (variation of the physicochemical parameters such as energy tension or capillarity). When ink is deposited on paper, the setting phase of the ink starts. During this phase the ink can penetrate into paper or alternatively spread on the surface. Capillarity, surface tension of the ink and surface energy of the paper, roughness, permeability, diffusivity are physical properties influencing the ink setting. The ink penetration and diffusion behavior has been well studied for multiple processes [190–198]. Physical dot gain affects the quality of the print, impacting especially the print through (strike through, show through), the optical density of the print, the color gamut, the print gloss, the color on color bleed, the edge fuzziness, etc. For simplifying reasons, the ink surface is often assumed to have constant thickness; however the actual ink thickness depends on the position on the printed dot. Figure 2.13 shows the ink setting for offset, inkjet and electrophotography. An increase of the dot size can be observed.

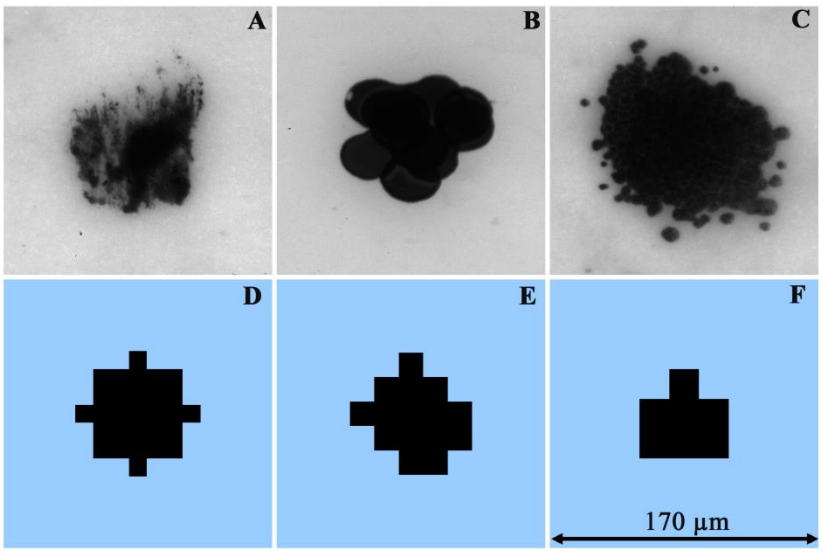

Figure 2.13: Single halftone dot: (A, B, C) printed and imaged and (D, E, F) printer input binary image, for (A) Offset, (B) Inkjet and (C) Electrophotography at 150 lpi.

2.5.2 Light scattering: the cause of optical dot gain

Scattering of light is generated by several directions deviations of the photons linear trajectories. Scattering of light has been studied since the 18th century by scientists. Lord Rayleigh used Maxwell equations to determine the air scattering power as a function of the wavelength and demonstrated the blue color of the sky. Mie extended Rayleight's work to diluted suspensions comprising dielectric spheres. More complicated materials such as paper, clouds, snow, called turbid materials cannot be solved with the Mie single scattering approach since multiple scatterings occur. The radiative transfer theory has been developed to solve multiple scatterings. However, the complexity of the general formulation is extremely high (integro-differential of five simultaneous variables). Multiple assumptions have been proposed for different applications leading to solutions of the radiative transfer theory such as the neutron theory, the Kubelka-Munk theory, the diffusion approximation theory, two dimensions 2 flux model, 3 dimensions two flux models and 4 flux models [4].

Light scattering into ink and paper generates a diffusion of the light causing the Yule-Nielsen effect, referred as optical dot gain. The optical dot gain occurs when viewing the print and results from the optical interactions of the light with the ink and the paper. The optical dot gain is fundamentally different from the physical dot gain. The optical dot gain can be observed by a shadowing around the dot edges, by a global darkening of the paper region and a global brightening of the ink regions, Figure 2.13. Several types of light interactions can occur when viewing the print, Figure 2.14.

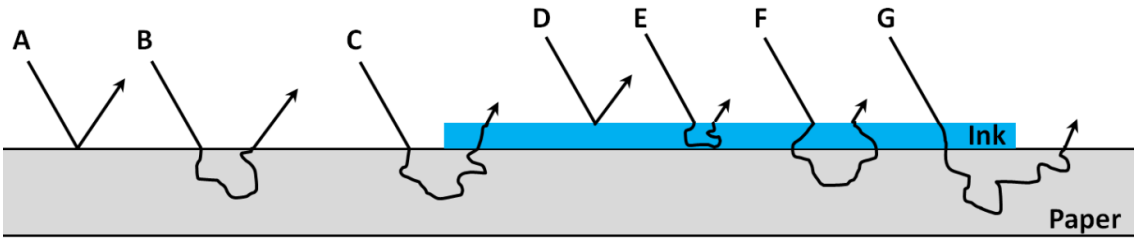

Figure 2.14: Light reflection situations on a halftone print. The internal reflections and scattering of light inside paper, inside ink and at the interfaces of paper and ink are not represented.

In the case A and D, photons are directly reflected at the surface of the paper and the ink. The direct reflections occur due to the difference of the refractive indexes (air – materials). The direct reflections are called the specular reflection and their direction depends on the direction of the incident light and on the orientation of the surface. For paper, the direct reflection orientations are distributed due to the paper surface roughness. The distribution can be characterized by a bidirectional reflectance distribution function [199]. Recent studies have pointed out that even if the photons were reflected at the surface of the material, interactions between photons and the material were still possible. Thus, photons from specular reflection could be partially absorbed in the case of ink and paper materials [200]. Specular reflections are usually cut off the measurements by adopting a specific measurement geometry (for example 45°/0°) or by using polarizer-analyzer filters. The internal reflections are induced also by the difference of the refractive indexes (air – materials). However the internal reflection occurs for photons exiting the ink-paper material. A part of the photons exit the print and another part are reflected back at the air-print boundary. These back reflections are called internal reflections [201].

For the B, C, E, F and G cases, photons enter either the paper or the ink and scatter inside the layer, Figure 2.14. In cases B and C the photons penetrate the paper and scatter inside the paper. The photons are attenuated by the paper absorption and exit the paper at a position different from the entering position. The distribution of photons exiting the paper as a function of the entering position is described by the point spread function of paper and has been studied and modelled continuously [202–207]. In the case of the reflection B, the photon diffusion does not change the integrated amount of photons over the surface. However in the case of reflection C, photons entering the paper are diffused and exit

the print through an inked surface. Parts of the photons passing through the ink layer are absorbed and the integrated photons over the surface are then smaller (the proportionality to the inked and non-inked surfaces is not maintained). The decrease of reflectances can be seen as an artificial increase of the ink coverage (i.e. Murray-Davies model) and is called the optical dot gain. This effect is counter-balanced by the opposite phenomena as illustrated by the reflection G: photons penetrating the ink layer and exiting aver a paper region. This increases the reflectance of the paper, compensating for the decrease due the reflection C. However it has to be noted that in the case of reflection G, the absorption of photons due to the relatively low transmittance of the ink layer cannot re-equilibrate fully the reflectance decrease of reflection C.

Reflections E and F differs as photons of reflection E are reflected on the surface of the paper and photons of reflection F penetrates into the paper. Reflection E and F do not participate in the dot gain phenomena, as photons arriving over an inked surface are reflected over an inked surface. In the case of low transmittance ink, reflections C, E, F and G could result in a total absorption of the photons, and thus no photons exiting the inked surface. It has to be noted that the wavelength of the photon in relation with the absorption characteristic of the ink layer has to be taken into consideration and can lead to a mixture of dot gain that are wavelength dependents. Finally, the optical dot gain when controlled can benefit the print, especially by saving ink and increasing the color gamut [208,209].

2.6 Print measurement methods

Prints can be characterized by different physical quantities and consequently multiple measurement methods were developed. In this section a selection of the measurement methods to characterize prints are presented, focusing on the characterization of the ink coverage, the optical and physical dot gain.

2.6.1 Optical macroscale print measurement methods

A fundamental quantity that can be measured to characterize a printed surface is the amount of light reflected, called the reflected spectral irradiance $I_r(\lambda)$. This quantity can be measured with a spectrophotometer, diffracting the light and measuring each diffracted group of wavelength with an array of photodiodes at the same time. The spectrophotometer measures then a spectral irradiance discretized according to the resolution of the device (for example from 400 nm to 730 nm with a resolution of 3 nm).

The reflected spectral irradiance is often expressed relatively to the incident spectral irradiance $I_0(\lambda)$ and the ratio is called the spectral reflectance $R(\lambda)$, equation [2.1]. Incident and reflected irradiances depend on the wavelength λ and consequently the spectral reflectance is also function of the wavelength. Calculating the spectral reflectance $R(\lambda)$, requires the knowledge of the incident spectral irradiance $I_0(\lambda)$. The illuminating source in a spectrophotometer may deviate while ageing and having $I_0(\lambda)$ as a constant in the spectrophotometer would lead to measurements deviations. The solution adopted is to measure $I_0(\lambda)$ for each set of measurements, by measuring the reflected spectral irradiance on a specific white ceramic tile.

Spectral reflectances can be integrated over the visible wavelength region resulting in a single value for the reflectance, equation [2.2] with $\Pi_x(\lambda)$ the spectral product (spectral filter for ink x and sensitivity of the sensor). R_x is calculated through standard spectral filters maximizing the response for each ink. Standards as the ISO 5-3:2009 and DIN 16536-2 define measurements conditions and integration conditions according to standard spectral sensitivities. The blue spectral filter of status E, matching the yellow inks is presented on Figure 2.15 (B). Note that the filter applies a weighting to the reflectances at each wavelength in order to favor the region of high absorbance of the ink.

Spectral reflectance

		Symbol	Unit	Denomination
[2.1]	$R(\lambda) = \frac{I_r(\lambda)}{I_0(\lambda)}$	$R(\lambda)$	1	Spectral reflectance
		$I_r(\lambda)$	$\frac{W}{m^2}$	Reflected spectral irradiance
		$I_0(\lambda)$	$\frac{W}{m^2}$	Incident spectral irradiance

Integrated reflectance

		Symbol	Unit	Denomination
[2.2]	$R_x = \int_\lambda \Pi_x(\lambda) R(\lambda) d\lambda$	R_x	1	Integrated reflectance for ink x
		$R(\lambda)$	1	Spectral reflectance
		$\Pi_x(\lambda)$	1	Ink x filter and sensor sensitivity

Another instrument called a densitometer measures directly the reflected integrated irradiance (the difference with a spectrophotometer is that the light is not split into groups of wavelength and the average irradiance of the entire spectrum is measured. The integrated reflectance can then be obtained by dividing I_r by I_0. I_0 is obtained by measuring an unprinted area of paper and allows a normalization of the paper reflectance R_p equal to 1. The densitometer uses standard optical filters in order to distinguish the level of reflected irradiance for each conventional ink (cyan, magenta, yellow and black).

Apertures of spectrophotometers are usually in the shape of a disc of 1.5 mm diameter. Mounting additional objectives on spectrophotometers was achieved by several authors in order to measure a small halftone surface, thus allowing a separate measurement of the reflectance of the ink and of the paper between the dots in a halftone configuration. In the work conducted by Engeldrum, the aperture diameter was downscaled to 130 µm [35]. More detail about the geometry of the measurement, the standard illuminants, the architecture of measuring devices can be found in [4,210,211].

The optical density is a simple logarithm transformation of the reflectance, equation [2.3]. It has to be noted that the optical density can also be expressed at a single wavelength (λ_0) as expressed in equation [2.4]. Spectral reflectance, integrated reflectance and optical density are the main measurements applied to macroscale print characterization however they do not give direct information on the ink coverage. By fitting models it is then possible to obtain a predicted ink coverage. It has to be noted that the optical dot gain impacts the measured reflectance, thus can impact the prediction of the ink surface and should be taken into consideration.

Optical density

		Symbol	Unit	Denomination
[2.3]	$D_x = -\log(R_x)$	D_x	1	Optical density for ink x
[2.4]	$D_{\lambda_0} = -\log[R(\lambda = \lambda_0)]$	D_{λ_0}	1	Optical density at wavelength λ_0
		R_x	1	Integrated reflectance for ink x
		$R(\lambda)$	1	Spectral reflectance

Similarly to optical densities, the color coordinates called the tri-stimulus values can be calculated from the spectral reflectances by integration, equation [2.5] with $L(\lambda)$ the normalized illuminant power spectra and $\bar{x}(\lambda)$, $\bar{y}(\lambda)$, $\bar{z}(\lambda)$ the color matching functions, as defined by the standard ISO 13655 and ISO 11664-1[212]. Λ_0 and λ_1 is the range of the integration and is defined as ranging

from $\lambda_0 = [380 - 400\ \text{nm}]$ to $\lambda_1 = [700 - 780\ \text{nm}]$. The tri-stimulus values can then be transformed into any colorimetric space such as, for example in the x, y space or the L*, a*, b* space.

Tri-stimulus values [212]

		Symbol	Unit	Denomination
[2.5]	$X = \int_{\lambda_0}^{\lambda_1} R(\lambda)\,\bar{x}(\lambda)\,L(\lambda)\ d\lambda$ $Y = \int_{\lambda_0}^{\lambda_1} R(\lambda)\,\bar{y}(\lambda)\,L(\lambda)\ d\lambda$ $Z = \int_{\lambda_0}^{\lambda_1} R(\lambda)\,\bar{z}(\lambda)\,L(\lambda)\ d\lambda$	X, Y, Z	1	Tri-stimulus values
		$R(\lambda)$	1	Spectral reflectance
		$L(\lambda)$	1	Illuminant spectral power
		$\bar{x}(\lambda), \bar{y}(\lambda), \bar{z}(\lambda)$	1	Color matching functions

Spectral reflectances for paper and cyan, magenta, yellow and black inks are presented on Figure 2.15 (A). Paper reflects almost all the incident light with reflectances close to 1 for all wavelengths between 400 and 700 nm. The paper measured has a blueish tint, as expressed by the higher reflectance in the 300 to 450 nm range. In that range the reflectance is found higher to 1, which should not be possible (i.e. the reflected irradiance cannot in principle be higher that the incident irradiance). However due to optical brightener agents, fluorescent phenomena occur, absorbing photons in the UV range, below 400 nm, and re-emitting them around 450 nm. That transfer of energy acts as an additional imaginary incident irradiance increasing the reflected irradiance. It can be noticed that the black ink absorbs as expected over the visible wavelength range (i.e. achromatic). Cyan, magenta and yellow inks either absorb or transmit the light depending on the wavelength region (i.e. chromatic) and act then as filters of the light spectra. The spectral reflectances of the yellow ink of electrophotography prints for various ink coverages are presented on Figure 2.15 (B). It can be noticed that going from the solid print (100%) to the paper, the reflectances in the absorbing regions of the ink are progressively increased to finally match the reflectances of the paper. The halftone ink surfaces and the paper surfaces are averaged over the measurement zone. The resulting reflectance spectrum is then a composition of the paper spectra and the ink spectra weighted by the ink coverage. The spectral reflectance is a function of the ink thickness as well. With the increase of the ink thickness, the spectral reflectance decreases. With increasing thickness, most inks reach a plateau where the spectral reflectance becomes constant with the increase of the ink thickness. The plateau depends mostly on the scattering properties of the ink [213].

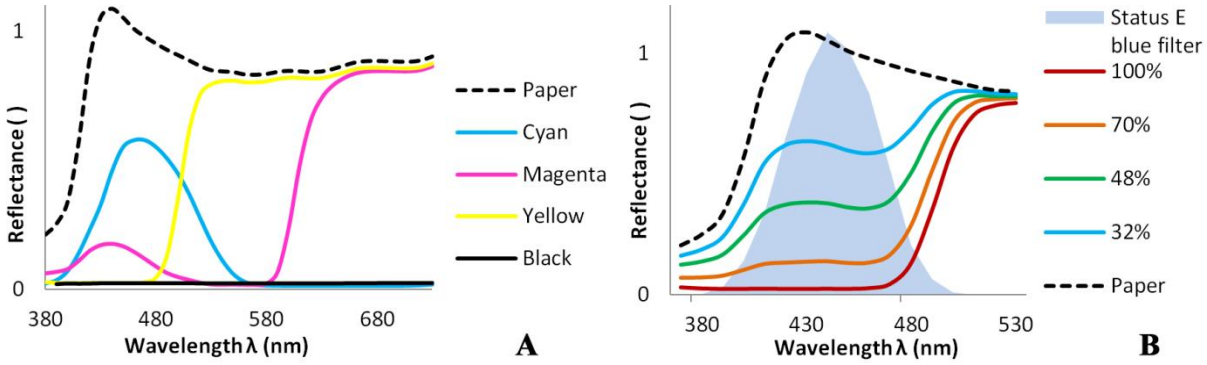

Figure 2.15: Spectral reflectances of an electrophotography print on mat coated paper: (A) Spectral reflectances of paper and cyan, magenta, yellow, and black inks. (B) Spectral reflectances of the yellow ink for solid area (100%), halftones of 70%, 48% and 32% of ink and bare paper. The blue region denoted "Status E blue filter" corresponds to the spectral filter for the yellow ink (Y-axis is the density weighting factor).

2.6.2 Optical microscale measurement methods

Optical densitometry and spectrophotometry allows obtaining macroscopic quantitative information about the print and are commonly used by the graphic industry. However, the macroscopic characterization of a microscopic system leads to a loss of information. Moreover, models have to be employed to obtain the ink coverage from the macroscale reflectance measurements. Gustavson and Tegenfeldt pointed out that the tristimulus colorimetric measurements should only be used to characterize the color and should not be used to compute ink coverages [208,214]. For these reasons, several studies were conducted using optical microscopic measurements and allowed to obtain directly the dots characteristics at the microscale [18,19,17,26,28,10]. The microscale approach retrieves further significant indexes such as the print quality [21], the optical dot gain, the ink penetration [22], the printer identification and the print authentication [26]. From microscale measurements it is possible to obtain directly the optical or physical dot gain. Physical and optical dot gains are related through the total dot gain:

$$\Delta a_{tot} = \Delta a_{opt} + \Delta a_{phy} = a_a - a_n \qquad [2.6]$$

with Δa_{tot} the total dot gain, Δa_{opt} the optical dot gain, Δa_{phy} the physical dot gain, a_a the apparent dot area and a_n the nominal dot area. It should be noted that in printing, the dot areas are systematically normalized to the surface of the halftone and are therefore in the range from 0 to 1 (usually expressed in percentage from 0% to 100%).

Multiple microscale measurement methods and strategies were developed in literature. These methods can be classified as direct optical measurements (planimeters), indirect optical measurements and non-optical methods, Figure 2.16. A planimeter is an apparatus comprising an imaging unit (optical microscope with a digital camera, numerical optical scanner, etc.) and an image processing unit allowing measuring the print characteristics. In research, most planimeters are custom built allowing tuning and controlling the measurements. This leads to a variation in results reported and a special attention has to be dedicated to the measurement method used in order to compare the different results. Indirect measurement methods target the measurement of quantities related to the print such as the light diffusion into paper (the cause of optical dot gain) or the print quality. Finally non-optical methods such as scanning electron microscopy, atomic force microscopy, etc. can be used to measure the print at the microscale.

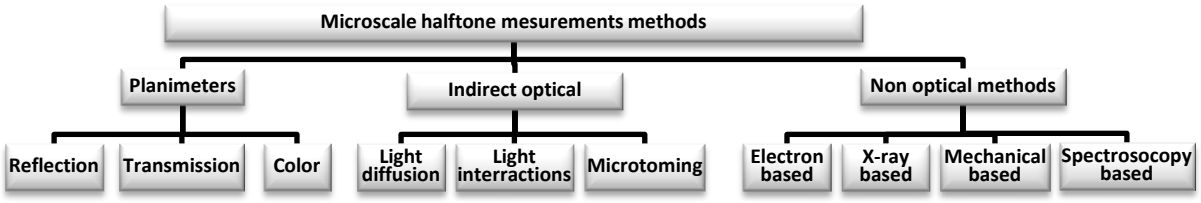

Figure 2.16: Classification of the microscale print measurement methods (non-exhaustive).

2.6.2.1 Reflectance based planimeters

Ocular micrometer scale

Among the first methods, Murray proposed using an optical microscope and an ocular micrometric scale. The print was clamped on the stage of a darkfield microscope (Leitz Ultropak illuminator). The geometry of the measure is close to 45°/0° reducing specular reflections. A micrometric scale calibrated at 2.06 µm/units (magnification of approximatively x200) helped Murray to measure manually two diameters corresponding to the max and the min diameters of the halftone dots. The dot surface computed was approximating the dots to perfect discs. Murray measured also the

distance between two adjacent dot centers and established the area of the halftone cell. The ink coverage was then obtained [2].

Modern imaging units

The improvement of the microscopy techniques and of digital imaging led to multiple imaging units used as planimeters. Comparing studies investigating printed dots at the microscale reveals that the definition of the microscale is not currently unified. The number of pixels used to image a dot at the printer resolution, 2540 dpi for offset for example, varies from 5 to 37 pixels/dot diameter, Table 2.2. According to the Nyquist sampling theorem, 2 to 3 pixels are necessary to sample a small point object of the dot shape. Thus the size of the sub-dots that could be resolved varies respectively from 5 µm to 0.81 µm. Sub-dots of 5 µm correspond to 50% of the printed dot width for a dot at 2540 dpi and perimeter shape cannot then be accurately resolved. Sub-dots of 0.81 µm corresponds to 8% of the printed dot width and allows for a more precise description of the dot perimeter shape. It has to be noted that increasing the imaging resolution with a constant sensor size results in a decrease of the number of halftone cells being imaged. Characterizing halftone prints can also directly benefit from research advances in paper surface characterization and other surface characterization fields [215–217].

Table 2.2: Comparison of the planimeters used in 5 recent studies.

Studies	Optic and sensor	Resolution µm/pixel	Pixel/dot width 2540 dpi	Field of view (µm²)	Number of halftone cell imaged (150 lpi)	Light source & geometry
Nyström [19]	Macro bench, CCD mono, 1.4 Mpix, 12 bits	2	5	2720 x 2048	192	Tungsten halogen 45°/0°
Ukishima [17]	Microscope, CCD mono, 11 Mpix, 12 bits	0.67	15	2685 x 1790	150	Halogen 0°/0° polarized
Happel [10]	Microscope, CCD mono, 2 Mpix, 12 bits	0.54	18	879 x 667	15	Green LED 0°/0° polarized
Namedanian [18]	Macro bench, CCD mono, 1.4 Mpix, 12 bits	1.94	5	2650 x 1990	165	Tungsten halogen 45°/0°
Rahaman [28]	Microscope, CCD RGB, 5 Mpix, 14 bits	0.57	18	1477 x 985	40	Not defined 45°/0°
Nguyen [26]	Microscope, CCD RGB, 5 Mpix, 12 bits	0.27	37	698 x 523	12	Tungsten halogen 65°/0° darkfield

Line scanning

Arney and coworkers method is based on the acquisition of halftone dots on a microscope with a digital monochrome camera and a ring fiber optic illuminator attached to the microscope objective. The pixel values are divided with the mean pixel value obtained from capturing unprinted paper and the reflectance is computed. It has to be noted that this integrated reflectance may somewhat be different from the integrated reflectance presented in equation [2.2] due to the difference of the term $\Pi_x(\lambda)$, the sensor having an uncorrected spectral sensitivity. The reflectances are plotted on a histogram, h(R), for 256 classes of reflectance, Figure 2.17 (A). This frequency distribution shows a peak for the ink and a peak for the paper. Finding a limit (R_{limit}) between these two peaks allows separating the ink from the paper. The method proposed by Arney and coworkers to find R_{limit} is based on spatial scans of the image in multiple directions. The borders of dots (transition from ink reflectance to paper reflectance) are detected and the rate of maximum reflectance change in the transition region is recorded. The R_{limit} is then obtained by averaging the maximum transition rate for multiple dots, equation [2.7]. Thus the ink region and paper region can be separated. The area under the histogram for the ink region corresponds to the ink coverage a_e, equation [2.8]. The mean ink and paper reflectances R_i and R_p in the halftone can be then obtained, equation [2.9]. Moreover the authors suggested that the reflectance peaks for the ink and for the paper, R_{ik} and R_{pk}, could be

measured from the histogram, taking the maximum of each respective peak, Figure 2.17 (A) [5,218]. The authors showed that the ink and paper reflectances depend on the ink coverage, Figure 2.17 (B) [5].

Ink and paper coverage from reflectance frequency distribution [5]

		Symbol	Unit	Denomination
[2.7]	$R_{limit} = R_a(x,y)$ where MAX $\left[\frac{dR_a(x,y)}{dx,dy}\right]$	R_{limit}	1	Ink-paper limit reflectance
[2.8]	$a_e = \frac{\int_0^{R_{limit}} h(R_a)dR_a}{\int_0^{255} h(R_a)dR_a}$	a_e	1	Effective ink surface
[2.9]	$R_i = \frac{\int_0^{R_{limit}} R_a\, h(R_a)dR_a}{\int_0^{255} h(R_a)dR_a}$ $R_p = \frac{\int_{R_{limit}+1}^{255} R_a\, h(R_a)dR_a}{\int_0^{255} h(R_a)dR_a}$	R_i	1	Ink reflectance in halftone
		R_p	1	Paper reflectance in halftone
		$R_a(x,y)$	1	Halftone spatial reflectance
		$h(R_a)$	1	Reflectance histogram

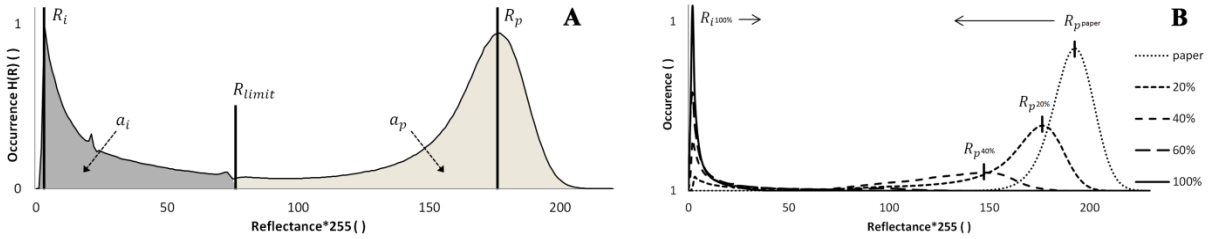

Figure 2.17: (A) Example of a reflectance histogram, (B) Ink and paper peak reflectances decrease with the increase of the ink coverage.

Methods based on image thresholding

Methods based on image thresholding are similar to the method presented by Arney and coworkers, however the strategy to obtain R_{limit} differs. Multiple threshold algorithms have been developed in literature. However, they were not developed specifically for the measurement of halftone dots [171].

Manual threshold: Engeldrum and Hsieh proposed a method adjusting manually the value of R_{limit} and displaying the pixels under R_{limit} in order to match the borders of the halftone dots [35,37]. This method depends highly on the settings of the display and on the experimenter judgment [219]. Moreover images of microscale halftone dots captured with an optical microscope contain a part of optical dot gain as suggested by Happel [36]. Thus, the direct measurement of physical dot gain from manually thresholded image may include a portion of optical dot gain.

Midpoint threshold: Nyström proposed to use an optical setup where the angle of illumination and the angle of measurement could be modified. A tungsten-halogen lamp with an IR cut-off filter was used to obtain an illuminant spectrum close to the spectrophotometers illuminants. A highly linear monochrome camera was used and images were compensated for dark current and calibrated against a white reference, allowing obtaining the measured reflectance $R(x,y)$. The author proposed to define R_{limit} as the midpoint between the measured R_{ik} and R_{pk} (the local maxima in the paper region and the ink region of the histogram). However testing this thresholding method revealed that it produced results less accurate than the line scanning method developed by Arney and coworkers. Another difference is that the author defined the ink coverage measured on the histogram, equation [2.8] as the physical ink coverage and considered that no optical dot gain was included [19,211,220–224].

Minimum: Namedanian extended Arney's line scanning method by stating that since the histogram is a representation of the gray level occurrences, the steepest slope going from the ink to the paper corresponds to the position on the histogram where the occurrence is minimal. The author stated that the benefit of working on the histogram instead of working on the image is that the halftone dot

configuration does not impact the measurement. For frequency modulated halftoning, performing line scanning may be more complicated than finding a minimum occurrence of a distribution [225].

First minimum of the first derivative threshold: Namedanian proposed a threshold method based on the histogram of halftone microscale image [226]. The histogram presents a bimodal distribution, the first peak corresponding to the ink and the second to paper. Namedanian noticed a rapid drop in the histogram occurrences going from the ink to the paper. This rapid drop occurred after the ink peak maximum and the author suggested that the signification of this drop was the switch from the ink region to the paper region. To obtain the position of this drop the author proposed to compute the first and the second derivative of the histogram and to detect the pixel value where the first derivative had its first minimum and where the second derivative was equal to 0. This algorithm strategy is similar to the empirical mode decomposition [227].

Literature threshold algorithms applied to halftone thresholding: Several authors have proposed to use threshold algorithms from literature to separate inked areas from paper areas. Nguyen proposed to use the maximum entropy threshold developed by Kapur [27,163]. Nguyen performed comparative measurements for different print processes and different papers and concluded that the results were valid if a similar threshold algorithm was employed. Poletti tested three different threshold methods: the entropy threshold developed by Kapur, the factorization threshold developed by Otsu and the moment threshold developed by Tsai and concluded that the factorization thresholding method was the best method for halftone dots printed with offset (visual assessment) [25,63,163,168,173].

Methods based on image segmentation

Latorre proposed to apply five segmentation algorithms to measure the ink coverage of multiple inks printed on ceramic tiles. The segmentation methods used were originally developed for different image processing purposes. The segmentation methods tested are the fuzzy C-means, the fuzzy C-means with contextual information based on a Markov random field, a mixture of Gaussians, and an iterated conditional mode algorithm. Results showed that the iterated conditional mode algorithm was the most accurate, however the performance analysis relies on the definition of a ground truth and its definition may have introduced a bias [228]. Rahaman proposed to use a k-mean segmentation algorithm with an initialization of 3 clusters: 1 cluster for the ink, 1 cluster for the paper and 1 cluster for the mix region (generated by optical dot gain). The k-means clustering algorithm groups pixels according to their value. At each step of the grouping the new mean value of the pixel groups are computed and a new search for neighbor pixels belonging to groups is performed. This segmentation algorithm shows accurate results and proposes a direct method to isolate the optical dot gain (mixed area) [20,28,28].

Commercial planimeters

A commercial microscope performing print and non-print regions separation is the Techkon SpectroPlate or the Techkon DMS 910. These apparatuses capture images of a printing plate using magnifying optics. Image analysis and especially threshold methods are applied to differentiate print and non-print regions. A quantification of the ink coverage can then be achieved. Unfortunately details of the image processing and of algorithms used by Techkon are not published and cannot be accessed in the software [229]. Happel argued that for measurements of ink dots printed on paper, the midpoint thresholding developed by Nyström was more reliable than the integrated algorithms of the Techkon software [19]. Moreover the performances of the image analysis performed by the Techkon were found dependent on the substrates [230,231].

Scanners

Scanners offer a limited optical resolution restraining the accuracy of the information obtained on the halftone dots at the microscale. Streckel stated that scanners were limited to measurements of 10 µm per pixel (only 1 pixel per printed dot at 2540 dpi) [232]. Scanning technology has improved but the optical resolution remains too low to measure halftone dots at the microscale accurately [231].

2.6.2.2 Transmittance based planimeters

Reflectance and transmittance combined measurements

Transmission optical images of paper are usually employed to characterize the paper formation, fiber aggregation and fiber distribution into the paper structure [233]. The transmittance of the paper as a function of the position may be highly heterogeneous. When measuring the transmittance of a paper with printed ink on its surface, the ink absorption is clearly visible and may be used for characterizing the physical ink coverage. For thick paper a limitation can appear and be solved using other radiations such as β radioactive radiations [215]. Takahashi and coworkers proposed a colorimetric determination of optical dot gain based on a microscale characterization. The authors combined reflection and transmission measurements in order to isolate optical dot gain [190,234].

Gustavson Transmittance / reflectance measurements

Gustavson proposed to measure the optical dot gain by combining transmission-reflectance measurements [235]. The author deduced theoretically that the optical dot gain should be excluded in transmission measurements, since the light enters first the paper, scatters and then passes through the ink layer. Gustavson used an Astromed cooled digital CCD camera placed on a microscope. 768 by 512 pixel images with 0.82 µm/pixel were achieved with a 16 bytes quantization. The microscope was configured to acquire darkfield reflection and brightfield transmission images. The darkfield illuminant was a horizontal, 20 cm long, 2.7 cm high, fluorescent tube forming a 35° angle with the microscope stage. The transmission illuminant was a halogen lamp equipped with a diffusing mirror. The samples were printed on either coated, uncoated or polyethylene white film with a high quality thermal transfer printer (Seiko Professional ColorPoint II). The authors obtained ink transmittance images and compared them with reflectance images to determine the optical dot gain. Their approach focused on measuring the paper point spread function by fitting the reflectance images simulated from the transmittance measurements with the reflectance images measured. The author states that a drawback of the method is that the transmission of light through paper is not homogeneous. Moreover they noticed that transmission images showed a slight shadowing near the edges of the dots, suggesting a possible dot gain effect. The authors credited the shadowing effects to either a lack of camera focus or more likely to internal reflections, invalidating the assumption of the absence of dot gain in transmission images. Nyström tried also to measure transmittance images of printed halftones. His system was associated with lower resolution: CCD camera (Pixelfly HiRes highly linear monochrome 1.4 Mega-pixels, 12 bits) mounted with an equivalent 2.4x objective (Schneider Kreuznach APO-CPN 2.8/40) allowing for a resolution of 1.94 µm/pixel with a field of view of 2.65x1.99 mm². The author observed similar paper transmittance heterogeneities in the measurements. Therefore the author claimed that reflectance-transmittance measurements could not be used to measure accurately the optical and physical dot gain [19,223]. Koopipat used a similar method to measure the ink transmittance of inkjet printed lines [236,237].

Ukishima iterative algorithm for ink transmittance computation

Ukishima proposed to determine the ink transmittance from spatial reflectance measurement of halftones [17,238]. The spatial reflectance was measured on an optical microscope (Olympus BX50, objective 4x, bright reflection 0°/0° geometry, crossed polarizer-analyzer filters), capturing the reflected light spectrally through a liquid crystal tunable filter (Cis VariSpec, 30 nm bandpass in the range from 430 nm to 700 nm) and with a monochrome CCD camera (Lumenera Infinity 4-11M, 12 bits, 1.96 µm/pixel resolution). Ukishima method differs from Gustavson and Koopipat reflection-transmission method since only measurements in reflection and the knowledge of the paper point spread function (PSF) is required. Ukishima suggested that based on the model of the light diffusion on halftones (equation [2.48]), the only unknown variable is the spatial description of the ink transmittance. The author suggested that a direct computation of the ink transmittance is problematic since the ink transmittance is convolved with the paper PSF. The author proposed then to solve the

equation by an iterative method, modifying the ink transmittance at each step and evaluating the convergence by the root mean square of the difference of the predicted reflectance and the measured reflectance. For each step the modification of the ink transmittance proposed by the author relies on the computed difference between the predicted reflectance and the measured reflectance. Ukishima showed that the iterative method was converging rapidly with 50 iterations. The author investigated the influence of the initialization and found that the number of iterations needed was not impacted significantly. The author found that the ink transmittance obtained with the iterative method had a lower ink transmittance the one obtained with reflectance/transmittance measurements. Knowing the ink transmittance function, it is possible to compute the physical dot gain. Setting the point spread function $H(x, y) = 1$, the author was able to visualize the halftone print without optical dot gain.

2.6.2.3 Color based planimeters

Wedin and Kruse color vector method

A method was developed by Wedin and Kruse and relied on the colorimetric measurements of halftone samples on a RGB bed scanner. The scanner (FENIX 6425-C flatbed scanner) has an optical resolution of 1024 dpi in both directions, with a calibration of 24.8 µm/pixel. The scanner is calibrated with a white reference. The sample RGB values are retrieved as a function of the spatial position. These coordinates are converted in the colorimetric XYZ space using a conversion matrix [239,240]. Kruse found that the color distribution for a halftone with a single ink is almost one dimensional in the X Y, Z space, laying on the vector linking the paper mean colorimetric coordinate to the mean ink colorimetric coordinate. This effect is also true for multiple inks print with the vector of colorants expressed between the mean colorimetric coordinate of two colorants. For example, for a cyan (C), magenta (M), yellow (Y) print on paper (P), there would be 7 colorants (C, M, Y, CM, CY, MY, CMY) and there would be 10 vectors (C-P, M-P, Y-M, CY-P, CM-C, YM-Y, CY-Y, CM-M, YM-M, CMY-P) [241]. It has to be noted that the position of the vectors are normalized between 0 and 1. An example for 3 cyan halftones of 25%, 50% and 75% ink coverage is presented in Figure 2.18 (A). The occurrence of each tint in the halftones (placed on the vector between the solid ink and paper) are equivalent to the reflectance histograms presented by Arney. With Wedin and Kruse methodology the positions of the ink and paper peaks are independent on the ink coverage. The authors defined the mean colorimetric coordinate of a colorant as the integration of the distribution from the solid print to the half-distance between the solid print and the paper.

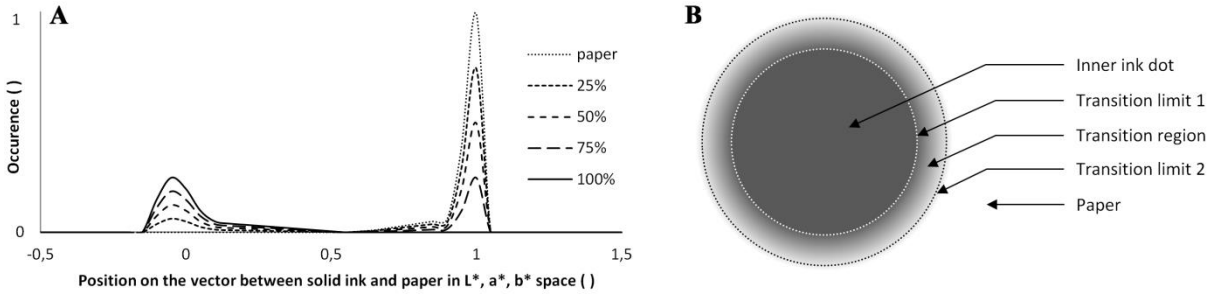

Figure 2.18: (A) Halftone tints distribution on the vector between the solid print and the paper in the colorimetric L, a*, b* space, adapted [239], (B) A halftone dot with the transition region and the two limits found with Wedin transition area method. Redrawn [231].*

Wedin and Kruse color threshold method

Another method to define the limit between ink and paper was proposed by Wedin and Kruse and is based on a threshold algorithm analyzing the maximal differences of occurrences for successive colorimetric values on the vector going from the ink to the paper [241]. Two limits were found, one between the ink region and the transition region and another one between the transition region and the paper region Figure 2.18 (B). The ink coverage was then defined by the authors as the area from the

center of the dot to the middle of the two limits. This method was tested on a 50% nominal ink coverage dots and results were extrapolated for other ink coverages.

Wedin and Kruse color shift method

The authors described a method to measure optical dot gain called the color shift method [241]. The method requires projecting the colorimetric coordinate of the tints of the halftone on the vector linking the two colorants. The projection is not normalized and tints projected on the vector linking the two colorants measured in total coverage conditions. The ink coverage including dot gain is then described by the authors as the integral of $C(x)$, the occurrences as a function of the colorimetric distances x on the vector:

$$a_e(x) = 1 - \int x\, C(x)\, dx \qquad [2.10]$$

with the colorimetric coordinate of the solid print at $x = 0$ and of the paper at $x = 1$. That integration is equivalent to the Murray-Davies model and to Arney integration of the reflectance distribution.

Nyström method

Nyström proposed a similar method based on the analysis of the 3D color histogram. The author performed a clustering of the colorants on a 3D XYZ histogram. The threshold value XYZ_{limit} (analog to the threshold limit R_{limit} in the case of single ink halftone) corresponding to the separation between two colorants is then defined as the mid-distance on the orthogonal vector between two centers colorants clusters. The authors claims then to obtain the physical ink coverage by integration of the occurrence projected on the vector linking two colorants [19,211,220–224].

2.6.2.4 Indirect optical methods: light diffusion on paper

The halftone reflectance is impacted by the light diffusion, thus an indirect measurement of the optical dot gain can be performed by characterizing the light diffusion in paper. The light diffusion can be expressed by the Edge Spread Function (ESF), by the Line Spread Function (LSF) or by the Point Spread Function (PSF). Corresponding functions can be transformed in the Fourier domain, the Modulation Transfer Function (MTF) being the transformation of the LSF. Two main categories of light diffusion measurements were established by Happel: the projection and contact methods [10]. In the projection method, the incident light is patterned with a mask before reaching paper (reflected light does not cross the mask). In the contact method, the mask is applied directly on paper and the reflected light passes through the mask when entering and exiting the paper. Another classification was proposed by Rogers depending on the type of patterns [242]. Rogers proposed 3 main patterns: a sinusoidal pattern, a bar pattern and an edge gradient pattern.

Yule-Nielsen early work [243–245]

Yule and Nielsen were the first to image a lamp filament projected on paper with a microscope. Instead of the sharp edge of the filament, the authors observed a spread of the light beyond the boundary of the filament. Images were captured by an analog camera. Uncoated paper showed larger light scattering than the coated paper and both showed larger scattering lengths than for reflections on a mirror [244].

Knife edge spread function measurements

Yule, Howe and Altman obtained the paper line spread function from edge spread function measurements [16]. Using an optical microscope, they projected a knife edge on paper. An optical 5.6x objective was used to project a reduction of the knife edge on paper. The light source was mounted in front of a condenser and aligned with the knife edge. The knife edge was a very sharp contrast image produced on a Kodak high resolution plate. The authors considered that a potential un-sharpness of the

knife edge would be attenuated by the optical reduction. A measuring stage comprising an objective, eyepiece, scanning slit field lens and photodetector was set at 0°. The scanning slit measured 2 µm and allowed to selectively measure light intensity on the knife edge as a function of the position. A correction for the diffusion of the apparatus was proposed by measuring a nickel coated glass. Correction of the instrument spreading could then be performed transforming the LSF in the Fourier domain and by dividing the paper MTF with the instrument MTF. Transforming back into the time domain gave a corrected paper LSF, corresponding to the deconvolution with the instrument LSF.

Arney and coworkers proposed a similar method with a black video tape clamped on the surface of paper [246]. Multiple line scans were performed and the average yielded the half edge spread function (reconstructed assuming symmetry).

Ukishima proposed to obtain the sharp edge using the iris diaphragm of a microscope (BX50 Olympus) equipped with a monochrome CCD camera (Lumenera Infinity 4-11M, 12 bits, 10.7 megapixels with a resolution of 0.76 µm/pixel on the image) [17,247]. The authors noticed that when using a microscope properly configured for Köhler illumination with geometry at 0°/0° (including polarizers and analyzers), the iris diaphragm of the microscope was located in a conjugate plane with the lamp collector lens and was thus imaged sharply on the object plane. Spectral bandpass filters were also added in order to measure the dependency of the paper MTF as a function of the wavelength. Ukishima proposed to measure the edge imperfections due to the projection and proposed to remove them from the measurements by deconvolution (division in the Fourier domain). To further reduce the noise of the deconvolution a threshold was introduced to cutoff the small frequencies. The author found that the MTF measurements were independent on the projected spot size. The author observed a dependency of the MTF on the wavelength (larger MTF associated with shorter wavelength).

Happel, Dörsam and Urban proposed a method to measure the edge function of paper accounting for the multiple sources of errors: specular reflections and scattering due to sample roughness, point spread function of the optical apparatus, inaccurate focusing, non-linear image sensor and light stray [10,36,248,249]. Their method was based on the knife edge projection. The authors used an optical microscope (Leitz Orthoplan, Ploemopak PL Apo 6.3) with narrow spectral light emitting diodes, red (632 nm), green (536 nm), blue (457 nm), reducing errors due to chromatic aberrations. The knife edge illumination was produced by placing a razor blade in the illumination path with a lens allowing focusing the edge of the razor blade on the sample. The illumination/measurement geometry was 0°/0° thus a set of polarizer and analyzer were used. Reflected light intensities were captured with a highly linear monochrome 2 mega pixels CCD sensor (Basler scA1600-14 gm) with 12 bit digitalization depth and 0.542 µm/pixel. A sample holding apparatus represented on Figure 2.19, allowed to set the focus on a reference material (aluminized first surface mirror) and then to shift to the sample surface maintaining the focus. The reference mirror and the sample are maintained at the same level thanks to springs. The method allowed a precise focusing on uncoated paper (rough surfaces). Moreover, the sample holder can rotate allowing measuring the anisotropy of light transport. Measurements were conducted capturing 4 images: the reference with and without knife edge illumination and the sample with and without knife edge illumination. The authors proposed 3 methods to calculate the line spread function for the edge spread function measurements. The first method was a direct deconvolution performed in the Fourier domain. However, errors were amplified by the deconvolution [247]. The second method was based on a model fitting, assuming a model of the line spread function and optimizing the parameters of the model to minimize the differences with the experiments. This method led to accurate results however the model of the line spread function had to be specified by the experimenter. The third method was to solve the quadratic problem with assumed properties: the LSF positive and symmetric with the point of symmetry located at its center, the LSF monotonically decreasing and convex, the LSF unimodality and the sum of the LSF equal to 1. The authors defined the light transport length as the distance from the knife edge (normalized a reflectance of 0.5) to the position where the reflectance reached 0.1. The authors measured the ESF of 32 different

papers with several surface treatments (glossy, mat, microporous, swellable and uncoated) and several paper basis weight 90 to 400 g/m². The authors found 3 classes of paper: coated and uncoated art papers (light transport length between 40 and 81 µm), microporous ink-jet papers (light transport length between 121 and 148 µm) and swellable ink-jet papers (light transport length between 216 and 243 µm). Studying the anisotropy of the light scattering for these 3 classes, the authors found a very small variation as a function of the orientation.

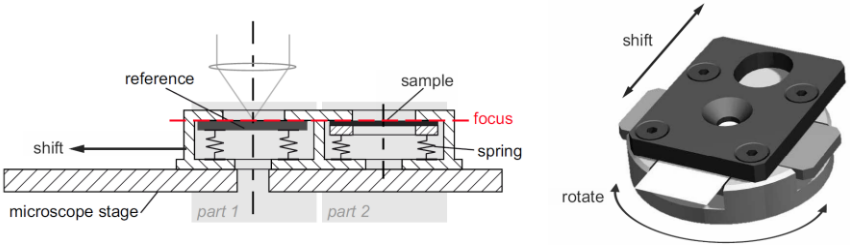

Figure 2.19: Sample holding apparatus allowing a setting the focus on a reference material (aluminized first surface mirror) and then to shift to the sample surface conserving the focus, reproduced [10].

Projection or contact bar target method

Rogers proposed a series-expansion bar target technique to measure the MTF of paper [242]. The principle was to use the Fourier transform of an image of a projection or of a contact film of a bar target on paper. The MTF of the paper was given by the series expansion coefficients of the Fourier transform of reflectance data. Rogers proposed to image only one bar target pattern and to plot the amplitudes of the bar target main frequency and its harmonics. Low frequency bar targets were preferred, since they had multiple harmonics. One could consider the method similar to the ESF measurement; however, the measure was performed on the amplitude of the harmonics in the Fourier domain, allowing obtaining the MTF without deconvolution. Rogers tested his method with simulation of paper MTF including a Gaussian noise. The measurement of the MTF was found in accordance with the MTF used for the simulation and the noise had only a limited effect on the measurements.

Arney and coworkers proposed to use a high contrast photography film imposed with a commercial graphic arts image setter [208]. Alternatively a standard glass slide resolution target USAF 1951 was used. A major drawback of the contact method is the increase of the interfacial reflections [6]. The films were then placed into vacuum contact with the paper to reduce the interfacial reflections. The author proposed to compute the contrast transfer function from measurements. Ukishima re-employed the method in order to investigate the paper MTF dependency on the illuminant geometric configuration [17,250]. The authors concluded that the angle of illumination was not significantly influencing the MTF of paper. Gustavson also proposed a "printless" method using photographic or physical grafted films projected onto papers.

Printed bar target method

Koopipat proposed to measure the MTF of paper using a bar target pattern printed directly on paper reducing the projection defocus and contact internal reflection problems [236]. The author proposed to image pattern in transmission conditions to obtain a measurement of the bar target pattern without optical dot gain (reference). The printed sample was mounted on a microscope (Olympus OX50, 10x objective) and imaged with a camera placed at normal angle with the paper (Kodak DCS420, 1.5 mega-pixels). Two illuminant sources, one illuminating the paper at 0° from above and one illuminating the paper at 0° from below were used respectively to acquire reflection and transmission images. A pair of polarization-analyzer filters allowed to cut-off specular reflection. The author observed that since the bar target was printed, the transmittance was not constant. Another drawback of the method was the difficulty to measure an accurate reference without optical dot gain.

Sinusoidal pattern method

Inoue, Miyake and Koopipat proposed to project or put into contact a sinusoidal pattern on the paper [251,252]. The MTF measurement is not direct and has to be extracted from the sinusoidal reflectance usually by Fourier transform [253]. Ukishima evaluated the method and found that it was extremely accurate. However, it could not be applied easily as it required to project and measure a large amount of sinusoidal patterns having different spatial frequencies [17,247].

2.6.2.5 Additional methods

Visual assessment

Preucil, Brunner and several other authors developed a scale to determine visually the amount of dot gain [252,254–263]. A special pattern printed on paper and its characterization leads to an estimation of the optical dot gain, Figure 2.20. The printed pattern was found to be also impacted by the physical dot gain. Nevertheless, it is an interesting solution to assess quickly the quality of a print in production.

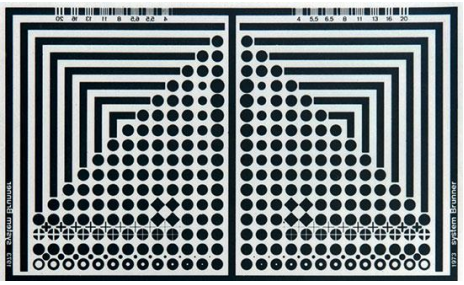

Figure 2.20: Brunner Super Micro Measuring target [254].

Analysis of optical dot gain through image quality

The optical dot gain was investigated by Ukishima, Inoue, Koopipat and Miyake by assessing the print quality [17,251,264–266]. The author proposed to simulate halftone prints at various screen resolutions, with different halftoning methods and with different light scattering lengths in paper. The model of the light diffusion on halftones (equation [2.48]) was used to simulate the halftone images. The author developed specific tests consisting in asking observers to grade the simulated images by comparing them to a reference. Indexes were defined in order to assess objectively the quality of the simulated images. The indexes took into account the contrast sensitivity function of the human eye as well as the modulation transfer function of the imaging system [267]. The author concluded that an increase of the PSF length was reducing the sharpness of the image. However, less paper granularity was visible, improving the print quality. It was found by the panel of observers that images with small PSF length were associated with the best image quality. Moreover, the author observed that the increase of optical dot gain generated for large PSF was giving the possibility to print less ink achieving the same tone.

Scatterometry, ellipsometry and scatterfield microscopy

Optical reflection microscopy images are acquired and diffraction intensities are measured. Using an inverse approach modeling, it is possible to obtain the shape of the 3D structures measured on the surface. Madsen developed an apparatus to measure micro and nano patterns on semi-transparent materials [268]. The current limitation of the method for an application on ink and paper is that it requires uniform periodical sample structures for the topography reconstruction. Ellipsometry and scatterfield microscopy can also potentially be used to study halftone dots at the microscale [269,270].

Laser focus (laser profilometry)

Laser profilometry allows obtaining the topography of a surface by focusing a laser spot on the sample. A mechanical stage scans the sample in x, y direction while the Z stage focuses the laser spot. Alternatively, laser triangulation can be achieved for faster measurements. However, the accuracy of the measurement is reduced. Chinga used laser profilometry to measure the paper surface on a 500 µm² area of measurement with lateral resolution of 1 µm [111,271].

Interferometric microscopy

Interferometric microscopy uses an optical microscope equipped by a special optic allowing a combination of two light paths, one reflected on a reference mirror and another reflected by the sample. By moving the microscope stage in the Z direction, the light path length reflected by the sample is changed. Interferences are produced by combining the two light paths and allow measuring accurately sample height. Interferometric microscopy has been used to measure paper and printed samples, Figure 2.21. A texture or a height difference is required to differentiate the ink from the paper since the reflectance information is not retrieved [272,273].

Figure 2.21: Interferometric microscopy, example of 3D reconstructed image, reproduced [274].

Confocal microscopy coupled with Raman and FTIR chemical analysis

Confocal microscopy, described in the digital optical microscopy section, has been used to characterize printed samples and paper surfaces [217,275,276]. This microscopy method allows obtaining accurate measurements of the surface topography. Authors have used confocal microscopy coupled with Raman spectroscopy in order to obtain the chemical composition of the measured surface. Raman spectroscopy uses a powerful monochromatic laser to excite the chemical molecules of the sample. These molecules relax then generating a backscattering yielding the chemical signature of the molecule. Confocal Raman microscopy can be used on two modes depth profiling or lateral mapping. Infrared spectroscopy (FTIR) was similarly used to measure directly chemical components of printed samples. Advanced authentication solutions have been proposed, based on confocal Raman microscopy [113,277–279].

Microtoming by resin inclusion

Yang and coworkers proposed to characterize the ink penetration by optical microtomography of printed paper combined with image analysis of optical captured images [194]. The halftone samples were first placed into a liquid methacrylate resin (Agar sci. LR white) under vacuum to force the resin inside the paper. After polymerization, the samples were trimmed and microtomed (Reichert-Jung 2050) in the cross section of the paper producing 3 µm thick slices. The slices were imaged on an optical microscope (Zeiss Axioplan, transmitted brightfield illumination, 20x objective) with a Nikon digital camera (DXM1200 1.31 Megapixels, RGB sensor, 0.425 µm/pixel). To adapt to the non-

perfectly flat slices z-stacks were captured and images were reconstructed (Average-Focus function, Easy Image Analysis 2000, Techno Optik AB). A color thresholding algorithm was then applied to identify the top and bottom limits of the paper and the position of the ink penetration limit. The measurement of the ink setting in the cross-section of the paper differs from the characterization of the inked surface on the paper. However, the tools proposed for these measurements can be adapted to measure the ink setting on the paper surface. Other applications of the microtomography with resin inclusion were reported, in particular to investigate the paper structure [217].

2.6.1 Non-optical microscale measurement methods

2.6.1.1 Electron and ion based methods

Scanning electron microscopy has been used in order to characterize prints and paper at the microscale [217,280,281]. Electrons are an interesting alternative source of particles to measure the print (photons are limited to measurements up to 200 nm while electrons are associated with a smaller limit, below 1 nm). Another advantage of using electrons is that paper diffuse less the electrons than it diffuses photons and a clear limit between the ink and the paper can be observed, Figure 2.22. On this image, defects of the print and edge position of the dots are clearly visible. However, scanning electron microscopes have to be precisely calibrated. Field geometry deformations can be induced and can influence the shape of the measured printed dot. Moreover, to obtain high resolution images such as in Figure 2.22 (A), a metalization of the sample is required. This metalization is permanent and optical measurement cannot be performed anymore. Low vacuum scanning electron microscopes allow imaging halftone dots without metalization however the imaging resolution is limited. Two modes can be used for imaging: the secondary electron imaging and the backscattered electron imaging. The secondary electron mode is useful to obtain an image of the surface of the sample. The backscattered electron mode allows obtaining the chemical content of the sample (high atomic weight atoms will produce a high brightness and low atomic weight atoms a low brightness). Multiple other methods based on electron measurements can be used to measure printed dots at the microscale such as the measurement of Auger electrons, energy dispersive X-ray (EDX), catho-luminescence, continuum X-ray, inelastic scattering, elastic scattering, incoherent elastic scattering, etc.

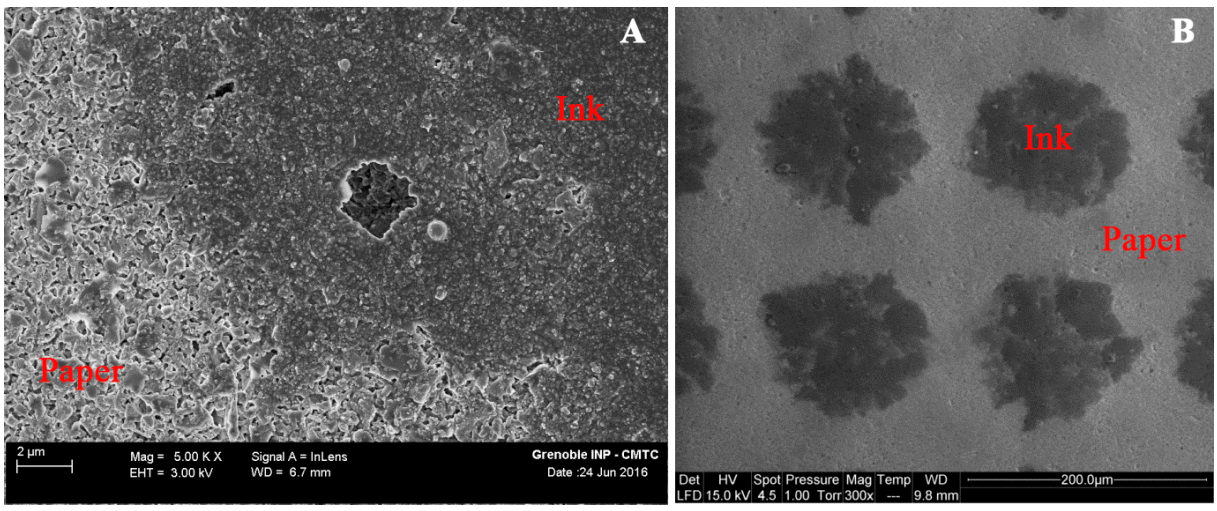

Figure 2.22: Scanning electron microscopy of an offset print (A) metalized with 5000x magnification, (B) non-metalized, low vacuum, 300x magnification.

Focused ion beam coupled with transmitted electrons microscopy is probably one of the most advanced microscopy analysis used in print characterization [217,282,283]. A printed sample is embedded in a resin. A focused ion mean is then used to perform a sectioning of the sample at high resolution. The ion beam is capable of focusing ions with a small beam size (7 to 300 nm). After slicing, a platinum organometallic gas injector is used to metalize the sample. Imaging can be conducted using a

transmitted electron achieving high resolutions up to 0.2 nm. These measurements can only be performed on small surface and sample preparation and sectioning is time consuming.

2.6.1.2 X-ray based methods

Kristiansson and coworkers developed a method to measure the physical ink setting on the paper excluding optical dot gain [32,284]. Their method was performed at the Lund nuclear microprobe facility performing particle induced X-ray emission measurement. For this purpose, a beam of 3x3 µm² and 1nA illuminated the sample and was emitted from an ion source accelerated to 2.55 MeV. X-ray induced emissions were consequently measured. The beam was then switched to different locations of the sample with 2 µm steps. The time for the acquisition of the X-ray induced emissions was set at 3 hours in order to obtain sufficient signal. 300x300 µm² were measured for each halftone configurations. Simultaneously a measure called the off-axis scanning transmission ion microscopy was performed in order to obtain the mass distribution of the ink as a function of the space. This method measures the energy loss of protons and allows retrieving an ink thickness. Kristiansson compared the X-ray measurements with optical measurements and was able to quantify the optical dot gain.

X-ray microtomography uses X-ray electromagnetic waves to produce an interaction with the sample and to obtain a contrast. The contrast contains the cross section information of the sample. By performing multiple X-ray images with multiple angles (called X-rays scans), a 3 dimensional reconstruction of the sample is possible. The advantage of that method is that the internal structure of the sample is imaged without destroying its integrity by sectioning. From the acquired image the microstructure of the sample can be reconstructed using powerful image processing tools. Artifacts such as the ring artifacts can be generated from this reconstruction and should be accounted for. Molecular weight differences between ink and paper are required in order to obtain the required contrast of the X-ray cross section images. Since ink and paper have similar molecular weight, a precise tuning of the parameters is required. The paper structure and mechanical properties were studied using x-ray microtomography [217,285]. These advanced methods are extremely accurate. However, they are slow, require expensive equipment and the measurable surface is limited.

2.6.1.3 Mechanical profilometry and atomic force microscopy methods

Mechanical profilometers are composed of an accurate motorized translation arm or stage allowing recording the displacements. A stylus (small tip) is applied on the sample with a standard force and the height is record. A stage moves precisely the sample in order to perform the measurement on multiple points of the surface. One advantage of that method is that the measurements are not influenced by the optical properties of the printed sample. One drawback is that only small surfaces can be measured. Mechanical profilometry has been used to measure paper characteristics at the microscale [286–288].

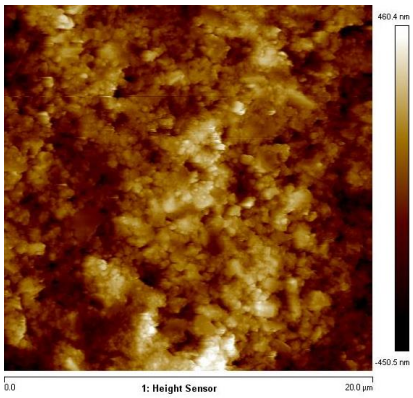

Figure 2.23: Atomic force microscopy of a dot printed on coated paper with offset.

Atomic force microscopy is similar to mechanical profilometry. However a higher resolution is achieved. A microscopic tip is put in contact with the sample with a piezo actuator. A laser performs triangulation in order to measure precisely the displacement of the microscopic tip. A tapping mode uses vibration of the tip in order to acquire the height of the sample faster. The resolution can reach 0.1 nm in the height and 0.01 µm in the x, y direction. When measuring thin ink films on non-flat surfaces the ink height can be "lost" in the roughness of the paper, Figure 2.23. Researchers used atomic force microscopy to measure printed dots with relative success [289,290].

2.7 Model based optical and physical dot gain characterization

A selection of the models proposed in literature is presented. The models described are commonly used to estimate the ink coverage by fit of the model predicted reflectances and of a set of measurements. The Murray-Davies model allows obtaining the effective ink coverage [2]. The Yule-Nielsen model allows obtaining an estimation of the physical ink coverage [244]. The probability model characterizes ink and paper reflectances dependencies with the halftone characteristics, allowing obtaining also an estimation of the physical ink coverage. Finally, the model of the light diffusion on halftones gives a spatial description of the light diffusion effects (optical dot gain) on halftones and therefore can allow obtaining also an estimation of the physical ink coverage. A discussion of the relations between the models and the dot gain is proposed. Other models such as the Clapper-Yule model can also be used to characterize the physical ink coverage [245]; however, they are not presented in this section for summarizing reasons. Moreover, the models presented are proposed in their single ink version but have been extended to multi-ink prints. Extended information and review of these models can be found in [3,212,291–293]. Print reflectance models are designed to predict the output reflectance of a printed halftone as a function of the ink and paper characteristics: the ink setting on paper, the ink reflectance, the ink transmittance, the diffusing properties of paper, etc. The reflectance $R(\lambda)$ is dependent on the wavelength and models can output the spectral reflectance or directly the integrated reflectance R. Models can alternatively output the optical density or the colorimetric coordinates. Transformations between the reflectance, optical density or color coordinates can be found in [212]. Authors have proposed to classify the prediction models into two categories: the regression based models and the first principal models [3]. Another classification has been proposed with three categories: the surface models, the physically inspired models and the ink spreading models. Surface models rely on the description of the surface coverage of colorants. The ink spreading models rely on the assessment of the dot gain.

The total dot gain Δa_{tot} is the sum of the physical dot gain Δa_{phy} (ink spreading) and of the optical dot gain Δa_{opt} (light diffusion effects), equation [2.11]. These dot gains are characterized by measuring the apparent a_a and effective a_e ink coverages compared to the nominal a_n ink coverage. The nominal ink coverage is the ink coverage set on the binary file sent to the printer. The apparent ink coverage is the surface coverage measured after printing and including the optical dot gain effects. The effective ink coverage corresponds to the effective surface where ink was deposited, thus including physical dot gain but excluding the optical dot gain.

$$\Delta a_{tot} = \Delta a_{opt} + \Delta a_{phy} = a_a - a_n \quad [2.11]$$

$$\Delta a_{phy} = a_e - a_n \quad [2.12]$$

2.7.1 Murray-Davies model

Murray and Davies developed their model based on optical microscopic measures of the inked surface in relation to the optical densities [2]. The model was originally designed for optical densities. Later, the Murray-Davies model was extended to reflectances, equation [2.13]. The Murray-Davies model is initially only valid for integrated reflectance measurements performed with an integrating sphere, but in practice limited solid angle measurements are used [294]. Arney, Engeldrum and Zeng described the Murray-Davies model as an expression of the law of conservation of energy for photons [5]. Reflectances are directly related to photons flux being returned from the print image. Photons have extensive properties, photons add and thus, reflectances should add too. The Murray-Davies model is then the addition of two photon fluxes: the one reflected over paper surface and the one reflected over the ink surface [5]. The same model, although presented under another analytical form was given by Buchdahl, Polglase and Schwalbe [295]. The total dot gain can be obtained by subtracting the apparent ink coverage with the nominal ink coverage, equation [2.14].

Murray-Davies model, adapted from original form

		Symbol	Unit	Denomination
[2.13]	$R_a(\lambda) = (1 - a_a)\, R_{ps}(\lambda) + a_a\, R_{is}(\lambda)$	$R_a(\lambda)$	1	Halftone reflectance
		$R_{is}(\lambda)$	1	Solid print reflectance
		$R_{ps}(\lambda)$	1	Bare paper reflectance
[2.14]	$\Delta a_{tot} = \dfrac{R_a(\lambda) - R_{ps}(\lambda)}{R_{is}(\lambda) - R_{ps}(\lambda)} - a_n$	a_a	1	Apparent ink surface
		a_n	1	Nominal ink surface
		Δa_{tot}	1	Total dot gain

2.7.2 Yule-Nielsen model

The construction of Yule-Nielsen model came from the analysis conducted by Yule and Nielsen of two special cases [244]. The first one is called the "complete light diffusion approximation" and considers that when the halftone period is small compared to the length of light diffusion, the probability that a ray of light exits the paper under a printed dot does not depend on the location where it entered the print. The Murray-Davies model should then be completed by adding the reflectance of the light entering paper and exiting paper under an inked surface and the reflectance of the light entering the ink and exiting in a paper area, Figure 2.24.

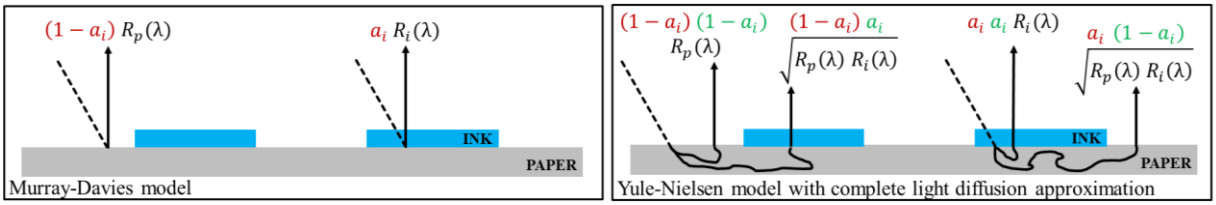

Figure 2.24: Illustrations of the components of the Murray-Davies model and the Yule-Nielsen model with complete light diffusion approximation.

For a solid print patch, the light goes through the ink layer and is reflected by the paper through the ink layer again:

$$R_{is}(\lambda) = T_i(\lambda)\, R_{ps}(\lambda)\, T_i(\lambda) \qquad [2.15]$$

When the light diffuses from paper to an inked surface, it goes only on time through the ink layer:

$$T_i(\lambda)\, R_{ps}(\lambda) = \sqrt{R_{is}(\lambda)\, R_{ps}(\lambda)} \qquad [2.16]$$

A summation of the terms presented for the Yule-Nielsen model with the complete light diffusion approximation leads to:

$$R_a(\lambda) = \left[(1 - a_e)R_{ps}(\lambda)^{\frac{1}{2}} + a_e R_{is}(\lambda)^{\frac{1}{2}}\right]^2 \qquad [2.17]$$

which corresponds to the Yule-Nielsen model with n=2. The second special case that Yule and Nielsen investigated is the case when the light does not diffuse. The sum of the terms lead then back to the Murray-Davies model, which corresponds to the Yule-Nielsen model with n=1. Yule and Nielsen defined their model for the cases where the light diffuses but the complete light diffusion approximation cannot be adopted, with 1 > n > 2, equation [2.18] [244]. It should be noted that the model allow obtaining the effective ink coverage only when using an accurate n parameter. The model was extended to spectral reflectances [296].

Yule Nielsen model, extended to spectral reflectances

[2.18] $$R_a(\lambda) = \left[(1 - a_e)R_{ps}(\lambda)^{\frac{1}{n}} + a_e R_{is}(\lambda)^{\frac{1}{n}}\right]^n$$

[2.19] $$\Delta a_{opt} = \frac{R_a(\lambda) - R_{ps}(\lambda)}{R_{is}(\lambda) - R_{ps}(\lambda)} - \frac{R_a(\lambda)^{\frac{1}{n}} - R_{ps}(\lambda)^{\frac{1}{n}}}{R_{is}(\lambda)^{\frac{1}{n}} - R_{ps}(\lambda)^{\frac{1}{n}}}$$

Symbol	Unit	Denomination
$R_a(\lambda)$	1	Halftone reflectance
$R_{is}(\lambda)$	1	Solid print reflectance
$R_{ps}(\lambda)$	1	Bare paper reflectance
a_e	1	Effective ink surface
n	1	Yule-Nielsen factor
Δa_{opt}	1	Optical dot gain

Although the Yule-Nielsen model is considered to be an empirical model, the two special cases studied can be considered as physical models, describing the conservation of energy law, considering fundamental assumptions: the ink has a constant thickness for all ink coverages and the multiple internal reflections due to different refractive indexes (air, print-paper) at the interfaces are not considered [13,297]. The model does not conserve the linearity of the Murray-Davies model but is instead linear in the 1/n reflectance space [292]. Viggiano demonstrated that working with integrated reflectances R and reflectances depending on the wavelength $R(\lambda)$ was not equivalent because of the non-linearity of the model [296]. Indeed, the inverse Cauchy-Schwartz inequality states that:

$$\sqrt{R_{\lambda=1}} + \sqrt{R_{\lambda=2}} + \cdots > \sqrt{R_{\lambda=1} + R_{\lambda=2} + \cdots} \qquad [2.20]$$

Viggiano suggested that performing the integration after the application of the Yule-Nielsen model lead to improved precision [296]. The optical dot gain can be obtained by subtracting the apparent ink coverage obtained from the Murray-Davies model with the effective ink coverage obtained with the Yule-Nielsen, equation [2.19].

The Yule-Nielsen n factor is often determined to fit the reflectance measurements. Multiple studies [3,20,22,34,35,211,231,244,291,297–306] have explored the effects of a n factor superior to 2. In some of these studies, a large n factor, up to n=100, was determined to best fit the measurements. Yule and Nielsen observed that, by computing the optical density with their model, the optical density was becoming linear versus the ink coverage with n tending to infinity. When n tends to infinity the Yule-Nielsen model tends to become similar to the Beer-Lambert-Bouguer law [307]. However, as Yule and Nielsen, Ruckdeschel and Hauser and Arney and Yamaguchi demonstrated, n factors superior to 2 do not have a physical signification. Ruckdeschel and Hauser proposed that an n fitting superior to 2 could originate from errors in the measurement of the effective ink coverage. Lewandowski and Viggiano showed that a negative n value fitted best their measurements in case of ceramic printing or in the case

of strong ink penetration into the substrate [308,309]. Attempts to determine the Yule-Nielsen n factor were performed empirically and physically. The Yule-Nielsen n factor can be obtained empirically through an optimization, minimizing the difference between the measured reflectance and the reflectance calculated with the Yule-Nielsen model (alternatively minimization of the color difference or specific weighting of the spectra).

Pearson conducted a study to correlate the n value with multiple printing conditions and obtained n factors between 1.4 and 1.8 [310]. The true ink surface was determined by measuring the transmittance of the transfer films where the halftone patterns were set before transferring to paper. The ink coverage demonstrated a small influence on the n factor. On the contrary the halftone frequency (65 and 150 lpi) as well as the nature of the paper (uncoated, newsprint and coated) revealed a large influence. However, Pearson's results should be interpreted with care since integrated optical densities were used. Other researchers have found that n is dependent on the length of light scattering in the paper as well as on the halftone size and on the ink coverage [16,311].

Ruckdeschel and Hauser tried to calculate the n factor of the Yule-Nielsen equation relying on the model initiated by Callahan, expressing the reflectance of the halftone image as the convolution of the transmittance of the ink and the paper point spread function multiplied by the transmittance of the ink and the reflectance of the paper [9]. Ruckdeschel and Hauser calculated the convolution using a normalized Gaussian point spread function and found that:

$$R_a = (1 - a_e)\left[C + \sqrt{1 - a_e}(1 - C)\right]^2 \quad [2.21]$$

$$C = \frac{\sum_{m=1}^{\infty} \frac{\sin^2\left(\frac{m\pi d}{f}\right)}{m^2} \exp\left(-\frac{m\pi\sigma}{f}\right)}{\sum_{m=1}^{\infty} \frac{\sin^2\left(\frac{m\pi d}{f}\right)}{m^2}} \quad [2.22]$$

with d the ink dot diameter, f the halftone period and σ the parameter of the Gaussian paper point spread function. Taking the hypothesis that the series are quick convergent and that R_{is} is equal to 0, the authors obtained for small $a_e \ll 1$:

$$n = 2 - \exp\left(-\frac{\pi\sigma}{f}\right)^2 \quad [2.23]$$

Furthermore, Ruckdeschel and Hauser showed that at $a_i > 50\%$ n was becoming dependent on the ink coverages. Their work showed analytically, for the first time, that the n parameter was dependent on the diffusion of the light in the paper and can be calculated from the paper point spread function, the halftone frequency and the ink coverage [13]. Ruckdeschel and Hauser's expression of n was rewritten by Arney and coworkers:

$$n = 2 - \exp(-k_1\, \sigma\, f) \quad [2.24]$$

with σ the light scattering length, f the halftone frequency for AM halftone [6]. k_1 depends mostly on the halftone configuration. Arney and coworkers suggested that σ could be determined by various approaches, by the analysis of the paper point spread function in the Fourier domain [312–314] or by measurement of periodic pattern of light projected onto paper [16,312,315,316]. According to Arney:

$$\sigma = \frac{1}{x} \quad \text{when} \quad MTF(x) = \frac{1}{2} \quad [2.25]$$

Arney and coworkers found that the K coefficient of the Kubelka-Munk model had a little influence on the Yule-Nielsen n factor. However, they found a great influence of the Kubelka-Munk S coefficient and established that for coated papers:

$$\sigma \approx \frac{10}{S} \qquad [2.26]$$

Iino and Berns proposed a modification of the Yule-Nielsen model by having the n parameter dependent on the wavelength [317]. Fitting of the n parameter was performed by least square regression techniques and with a nonlinear simplex method. The authors showed that by allowing the dependency of n to the wavelength, improved predictions of the model could be obtained.

2.7.3 Arney probability model

Callahan was the first to determine that the ink and paper reflectances were dependent on the ink coverage and could be described from the bare paper and solid print reflectances [9]. Arney, Engeldrum and Zeng suggested that the reflectances of paper and ink in the Murray-Davies and in the Yule-Nielsen model do not refer to the same quantities [5,7,297]. In the Yule-Nielsen model the reflectances expressed are reflectances of solid print and paper measured outside of the halftone image. The reflectances expressed in the Murray-Davies model are conversely the reflectances of the ink and of the paper measured in a halftone surface. This suggests that the reflectances in the Murray-Davies model are dependent on the ink coverage, the halftone frequency, and pattern and on the paper properties. Thus, Arney studied reflectances of paper and ink measured in a halftone image for multiple ink coverages [7]. The measurements show the dependency of the reflectance of the ink and the paper versus the ink coverage. In the case of the complete light diffusion approximation, relations between reflectances of paper and ink, inside a halftone image, respectively $R_p(a_e)$ and $R_i(a_e)$ can be expressed as a function of the reflectances of bare paper R_{ps} and solid print R_{is} [297] (the wavelength dependencies of the reflectances are not expressed for simplicity):

$$R_p(a_e) = (1 - a_e)\, R_{ps} + \; a_e \sqrt{R_{ps}\, R_{is}} \qquad [2.27]$$

$$R_i(a_e) = \; a_e\, R_{is} + \; (1 - a_e) \sqrt{R_{ps}\, R_{is}} \qquad [2.28]$$

The prediction of the halftone reflectance is then obtained similarly than with the Murray-Davies model, equation [2.29] [35]. Later, Wakeshima, Kunishi and Kaneko suggested the same ink and paper reflectances dependencies and proposed a model based on the diffusion of the light in the print [318] yielding to the Yule-Nielsen model with n=2. Studies have shown that the complete light diffusion approximation is a valid hypothesis when the ratio between the length of the light diffusion and the frequency of the halftone pattern exceeds or is equal to 1 [7,213,319]. Thus, to adapt the model to halftone where the complete light diffusion approximation is not valid, researchers proposed several functions linking the ink and paper reflectances in the halftone, $R_p(a_e)$ and $R_i(a_e)$ to the effective ink coverage, to the halftone size and to the paper type and to several other parameters. For the purpose of this study the functions developed are called f functions, equation [2.30].

Expanded Murray-Davies model

		Symbol	Unit	Denomination
[2.29]	$R_a = (1 - a_e)R_p(a_e) + a_e R_i(a_e)$	R_a	1	Halftone reflectance
[2.30]	$R_p(a_e) = f_p(a_e, R_{ps})$ $R_i(a_e) = f_i(a_e, R_{is})$	R_{is}	1	Solid print reflectance
		R_{ps}	1	Bare paper reflectance
[2.31]	$\Delta a_{opt} = \frac{R_a - R_{ps}}{R_{is} - R_{ps}} - \frac{R_a - R_p}{R_i - R_p}$	a_e	1	Effective ink surface
		f_p, f_i	1	Specific "f" functions
		Δa_{opt}	1	Optical dot gain

Arney, Engeldrum and Zeng proposed f functions presenting empirical modifications to account for cases where the complete light diffusion approximation could not be adopted and for cases with non-constant thicknesses [5,297]. The authors introduced two terms: w to account for the light diffusion in relation to the dot size and v to account for the ink thickness variation on the edges of the dots.

$$R_i(a_e) = R_{ps}(1-(1-T_i)a_e^w)(1-(1-T_i)a_e^v) \quad [2.32]$$

$$R_p(a_e) = R_{ps}\left(1-(1-T_i)(1-a_e^w)\right)\left(1-(1-T_i)(1-a_e^v)\right) \quad [2.33]$$

$$\text{with } T_i = \sqrt{\frac{R_{is}}{R_{ps}}} \quad [2.34]$$

The two empirical factors w and v are determined by minimizing the differences between the predicted reflectances and the measured reflectances for training set. Arney, Engeldrum and Zeng compared their model with the Yule-Nielsen model and found that their model was not increasing the prediction accuracy of the measured reflectance. Nyström showed experimentally that this model was not adapted for high screen frequency halftones [19]. An example of the prediction of $R_p(a_e)$ and $R_i(a_e)$ obtained with the model, is given in Figure 2.25 (A) and is compared to experimental data.

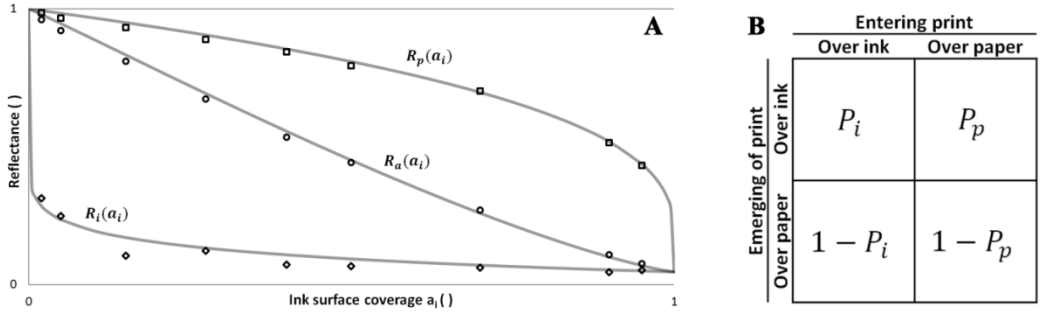

Figure 2.25: (A) Measured R_a, R_p and R_i as a function of the ink coverage. Model (solid lines) with $w = 0.35$ and $v = 0.05$, adapted [218].(B) Probability of photons path in the case of monochrome printing, adapted [7].

Arney and coworkers proposed another set of functions f to describe the ink and paper reflectances as a function of the ink coverage. Their approach called the probability model, is based on Hunstman model describing the probabilities of photons entering the paper to leave the paper under an inked surface or over the paper area [6,7,320]. The probability of photons arriving over an inked surface is also expressed. Four cases arise with associated probabilities, Figure 2.25 (B) [7]:

- light entering over paper and reflected over paper: $R_{p1}(a_e) = R_{ps}\left(1-P_p(a_e)\right)$ [2.35]
- light entering over paper and reflected over the ink: $R_{i1}(a_e) = R_{ps}\,T_i\left(1-P_i(a_e)\right)$ [2.36]
- light entering over the ink and reflected over paper: $R_{p2}(a_e) = R_{ps}\,T_i\;P_p(a_e)$ [2.37]
- light entering over the ink and reflected over the ink: $R_{i2}(a_e) = R_{ps}\,T_i^2\,P_i(a_e)$ [2.38]

Then, the total reflectance of the paper surface and of the ink surface is given by the sum of the four cases multiplied by the respective ink coverages, equation [2.39]. $R_i(a_e)$ and $R_p(a_e)$ can be obtained similarly, equation [2.40].

Probability model

		Symbol	Unit	Denomination
[2.39]	$R_a = (1 - a_e)\left(R_{p1}(a_e) + R_{p2}(a_e)\right) + a_e\left(R_{i1}(a_e) + R_{i2}(a_e)\right)$	R_a	1	Halftone reflectance
		T_i	1	Ink transmittance
[2.40]	$R_i(a_e) = R_{ps}\, T_i\left(1 - P_i(a_e)(1 - T_i)\right)$ $R_p(a_e) = R_{ps}\left(1 - P_p(a_e)(1 - T_i)\right)$	R_{ps}	1	Bare paper reflectance
		a_e	1	Effective ink surface
		$P_i(a_e)$, $P_p(a_e)$	1	Probability functions

The authors observed that the following empirical probability functions fitted the best the experiments for AM halftoning:

$$P_p(a_e) = a_e(1 - (1 - a_e)^w + (1 - a_e^w) \quad [2.41]$$

$$P_i(a_e) = (1 - a_e)(a_e^w - 1) + (1 - a_e)^{w+1} + a_e \quad [2.42]$$

Similarly, for FM halftoning:

$$P_p(a_e) = w\left(1 - (1 - a_e)^B\right) \quad [2.43]$$

$$P_i(a_e) = 1 - \frac{w}{a_e}[(1 - a_e)(1 - a_e)^{B+1}] \quad [2.44]$$

with w the light diffusion factor and B the geometry dot factor [7]. The authors suggested that the probability model has the advantage to establish simpler relations than the models based on the point spread function. An insight of determining the probability function by derivation of the point spread function is given by the Z-sum theory established by Rogers [321].

2.7.4 Model of the light diffusion on halftones

Callahan is the first author to describe the optical dot gain on paper by writing the convolution of a point spread function with the ink transmittance [9]. This led to the model of the light diffusion on halftones, equation [2.48]. Assumptions are taken for the model of the light diffusion on halftones: the ink is on the surface of the paper without penetration into paper. No specular reflection, internal reflections and diffuse reflections due to scattering within the ink are accounted [235]. Moreover, it is assumed that the incident irradiance $I_0(x, y, \lambda)$ is uniformly distributed over the surface, so it can be expressed by $I_0(\lambda)$. This incident light goes through a first layer composed either of ink or of non-ink of transmittance $T_i(x, y, \lambda)$. The transmittance varies between 0 and 1 dependently on the x, y position (either if ink was deposited at that position x, y, or if there is only paper), on the thickness of the ink and on the spectral response of the ink. When the light goes through the first layer, the irradiance is written:

$$I_r(x, y, \lambda) = I_0(\lambda) T_i(x, y, \lambda) \quad [2.45]$$

These photons reach then paper and diffuse. The diffusion is modelled by the convolution of $I_r(x, y, \lambda)$ with a point spread function $H(x, y, \lambda)$. This convolution is the equivalent of a blurring convolution with a kernel specified by the optical properties of the paper. Photons are then reflected by the paper with a reflectance of $R_{ps}(x, y, \lambda)$ and the reflected irradiance is equal to:

$$I_r(x, y, \lambda) = R_{ps}(x, y, \lambda)\, [I_0(\lambda)\, T_i(x, y, \lambda) \circledast H(x, y, \lambda)] \quad [2.46]$$

The light reflected by the paper will then be transmitted again through the ink or non-ink layer of transmittance $T_i(x, y, \lambda)$. Thus, the final irradiance reflected by the halftone is:

$$I_r(x, y, \lambda) = T_i(x, y, \lambda)\, R_{ps}(x, y, \lambda)\, [I_0(\lambda)\, T_i(x, y, \lambda) \circledast H(x, y, \lambda)] \quad [2.47]$$

The halftone reflectance is the ratio between reflected irradiance and incident irradiance and considering the associative property of the point spread function, equation [2.48] is obtained.

By setting the paper point spread function to 1, the halftone reflectance without light diffusion R_{aw} (including only the physical dot gain) can be computed, equation [2.49]. The ink coverage, a_e, is expressed in the transmittance function $T_i(x,y,\lambda)$. Since the transmittance depends on the ink thickness, the ink coverage is expressed as a function of the ink thickness. Nevertheless, the equivalent ink coverage independent from the ink thickness can be retrieved using the Murray-Davies equations with the bare paper reflectance, the solid print reflectance and the two calculated halftone reflectances: $R_a(x,y,\lambda)$ including light diffusion and $R_{aw}(x,y,\lambda)$ excluding light diffusion, equation [2.50].

Gustavson argued that the assumed separability from all stages is only true in the case where the ink is rigorously at the surface of the paper, without ink penetration in the paper and the paper having no roughness [235]. With ink penetration into the paper and paper roughness, a 3 dimensional approach should be adopted, with a 3 dimensional convolution, a 3 dimensional paper point spread function and a 3 dimensional transmittance layer. The model of light diffusion on halftones also assumes that no internal reflections are occurring, however the effects of internal reflections were observed for coated paper by Williams and Clapper [322]. Kruse and Wedin proposed to add direct reflections to the light diffusion halftone model [208,231,240]. Multiples studies were conducted to relate empirical point spread functions to physical parameters or to predict the reflectance of a halftone by computer simulations [9,11,13,16,208,235,261,315,323].

The model of light diffusion on halftones

[2.48] $$R_a(x,y,\lambda) = R_{ps}(x,y,\lambda)\, T_i(x,y,\lambda)\, [T_i(x,y,\lambda) \circledast H(x,y,\lambda)]$$

[2.49] $$R_{aw}(x,y,\lambda) = R_{ps}(x,y,\lambda)\, T_i(x,y,\lambda)^2$$

[2.50] $$\Delta a_{opt} = \frac{R_a(\lambda) - R_{ps}(\lambda)}{R_{is}(\lambda) - R_{ps}(\lambda)} - \frac{R_{aw}(\lambda) - R_{ps}(\lambda)}{R_{is}(\lambda) - R_{ps}(\lambda)}$$

Symbol	Unit	Denomination
$R_a(x,y,\lambda)$	1	Halftone reflectance
$R_{aw}(x,y,\lambda)$	1	Halftone reflectance without light diffusion
$T_i(x,y,\lambda)$	1	Ink layer transmittance
$R_{ps}(x,y,\lambda)$	1	Spatial bare paper reflectance
$R_{ps}(\lambda)$	1	Bare paper reflectance
$R_{is}(\lambda)$	1	Solid print reflectance
$H(x,y,\lambda)$	1	Paper point spread function

Multiple assumptions have been proposed to solve the radiation transfer equation such as the neutron theory, the Kubelka-Munk theory, the diffusion approximation theory, two dimensions 2 flux model, 3 dimensions two flux models and 4 flux models. Berg and Mourad introduced cellular models to describe the transport of light laterally. Arney proposed to extend the cellular approach to allow for lateral transports over multiple cells [8,324–326]. The radiative transfer theory has also been approached numerically, with solutions obtained by Monte-Carlo simulations [202–204,327–331]. Linder, Löbjörn and Coppel simulated recently the modulation transfer function using phase functions from an analytical solution of the scattering by an infinite cylinder with a Monte Carlo approach. The authors found that their method was more accurate than the MTF obtained from rotationally invariant single scattering phase functions. However, the level of light scattering simulated remained inferior to the experimental measurements due to the hollow lumen of wood fibers. A similar approach was proposed by Coppel, Neuman and Edström, using the Henyey-Greenstein phase function with two different asymmetry factors [8,207,312,332–335]. Kruse and Wedin proposed a simulation of the light path into paper based on a transmission PSF [231,241,323,336]. The main point spread functions proposed in literature are:

- Gaussian point spread function: Inoue, Tsumura and Miyake proposed a normalized Gaussian point spread function to simulate the optical dot gain effects with σ the standard deviation representing length of light diffusion in a paper [261] :

$$H(x,y) = \frac{\exp\left(-\frac{x^2+y^2}{2\,\sigma^2}\right)}{2\,\pi\,\sigma^2} \quad [2.51]$$

- Sum of Gaussian point spread function: Neumann, Coppel and Edström investigated the point spread function dependence with anisotropic single scattering and proposed a sum of Gaussians function where α_I and σ are determined from the asymmetry of the single scattering, the scattering albedo, the mean free path and the medium thickness [334,337]:

$$H(x,y) = \sum_i \alpha_i \exp_i\left(-\sigma\,(x^2+y^2)\right) \quad [2.52]$$

- Exponential point spread function: Koopipat performed experimental measurements of the paper MTF and proposed an exponential point spread function [236,266] :

$$H(x,y) = \frac{1}{2\,\pi\,\sigma^2}\exp\left(-\frac{\sqrt{x^2+y^2}}{\sigma}\right) \quad [2.53]$$

- Modified exponential point spread function: Gustavson derived point spread functions theoretically simulating spatial and angular distributions of photons. The author proposed a modified exponential point spread function with R_1 the total reflectance of the substrate and σ the PSF length [208,235,336,338] :

$$H(x,y) = R_1\,\frac{\sigma}{2\,\pi\sqrt{x^2+y^2}}\exp\left(-\sigma\sqrt{x^2+y^2}\right) \quad [2.54]$$

- Laurentzian point spread function: Modrić and coworkers proposed a Laurentzian PSF function based on a Monte-Carlo simulation with σ the length of light transport in paper and γ a normalization factor [203,339]:

$$H(x,y) = \gamma\,\frac{\sigma}{2}\left(\pi\left((x^2+y^2)+\left(\frac{\sigma}{2}\right)^2\right)\right)^{-1} \quad [2.55]$$

It should be noted that to satisfy the energy conservation law, the sum of the PSF function (at the kernel size) should be equal to 1. To enable a precise comparison of the PSF fittings, Modrić and coworkers proposed a novel approach based on the Akaike information criterion applied on the edge of a halftone dot. This methodology confirmed that the Laurentzian function is providing an accurate modelling of the measurements [12,340].

2.8 Optical and physical dot gain impact

2.8.1 Measurement method impact

2.8.1.1 Reflection and transmission microscopy

Reflection and transmission microscopy are often used to characterize optical dot gain. Several authors have developed methods with the assumption that there is only physical dot gain with transmission images of a printed sample. As it can be observed on Figure 2.26, the optical dot gain at the border of the dots obtained by reflection microscopy cannot be clearly identified as on transmitted images. On another hand the paper transmittance obtained with transmission microscopy shows large heterogeneities. Special attention should be applied to optical dot gain measurements with combined reflection - transmission microcopy images. However as highlighted by Gustavson [208], combined reflection - transmission shows greater results when applied on homogeneous materials such as plastic substrates. Images obtained by Gustavson show a greater shadowed region in reflection than in transmission measurements, Figure 2.26. It has to be noted that these reflection - transmission measures are extremely sensitive to microscope focus, which can be difficult to set.

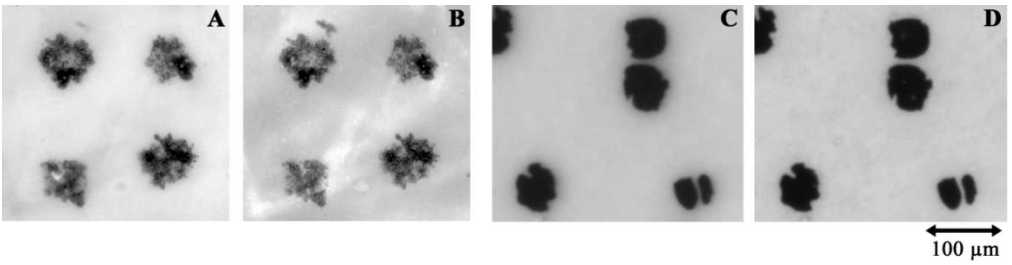

Figure 2.26: (A) Reflection and (B) transmission microscope images of halftone dots printed on paper with offset.(C) Reflection and (D) transmission microscopy of halftone dots printed with thermal transfer on white polyethylene, adapted from Gustavson [208].

2.8.1.2 Methods of measurement

Methods used to obtain the ink coverage can influence the result and accuracy. Different levels of dot gain are obtained depending on the method used: a densitometer (total dot gain), a scanner associated with the transition area threshold method (physical dot gain) and a scanner with the color shift method (total dot gain). Distinction between methods measuring total dot gain and physical dot gain highly depends on the assumptions adopted by researchers and results can vary significantly Figure 2.27.

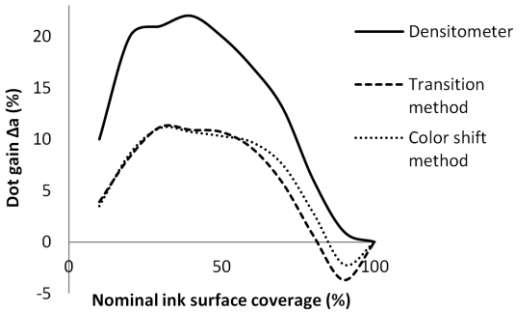

Figure 2.27: Dot gain as a function of the nominal ink coverage measured with 3 methods: Densitometer Xrite 414, Scanner (flatbed FENIX 6425-C) with transition area threshold method and Scanner with color shift method. Thermal transfer print: Seiko professional ColorPoint 2, 300 lpi, Seiko advanced halftoning, cyan ink.

2.8.1.3 Spectral dependency

Iino and Berns studied the dependency of the Yule-Nielsen n parameter with the wavelength [317]. The Yule-Nielsen model is admitted to be a physical model if n is found between 1 and 2, as explicated by Ruckdeschel and Hauser [13]. Iino and Berns fitted the model to spectrophotometric measurements, allowing a dependency of n to the wavelength. As illustrated on Figure 2.28, the fitted $n(\lambda)$ is dependent on the wavelength and is comprised between 1.26 and 1.69. It has to be noted that the average of the parameter value is found at 1.57, a value close to the recommended n value of 1.7 given by Pearson [310]. However, as mentioned by Yang, the n value fitted is extremely dependent on the ink coverages or colorants surface coverages adopted in the regression. In cases where the nominal ink coverages are used, the n value loses its physical meaning as it compensates for physical dot gain. Hübler demonstrated that the optical dot gain had a "color", meaning that the effect of the optical dot gain was dependent on the wavelength [341].

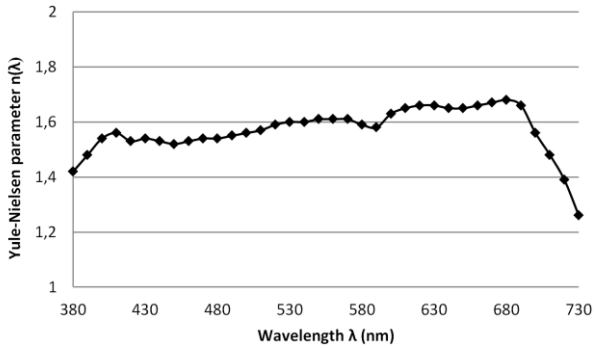

Figure 2.28: Yule-Nielsen parameter n(λ) fitted as a function of the wavelength λ, reproduced from Iino [317].

2.8.1 Print method impact

2.8.1.1 Print process influence

As presented on Figure 2.29, the total dot gain depends on the printing process. The physical spreading on the ink is directly dependent on the process. The printed dot spreading, penetration, thickness and geometry have an influence on optical dot gain: for example a fuzzy dot edge will be more sensitive on optical dot gain than sharp edges. The dot gain obtained with two identical processes can also differ depending on print parameters and on process accuracy (illustrated on the graph by thermal transfer I and II). Dot gain effects were measured with a densitometer (Xrite 414).

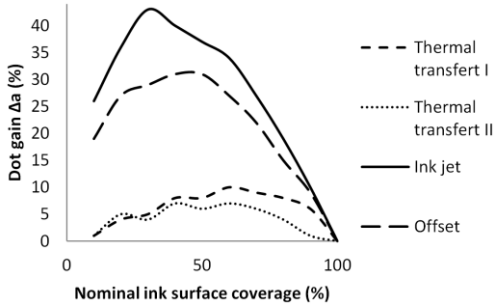

Figure 2.29: Dot gain as a function of the nominal ink coverage for 4 printers: thermal transfer I and II (Seiko professional ColorPoint 2, 300 dpi and QMS ColorScipt 100, 300 dpi), inkjet (Hewlett-Packard PaintJet XL300, 300 dpi) and offset 30 lpi. Plotted from data presented by Wedin [231].

2.8.1.1 Halftone method influence

Wedin observed that the halftoning method had also an influence on the amount of dot gain. Similar dot surfaces can be obtained from extremely different dot geometry yielding to different effects of optical dot gain [231]. Consequently, the geometry and perimeter length of the dots can differ

according to halftone methods. The optical dot gain is sensitive to the perimeter length of the dots and the length of un-inked paper regions between the dots. The physical dot gain is sensitive to the geometry of the halftone. The resulting total dot gain difference is illustrated on Figure 2.30. Nyström studied amplitude modulated and frequency modulated halftoning with various screen frequencies [19]. The authors plotted the measured total reflectance, the ink reflectance and the paper reflectance as a function of the measured physical ink coverage. As described by Arney and coworkers, the effective ink and paper reflectances of a halftone patch depends on the ink coverage, [5]. As observed on Figure 2.31, the variation of the ink and paper reflectances compared to the reflectance of the bare paper and of the solid print is dependent on the halftone method and on the screen frequency. A stronger variation is observed when the halftone patch presents small dots. With smaller halftone dots, the distance between ink and paper is smaller and the optical dot gain is stronger. Hübler demonstrated that the ink coverage at which the optical dot gain is maximal was depending on the perimeter of the printed dots [341].

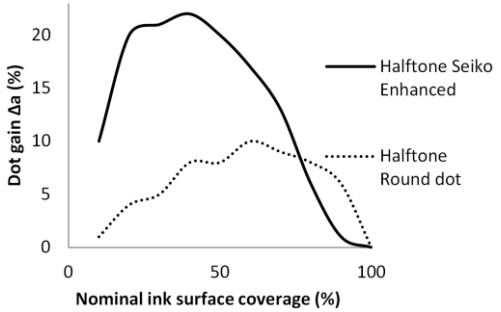

Figure 2.30: Dot gain as a function of the nominal ink coverage for 2 different halftoning methods: the Seiko enhanced and the round dot oriented at 0°. Printed by thermal transfer (Seiko professional ColorPoint 2, 300 dpi) and measured with densitometer (Xrite 414). Plotted from data presented by Wedin [231].

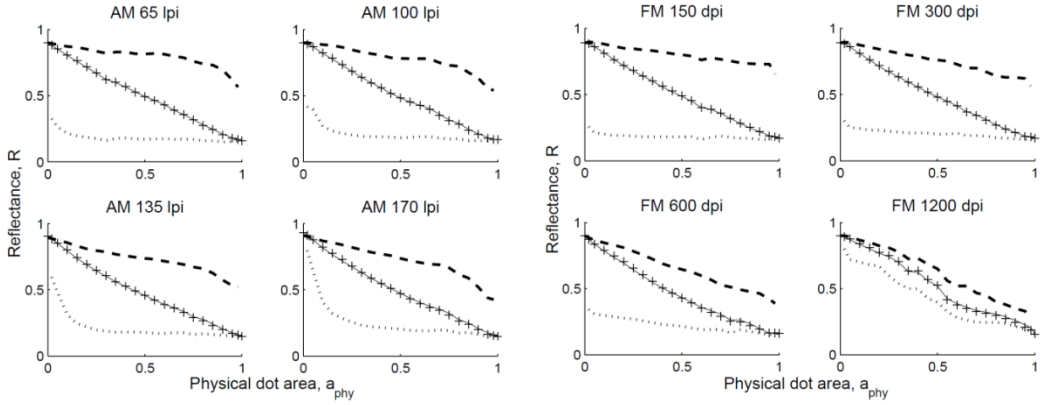

Figure 2.31: Ink, paper and halftone reflectances as a function of the effective ink coverage for AM and FM halftones with different halftone sizes. Ink reflectances are represented with dotted lines, paper reflectances are represented with dashed lines and mean reflectances are represented with the solid lines. The (+) lines represents the results of Nyström model. Reproduced from Nyström [19].

2.8.1.1 Halftone frequency influence

Yule, Howe and Altman studied the influence of the halftone frequency on the dot gain for offset prints. Figure 2.32 shows the evolution of the measured dot area (apparent ink coverage) comprising optical dot gain and physical dot gain as a function of the nominal ink coverage. The dot gain increases with the increase of the halftone frequency. At 50% nominal ink coverage the authors obtained 25% 16% and 9% dot gain for respectively the 266, 135 and 66 lpi halftone frequencies [16]. Nyström also observed the influence of the halftone frequency on the total dot gain. Nyström measurements of physical ink coverage allowed to separate the total dot gain from physical dot gain, allowing measuring the optical dot gain. The author showed that for frequency modulated halftoning,

the frequency increase was associated with an increase in optical dot gain and in physical dot gain. The physical dot gain is shown to be the most sensitive to the increase of the halftone frequency. As previously demonstrated by Yang [342], the optical dot gain loses its symmetry with the increase of the screen frequency. The maximum optical dot gain is then shifted toward lower ink coverage (20-25%), Figure 2.33 (A). Nyström proved that the asymmetry of optical dot gain was due to physical dot gain by plotting the deducted optical dot gain as a function of the measured physical dot gain, Figure 2.33 (B). On this graph, only the maximal value of optical dot gain depends on the halftone frequency, the position of these maxima are always centered at 50% physical ink coverage [19].

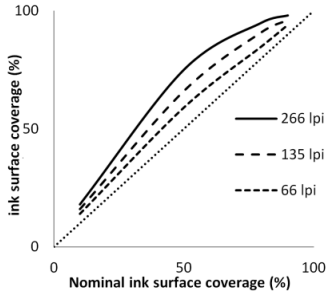

Figure 2.32: Apparent ink coverage as a function of the nominal ink coverage for 3 halftone frequencies on coated paper. In dotted line is the y=x curve representing no dot gain. Adapted from Yule, Howe and Altman [16].

2.8.2 Ink and paper impact

2.8.2.1 Inks influence

Yang measured total dot gain on inkjet prints with inks of different colors [342]. The author fitted then the measurements with his unified model including optical and physical dot gain. As demonstrated on Figure 2.34, the total dot gain depends on the ink. Moreover Yang's model suggests a symmetric optical dot gain with the axis of symmetry at 50% nominal ink coverage. On another hand, the physical dot gain shows an asymmetric behavior with maxima between 20% and 30% nominal ink coverage.

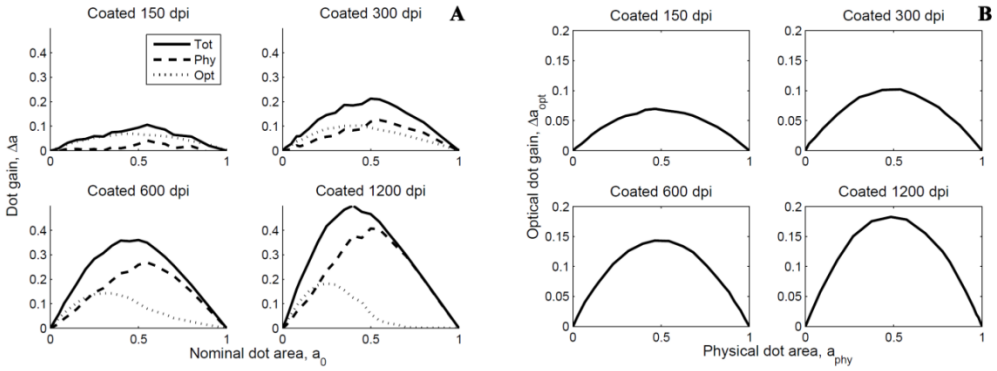

Figure 2.33: (A) Total, physical and optical dot gains as a function of the nominal ink coverage for FM halftones with different frequencies. (B) Optical dot gain as a function of the effective ink coverage measured for FM halftones with different frequencies. Reproduced from Nyström [19].

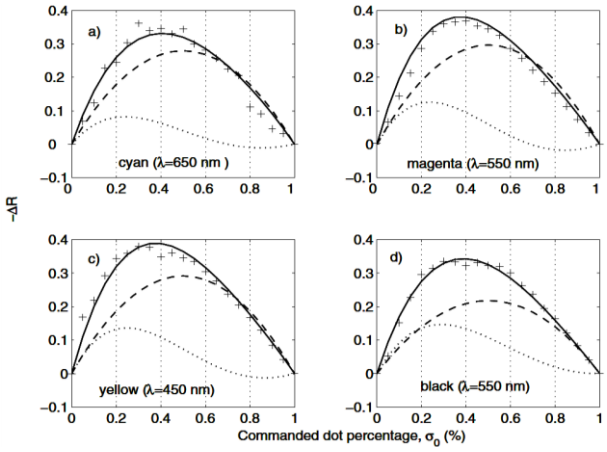

Figure 2.34: Total dot gain as a function of the nominal ink coverage for 4 inks. Measured total dot gain is represented by crosses, simulated total dot gain, optical and physical dot gain are represented respectively by solid line, dotted line and dashed line. Reproduction from Yang [342].

2.8.2.1 Paper influence

Optical and physical dot gains are sensitive to the paper on which the halftone pattern is printed. As presented by Yule, Howe and Altman [16] and adapted on Figure 2.35, uncoated papers are associated with higher total dot gain. Differences can also be observed for papers with different coating. This behavior is related, as highlighted by the authors, to the scattering properties of the substrate. High scattering will lead to small light path into paper before being reflected and thus is associated with reduced diffusion length. On the opposite, uncoated paper has a relative low refraction index and light path before reflection can be large. The diffusion length will therefore be larger [16].

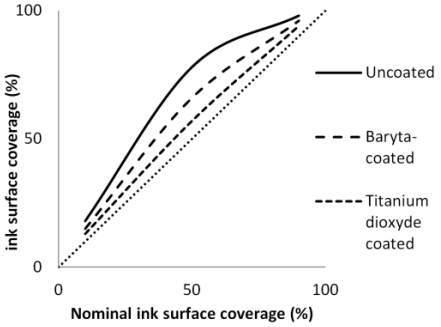

Figure 2.35: Apparent ink coverage as a function of the nominal ink coverage for 3 papers printed at 133 lpi. In dotted line is the y=x curve representing no dot gain. Adapted from Yule, Howe and Altman [16].

2.9 Conclusion

Printing and halftoning were developed as a mainstream support to share information in societies. The recent technological boom brought alternative ways of distributing the information, nevertheless printing remains an essential media in the modern societies. The currency is an example of the printing applications. Researches are conducted continuously to secure the printed money and multiple printed anti-counterfeit solutions are proposed. The most secured anti-counterfeit solutions rely on an accurate control and measurement of the printed ink dot morphologies. Similarly researches are conducted to improve the relation between the print process control and the resulting print perception obtained.

The literature study showed that models are progressively going from a macroscale description of the print to a microscale description. This change of scale allows scientists to better understand the print deformations on the halftone dots referred as the physical dot gain. Measuring the print at the microscale present multiple drawbacks and multiple measurements apparatus and methodologies are proposed. Most of measurement methods that demonstrated accurate results for halftone prints are based on optical microscopy measurements.

A central problem with optical measurements is the interactions between ink, paper and light. These interactions are responsible for the well-known phenomenon called optical dot gain. Multiple studies were conducted to understand the influence of optical dot gain on the print. Moreover, the parameters influencing the amount of optical dot gain were also studied. These studies are nevertheless difficult to consolidate objectively since different printing processes, printing parameters and paper types were used. The state of the art demonstrated that more accurate measurements of the halftone dots at the microscale could help understanding the relations between the dot morphology and the print parameters. Moreover, more accurate measurements of the halftone dots at the microscale could help improving the understanding of the ink, paper and light interactions, helping to characterize the dependencies and effects of optical dot gain.

The requirement of performing a large amount of measurements to obtain significant statistical results for multiple types of halftone configurations was also demonstrated from the state of the art. To our knowledge, no automated measurement of halftone dots at the microscale was developed. Developing an automated reliable measurement apparatus is then essential in order to obtain significant results.

Multiple image processing strategies were proposed to numerically separate the ink from the paper. Nevertheless, it appears that these image processing strategies were not evaluated. An evaluation could then help determining the best image processing strategies.

Following the technology development, multispectral microscale measurements are starting to be employed to obtain more accurate measurements of the halftone dots at the microscale. These improvements require redeveloping the measurements process and image treatments. A continuation of this state of the art could then focus on the solutions to integrate multispectral 3-dimensional captured images into the processing chain. The focus could then be turned toward the improvement of the measurement and processing time.

Chapter 3 Material and methods

Design of test forms, print and characterizations

Louis Vallat-Evrard, Lionel Chagas, Raphaël Passas, Nadège Reverdy-Bruas
Univ. Grenoble Alpes, CNRS, Grenoble INP*, LGP2, F-38000 Grenoble, France
Agefpi, LGP2, F-38000 Grenoble, France

3.1 Introduction

In the last century, multiple methods to measure the halftone dots have been developed. The first goal in this work is to develop a framework allowing a control of all aspects from the generation of the test form to the measurement of the halftone dots. The objective is, in fine, to obtain more accurate measurements of the halftone dots at the microscale, in order to characterize the spatial reflectances of the halftone dots surfaces. A detailed attention is brought on the control of the measure uncertainty and stability. The test forms are designed specifically in Python, allowing a free control of the designs. The methodology and the design of the experiment are presented in section 2. The control of the printing process is performed tuning the parameters available in the raster image processing (RIP) of each printing machine and is presented in section 3. The sample preparation after printing is also presented in section 3. A specific apparatus is developed in order to measure the halftone dots at the microscale. This apparatus is fully controlled using a graphical user interface developed specifically. The development of the apparatus as well as the presentation of the performances of the apparatus is proposed in section 4. One major drawback with optical measurements is the influence of optical dot gain in the measured images. A controversy was raised regarding the presence of optical dot gain when imaging halftone dots at the microscale in transmission mode. Effects of this measurement configuration are investigated and insights toward a novel measurement strategy are discussed in section 5. The test forms, prints and characterizations are analyzed for black ink on a white paper. Nevertheless the continuation of this work will be to extend these methods to color printing. For this purpose an automatic filter wheel is developed in order to perform multispectral high resolution halftone dots measurements, section 6.

3.2 Design of test forms

Test forms are generated in python using the Numpy extension handling multidimensional arrays. The test form is composed of 3 sets of experiments and of elements for visual inspection, ink demand compensation, ink variation controls, Figure 3.1. For each process, the test forms and added elements are re-generated in order to adapt to the native resolution of each printer.

3.2.1 Print characterization test forms

The first set of experiments is focused on the characterization of the print. It contains 2 halftoned grayscale bars with 14 different tones, Figure 3.1 markers (2) and (3). These two halftone bars originate from a single continuous tone grayscale bar generated in Python. A patch size of 10 mm by 10 mm is chosen and a grayscale value is determined as a function of a targeted area coverages

going from 5.00% to 95.00% and spaced by either 5.00% or 10.00%, Table 3.1. The continuous tones grayscale bar is encoded on 8 bits giving 256 different tone levels, Figure 3.2 (A). This encoding generates a tone error due to the limited amount of levels (quantization). The mean absolute error associated with the quantization is found at 0.11% +/- 0.08%. Each continuous tone patch is stacked with a border of black color of 0.2 mm width. The patches are assembled in an array. A halftoning of the continuous tones is then performed adopting the native resolution of the printer as the output image size (no resizing of the continuous tone image) with a halftone cell size of respectively 150 lpi (Line Per Inch) and 200 lpi. The halftoning is performed using Photoshop CS6 Bitmap function using a halftoning with circle cells, Figure 3.2 (B). The resulting patches are composed of halftone dots with ink coverages corresponding to the grayscale tones. The halftoning induces a further shift of the patches tones. For example by halftoning at 2540 dpi (Dot Per Inch) and 150 lpi, the halftone cell size corresponds to squares of 17 by 17 pixels, resulting in different 290 tones. On another side, the halftoning at 1200 dpi and 200 lpi would result in only 37 different tones addressable. The Photoshop halftone tint function introduces a variation of the dot sizes from adjacent cells allowing an increase of the amount of tones addressable. Ink coverage errors are nevertheless introduced and should be taken into account, Table 3.1. The largest absolute mean errors are found at a level of 0.15% +/- 0.10% for the grayscale bar at 1440 dpi and 200 lpi. Average errors for other configurations are found smaller around 0.11%. Over all halftoning configurations the targeted tones of 30.00% and 50.00% are the most impacted by errors with average absolute errors of respectively 0.24% +/-0.11% and 0.24% +/- 0.14%. These errors remain small compared to the ink coverages and should not influence significantly the results.

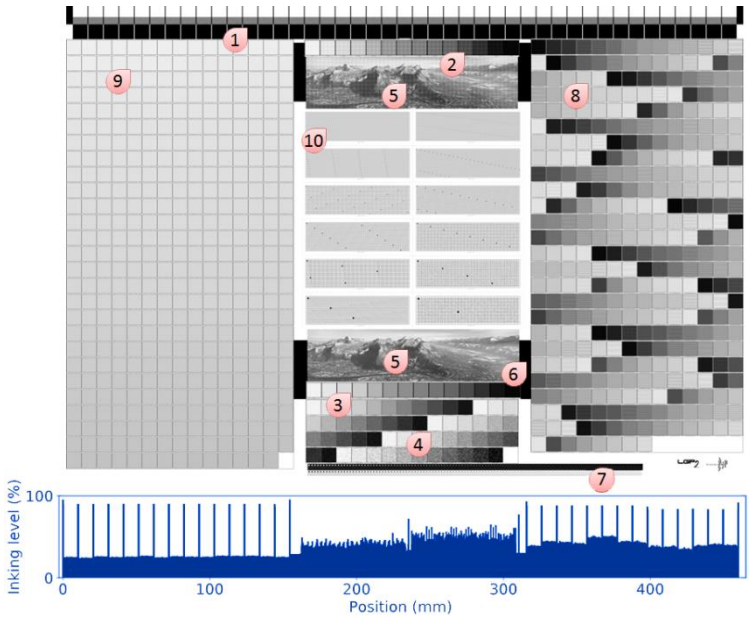

Figure 3.1: Test form. Red bubbles show the different experiments. Inking level graph represented in blue color.

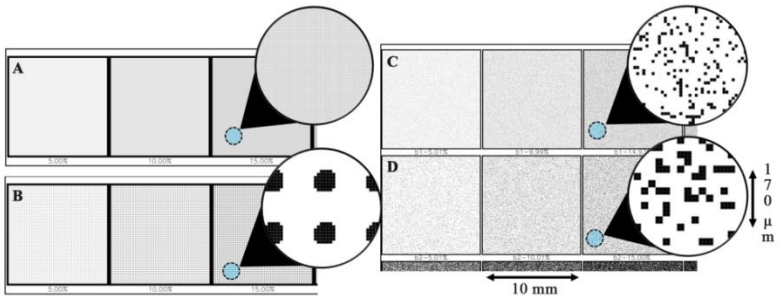

Figure 3.2: Grayscale bar test forms - (A) 8-bits continuous tones (B) Halftoned (2540 dpi, 150 lpi), (C) Random dots at native resolution of the printer and (D) Random dots with a binning of 2 (1270 dpi).

Table 3.1: Tones and ink coverages as a function of the bit quantization, of the halftone parameters and of the printer native resolution.

Tone target (%)	Tone bit quantization (%)	Coverage 2540 dpi 150 lpi (%)	Coverage 2540 dpi 200 lpi (%)	Coverage 1440 dpi 150 lpi (%)	Coverage 1440 dpi 200 lpi (%)	Coverage 1200 dpi 150 lpi (%)	Coverage 1200 dpi 200 lpi (%)
5.00	5.10	5.19	5.03	5.00	5.10	5.08	5.21
10.00	10.20	10.04	10.06	10.25	10.20	10.16	10.07
15.00	14.90	14.88	14.79	15.00	14.80	14.84	14.93
20.00	20.00	20.07	20.12	20.00	19.90	19.92	20.14
30.00	29.80	29.76	29.88	29.75	29.59	29.69	29.86
40.00	40.00	40.14	39.94	40.00	39.80	39.84	39.93
45.00	45.10	44.98	44.97	45.00	44.90	44.92	45.14
50.00	49.80	49.83	49.70	49.75	50.00	49.61	49.65
55.00	54.90	55.02	55.03	55.00	55.10	55.08	54.86
60.00	60.00	59.86	60.06	60.00	60.20	60.16	60.07
70.00	69.80	69.90	69.82	69.75	69.90	69.92	69.79
80.00	80.00	79.93	79.88	80.00	80.10	80.08	79.86
90.00	89.80	89.97	89.94	89.75	89.80	89.84	89.93
95.00	94.90	94.81	94.97	95.00	94.90	94.92	94.79

The first set of experiments also includes grayscale bars composed of different ink coverage obtained by random disposition of dots. Ink coverages from 5.00% to 90.00% with a step of 5.00% to 10.00% are generated for multiple binning, Figure 3.2 (C & D). The binning corresponds to the size of the nominal dot compared to the native resolution of the printer. For example for inkjet, the print resolution is 1440 dpi (corresponding to a width of 17.6 µm), a binning of 2 will result in a dot size of 720 dpi (corresponding to a width of 35.3 µm). The patches are generated using Python and Numpy. Each halftone patch is designed to measure 10 mm. A random value between 0 and 100 is attributed for each addressable position on the patch. A threshold is then applied on the patch to obtain the targeted surface coverage. In the case of a targeted 30% ink coverage, the pixel locations with values superior to 30 are filled with ones and the pixels location with values below or equal to 30 are filled with zeros. Borders of 0.1 mm are applied around the patch and patches are concatenated together. When a grayscale bar with a binning superior to 1 is generated, a similar process is applied. An additional step is required and corresponds to the binning process. In the case of a binning of 2 for example, pixels are duplicated one time in the x direction. The pixels are then duplicated one time in the y direction. The generated image will be at the resolution of the printer and each dot will be composed of 4 pixels (4 dots at the native resolution of the printer). Grayscale bars with random dots are generated at binnings of 1, 2, 3, 4 and 8, Figure 3.1, marker (4).

Superformula[343]

[3.1] $$\frac{1}{r} = \sqrt[e_2]{\left|\frac{1}{e_5}cos\left(\frac{e_1}{4}\theta\right)\right|^{e_3} + \left|\frac{1}{e_6}sin\left(\frac{e_1}{4}\theta\right)\right|^{e_4}}$$

Symbol	Unit	Denomination
r	1	Radius
θ	°	Angle
e_1	1	Real number
e_2	1	Real number
e_3	1	Real number
e_4	1	Real number
e_5	1	Real number excluding 0
e_6	1	Real number excluding 0

3.2.2 Optical dot gain characterization test forms

The second set of experiments is designed to characterize the relations between the halftone dots and the optical and physical dot gain. The second set is divided in two experiments. The first experiment is a set of 358 patches where the size of the halftone dots and the spacing between the halftone dots are changed, Figure 3.1, marker (8). In order to generate the halftone dots the Superformula developed by J.Gielis [343] is used, equation [3.1]. This formula allows obtaining a wide range of particle shapes by choosing carefully the parameters ($e_1, e_2, e_3, e_4, e_5, e_6$). Thus, circle dots, triangle dots with angles of 0°, 45° and 90°, square dots with angles of 0°, 45° and 90°, pentagon dots and hexagon dots at angles of 0°, 45° and 90° are generated, Figure 3.3. Moreover these dots are generated at different diameters of 5 pixels, 9 pixels and 17 pixels, giving sizes of respectively 50 µm, 90 µm and 170 µm for dots printed with offset, 88 µm, 159 µm and 300 µm for dots printed with inkjet and 106 µm, 191 µm and 360 µm for dots printed with electrophotography. These dots are placed with several different spacing distances in patches. A honeycomb configuration is adopted to conserve similar distances between dots in different directions. For example, for circle dots with a diameter of 17 pixels, a patch is produced for each of the dot spacing of: 1, 2, 3, 4, 5, 6, 8, 10, 11, 13, 14, 16, 20, 24, 32 pixels. For dots with different shapes, different combinations of distances are chosen in order to represent accurately the range of ink coverages, Figure 3.3. The second experiment of this set is designed to explore the optical dot gain effects of the perimeter of the halftone dots with constant area, Figure 3.1, marker (9). 200000 dot shapes have been generated by variating the parameters of the Superformula: e_1 from 0.00 to 6.00 with a step of 0.25, e_2 from 0.10 to 3.85 with a step of 0.25, e_3 from 0.00 to 2.25 with a step of 0.25, e_4 from 0.00 to 2.25 with a step of 0.25, e_5=1.00, e_6 from 0.50 to 2.50 with a step of 0.50. The area and perimeter are computed by connected component analysis (OpenCV). Halftone dots with similar areas and with multiple different perimeters are selected. Patches are then generated using the selected halftone dots with a constant spacing between the dots of 12 pixels. For both experiments, the halftone dots are generated by executing scripts written in Python with Numpy and OpenCV extensions. All patches are labelled and borders of 0.10 mm are generated.

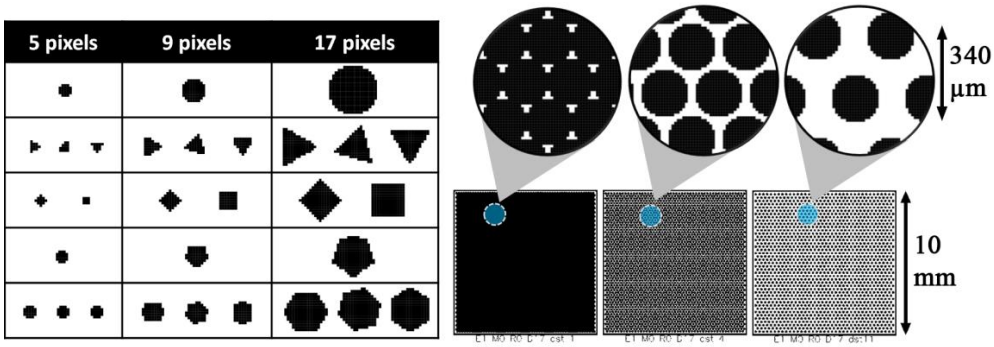

Figure 3.3: Shape of the halftone dots generated with different parameters inputted in the Superformula. Halftone dots placed in patches with several spacing distances (from left to right: 10 µm, 40 µm and 110 µm).

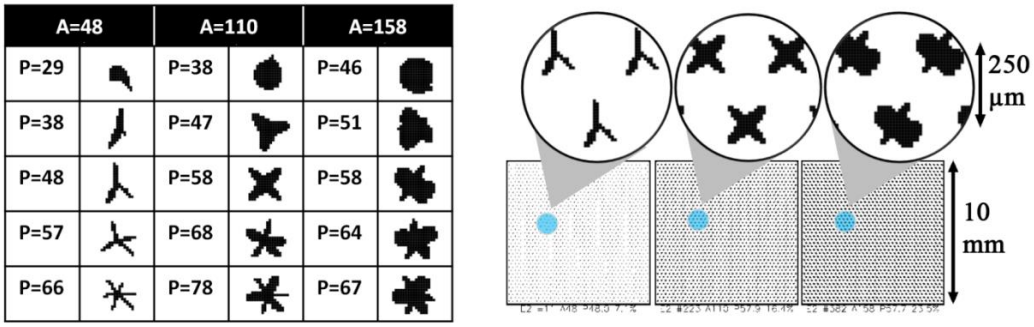

Figure 3.4: Example of halftone dots of area A and with different perimeters P. Halftone dots placed in patches.

3.2.3 Physical dot characterization test forms

The third set of experiments aims at evaluating the physical dot gain for the three print processes, Figure 3.1, marker (10). The first experiment of this set is composed of a large array with stacks of patches, Figure 3.5 (A). A patch is composed of a matrix of 3 pixels by 3 pixels at the center, 4 pixels white margins around and 1 pixel black borders. By generating all the inking configurations of the 3 by 3 matrix, 512 inking configurations are obtained. The interactions between printed dots can then be studied. The shape of the dot varies due to random variations in the print process. For this reason the 512 inking configurations are reproduced multiple times. Each redundancy is separated by a patch inked over its entire surface. Borders and markings are added to the large array of patches. The array allows registering and retrieving the location of each patch after printing. These arrays are produced at the native resolution of the printer with different binnings. A patch designed for the offset printing, at the resolution of 2540 dpi with a binning of 1 will have an effective resolution of 2540 lpi and will therefore measure 130 µm. A similar patch with a binning of 6 will have an effective resolution of 423 lpi and will therefore measure 780 µm, Figure 3.5. In the case of a binning of 6, all pixels at the effective resolution will be composed of 36 pixels (6 by 6 pixels) at the native resolution of the printer. The second experiment is similar to the first, with the difference that a 5 by 5 matrix is used, Figure 3.5 (B). Since the amount of the inking configurations in the 5 by 5 matrix is large with more than $3x10^7$ configurations, the generation of the configurations is performed randomly. This inking generation results in highly complex shapes, allowing characterizing precisely the print performances and the physical dot gains.

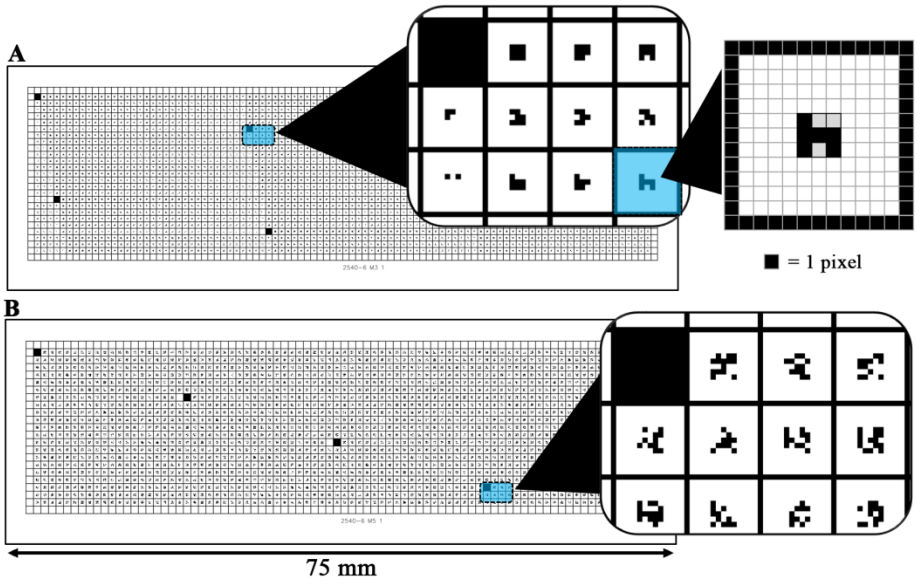

Figure 3.5: Test form with 3 by 3 matrix (A) and 5 by 5 matrix (B). Each matrix is placed in a patch having white margins and black borders. Patches are stacked together in a large array corresponding to the size of a microscope slide. The black patch corresponds to the beginning of the series of patches.

Additional elements are added to the test form:

- A bar covering the total width of printing composed of full tone patches, 50% ink coverages patches and bare paper patches, providing a reference to measure the inking and paper variations along the width of the paper, Figure 3.1, marker (1).
- Full tone rectangles to distribute more evenly the ink demand, Figure 3.1 marker (6).
- Two images (150 lpi and 200 lpi, Photoshop CS6 Bitmap function using halftone tints with circle cells) to evaluate the print visually, Figure 3.1 marker (5).
- Black and white single dots with different diameters to evaluate visually the ability of the printer to reproduce fine details, Figure 3.1 marker (7).

3.3 Print setup and sample preparation

3.3.1 Print processes

The test forms are printed with 3 print processes: offset, inkjet and electrophotography, Table 3.2. For each printer a specific protocol is developed in order to optimize the printing conditions. The binary test forms are merged with Photoshop CS6, saved in 1 bit .tif image format.

For offset, the image obtained measures 46000 pixels by 32000 pixels which gives, at the printer resolution of 2540 dpi, a printed size of 460 mm by 320 mm. The file is sent to a computer to plate, Heidelberg Prosetter P52. Kodak Libra VP photopolymer digital plates are used. The computer to plate can produce 645 mm by 525 mm images on plates. A 30 mW laser in the violet range of 405 nm is used to expose the photosensitive plate. Resolution of the computer to plate is fixed to 2540 dpi but could be extended to 3386 dpi with a theoretical repeatability of +/- 5 µm (5080 dpi) relative to the punch position and +/-25 µm (1016 dpi) relative to the edge of the plate. The plates used are negative photopolymer digital plates based on electrochemically grained and anodized aluminum. The spectral sensitivity of the plate is centered at 405 nm and a laser energy of 30 to 50 µJ/cm² is required. The resolution achieved is announced with a minimum of 2% at 200 lpi giving halftone dots of 18 µm of diameter (1414 dpi). Plates are mounted on a Heidelberg Speedmaster SM 52-1 offset press. The press has 18 rollers for the inking unit and 16 inking zones. The dampening system is a Alcolor continuous-type dampening with 5 cylinders. The maximum dimension of paper handled by the printing press is 370 mm by 520 mm. The press is set according to ISO 12647-2. A conventional Novavit 918 supreme black ink is used.

For inkjet an Epson Stylus Pro 4900 digital printer is used. This printer allows a maximum resolution of 2880 dpi by 1440 dpi. The print head is composed of 10 channels and of 360 Micro Piezo advanced TFP nozzles. The printer carries 11 cartridges including 4 different black inks (photo black, matte black, light black, light-light black), 3 conventional color inks (cyan, vivid magenta, yellow), 2 extra color inks (orange, green) and two light color inks (light cyan, vivid light magenta). The printer can print paper formats up to 420 mm by 594 mm. The binary test forms generated at 1440 dpi are merged in 3 different images to adapt to a paper size of 210 mm by 297 mm (A4 format). Three raster image processors (RIP) are tested to feed data to the Epson Stylus Pro 4900. The first RIP tested is the Epson Stylus Pro 4900 proprietary driver. The file is fed to the driver through the Windows photo viewer software using the print function. The options proposed in the print function of the Windows photo viewer are set according to Epson's recommendations: deselect fit picture to frame and deselect activate sharpen for printing. The choice of the media type in the RIP influenced the printing. For example by selecting "Standard Proof paper (240)", the printer is printing with all colors. By selecting "Singleweight Matte paper" only the matte black ink is printed. The maximal RIP resolution selectable depends also on the choice of media. Thus, the maximal resolution when printing with "Singleweight Matte paper (line drawing)" is 1440 dpi by 1440 dpi. It is interesting to note that the Epson proprietary driver allows selecting a gamma of either 1.8 or 2.2 in the color options. The gamma level influences also the results of the printing. The second RIP tested is the GMG ColorProof. This RIP behaves similarly to the Epson proprietary driver. The third RIP tested is the Wasatch SoftRIP SP. This RIP is designed to produce print forms for screen printing, flexography and lithography. Thus, the test forms can be printed with a single ink (i.e. photo black or matte black ink) at the resolution of 1440 dpi by 1440 dpi. An option allows selecting the volume of the droplets (3.5 pL or 5.2 pL) ejected. The volume of each droplet influences the print result. Best performances are found for 3.5 pL droplets. The Wasatch RIP is associated with the smallest distortion from the test form to print result and is then used in this work.

For electrophotography, two machines and associated RIP are used as a consequence of the implementation of the printing fleet of the lab. The first press is a Ricoh Aficio C2800 equipped with a dry electrostatic toner transfer system and with dual components magnetic brushes. A resolution of 1200 dpi by 1200 dpi is achieved with Ricoh proprietary RIP driver and Adobe Postscript 3 extension. The Ricoh Aficio C2800 press handles up to 297 mm by 420 mm paper sheets. The binary test form is sent directly to the printer with the print function of Windows picture viewer. The printer RIP driver allows setting a dot compensation and a gamma level. The best printing parameters are found with the dot compensation activated and a gamma of 1.8. The second electrophotography press is a Xerox Versant 180. This machine has a resolution 2400 dpi by 2400 dpi. However a maximum render of 1200 dpi by 1200 dpi is announced by the manufacturer. The maximum paper size is 330 mm by 660 mm. The machine is equipped with a dry electrostatic toner transfer system with uniform low temperature setting toner particles. Xerox FreeFlow Print Server is associated with the press. Xerox FreeFlow Print Server requires selecting the type of halftoning. When imputing a .tif file, a stochastic halftone of resolution of maximum 600 dpi can be accessed. It could not be determined if the RIP was performing a halftoning with binary .tif files. Multiple print settings (halftoning method, line thickness), test form resolutions (600 dpi and 1200 dpi) and file formats (.pdf, .eps, .jpeg) are analyzed and the .tif file format with a resolution of 1200 dpi gives the best results.

Table 3.2: Printing processes, resolutions and inks.

Printing process	Resolution	Dot size	Ink (Black)
Offset: Heidelberg Speedmaster 52	2540 dpi	10.0 µm²	Novavit 918 supreme
Inkjet: Epson Stylus Pro 4900	1440 dpi	17.6 µm²	Epson PK T6531, MK T6538
Electrophotography: Ricoh Aficio C2800	1200 dpi	21.2 µm²	Ricoh MP C3000 Black
Electrophotography: Xerox Versant 180	1200 dpi	21.2 µm²	Xerox Versant 80 black

3.3.2 Sample preparation

Once printed the test forms are cut and placed on a microscope slice. The following protocol is systematically applied: a double face (Tesa, “Fixer sols, Double-face fort”, ref 56138, white) is applied on a microscope slide of 76 by 26 mm. The tape is laminated by hand with a spatula. Extra caution is applied to prevent air bubbles between the glass and the adhesive. The test form is cut on a Teflon board with a sharp razor blade. The test form is then laminated on the top of the slide. The lamination is performed without applying a shear force on the surface of the test form to prevent generating damages to the print. The slide is then placed between two microscope slides under vacuum to remove potential small air bubbles.

3.3.3 Ink and paper characterization

Four papers are used for printing: two glossy coated papers, one inkjet proofing paper and one uncoated paper including mineral fillers, Table 3.3. The two coated paper are associated with the smallest basis weight and thickness respectively 139 g/m² and 98 µm. The uncoated paper is slightly heavier with 169 g/m² and is thicker with 159 µm. The roughness of the coated papers is smaller than the uncoated paper with 214 nm compared to 1150 nm. The Epson paper is different and includes a coated layer for high quality inkjet printing. The basis weight and thicknesses reach 242 g/m² and 220 µm. The surface roughness is found at 513 nm, however the top coated layer is transparent yielding to inaccurate measurements with the Alicona infinite focus. Scanning electron microscopy (SEM) allows visualizing the surface morphology of the papers. The two coated papers Figure 3.6 (A, B) present a layer with mineral particles and bounding agents covering totally the cellulose fibers. The two coated papers present particles with similar sizes and organization. The surface presents small holes. The surface of the Glossy 2 paper is slightly less open than for the Glossy 1 paper. The surface of the Epson paper, Figure 3.6 (C) presents extremely small particles on its surface compared to the two coated papers. This confirms that the roughness measurement with the Alicona is inaccurate due to the transparency of the layer. The uncoated paper, Figure 3.6 (D), differs, presenting apparent

cellulose fibers and mineral fillers. The surface roughness is therefore more pronounced. It has to be noted that the SEM image is less magnified for this paper.

The apparatuses used for the characterization are: an EFI Quanta 200 environmental scanning electron microscope, a spectrophotometer Techkon SpectroDens B104052, with polarized filter and ISO E density filter and a 3D optical profilometer Alicona Infinite focus.

Table 3.3: Papers characterization.

Papers	**Glossy 1**	**Glossy 2**	**Epson**	**Uncoated**
Supplier	Unknown	Mondi	Epson	Inapa
Commercial name	-	Color Copy	Proofing	Tecno colour laser
Type	Coated glossy	Coated glossy	Coated for inkjet	Mineral fillers
Basis weight (g/m²)	138.0 +/- 1.2	140.1 +/- 1.3	242.1 +/- 2.1	168.7 +/- 0.8
Thickness (µm)	90.9 +/- 1.0	104.2 +/- 1.1	219.7 +/- 0.8	158.5 +/- 1.2
Surface roughness (nm)	220.8 +/- 36.2	206.4 +/- 18.7	513.1 +/- 44.2	1149.3 +/- 55.0
Opacity (ISO 2471:2008)	95.65 +/- 0.20	95.60 +/- 0.08	95.41 +/- 0.10	98.96 +/- 0.25
Brightness R457 (ISO 2470:2009)	87.55 +/- 0.21	92.05 +/- 0.24	87.68 +/- 0.11	97.72 +/- 0.27

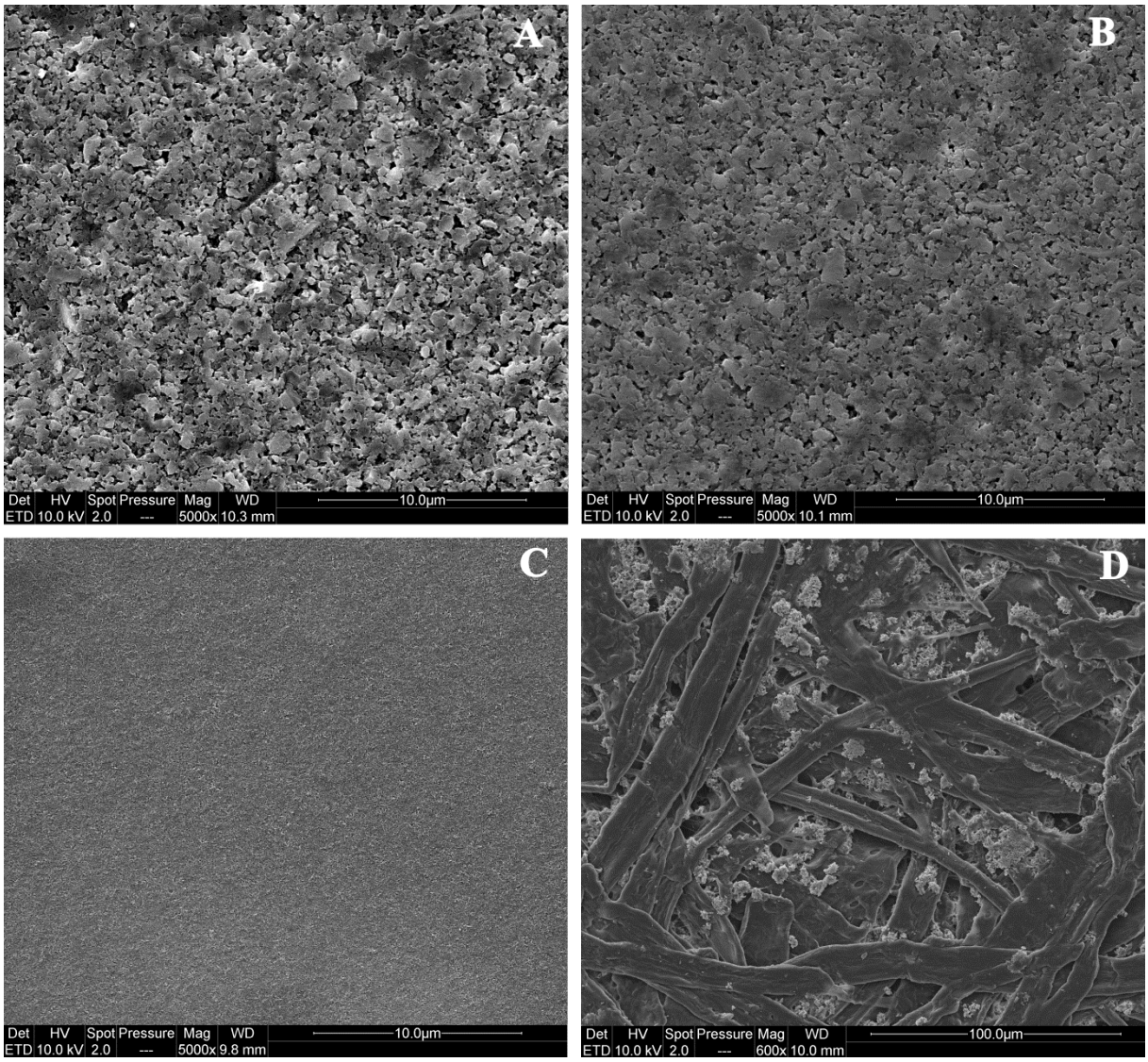

Figure 3.6: SEM images of the four tested papers: (A) Glossy 1, (B) Glossy 2, (C) Epson, (D) Uncoated. Image magnification for (D) differs from (A, B, C).

Scanning electron microscope (SEM) images are employed to analyze the morphology of the ink layer. For the offset print, Figure 3.7 (A) the ink layer is thin, following the topology variations of the coating layer. Small rounded particles are observed in the ink layer. The limit between the ink layer and the paper is well defined and ink layer defects can be observed on the surface of the print. For the electrophotography, Figure 3.7 (B) the ink layer is thicker and covers totally the coated surface of the paper. The ink layer is more homogeneous than for the offset print. Bounding of the toner with the coating is visible with a penetration on the surface of the coating layer. For the two inks printed in Inkjet, Figure 3.7 (C, D) no change of the surface morphology is observed. This is coherent with the fact that the coating layer absorbs and captures the ink. Contrast differences appear between the two inks, however on conclusion can be drawn since the observation conditions had to be adapted (contrast and brightness). A difference also appears with the presence of cracks near the superposition of two droplets for the ink matte black ink. For both inks, the ink layer is homogeneous on the surface.

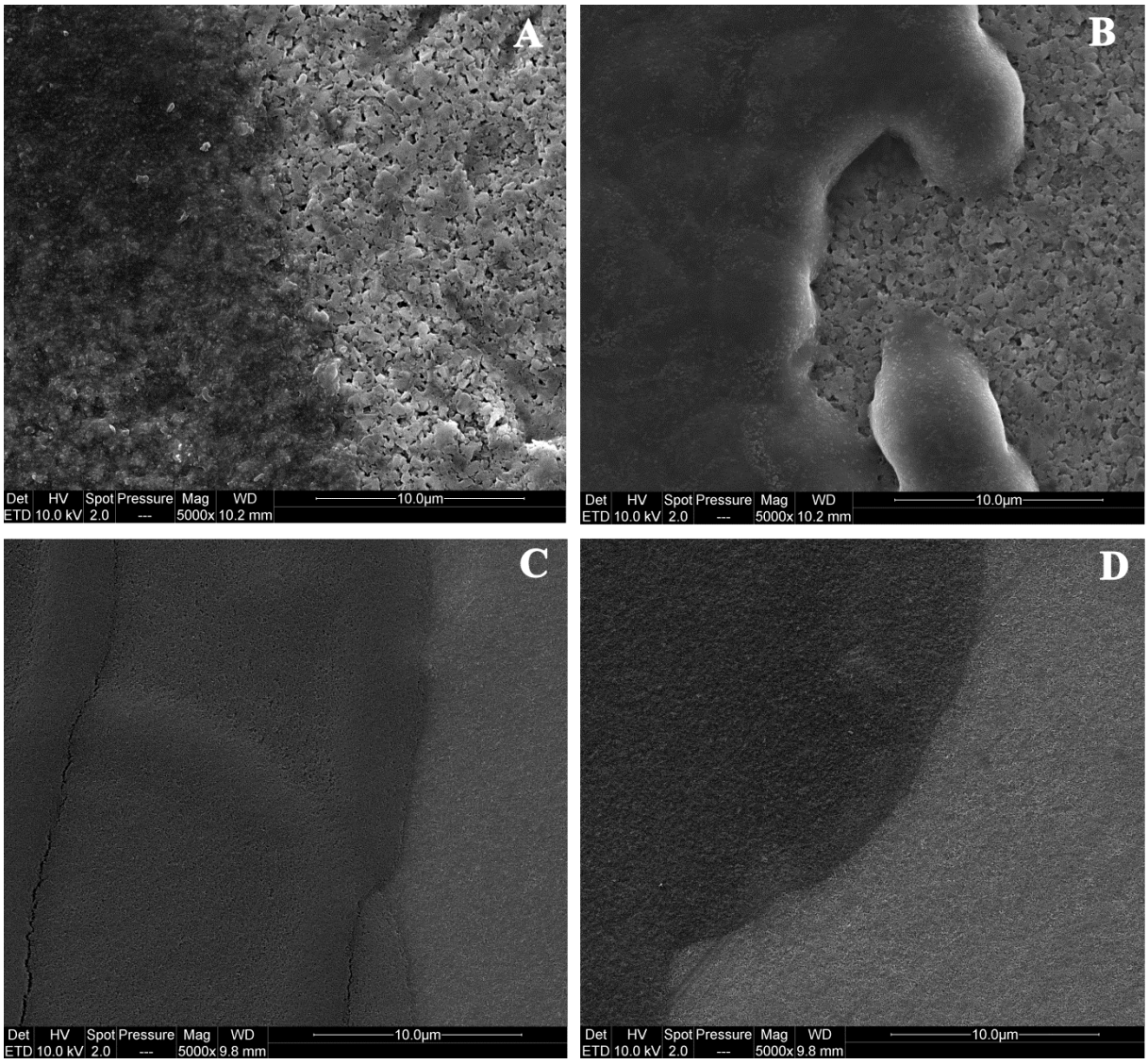

Figure 3.7: SEM images of the four printed inks: (A) Offset Novavit 918 supreme on Glossy 1 paper, (B) Xerox Versant 80 black on Glossy 1 paper, (C) Epson MK T6538 on Epson paper, (D) Epson PK T6531 on Epson paper.

3.4 High resolution optical measurement of halftone dots

3.4.1 Optical microscope

Multiple measurement apparatuses to characterize halftone dots at the microscale have been presented in chapter 2. An apparatus with improved resolution is developed for this study. Optical microscopy is the most straightforward measurement type for halftone dots printed on paper. Thus, a Zeiss Axio Imager M1m optical microscope mounted with EC Epiplan Neofluar objectives, is adopted, Figure 3.8. The microscope is mounted with 3 objectives: 5x/0.13 HD DIC, a 10x/0.25 HD DIC and a 20x/0.50 HD DIC. These objectives are color corrected (Zeiss Infinity Color Corrected System) and ensure that no geometric aberrations occurs (flatness correction). The field of view diameter reaches 5 mm for the 5x, 2.5 mm for the 10x and 1.25 mm for the 20x. The transmittance curves of the 3 objectives show a plateau from 400 nm to 700 nm with transmittance larger than 90%. Between 700 nm and 800 nm transmittances decrease for the 3 objectives going from transmittances superior 90% to transmittances superior to 80%. The Numerical aperture is different for the 3 objective giving different optical resolutions. According to the Abbe limit [344], at a mean wavelength of 550 nm, the 5x objective can resolve distances between objects larger than 2.1 µm, the 10x objective can resolve 1.1 µm and the 20x objective can resolve 0.6 µm. The Zeiss Axio Imager M1m coupled with these objectives allows different illumination modes: transmitted or reflected light, brightfield, darkfield and polarized light.

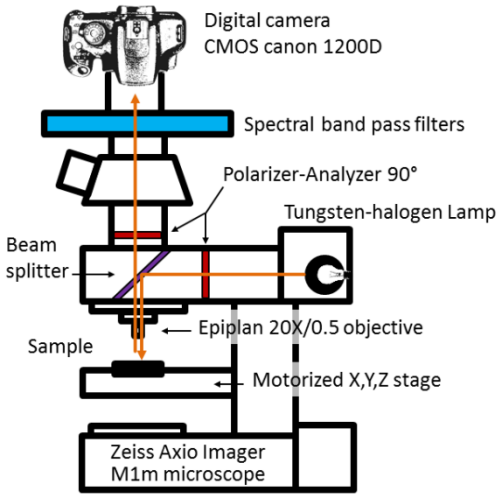

Figure 3.8: Diagram of the microscope and the digital camera with the illuminant path configuration.

3.4.2 Illuminant

A Zeiss HAL 100 tungsten-halogen lamp is used. The lamp is powered by a highly stabilized DC source. The voltage can be tuned from 0 to 12 V. Low voltage tends to produce a spectrum shifting toward large wavelength (toward 800 nm). The relative radiant flux per unit area increase of the source is not linear with the voltage increase but is rather associated with an exponential increase, Figure 3.9 (A). This can be explained by the fact that the radiant flux per unit area is defined according to the standard sensitivity of the human eye (CIE photopic luminosity function [345]) having a shape close to a Gaussian function with a center around 550 nm and a full width at half maximum of approximately 100 nm. For low tensions, the lamp filament is cooler with only a small portion of the radiated energy in the CIE sensitivity function and a large portion in the infrared region. With the increase of the tension the maximum of radiated energy shift toward smaller wavelengths. For optical imaging of halftone at the microscale, high irradiance is required and a source tension of 10.0 V is adopted. The illuminant with a source at 10.0 V has a spectrum close to a standard illuminant of type

A, Figure 3.9 (B). A blue filter is placed to correct the illuminant and obtain a spectrum close to the standard D65. The standard illuminant D65 provides a more constant irradiance over the spectrum, Figure 3.9 (A) and Table 3.4. It has to be noted that the radiant flux sensor (Voltcraft MS-1300) is given was modified to fit at the object plane of the microscope and the sensor calibration was lost. Values are then considered relatively. The objective does not influence significantly the level of radiant flux of the illuminant. Spectra for the 3 objectives superpose showing that the objectives transmit similarly the light, Figure 3.9 (C). For the 3 objectives, 9 measurements are performed and demonstrated small variations with mean standard deviations over the spectrum of respectively 0.01, 0.04 and 0.16 for the 20x, 10x and 5x objectives. Finally, density filters can be placed in the light path and reduce the radiant flux of the illuminant without altering its spectrum, Figure 3.9 (D). The relative spectral radiant flux is reduced from 27.22 to 5.66 and to 0.79 going respectively from the density filters N° 1 to N° 2 and to N° 3. The analyzer and polarizer alter slightly the illuminant spectrum but do not change the global tendency of the spectrum, Figure 3.9 (D). The analyzer and polarizer decrease significantly the relative spectral radiant flux with 203.36 at first, 66.93 with the polarizer and 27.38 with analyzer and polarizer. Nevertheless polarizer and analyzer are essential to perform an imaging of the halftone dots at the microscale with a 0°/0° geometry excluding specular surface reflections [17] (crossed polarizer and analyzer). To characterize the illuminant a spectrophotometer Eye One Pro 2 measuring in the 370 nm to 700 nm range with a sampling of 3.5 nm was used. The spectral resolution of this instrument is 10 nm. The measuring aperture measures 4.5 mm. The spectrophotometer was used with the software HCFR 3.5.1.4 to retrieve the spectrum and measurements were performed in monitor mode (to measure emitted light).

Table 3.4: Mean relative spectral radiant flux measured on the surface plane of the camera sensor with different illuminant conditions on the microscope.

	20x	**20x+Blue filter**	**10x+Blue filter**	**5x+Blue filter**	**Density filter 1**	**Density filter 2**	**Density filter 3**	**No analyzer**	**No analyzer No polarizer**
Mean relative spectral radiant flux ( )	27.38 +/- 0.11	5.48 +/- 0.01	5.58 +/- 0.04	5.06 +/- 0.16	27.22	5.66	0.79	66.93	203.36

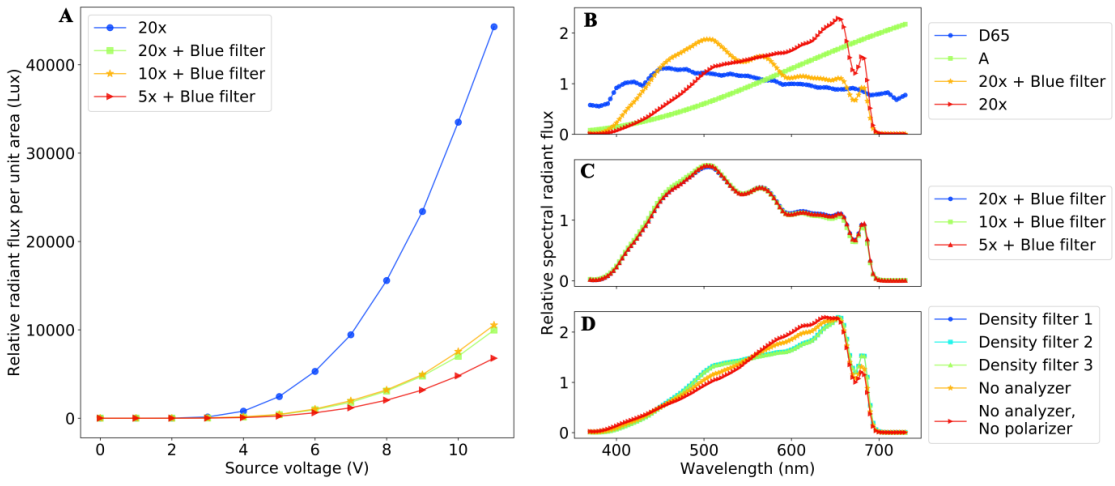

Figure 3.9: (A) Relative radiant flux per unit area as a function of the source voltage. (B, C, D) Spectrum measured on the surface plane of the camera with different illuminant conditions - (B) 20x objective, source 10.0 V, density filter 1, polarizer and analyzer, with or without blue filter; A and D65 are standard illuminants, (C) source 10.0 V, density filter 1, blue filter, polarizer and analyzer and 5x, 10x and 20x objectives and (D) 20x objective, source 10.0 V, without blue filter, density filters 1, 2, 3 and without analyzer, without polarizer and analyzer. Spectra are normalized.

3.4.3 Microscope stage

The microscope is equipped with a motorized X, Y, Z stage. The X and Y motorized axis allow controlling the displacement of the samples to perform multiple image acquisition (tiles acquisitions) and reconstruct an image larger than the optical field of view. The motorized Z displacement of the stage allows controlling precisely the focus on the microscope and allows performing autofocus. The stage used has a displacement of 75 mm on the X axis and 50 mm on the Y axis. These displacements allow covering the entire surface of the microscope slides. The precision for the X and Y and the Z axis differs. The displacement resolution reaches 0.1 µm for the X and Y axis with a reproducibility of +/- 1 µm and an absolute accuracy of +/- 5 µm. It has to be noted that the nominal halftone dot at 2540 dpi has a diameter of 10 µm. The resolution and reproducibility of the microscope stage are then compatible with imaging of a single dot at the maximum printed resolution employed in this study. The microscope stage can be move on the Z axis with a resolution of 25 nm and a reproducibility of +/- 75 nm.

3.4.4 Camera

A commercial reflex camera, Canon 1200D, RGGB CMOS sensor is used to image the halftone dots. Other studies have adopted commercial photo camera for scientific applications, [346–348]. The choice for this camera was made based on the possibility:

- to control remotely the camera through a USB protocol
- to capture and save the images in raw mode (Canon .CR2 format) preventing from automatic processing of the image (interpolation, white balance, exposition and gamma compensation)
- to capture multiple halftone dots simultaneously with high resolution (large sensor size APS-C)

The Canon 1200D has a CMOS sensor of 22.3 mm by 14.9 mm with 18.7 million of pixels (5344 pixels by 3516 pixels, retrieved from metadata of raw captures) and with a quantization on 14 bits. The pixel size reaches 4.21 µm by 4.21 µm. The effective amount of pixels (pixels used for imaging) is equal to 17.9 million of pixels with images of 5184 pixels by 3456 pixels.

3.4.4.1 Removing the Bayer filter

One major drawback of this sensor is that it includes a Bayer filter (array of color filters required to capture color images). The Canon 1200D is then transformed to monochromatic by removing the Bayer filter. This transformation allows obtaining a sensor more sensitive to light and also to exploit the full resolution of the sensor without the need of interpolation. Moreover the reconstruction of the spectrum is simplified when measuring with the band pass filters. The transformation is performed adapting the techniques given in the Stargazers Lounge astronomy forum [349]. First the camera is disassembled in order to extract the CMOS sensor, Figure 3.10 (A, B). The IR-blocking filter is then disassembled from the sensor. The front sealed glass cover of the sensor is removed with a milling machine. This operation is delicate since extremely small wires connect the silicon chip to the printed circuit board. These wires are then protected by casting an epoxy resin between the edge of the sensor frame and the edge of the silicon chip, Figure 3.10 (C). The array of color filters (Bayer array) is located directly on the surface of the silicon chip. On the top of the Bayer array, an array of microlens is superposed in order to collected light on the entire surface of the pixel. Unfortunately, to remove the Bayer layer, the array of photodiodes has also to be removed. These operations are performed by pealing mechanically the two layers. A wooden micro scraper is used for the first pass. Then the sensor is polished using a kit to restore automobile headlights (“Auto Pratic Kit Rénovation Optiques de Phares”) and cotton swabs. The sensor is then cleaned with a Zeiss lens cleaning solution and the IR-blocking filter is remounted in front of the sensor, sealing back the sensor, Figure 3.10 (D). The Bayer filter is still partially visible on the edges of the sensor in regions covered by the epoxy resin.

The camera is reassembled and an image is captured mounting the camera on the microscope and placing a mirror in the object plane. From this image the regions without Bayer filters are observed, Figure 3.10 (E). The image of the mirror (white frame) shows a homogeneous frame with a constant illumination, Figure 3.10 (F). Two row of pixels and two columns of pixels have been permanently damaged in the operation. An interpolation is then performed for these dead pixels. Cropping on the side of the sensor is necessary to remove regions where the Bayer filter remains. After cropping, the image size reaches 4600 pixels by 3000 pixels, giving an effective capture surface of 13.8 million of pixels.

3.4.4.2 Removing the rotating mirror

The camera is equipped with a rotating mirror allowing the visualization of the scene before capturing an image. The camera rotates the mirror at each capture, generating vibrations transmitted to the microscope and inducing a blurring of the capture frames. The mirror and the actuating mechanism are then removed from the camera. A metal cover is then placed on the viewing aperture to prevent light pollution of the sensor. The exposition of the sensor to the light is activated through a mechanical focal plane curtain shutter. This mechanical shutter is essential to capture images with this camera and produces only a small amount of vibrations limiting the blurring effect. The complete setup is shown on Figure 3.10 (G) and each part is annotated on Figure 3.8.

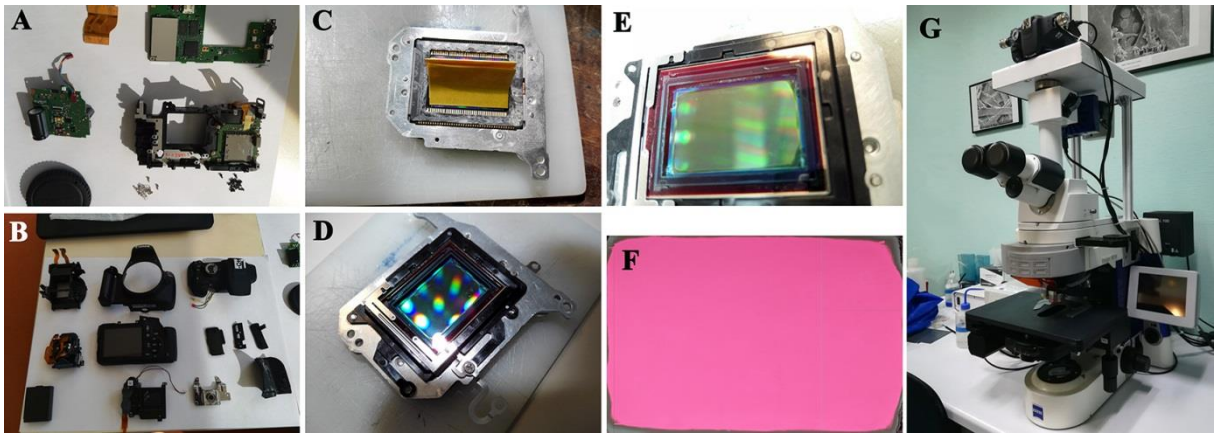

Figure 3.10: Illustrations of the transformation steps of the Canon 1200D CMOS sensor to monochromatic (A, B, C, D, E). Image of the surface of a mirror captured on the microscope (F). The camera is placed on top of the microscope (G).

3.4.4.3 Dimensional calibration

A geometry characterization of the captured image is performed placing, in the object plane, a stage micrometer (Zeiss 474027-9801-000, 5 mm/5 + 1 mm/100). This calibrated slide is designed for reflected light imaging and is calibrated (DIN EN ISO/IEC 17025 accredited). The slide is composed of 5 marks with an interval of 1 mm and of 100 marks with an interval of 0.01 mm. Images of this slide are captured placing the marks in all regions of the field of view to verify that no optical deformations are induced. The results for images with the 20x objective give a pixel size on the image of 0.2096 +/- 0.0001 µm/pixel in the X direction and 0.2102 +/- 0.0002 µm/pixel in the y direction with a variation of respectively 0.06% and 0.08% on different regions of the image. The images with the 10x objective reach 0.4216 +/- 0.0018 µm/pixel in the X direction and 0.4213 +/- 0.0014 µm/pixel in the y direction with a variation of respectively 0.43% and 0.34% on the different regions of the image. For image with the 5x objective reach 0.8396 +/- 0.0026 µm/pixel in the X direction and 0.8391 +/- 0.0013 µm/pixel in the y direction with a variation of respectively 0.31% and 0.15% on different regions of the image. Given the extremely small variations between the X and Y directions, a

single calibration term is computed. A mean calibration of 0.2101 +/- 0.0007 µm/pixel is adopted for the 20x objective. The calibrations are computed proportionally for the other objectives.

3.4.4.4 Additional sensors

A thermocouple was inserted on the side of the CMOS sensor and the temperature value is automatically read and stored for each capture. The device used is the Yocto-Thermocouple THRMCPL1 from Yoctopuce associated with a thermocouple type K. The measurement resolution is 0.2 °C with a precision of 1 °C. The radiant flux of the illuminant is automatically measured and stored for each capture. A photodiode is inserted in the light path near the lamp source. The device used is a Yocto-Light-V3 LIGHTMK3 from Yoctopuce. The photodiode, produced by Rohms and referenced BH1751FVI, can measure in the range of 0 to 100000 lux with a resolution of 0.25 lux. Both sensors are controlled by USB.

3.4.5 Control and automation

The camera can be controlled directly on a computer with a graphical user interface named Canon EOS utility. A USB cable links the camera to the computer. Although efficient, the software is not developed for microscopy applications and is not open source, preventing from adding functions. It was then necessary to develop a specific graphic interface that could handle simultaneously the camera, light and temperature sensors and microscope actuators (X, Y, Z stage, etc.).

3.4.5.1 Reverse engineering

To develop this application the communication (command and data) with the camera was reversed-engineered by “sniffing” the communication port between the EOS utility software and the camera using USBlyzer 2.2. This operation is time consuming and difficult since the structure of the commands and answers are not known. An example of the hexadecimal command required to trigger a capture after having initialized the communication with the camera is given in Figure 3.11. The first 4 hexadecimal values are used to encode the size of the command, the next 4 hexadecimal values are used to encode the type of command, the next 4 hexadecimal values to encode the command number and the rest of the hexadecimal values contain the data of the command. The commands are written with little-endian format and the integers are unsigned. The following functions are reversed engineered:

- camera initialization and closing
- live-view initialization, actualization and closing
- live-view zoom initialization at the x, y location, actualization and closing
- live-view “200x” zoom initialization at the x, y location, actualization and closing
- exposure time reading and setting
- image capture

When triggering an image capture, the camera sends the image as a stream of data packets. These packets are collected, identified and consolidated to form the Canon raw .cr2 file. The communication with the camera was established in Python programming with the PyUsb module. The port configuration for the dialog is the IdVendor: 0x04A9 and the IdProduct=0x327F with outbound commands on the 0x02 endpoint, with inbound data on the 0x81 endpoint and with maximal packet size of 2093056 bytes (2.09 megabytes). The raw images are then opened in Python with the Rawpy module allowing the generation of an array with the raw pixel values. Alternatively the raw images are visualized for a quick inspection with the Raw Digger 1.2.10 software. The metadata of the captured image are accessed in Python with the Exifread module and are occasionally accessed for a quick inspection with Exiftool 10.07.

Command #1: 14 00 00 00 01 00 28 91 05 00 00 00 01 00 00 00 01 00 00 00
Command #2: 10 00 00 00 01 00 29 91 06 00 00 00 01 00 00 00
Command #3: 14 00 00 00 01 00 28 91 07 00 00 00 03 00 00 00 01 00 00 00
Command #4: 10 00 00 00 01 00 29 91 08 00 00 00 02 00 00 00
Command #5: 0c 00 00 00 01 00 16 91 09 00 00 00

Figure 3.11: Hexadecimal commands to trigger a capture on a Canon 1200D camera.

3.4.5.2 Graphical user interface

A graphical user interface (GUI) is developed in order to control all the sensors and actuators of the apparatus simultaneously, allowing an automation of the image acquisition, Figure 3.12. The version of the main Python modules used to develop the set of tools is given in Table 3.5. PyQt module is used to code the GUI functions, associated with the software QtDesigner 5.6.0 to design directly all elements of the GUI.

Table 3.5: List of Python modules selected and version associated.

Package	Python	Numpy	OpenCV	Pyusb	Rawpy	Pyserial	Exifread	Yoctopuce	PyQt5
Version	3.6	1.14.3	3.4.1	1.0.0	0.9.0	3.3	2.1.2	1.10.30378	5.6.0

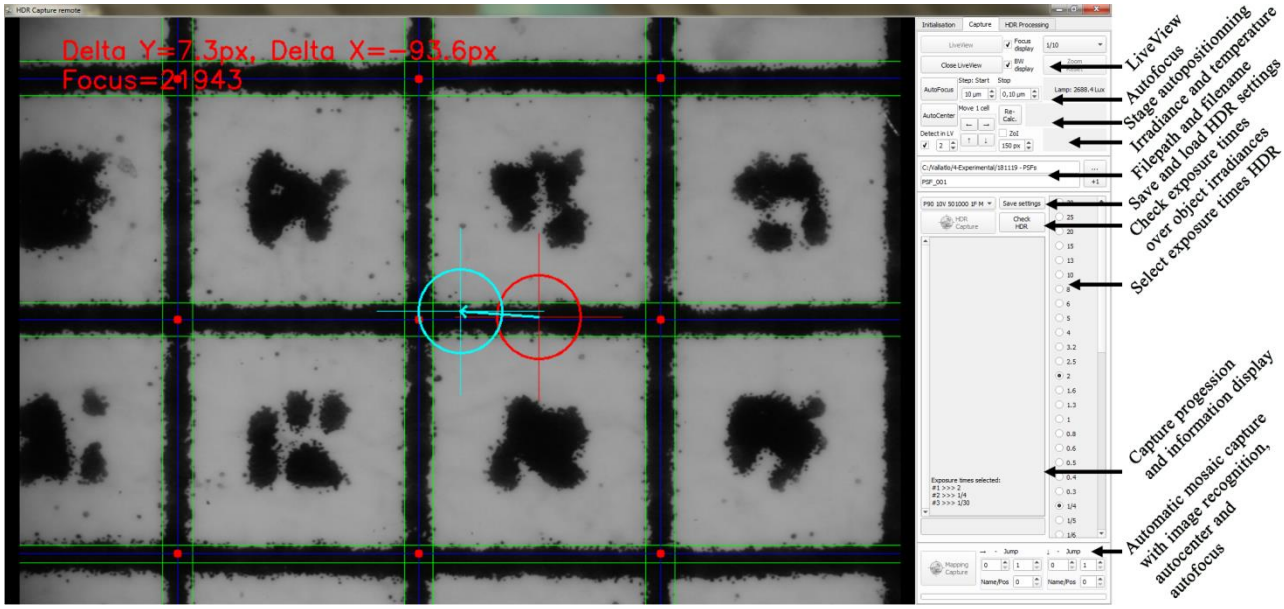

Figure 3.12: Graphic user interface integrating all sensors and actuators of the apparatus to perform: autofocus, auto-positioning, mosaic capture with image recognition and high dynamic range capture (HDR).

The GUI designed is called HDR (High Dynamic Range) capture remote and is composed of 3 main tabs: “Initialization”, “Capture” and “HDR Processing”. The “Initialization” tab is used to manage the communication of each element of the apparatus. The “Capture” tab is used to set and control the capture of halftone dots at the microscale. Finally the “HDR processing” tab is used to reconstruct HDR images from the captured images with specific settings. Several capture functions are developed in order to allow a faster and more accurate automated capture.

- A LiveView function allows obtaining a live visualization of the image plane of the microscope. This visualization is triggered by sending commands to the camera and multiple .jpg images are received at a rate estimated at 20 frames per second. The images received are 8 bit depth on 3 channels (red, green and blue). With the sensor modified to monochromatic, retrieving color images do not give additional information. An option converting the images to grayscale is added and allows switching the live preview to monochromatic. By double clicking on a region of the

image, the position of the cursor is recorded and converted to send to the camera the position at which new frames with a zoom should be captured. Images of the regions with a zoom are then sent back, treated and displayed. It allows for accurate manual focusing and to visualize more accurately fine details.

- A focus can be performed automatically (to ensure reproductible and unbiased measurements) by pressing the Autofocus button. This triggers the execution of an algorithm moving the Z stage of microscope by dichotomy to find the maximum of a focus index. Verifications were performed to ensure that the focus index as a function of the Z stage position had a bell shape, in such way that the maximum could be accurately determined by dichotomy. The focus index is displayed in a text overlay on the preview image. The focus index is calculated from the preview image as described: the image is converted to grayscale and is cropped to the region of interest (ZoI) specified in the GUI. Restraining to a region of interest allows obtaining a more precise autofocus for images where the surface is rougher than the optical depth of field. A double convolution is then applied to the image with two modified Laplacian operators, 1 in the X direction and 1 in the Y direction [350]. The focus is computed as the double sum in both directions of the result of the absolute of the convolution squared. Multiple tests showed that the focus index was having a gradient near the focal point but was then rapidly becoming constant away from the focal point. The index was then modified, equation [3.2] removing the square term and adding a dependency with the standard deviation (focused images have sharp edges resulting in larger pixel values differences). Tests showed that the focus index function was presenting a bell shape with a gradient even on Z stages positions largely shifted from the focal position. The starting step and stopping step defining the initial and final offset movement of the Z stage for the dichotomy is tuned directly in the GUI as well as the size of the region of interest.

Focus index

[3.2]
$$FI = \left(\sum_x \left|LapK_x \circledast IM\right| + \sum_y \left|LapK_y \circledast IM\right|\right)\left(\sqrt{\frac{\sum_{i=1}^{N}(px_i - \overline{px})^2}{N-1}}\right)^2$$

Symbol	Unit	Denomination
FI	1	Focus index
LapK	1	Laplacian kernel
IM	1	Image LiveView
px_i	1	Pixel value i
$\overline{px}$	1	Mean pixel value
$\circledast$	-	Convolution operator

- A function allows detecting automatically specific features of the print in order to center the halftone in the X-Y plane. This automatic detection and centering algorithm is especially developed for automatic measurement of a large amount of halftone dots placed in a printed array, Figure 3.5 and Figure 3.12. The LiveView image is first smoothened applying a median blur filter and a box blur filter and is then thresholded using the mean method. The detection algorithm computes then the sum of black pixels in the X and Y directions. Ink edges (of an array or of patches borders) can then be identified by tracking the maxima of the sum in the two directions. Multiple conditions are checked in order to circumvent potential defects in the image (dust particles, incomplete printing and print margins). Four different centering locations are developed in relation to the array including the halftone dots: the intersection of an array column and line, the center of a cell line, the center of a cell column and the center of a cell. This centering location is set in the GUI under the "Detect in LV" caption. Buttons with arrows in the four directions (up, down, right left) allowed toggling between the cell of the array, moving by one cell distance in the specified direction. This distance is automatically computed from the array edge detection on the preview image and is converted into microscope stage displacement quantities as a function of the objective magnification. A button on the GUI interface allows resetting this distance when switching slides.

- A function is then added on the GUI to set the parameters of the automated capture and to trigger it. The parameters allow choosing the number of images to capture in the X and Y directions and setting the displacement between each capture. After a displacement, the auto-centering algorithm is systematically applied and an autofocus is performed. The capture speed is measured at 32 seconds per image including the stage movement and centering, the autofocus and the image capture.
- A high dynamic range method is developed in order to extend the dynamic range (HDR) of the measured images. The development of the method is presented in section 3.5. On the GUI, a HDR a capture is enabled by selecting multiple exposure times. The exposure time selection can be saved and loaded in order to set the settings quickly. When triggering a HDR capture, the software sends commands the camera to set the exposure time and capture an image. A function to check if the selected exposure times cover the dynamic range of the halftone imaged is added.

3.5 High dynamic range capture method

A High Dynamic Range (HDR) method to capture printed dots at the microscale is then proposed. The HDR reconstruction method is developed to improve the accuracy of the ink and paper reflectances measurements. The HDR has already been used in the field of microscopy [351,352,123], however to the method was not commonly applied to microscale print measurements. A characterization of the camera is first proposed. Then the HDR method developed is presented and its performances are investigated. Offset, inkjet and electrophotography halftone dots are measured with HDR and compared to macroscale measurements.

3.5.1 Camera characterization

A characterization of the camera mounted on the microscope is conducted. A comparison is performed with a non-modified sensor of the same camera model to evaluate the effect of the transformation into a monochromatic and insure the validity of the measurements. The modified sensor is referred to as sensor MONO and the original sensor is referred to as sensor RGGB. The level of electron amplification (ISO level) is set to 800 (best compromise to reduce exposure time noise compared to amplification noise) and the time for the integration of the photons (exposure time) is selected independently for each experiment.

3.5.1.1 Black frame subtraction

Black frame characterizations allow removing constant defects of the sensor. Captures at all exposure times (30, 25, 20, 15, 13, 10, 8, 6, 5, 4, 16/5, 5/2, 2, 8/5, 13/10, 1, 4/5, 3/5, ½, 2/5, 3/10, ¼, 1/5, 1/6, 1/8, 1/10, 1/13, 1/15, 1/20, 1/25, 1/30, 1/40, 1/50, 1/60, 1/80, 1/100, 1/125, 1/160, 1/200, 1/250, 1/320, 1/400, 1/500, 1/640, 1/800, 1/1000, 1/1250, 1/1600, 1/2000, 1/2500, 1/3200 and 1/4000 seconds) are performed without exposition to photons. Ten frames are captured for each exposure time. Black references for each exposure time are obtained by averaging the pixel values respectively at each pixel position. The black reference can then be subtracted from a captured image by retrieving the exposure time of a captured image. In order to characterize the effect of black frame subtraction, two measurements are adopted: the average and standard deviation of the array of pixels values. Since 10 images at each exposure time are captured, the average over the ten frames of the average over each frame is computed. The average over the ten frames of the standard deviation over each frame is also computed, Figure 3.13 (A). The average measured is not equal to 0 but is found at the pixel value 2047.8 +/- 0.3 for the MONO sensor and at the pixel value 2047.7 +/- 0.6 for the RGGB sensor. This offset is introduced by the camera to enable the recording of negative pixel values. Theoretically, photons can only be added on the photodetectors, however due to defects on particular photosites,

negative values are measured and recorded to prevent a bias at the 0 level. A decrease of the mean pixel value is observed with longer exposures, mostly due to the dark current noise. The standard deviation becomes consequently larger. No significant influence of the sensor modification is observed. Results of the black frame subtraction are presented on Figure 3.13 (B). Thanks to the subtraction, the mean pixel level over the ten frames is found at the level 0.0000 +/- 0.0001 for the sensor MONO and at 0.0218 +/- 0.0375 for the sensor RGGB. The standard deviations remain similar after black frame subtraction.

Theoretically capturing a black frame should produce a pixel array with constant pixel level. However, measuring the average of the standard deviations over the pixel arrays shows variabilities in the range of 10 to 84 pixel levels, Figure 3.13 (C). The mean standard deviation depends on the exposure time and on the sensor modification. Exposure times over 1 second are associated with a large increase from +/-19 to +/-84 pixel levels for sensor MONO. This effect is more subtle for sensor RGGB with an increased from +/-14 to +/-26. Pixel deterioration after the monochromatic modification may cause these differences. After applying the black reference subtraction, the mean standard deviations are reduced for all exposure times. The two sensors are found within the same levels of mean standard deviation, slightly increasing with the increase of exposure time, from +/-10 to +/- 18 for the MONO sensor and from +/-11 to +/- 19 for the RGGB sensor.

The distribution of the pixel values is found closer to a Gaussian distribution after the black reference subtraction. This shows that the method reduces the sources of noise that were not random. The black frame subtraction method will then be applied systematically.

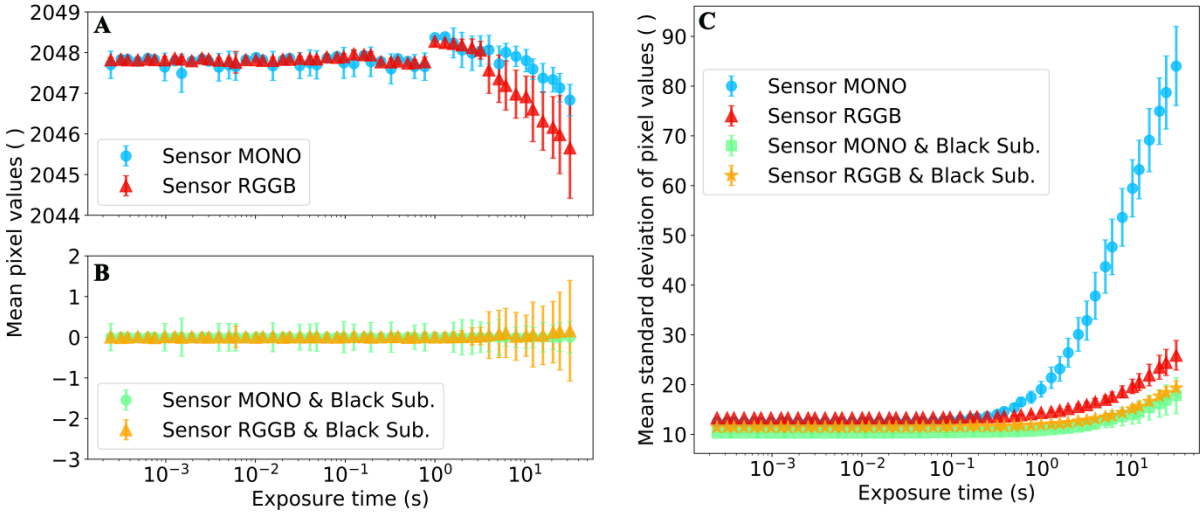

Figure 3.13: (A) Average and standard deviation of 10 black frames pixel levels as a function of the exposure time and (B) with black subtraction. (C) Average of standard deviation over the pixels locations of each capture.

3.5.1.2 Sensor saturation

Sensors maximum recordable pixel value is measured using a halogen illuminant Lumina FO-150 from Chiu Technology Corporation, equipped with an optical fiber and a rotary dimmer. The sensor is illuminated with a level of irradiance that produces saturation on the photosites of the sensor at exposure time 1/4000 second. A single image is then captured for each exposure times and averages of the pixel values are calculated for each exposure time (with black subtraction). Figure 3.14 (A) shows the maximal pixel value recordable. The average for exposures smaller than 1 second is found at 13255.5 +/- 0.3 for the MONO sensor and 13255.6 +/- 0.2 for the RGGB sensor. For longer exposure times, the maximal pixel value recordable decreases for both sensors, down to 13155.7 for the MONO sensor and down to 13182.3 for the RGGB sensor. This behavior results from noise build up over long exposure times and represents 0.8% of variation for the MONO sensor and 0.6% of variation for the RGGB sensor. The standard deviation as a function of the exposure times increases

with the increase of exposure time, from +/- 7.3 to +/- 213.1 for the MONO sensor and from +/- 7.2 to +/- 132.3 for the RGGB sensor. This behavior is explained by a charge overflow reaching the masked pixels on the edge of the sensor (used to set the dark current level) [353]. The irradiance homogeneity is studied by capturing images of a mirror under the microscope. The pixel values as a function of the position in the field of view are then analyzed and corrections are computed and applied.

3.5.1.3 Illuminant and sensor stability

In order to investigate the light source stability, images of reflected light on a photodiode are captured on the microscope for 120 minutes with intervals of 1 minute. The mean pixel value is computed for each frame and is compared to the radiant flux measured directly. The radiant flux is measured at the focal point of the object plane and the camera mean pixel value is measured at the focal point of the image plane. Both measurements are presented relatively to their first recorded level, Figure 3.14 (C). The temperature of the camera processor located behind the CMOS sensor is retrieved from the metadata of each captured image. The temperature of the processor has a precision of +/-1°C and a gradient between the CMOS sensor and the processor appears. First the stability of the light source is investigated from 0 to the 60th minute with a constant processor temperature. An increase of the processor temperature is then triggered periodically by increasing the load on the processor (live-view function). From 0 to the 60th minute, the camera mean pixel values and the radiant flux show similar relative variations in the range of +2.8% to -7.5%. These variations, representing a standard deviation of 2.3%, are caused by the lamp irradiance variation in time. 15 minutes periods are observed. A correction factor accounting for the lamp irradiance variations is computed and applied on the captured image. The measured pixel value variations with the correction are reduced to a range of +1.1% to -0.7% with a standard deviation of 0.3%. To perform this correction automatically when measuring halftone images, a photodiode is inserted in the light path near the lamp source.

On the second part of the curve, Figure 3.14 (C), an increase of the processor temperature is triggered. The measured pixel value starts to present an offset with the measured radiant flux. This shows that the measured pixel value is sensitive to the camera temperature, with a relative pixel value increase from 0 to 5% with an increase of the processor temperature from 27 °C to 47 °C. In standard image capture conditions, the CMOS sensor temperature stabilizes reducing the influence on the measured pixel value. For this purpose the sensor and the lamp are turned on 30 minutes before the measurements. Moreover a thermocouple was inserted on the side of the CMOS sensor and the temperature value is automatically read and stored for each capture.

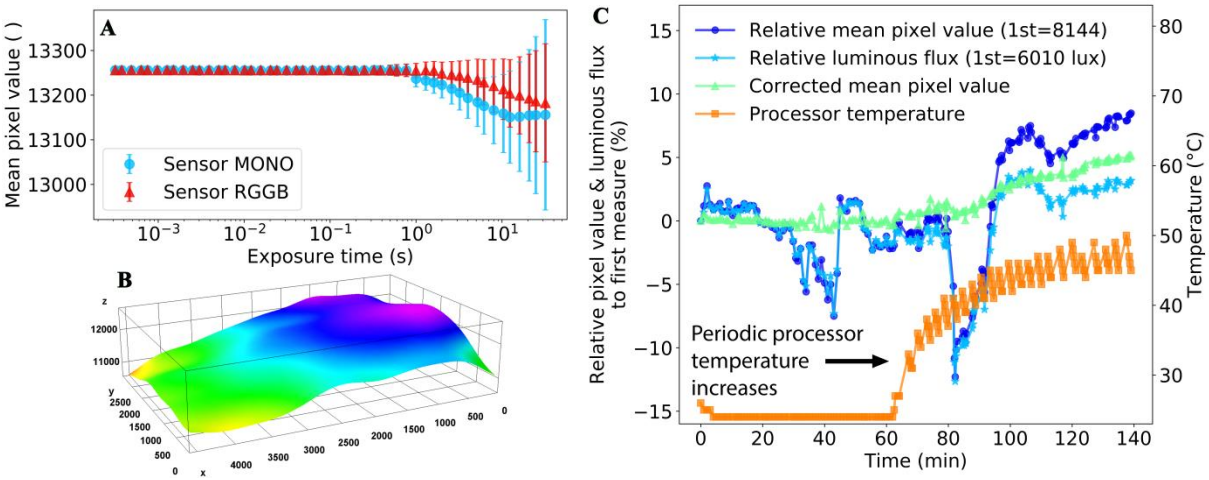

Figure 3.14: (A) Pixel value as a function of the exposure time for a capture with a high irradiance illuminant saturating. (B) Heterogeneity of illuminant irradiance. (C) Mean pixel value and radiant flux per unit area (relative to first measure) and camera processor temperature as a function of time for sensor MONO.

3.5.1.4 Exposure time characterization

Analyzing the metadata of each captured frames shows that the camera is providing two separate exposure times: the first one called "exposure" and the second time called "shutter time". The shutter time is stored in the metadata as minus the logarithm in base 2 of the time in seconds. Thus the exposure and the antilog of minus the shutter time differ. For example a frame could have in the metadata an exposure of 15 seconds and a shutter time of -4. The antilog in base 2 of minus the shutter time would be 2^4=16 seconds. By recording the sound of the mechanical shuttering, it was found that for long exposure times the shutter time is more representative of the time while the sensor is exposed to light. As the exposure time decreases it becomes more difficult to measure the exact opening and closing of the shutter curtain. The exposure time based on the shutter time is then adopted.

The effect of the exposure time on the amount of noise is investigated by capturing 10 images of the same region of a coated paper. The standard deviation for each pixel location of the 10 frames is computed. The mean standard deviation of the capture is obtained by averaging the standard deviation of each pixel location. This measurement is conducted for multiple exposure times with the irradiance adjusted by placing neutral density filters in the illuminant path, allowing the recording of pixel values in the similar range. Results show that the mean coefficient of variation does not depend on the exposure time and is found between 2.10% +/- 0.32 and 2.60% +/- 0.24, Table 3.6. Thus, the amount of noise does not significantly depend on the exposure time selected (in the range of this experiment).

Table 3.6: Mean coefficients of variation for multiple exposure times with similar mean pixel values.

Exposure (s)	Mean coefficient of variation (%)	Mean pixel values ( )
10.4	2.10 +/- 0.32	8600 +/- 398
3.22	2.28 +/- 0.25	6715 +/- 293
1.00	2.39 +/- 0.24	6397 +/- 296
0.0964	2.60 +/- 0.24	5295 +/- 234
0.0482	2.31 +/- 0.24	6334 +/- 294

3.5.1.5 Sensor linearity and noise dependency

CMOS and CCD sensors are not linear in their entire measuring range. Similarly the level of noise depends on the level of irradiance measured. Thus, in order to obtain quantitative information about a halftone print, the pixel values measured must be in the linear range of the sensor and associated with a limited measurement noise. In the following section the dependencies with pixel values as well as the linearity of the sensor are investigated.

Sensor linearity

The sensor linearity is investigated through the total range of exposure times. For this purpose, inkjet printed halftone dots with nominal ink coverage of 40% are captured at all discrete exposure times available on the sensor in the range of 30 seconds to 1/4000 seconds. This nominal ink coverage is chosen as there will be at the same time a high reflectance surface (paper) and a low reflectance surface (ink). Five different exposure times are selected (5, 8/5, 3/5, 1/5 and 1/15 seconds) where more than 50 pixel locations are found at an identical pixel value around the targeted pixel value of 5000, as represented in Table 3.7. The pixel locations of five different levels of pseudo-irradiance are obtained and are representative of the range encountered when measuring halftone dots. The pixel levels of each pixel locations for each exposure time are then collected and averaged. The pixel level is plotted as a function of the exposure time, Figure 3.15 (A).

Table 3.7: Irradiance levels selected and number of pixel location tracked for each exposure times.

Pixel value	**4770**	**4147**	**4665**	**4665**	**4666**
Exposure time (s)	5	8/5	3/5	1/5	1/15
Pseudo-irradiance level selected	954	2592	7775	23325	69990
Number of pixel location tracked	67	895	263	56	179

A well-known S shape curve is found for the CMOS sensor. Analyzing the curve reveals three operating regions. The first region is observed for low pixel values, below the pixel value 100. In this region, the pixel values show large random variations, as observed on the rounded dot curve. The number of photons integrated on the photosites during the exposure time becomes too small compared to the signal due to noise. Thus, the response over different exposure times is not linear anymore. The second region consists in a linear region, where the pixel values measured are proportional to the exposure times. This region is observed for the five curves. The range linearity appears at different exposure ranges, depending on the level of irradiance considered. However, the pixel levels where the linearity is observed are always in the same range between 100 and 10000. The third region, called the saturation limit, is observed, for high pixel values, when the pixel levels converge toward a constant value as the exposure time increases. This region is observed especially for the curve of pseudo-Irradiance 69990. Photons are converted to electrons on the CMOS sensor and these electrons are stored during the integration time. The storage capacity depends on the capacitance of the photocell. When the capacitance is saturated with electrons, photons arriving cannot be stored as electrons and thus cannot be measured. In order to measure accurately, it is required to consider only pixel level measured in the linear part of the sensor. The transition between the second region to the third region can be clearly identified above the pixel value 12500. In order to insure that no saturation will happen the pixel 10000 is adopted as the higher limit of linear range. The limit between the first and the second region is however more difficult to define.

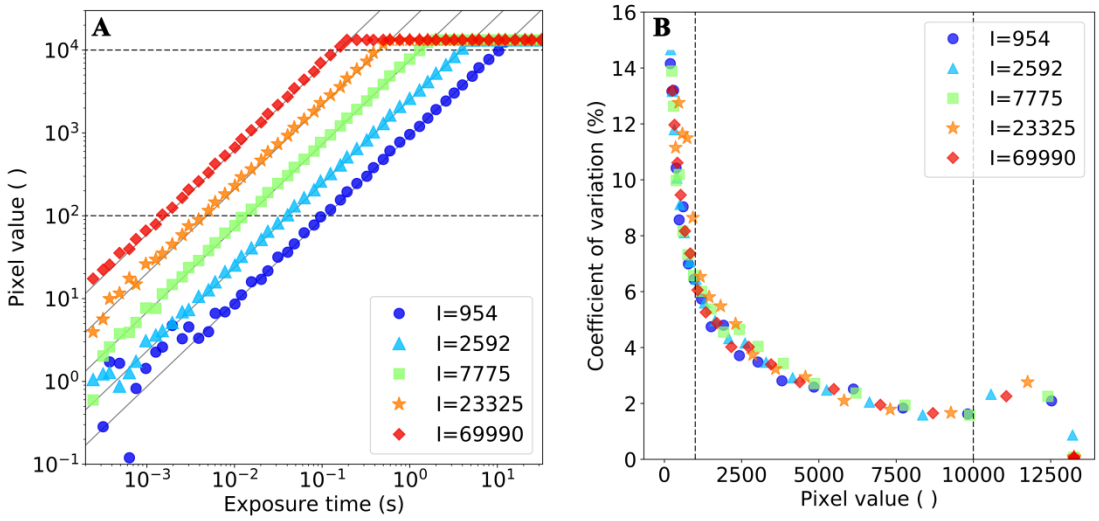

Figure 3.15: (A) Mean pixel values as a function of the exposure time and (B) coefficients of variation as a function of the pixel values, for different pseudo-irradiance levels (I) on a 40% NIC inkjet print.

The coefficient of variation, obtained from the pixel location for each exposure times, as a function of the pixel value demonstrates the effect of noise induced by a non-linearity in the first region of the sensor, as presented on Figure 3.15 (B). The curve obtained has a 1/x shape with a large increase of the coefficient of variation as the pixel level tends to become smaller than 1000. This behavior shows that to prevent high noise in the measurement, a limit at 1000 should then be adopted for the transition between the first region to the linear region. This linear range between the pixel value 1000 and 10000 is then adopted in the following of the study.

Regression through the origin

A set of images are captured by imaging a mirror surface with different optical density filters attenuating the irradiance of the illuminant. A linear regression through the origin is used to quantify the linearity of the camera response, as presented on Figure 3.16, and allows validating the linearity range defined on Figure 3.15. Different levels of pseudo-irradiance are represented by different slopes of the linear regressions, going from I=6993 to I=108351. Regressions were performed for 7 illuminant irradiances and coefficients of determination R^2 are found at an average of 0.9990 +/- 0.0007. This shows a high linearity of the sensor for the pixel value measured at different exposure times. Uncertainties in the pixel values, as well as uncertainties in the exposure times are responsible for the slight variations around the regression line. Equation [3.3] models this linear region. Using this model a quantity analog to the irradiance can be computed, by dividing the pixel level by the exposure time. Using multiple images at multiple exposure times in the range of linearity of the sensor allows improving the range of the irradiance that can be measured.

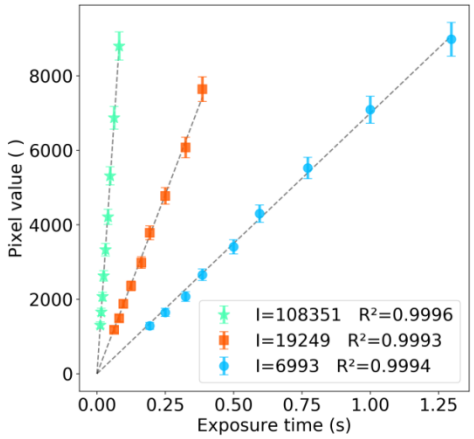

Figure 3.16: Linear regression through the origin of pixel values as a function of exposure times to determine the pseudo-irradiance of illuminant irradiances measured by a reflection on a mirror.

Pseudo-Irradiance

		Symbol	Unit	Denomination
[3.3]	$I(x,y) = \frac{px_i(x,y)}{E(i)} + \varepsilon(px_i)$	$I(x,y)$	s^{-1}	Pseudo irradiance
		$px_i(x,y)$	1	Pixel value frame i
		$E(i)$	s	Exposure time frame i
		$\varepsilon(px_i)$	s^{-1}	Pixel value error

3.5.2 High dynamic range

3.5.2.1 Single capture

As demonstrated on Figure 3.15 the sensor has a linear range going from the pixel value 1000 to almost 10000. A single image of printed inkjet halftone dots with 40% theoretical surface coverage captured at an exposure time of 0.2 seconds is analyzed. As shown on Figure 3.17, when capturing printed inkjet halftone dots on a microscope, the irradiance level of the paper and the irradiance level of the ink fall respectively in the upper non-linear and in the lower non-linear range of the sensor (regions represented in red). With a single capture, 30.0% of the pixels are inferior to the value 1000 and 40.6% of the pixel are over 10000. Thus, the dynamic range of the sensor is not large enough to obtain reliable pixel levels from a single capture for printed halftone dots. Capturing with shorter exposure time would result in fewer pixels in the upper non-linear range and would reduce the red regions on Figure 3.17 (B). However, the image would have more pixels in the lower non-linear range

and thus the red region would be larger on Figure 3.17 (A). Computing the optical density or analyzing the pixel levels from a single image could then be inaccurate. The high dynamic range allows overcoming this measurement limit.

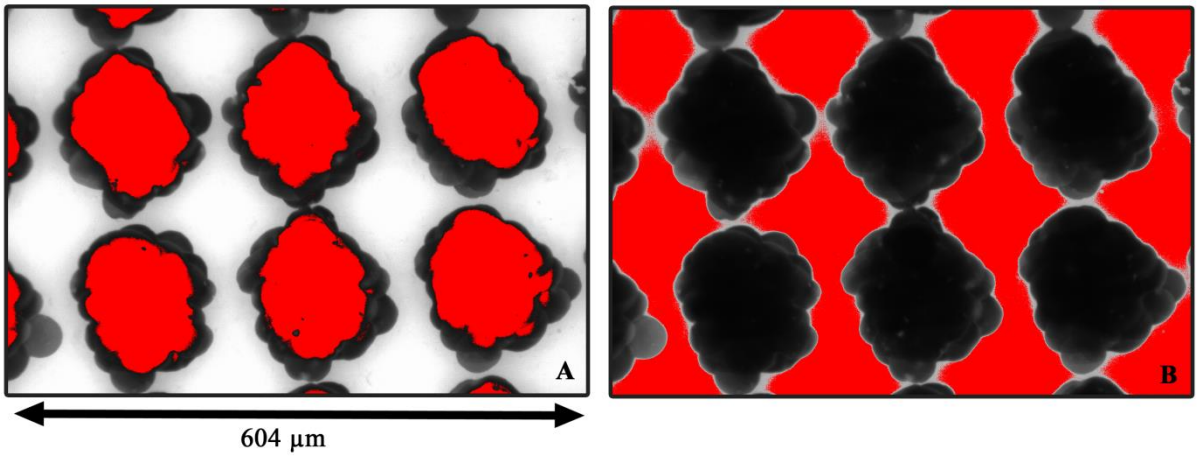

Figure 3.17: Dynamic range of the sensor for inkjet halftone dots with 40% nominal ink coverage: (A) pixel values inferior to 1000 displayed in red, (B) pixel values superior to 10000 displayed in red.

3.5.2.2 High dynamic range method

HDR principle

Offset halftones of 30% nominal ink coverage are imaged with a single exposure time of 1/10 seconds on Figure 3.18 (A). The mean pixel value in an inked area is equal to 259, which is lower than 1000. Referring to Figure 3.15, the pixel values under 1000 are associated with a large increasing noise. The transition region, between the ink and the paper is measured at the mean pixel level of 4271. This measurement is in the linear zone of the sensor. Finally, the paper region is measured at a mean pixel value equal to 11247. This pixel level is superior to 10000 and could then be subjected to saturation, as presented on Figure 3.15. Adjusting the exposure time for each region requires a minimum of one capture for each region and allows measuring while being in the linear part of the sensor, as presented on Figure 3.18 (B). The pixel level for the ink region is now found at the mean pixel value of 4144 for an exposure time of 1.6 seconds. The transition region was captured at the same exposure time as the image corresponding to a single exposure time and remained unchanged. The paper region was found at a mean pixel value of 4499 and was captured at an exposure time of 1/25 seconds. This observation illustrates the basic principle of the HDR method.

High dynamic range capture is achieved by capturing multiple images at different exposure times [124]. A single image is then computed from the multiple images captured at different exposure times. This computation is called image fusion. Instead of retrieving a relative pixel value when performing the fusion to a single image, the pseudo-irradiance I is computed, equation [3.3]. The method used to perform the fusion is a linear regression through the origin over the pixel values at each pixel location as a function of the exposure time, as described by equation [3.4]. Computation of the linear regression through the origin is based on the mathematical work of Eisenhauer [354]. These methods are systemically performed in the linear region of the sensor, thus pixel levels lower than 1000 and higher than 10000 are excluded.

Regression through the origin based pseudo-irradiance

		Symbol	Unit	Denomination
[3.4]	$I(x,y) = \frac{\sum_i (px_i(x,y)\ E(i))}{\sum_i (E(i)^2)}$	$I(x,y)$	s^{-1}	Pseudo irradiance
		$px_i(x,y)$	1	Pixel value frame i
		$E(i)$	s^{-1}	Exposure time frame i

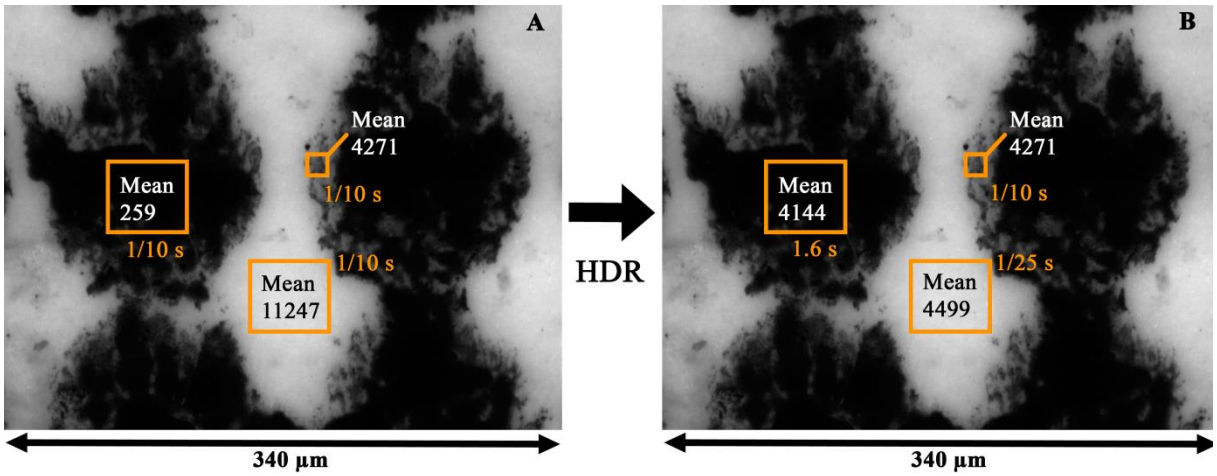

Figure 3.18: Mean pixel values of an ink, paper and transition region of an offset halftone of 30% nominal ink coverage captured at (A) a single exposure time and (B) with multiple exposure times. Exposure times are represented in orange color. "Mean" corresponds to the mean pixel value of the orange square.

Exposure time selection protocol

Selecting properly the exposure times for an HDR capture is extremely important. The following protocol is used to optimize the HDR capture:

1. Select exposure time A with pixel values close but inferior to 10000 for the paper region
2. Select exposure time B with pixel values close but superior to 1000 for the ink region
3. Compute pseudo-irradiance and determine if the pseudo-irradiance of the two exposure times A and B overlap. If no, add an exposure time C in the middle of the pseudo-irradiance gap
4. Extend the exposure times A and B to minimize the overlapping of the pseudo-irradiance that can be linearly captured
5. Offset the exposure time A, B and C in order to match the initial exposure time B
6. Optionally add sub-exposure times to increase the number of HDR frames

Encoding

Since the exposure times are predefined in the camera and are stepped almost following an anti-logarithm base 2 function, computing the pseudo-irradiance value with a logarithm base 2 tends to linearize the range. Then, the encoding algorithm applies an offset in order to shift to zero the minimum pseudo-irradiance value. The range of the pseudo-irradiance is then extended or reduced to fit into the range available when coding on 16 bits: range from 0 to 65535 with a step of 1. The encoding method is called 'LOG2' encoding and is presented in equation [3.5]. The key parameters determined for encoding are the minimum and maximum pseudo-irradiance and the minimum and maximum exposure times. These parameters are also encoded on 16 bits and stored in the first row of the image.

'LOG2' encoding

		Symbol	Unit	Denomination
[3.5]	$I_e(x,y) = \frac{\log_2(I(x,y)) - \log_2(\min(I(x,y)))}{\log_2(\max(I(x,y)))} (2^{16} - 1)$	$I_e(x,y)$	s^{-1}	Encoded pseudo irradiance
		$I(x,y)$	s^{-1}	Measured pseudo irradiance

The high dynamic range image is compared to a single exposure time image captured at exposure time 1/10 seconds. The high dynamic range image is also compared to the average of 9 single exposure time images captured with identical conditions at the optimized exposure time of 1/10 seconds. The high dynamic range method is performed with an average of 3 frames for each pixel location, and requires in order to cover the irradiance range, a total of 9 images at exposure times: 6, 4,

2, 1, 1/2, 1/4, 1/10, 1/13, 1/15 seconds. The pixel pseudo-irradiance values, reconstructed by the high dynamic range method associated with the regression through the origin are plotted as a function of the position along two lines, one in the ink region and one in the paper region.

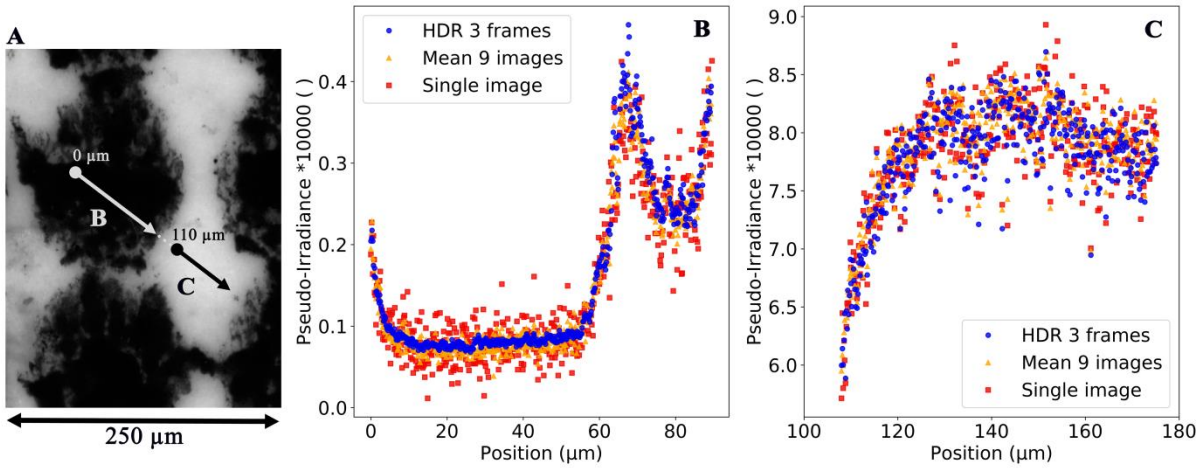

Figure 3.19: (A) Measured offset print and relative pixel values as a function of the position along a line of an offset halftone of 30% nominal ink coverage. (B) in the inked region, (C) in the paper region.

In the dark region, the pseudo-irradiance values for a single image (red squares) are dispersed, with a 29.3% coefficient of variation around the mean pseudo-irradiance of 761.2 between the position 10.2 and 50.0 µm, Figure 3.19. The dispersion of the pseudo-irradiance values reduces when taking into account the average of 9 images (orange triangles), with a 12.5% coefficient of variation around the mean pseudo-irradiance of 761.0. Using the regression method with 9 images captured at different exposure times, an average of 3 frames in the pixel range from 1000 to 10000 is considered for each pixel location. The resulting coefficient of variation is reduced to 5.9% around the mean pseudo-irradiance of 793.5. The reduction of dispersion obtained with the high dynamic range is explained by the fact that each irradiance level is measured with an adapted exposure time, having each irradiance level sampled in the linear region of the sensor. Moreover as it was shown on Figure 3.15, the coefficient of variation becomes lower with the increase of the measured pixel value and extremely high when capturing in the sensor range below the pixel value 500. Thus, the high dynamic range method, benefits from measuring at higher pixel value by selecting the exposure time, as well as an averaging effect, using 3 frames with different exposure times for each pixel location. On the opposite, when using a single image or an average of images at the same exposure times, since the dynamic range of the sensor is too small to capture irradiance level while having pixel value higher than 500 and lower than 10000, the measure is associated with a large uncertainty.

The difference of the average value between the single image, the mean of 9 images with a similar exposure time and with the high dynamic range image can be explained by the fact that there is an uncertainty on the exposure time retrieved from the camera metadata. The average obtained with the single image and the mean of 9 images depends on the accuracy of a single exposure time, as the HDR image rely on an average of 3 exposure times. The difference of 32.5 pseudo-irradiance levels corresponds to an error on the exposure time of 4.1 ms when measuring at 1/10 seconds for the single exposure time. On higher pixel values the high dynamic range dispersion is similar to the single image and the average of 9 images at a single exposure time, as shown on Figure 3.19. For the single image and the average, the paper region, measured from the position 130.1 to 170 µm, is captured with the selected exposure time at a mean pixel value of 7731 and 7759 respectively. These measurements take place in the linear region of the sensor and thus only a slight improvement is demonstrated by the HDR image. The coefficients of variation are found for the single image at 3.8% with a pseudo-irradiance of 80201.5, for the average image at 3.1% with a pseudo-irradiance of 80492.7 and for the HDR image at 3.3% with a pseudo-irradiance of 79839.1. The measurement error is not significantly

improved regarding the error on measured pixel values, however the error due to the exposure time is improved by the fusion of multiple exposure times. It has to be pointed out that the paper region and the ink region are not necessarily homogeneous and may be a source of dispersion of the measured values. The coefficient of variation is then only valid for comparison with the measurement methods and does not indicate the absolute measurement performances.

3.5.2.3 High dynamic range applications

From microscale images of halftone prints a few measurements are classically computed such as: the ink coverage using a threshold method, the histogram peaks of the paper region and of the ink region and dots shape descriptor indexes [17,19,355]. Quantities such as the optical density and the surface coverage using the Yule-Nielsen model can also be obtained from microscale measurements. However these quantities are traditionally obtained macroscopically and microscale measurements do not seem to increase their precision. Nevertheless, comparing microscale and macroscale measurement allow validating the microscale measurements. Moreover the microscale measurement benefits from the HDR method. The measuring range can be therefore extended.

Light spreading measurements

Ukishima and Happel used microscale images on an edge illumination in order to measure the point spread function of the paper [10,17]. To perform the measurements the aperture of the microscope is closed, giving a sharp edge illumination of the shape of an octagon. The sensitivity of these measurements can be improved using the HDR method, since the measurement of a high irradiance region and low irradiance region have to be measured at the same time, Figure 3.20 (A). The paper with full illumination is also captured using both the HDR method and a single capture, Figure 3.20 (B). The area corresponding to the illuminated region on the image captured with the closed aperture is obtained by performing an Otsu thresholding and by counting the number of pixels thresholded. Similarly, the threshold level obtained is used to compute the mean pseudo-irradiance value inside the illuminated region, using the image histogram.

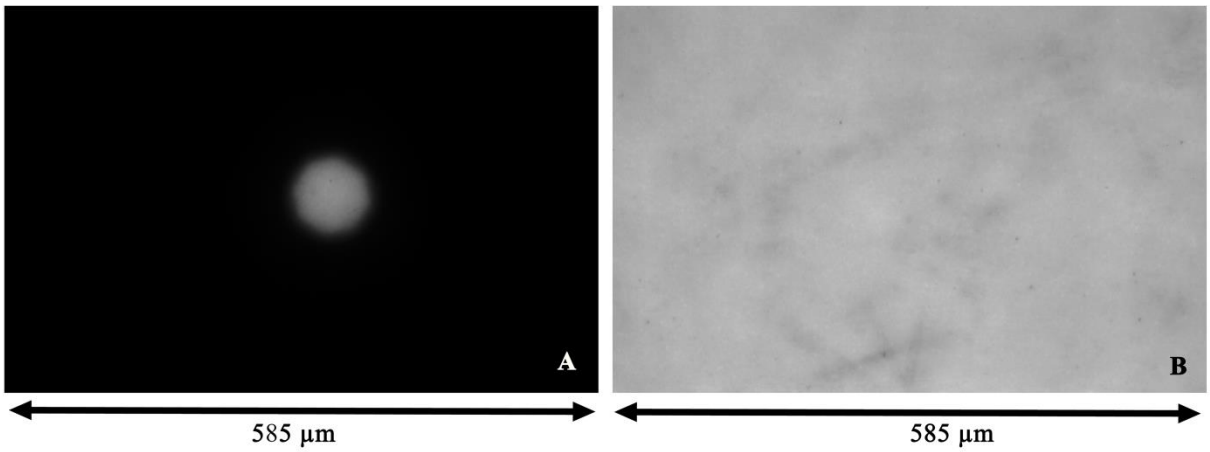

Figure 3.20: Radiance flux conservation experiment (A) knife edge illumination on glossy coated paper, (B) glossy coated paper with full illumination.

A consequence of the light scattering on paper is that the pseudo-irradiance values measured are not identical on the area inside the knife edge illumination and on the paper with full illumination. The mean pseudo-irradiance recorded inside the knife edge illumination is determined at 18776 +/- 1345 and the mean pseudo-irradiance of the paper with full illumination is found at 33338 +/- 680 for the HDR method. These differences represent a decrease of pseudo-irradiance of 43.7%. By computing the sum of the pseudo-irradiance levels on the total area of the two images and by dividing by their effective lighted areas, respectively 4930 µm² for the knife edge illumination and 244108 µm² for the full area, similar mean pseudo-irradiance are obtained, respectively 31382 +/- 1443 and 33338 +/- 680.

The difference between the two mean pseudo-irradiance is now 4.3%. This shows that although the light scatters in the paper in Figure 3.20 (A), it is possible to capture this light scattering outside the knife edge illumination using the HDR method. Thus, the HDR method allows verifying that the total light sent and reflected by the paper weighted by the area of illumination is conserved. Performing the same experiment with a single image capture produces a larger difference of pseudo-irradiance with an initial difference of 44.9% and a difference of 10.2% after the averaging over the surface. This shows that using a single image method leads to less precise measurement of the paper point spread function .

Shape descriptor indexes

The measurement improvement of the high dynamic range capture is also revealed when analyzing the ink distribution on the ink dots. The shape descriptor of printed dots is a measurement allowing a quantification of the relations between light, ink and paper. Moreover shape of printed dots can be used to assess print quality, print identification and define anti-counterfeiting signatures. The shape descriptor indexes are obtained performing image treatments on halftone dots of 30% nominal ink coverage printed with offset, inkjet and electrophotography. ImageJ particle analysis and segmentation was used [356]. The sub-dots obtained for each halftone dots are classified according to their surfaces (area classes). Shape descriptor indexes are obtained from the segmented sub-dots by computing their area, perimeter, convex area and the major and minor axis lengths of the fitted ellipse. More information can be found in Olson's work and ImageJ user guide [185,357].

Shape descriptors

[3.6]

$$\text{Solidity} = \frac{A}{A_c}$$
$$\text{Aspect ratio} = \frac{D_{min}}{D_{max}}$$
$$\text{Convexity} = \frac{P_c}{P}$$
$$\text{Circularity} = \sqrt{\frac{4\pi A}{P^2}}$$

Symbol	Unit	Denomination
A	μm^2	Area
A_c	μm^2	Convex area
P	µm	Perimeter
P_c	µm	Convex perimeter
$D_{min,max}$	µm	Feret diameters

As presented on Figure 3.21, the red regions correspond to the first 16.1% of the ink transmittance regions for HDR and 15.5% for a single capture. By comparing the ink regions selected on the image obtained with the high dynamic range method (A) and with the single frame capture (B), differences in the edges of the regions are visible. On the HDR image the edges are clearly defined. On the single image, the edges are fuzzy and the shapes of the regions are not easily identifiable. These differences are shown by the enlargement produced at the top of Figure 3.21. With HDR the shape is well defined and on the contrary with a single frame the shape is less defined and is associated with more random noise. Performing shape descriptor indexes computations is more likely to give reliable results with the HDR method as less isolated pixels are present. The results are similar for inkjet and electrophotography with improved defined edges and shapes with HDR.

As presented on Figure 3.21, ink sub-dots can be extracted from the selected regions of the halftone dots. The area distributions of these sub-dots are represented in Table 3.8 as a function of the print process and as a function of the capture method. Although the edges and shapes of the sub-dots are less precise with a single image capture, it appears that the number of segmented sub-dots is similar for the large area classes, corresponding to sub-dots surfaces greater than 17.7 µm². Below 17.7 µm², the number of sub-dots depends on the capture method. A difference of the number of sub-dots segmented is observed from 17.7 to 1.77 µm² however no clear tendency can be pointed out from the analysis of the 3 print processes. Below 1.77 µm², the single image method is associated with a larger amount of segmented sub-dots. This can be interpreted as a higher amount of noise, thus influencing a correct interpretation of the shape and position of the ink transmittance patterns. That effect is stronger for extremely small sub-dots, inferior to 0.17 µm² going for example from 445 for

the HDR method to 3147 for the single image method for offset prints. The shape descriptor indexes are computed from the class 17.7-1770 µm² for offset and electrophotography and from the class > 1770 µm² for inkjet (Table 3.9).

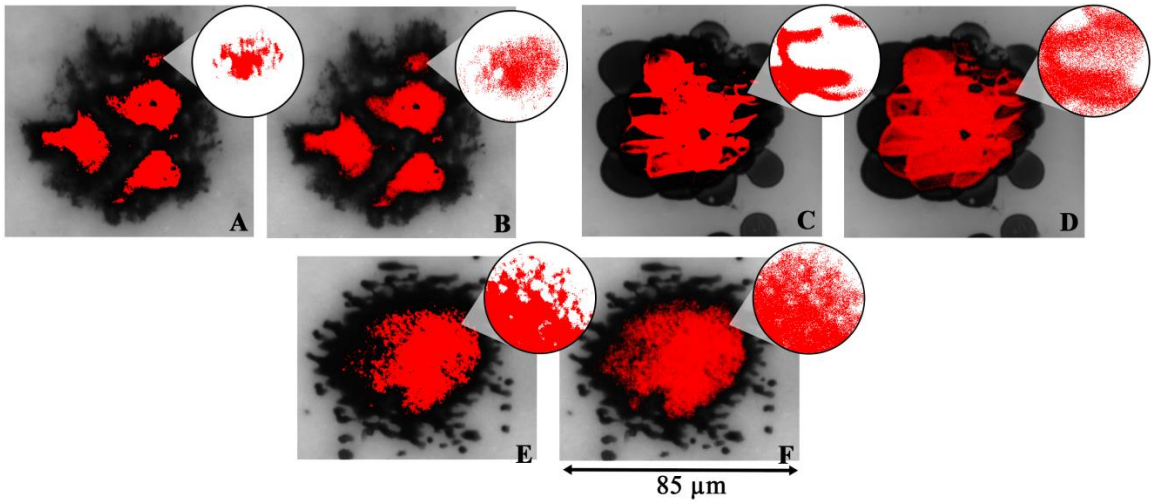

Figure 3.21: Halftone dot at 30% nominal ink coverage printed with offset (A, B), inkjet (C, D) and electrophotography (E, F) and imaged with the HDR method (A, C, E) and using a single capture (B, D, F).

For the 3 processes the sub-dots present a smaller surface when analyzing a single image, with respectively a scaling down of 10.0% for offset, 15.1% for inkjet and 15.0% for electrophotography. This scaling down is relatively small and can be explained by the fuzziness of the edges of the sub-dots obtained with a single image. The difference of the perimeter is important between the two capture methods with a perimeter from the HDR method to the single image method multiplied by 1.71 for offset, 1.86 for inkjet and 2.28 for electrophotography. These increases in perimeter are attributed to the fuzziness of the edges on the single image method. These differences are more problematic, as previous studies have shown that the optical dot gain could be dependent on the perimeter of the halftone dots [18]. Diameters and angles are obtained from an ellipse fit. From Table 3.9, it can be observed that the sub-dots edges and shapes differ. Nevertheless, the diameters found are similar with 0.94 for offset, 0.91 for inkjet and 0.90 for electrophotography. The angles determined are similar except for inkjet with 9.3° difference between the two methods. Four shape descriptor indexes are then calculated. The aspect ratio and the convexity are similar for both capture methods. The circularity and the solidity differ from the two methods. A circularity decrease of 3.8 times is obtained with the single image compared to the HDR. The single image method shows a decreased solidity with a difference of about 1.2 times with the HDR method. These variations are attributed to the fuzziness of the edges of the sub-dots of the single image method. Similarly, the solidity takes into account the convex area, which also depends on the fuzziness of the sub-dots edges.

Table 3.8: Number of sub-dots identified in each area classes defined for the first ink region of a 30% NIC halftone dot printed with respectively offset, inkjet and electrophotography.

Number of sub-dots ( )	**Offset**		**Electrophoto.**		**Inkjet.**	
Area classes	**HDR**	**Single**	**HDR**	**Single**	**HDR**	**Single**
> 1770 µm²	0	0	0	0	1	1
17.7-1770 µm²	3	3	2	2	0	0
17.7-1.77 µm²	8	5	17	13	5	10
1.77-0.17 µm²	19	89	88	262	41	295
< 0.17 µm²	445	3147	1052	6748	1383	1965

Table 3.9: Shape descriptor indexes of class 17.7-1770 µm² for offset and electrophotography and of the class > 1770 µm² for inkjet for a 30% NIC halftone dot.

	Offset		Electrophoto.		Inkjet.	
Imaging method	**HDR**	**Single**	**HDR**	**Single**	**HDR**	**Single**
Area (µm²)	704	634	1691	1438	1485	2768
Perimeter (µm)	253	434	689	1574	649	590
Diameter (µm)	262	246	421	381	117	126
Angle (°)	61.1	61.6	56.4	55.8	0.03	0.01
Circularity ( )	0.14	0.04	0.05	0.01	1.13	1.10
Aspect ratio ( )	1.37	1.34	1.46	1.40	0.88	0.91
Convexity ( )	0.74	0.75	0.69	0.71	0.68	0.54
Solidity ( )	0.79	0.70	0.66	0.52	1485	2768

Optical density and effective ink coverage

Using the microscale measurement to compute the optical density can be of interest in order to extract most information from the microscale capture. The optical density is computed with equation [3.7]. I_{is} and I_{ps} are computed by averaging the pseudo-irradiance values obtained on the images of respectively halftone samples and the images of the paper samples. The optical density is also measured at the macroscale using a conventional spectrophotometer: Techkon SpectroDens B104052, with polarized filter and Iso E density filter. For both methods, the optical density is measured 5 times, on different locations of the patch. The HDR apparatus has a field of view of 0.61 mm² and can capture 15 halftone cells at once. The spectrophotometer has a round aperture of 3 mm diameter and measures approximately 244 halftone cells at once.

Optical density

[3.7] $$D = -\log\left(\frac{\frac{1}{k}\sum_{x,y} I_{is}(x,y)}{\frac{1}{k}\sum_{x,y} I_{ps}(x,y)}\right)$$

Symbol	Unit	Denomination
D	1	Optical density
$I_{is}(x,y)$	1	Pseudo irradiance ink region
$I_{ps}(x,y)$	1	Pseudo irradiance paper region
x,y	1	Pixel coordinates
k	1	Number of pixels

The measurement of the solid print patches for offset reveals similar optical density values for the microscale HDR method and the macroscale spectrophotometer approach, Table 3.10. On another side, measured optical densities differ for electrophotography and inkjet for both methods. These differences can be explained by the accuracy limitation of the spectrophotometer to a maximum optical density of 2.50, as well as differences in the measurement conditions (illuminant, geometry, standard filters, scaling effects). Although an offset appears in the measured optical densities, similar tendencies are measured comparing the optical density obtained by the HDR images and the spectrophotometer on printed halftone patch at 150 lpi shows similar tendencies, Figure 3.22. The offset raises at different nominal surface coverages depending on the process: from 60% for offset, 40% for electrophotography and 70% for inkjet. The offset tends to increase with the increase of the nominal ink coverage. This offset can be explained by a difference in the sensibility of the two measurement methods. For both measurements the uncertainties are small. This shows that the optical density can be estimated from HDR microscale images. This measurement can then be used coupled with other measurements obtained from microscale images, such as the effective ink coverage in order to fit precisely the Yule-Nielsen model for example or to study the effect of the halftone dot morphology on the optical dot gain.

Table 3.10: Average and standard deviation of the optical densities for solid print samples printed by offset, electrophotography and inkjet measured with HDR and with a densitometer.

	Offset	Electrophoto.	Inkjet
HDR	1.60 +/- 0.04	2.49 +/- 0.01	2.65 +/- 0.06
Densitometer	1.65 +/- 0.03	2.81 +/- 0.04	3.11 +/- 0.05

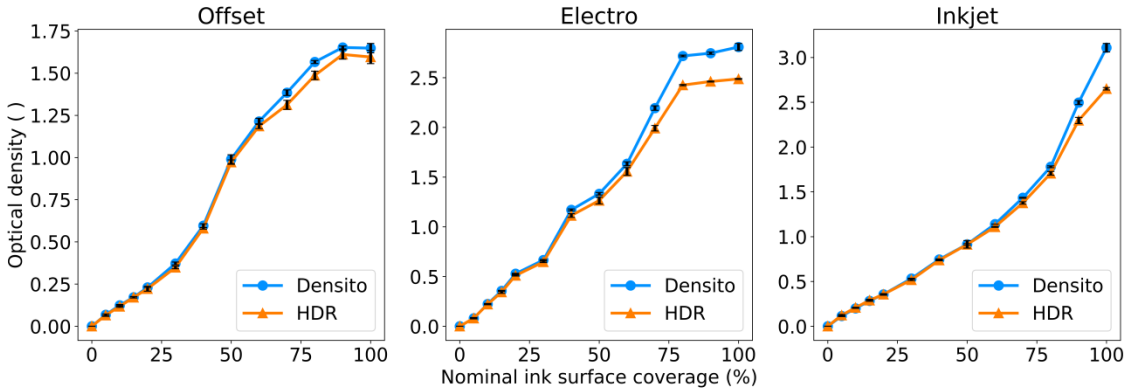

Figure 3.22: Optical density as a function of the nominal ink coverage measured with: (Densito) a densitometer and (HDR) HDR images.

3.6 Multispectral high resolution apparatus development

A set of band pass filters is mounted on the microscope next to the camera sensor. These band pass filters coupled with the monochromatic camera allow obtaining a spectral measurement of the halftone dots at the microscale (spectral response for all pixels in the field of view). To cover the range between 400 nm and 800 nm, 17 filters with a bandwidth of 25 nm are acquired from Edmunds Optics (Hard Coated OD 4 25 nm Bandpass Filters, 25 mm of diameter). The spectral characteristics of these filters can be obtained from the manufacturer's website [358]. The tolerance of the central wavelength is given at +/- 3 nm and the bandwidth tolerance at +/- 3 nm. The optical density of the filter outside the pass band is superior to 4.0 and the transmission in the pass band is superior to 90%. A custom rotating filter wheel is designed to position to switch the filters automatically. The mechanical design and construction is performed by the LGP2 engineering team (Maxime Terrien and Chu Ly Bliamay), Figure 3.23. A step motor was added to rotate the filter wheel. This step motor, a Trinamic Pandrive PD2-013-42 is controlled through a serial RS485 port, implemented directly in Python with the Pyserial module. A micro-switch is used to calibrate the position of the filter wheel upon startups. The integration on the microscope can be seen on Figure 3.8 and Figure 3.10 (G).

The multispectral apparatus was characterized by measuring the spectral region where the light would pass for each filters, Figure 3.24 (A). It can be observed that the relative radiant flux decrease strongly near the wavelength 700 nm and is then close to 0 for wavelength larger than 700 nm. This behavior probably results from the "heat shield filter" near the illuminant source, blocking the illuminant in the near infrared. Therefore bandpass filters with a center passband higher than 700 nm could not be characterized. The central wavelength of the bandpass filters were found close to their nominal values with 403 nm for the 400 nm filter, 427 nm for the 425 nm filter, 450 nm for the 450 nm filter, 477 nm for the 475 nm filter, 500 nm for the 500 nm filter, 523 nm for the 525 nm filter, 550 nm for the 550 nm filter, 573 nm for the 575 nm filter, 600 nm for the 600 nm filter, 623 nm for the 625 nm filter, 647 nm for the 650 nm filter, 677 nm for the 675 nm filter and 697 nm for the 700 nm filter. The band pass widths of the filters were found at an average of 24 nm +/- 2 nm with the exception of the filter at 700 nm that had a measured band pass of 17 nm. This may be due to the

spectral cut off of the illuminant at 700 nm. It has to be noted that the transmission of this filter is also found lower at 75%. It can be concluded from this analysis that this system is ready to measure color halftone dots composed of multiple inks.

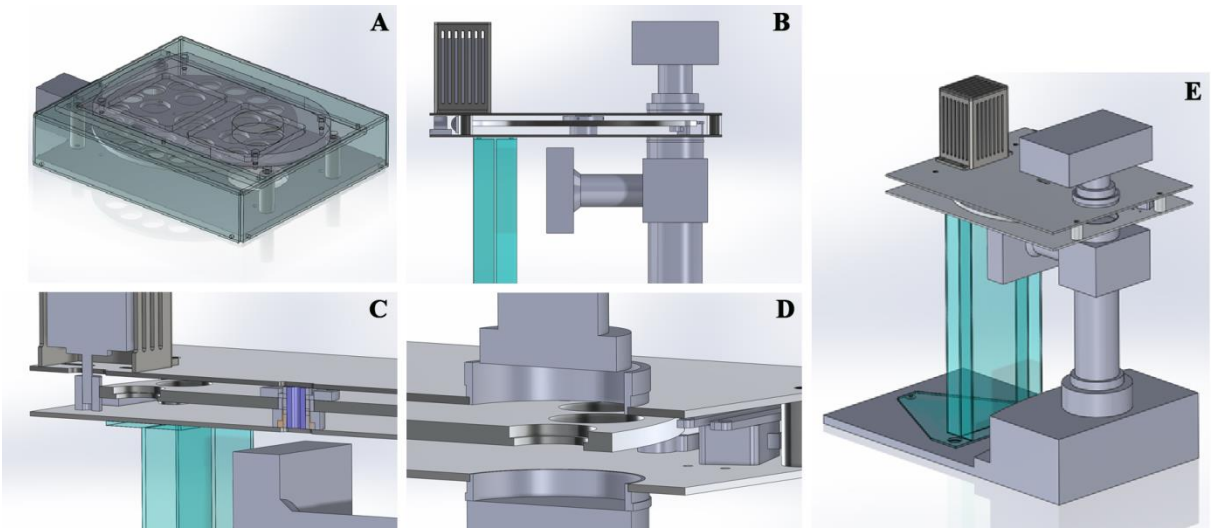

Figure 3.23: Computer assisted design view of the rotating filter wheel and microscope integration.

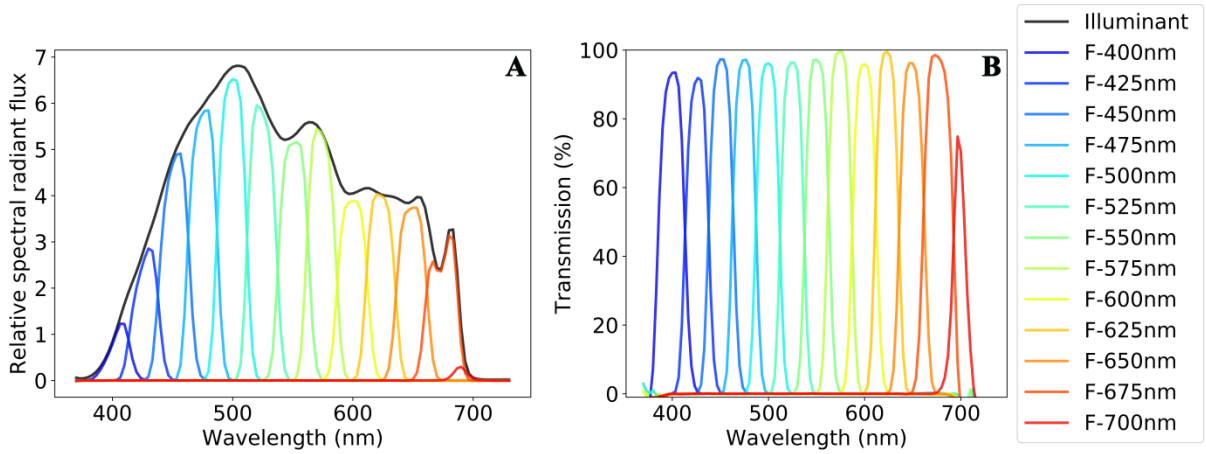

Figure 3.24: Spectral measurements of the illuminant with a blue filter and with the 17 bandpass filters. Measurements performed at the image plane of the microscope with a mirror on the object plane.

3.7 Conclusion

First the test forms were designed. Ten different test forms were produced in order to study the optical and physical dot gain as a function of the dot shape and organization. Conventional amplitude modulated halftone were obtained with Photoshop and a study of the distortion of the ink coverage from the test form 8 bit test form to the binary test form was performed. This study showed that the maximum mean distortion reached 0.15% and was then considered not significant. The Superformula was used to produce multiple dot shapes having constant ink surface with multiple edge perimeters. Halftone dots configurations were generated and placed in an array in order to measure the dot-dot interactions on the shape of the halftone dot.

The three the print processes where then presented and optimized. The morphology of the ink deposition was analyzed using scanning electron images. This revealed that the offset ink deposited

was extremely thin with particles visible in the layer. The inkjet inks had penetrated in the first layer of the paper coating. The matte inkjet ink produced cracks at the edges of the superposition of two droplets. The electrophotography ink deposited produced a thick layer totally covering the paper coating particles. Four papers were used for printing and were analyzed. The two different glossy coated papers showed a layer of mineral particles and bounding agent covering totally the cellulose fibers. The inkjet paper also had a coating on its surface however the roughness of its surface appeared to be much smaller than with the glossy coated paper. Finally the uncoated paper displayed a rough surface with apparent cellulose fibers and mineral fillers.

A specific apparatus designed to measure halftone dots at the microscale automatically was then developed and presented. This apparatus was composed of the shelf optical microscope (Zeiss Axio Imager M1m) equipped with a motorized X, Y, Z stage and mounted with a commercial digital camera (Canon 1200D). This allowed to capture images in a raw format (.CR2) without camera processing such as pixel interpolation, white balance, exposition compensation and gamma processing. The camera was modified to monochromatic to enable a capture without pixel binning. The temperature of the camera and the radiant flux of the illuminant were controlled by installing specific sensors. A filter wheel, with pass band filters of 25 nm bandwidth and 25 nm steps was designed and custom built. All sensors and actuators of the apparatus were controlled and set in a graphic user interface developed in Python programming with the PyQt module. Function such as an autofocus and an auto-positioning of the stage were developed to allow an automatic capture of the halftone dots.

A characterization of the apparatus has been performed and showed accurate measurements. The exposure time did not impact significantly the accuracy of the measurements in the tested range corresponding to conditions for print measurements (with black frame subtraction). However, the coefficient of variation of measurements increased exponentially as the pixel values were decreasing. The linearity investigation of the CMOS sensor showed that three operating regions were present. The first region was observed for pixel values inferior to 1000 and was characterized by an increased noise. The second region was observed for pixel values in-between 1000 and 10000 and was linear with an associated coefficient of determination for the linear regression through the origin of 0.9990 +/- 0.0007. The third region with pixel values superior to 10000 corresponded to the saturation of the sensor. The study of an image of halftone dots captured at a single exposure time showed that 30.0% of the pixel values were inferior to 1000 while at the same time 40.6% of the pixels were superior to 10000. This demonstrated that with a single exposure time capture, saturation and sensor noise from the non-linear region could be expected.

The high dynamic range was consequently developed to improve the measurement accuracy. The HDR method processed capturing frames at different exposure time of the same halftone region and processed then to a fusion of the different images. The improvement of that method was demonstrated by studying the pixel values along a line in an inked region of a halftone image and along a line in the paper region. A large dispersion of the measurement in the inked region is observed with a coefficient of variation of 29.3% for a single exposure time capture. The high dynamic range showed the best improvement with a coefficient of variation of 5.9%. On the paper region only a slight improvement was demonstrated using the high dynamic range method and is due to fact that the paper falls into the linear range with the selected parameters. The HDR method also improved the definition of the ink distribution. On the HDR images the study of the ink transmittance regions showed that the edges were clearly defined. On the single image, the edges were fuzzier and the shapes of the regions were less easily identifiable. The HDR method allows then to improve the microscale measurements of the halftone printed dots.

Chapter 4 Gaussian fit method for automated ink and paper peak measurements

Louis Vallat-Evrard, Lionel Chagas, Raphaël Passas, Nadège Reverdy-Bruas
Univ. Grenoble Alpes, CNRS, Grenoble INP*, LGP2, F-38000 Grenoble, France
Agefpi, LGP2, F-38000 Grenoble, France

4.1 Introduction and background

Recent studies developed approaches to measure precisely dots characteristics at the microscale [7,19,17,18,26,28]. A benefit of the microscale measurements is the possibility to study not only the spatial organization of the halftone dots but also the frequency distribution obtained. Many studies have used the frequency distribution of halftone dots to separate the ink regions from the paper regions [5,19,27,28,35–38]. This separation is required in order to measure the ink and paper coverages. A further analysis of the frequency distribution lead Arney to the observation that the mean reflectance of the ink and of the paper were dependent on the ink coverage [5]. Arney proposed a model, called the expanded Murray-Davies, equation [4.1] [5]. In this model it can be observed that the ink and paper reflectances are dependent on the ink coverage. Arney proposed an empirical formula to obtain the ink and paper reflectances as a function of the ink coverage. This model was constructed from multiple measurements of the ink and paper reflectances as a function of the ink coverage. These measurements were performed manually by the experimenter. An example of ink and paper dependency to the ink coverage is presented in Figure 4.1. For the ink a shifting to higher reflectance values with the increase of the ink coverage can be noticed. For the paper a decrease of the reflectance values can be observed with the decrease of the ink coverage can be also noticed. These dependencies are dictated by the light diffusion on the halftone print and is an expression of the phenomena called optical dot gain. Arney suggested that the ink and paper reflectances could be measured taking the maximum of the peak in the ink region and the maximum of the peak in the paper region. This approach is valid for halftones where there is a significant amount of either ink or paper resulting in visible peaks for the ink and paper regions. However as presented on Figure 4.1, for the 5% nominal ink coverage halftone, the peak corresponding the ink is small and hard to identify using a maximum search. Similarly starting from 50% ink coverage the paper peak is difficult to identify, even when using a log-log transformation. An automatic method to measure the ink and paper mean reflectance could then lead to an improvement of the accuracy of the model.

Expanded Murray-Davies model

		Symbol	Unit	Denomination
[4.1]	$R_a = (1 - a_e)R_p(a_e) + a_e R_i(a_e)$	R_a	1	Halftone reflectance
		$R_i(a_e)$	1	Ink reflectance in halftone
		$R_p(a_e)$	1	Paper reflectance in halftone
		a_e	1	Effective ink surface

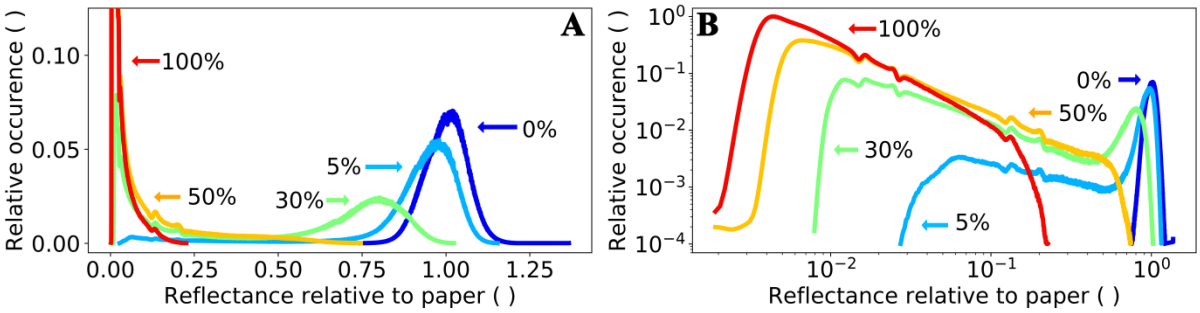

Figure 4.1: Reflectance distributions (histograms) for solid print, paper and halftone of 5% and 50% nominal ink coverages printed with offset. (A) Linear axis, (B) Log-Log axis.

Therefore a method is proposed in this work to measure automatically the ink and paper reflectance peaks for all ink coverages. The method is based on the observation that solid print and paper have reflectance distributions close to Gaussian functions. The approach proposed fit a Gaussian function to the ink and paper peaks, allowing an automatic measurement of the center of the ink and paper reflectances peaks. It can be observed on Figure 4.1 that the light scattering into paper can spread the reflectance values and transform the Gaussian distribution to a non-Gaussian distribution (for example paper peak on the 50% nominal ink coverage curve). The effect of fitting a Gaussian curve to non-Gaussian reflectance distributions will be studied to validate the proposed method. The work presented focuses first on a presentation of the method developed, on a validation of the hypothesis adopted for the convergence and on a validation of the criteria used for the optimization. Then in a second part, the method will be evaluated on simulated halftone dots. Finally in a third part the method will be applied to halftone dots measured with an optical microscope. The ink and paper reflectances obtained will be compared to manual measurements and to models from literature.

4.2 Materials and methods

4.2.1 Printed samples and acquisition

Ink and paper mean reflectances are measured on printed halftones, prepared with three different processes: offset, inkjet and electrophotography. Specifications of the print processes are presented in Table 4.1. Inks and papers selected are optimized for each process and a specific test form is generated for each print processes at the native print resolution of the device. Test forms are prepared and consist of halftone patches going from 0 to 100% ink coverage with 10% increments. For low ink coverages halftone patches of 5% and 15% are added. Two test forms are generated with amplitude modulated halftoning of 150 and 200 lpi using Photoshop CS6 circular dot bitmap function.

Printed halftone dots are measured with a modified optical microscope, based on a Zeiss Axio Imager M1m optical microscope mounted with an EC Epiplan Neofluar 20x/0.5 HD DIC objective. A 90° polarized reflected light configuration with a 0°/0° geometry is chosen to capture halftone dots, thus excluding specular reflections. A halogen lamp Zeiss Hal 100 is used as light source for the microscope and the lamp voltage is set to 10.0 V. The source used does not match with a standard illuminant however is considered close to D65 standard illuminant. A Canon 1200D camera, equipped with a modified monochromatic CMOS sensor is used to image the halftone dots. The sensor is composed of 13.8 mega pixels: 4600 columns and of 3000 rows of photodetectors having a physical pixel width of 4.21 µm. The resolution at the focal point of the sensor is equal to 0.2101 µm/pixel, giving an observation field of 966x630 µm². Images are saved in ".CR2" raw format, to preserve the unprocessed pixel values. Parameters imposed are the level of electron amplification (ISO level), set at 800 (best compromise to reduce exposure time noise compared to amplification noise) and the

integration time for the integration of the photons on the surface of the photodetectors (exposure time), set at 1.6, 1/5 and 1/40 seconds for offset prints and at 2.5, 0.3 and 1/30 seconds for electrophotography and inkjet prints. High dynamic range is performed in order to extract richer information from the measurements. The captures are corrected with black frame subtraction; the illumination of the field of view is corrected for uniformity; the illuminant mean irradiance is measured and compensated for each capture and the temperature of the sensor is monitored.

Table 4.1: Paper, ink and printing processes.

Printing process	Resolution	Dot size	Paper (g/m²)	Ink (Black)
Offset: Heidelberg Speedmaster 52	2540 dpi	10.0 µm²	Glossy 1: Unknown supplier, coated, 135	Novavit 918 supreme
Inkjet: Epson Stylus Pro 4900	1440 dpi	17.6 µm²	Epson: Epson proofing, coated 205	Epson PK T6531
Electrophotography: Xerox Versant 180 Press	1200 dpi	21.2 µm²	Glossy 1: Unknown supplier, coated 135	Xerox Versant 80 Press
Electrophotography: Xerox Versant 180 Press	1200 dpi	21.2 µm²	Glossy 2: Mondi, coated, 135	Xerox Versant 80 Press
Electrophotography: Xerox Versant 180 Press	1200 dpi	21.2 µm²	Epson: Epson proofing, coated 205	Xerox Versant 80 Press
Electrophotography: Xerox Versant 180 Press	1200 dpi	21.2 µm²	Uncoated: Inapa, uncoated, 160	Xerox Versant 80 Press

4.2.2 Ink and paper reflectance peaks determinations

An algorithm based on a Gaussian fitting of the histogram is proposed in order to determine ink and paper peaks:

- Starting from an image of halftone dots with reflectances normalized (by dividing the halftone image by the average reflectance value of the bare paper), the pixel array is smoothened with a Gaussian kernel of size 3. This removes reflectance extrema and pixel values from defective photosites.
- Numpy 1.14.3 histogram function is used in Python 3.5 with 100,000 bins in the range of the maximum and minimum pixel value of the image.
- The zero counts of the histogram are removed and a smoothing is performed using a convolution with a Gaussian kernel size corresponding to 0.5% of the histogram length.
- The histogram is then separated in two sub-histograms. The reflectance value for this separation, called x_T , is obtained at 0.1 of the histogram length. Theoretically the ink peak should then be found between the ink reflectance and the ink transmittance values and the paper peak should then be found between the ink transmittance and the paper reflectance. However due to several effects such as the variation of the ink thickness, it was found that a separation corresponding to 0.1 of the histogram length would work better. The first sub-histogram ranges from the reflectance value x_0 to x_T and the second sub-histogram ranges from x_T to x_1.
- On each sub-histogram a double optimization is performed on order to find the ink and paper peaks. A double optimization is used in order to fit two parameters of the Gaussian function: the width of the Gaussian σ and the position of the center of the Gaussian µ. The third parameter of the Gaussian function is fixed: the height of the Gaussian γ is set to be equal to the height of the histogram distribution at a given reflectance. The Gaussian function is presented in equation [4.2]. The optimization of the parameters of the Gaussian are performed in two steps. For all positions x on each sub-histogram an optimization of the width of the Gaussian σ is performed with $\mu = x$. The optimization strategy employed is described in paragraph 4.2.2.1. A criterion is computed for each σ optimized Gaussian at each µ position and the maximum of this criterion gives the position where the Gaussian function fits the best the histogram distribution. The optimization strategy for

the position μ is described in paragraph 4.2.2.2. Both optimization criteria, Crit_σ, equation [4.3], and Crit_μ, equation [4.4], are defined empirically. For Crit_σ, an average of the absolute differences between the Gaussian curve and the histogram distribution is computed for each reflectance value in the selected range. For Crit_μ, three indexes are multiplied according to the following hypothesis: the fitted Gaussian function should be closest to the histogram distribution, the width of the Gaussian function should be as small as possible and the height of the Gaussian should be as high as possible.

Gaussian function

		Symbol	Unit	Denomination
[4.2]	$G(x)_{\mu,\gamma,\sigma} = \gamma \exp\left(-\frac{(x-\mu)^2}{2\sigma^2}\right)$	$G(x)$	1	Gaussian function
		μ	1	Position peak center
		γ	1	Height of peak
		σ	1	Width of the peak

σ optimization criterion

		Symbol	Unit	Denomination
[4.3]	$\mathrm{Crit}_\sigma = \frac{\sum_{x=i}^{N} \sqrt{\left(G(x)_{\mu,h,\sigma} - h_s(x)\right)^2}}{N}$	Crit_σ	1	σ Optimization criterion
		$G(x)$	1	Gaussian function
		$h_s(x)$	1	Sub-histogram
		x	1	Reflectance position

μ optimization criterion

		Symbol	Unit	Denomination
[4.4]	$\mathrm{Crit}_\mu = -\log_{10}\frac{\mathrm{Crit}_\sigma\,\sigma}{\gamma}$	Crit_μ	1	μ Optimization criterion
		Crit_σ	1	σ Optimization criterion
		γ	1	Fitted Gaussian height
		σ	1	Fitted Gaussian width

4.2.2.1 Optimization of σ

The optimization of the width of the Gaussian peak is performed based on the assumption that the curve representing the optimization criterion Crit_σ, equation [4.3], as a function of the width σ, has an inverse bell shape. A bisection algorithm strategy is adopted. Starting from one edge of the bell, the optimization loop increments σ with a fixed step. The optimization criterion of the incremented σ is compared to the non-incremented σ. In the case of a smaller Crit_σ with the incremented σ, the incremented σ is adopted and re-incremented in the same direction. In the other case, the direction of the increment is reversed and the step is reduced by a division of 1.2. In this way the algorithm finds quickly the minimum of the inverse bell shape of the $\mathrm{Crit}_\sigma(\sigma)$ function. The algorithm is stopped when the step becomes smaller than a defined value and the best fitting σ is returned. The starting step is equal to 90% and the stop step is equal to 0.001% of the distribution length.

4.2.2.2 Optimization of μ

The optimization of the position cannot adopt a bisection algorithm since the optimization criterion as a function of the position has multiple local maxima. A strategy using multi-pass is then adopted. For the first pass, the position is incremented from x_0 to x_T and from x_T to x_1 with a step corresponding to 0.3% of the range length. For each increment, $\mu = x$ is set, σ is optimized and Crit_μ

is computed, equation [4.4]. $Crit_{\mu}$ as a function of the position is then obtained. This function is analyzed and a maximum is validated if this maximum is not on the edge of the range and if the maximum height is superior to 1.1 times the height at the position x_T. If these conditions are not fulfilled, the first derivative of the $Crit_{\mu}$ is computed. The position corresponding to the middle between the maximum and the edge of the function is then adopted. The maximum of the derivative corresponds to the largest gradient of $Crit_{\mu}$ and is proven to be significant when ink or paper peaks are spread (for example paper peak on the 50% nominal ink coverage curve on Figure 4.1). The best fitting position x is then stored. The second pass processes in the same way with a step divided by 10 in a reduced x range centered on the best fitted μ obtained during the first pass and with a range width of +/- 10 times the step. Next passes occur similarly and the algorithm is stopped when the step becomes inferior to 1 (the bin width of the histogram). The best fitting position μ is then returned.

4.2.3 Optical dot gain simulations and applications on halftone images

Optical dot gain simulations

Optical dot gain simulations are conducted to understand the impact on the ink and paper reflectance distributions. The influences of the PSF (Point Spread Function) size, of the ink dot size, of the ink coverage and of the halftone configuration are analyzed. These simulations are performed with the model of light diffusion on halftone, equation [4.6]. This model has been introduced by Callahan, Yule and Lehmbeck [8–16]. The model takes as input the ink transmittance function (2D description of the ink surface), the paper reflectance function (2D description of the bare paper reflectance) and the point spread function (2D description of the light diffusion into paper).Thus in this model the ink thickness can be heterogeneous and also depends on the ink spectral absorption characteristics. It has to be noted that in this work T_i and R_{ps} can be expressed without expressing their dependencies (x, y, λ). To perform optical dot gain simulations, the ink transmittance, the paper reflectance and the point spread function are generated. A smoothening with a Gaussian kernel of size 3 is used to remove the extrema and to reduce the amount of noise. T_i and R_{ps} distributions are generated using a Gaussian function with averages and standard deviations obtained by analyzing the ink and paper distribution of an electrophotography printed solid image and a bare paper image. To obtain the ink transmittance average and standard deviation, the square roots of the solid reflectances have to be computed:

$$T_i = \sqrt{\frac{R_{is}}{R_{ps}}} \qquad [4.5]$$

The halftone patterns are generated with a Python algorithm generating an array of discs. The generation of the point spread function is performed using a Gaussian function with 3 parameters: the Gaussian width, the Gaussian height and the distribution length. An example of PSF generated is presented on Figure 4.8 (C).

Model of light diffusion on halftone

		Symbol	Unit	Denomination
[4.6]	$R_a(x,y) = R_{ps}(x,y)\, T_i(x,y)$ $[T_i(x,y) \circledast H(x,y)]$	$R_a(x,y)$	1	Halftone reflectance
		$T_i(x,y)$	1	Ink transmittance
		$R_{ps}(x,y)$	1	Bare paper reflectance
		$H(x,y)$	1	Paper point spread function
		$\circledast$	-	Convolution operator

Optical dot gain simulations are also performed on measured halftone dots printed with electrophotography, offset and inkjet at 150 lpi and 200 lpi. The ink transmittance function is obtained

by thresholding the images of the printed halftones with Otsu threshold [168] algorithm. The ink and the paper reflectance distributions are then simulated similarly than for the simulated dots.

Manual measurements

Manual measurements are performed with ImageJ 1.51d [357] using multiple selections of respectively the ink and the paper regions and by computing the mean reflectance of the selected positions, Figure 4.2. It has to be noted that for cases where the paper surface is extremely small, a modification of the viewing conditions is performed in ImageJ in order to improve the visual separation of the ink and of the paper. This modification does not change the measured reflectance.

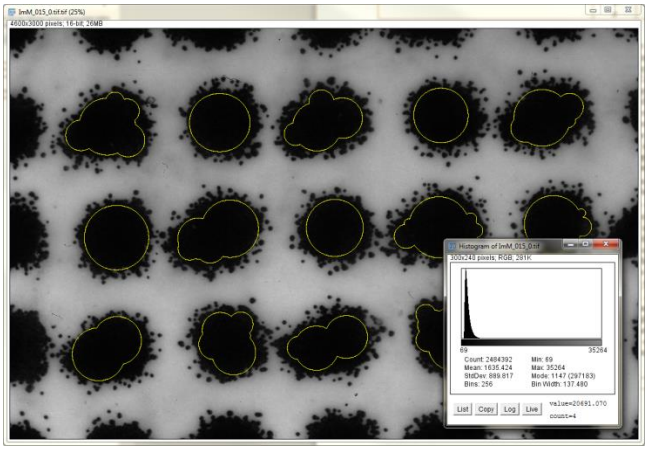

Figure 4.2: Manual measurement of the ink reflectance on a 15% nominal ink coverage 150 lpi halftone printed with electrophotography using the ImageJ software.

Ground truth

The ground truth is obtained by computing the mean reflectance over the ink and paper regions prior to the optical dot gain simulation.

Complete light diffusion

The complete light diffusion approximation corresponds to the situation where the photons diffusion is large compared to the halftone size. In that case paper and ink reflectances do not depend on the position on the halftone (distance with an ink/paper interface). In this case the ink and paper reflectances can be obtained theoretically as a function of the ink coverage. Two singular ink coverages for the ink and two singular ink coverages for the paper can be considered:

- for the ink when the ink coverage is extremely small, only photons diffusing from the paper will emerge over the inked region and the reflectance is equal to $R_{ps}T_i$
- for the ink when the ink coverage is almost total, it can be considered that no photons from the paper will exit above an ink region and thus the reflectance associated is $R_{ps}T_i^2$
- for the paper a reflectance equal to R_{ps} is obtained for extremely small ink coverages
- for the paper when the ink coverage is almost total a reflectance equal to $R_{ps}T_I$ is obtained

In between these singular ink coverages an average weighted by the ink coverage gives the ink and the paper reflectance:

$$R_i(a) = (1-a)\,R_{ps}T_i + a\,R_{ps}T_i^2 \qquad [4.7]$$

$$R_p(a) = (1-a)\,R_{ps} + a\,R_{ps}T_i \qquad [4.8]$$

It has to be noted that for the halftone printed with offset, the complete light diffusion model was modified since the solid print surface included inking defects. These defects reduced the ink coverage to 86.2%. The computation of the ink transmittance for an ink region that is solid does not

satisfy the conditions (i.e. homogeneous optical dot gain). The best approximation achievable in that case is to select manually ink regions that are located far away from paper defects, to compute the mean reflectance value over these regions and to use it as if it corresponded to the reflectance of the solid print patch.

Mean absolute difference index

To quantify the differences between the three measurements (Gaussian fit, manual measurement and ground truth), an index corresponding to the mean absolute differences is proposed. The mean absolute differences are expressed in percentage relative to the ground truth.

4.3 Results and Discussions

4.3.1 Ink and paper reflectance peaks determinations

The ink and paper peak determination by Gaussian fit is applied to a solid print patch, a paper patch and as well as on a 30% nominal ink coverage halftone printed with electrophotography. Results of the fits are presented on Figure 4.3. In the case of solid print, the Gaussian fits more accurately the left side of the distribution. The solid print region appear to be composed of multiple Gaussian distributions caused by different ink thicknesses. The electrophotography process deposits solid print particles, called toner at the surface of the paper. If a variation of the number of toner particles stacked at a location occurs, regions with different reflectances would appear and the ink reflectance distribution would be spread. Nevertheless the single Gaussian fitting the ink distribution covers 85.2% of the ink distribution in the $1.56x10^{-3}$ to $4.56x10^{-3}$ reflectance range, Figure 4.3 (A). The ink distribution average reflectance is found at the reflectance of $3.09\ x10^{-3}$ and the fitted Gaussian center at $3.06x10^{-3}$. This difference corresponds to an optical density difference of 0.004 and is not significant. The glossy coated paper has a reflectance distribution fitted almost accurately with a single Gaussian, Figure 4.3 (B). The Gaussian curve covers 99.2% of the ink distribution in the 0.81 to 1.20 reflectance range. The choice of a Gaussian fit to determine the paper mode is then justified. The paper peak distribution average is found at the reflectance of 1.0064 and the fitted Gaussian center at 1.0032. The difference is not significant. It has to be noted that the reflectance values obtained are relative to the mean reflectance value of bare paper. For that reason reflectance values superior to one are obtained.

Subsequently, the halftone patch at 30% ink coverage is fitted by two Gaussian functions, one for the ink and one for paper. Gaussian functions fit correctly the distribution for ink and paper on respectively the left of the ink peak and the right of the paper peak, Figure 4.3 (C) and (D. On the other half part, the Gaussian fits for the ink and paper do not follow the halftone reflectance distribution. This is attributed to optical dot gain [225], acting similarly than a smoothening filter and spreading the ink and paper reflectances. It has to be noted that for the ink the spreading of the reflectance distribution may be attributed to other factors such as ink penetration for example [359]. The ink peak fitted with the Gaussian is found at the reflectance value of $1.09x10^{-2}$. The peak maximum is measured at $1.11x10^{-2}$ and a difference of 0.039 of optical density is found. This difference is small, showing that the optimization criteria $Crit_{\mu}$ takes correctly into account the search for the maximum occurrence, similar to the ink mode. In the case of paper, the fitted Gaussian center is found at the relative reflectance value of $6.83x10^{-1}$. The peak maximum is measured at $7.09x10^{-1}$ and a difference of 0.016 of optical density is found. For this case, the fitted Gaussian is shifted toward lower reflectance and shows more accurately the effects from the optical dot gain than by using the mode. Moreover the mode method has a limit when no paper peak can be distinguished, especially for large effective ink coverages. The Gaussian fitting is not designed to find a local maximum but instead is designed to find the Gaussian center and width that will represent best the fitted the peak.

The reflectance of the ink in the halftone patch is observed to have shifted toward higher reflectance values with a decrease of the optical density of 0.552. Similarly the paper reflectance in the halftone is observed to have shifted toward lower reflectance values with an increase of the optical density of 0.167. It has to be noted that the ink distribution in the halftone patch shows a variation at the reflectance 1.67×10^{-2}. This variation is an artifact generated from the HDR (High Dynamic Range) reconstruction (when two captured images overlap) and is therefore not an attribute of the halftone. These artifacts are tracked to monitor their influence.

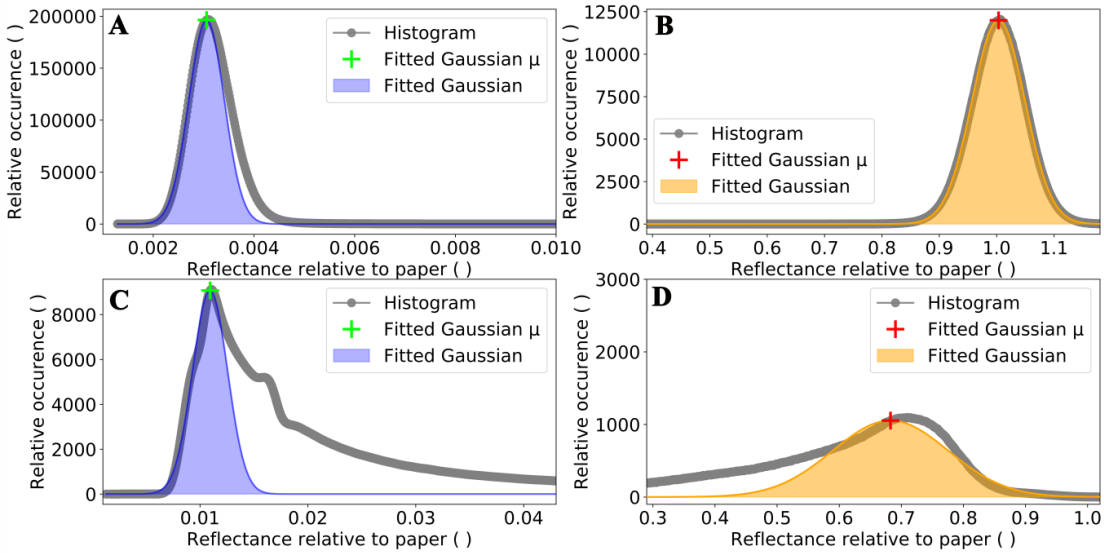

Figure 4.3: Gaussian fittings of the reflectance for (A) solid print, (B) paper, (C and D) ink and paper regions of a 30% nominal ink coverage halftone printed with electrophotography.

The repeatability of the Gaussian fitting is analyzed on 5 images of a 30% nominal ink coverage halftone printed with electrophotography, Table 4.2. In order to separate the variations associated with the print and the variations associated the Gaussian fitting, the average of the reflectances of the halftone is computed. The variations of the Gaussian fittings are smaller than the variations of the halftone and thus the Gaussian fitting method is accurate and reproducible. Often in the print industry the reflectance measurement is transformed into optical density. It can be observed that the variation associated with the Gaussian fitting of the ink peak is found largely inferior to the variation of the halftone. For the paper the Gaussian fitting shows larger relative variations than the halftone. This variation is nevertheless globally small and it can be concluded that the fitting Gaussian method is consistent for multiple measurements.

Table 4.2: Halftone, ink and paper reflectances (R) and optical density (OD) measurements based on 5 images captured at different locations on a single 30% nominal ink coverage halftone patch printed with electrophotography.

	Average	Coefficient of variation (%)
R_a	0.243	3.07
R_i fitted	0.011	1.68
R_p fitted	0.692	2.32
OD_a	0.614	2.16
OD_i fitted	1.960	0.37
OD_p fitted	0.160	6.32

The convergence curves of the two optimization algorithms are investigated in order to validate the hypothesis adopted for these two algorithms. The optimization criteria $Crit_\sigma$ described in equation [4.3] is plotted as a function of the Gaussian width σ for ink and paper, Figure 4.4 (A) and (B). It can be observed for ink and paper that the optimization criterion has local minima. However since the

algorithm looks for the minimum with a decreasing step, the optimization would converge automatically toward the global minimum. A small error may occur if the optimization algorithm converges toward a local minimum next to the global minimum (potential error of 1.02% of the fitting range for the paper on Figure 4.4 (B)). The accuracy of the convergence of the optimization algorithm could be improved, however since an optimization of the Gaussian width is required at each step of the optimization of the Gaussian position μ, the computation speed is also a factor of consideration. The choice of the bisection algorithm allows having an average of 80 +/- 25 Crit_σ iterations (average over 2300 optimizations) to converge as compared with 90000 Crit_σ iterations for a direct search (with similar range and step).

The optimization criterion Crit_μ described in equation [4.4] is plotted as a function of the Gaussian position parameter μ for ink and paper fits, Figure 4.4 (C) and (D). These curves present multiple discontinuities. A bisection algorithm might not lead to the global maximum. However global maxima are present on both the optimization function for the ink and for the paper. A multi-pass algorithm is then adopted. The first pass will have large steps in order to obtain the global shape of the function. The steps are then decreased and the range reduced around the previous maximum of the function. It has to be noted that for the fitting of the Gaussian position, the optimization criterion has a dependency to the height and to the width of the fitted Gaussian. By adding these dependencies, Crit_μ presents a global maximum improving the definition of the position of the ink or the paper peak.

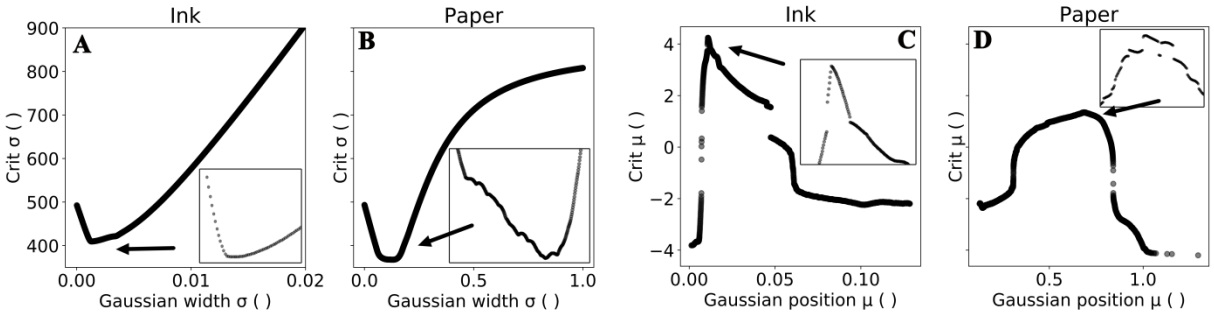

Figure 4.4: Optimization criteria curves as a function of the Gaussian parameter for the two algorithms: (A) and (B) optimization of σ, (C) and (D) optimization of μ, of a 30% nominal ink coverage halftone printed with electrophotography.

The bin size as well as the size of the Gaussian kernel used for smoothing the histogram are investigated, Figure 4.5. The bin size effect is directly linked to the image capture parameters and influences the shape of the histogram, as explored by Wand [360]. Since high dynamic range is performed, the reflectance step (pixel value step divided by the exposure time) for each image of the HDR differs and the reconstructed image has "composed" sampling frequencies. A limit appears above the bin size equal to 10^4 where the shape of the histogram is not influenced anymore by the increase of the bin size Figure 4.5 (A). Then with the increase of the number of bins the occurrences are found smaller (bin sizes become smaller). In order to obtain accurate ink and paper reflectance measurements, clear count differences between the different regions of the histogram are required. This is obtained by reducing the bin size. However small bin sizes lead to a reduced accuracy of the measured ink and paper reflectances. A single image is encoded on 14 bits with an offset of 2048 and a maximum at 15306. Thus 13258 irradiance levels are discretized per single image. The high dynamic range is performed with 3 images with a potential amount of 39774 reflectance level discretized. The bin size of 10^4 could potentially be insufficient regarding the potential amount of pixel levels.

The effect of the bin size and of the smoothening kernel size is investigated on the ink and paper peaks reflectances obtained by the Gaussian fitting, Figure 4.6 (A, B, C, D). The effect on the fitted Gaussian peak width is investigated as well, Figure 4.6 (E, F, G, H). The measured reflectances of the ink and paper peaks are sensitive to the bin size of the histogram and to the size of the smoothening

kernel. It can be observed that when increasing the bin size, the ink and paper reflectances and fitted Gaussian width stabilize. This stabilization appears starting from the bin size equal to 10^4 for the ink and 10^5 for paper. The dispersion of the reflectance measurements for the ink and paper are also dependent on the bin size with a global decrease of the dispersion with the increase of the bin size. For these reasons the bin size of 10^5 is adopted.

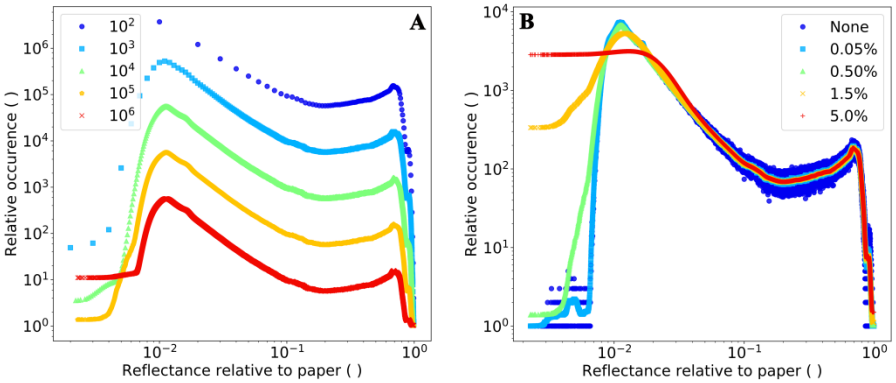

Figure 4.5: (A) Effect of bin size and (B) effect of the Gaussian smoothing on the histogram of a 30% nominal ink coverage 150 lpi halftone printed with electrophotography.

The choice of the size of the smoothening relative to the histogram length has also an important influence on the histogram shape, Figure 4.5 (B). For a smoothening with a small kernel size, the histogram shows large dispersions due to noise in the quantization of pixel levels of the captured image. A large noise is observed, especially when no smoothening is performed in the region around the paper peak. Smoothening solves this issue, however it can change significantly the histogram shape as shown with relative kernel sizes larger than 0.5%. The maximum of the ink peak is translated to the right with the increase of the kernel size. For the paper peak, the smoothening with increasing kernel sizes does not change the shape of the peak. Smoothening with the kernel size of 0.5% appears to reduce the histogram dispersion without introducing significant deformations of the histogram.

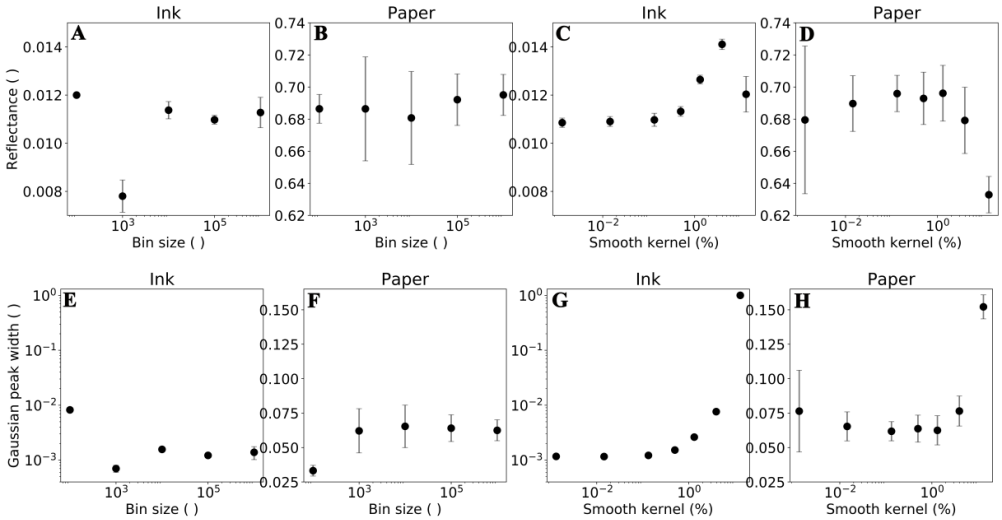

Figure 4.6: Ink and paper reflectances (center of the fitted Gaussians) as a function of the histogram bin size (A), (B) and as a function of the smoothening kernel size (C), (D). Fitted Gaussian widths as a function of the histogram bin size (E), (F) and as a function of the smoothening kernel size (G), (H).

The smoothening has also an effect on the fitted ink and paper reflectances and on the fitted Gaussian peak width, Figure 4.6 (C), (D), (G), (H). The fitted reflectance for the ink has a tendency to increase with the increase of the smoothing kernel caused by a translation of the distribution toward higher reflectance values and by a broadening of the ink peak width. For smoothening with kernel size below 0.5% of the distribution size, the fitted reflectance increase remains small compared to the fitted

reflectance without smoothening. The associated measurement dispersion is small. For the paper peak, the increase of the smoothening kernel does not affect the fitted paper peak reflectance for kernel sizes from 0.01% to 1.3%. A reflectance decrease is then observed for kernel size larger than 1.3%. The dispersion of the fitted paper reflectance is larger without smoothening than with a small smoothening. The fitted Gaussian width also benefits from a smoothening with a small kernel size. Taking into consideration the fitted ink and paper reflectance peaks, the fitted Gaussian width and the dispersion associated with these measurements a bin size of 10^5 with a smoothening kernel of 0.5% of the distribution size are found to be best suited for the application.

4.3.2 Optical dot gain simulations

Simulations are conducted to understand the capabilities and limits of the Gaussian fit method. First simulations of the impact of different optical dot gains on a single ink and paper dots of 17 µm in diameter are conducted, Figure 4.7. The ink and paper distributions are simulated based on a Gaussian distribution with the ink transmittance equal to 0.056 +/- 0.003 and the paper reflectance equal to 1.003 +/- 0.035. The initial distributions are represented on "PSF 0", Figure 4.7. It can be observed that the simulation of the optical dot gain produces a shift of the Gaussian distributions to the right for the ink reflectances and to the left for the paper reflectances. Simulations with large PSF show distributions with larger shifts. A shift limit is observed and corresponds to the ink transmittance value T_i. This limit can is demonstrated with the model of light diffusion on halftone. If the ink surface is very small, the convolution with a large PSF will leads to:

$$[T_i \circledast H] = 1 \text{ for } a_e \to 0 \quad [4.9]$$

with R_{ps} normalized to 1 the ink reflectance is then equal to:

$$R_i = T_i \text{ for } a_e \to 0 \quad [4.10]$$

Similarly if the ink surface is large:

$$[T_i \circledast H] = T_i \text{ for } a_e \to 1 \quad [4.11]$$

the paper region will then be equal to:

$$R_p = T_i \text{ for } a_e \to 1 \quad [4.12]$$

Nevertheless, this limit cannot be used directly to separate the ink from the paper, since the halftone reflectances are influenced by ink thickness variations and by complementary optical effects (internal reflection, ink penetration, etc.).

The initial Gaussian distribution shape for ink and paper can spread depending on the ratio between the ink dot size and the PSF length, Figure 4.7. For ratios above 0.5, the ink peak spreads and the distribution is not Gaussian anymore. With larger PSF sizes, (ratios below 0.5) only a uniform decrease of the paper reflectance can be observed. Similarly the increase of the ink reflectance tends to be more uniform and the distribution is kept Gaussian. Authors have shown that a ratio below 0.5 was corresponding to the complete light diffusion approximation (CLDA): the probability of measuring a photon being independent on the position on the halftone [319,361]. The CDLA corresponds to the case of the Yule-Nielsen model with n=2. This effect can be observed by comparing PSF 0 PSF 2 and PSF 7 on Figure 4.7 (D). The ink and paper peak fittings rely on the assumption of a Gaussian distribution, thus the fitting when the distribution is not Gaussian may lead to incorrect ink and paper peaks reflectances. Nevertheless, errors induced can be controlled by monitoring the ratio of the surface peak covered by the fitted Gaussian peak.

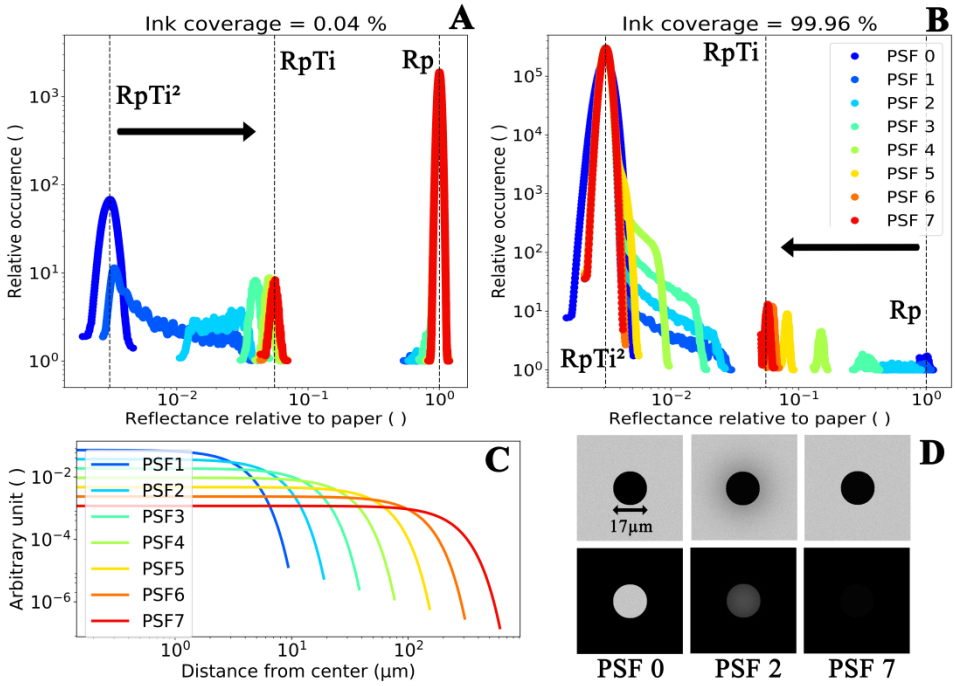

Figure 4.7: Optical dot gain simulations with multiple PSF kernel sizes: (A) Reflectance histograms of a single small ink dot on paper, (B) Reflectance histograms of a single small unprinted dot on solid printed paper, (C) Shape of the PSF to simulate the reflectance images, (D) Examples of a single small inked dot on paper and of a small unprinted dot on solid printed paper simulated with different PSF. PSF 0: ink and paper distribution without optical dot gain simulation. PSF 1 to 7 simulations with PSF length of respectively 9.6, 19.2, 38.3, 76.6, 153.2, 306.4 and 612.9 µm. T_i is the bare ink transmittance and R_{ps} the bare paper reflectance.

Halftone images with multiple halftone cells are generated. The PSF used has a length of 100 µm, Figure 4.8 (C). Results of the optical dot gain simulation can be observed on Figure 4.8 (E) for 50% nominal ink coverage halftone dots with different cell width: 75 lpi and 300 lpi. The simulation for the halftone dots with 75 lpi shows a large shadow around the dots corresponding to optical dot gain with incomplete light diffusion. In this case, the ink and paper reflectances are heterogeneous and depend on the position on the surface of the halftone. The associated histogram will therefore be associated with spread peaks. The simulation for the halftone dots with 300 lpi shows a global decrease of the reflectance of the paper and an increase of the reflectance for the ink. Paper and ink reflectances are more homogeneous and will be associated with well-defined peaks. For 300 lpi halftone cells with a 100 µm PSF the complete light diffusion occurs.

From these simulated images, the ink and the paper reflectances measured with the Gaussian fitting method are compared to the ground truth and to manual measures, Figure 4.8 (A) and (B). The ground truth is the absolute reference and is obtained by measuring the average reflectances of the ink and paper regions defined before optical dot gain simulation. For halftone cells above 300 lpi, the Gaussian fit and manual measurements give results similar to the ground truth. Relative mean differences between the Gaussian fit and the ground truth for the three ink coverages (25%, 50% and 75%), reach 0.52% +/- 0.15% for the ink and 0.31% +/- 0.10% for the paper. These relative differences are similar to the differences between the manual measurement and the ground truth reaching 0.36% +/- 0.70% for the ink and 0.27% +/- 0.43% for the paper. Below 300 lpi results show a greater variation of the Gaussian fittings compared to the ground truth with mean differences of 25.6% +/- 31.1% for the ink and 10.0% +/- 8.0% for the paper. Similar mean differences associated with a smaller dispersion are observed with the manual measurement with 25.6% +/- 10.6% for the ink and 11.0% +/- 4.0% for the paper. From these results the Gaussian fit does not show an improved accuracy compared to the manual measurements. However the proposed method can be computed automatically and is therefore unbiased. Moreover it has to be noted that the simulation of theoretical perfect dots

leads to a large spreading of the reflectance distribution and can explain the lack of performance of the proposed method.

With the increase of the halftone cell lpi, a respective decrease of the ink reflectance and increase of the paper reflectance is visible, Figure 4.8 (A) and (B). It is interesting to note that when the complete light diffusion approximation applies the ink and paper reflectances reach a plateau. The value of this plateau only depends on the ink coverage of the halftone and can be modeled by:

$$R_i(a) = \left(R_{ps}T_i^2 - R_{ps}T_i\right)a + R_{ps}T_i \quad [4.13]$$

$$R_p(a) = \left(R_{ps}T_i - R_{ps}\right)a + R_{ps} \quad [4.14]$$

with T_i the ink transmittance and R_{ps} the bare paper reflectance, Figure 4.8 (D). By placing $R_i(a)$ and $R_p(a)$ in the Murray-Davies model, the Yule-Nielsen with n=2 is obtained.

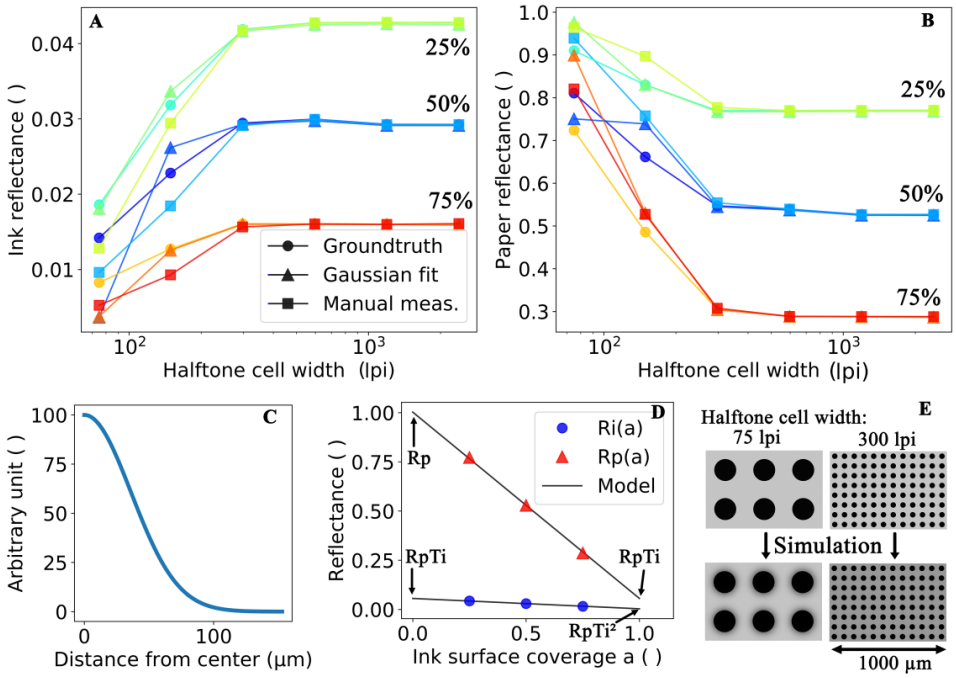

Figure 4.8: Optical dot gain simulations for multiple halftone cell widths: (A) Ink reflectance measurements, (B) Paper reflectance measurements, (C) Shape of the PSF to simulate the reflectance images used to compute the reflectance histograms, (D) Ink and paper reflectances for simulated halftone with small halftone cell width (large lpi) and Yule-Nielsen model with n=2, (E) Examples of optical dot gain simulations on 50% ink coverage halftone with 75 lpi and 300 lpi cell widths.

Next optical dot gain simulations are conducted with real halftone dot geometries in order to analyze the performances of the Gaussian fitting method. The choice of performing an optical dot gain simulation rather than analyzing directly the halftone images was adopted because it allowed obtaining an accurate ground truth (ink and paper average reflectance over regions where there were initially only ink and only paper). Printed halftone dots at 150 lpi and 200 lpi with electrophotography, offset and inkjet are used for the simulation in order to have different dot geometries. To allow comparisons between the different processes, similar ink transmittance paper reflectances are used. The point spread function adopted is identical to the one used for theoretical halftone dots.

Comparing the manual measurement with the Gaussian fit relatively to the ground truth shows that the Gaussian fit is more accurate than the manual measurement. The relative average difference of the Gaussian fit with the ground truth over all effective ink coverages reaches 8.7% for the ink and 3.1% for paper for electrophotography at 150 lpi, respectively 6.9% and 2.0% for offset and 11.3% and 3.8% for inkjet. On another hand the relative average difference of the manual measurement with the ground truth reaches 24.9% for the ink and 12.5% for paper for electrophotography at 150 lpi,

21.0% and 10.6% for offset and 24.9% and 6.8% for inkjet. For smaller halftone dots the Gaussian fit gives similar accurate results compared to the ground truth. The manual measurements tend to perform better since the ink and paper reflectances are more homogeneous over the regions. The relative average difference of the Gaussian fit with the ground truth over all effective ink coverages reaches 2.4% for the ink and 5.4% for paper for electrophotography at 200 lpi, 2.9% and 0.9% for offset and 3.7% and 5.6% for inkjet. The relative average difference of the manual measurement with the ground truth reaches 10.4% for the ink and 10.0% for paper for electrophotography at 200 lpi, 8.9% and 7.3% for offset and 6.4% and 2.5% for inkjet.

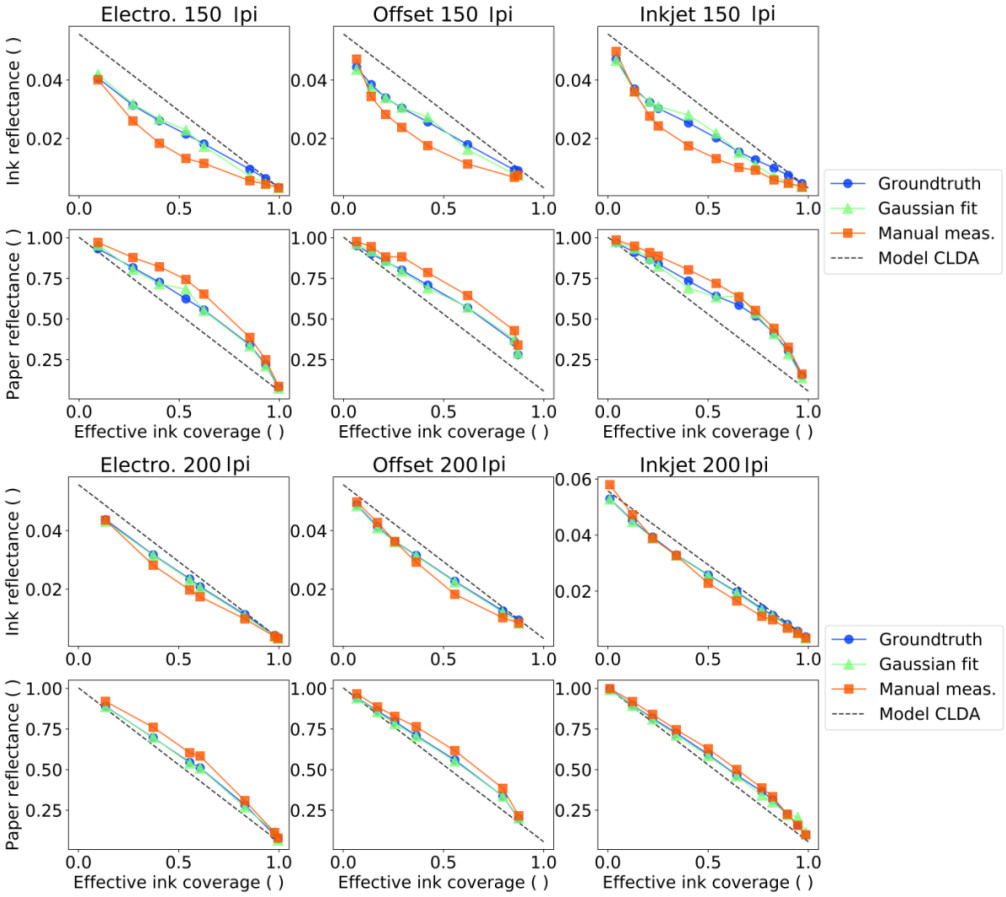

Figure 4.9: Ink and paper reflectances as a function of the effective ink coverage (normalized between 0 and 1) measured with the Gaussian fitting method, measured manually, ground truth and model based on the complete light diffusion approximation (CLDA). Halftone dots printed with electrophotography, offset and inkjet at 150 lpi and 200 lpi, thresholded to obtain the dot geometries.

Finally it can be observed that the largest relative errors of the Gaussian fit are generated by halftone dots with high effective coverage. By removing the results of the simulation for effective ink coverage over 0.8, the relative differences between the Gaussian fit and the ground truth are reduced, reaching 2.9% for the ink and 3.1% for paper for electrophotography at 150 lpi, 3.5% and 1.3% for offset, 5.0% and 3.2% for inkjet. Similarly at 200 lpi, the relative differences between the Gaussian fit and the ground truth are reduced, reaching 0.9% and 0.6% for electrophotography, 1.3% and 0.8% for offset and 1.3% and 1.7% for inkjet. The relative differences between the manual measurements and the ground truth remain large. It can be concluded that the Gaussian fit is more accurate to determine the ink and paper reflectances as a function of the ink coverage than manual measurements. Moreover the Gaussian fit method is computed without the input of an experimenter and is therefore unbiased.

It is interesting to note that as the size of the ink dot fluctuates inside the halftone cell the actual ratio of the CLDA fluctuates as well. For this reason it appears that the ground truth for all halftone dots at 150 lpi for the ink reflectance and the paper reflectance differ the most from the CLDA at

effective ink coverage of 50%, Figure 4.9. The effective ink coverage of 50% is indeed where the halftone dots and paper areas are the largest. This tendency can be observed also for 200 lpi halftones, however is less pronounced. For effective ink coverage extrema, the ink and paper reflectances tend to converge toward the CLDA model.

4.3.3 Applications on halftone images

Ink and paper reflectances are measured with the Gaussian fit method and are compared to manual measurements for printed halftone dots. For these measurements a ground truth cannot be obtained accurately since it requires knowing precisely the ink and paper position on the halftone.

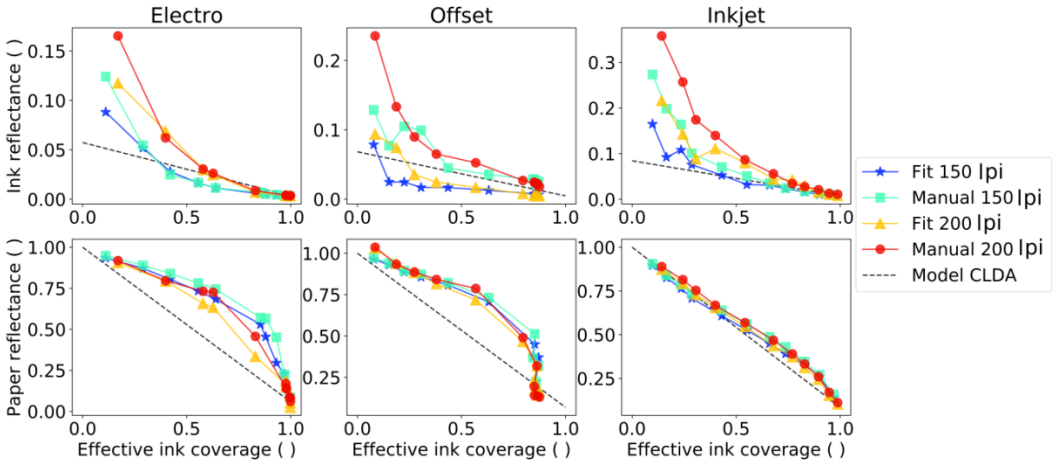

Figure 4.10: Ink and paper reflectances as a function of the effective ink coverage (normalized between 0 and 1) measured with the Gaussian fitting method and measured manually. Model based on the complete light diffusion approximation (CLDA). Halftone dots printed with electrophotography, offset and inkjet at 150 lpi and 200 lpi.

It can be observed on Figure 4.10 that the Gaussian fit measurements and the manual measurements show similar tendencies. An exception is presented for the ink reflectance measurements of the halftones printed with offset. No significant impact of the halftone size can be observed when comparing the obtained Gaussian fit and the manual measurements. However an impact of the halftone size appears on the measured reflectance levels. It has to be noted that for the ink, the Gaussian fit and manual measurements differences are globally less significant than when performing simulations with the similar ink setting. This effect is mostly related to the ink and paper reflectances distributions. The paper reflectance distribution for a 15% nominal ink coverage 150 lpi halftone printed with electrophotography differs comparing the measured reflectances and the simulated reflectances, Figure 4.11. These differences are produced by simplifications from the model of light diffusion on halftone. Going from the highlighted 20% of paper to 50% of paper it can be observed that the reflectance positions are dispersed and depend less on the position between the printed dots for the measured halftones. For the simulated halftones it can be seen that the highest reflectance regions are located at the largest distances of the printed dots. The paper reflectances are then decreasing when going toward ink dots. This behavior tends to influence strongly the manual measurements as manual paper reflectance measurements are mostly performed away from the border of the printed dots. The resulting reflectance will then be respectively higher for the paper and lower for the ink.

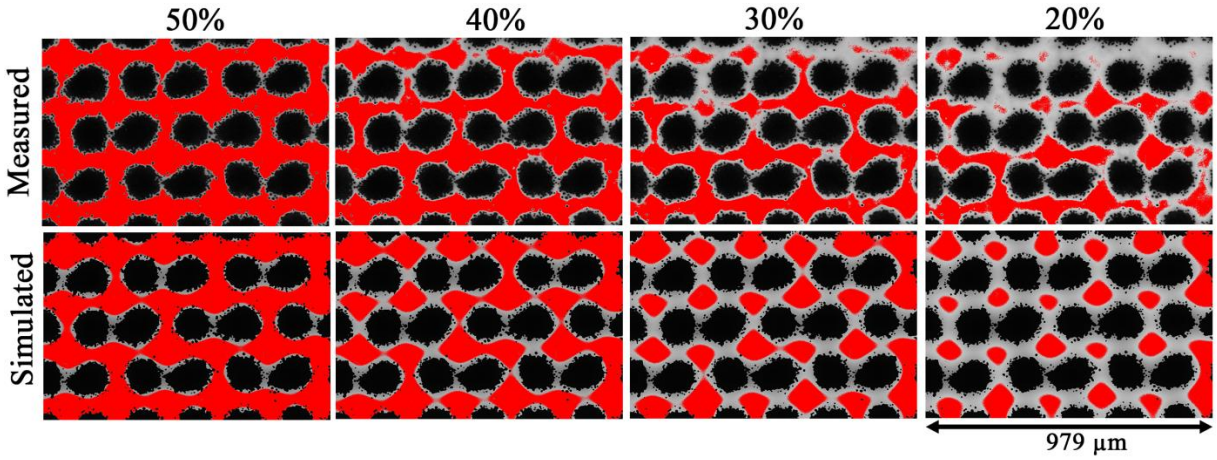

Figure 4.11: Measured and simulated 15% nominal ink coverage 150 lpi halftones printed with electrophotography and paper reflectance distribution highlighted in red: selecting the reflectance values from the paper to the ink reflectances to obtain respectively 50%, 40%, 30%, 20% of the surface of the halftone.

For the halftone printed with electrophotography at 150 lpi, it can be observed that the Gaussian fit measurement for the ink follows precisely the manual measurements for all surface coverages, reaching an absolute difference relative to the complete light diffusion approximation of 3.6%, Figure 4.10. An exception occurs for the halftone with effective surface coverage of 10.2%, with an absolute difference reaching 69.6%. For the paper an offset is observed between the Gaussian fit measurements and the manual measurements and higher paper reflectances are obtained with the manual measurements (relative difference of 7.2% excluding the effective ink coverage of 83.4% and 89.4%). The relative differences for these two surface coverages are respectively 52.1% and 99.3%. This tendencies for the paper are similar than for the simulations. Similar observations are obtained for the 200 lpi halftone printed with electrophotography with a mean relative difference between the Gaussian fit the manual measurements of 2.1% for the ink (excluding the halftones with effective surface coverage of 15.8% and 36.8%) and 10.5% for the paper (excluding the effective ink coverage of 99.5%).

For the halftone printed with offset large relative differences between the Gaussian fit and the manual measurement appear for the ink reflectances with 121.0% for the 150 lpi halftone and 115.1% for the 200 lpi. It can be observed that the Gaussian fit measurements and the manual measurement follow the same tendency and an offset appears between the two types of measurements. This offset is generated by a heterogeneous printed ink layer presenting numerous holes. Optical dot gain occurs and therefore these holes are accounted as ink when performing manual ink peak measurements. The manual measurement ink reflectances are therefore obtained higher, as shown on Figure 4.10. Another consequence of these defects is that the 100% effective ink coverage cannot be reached and a final coverage of 86.2% for 150 lpi and 87.5% for 200 lpi is reached. For the paper reflectance measurements the difference between the Gaussian fit and the manual method is smaller with respectively a relative difference of 7.3% and 7.0% for 150 lpi and for 200 lpi.

For halftones printed with inkjet, relative differences between the Gaussian fit and the manual measurement of 24% for 150 lpi and 23.9% for 200 lpi are obtained. The first three halftone of nominal ink coverage of 5%, 10% and 15% have larger relative differences of respectively 151.3%, 159.1% and 88.4% for 150 lpi and respectively 197.1%, 171.2% and 135.4% for 200 lpi and were removed from the computed average. These differences can be explained by the non-constant ink thickness due to the superposition of a different number of ink droplets depending on the position on the halftone dot. For the reflectance of the paper, both the Gaussian fit and the manual method give similar results. The relative differences between the two methods are obtained at respectively 6.1% and 4.9%. From these observations, the Gaussian fit method is validated as an automated method to obtain the ink and paper reflectances as a function of the ink coverage.

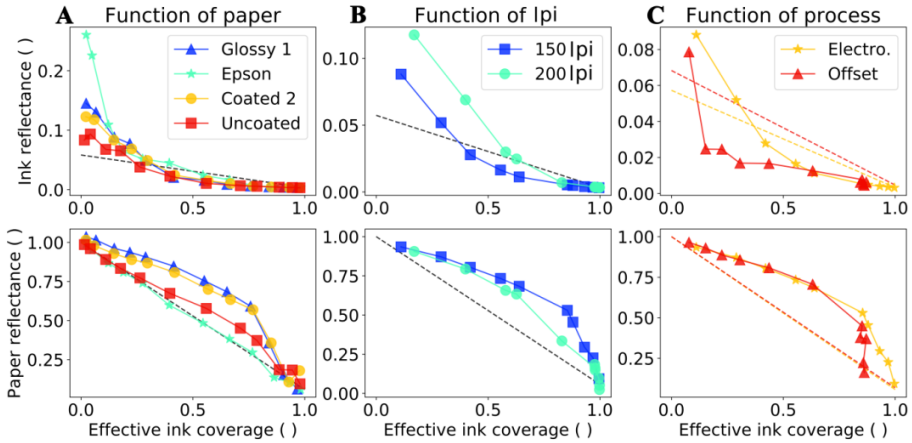

Figure 4.12: Ink and paper reflectances as a function of the effective ink surface coverages (normalized between 0 and 1) measured with the Gaussian fitting method. (A) Halftones at 150 lpi printed in electrophotography on four different papers, (B) Halftones at 150 lpi and 200 lpi printed in electrophotography on glossy 1 coated paper. (C) Halftones at 150 lpi printed in electrophotography and offset on glossy 1 coated paper. Model based on the complete light diffusion approximation (CLDA) represented on dashed curves.

Influences of the type of paper, of the halftone size and of the printing process are investigated by analyzing the measured ink and paper reflectance as a function of the ink surface coverage, Figure 4.12. Four papers were printed with electrophotography at 150 lpi. The paper reflectance as a function of the effective ink surface coverages has a shape going from a line shape to a bell shape depending on the type of paper. The two coated glossy papers (Glossy 1 and Glossy 2), are associated with a similar shape and are associated with the bell shape. The uncoated paper presents an attenuated bell shape. The inkjet proofing paper (Epson) paper is associated with a line shape, superposing with the complete light diffusion approximation. These results show that the different papers are associated with more or less light diffusion depending on their type. The inkjet proofing paper diffuses strongly the light compared to the halftone cell size of 150 lpi and complies with the CLDA with a relative difference of 0.6% with the complete light diffusion approximation at 54.5% of effective ink coverage. The uncoated paper diffuses less light and thus differs from the complete light diffusion approximation, with a relative difference of 22.3% with the complete light diffusion approximation at 56.0% of effective ink coverage. The two glossy coated papers are similar and diffuse less the light. These papers have reflectance differences with the complete light diffusion approximation of respectively 56.9% and 50.4% at the effective ink coverage of 55.1% and 56.8%. A large difference between the four papers tested appears for the ink reflectances in the low ink surface coverages. With the exception of the uncoated paper, these differences are inversed compared to the tendencies that are expected in regard with the complete light diffusion approximation. Thus it can be concluded that further phenomena impact the print such as ink thickness variations and penetrations and internal reflections. Similarly for the high ink surface coverages, the paper reflectance can be observed below the theoretical limit. A cause identified is an error of the threshold algorithm for the high ink surface coverages, outputting an effective ink surface coverage smaller than the actual surface coverage..

By comparing the influence of the halftone cell size, it can be observed that the 150 lpi halftone reflectances differ more from the complete light diffusion approximation than the 200 lpi halftones. This shows the influence of the size of the dots compared to the paper point spread function length.

Electrophotography and offset halftones were printed on a similar paper and are Figure 4.12. For the 150 lpi halftone cell size, the ink reflectances of both processes are similar for effective ink coverages higher than 50%. Below 50% the ink reflectances of electrophotography are found higher than for offset. This can be attributed to variations of the ink thickness as a function of the surface coverage different from the electrophotography and the offset prints. The paper reflectance differences appear for effective ink coverages higher than 50%. These differences are mainly caused by the error

of measurement of the effective ink coverage for the offset prints due to non-inked regions on the printed dots. Similar tendencies are observed for the 200 lpi halftone cell sizes.

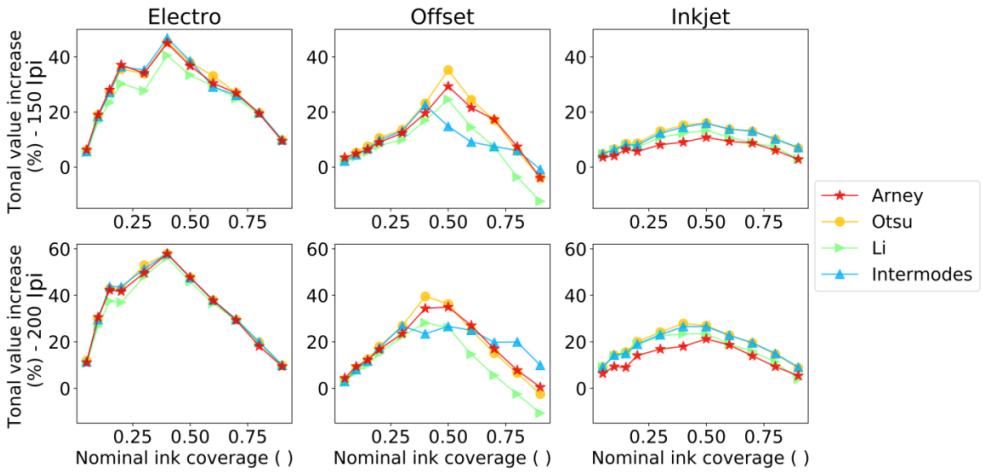

Figure 4.13: Physical dot gain as a function of the nominal ink coverage (normalized between 0 and 1) measured with the Gaussian fitting method with Arney model (Arney) and compared to physical dot gain obtained with threshold algorithms (Otsu, Li, Intermodes). Halftone dots printed with electrophotography, offset and inkjet at 150 lpi and 200 lpi.

The physical dot gain obtained inversing Arney's model, equation [4.1], with the ink and paper reflectances measured as a function of the ink coverage is compared to the physical dot gain obtained with three thresholding algorithms, Figure 4.13. For electrophotography at 150 lpi both the Otsu and the intermodes thresholds give values similar to the Arney model with a mean absolute difference of coverage of respectively 0.71% +/- 0.82% and 0.94% +/- 0.53%. Similarly for electrophotography at 200 lpi, the best threshold algorithms are the Otsu threshold with 0.83% +/- 0.98% and the intermodes with 0.89% +/- 0.71%. For halftones printed with offset, larger differences between the threshold algorithms and Arney's model appear. Negative physical dot gains can be observed for high ink coverage halftones and are caused by non-inked regions in the ink layer. The Otsu threshold algorithm is found the closest to Arney's model with respectively 1.78% +/- 1.76% and 1.90% +/- 1.44% for 150 lpi and 200 lpi. The Li algorithm reproduces accurately the variations of the model however an offset appears. The intermodes algorithm does not follow the variations of the model starting from the nominal ink coverage of 60% for 150 lpi and 50% for 200 lpi. For the halftone printed with inkjet, the three threshold algorithms are associated with larger physical dot gains than Arney's model. The three algorithms reproduce accurately the variation of Arney's model however an offset appears. The Li threshold algorithm is nevertheless found the closest to the model with an absolute mean difference of 1.61% +/- 0.98% for 150 lpi and 3.34% +/- 1.92% for 200 lpi. From these results it can be concluded that the threshold algorithms can effectively separate the ink from the paper, outputting the effective ink coverage (including physical dot gain but excluding optical dot gain). However the performances of these algorithms seem to depend on the print processes and on the imaging conditions. Measuring the ink and paper reflectance as a function of the ink coverage allow with the Arney model to obtain accurately the effective surface coverage and is a direct benefit from this approach.

4.4 Conclusion

Based on the work conducted by Arney it was observed that the ink and the paper reflectances were dependent on the ink coverage at the microscale. A method was proposed to measure automatically the ink and paper reflectances. This method is based on a Gaussian fitting of the ink and paper peaks on the histogram of the microscale image of the halftone. The Gaussian fitting was

performed by optimizing two parameters, the Gaussian width and the Gaussian center position, in a two steps algorithm. The first step was to optimize the Gaussian width for a given Gaussian center position. The second step was to find the Gaussian center positions where the optimization criterion is maximized. The height of the Gaussian curve was fixed to the height of the reflectance distribution at the position corresponding to the center of the Gaussian. Two optimization criteria were developed accordingly. The effect of the bin width of the reflectance histogram was studied and a bin width of 10^5 was adopted. It has to be noted that the choice of the optimal histogram bin width relies mainly on the acquisition parameters. Similarly the effect of the smoothening of the histogram was investigated. A smoothening of 0.5% the size of the histogram was associated with a large reduction of the dispersion and did not introduce significant shape deformations of the distribution.

The performance of the Gaussian fit of the histogram ink and paper peaks was then analyzed. First the accuracy of a Gaussian fits on a solid patch printed in electrophotography and on a bare paper were analyzed. It was found that the paper reflectance distribution was found very close to the Gaussian fit with 99.2% of the paper peak covered by the Gaussian fitting. For the solid print, the reflectance distribution was also close to the Gaussian fit with 85.2% of the ink peak covered by the fitted Gaussian. The Gaussian followed accurately the ink reflectance distribution on the left of the peak. The peak however seemed composed of multiple Gaussian curves and a single Gaussian could not fit accurately the right hand side of the ink peak. The repeatability of the Gaussian fitting was verified and it was concluded that the Gaussian fit method was reproductible.

Simulations of the dot gain with real halftone dot geometries were investigated in order to evaluate the performance of Gaussian fit measurements compared to manual measurements with an absolute reference (ground truth). The Gaussian fit measurements were found closer to the ground truth than manual measurements. For the three print processes at 150 lpi, the relative average differences between the Gaussian fit and the ground truth reached 9.0% for the ink reflectances and 3.0% for the paper reflectances. This can be compared to the manual measurements reaching 23.6% for the ink reflectances and 10.0% for the paper reflectances. At 200 lpi relative average differences were smaller with 3.0% for the ink and 4.0% for paper for the Gaussian fit compared to 8.6% and 6.6% for the manual measurements.

The Gaussian fit method was then applied on four different papers having different light diffusion characteristics. The inkjet proofing paper was associated with the largest light diffusion and corresponded to the complete light diffusion approximation. The two glossy coated papers, the paper reflectance values had a large bell shape above from the complete light diffusion approximation. The physical dot gain obtained with Arney's model was compared to three thresholding algorithms. It was found that the best threshold algorithm depended on the print process. The halftone cell size did not influence the performances of the threshold algorithms. The best threshold algorithm was the Otsu threshold for electrophotography and offset printed halftones and the Li threshold for inkjet printed halftones. This suggested that the performances of the threshold algorithms were mainly affected by the level of optical dot gain.

From this analysis it was determined that the Gaussian fit method is valid as an alternative automated method to obtain the ink and paper reflectances as a function of the ink coverage.

Chapter 5 Convolution strategies to differentiate physical and optical dot gain

Louis Vallat-Evrard, Lionel Chagas, Raphaël Passas, Nadège Reverdy-Bruas
Univ. Grenoble Alpes, CNRS, Grenoble INP*, LGP2, F-38000 Grenoble, France
Agefpi, LGP2, F-38000 Grenoble, France

5.1 Introduction and background

By observing a halftone print or by measuring a halftone area with optical devices (i.e. densitometry, spectrophotometry or microscopy) a phenomenon called optical dot gain or Yule-Nielsen effect occurs. Depending on the paper properties, this phenomenon tends to reduce the perceived or measured reflectance of prints [244]. The optical dot gain effect is caused by the lateral light transport in paper (light diffusion). In fact, an incident photon arriving on the paper will not necessarily be reflected at the exact same location of its entering location. Dictated by the point spread function (PSF) of the paper, the photon arriving at $r = 0$ will have a probability to exit the paper at a location (r, θ) given by the probability density described by the PSF. This light diffusion is not problematic on bare paper, however, the ink having the property of absorbing part of the light, photons arriving at a location of paper, diffuse and can exit the paper under an inked surface. These photons are then absorbed by the ink, resulting in a decrease of the spectral reflectance. The optical dot gain effect has been carefully studied and modeled [4], in order to improve models predicting the output reflectance of a print. However fewer studies have investigated the impact of the optical dot gain on the microscopic measurement of halftone dots. To obtain the effective surface of an ink deposition at the microscale, it is then required to separate the local reflectances generated from optical dot gain effect and the local reflectances from the ink absorption. To perform this separation authors have investigated different methods. Yang and Hersch proposed a method based on physical models describing either the spectral reflectance or transmittance [22,31]. Namedanian, Rahaman and Fleming proposed a method based on the analysis of histograms of the captured images [18,28,30]. Nyström and Ukishima proposed a method combining optical transmission and reflection microscopy to isolate optical dot gain [17,19]. Finally, Kristiansson proposed to measure directly the optical dot gain with the Lund microscopy method [32]. These methods are promising however they are either difficult to use for large number of measurements, depend on image acquisition characteristics or perform only a partial separation.

In this work an image processing is proposed allowing a separation of optical dot gain and ink spreading on the surface of the paper. A separation of the optical dot gain from the captured image is then performed following two strategies developed according to the model of the light diffusion of halftones [8,12]. Results of the two separation strategies are then analyzed and compared to optical dot gains found in literature.

5.2 Materials and Methods

5.2.1 Paper, printing and test forms

The microscope acquisition and optical dot gain separation methods are tested on three different processes: offset, inkjet and electrophotography. The specifications for these three processes are detailed in Table 5.1. The printing form consists in a series of patches of different gray levels, ranging from 0% to 100% of grayscale. In order to print these continuous tones, halftoning was performed with Photoshop CS6 bitmap function, setting the output resolution to the resolution of the printer, the line per inch to 150 lpi and the shape of halftone dots to circular.

Table 5.1: Paper, printing and test form specification.

Printing process	Printing resolution [dpi]	Halftone cell size [px²]	Singular pixel size [µm²]	Paper	Ink
Offset: Heidelberg Speedmaster 52	2540	17 x 17	10.0 x 10.0	Glossy coated paper 135 g/m²	Black Novavit 918 supreme bio
Inkjet: Epson Stylus Pro 4900	1440	10 x 10	17.6 x 17.6	Epson standard proofing 205 g/m²	Epson PK T6531 Black
Electrophotography: Ricoh Aficio MP C2800	1200	8 x 8	21.2 x 21.2	Glossy coated paper 135 g/m²	Ricoh MP C3000 Black

A Zeiss Axio Imager M1m optical microscope mounted with a Canon 1200D reflex camera (RGGB sensor, modified to monochromatic, 18.8 megapixels, CMOS camera) is used with an EC Epiplan Neofluar 20x/0.5 HD DIC objective. Total magnification on sensor is 32X with a physical pixel size of 4.3 µm/pixel. Thus, the calibrated system captures images of 0.1330 µm/pixel, giving an observation field of 585 x 391µm² (reduction of sensor surface due to the modification into monochromatic sensor). The Canon 1200D camera is set to save images in .CR2 raw format, allowing us to retrieve the measured value of reflectance for each photodetector. Using this raw format, no white balance compensation or interpolation is performed by the camera. The only controls for the sensor is the level of photon (in fine electron) amplification: iso level and the time for the integration of the photons on the surface of the photodetectors: exposure time. The iso parameter is set to 800 and exposure time is independently fixed for each image captured, ranging from 3.125 ms to 10 s. 90° polarized reflected light microscopy configuration is chosen to capture halftone dots, thus excluding specular reflections and taking into account optical dot gain [19]. A halogen lamp Zeiss Hal 100 is used as light source for the microscope and the lamp voltage is set to 10.7 V. The source used is not a standard illuminant however a blue filter is applied to have a spectrum closer to D65 standard illuminant. 42200 lux is measured with a luxmeter and this luminance is set for all measurements.

5.2.2 Line spread function measurement

From the captured image of a projected knife edge realized by closing the focal aperture of the incident illuminant on the microscope, an image showing light diffusion is obtained Figure 5.2 (B) and (C). By subtracting this image to the image of the reference containing the representation of the focal aperture Figure 5.2 (A), the half edge spread function (ESF) of the paper in all directions can be computed. This subtraction method allows reducing the amount of noise generated in the second half on the ESF that is due to paper reflectance heterogeneities. From the half ESF, the complete ESF can be recovered thanks to the ESF assumed symmetry, represented in Figure 5.1. It is then possible to calculate the line spread function (LSF) by derivation of the edge spread function. The hypothesis that the light scattering on paper is isotropic is adopted. By averaging the LSF and applying a 2π rotational symmetry, an approximation of the point spread function (PSF) is obtained.

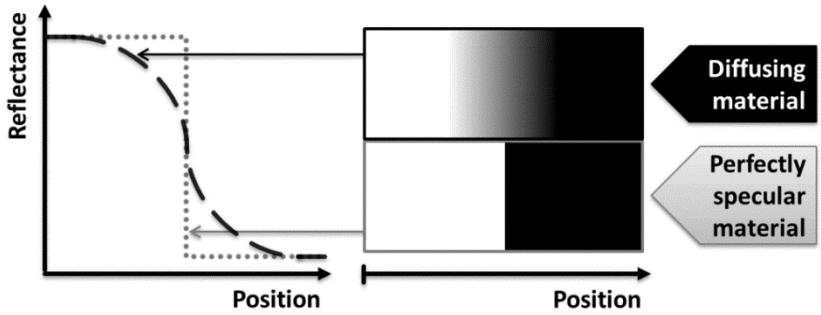

Figure 5.1: Edge spread function for a diffusing material (long dashes line) and for a perfectly specular material (round dots line) and 2D representation.

Figure 5.2: Knife edge illumination measurements: (A) perfect specular mirror, (B) glossy coated paper, (C) Epson standard proofing paper.

5.2.3 Optical dot gain separation method on captured images

The method to separate the optical dot gain is based on the model of the light diffusion on halftones introduced by Callahan, Yule and Lehmbeck [8–16] and discussed by Modrić [12], equation [5.1]. This model establishes the relation between the halftone reflectance at each point of a surface $R_a(x,y)$, as a function of the paper reflectance $R_{ps}(x,y)$, the ink transmittance $T_i(x,y)$ and the convolution of with the paper point spread function $H(x,y)$. The aim of the separation method is to obtain a halftone reflectance without optical dot gain $R_{aw}(x,y)$. As shown in equation [5.2], the halftone reflectance without optical dot gain is equivalent to halftone reflectance, except that the paper point spread function is set to 1. The ink transmittance can then be written as the square root of the fraction of the halftone reflectance without optical dot gain and the halftone reflectance. By knowing ink transmittance, the halftone reflectance without optical dot gain can be computed.

Model of light diffusion on halftone

		Symbol	Unit	Denomination
[5.1]	$R_a(x,y) = R_{ps}(x,y)\, T_i(x,y)\, [T_i(x,y) \circledast H(x,y)]$	$R_a(x,y)$	1	Halftone reflectance
		$T_i(x,y)$	1	Ink transmittance
		$R_{ps}(x,y)$	1	Bare paper reflectance
		$H(x,y)$	1	Paper point spread function
		$\circledast$	-	Convolution operator

Two strategies are developed to compute ink transmittance from the halftone reflectance. The first strategy is developed from the following hypothesis: the convolution of ink transmittance and paper point spread function can be approximated by the convolution of the paper point spread function and of the square root of the fraction of the halftone reflectance divided by the paper reflectance. This hypothesis theoretically overestimates the optical dot gain effect: the ink coverage is larger on the

transmittance calculated from the reflectance than on the true transmittance. Once the convolution term is calculated, it is possible to obtain the ink transmittance by dividing the halftone reflectance with the convolution of the ink transmittance with the paper point spread function, equation [5.3]. It is then straightforward to compute the halftone reflectance without optical dot gain, equation [5.2].

Model of light diffusion on halftones without optical dot gain

		Symbol	Unit	Denomination
[5.2]	$R_{aw}(x,y) = R_{ps}(x,y)\, T_i(x,y)^2$	$R_{aw}(x,y)$	1	Halftone reflectance without optical dot gain
		$T_i(x,y)$	1	Ink transmittance
		$R_{ps}(x,y)$	1	Bare paper reflectance
		$\circledast$	-	Convolution operator

Ink transmittance approximation

		Symbol	Unit	Denomination
[5.3]	$T_i(x,y) \cong \dfrac{R_a(x,y)}{R_{ps}(x,y)\left[\sqrt{\dfrac{R_a(x,y)}{R_{ps}(x,y)}} \circledast H(x,y)\right]}$	$T_i(x,y)$	1	Ink transmittance
		$R_a(x,y)$	1	Halftone reflectance
		$R_{ps}(x,y)$	1	Bare paper reflectance
		$\circledast$	-	Convolution operator

The second strategy also focuses in obtaining the ink transmittance but uses a different hypothesis. The following hypothesis is formulated: the ink transmittance can be obtained by the thresholding of the halftone reflectance at a threshold value K, equation [5.4].

To find the threshold value describing the ink transmittance the most accurately, the measured halftone reflectance is compared to all simulated halftone reflectance computed using equation [5.1]. The threshold value is then determined by minimizing the root mean square of reflectances differences. Obtaining the halftone reflectance without optical dot gain becomes straightforward by computing equation [5.2].

Ink transmittance approximation

		Symbol	Unit	Denomination
[5.4]	$T_i(x,y) \cong \begin{cases} \sqrt{\dfrac{R_{is}}{R_{ps}}} & \text{where } R_a(x,y) \le K \\ R_{ps} & \text{where } R_a(x,y) > K \end{cases}$	$T_i(x,y)$	1	Ink transmittance
		$R_a(x,y)$	1	Halftone reflectance
		R_{ps}	1	Bare paper reflectance
		R_{is}	1	Solid ink reflectance
		K	1	Threshold value

The two strategies are computed for the three different printing processes: offset, inkjet and electrophotography, for patches ranging from 0% to 100% coverage. The resulting separations are analyzed by two different approaches:

- Computing the effective ink coverages calculated with the Murray-Davies formula based on optical densities obtained with the microscope captured images.
- Computing the effective ink coverages by thresholding the halftone image using the Otsu method and counting the number of pixels attributed to the ink region. It has to be noted that the definition given by the Murray-Davies model is that a solid print patch represents 100% of coverage. To respect this definition, the effective ink coverages are multiplied by a constant to obtain 100% for the solid print patch.

5.3 Results and Discussions

5.3.1 Line spread function of paper

The line spread functions of various papers including the papers presented in this work are measured Figure 5.3. Globally, a difference between coated and uncoated papers is pointed out. It is interesting to note that the Glossy coated paper used in the present study behaves as a coated paper with a shallower line spread function. On the contrary, the Epson standard proofing paper, although coated, behaves more like an uncoated paper having a larger line spread function. These results are consistent with literature, with a global light scattering of about 100 µm [332,340].

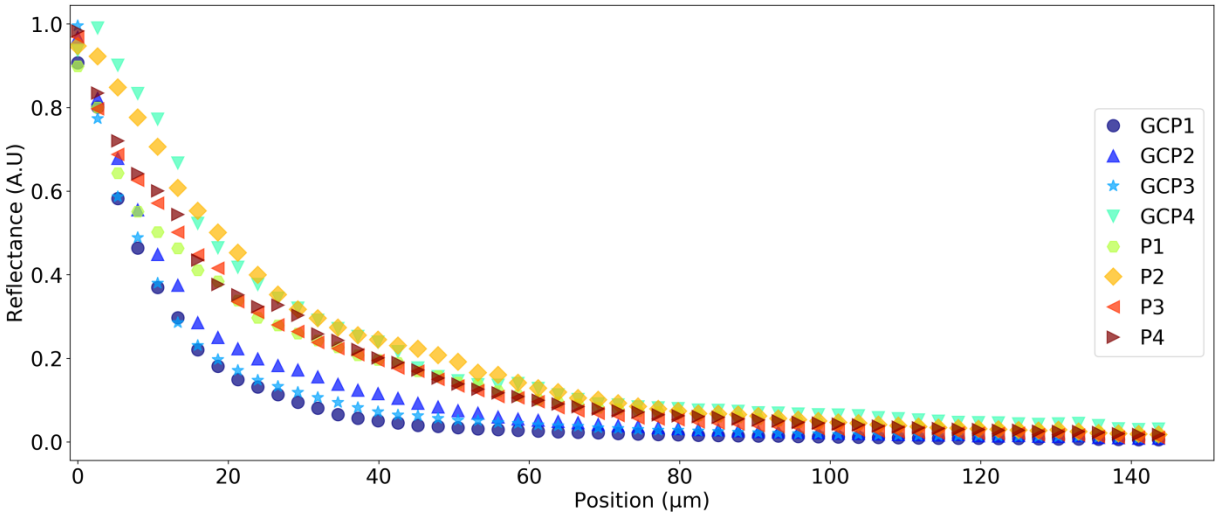

Figure 5.3: Line spread function of: GCP1=Glossy coated paper used in this study, GCP2=Silver blade coated paper, GCP3=Mondy "the glossy paper", GCP4=Epson standard proofing paper, P1=Condat offset paper, P2=Clairefontaine clairalfa paper, P3=Vertaris recycled, P4= Inapa laser classic paper.

5.3.2 Separation of optical dot gain from total dot gain

In Figure 5.4, the results of the separation of optical dot gain from total dot gain of offset printing patches are depicted. Comparing row 2 and 3 from row 1, the areas where the optical dot gain was impacting the print are observed. Small unprinted areas on the inked dots appear dark on images presenting total dot gain. Images without optical dot gain showed unprinted areas inside the ink region more clearly. The separation of optical dot gain seems to be more pronounced for the second strategy. Indeed, due to the thresholding used for the strategy 2, only a single ink thickness is kept, neglecting areas of light inking on the edges of the dots. The optical dot gain separation results for ink-jet and electrophotography were also investigated, Figure 5.5, Figure 5.6. For these two processes presenting less unprinted areas on the ink regions, the effect of optical dot gain removal, is observed particularly around the dots. For inkjet an over separation appears for strategy 1. This behavior may be induced by a different light scattering effect due to penetration of the ink into the first layers of the substrate.

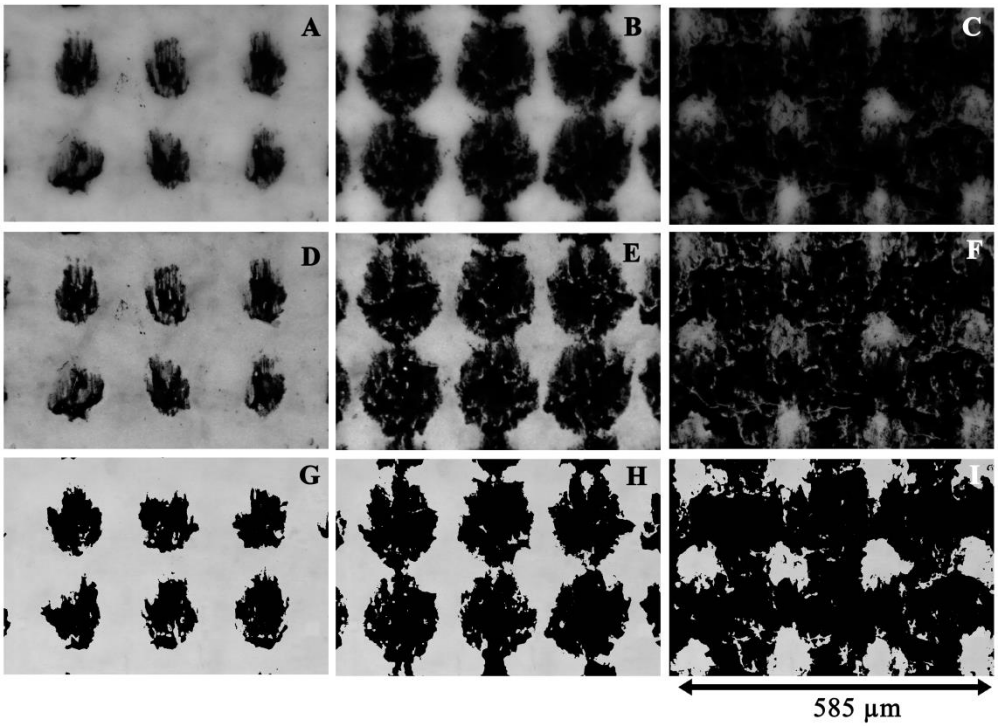

Figure 5.4: Results of the separation of optical dot gain for offset. (A, D, G) 10% of nominal ink coverage, (B, E, H) 40% and (C, F, I) 60%. (A, B, C) images of total dot gain, (D, E, F) images obtained with strategy 1 and (G, H, I) images obtained with strategy 2.

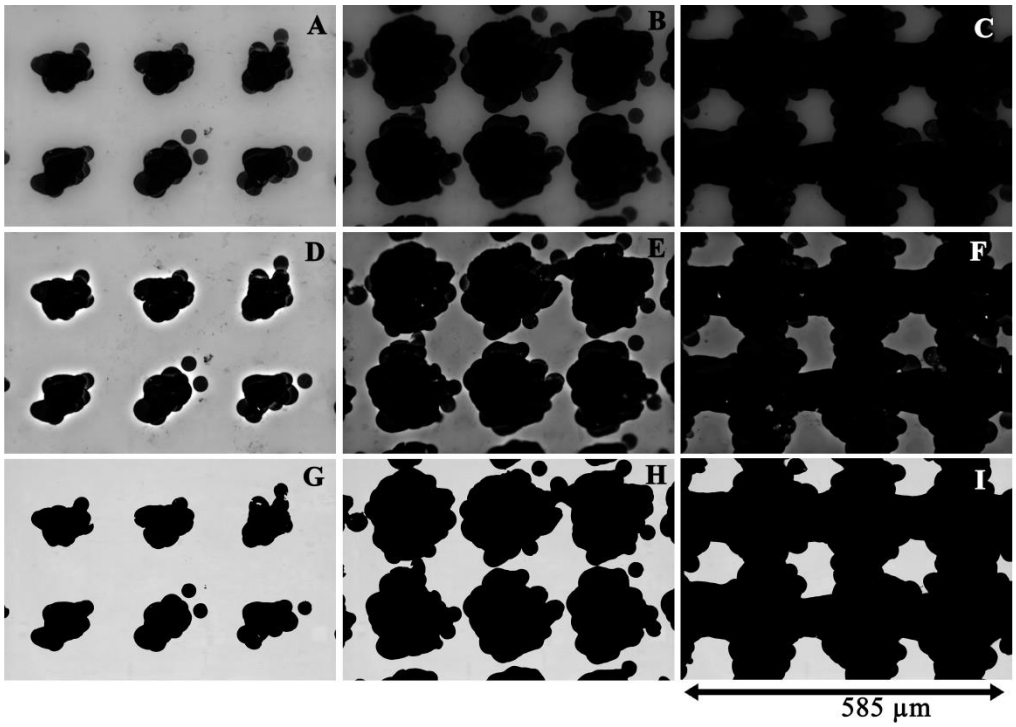

Figure 5.5: Results of the separation of optical dot gain for inkjet. (A, D, G) 10% of nominal ink coverage, (B, E, H) 40% and (C, F, I) 60%. (A, B, C) images of total dot gain, (D, E, F) images obtained with strategy 1 and (G, H, I) images obtained with strategy 2.

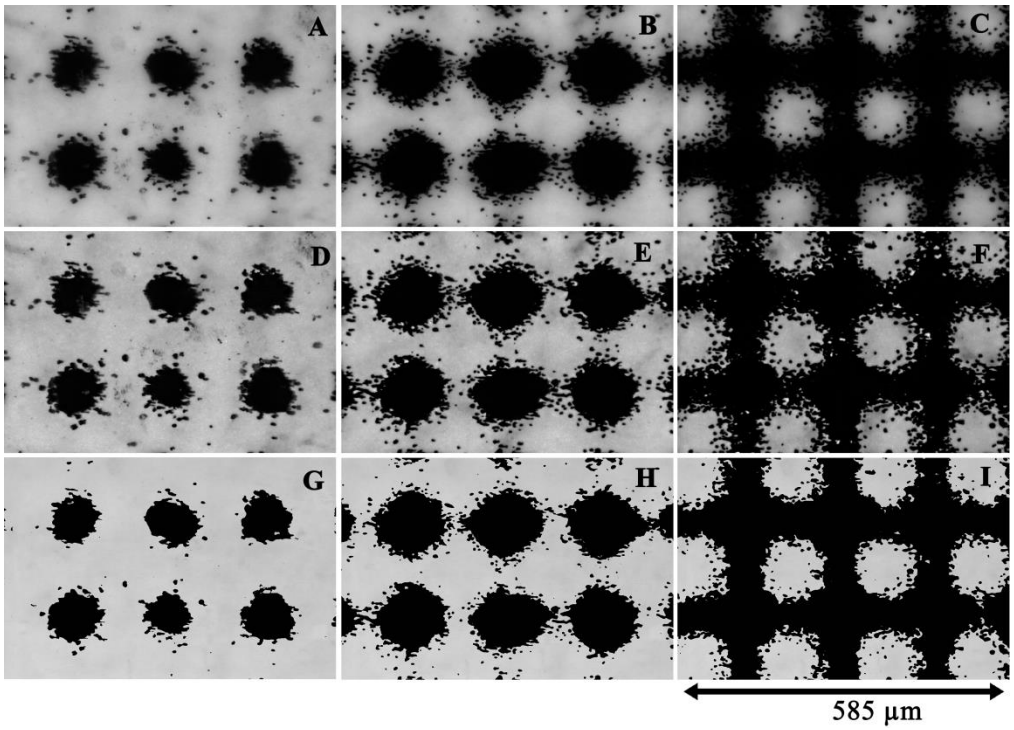

Figure 5.6: Results of the separation of optical dot gain for electrophotography. (A, D, G) 10% of nominal ink coverage, (B, E, H) 40% and (C, F, I) 60%. (A, B, C) images of total dot gain, (D, E, F) images obtained with strategy 1 and (G, H, I) images obtained with strategy 2.

The separation of optical dot gain was analyzed comparing effective ink coverage calculated with the microscopic optical density and thresholding image processing methods, Figure 5.7, Figure 5.8 and Figure 5.9. For the offset process, considering the measurement based on the micro optical densities, Figure 5.7 (A), the removal of the optical dot gain reduces, for the first strategy, the tonal value increases of a maximum of 1.7% at 30% nominal ink coverage. High and low nominal ink coverages are less impacted by the optical dot gain, since there is less paper surface to diffuse the light or ink surface to absorb the diffused light. For strategy 2, results show a higher optical dot gain, with a maximum of 23.6% at 20% nominal ink coverage. The optical dot gain calculated with the second strategy reduces with the increase of ink coverage. Interestingly low nominal ink coverages are mostly impacted by optical dot gain, suggesting that there would be no ink spreading below 20% nominal ink coverage. Looking at the strategy 1 measured with the thresholding method, Figure 5.7 (B), a higher optical dot gain is observed with a maximum of optical dot gain of 8.4% at 50% nominal ink coverage.

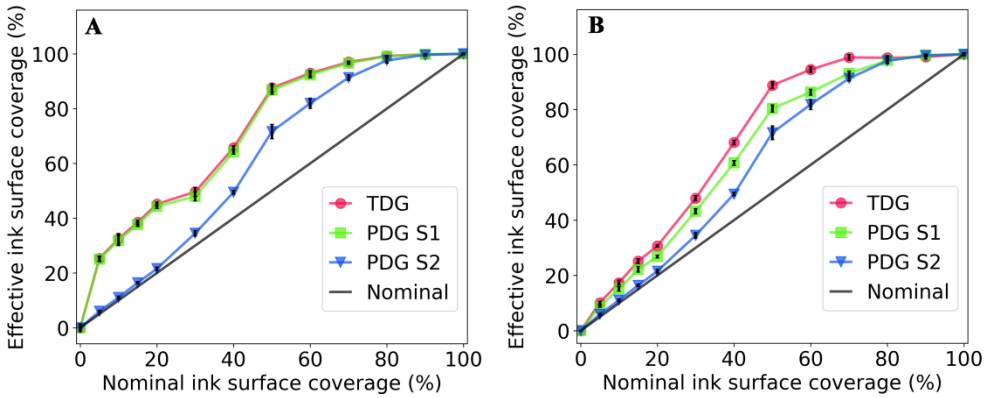

Figure 5.7: Effective ink coverage as a function of the nominal ink coverage for offset patches - total dot gain (TDG), with optical dot gain removed with strategy 1 (PDG S1) and strategy 2 (PDG S2): (A) Murray-Davies micro optical density method, (B) thresholding method.

Comparing the histogram of the gray values, it can be noticed that the halftone image with the total dot gain has a larger distribution than the one having no optical dot gain obtained with strategy 1. This difference in distribution occurs mostly when the un-inked surface becomes small. Since the threshold algorithm is based on the analysis of the gray values distribution, ink coverage calculated could become biased. However, this is not the case as both measurement methods give similar results for optical dot gain above 80% nominal ink coverage. For strategy 2, the results of effective ink coverage measurements based on the threshold method gives similar result than the method based on micro optical densities. The maximum optical dot gain is found at 18.7% at a nominal ink coverage of 40% and decreases for high and low nominal ink coverages.

Similar trends are observed for the electrophotography and inkjet processes, as illustrated in Figure 5.8 and Figure 5.9. For electrophotography, the maximum optical dot gain is found respectively at 4.2% and 14.3% at 50% nominal ink coverage for strategy 1 and strategy 2 and for the measure based on micro optical densities. For the measure based on thresholding, maxima are measured at 5.0% and 6.9% at 50% nominal ink coverage for strategy 1 and strategy 2. For inkjet, the maximum optical dot gain is found respectively at 4.9% and 20.0% at 30% nominal ink coverage for strategy 1 and strategy 2 and for the measure based on micro optical densities. For the measure based on thresholding, maxima are measured at 1.0% 30% nominal ink coverage for both strategies. Classical values for optical dot gain for the offset process (printer at 1200 dpi, halftone at 150 lpi) with coated paper, are found in literature between 5% to 15%, [19,226]. The values found for optical dot gain for the offset process are then in the same range or slightly higher than classical optical dot gain found in literature.

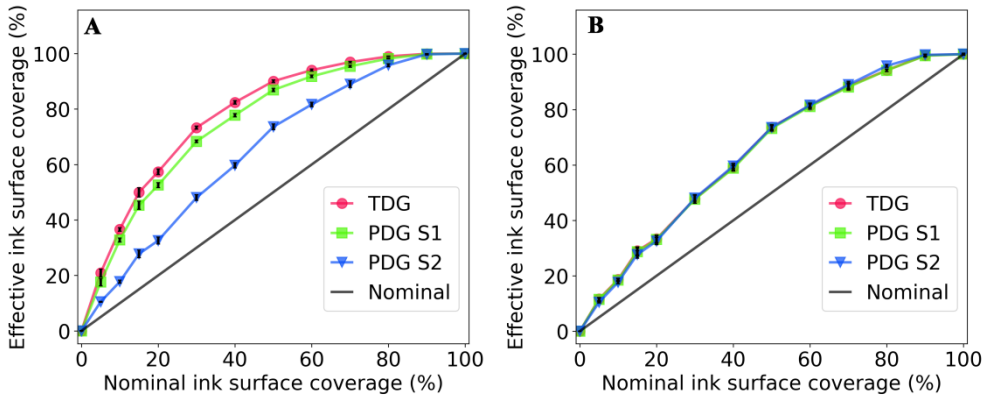

Figure 5.8: Effective ink coverage as a function of the nominal ink coverage for inkjet patches - total dot gain (TDG), with optical dot gain removed with strategy 1 (PDG S1) and strategy 2 (PDG S2): (A) Murray-Davies micro optical density method, (B) thresholding method.

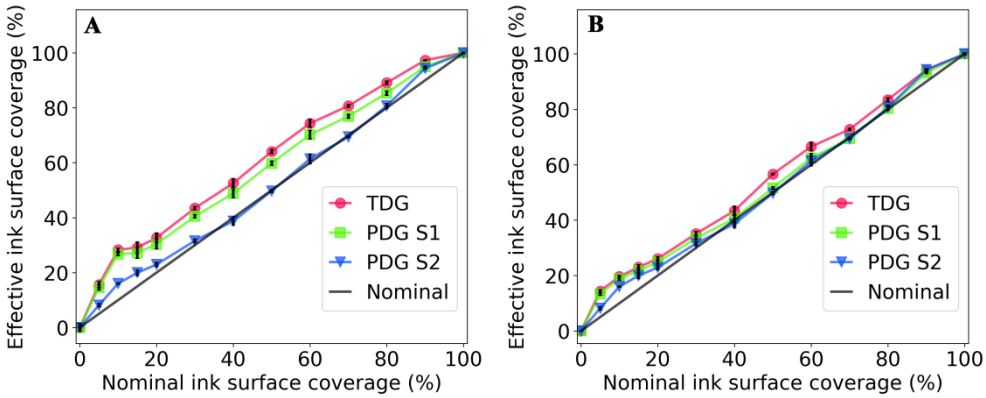

Figure 5.9: Effective ink coverage as a function of the nominal ink coverage for electrophotography patches - total dot gain (TDG), with optical dot gain removed with strategy 1 (PDG S1) and strategy 2 (PDG S2): (A) Murray-Davies micro optical density method, (B) thresholding method.

5.3.3 Optical dot gain separation analysis

With the difficulty to obtain reliable references, an evaluation of performances of the two optical dot gain separation methods is difficult to conduct. An analysis of the performance of the methods by qualitative determination of the reflectance evolution (with optical dot gain and without) is then conducted Figure 5.10. It can be noticed, on the graph, that there are 3 main reflectance values families. The first one located in the low reflectance values represents the ink. The second located in the high reflectance values represents the paper. The in-between reflectance values family with levels around 20000/65535 represents the area most impacted by optical dot gain. This third reflectance values family is mostly present for the printed dot with total dot gain. The effects of the optical dot gain separation strategies can be observed with sharper peaks and transitions from ink to paper (highlighted by the arrows). Globally, ink reflectance values level and paper reflectance values level remain the same after the separation of optical dot gain for the two strategies compared to the total dot gain. A small offset is found for the paper reflectance value levels obtained with the second separation strategy, with the reflectances values found closer to the reflectance values of bare paper. A decrease of the paper reflectances due to optical dot gain is observed for the total dot gain printed dots. The optical dot gain separation strategy 1 should theoretically remove this effect and reflectance values for paper should be similar to the one on bare paper. It is not completely the case for the first strategy and it shows that the optical dot gain removal is not complete. Overall, the two strategies show satisfying removals of optical dot gains on the inked surfaces. Similar observations are conducted for inkjet and electrophotography, Figure 5.11 and Figure 5.12. For the inkjet process the differences between paper reflectance values are even more marked. It should be noted that the reflectances are represented by the gray values on the figures.

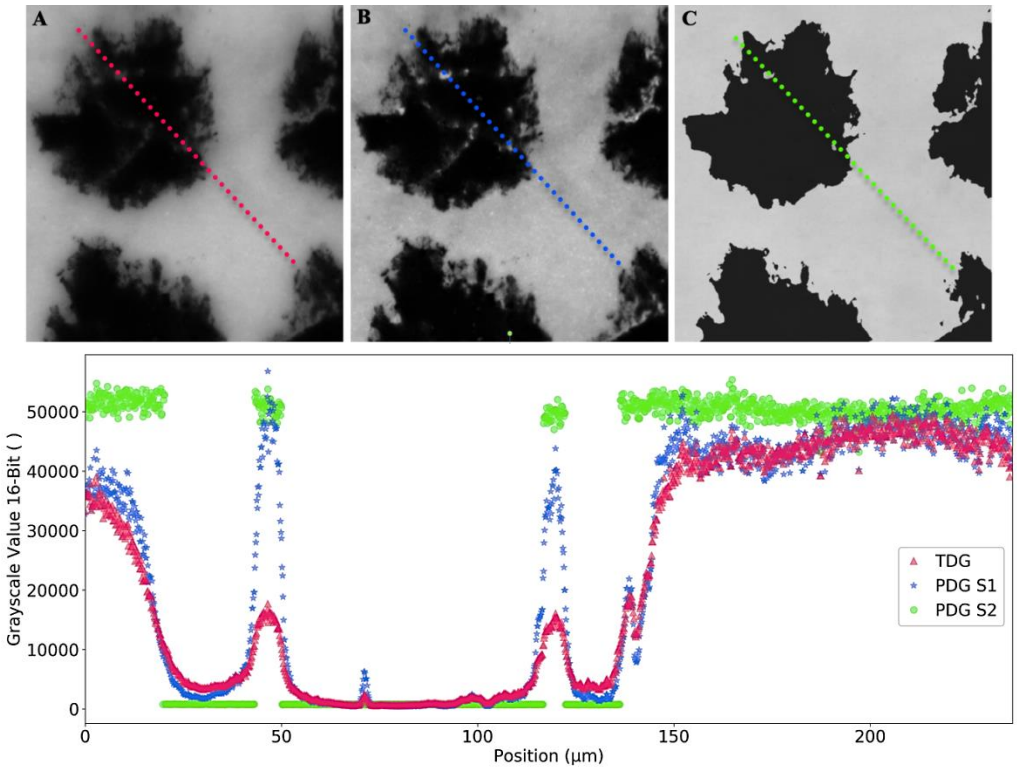

Figure 5.10: Profile of a offset printed dot of 30% nominal ink coverage on paper - total dot gain (TDG), with optical dot gain removed with strategy 1 (PDG S1) and strategy 2 (PDG S2). Gray values as a function of the position along the lines represented on images (A, B, C).

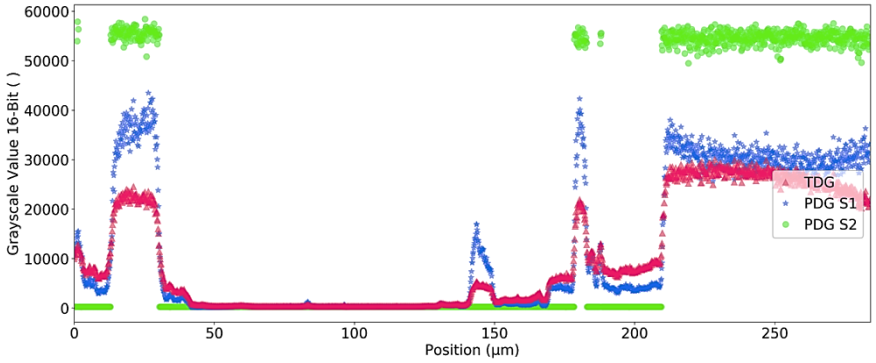

Figure 5.11 : Profile of a inkjet printed dot of 30% nominal ink coverage on paper - total dot gain (TDG), with optical dot gain removed with strategy 1 (PDG S1) and strategy 2 (PDG S2).

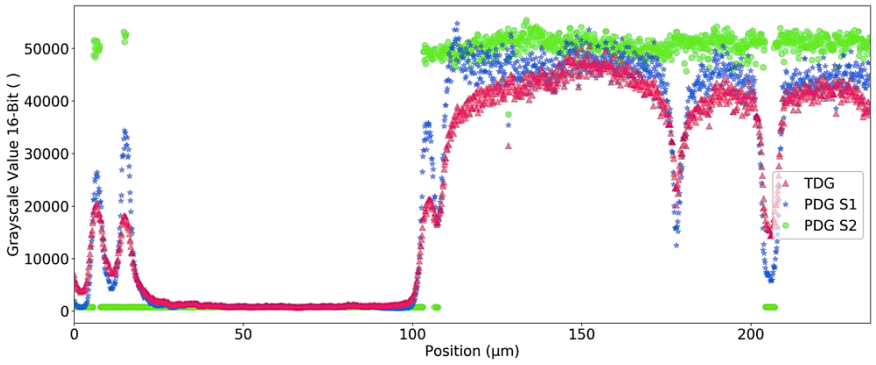

Figure 5.12: Profile of a electrophotography printed dot of 30% nominal ink coverage on paper - total dot gain (TDG), with optical dot gain removed with strategy 1 (PDG S1) and strategy 2 (PDG S2).

5.4 Conclusion

The convolution strategy presented in this work allowed to separate optical dot gain from total dot gain. PSF for the papers used in the present experiments were measured and compared to other papers PSF. It was shown that the papers considered in this study behaved similarly to papers referenced in literature, with a global light scattering around 100 µm. Two optical dot gain separation strategies were presented and investigated. The two methods showed an effective separation and images treated revealed un-inked surfaces previously impacted by the optical dot gain. For the first strategy (S1), the two effective ink coverage measurement methods, the Murray-Davies based on micro optical densities and the image processing threshold methods, showed a maximum optical dot gain impact of respectively 1.7% and 8.4% for offset, 4.9% and 1.0% for ink-jet and 4.2% and 5.0% for electrophotography. For the second strategy (S2), these global optical dot gain impacts were raised to respectively 23.6% and 18.7% for offset, 20.0% and 1.0% for ink-jet and 14.3% and 6.9% for electrophotography. Results of optical dot gain were compared to literature for the offset processes where optical dot gains were measured between 5 to 15%. The values found for optical dot gain for the offset process were then in the same range than classical optical dot gain found in literature. Analyses of the impact of the two optical separation strategies were conducted by comparing the reflectance values along a halftone dot profile. It was found that the results of the two strategies were closer to a bimodal distribution. These analyses showed the positive effect of removal of optical dot gain on the inked surfaces. However, paper reflectance levels for strategy 1 were not exactly matching the reflectance levels of bare paper, showing that the optical dot gain removal was not total. It was concluded that the method proposed allowed a first optical dot gain separation. Quantitative evaluation of the two separation strategies performances remained difficult because of the difficulty in obtaining a reliable reference of the ink distribution on paper.

Chapter 6 Threshold algorithms for ink and paper regions separation

Louis Vallat-Evrard, Lionel Chagas, Raphaël Passas, Nadège Reverdy-Bruas
Univ. Grenoble Alpes, CNRS, Grenoble INP*, LGP2, F-38000 Grenoble, France
Agefpi, LGP2, F-38000 Grenoble, France

Fast and accurate measurements of the printed dots at the microscale are required. Images of the inked dots at the microscale are obtained using an optical microscope equipped with a digital camera. However measuring inked dots on a color or grayscale image is not trivial because there are no direct relations to differentiate pixels belonging to the ink from pixels belonging to the paper, Figure 6.1. The optical dot gain is the consequence of the interactions between light ink and paper and generates a shift of ink and paper reflectances. The shift is spatially dependent and thus mixed regions appear. The mixed regions are regions where the limit between the ink and the paper is not clearly defined. Moreovers the amount of optical dot gain depends on the ink coverage as well as on the halftone cell size, dot resolution, halftoning method, etc. Image analysis tools are then required to separate pixels belonging to the ink region and pixels belonging to the paper region. Different methods, called thresholding methods, were employed to perform this separation [17–19,28,29].

Image thresholding to obtain a binary image can be divided into two steps: first, a threshold value is defined, then, pixels having a gray level below the threshold value are assigned to the ink and the remaining pixels are assigned to the paper. This binary image has ideally only the ink represented by the first level and only the paper represented by the second level. Measurements from the thresholded image become then straightforward: measuring the attributes of the first or the second level of pixels. Other fields of research have pushed researchers to develop multiple threshold algorithms. These algorithms were then evaluated with various images of material sciences and document reconstruction [171]. However, their performances were not tested for microscale halftone images. Evaluating objectively threshold algorithms is then a necessary step to obtain reliable measurements of halftones and to improve the accuracy of applications requiring microscale halftone dots characteristics. Two novel threshold algorithms, specifically developed for halftone dot processing were then proposed.

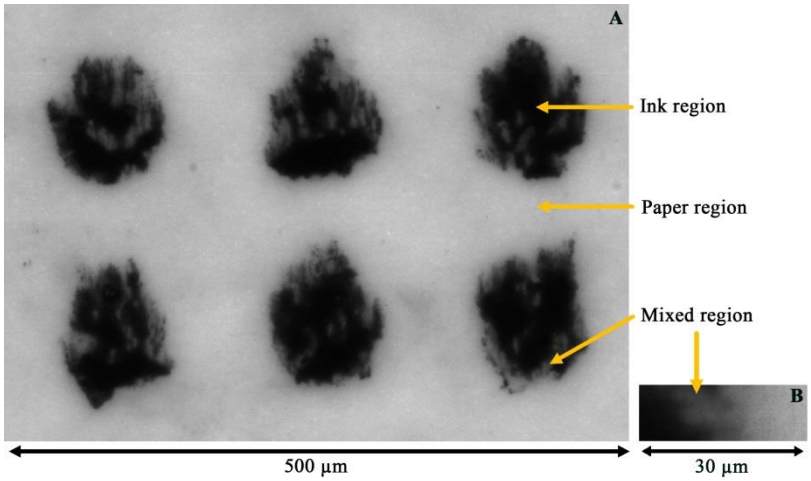

Figure 6.1: (A) Six halftone cells of a 15% ink coverage offset print on glossy 1 paper. (B) Enlargement of a mixed ink-paper region, illustrating the effects of optical dot gain.

6.1 Supervised evaluation of threshold algorithms applied to halftone dots analysis

6.1.1 Threshold algorithms evaluation

Multiple threshold evaluations were proposed in literature and can be classified in four approaches Figure 6.2 [176,178,180,182,183,362].The first approach, called the analytical evaluation, assesses the algorithm principle and complexity. This evaluation can be useful when developing new threshold algorithms. However, it does not assess the performance of the threshold algorithm for specific applications. For example, the targeted results differ greatly when thresholding scanned texts for optical character recognition or when thresholding topographic satellite images. To evaluate the performance of a threshold algorithm for a particular application a specific evaluation is required. The second approach consists in a visual evaluation of the result of a threshold algorithm. Although this approach is quite subjective, it is often used for its simplicity. The third and fourth evaluation approaches are based on a quantitative evaluation of the threshold algorithms and differ only from the type of evaluation criteria. The third approach is said unsupervised and assesses the performances of threshold algorithms through thresholded image quality criteria, such as uniformity of the regions, sharpness of the edges or roughness of the regions. This approach presents the advantage that an optimization of the threshold algorithm can be performed to return an image maximizing the selected criteria. In the case of optical character recognition for example this strategy is suitable. However, the experimenter is required to define specific criteria (for example, the level of edges sharpness, the smoothness degree of regions, etc.). With printed dots the experimenter cannot determine the quality indexes without introducing a potential bias in the results. The fourth approach, called supervised evaluation, is then the best suited to evaluate threshold algorithms for printed dots processing. The approach works by measuring the differences between a reference (called ground truth) and the result of the threshold. The supervised evaluation can be split in two methods, Figure 6.3. The first one requires the user to generate the ground truth manually, which introduces subjectivity in the evaluation, as explained by Johnson and Xie [183]. The second method was developed by Zhang [363] and differs, generating automatically a simulated image from a ground truth. The simulated image is then thresholded and compared to the ground truth. This method is therefore more objective but, to our knowledge, was never applied to an evaluation of threshold algorithms with halftone images. Applying this objective threshold evaluation to halftone images requires to develop a method to generate the simulated microscope images.

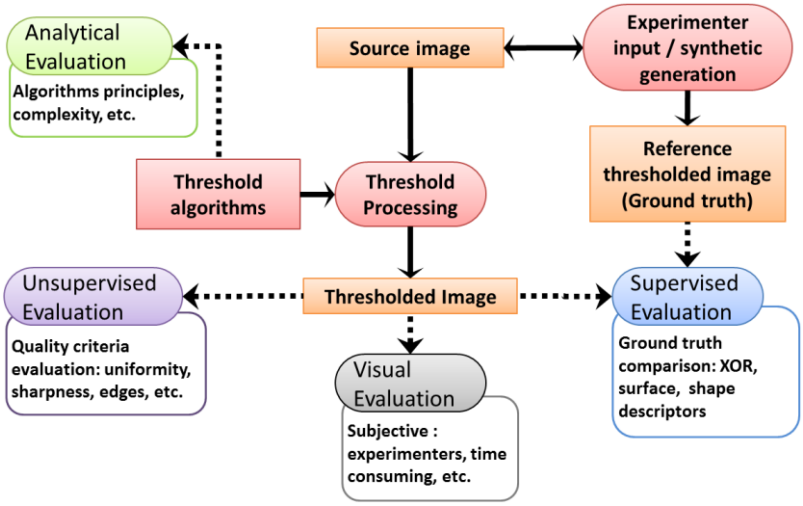

Figure 6.2: Approaches to evaluate the performance of threshold algorithms.

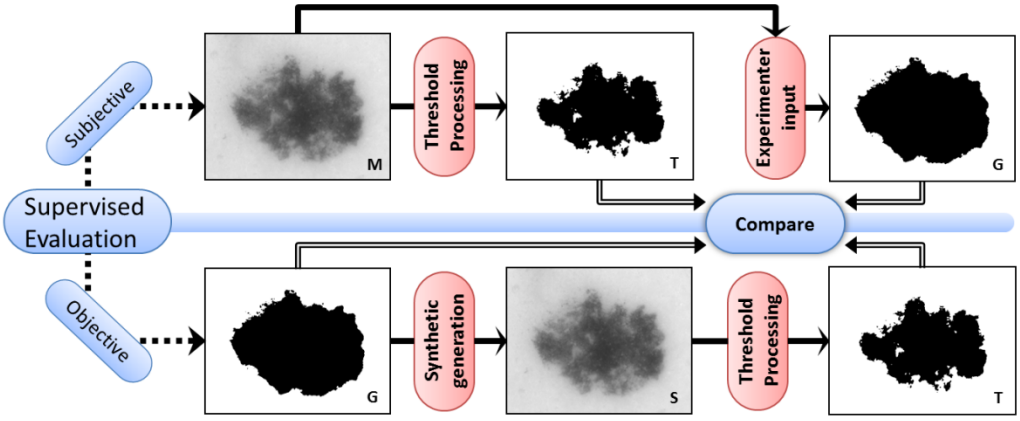

Figure 6.3: Subjective and objective supervised evaluation methods. M: test image, T: thresholded image, G: ground truth image, S: simulated test image.

Thus, in this work, a novel method is proposed to generate simulated microscope images reproducing alterations encountered during printing and imaging. The simulated image generation will then allow performing an objective evaluation of the threshold algorithms with halftone images. This evaluation is then required to define the best suited thresholding algorithm and to measure accurately halftone dots at the microscale. This study is split in two parts. First, a description of the proposed threshold evaluation method is conducted and an evaluation of the similarity of the simulated image compared to the real image is performed. Then, the second part of the study focuses on applying the method developed to determine the threshold algorithms that are best suited for printed halftone dots processing.

6.1.2 Materials and methods

6.1.2.1 Supervised objective evaluation method

Generation of the ground truth image

Following the principles of the supervised objective evaluation presented in Figure 6.3, ground truth images have first to be generated. The ground truth images can be generated with multiple methods. Two different methods are selected and developed in this work.

The first method is based on an automatic threshold of a halftone image captured. In order to obtain ground truth images with ink regions similar to the ink regions of halftone prints, the threshold algorithm should discard most optical dot gain. The Otsu threshold algorithm, Table 6.2 is selected based for its apparent ability to threshold correctly all ink coverages in the mixed regions. The choice of this threshold algorithm should not influence particularly the threshold evaluation since the ground truth image is only a reference image and since the simulated image that will be thresholded for the evaluation is synthetized directly from the ground truth. The only requirements are that the morphology and homogeneity of the halftone dots on the ground truth image should be similar to the morphologies of the halftone dots on the microscope image. The advantages of generating the ground truth image from measured halftone prints are that the ink morphology and homogeneity obtained follow precisely the images that will be expected to be thresholded after the selection of the best threshold algorithm based on the evaluation performed. In the following of this study, the Microscope Captured Images will be referred as MCI, the Ground Truth Image will be referred as GTI and the Simulated Microscope Image obtained will be referred as SMI.

The second method to produce a GTI is based on a simulation of the deformations induced when printing. Ideal halftone dots are numerically generated and defects are applied to either reproduce the deformations observed on real halftone images or to produce dot deformations more complex. In order to evaluate the performance of the generation of the GTI and of the SMI, the

strategy to simulate a GTI similar to a measured halftone image is adopted. The method to generate such a GTI is more specific however, the main principles are similar than for classical GTI. Starting from the microscope captured image Figure 6.4 (A), the first step is to build an image with ideal dots. The microscope captured image is analyzed with the OpenCV connected components function and centroids of all dots as well as morphological properties are extracted. Ideal dots are then generated at the locations of the measured centroids using an elliptical model with major and minor dimensions determined following the size distribution measured, Figure 6.4 (B). The angle of the ellipses was set at 45°. These ideal dots do not incorporate the physical dot gain (i.e. ink spreading, etc.) encountered during printing, as shown by the differences in the morphology of the dots Figure 6.4 (A and B). Consequently further treatments are applied to simulate the deformations that impact the morphology of the dot during printing. Miss-inking in the ink region is generated by introducing small circular paper particles inside the ink region, Figure 6.4 (C). The number of these particles, size distribution and position is controlled and reproduces the miss inking observed. Moreover, the pixel values of these circles are distributed since it is observed that a miss-ink region presents often ink residues. The deformations induced by the ink transfer are then simulated. A pixel dislocation function was designed for this purpose. This function selects a set of pixels with a specified length and thickness in a specified direction (X or Y direction) at a specified position of the image. The selected pixels are then dislocated with a specified distance and in a specified direction. The parameters of this function (i.e. set of pixel length, thickness, centroid, distance and direction) are selected in a specified distribution. The number of dislocations impacts the results of the simulation and is set to match the MCI, Figure 6.4 (D'). Extended information on this generation can be found in a previous work [364]. A smoothening is then applied to the ground truth with a median blur filter followed with a mean blur filter. These filters are obtained by the convolution of the image with a defined kernel, [365]. The smoothening helps reducing artifacts induced by the pixel dislocation generation producing rectilinear groups of pixels. Finally, the last operation is a filtering of the ground truth with a low pass filter on the pixel value Figure 6.4 (D''). In this way, it allows the ground truth image to have different ink pixel values caused by different ink thicknesses deposited, Figure 6.4 (D).

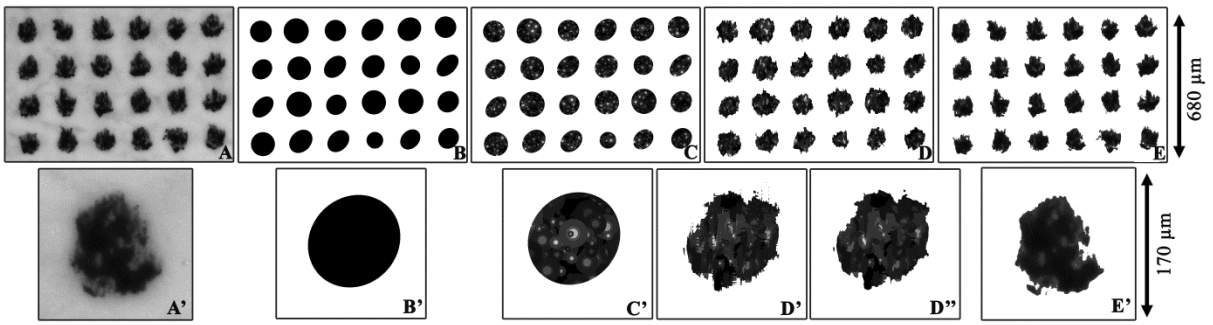

Figure 6.4: Generation of the GTI: (A, A') Halftone dots of 15% ink coverage printed on glossy 1 paper with offset and imaged with an optical microscope, (B, B') Generation of ellipses at the centroid of the printed dots, (C, C') Ink defects generation inside the ink region, (D, D') ink spreading defect generation, (D'') smoothening and low pass filter, (E, E') thresholded MCI.

It has to be noted that the deformations of the printed dots depend greatly on the printing process and on the printing parameters [366]. To test the performance of the GTI generation, the offset process was chosen and defects were generated specifically. The parameter selected for the generation are then 4800 iterations of miss inking with radius of 3 to 19 µm. The distribution of the pixel value is determined from the histogram distribution of the microscope image considering pixel values superior to the threshold value obtained with a mean thresholding. The ink dislocation generation is set with 10000 iterations with mean block length of 13 µm and mean block width of 8 µm. The mean displacement is fixed at 5 µm with 90% of the dislocations targeted in the Y direction. The kernel size of the two smoothening filters is set for the example at 2 µm. The low pass filter is set at the pixel value 70 for this example. The result of the simulation with the selected process and parameters show

an accurate reproduction of the dot deformations observed, Figure 6.4 (D, D'' and E, E'). It has to be noted that the generated ground truth and microscope captured ground truth are thresholded by setting only the paper layer to 1, in order to conserve the ink thickness variations (only for the comparison).

Generation of the microscope simulated image

Starting from the ground truth images, microscope simulated images simulating the deformations observed on images captured by the microscope are generated. When imaging halftone dots with a microscope, three types of deformations are observed: a light trapping (optical dot gain), dust or particles in the optical system defects and blur and noise due to the limit of the resolution of the microscope optics and imaging camera. The light trapping effect, generating optical dot gain, was modelled by Callahan, Yule and Lehmbeck [8–16] and is called the model of light diffusion on halftone, equation [6.1]. The model takes as input the ink transmittance function $T_i(x,y)$ (obtained from ground truth image), the bare paper reflectance function $R_{ps}(x,y)$ (bare paper image) and the point spread function $H(x,y)$ (2D description of the light diffusion into paper). The point spread function chosen is a Gaussian function with a half width of 80 µm corresponding to values measured for coated offset papers. Then, dust defects are added to the image by generating circular particles with pixel values darker than the paper. 30 particles were generated with a diameter in the range of 0.5 to 5 µm and pixel values in the range of 230/255 to 250/255. The optical resolution limit of the microscope induced a small amount of blur which is modelled by applying a Gaussian blur filter to the simulated image. The kernel for Gaussian blur filter has a size of 3.15 µm. A second Gaussian blur is applied to account for the camera optical resolution limit. The kernel for the second Gaussian blur has a size of 0.63 µm. Finally, a noise mask, modelling the sensor measurement errors, is applied to the image. The noise mask is composed of random uniform distributed values in the range of 0.96 to 1.04. The simulated image is then multiplied by the image of a bare paper to reproduce accurately the variations of the paper region. The aim of thresholding will be to discard most of the effects induced by this generation in order to obtain an image having the same properties as the ground truth.

Model of light diffusion on halftones

[6.1] $$R_a(x,y) = R_{ps}(x,y)\,T_i(x,y)\,[T_i(x,y) \circledast H(x,y)]$$

Symbol	Unit	Denomination
$R_a(x,y)$	1	Halftone reflectance
$T_i(x,y)$	1	Ink transmittance
$R_{ps}(x,y)$	1	Bare paper reflectance
$H(x,y)$	1	Paper point spread function
$\circledast$	-	Convolution operator

6.1.2.2 Performance of the objective supervised evaluation method

The performance of the objective supervised evaluation method relies on the similarity between the SMI and the MCI. An evaluation of this similarity is performed with five criteria:

- The first criterion is a frequency comparison of the MCI and the SMI. A ratio of similarity between the two histograms is calculated based on the Pearsons chi-square statistic test, equation [6.2] [367]. The statistic test compares the two distributions and gives an index of similarity in the range of 0 to 100; 100 corresponding to two identical distributions and 0 corresponding to two very different distributions. Since the index is bounded between 0 and 100, it will be expressed in percent.
- The second criterion consists in a modified exclusive disjunction logical operation (XOR). The modified XOR operation is performed on the MCI and SMI thresholded at the same threshold level of 100/255. Over and under inking ratios are computed by counting the number of pixels that are missing on the SMI compared to the MCI (under inking) and the number of pixels that are

added compared to the MCI (over inking). A ratio called the binary fidelity ratio (FD_b) is then expressed by the modulus of the difference of the over inked pixels count and the under inked pixel count relatively to the inked pixel surface of the GTI, equation [6.3]. The FD_b ratio depends highly on the threshold value selected to process the MCI and SMI.

- The third criterion is a coupled frequency and spatial approach, calculating the binary fidelity ratio for each threshold value in the range of 0 to 255. The frequency-spatial coupling allows comparing the behavior of the MCI and the SMI for all possible threshold values; the calculated binary fidelity ratio showing at each threshold value the similarity of the MCI and SMI. This coupled analysis is extremely helpful to determine the similarity between the MCI and the SMI. However, the analysis is slow since it requires to compute the binary ratio at each threshold value.
- The fourth criterion, called the grayscale fidelity ratio (FD_g), is introduced to compute rapidly the level of spatial and frequency similarity between the MCI and the SMI, equation [6.4]. The grayscale fidelity ratio computes the average of the absolute pixel value difference of the MCI and SMI for each pixel location. The grayscale fidelity ratio is expressed in percent.
- The fifth criterion is a comparison of the shape descriptors [185,186] of the halftone dots obtained after thresholding the MCI and SMI. Four shape descriptors based on the ISO 9276-6 were considered, equations [6.5]. The solidity describes the degree to which the area of the particle is closed (i.e. composed of only convex surfaces). The aspect ratio describes the shape of the particle. An aspect ratio converging to 1 means that the particle has identical dimensions in perpendicular directions. The circularity describes the degree to which a dot is close to a disc. The circularity is directly linked to the particle roughness and has to be analyzed in conjunction with it. The convexity describes the roughness of the edges of the particle. The shape descriptors are computed with the OpenCV connected component function (used to individualize the dots and obtain a measurement of their area). The OpenCV find contours function was used to identify the edges of the dots and compute their perimeter. The OpenCV convex hull function was used to compute the convex perimeter. The OpenCV fit ellipse function was used to find the major and minor axis and angle of the ellipse fitting the dots. The major and minor axis lengths were used to compute the aspect ratio. It differs from the ISO standard, as the ISO aspect ratio relies on the ferret diameters. For printed dots, the ellipse fitting method was found to be more effective. A limitation of the shape descriptor analysis is that halftone dots must be separable from each other in order to analyze them individually. This analysis is then mostly restricted to low ink coverage patches.

Histogram similarity index inspired from the Pearsons chi-square test

[6.2] $$BP_e = 1 - \sum_i \begin{cases} \frac{\left(h_1(i) - h_2(i)\right)^2}{h_1(i) + h_2(i)} 1 & \text{if } h_1(i) + h_2(i) > 0 \\ 0 & \text{else} \end{cases}$$

Symbol	Unit	Denomination
BP_e	1	Histogram similarity index
$h_{1,2}(i)$	1	Histograms
i	1	Histogram bin

Binary fidelity index

[6.3] $$FD_b = \begin{cases} FD_b & \text{if } FD_b > 0 \\ 0 & \text{else} \end{cases}$$

$$FD_b = \left(1 - \frac{\left|\sum_x \sum_y O(x,y) - \sum_x \sum_y U(x,y)\right|}{\sum_x \sum_y IM_G(x,y)}\right)$$

$$O(x,y) = 1 \quad \text{where } IM_K(x,y) < IM_G(x,y)$$

$$U(x,y) = 1 \quad \text{where } IM_K(x,y) > IM_G(x,y)$$

$$IM_k(x,y) = \begin{cases} 1 & \text{where } IM_{SMI}(x,y) \le K \\ 0 & \text{where } IM_{SMI}(x,y) > K \end{cases}$$

Symbol	Unit	Denomination
FD_b	1	Binary fidelity index
$IM_{SMI}(x,y)$	1	SMI image
$IM_K(x,y)$	1	Thresholded image
K	1	Threshold value
$IM_G(x,y)$	1	Ground truth image
$O(x,y)$	1	Over inked region
$U(x,y)$	1	Under inked region

Grayscale Fidelity index

[6.4] $$FD_g = \left(1 - \frac{\sum_x \sum_y |IM_{SMI}(x,y) - IM_{MCI}(x,y)|}{xy * DLv}\right)$$

Symbol	Unit	Denomination
FD_g	1	Grayscale fidelity index
$IM_{SMI}(x,y)$	1	SMI image
$IM_{MCI}(x,y)$	1	MCI image
DLv	1	Discretization level

Shape descriptors

[6.5] $$\text{Solidity} = \frac{A}{A_c}$$ $$\text{Aspect ratio} = \frac{D_{min}}{D_{max}}$$ $$\text{Convexity} = \frac{P_c}{P}$$ $$\text{Circularity} = \sqrt{\frac{4\pi A}{P^2}}$$

Symbol	Unit	Denomination
A	μm^2	Area
A_c	μm^2	Convex area
P	µm	Perimeter
P_c	µm	Convex perimeter
$D_{min,max}$	µm	Feret diameters

6.1.2.3 Paper, printing and optical microscope measurement

To produce the printed samples, three different processes are employed: offset, inkjet and electrophotography with four different types of paper, Table 6.1. Grayscale patches consisting of 14 different gray patches with targeted ink coverage of 0%, 2%, 5%, 10%, 15%, 20%, 30%, 40%, 50%, 60%, 70%, 80%, 90%, 100% are generated with Python 3.6 and halftoned with Photoshop CS6 amplitude modulated halftoning (AM). Two different series of patches are generated with a halftone cell size of 150 lines per inch (lpi) and 200 lpi. The resolution is adapted to the native resolution of the printer: 2540 dots per inch (dpi) for offset, 1440 dpi for inkjet and 1200 dpi for electrophotography. Halftone patches are also generated with a frequency modulated halftoning (FM) implemented in Python programming (random distribution of dots with a fixed size). 13 different gray patches with targeted ink coverage of 0%, 5%, 10%, 15%, 20%, 30%, 40%, 50%, 60%, 70%, 80%, 90%, 100% are set. Five series of gray patches are generated with different nominal dot sizes: equal to 1, 2, 3, 4 and 8 times the native resolution of the printer.

Table 6.1: Ink, paper and printing process.

Printing process	Paper	Ink (Black)
Offset: Heidelberg Speedmaster 52, 2540 dpi	· Unknown supplier, glossy coated, 135 g/m² (Glossy 1)	Novavit 918 supreme
Inkjet: Epson Stylus Pro 4900, 1440 dpi	· Epson proofing, inkjet coated, 205 g/m² (Epson)	Epson PK T6531 Epson MK T6538
Electrophotography: Xerox Versant 180 Press, 1200 dpi	· Unknown supplier, glossy coated, 135 g/m² (Glossy 1) Mondi, glossy coated, 135 g/m² (Glossy 2) · Epson proofing, inkjet coated, 205 g/m² (Epson) · Inapa, uncoated, 160 g/m² (Uncoated)	Xerox Versant 180

A Zeiss Axio Imager M1m optical microscope mounted with two EC Epiplan Neofluar HD DIC 10x/0.25 and 20x/0.50 objectives is used with a modified Canon 1200D camera (monochrome, CMOS, 13.8 megapixels). Total magnification on sensor is 10x and alternatively 20x with a physical pixel size on sensor of 4.21 µm/pixel. The calibrated system captures images of respectively 0.4202 µm/pixel for the 10x objective and 0.2101 µm/pixel for the 20x objective. Crossed analyzer-polarizer (90°) reflected light microscopy with a 0°/0° geometry is chosen to capture images excluding the specular reflections. A halogen lamp Zeiss Hal 100 is used as light source for the microscope with

a blue filter giving a spectrum similar to the standard D65 illuminant. The source voltage is regulated and set at 10.0V. The source luminance variations are recorded with a luxmeter placed on the side of the light path and images captured are corrected accordingly. The iso of the camera is set at 800 and exposure times are selected to perform high dynamic range captures. Images are saved in raw .CR2 format and processed with Python 3.6 to perform black frame subtraction, to correct the uniformity of the field of view and to obtain richer information processing the high dynamic range, Figure 6.1. The ink coverage is obtained by counting the amount of thresholded pixels belonging to the ink.

6.1.2.4 Evaluation of the threshold algorithms

Threshold algorithms evaluated

Threshold algorithms are developed in order to find the best threshold algorithm for halftone prints. The evaluation allows also the threshold algorithms performances dependencies on the print process, the ink coverage, the halftone method or on other parameters linked to the printing process. Thirty threshold algorithms from literature are then evaluated, Table 6.2. The threshold algorithms tested are a selection of the threshold algorithms available in literature. Multiple other threshold algorithms have been developed [171]. Four of the threshold algorithms have been specifically proposed for halftone dot processing:

- Engeldrum and Hsieh proposed a manual thresholding, not implemented in this study since it cannot be automated and depends mostly on the experimenter [219].
- Arney [5,218]and then later Namedanian proposed a threshold algorithm computing the threshold value at the position on the histogram where the occurrence is minimal in between the ink and paper peaks [225]. The method is similar to Prewitt's minimum threshold algorithm.
- Nyström proposed to define the threshold value as the midpoint between the local maxima in the paper region and the ink region [19,211,220–224]. Nyström algorithm is similar to Prewitt's intermodes threshold algorithm.
- Namedanian proposed also a threshold method based on the analysis of the histogram shape and defined the threshold value as the rapid drop occurring after the ink peak maximum [226]. Noise in the measurement may alter the shape of the histogram and thus, give unstable threshold results. The threshold algorithm was then not implemented in this work.

Sezgin and coworkers proposed a classification of the threshold algorithms according to the algorithm strategy. This classification is used in order to present the selected threshold algorithms. The classification is composed of 6 categories called: shape, attributes, cluster, entropy, spatial and local.

- Shape threshold algorithms are based on strategies over the shape (peaks, valleys) of the histogram (distribution of pixel values over the pixel value range).
- Cluster threshold algorithms are based on a classification of the pixel value distribution in two classes: the object class and the background class.
- Entropy threshold algorithms are based on the minimization of the entropy of the objects or of the background classes.
- Attribute threshold algorithms are based on the properties of the object or of the background, considering, for example, fuzziness of the class.
- Local threshold algorithms can be associated with the shape, cluster, entropy and attribute categories; however, they differ by setting a local threshold for each pixel instead of defining a global threshold. The local threshold is computed over a defined window. It has to be noted regarding the local threshold algorithms that applying a local threshold can improve the results when the image background pixel values depend on the position (non-flat background). In this study, a field flatness compensation is applied after the measurement on the microscope.

- Spatial threshold algorithms are based on a combination of the global and local approaches with a global threshold defined from the analysis of local properties.

A definition of the histogram moments is given in appendix, equation [A.1]. The threshold algorithms are implemented on 8 bits.

Table 6.2: Threshold algorithms implemented. Corresponding equations are presented in appendix.

Name	Author	Type	Principle
Mean	Doyle [368]	Cluster	K= average of the pixel values
Median	Doyle [368]	Cluster	K = median of the pixel values
Percentile	Doyle [368]	Cluster	K in order to have the relative sum of pixel count from 0 to K equal to p. In this work p is computed automatically (one minus the average of the pixel values).
MinError	Kittler [164]	Cluster	Object and background are assumed normally distributed. $K = t$ when $CT_k(t)$ is minimized. Equation [A.2].
PalBhandari	Pal Bhandari [369]	Cluster	Variation of the Kittler algorithm. $K = t$ when $CT_{pb}(t)$ is minimized. Equation [A.3].
IsoData	Ridler [170]	Cluster	Variation of Ridler algorithm. Iterative search of K in the range of pixel values. $K = t$ when first $CT_r(t) > t$. Equation [A.4].
SimpsonGobat	Simpson Gobat [370]	Cluster	Variation of Ridler algorithm with different iterative search: initialization t = average of the pixel values, then iterations of $t = CT_r(t)$ until t remains constant.
Otsu	Otsu [168]	Cluster	Iterative search based on the maximization of $CT_r(t)$: variance in-between of objects and backgrounds regions. Equation [A.5].
Intermodes	Prewitt [371]	Shape	Smoothening of the histogram until there are only two maxima. K = average of the two maxima
Minimum	Prewitt [371]	Shape	Similar to intermodes. K = minimum between the two maxima
Triangle	Zack [372]	Shape	A triangle is constructed by linking the maximum of the histogram, the minimum furthest away and a point in-between. K is the pixel value of the point maximizing the altitude.
Rosenfeld	Rosenfeld [373]	Shape	The histogram shape is compared to its convex hull. K is the pixel value where the cavity between the histogram and the convex hull is the largest.
Whatmough	Whatmough [174]	Shape	The histogram shape is compared to its exponential hull. K is the pixel value where the cavity between the histogram and the convex hull is the largest.
MaxEntropy	Kapur [163]	Entropy	Divides the histogram into two probability distributions. $K = t$ when the sum of the entropies of the two distributions $CT_a(t)$ is maximum. Equation [A.6].
RenyiEntropy	Sahoo [374]	Entropy	Renyi entropy $CT_y(t, \alpha)$ is computed with equation [A.7]. $CT_y(t, \alpha)$ is maximized for three values of α and the K_α obtained are combined with equation [A.8] yielding K.
Yen	Yen [375]	Entropy	Special case of Renyi entropy, equation with $\alpha = 2$. $K = t$ when $CT_y(t, 2)$ is maximum.
Li	Li [376]	Entropy	Divides the histogram in two distributions. $K = t$ when the sum of cross-entropies $CT_l(t)$ is minimum. Equation [A.9].
Shanbhag	Shanbhag [172]	Entropy	Divides the histogram into two probability distributions. $K = t$ when the sum of the fuzzy entropies $CT_s(t)$ is minimum. Equation [A.10].
Moments	Tsai [173]	Attribute	First three moments are kept unchanged before and after thresholding. K is found solving equation [A.11].
Huang	Huang [162]	Attribute	$K = t$ when the fuzziness $CT_h(t)$is minimized, equation [A.12].
PalDasgupta	Pal Dasgupta [377]	Attribute	$K = t$ when the Pal Dasgupta ambiguity $CT_{pd}(t)$ is minimized, equation [A.13].

Abutaleb	Abutaleb [378]	Spatial	A 2D probability function (2D histogram) is generated by superposing the halftone image $I_h(t)$ and the image representing the local average of the halftone over a region of size k x k, $I_m(s)$, equation [A.14]. $K = t$ when the total entropy $CT_u(t,s)$ is maximized, equation [A.15].
Brink	Brink [379]	Spatial	Similar to Abutaleb, except that the minimum of the two entropies $(CT_{ba}(t,s), CT_{bb}(t,s))$ are selected. K is found at the position of the maximum of the these minima, equation [A.16].
Local_Mean	Doyle [368]	Local	K defined independently for all pixels. Average of the pixel values over a window of size k x k.
Local_Median	Doyle [368]	Local	K defined independently for all pixels. Median of the pixel values over a window of size k x k.
Local_ Contrast	Soille [380]	Local	K defined independently for all pixels. If K is closest to the local maximum sets to background, otherwise set to foreground.
Local_Bernsen	Bernsen [381]	Local	Similar to local contrast threshold method. If the local contrast $(t_{max} - t_{min}) < 15$, the neighborhood consists of only a single class and K is defined from the global contrast. Else K is defined from the local contrast.
Local_Niblack	Niblack [382]	Local	K_n computed from moments independently for all pixels, equation [A.17], window of size k x k. Parameter $e = 0.2$.
Local_Sauvola	Sauvola [383]	Local	K_s computed from moments independently for all pixels, equation [A.18], window of size k x k. Parameter $e = 0.5$, $r = 0.5$.
Local_ Phansalkar	Phansalkar [384]	Local	K_p computed from moments independently for all pixels, equation [A.19], window of size k x k. Parameter $e = 0.5$, $r = 0.5, f = 2, g = 10$.

GTI and SMI generated for the evaluation

3920 SMI are generated in order to evaluate the threshold algorithms. The generation can be split in two categories: SMI from thresholded MCI and SMI generated from synthetic GTI. The two strategies are complementary.

1320 SMI are generated from GTI obtained from thresholded MCI and present the advantage to follow precisely real halftone dots morphologies and homogeneities. They allow then to give an evaluation that will be relevant when using the threshold algorithm later on, processing real halftones. Following the methodology developed in section 2.1, the GTI are obtained by thresholding the MCI with Otsu threshold algorithm. The SMI are then generated from the GTI with the point spread functions and ink transmittances given in Table 6.3 (optical densities). The point spread functions chosen are Gaussian functions. It was found that a second convolution with a small Gaussian point spread function was reproducing better the mixed region. Therefore, two different convolutions with two different point spread functions are applied. The ink transmittances employed were measured on the corresponding solid ink MCI patches. For simplification reasons, no dust defects are generated and diffusion from the microscope is set to Gaussian blur with a half width kernel of 3 µm. No diffusion from the camera and no sensor noise errors are applied.

2600 GTI were generated from synthetic GTI. Half of the GTI generated followed an amplitude modulated halftone scheme and the other half followed a frequency modulated halftone scheme. Combinations of the different parameters used for the synthetic generation of the GTI are given in Table 6.4. The synthetic generation of the GTI allows exploring unusual halftone configurations with high resolutions up to 605 lpi for AM halftones and 2419 dpi and 4838 dpi for FM halftones. Halftones with rounded dots and elliptical dots are generated. Small and large ink coverages are explored without printer distortion affecting the targeted ink coverages. Halftones with homogeneous and heterogeneous ink surfaces are introduced by variating the number of mis-inked dots. Different edges fuzziness of the halftone dots are also generated by variating the number of pixel dislocation

iterations. Three different ink reflectances are used in order to simulate different types of prints with respective optical densities of 2.52, 1.52 and 1.00. Three different Gaussian paper point spread function combinations are used to generate halftones with different light trapping effects.

Table 6.3: Solid ink optical densities and specificities of MCI halftones used to obtain by threshold a set of GTI.

Process	Halftone type and resolution	Specificities	Solid ink optical density
Offset	AM: 150 and 200 lpi	Inking: Light	1.01
Offset	AM: 150 and 200 lpi	Inking: Normal	1.91
Offset	AM: 150 and 200 lpi FM: 2540, 1270, 847, 635, 318 dpi	Inking: Strong	2.37
Electrophotography	AM: 150 and 200 lpi FM: 1200, 600, 400, 300, 150 dpi	Paper: Glossy 1	2.51
Electrophotography	AM: 150 and 200 lpi	Paper: Glossy 2	2.52
Electrophotography	AM: 150 and 200 lpi	Paper: Epson	2.47
Electrophotography	AM: 150 and 200 lpi	Paper: Uncoated	2.51
Inkjet	AM: 150 and 200 lpi FM: 1440, 720, 480, 360, 180 dpi	Ink: Epson MK	2.65
Inkjet	AM: 150 and 200 lpi	Ink: Epson PK	2.21

Table 6.4: Experimental parameters for the generation of the set of synthetic GTI and SMI.

Halftone	AM	FM
Halftone cell size / dot size	101, 151, 202, 302 and 605 lpi	403, 806, 1210, 2419, 4838 dpi
Dot aspect ratio	1.0+/-0.0 and 0.7+/-0.0 only associated with 0 mis-inked dots	
Dot rotation	45°+/-0°	
Ink coverage	2, 5, 10, 20, 30, 40, 50, 60, 70, 80, 90, 95 and 98%	
Mis-inked dots number	0, 200 and 500 dots	
	Diameter: 5 µm +/- 4 µm	
Pixel dislocation function	100 and 10000 iterations only associated with 200 mis-inked dots	
	Set of pixels length: 10.5 µm	
	Set of pixels thickness: 6.3 µm	
	Set of pixels direction: 90% in the Y direction	
	Set of pixels distance: 4.2 µm	
Smoothening and filtering	Median blur with kernel 1.9 µm	
	Mean blur with kernel 1.9 µm	
	Threshold algorithm: Mean	
Ink reflectance / Optical density	Ri=0.003, 0.03 and 0.1 / OD=2.52, 1.52 and 1.00	
Point spread function: Gaussian function	Half width of 105 µm + 21 µm Half width of 157 µm + 52 µm (only with Ri=0.003) Half width of 52 µm + 2 µm (only with Ri=0.003)	

GTI and SMI comparison metrics

The first index proposed compares the ink coverage of SMI and GTI. The index, called the Ink Coverage Difference (ICD), is computed by subtracting the GTI ink coverage to the thresholded ink coverage. An average over multiple images can be computed, nevertheless the average is computed on the absolute values of the ICD. The ICD is expressed in percentage and the best threshold performance is associated with an ICD converging toward 0. The second index proposed is based on the binary fidelity index, equation [6.3]. The binary fidelity ratio is more accurate since it compensates the over inked and under inked regions. Additional indexes required to compute the binary fidelity index, such as the over inked ratio and the under inked ratio are also computed and help the performance analysis. It has to be noted that the grayscale fidelity ratio, equation [6.4] is computed for the SMI generated from the MCI in order to evaluate the performance of the simulation.

Ink coverage difference (ICD)

$$ICD = \frac{\left|\sum_x \sum_y IM_K(x,y) - \sum_x \sum_y IM_G(x,y)\right|}{xy} \quad [6.6]$$

$$IM_K(x,y) = \begin{cases} 1 \text{ where } IM_{SMI}(x,y) \leq K \\ 0 \text{ where } IM_{SMI}(x,y) > K \end{cases}$$

Symbol	Unit	Denomination
FD_b	1	Ink coverage difference
$IM_{SMI}(x,y)$	1	SMI image
$IM_K(x,y)$	1	Thresholded image (binary)
K	1	Threshold value
$IM_G(x,y)$	1	Ground truth image (binary)

6.1.3 Results and interpretations

6.1.3.1 Performances of the objective supervised evaluation method

The performance of the objective supervised evaluation method is analyzed by generating 10 SMI from synthetic GTI. The synthetic GTI were simulated following the halftone dots placements, morphologies and homogeneities of 10 MCI of 150 lpi amplitude modulated halftones of 15% nominal ink coverage printed with offset on offset gloss coated paper (Glossy 1). Illustrations of the generation are given in Figure 6.4. The similarities between the SMI and MCI are then investigated with qualitative (i.e. visual comparison) and quantitative (frequency, spatial, coupled and morphological measurements) approaches. The MCI and the SMI are visually similar, Figure 6.5 (A, D). Heterogeneous background is observed for the SMI and MCI with shadows and random background noise generated by paper fibers and surface coating. Background defects such as dust in the optical path or ink residues on the paper are also visible for both images. However, dust in the optical path or ink residues on the paper appear smaller and in a greater number on the MCI. Comparing the halftone dots of the two images, the shapes and sizes distributions are globally similar. The halftone dots have fuzzy edges. Dark levels are more pronounced on the SMI with at the same time a larger range of gray levels. The missing areas inside the halftone dots are well simulated on the SMI. Shapes of single halftone dots can be compared for the two images considering the two selected dots Figure 6.5 (B, E). The edges sharpness, shape aspect, size, shadows (optical dot gain), satellite defects, miss-inking and over-inking are similar. The simulated dot gives an impression of a sharper version of the real dot. This effect disappears when thresholding the two images with a fixed threshold value define at 100/255, Figure 6.5 (C, F). However, the morphologies and edges roughness of the MCI dots are slightly rougher than the SMI dots. From this first qualitative analysis, it can be concluded that the SMI simulates correctly the MCI. It has to be noted that this comparison is based on a synthetic GTI. The exact dot shapes differ then from the MCI. A simulation with a GTI obtained directly from a MCI would result in exactly identical dot shapes. However, comparing the two images with a generation from a synthetic GTI, allowed illustrating the performances of the GTI generation.

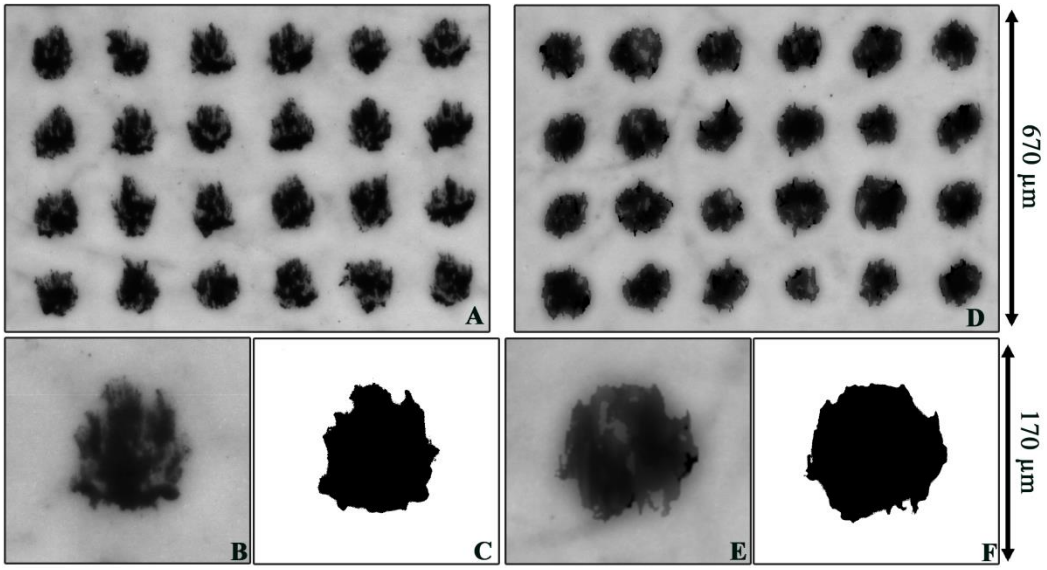

Figure 6.5: MCI (A, B) and SMI (D, E), thresholded MCI (C), thresholded SMI (F), 150 lpi AM halftone of 15% nominal ink coverage printed with offset on Glossy 1.

The frequency analysis based on the histograms of the MCI and SDI images allows determining the gray levels distribution similarities. It is interesting to study the histograms because most threshold algorithms operate on the gray level distribution. Images that give accurate threshold results usually have a histogram with two maxima: one located in the low gray levels (i.e. dark areas corresponding to the ink) and another one located in the high gray levels (i.e. lighter areas corresponding to the paper). Threshold of this ideal histogram takes place in between the two peaks maxima. The two histograms obtained are presented in Figure 6.6 and show for the MCI and SMI a wide plateau between two peaks. The presence of this large non-zero plateau between the two peaks illustrates the presence of mixed ink and paper regions (also caused by dust defects, imaging defects etc.). The exact position of the threshold required to separate the ink from the paper in the mixed region is then difficult to obtain. Nevertheless, the two histograms are globally similar, demonstrating that the gray level distribution on both the SMI and MCI are similar. It has to be noted that the SMI histogram was obtained by averaging 10 SMI. The associated standard deviation is shown in dark cyan color. It can be observed that the MCI and SMI histograms are very similar between the gray levels 10 to 255. Regions where the two histograms differ slightly are located near the two peaks. These regions are also associated with the largest variations from SMI generations. The SMI first peak in the low gray levels is wider than the MCI peak and, in reverse, the peak in the high gray levels is narrower than the MCI. These variations tend to be small and should not influence significantly the threshold algorithms results. In the 0 to 10 gray level range, the SMI presents a different distribution than for the MCI with a small peak near the gray level 0. This peak could influence threshold methods. To quantify the similarity of the two histograms, the metric based on the Pearsons chi square statistic test (BP_e) is computed. A BP_e of 94.3% +/-0.2% is obtained. This high value shows the similarity of both histograms. The generation simulates globally correctly the frequency distribution of the MCI. For both distributions, maxima are located at the same levels. It has to be noted that in the low gray levels for the MCI and SMI, the first peak shows distributions that are less close to Gaussian distribution than for the following peak located in the high gray levels.

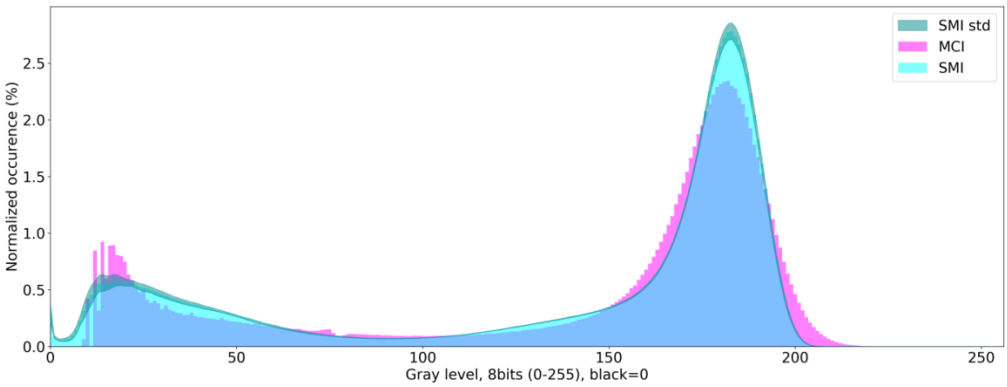

Figure 6.6: Histograms of the MCI and of the average of 10 SMI. Standard deviation of the 10 SMI denoted "SMI std". Superposition of MCI and MCI histograms in blue color.

A spatial analysis is then conducted by thresholding the MCI and SMI at a similar threshold value of 100/255. The numbers of misregistered over-inked and under-inked pixels are obtained with a modified XOR operation, Figure 6.7. For the SMI an average over the 10 thresholded SMI is computed. The ink coverage of the thresholded MCI and SMI are globally similar with respectively 24.0% and 25.6% +/-1.0%. This similarity can be observed on the modified XOR image, with the superposition of the ink region of the thresholded MCI and SMI represented in blue color. Cyan and magenta colors represent over and under inked regions. Comparing the over-inked region and under-inked region, it can be observed that thresholded SMI has larger over-inked regions than under-inked regions with respectively 19.4% +/- 2.7% and 12.7% +/-1.6%, relative to the thresholded MCI dot area. The binary fidelity ratio index reaches 93.3% +/- 4.1% showing a high spatial similarity of thresholded SMI compared to the thresholded MCI. The standard deviation remains acceptable, illustrating that the dot shape variations due to the multiple GTI and SMI generations are small; the halftone dots of all the generations remaining similar to the thresholded MCI. The optical densities of the SMI and MCI are then computed. The results show a global similarity between the two images, with an optical density of 0.56 for the MCI and 0.55 +/- 0.01 for the SMI. The difference in optical density can be caused by two factors: a difference in inked surface or a difference in ink reflectance over the ink and paper regions. It is interesting to notice that the smaller ink coverage of the MCI image is associated with the larger optical density. This shows that although the global distributions are similar small differences of the ink or paper gray value local distributions lead to the small difference of optical density.

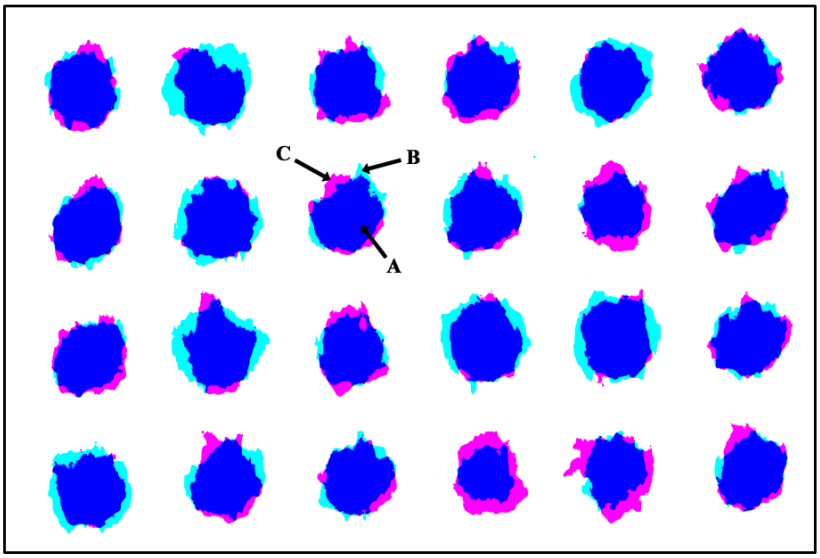

Figure 6.7: Modified XOR result image illustrating the comparison of the thresholded MCI and SMI. (A) In blue similar pixels belonging to the ink region, (B) in cyan the SMI over-thresholded ink pixels, (C) in magenta the under-thresholded ink pixels.

A further investigation of the performance of the SMI generation is performed by comparing the shape descriptor indexes for the thresholded SMI and MCI, Table 6.5. The circularity, qualifying how spherical and smooth the dots are shows a difference of 0.090 for the mean value calculated on 24 dots. This difference is mainly due to the difference in smoothness of the dot edges, as confirmed by the analysis of the convexity. The convexity index shows a difference between the two images of 0.092. This difference shows that the roughness of the dots of the thresholded MCI and SMI are different. The solidity describes the degree to which the area is closed. The solidity obtained is similar for the two images with 0.893 +/- 0.028 for the thresholded MCI and 0.903 +/- 0.021 for the thresholded SMI. The aspect ratio and orientation give similar results for the two images with an aspect ratio of 0.889 +/- 0.075 and an orientation of °140 +/- 23.4° for the thresholded MCI and 0.907 +/- 0.075 and 133° +/- 29.5° for the thresholded SMI. It can be concluded that the SMI is highly similar to the MCI at a threshold value of 100/255. The spatial evaluation relies on the threshold value chosen. Coupling spatial and frequency analysis is then extremely interesting to test the performance of the SMI generation.

Table 6.5: Circularity, convexity, solidity and aspect ratio average of 24 dots of the thresholded MCI and SMI.

	MCI (1 image)	**SMI (1 image)**
Dots analyzed	24	24
Circularity	0.542 +/- 0.031	0.632 +/- 0.041
Convexity	0.630 +/- 0.025	0.722 +/- 0.040
Solidity	0.893 +/- 0.028	0.903 +/- 0.021
Aspect ratio	0.889 +/- 0.075	0.907 +/- 0.075
Orientation	140° +/- 23.4°	133° +/- 29.5°

Coupled spatial and frequency analysis gives access to the binary fidelity ratio as a function of the threshold value. The results are shown in Figure 6.8. The FD_b is higher than 80% for all threshold values. For threshold values higher than 210, the FD_b reaches 100%. There is then no difference between the MCI and SMI, since the thresholded ink region covers the total surface of the image. These threshold results are however not in the range of interest since it does not represent a separation of the ink and the paper. Two peaks of FD_b can be seen when respectively increasing the threshold values on the left of the graph and decreasing the threshold values on the right of the graph. These peaks are associated to local minima and correspond to large differences between the two images (at threshold value 190 for example). These peaks are generated by a small difference of the pixel value distribution in the ink dot regions and in the mixed regions. With differences in the morphology of the inked dots between the different generations of the SMI, small differences appear and thus the standard deviation of the FD_b rises between the threshold values 60/255 to 150/255. Between these threshold values, the ink and paper regions are separated correctly (at threshold values 60, 100 and 150 for example). The purpose of the coupled spatial frequency analysis is not to define the best threshold value separating the ink and the paper but is, however, to determine if the MCI and SMI behave similarly depending on the threshold value. In the 50 to 150 threshold range the maximum similarity is found around threshold level 100. The ink coverages measured on the MCI and SMI are the closest for that threshold value. Small differences of ink coverages of respectively +2.54% and 2.83% are recorded at threshold levels of 60 and 150. These differences generate a local drop of the FD_b from 93.3% to 89.4% and 88.2% respectively. From the couple analysis it can be concluded that the MCI and SMI images are extremely similar. Small differences of pixel value spatial and frequency distribution appear; nevertheless it should not impact the performance of the threshold algorithm evaluation. From this coupled spatial frequency analysis the main difficulty of the threshold processing is well illustrated in between the threshold values of 50 and 150, the ink coverage increases continuously without significant variation: the valley corresponds to the mixed region between ink and paper. When increasing the threshold value from 50 to 150, less and less inked regions are thresholded as paper and more and more mixed region are thresholded as inked region. The correct threshold value

should effectively find the limit where the ink region is totally thresholded as ink and the mixed region is accurately separated into ink and paper regions. Since the mixed region position and shape depend on the ink dot morphology, a correct separation is difficult to conduct. An evaluation of the performances of threshold algorithms with multiple dot morphologies is then required. Finally the grayscale fidelity ratio is computed in order to assess rapidly the similarity between the SMI and the MCI. The FD_g obtained reaches 92.81% of similarity. The FD_g gives then results similar to the coupled frequency-spatial analysis, especially for thresholds in between the pixel values 50 and 150.

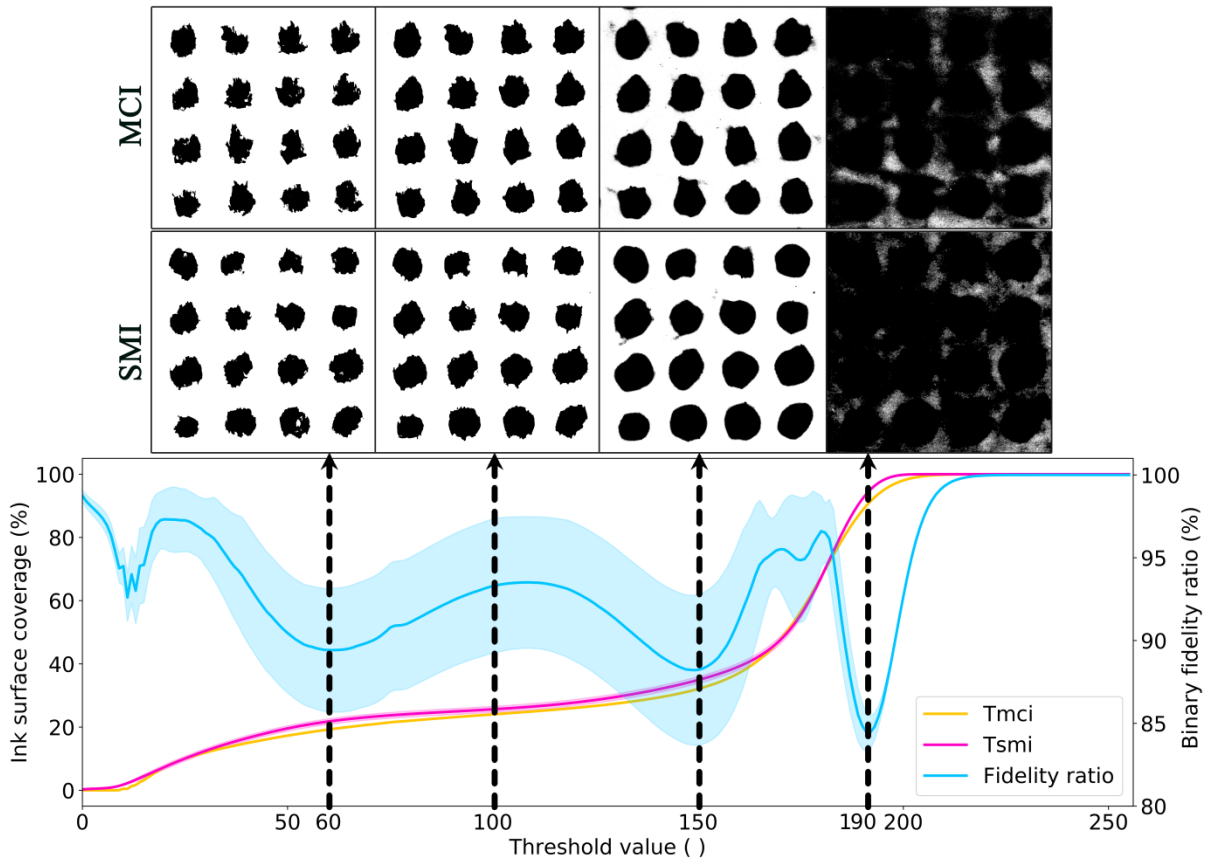

Figure 6.8: Binary fidelity ratio, ink coverage of T_{MCI} and T_{SMI} as a function of the threshold values. 150 lpi AM halftone of 15% nominal ink coverage printed with offset on Glossy 1.

6.1.3.2 Thresholding methods evaluation

The performance of the SMI generation from thresholded MCI is analyzed with the FD_g, Figure 6.9. An accurate average FD_g of 96.06% +/- 2.82% is obtained. Electrophotography, inkjet and offset demonstrate almost equivalent performances with respectively 97.05% +/- 2.19%, 95.03% +/- 3.98% and 94.92% +/- 2.89%. Amplitude modulated halftoning and frequency modulated halftoning are associated with similar mean performances with respectively 95.56% +/- 3.17% and 96.01% +/- 3.01. A dependency of the performance of the generation can be observed as a function of ink coverage. The best performance tends to be achieved for low and high ink coverages. The solid ink patches are better simulated with a mean FD_g of 98.94% +/- 2.58%. The bare paper has intrinsic variations, with an intrinsic FD_g of 97.39% +/- 0.24%. This corresponds to the level reached for the SMI generation for small ink coverages. The performances were lowest for ink coverages around 50%. The optical dot gain is also known to be maximal at that ink coverage. The fidelity ratio remains nevertheless high at 50% ink coverage with a 94.52% +/- 1.72% FD_g average between 45% and 55% of ink coverage. A series of lower performances can be observed around 60% ink coverage and are caused by the offset prints. The thresholded offset MCI present heterogeneous ink regions that produce large mixed regions on the SMI, Figure 6.9.

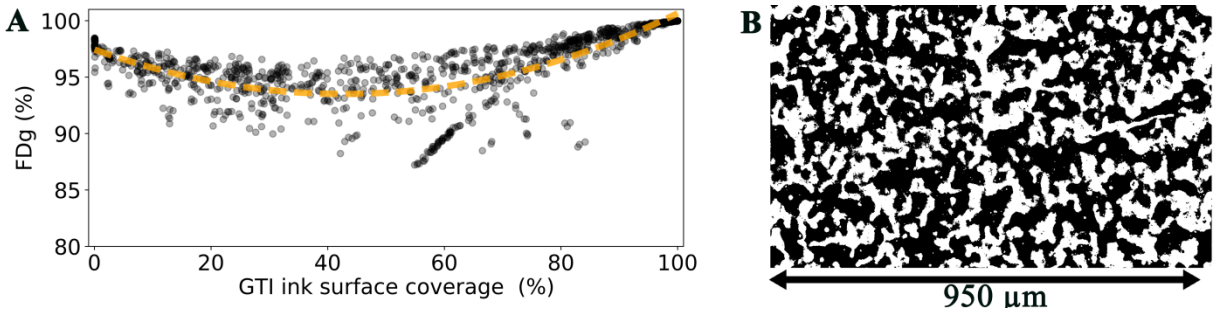

Figure 6.9: (A) Grayscale fidelity ratio as a function of the ink coverage for the 1320 SMI generated from thresholded MCI (orange line: mean tendency). (B) GTI offset AM 200 lpi 80% nominal ink coverage.

The evaluation of the threshold algorithms was performed on the 3920 SMI generated. The evaluation considering all generated SMI presents a large dispersion as the performance of a threshold algorithms depend on the print process, the solid ink reflectance, the paper, the halftone type, the print resolution, the halftone resolution, the ink homogeneity, etc. Nevertheless, the aim of this study is to evaluate the threshold algorithms for all types of prints. A global evaluation is then relevant to discard algorithms that would present poor performances on particular print conditions. The binary fidelity ratio as a function of the ink coverage allows a quick assessment of the thresholds performances, Figure 6.10. The mean FD_b and mean ink coverage differences are also computed to evaluate the threshold algorithms performances, Table 6.6. Based on the mean FD_b obtained, the graphs of Figure 6.10 were classified in three categories (according to the mean binary fidelity ratio in the 10-90% ink coverage range) : threshold algorithms with FD_b superior to 90%, threshold algorithms with FD_b in between 70% and 90% and threshold algorithms with FD_b inferior to 70%. Globally, the best suited threshold algorithms represented in green are the Li, PalBhandari, Huang, Minimum, SimpsonGobat, Otsu, IsoData, Intermodes and Phansalkar algorithms. These algorithms present a limited dependency on the ink coverage. On another hand, the threshold algorithms represented in orange and red present either a dependency to the ink coverage or a large global dispersion of the results. Threshold algorithms such as Mean, Median, Percentile, MaxEntropy, RenyiEntropy, Yen, PalDasgupta, Local mean, Local median, Contrast and Niblack present a large dependency of the algorithms performances on the ink coverage. It is observed that for these threshold algorithms the performances increase systematically with the ink coverage. Threshold algorithms such as the MinError, Triangle, Rosenfeld, Whatmough and Moments are associated with only a small dependency on the ink coverage. However, these algorithms present either a large performance dispersion or a large performance decrease for small ink coverages. Finally, the Shanbhag, Abutaleb, Brink, Bernsen and Sauvola threshold algorithms are associated with largely dispersed results (fuzzy results) that show the non-match between the threshold algorithm and images of printed halftones. It is interesting to notice that the performances of the threshold algorithms are not associated with the algorithms classification proposed by Sezgin. Threshold algorithms performing the best are classified in categories such as: cluster, shape, entropy, attribute and local.

The mean absolute ink coverage differences (ICD) between the GTI and the SMI follow the binary fidelity ratio tendencies. For the best performing threshold algorithms, the mean ICD reaches 1.78% for Li, 7.81% for PalBhandari, 2.22% for Huang, 2.87% for Minimum, 2.57% for SimpsonGobat, 1.84% for Otsu, 3.24% for Isodata, 3.30% for Intermodes and 2.44% for Phansalkar. Low ink coverages and high ink coverages are the most difficult ink coverages to threshold as shown by the increase of performances when computing the average for the ink coverages between 10% and 90%. Increased performances of 0.90% for Li, 0.88% for PalBhandari, 1.46% for Huang, 1.95% for Minimum, 1.99% for SimpsonGobat, 2.27% for Isodata and 2.59% for Intermodes are then observed. This is caused by the increase of differentiation of the bimodal distribution. The Otsu algorithm does not follow this tendency for large ink coverages with high performances for Otsu with a mean ICD of 0.48% for ink coverages superior to 90%. Similarly, the PalBhandari threshold algorithm performs

well for small ink coverages with a mean absolute ICD of 0.72% for ink coverages inferior to 10%. On another hand, the PalBhandari threshold algorithm miss-performs for small ink coverages with a mean ICD of 52.48% for ink coverages inferior to 10%. Similarly the Minimum, IsoData and Intermodes threshold algorithms miss-perform especially for large ink coverages with a mean ICD of respectively 10.75%, 12.00% and 10.55% for ink coverages superior to 90%. It is interesting to note that these three algorithms belong to the same thresholding classification category: shape. Globally the best threshold algorithm is the Li cross entropy algorithm with a mean ICD of 1.78% +/- 6.64% and a mean ICD in between 10% and 90% of ink coverage of 0.90% +/- 0.98%. The IsoData threshold algorithm based on the clustering of the histogram perform the best for ink coverages inferior to 10% with a mean ICD of 0.31% +/- 0.26%. The Otsu threshold algorithm also based on the clustering of the histogram performs the best for ink coverages superior to 90% with a mean ICD of 0.48% +/- 0.67%. It has to be noted that the SMI generated with ink coverages inferior to 10% represented 13.5% of the total amount of the SMI generated and the SMI generated with ink coverages superior to 90% represented 12.8%.

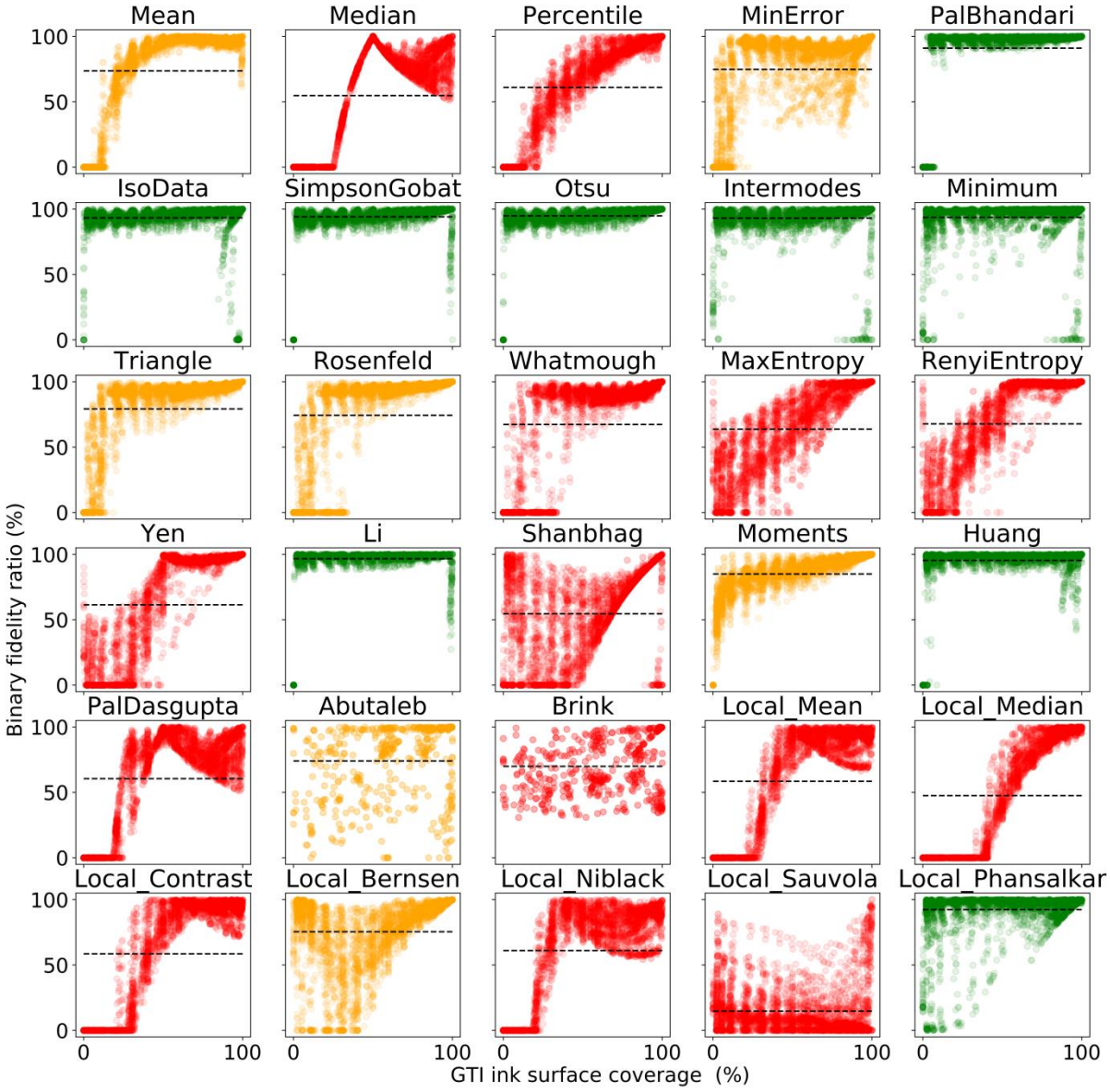

Figure 6.10: Binary fidelity ratio as a function of the ink coverage of the ground truth for the 3920 SMI generated. Black dashed line represents the binary fidelity ratio average over all ink coverages.

Table 6.6: Mean binary fidelity ratio and mean absolute ink coverage difference for the 3920 SMI generated. The greenest and the bluest results are associated with the best performances.

	Mean binary fidelity ratio (%)				Mean absolute ink coverage difference (%)			
Ground truth ink coverage	[0-100%]		[10-90%]		[10-90%]		[<10%]	[>90%]
Li	96.68	+/- 10.45	98.12	+/- 1.96	0.90	+/- 0.98	3.65	4.89
PalBhandari	91.06	+/- 25.64	98.12	+/- 2.02	0.88	+/- 0.94	52.48	0.54
Huang	95.35	+/- 12.72	97.29	+/- 3.48	1.46	+/- 2.68	4.44	4.26
Minimum	93.59	+/- 15.77	96.16	+/- 7.79	1.95	+/- 5.60	0.44	10.75
SimpsonGobat	94.07	+/- 10.79	95.35	+/- 3.67	1.99	+/- 1.69	3.35	5.08
Otsu	94.82	+/- 8.89	95.33	+/- 3.65	2.01	+/- 1.71	2.16	0.48
IsoData	93.34	+/- 12.68	95.11	+/- 4.74	2.27	+/- 3.40	0.31	12.00
Intermodes	93.04	+/- 13.83	94.60	+/- 7.24	2.59	+/- 5.34	0.31	10.55
Phansalkar	92.33	+/- 16.67	93.97	+/- 12.52	2.80	+/- 4.63	0.72	2.16
Triangle	79.23	+/- 30.56	87.97	+/- 15.95	4.32	+/- 2.92	4.57	2.01
Moments	85.05	+/- 15.62	87.72	+/- 8.69	4.80	+/- 2.59	1.82	0.95
Mean	73.67	+/- 36.91	83.45	+/- 25.99	3.97	+/- 3.57	22.18	4.71
Rosenfeld	74.33	+/- 36.93	81.73	+/- 29.55	7.18	+/- 12.03	15.89	1.28
MinError	74.77	+/- 30.16	81.55	+/- 20.10	9.00	+/- 10.05	4.07	5.02
Abutaleb	74.03	+/- 28.76	74.00	+/- 26.92	23.68	+/- 18.11	52.31	19.55
Whatmough	67.31	+/- 39.42	73.97	+/- 33.57	12.26	+/- 15.72	36.39	2.94
RenyiEntropy	67.69	+/- 36.75	72.40	+/- 31.68	7.68	+/- 7.40	5.17	1.00
Bernsen	75.48	+/- 26.42	70.09	+/- 26.77	12.75	+/- 10.40	0.70	1.92
Niblack	61.03	+/- 36.71	67.83	+/- 31.09	13.00	+/- 8.82	35.13	12.96
Brink	69.88	+/- 20.87	67.74	+/- 18.01	30.09	+/- 20.79	57.33	19.50
PalDasgupta	60.58	+/- 36.52	67.62	+/- 31.01	13.86	+/- 9.96	46.87	15.21
Percentile	61.05	+/- 36.58	65.94	+/- 29.60	11.37	+/- 5.32	14.01	2.33
MaxEntropy	63.73	+/- 33.14	65.79	+/- 28.76	11.91	+/- 8.44	3.98	1.13
Yen	61.40	+/- 40.98	64.48	+/- 38.52	11.19	+/- 10.68	6.01	1.20
Mean (local)	58.52	+/- 40.67	63.66	+/- 37.36	14.26	+/- 11.72	45.49	8.76
Contrast	58.58	+/- 42.09	63.46	+/- 39.28	14.54	+/- 13.93	52.05	7.23
Median	54.74	+/- 37.78	59.68	+/- 34.38	18.10	+/- 11.40	49.48	15.04
Shanbhag	54.54	+/- 33.46	50.19	+/- 30.28	21.99	+/- 11.17	6.03	17.20
Median (local)	47.57	+/- 42.65	47.61	+/- 40.19	27.13	+/- 19.58	65.54	2.04
Sauvola	14.72	+/- 19.48	10.97	+/- 13.94	46.85	+/- 24.23	3.35	67.03

The best six threshold algorithms based on the mean absolute FD_b between the ink coverage of 10 and 90% (Li, PalBhandari, Huang, Minimum, SimpsonGobat and Otsu algorithms) are selected to conduct a further analysis of the threshold performance dependencies, Figure 6.11. The dependency on the ink coverage can already be observed on Figure 6.10, nevertheless a better sensitivity is achieved on Figure 6.11. The SMI only generated from thresholded MCI are considered for this analysis in order to remove extreme conditions. It can be observed that the SimpsonGobat and Otsu algorithms perform similarly with a large dependency on the ink coverage. It is interesting to note that the optical dot gain is also dependent on the ink coverage and follows a similar theoretical bell-shaped curve. Thus, both thresholds algorithms appear to be sensitive to optical dot gain, over thresholding the ink in the mixed regions. Between the ink coverages of 45% and 55%, the SimpsonGobat reaches a mean ICD of 3.09% +/- 1.28% and the Otsu reaches 3.10% +/- 1.30%. Both algorithms belong to the cluster class. The Minimum and Huang threshold algorithms have an inversed bell shape. The Minimum algorithm under thresholds the ink below 50% ink coverage and over thresholds above 50% with a large dispersion for large ink coverages. The Huang algorithm first over thresholds the ink below 50% ink coverage and then under thresholds the ink above 50%. A large dispersion is also observed for the Huang algorithm above 50% ink coverage. It has to be noted that the classification of both algorithms differs, with the Minimum belonging to the shape class and the Huang belonging to the attribute class. Nevertheless with the exception of the extreme ink coverages, the dependency of both algorithms with

the ink coverage is limited. Both algorithms present a high performance between ink coverages of 45% and 55% with for the Minimum algorithm a mean ICD of 1.27% +/- 2.76% and for the Huang 0.79% +/- 0.68%. The PalBhandari and Li threshold algorithms are associated with a linear ICD shape. Below 50% ink coverage both algorithms perform very well with a small tendency to under threshold the ink region. This tendency is conserved for ink coverages above 50% and is associated with a larger dispersion of the ICD. These two algorithms globally under threshold the ink for all ink coverages which reduces the errors induced when measuring grayscale patches over the whole ink coverage range. A high performance between ink coverages of 45% and 55% is reached for the PalBhandari algorithm a mean ICD of 0.80% +/- 0.87% and for the Li 0.63% +/- 0.47%. It is interesting to note that although both algorithms have similar performances, they belong to different classes: cluster for the PalBhandari algorithm and entropy for the Li algorithm. It has to be noted that the results presented differ from Table 6.6 since only the SMI from thresholded MCI are considered. It can be concluded that for SMI obtained from thresholded MCI, the PalBhandari and Li threshold algorithms perform the best with mean absolute ICD of 0.76% +/- 0.75% and 0.76% +/- 0.71%. The global standard deviation expected when thresholding halftone is then inferior to +/- 1.51% when measuring with these two threshold algorithms in the ink coverage range from 10% to 90%.

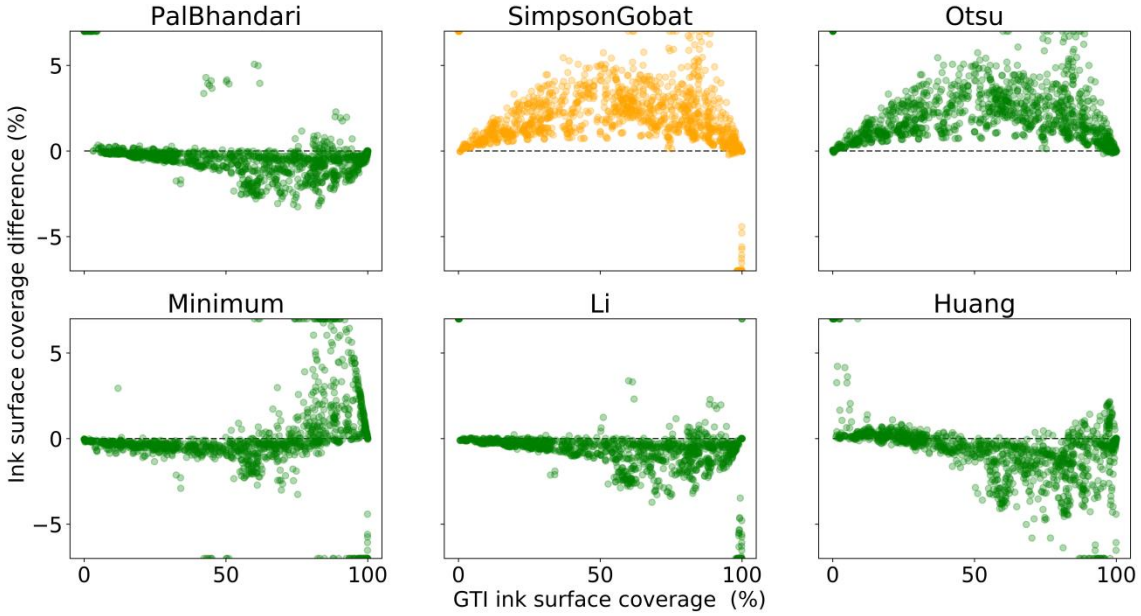

Figure 6.11: Ink coverage difference as a function of the ground truth ink coverage for the 6 selected threshold algorithms and the 1320 SMI generated from thresholded MCI. Ink coverage differences larger and smaller than 7% and -7% are represented at these limits.

An extended analysis of the performances of PalBhandari and Li threshold algorithms is performed as a function of the discretization level. For processing time reasons the threshold algorithms were computed with 8 bits histograms associated with 255 different discretized ink reflectance levels. The source images are based comparatively on a minimum of 14 bits (depending on the high dynamic range) associated with 16384 discretized ink reflectance levels. Results show that most differences between the two levels of discretization were found for small and large ink coverages. 5 over 9 images are not correctly thresholded with the PalBhandari threshold algorithm for ink coverages smaller than 10% with 8 bits discretization and none are found with 14 bits discretization. A FD_b of 98.1% +/- 1.3% is reached for these small ink coverages when processed on 14 bits. Similarly for the Li threshold algorithm, 4 over 13 images are not correctly thresholded for ink coverages larger than 90% with 8 bits discretization and none are found with 14 bits discretization. A FD_b of 99.3% +/- 0.5% is reached for the a 14 bit discretization. Apart from the small and large ink coverages, almost no differences are observed between the two levels of discretization: for the PalBhandari a mean absolute ICD of 0.60% +/- 0.63% on bits compared to 0.67% +/- 0.70% on 14

bits, for the Li, 0.61% +/- 0.66% for 8 bits and 0.67% +/- 0.70% for 14 bits. For both threshold algorithms, the increase of discretization reduces the mean performances and increases the standard deviations. Noise in the histogram, less smoothened by a larger discretization causes this decrease. Moreover, the average of the differences of the ICD for the two levels of discretization reached 0.12% +/- 0.09% for the PalBhandari threshold algorithm and 0.07% +/- 0.08% for the Li threshold algorithm. These differences are small compared to the level of performances of both algorithms and thus, it can be concluded that an 8 bits discretization does not influence significantly the threshold performances excepting for small and large ink coverages.

A qualitative synthesis of the performances evaluation of the 6 selected threshold algorithms is performed, Table 6.7. It can be concluded that the PalBhandari and the Li are the threshold algorithms that are most suited for halftone images processing. The Huang algorithm should also be cited as it performs averagely in all categories considered. The Otsu algorithm can be interesting to measure small and large ink coverages, however the dependency with the ink coverage can reduce the measurement accuracy on medium ink coverages. Finally, the SimpsonGobat and Minimum algorithms are associated with the lowest performances of the 6 selected threshold algorithms.

Table 6.7: Synthesis of the performances evaluation of the 6 selected threshold algorithms. +: high performance, o: average performance, -: low performance.

	10-90%	<10%	>90%	Independent of ink coverage
PalBhandari	+	-	+	+
SimpsonGobat	-	+	-	-
Otsu	-	+	+	-
Minimum	-	+	-	o
Li	+	+	-	+
Huang	o	o	o	o

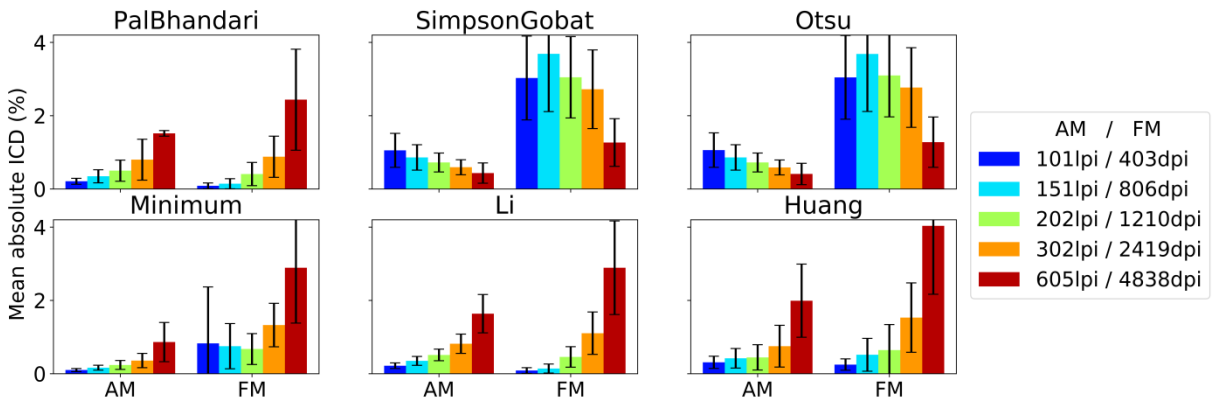

Figure 6.12: Mean absolute ink coverage difference as a function of the halftone type and dot size (SMI solid ink optical density of 2.52, paper PSF of 105 µm+21 µm).

The performances of the 6 selected threshold algorithms are then investigated as a function of the halftone resolution and the halftone type (AM or FM), Figure 6.12. It has to be noted that the halftones inferior to 10% and superior to 90% ink coverage were discarded from the mean ICD measurement to remove a source of noise. Two different global behaviors of the threshold algorithms can be observed: an increase of the mean ICD with the decrease of the dot size for the PalBhandari, Minimum, Li and Huang threshold algorithms and a decrease of the mean ICD with the decrease of the dot size for the SimpsonGobat and the Otsu algorithms. These tendencies have to be considered carefully as the standard deviations associated are large. For the SimpsonGobat, Otsu and Minimum threshold algorithms the obtained mean absolute ICD are larger for FM halftones than for AM halftones, with respectively 2.75% and 0.73% for the SimpsonGobat, 2.77% and 0.73% for the Otsu

and 1.29% and 0.34% for the Minimum. For the PalBhandari, Minimum, Li and Huang threshold algorithms the rate of mean ICD increase as a function of the dot size is almost linear with coefficient of determination of linear regression of respectively 0.9969, 0.9964, 0.9992, 0.9752 for the AM halftones and 0.9862, 0.9357, 0.9907 and 0.9842 for the FM halftones. This linearity is interesting and is related to the global amount of optical dot gain. The dot sizes classically used in the printing industry are mostly equal or inferior to 200 lpi for AM halftones and inferior to 1200 dpi for FM halftones. Below 202 lpi the PalBhandari, Minimum, Li and Huang threshold algorithms are associated with an error below +/- 0.50% demonstrating a high performance. Similar tendencies are observed for SMI with smaller solid ink optical densities and for SMI with smaller and larger paper point spread function (PSF).

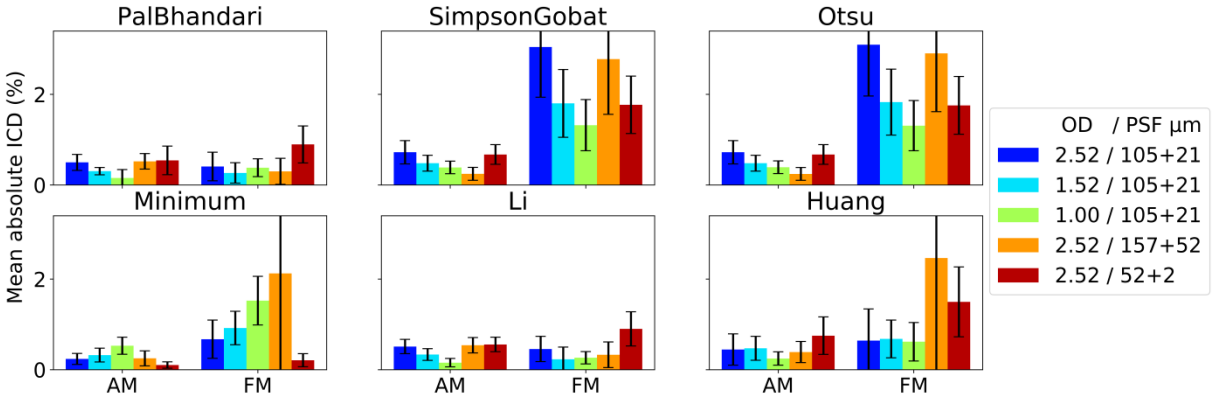

Figure 6.13: Mean absolute ink coverage difference as a function of the halftone type, optical density and simulated paper PSF. (Halftone size of 202 lpi for AM and 1210 dpi for FM).

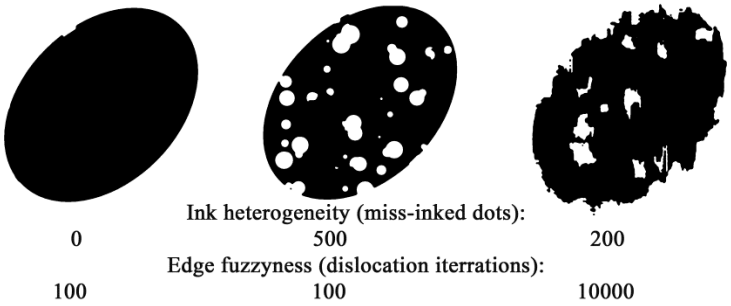

Figure 6.14: Example of 3 halftone dots with different levels of ink heterogeneities and edges fuzziness. AM 101 lpi 40% ink coverage, 0.7 aspect ratio and 45° rotation halftone.

The dependency on the optical density of the solid ink as well as on the simulated paper PSF was analyzed for the 6 selected threshold algorithms, Figure 6.13. The variations observed when decreasing the solid ink optical density are small for the AM halftones. For FM halftones the variations are more pronounced, especially for the SimpsonGobat algorithm, the Otsu and the Minimum algorithms. Although small, the decrease of solid ink optical density tends to increase the performances of the PalBhandari, SimpsonGobat, Otsu and Li algorithms for AM halftones. For FM halftones only the performances of the SimpsonGobat and Otsu are increased. The minimum threshold algorithm behaves in an opposed direction, with a decrease of the performances with the decrease of the solid ink optical density. The Huang algorithm seams unaffected by the solid ink optical density decrease. The dependency on the paper PSF is more difficult to establish. The tendency is only marked for the minimum threshold algorithm showing a decrease of the performances with the increase of the PSF size. Other thresholds such as the PalBhandari and Li show a small increase of the performances with the increase of the PSF for the FM halftones only. The dependency on the solid ink optical density and PSF was also analyzed on smaller and larger halftone sizes. It was found that the tendencies observed remained similar.

The heterogeneous inking as well as the dot edge fuzziness have a direct dependency on the dot sizes, since the generation of both defects dimensions are kept constant for all dot sizes. Thus, an analysis for the different dot sizes is required. Three halftones dots with different ink heterogeneity and edge fuzziness are presented in Figure 6.14. It can be observed that an increase of the ink heterogeneity increases the number of un-inked gaps in the ink region of the halftone dot. The edge fuzziness generates non-circular edges and the shapes of the un-inked surface become distorted. Introducing ink heterogeneities and edges fuzziness increase the optical dot gain since lengths of paper-inked interface are increased and since the distances between paper ink and paper regions are decreased. For large halftone size, it can be observed that the introduction of ink heterogeneities strongly decreases the performances of all threshold algorithms for the AM and FM halftones, Figure 6.15. The performances decreases are more marked for the SimpsonGobat, the Otsu and the Minimum algorithms. With the decrease of the halftone size the heterogeneous inking continue to impact the performances of the threshold algorithms. However, the differences are less marked. In some cases the performances of the thresholds algorithms can be increased. These increases of threshold performances may, however, be attributed to the large standard deviation of the mean ICD measurements. It can be concluded that an increase of the ink heterogeneity globally decreases performances of the selected threshold algorithms with a reinforced effect for the large dot sizes. The edge fuzziness also depends on the dot size and a first increase of all thresholds performances are observed for the AM and FM halftones with halftone sizes of 101 lpi and 403 dpi, Figure 6.16. This improvement is more pronounced for the SimpsonGobat, Otsu and Minimum algorithms for the AM halftones and for the Minimum algorithms for FM halftones. When decreasing the halftone size, the performances improvements are reduced and can even be reversed for very small halftone sizes. For very small halftone sizes, dots with regular edges are thresholded with slightly improved performances. The minimum threshold algorithm presents an exception with variating performances.

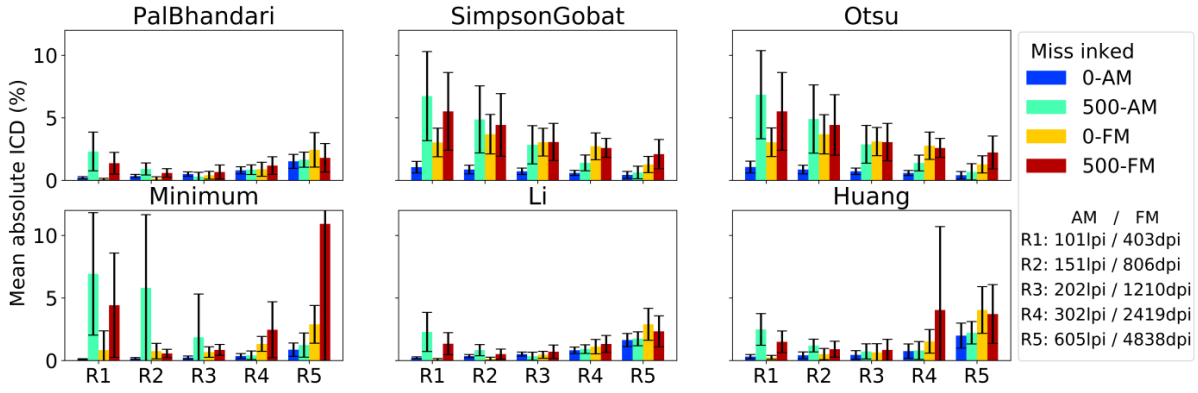

Figure 6.15: Mean absolute ink coverage difference as a function of the halftone type, dot size and ink homogeneity (solid dots or dots with un-inked regions).

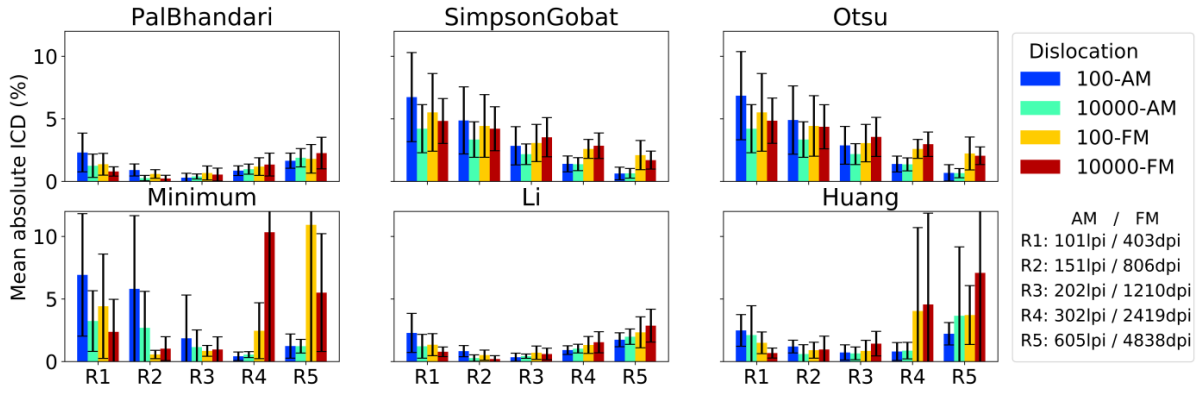

Figure 6.16: Mean absolute ink coverage differences as a function of the halftone type, dot size and dot morphology (sharp circular edges or fuzzy edges). (solid ink optical density of 2.52).

6.1.4 Conclusion

In this work, a method to evaluate objectively the threshold algorithms was presented. The method was specifically designed to evaluate the performances of the threshold algorithms on halftone prints images. The method was based on a generation of ground truth images, obtained either by thresholding halftones images captured on the microscope or by generating synthetically halftone dots configurations and defects. Then, a simulation of the optical dot gain effects and of the microscope distortions was performed to obtain simulated microscope images that have similar characteristics than the images measured on the microscope. The simulated images were then processed by the threshold algorithms and the performances of these threshold algorithms were evaluated by comparing the thresholded images with the ground truth.

An evaluation of the proposed evaluation method was performed. Visual comparison showed that the two images, the MCI and SMI appeared similar. Heterogeneous backgrounds were observed for the simulated and real image, with shadows, fuzzy edges of halftone dots, random background noises and background defects such as dust in the optical path or ink residues on the paper. A frequency analysis showed that the two image histograms were similar with maxima and minima located at the same levels. The SMI showed a distribution less similar to Gaussian distribution. The Pearsons chi square statistic was computed to quantify the similarity between the two histograms and a similarity of 94.3% +/-0.24% was obtained. A spatial analysis was performed after thresholding both images at the same level of 100/255. A binary fidelity ratio based on a modified XOR operation and accounting for over and under thresholded regions was proposed and reached 93.3% for the thresholded SMI and MCI. A large similarity was demonstrated between the two images. The differences were mainly caused by the randomness of the shape of the inked dot generated with the synthetic GTI generation, as demonstrated by the analysis of the shape descriptor indexes. Coupled spatial and frequency analysis finally showed that the generated SMI were stable with a fidelity ratio above 90% for thresholding in the 50/255-150/255 interval range. A grayscale fidelity ratio was also proposed to provide a fast coupled spatial and frequency comparison and reached 92.81%.

Thirty threshold algorithms were evaluated with the 3920 generated SMI. 1320 images were generated based on thresholded microscope captured images and 2600 images were generated based on synthetic generated ground truth images. The 1320 generated images based on the microscope images were found to be extremely similar to the references with a grayscale fidelity ratio of 96.06% +/- 2.82%. A dependency on the ink coverages of the SMI generation performances was observed, with a decrease of the performances toward the 50% ink coverage. Globally, the best suited threshold algorithms with ratios superior to 90%, were the PalBhandari, IsoData, SimpsonGobat, Otsu, Intermodes, Minimum, Li, Huang and Phansalkar algorithms. These algorithms presented a limited dependency to the ink coverage. Threshold algorithms such as the MinError, Triangle, Rosenfeld, Whatmough and Moments were associated with only a small dependency to the ink coverage. However, these algorithms presented either a large performance dispersion or a large performance decrease for small ink coverages. Finally, threshold algorithms such as the Mean, Median, Percentile, MaxEntropy, RenyiEntropy, Yen, PalDasgupta, Local mean, Local median, Contrast and Niblack presented a large dependency of the algorithms performances on the ink coverage and were associated with binary fidelity ratio inferior to 90%.

Over the 3920 images measured the mean ICD reached 1.78% for Li, 7.81% for PalBhandari, 2.22% for Huang, 2.87% for Minimum, 2.57% for SimpsonGobat, 1.84% for Otsu, 3.24% for Isodata, 3.30% for Intermodes and 2.44% for Phansalkar. These results were refined considering only the 1320 ground truth images obtained from the microscope images and restricting the ink surface range to exclude the ink coverage below 10% and above 90%. Within these conditions, the mean ICD were improved to 0.79% for Li, 0.79% for PalBhandari, 1.13% for Huang, 2.04% for Minimum, 2.35% for SimpsonGobat, 2.26% for Isodata, and 1.97% for Phansalkar. The Otsu and Intermodes performance were not increased within these conditions. The two best threshold algorithms obtained are then the Li

and PalBhandari. Considering the standard deviation and averages of the absolute ICD, the thresholding error expected when using these two algorithms to threshold halftones captured on the microscope is inferior to 1.51%.

Finally, the dependencies of the 6 selected threshold algorithms on the dot size, solid ink optical density, paper PSF, ink heterogeneities and edges fuzziness were investigated. It was found that for the Li and PalBhandari threshold algorithms, an increase of the dot size increased the threshold performances and the decrease of the ink solid optical density increased also the threshold performance. The paper PSF did not affect the global performances. The ink heterogeneity increase decreased the performances of the two threshold algorithms and edge fuzziness increase presented first an increase of the threshold performances for the large dot sizes and the tendency was then reversed for the small dot sizes.

This work allowed evaluating and determining the most suited threshold algorithms. The performances obtained were high considering that these threshold algorithms were not developed specifically to threshold halftone dots. Designing a threshold algorithm specifically for halftone dots can help improve the performances of the ink and paper separation for all ink coverages.

6.2 New threshold algorithms developed specifically for halftone dots analysis

6.2.1 Threshold algorithms for halftone dots analysis

More than 100 threshold algorithms were developed and reported by Sezgin [171]. Only four threshold algorithms were found in literature to have been developed specifically for halftone dot processing. Engeldrum and Hsieh proposed a manual thresholding, adjusting manually the threshold value and displaying the thresholded pixels belonging to the ink region in order to match the borders of the halftone dots [35,37]. This technique highly depends on the settings of the display screen and on the experimenter [219]. Moreover this method cannot be automated. Arney and coworkers method is based on scans of the spatial image of halftone dots in multiple directions. The borders of ink dots (transition from ink reflectance to paper reflectance) are detected and the rate of maximum reflectance change in the transition region is recorded. The limit of reflectance is then obtained by averaging the maximum transition rate for multiple ink dots, equation [5,218]. Nyström proposed to extend Arney and Engeldrum approaches to the analysis of the histogram of the image obtained [19,211,220–224]. The author proposed to define the threshold value as the midpoint between the measured R_i and R_p (the local maxima in the paper region and the ink region of the histogram). Nyström algorithm is similar to Prewitt's Intermodes threshold algorithm [371]. However, setting the threshold limit in-between the ink and paper peaks differs from the complete light approximation where the limit between the ink and paper converges toward R_pT_i. Another limitation is for small and large ink coverages where respectively the ink and paper peaks may be difficult to identify on the histogram. Namedanian also proposed to extend Arney's line scanning method by stating that since the histogram is a representation of the gray level occurrence, the steepest slope going from the ink dot to the paper corresponds to the position on the histogram where the occurrence is minimal. The author stated that the benefit of working on the histogram instead of working on the image is that the halftone dot configuration does not impact the measurement [225]. This method is similar to Prewitt's Minimum threshold algorithm [371]. This approach may lead to more accurate results, however, small and large ink coverages may still present peak identification difficulties. Namedanian proposed also a threshold method based on the shape of the histogram of halftone microscale image [226]. Namedanian noticed a rapid drop in the histogram occurrences going from the ink to the paper. This rapid drop occurs after the ink peak maximum and the author suggested that the signification of this drop is the transition from ink to paper. To obtain the

position of this drop the author proposed to compute the first and the second derivative of the histogram and to detect the pixel value where the first derivative has its first minimum and where the second derivative is equal to 0. Noise in the measurement coming from the camera, the microscope or any image treatment (field light flatness, focusing, sampling, white balance, gamma, etc.) may alter the shape of the histogram and can change this drop, reducing the reliability of this threshold algorithm. Multiple authors have proposed to use threshold algorithms from literature to separate inked areas from paper areas. Nguyen proposed to use the maximum entropy threshold developed by Kapur [27,163]. Poletti proposed to use the factorization method developed by Otsu [25,63,168].

Therefore two new threshold methods specifically developed for halftone dots analysis are proposed in this work. The first method is based on an analysis of the ink peak shifting on the histogram developed in chapter 4. This peak shifting was first studied by Arney and was proven to be directly related to the specificities of the halftone (ink dot morphology and size, halftoning method, light scattering in the paper, etc.). The second threshold method proposed relies on the pseudo deconvolution strategy developed in chapter 5. The threshold algorithm applies local modifications of the halftone image in order to remove the mixed area generated by optical dot gain. The threshold of the halftone image without mixed area becomes straightforward. The two threshold algorithm developed will be first presented and evaluated using the threshold evaluation method developed. Then, in a second part, the benefit from an accurate separation of the optical and the physical dot gain will be explored by studying parameters influencing the dot gain.

6.2.2 Materials and methods

6.2.2.1 LveShape threshold algorithm

The first threshold algorithm proposed relies on Arney's observations that the ink and paper reflectances are not constant but depend on the ink coverage [5,218]. The ink reflectances are shifted toward larger values as the ink coverage decreases. The paper is shifted toward smaller reflectance values as the ink coverage increases. This phenomenon can be observed on the histogram of halftone images with different ink coverages, Figure 6.17. Researchers have linked this phenomenon to the interactions between ink, light and paper. The light diffusion and scattering into paper causes photons incident over a paper region to be scattered and reflected back under an inked region causing then an increase of the ink reflectance and a decrease of the paper reflectance. The amount of light trapping depends on multiple parameters and especially on the ink and paper regions morphologies and sizes. This induces a dependency with the ink coverage. For small ink coverages, the ink peak is strongly shifted toward larger reflectance values and the paper is only slightly shifted toward smaller reflectance values. On the opposite, for large ink coverages, the ink peak is only slightly shifted toward large reflectance values and the paper peak is strongly shifted toward smaller reflectances value. These ink and paper reflectances shifts are the principle cause of the difficulty to separate the ink from the paper. Thresholding the halftone image at a constant value cannot gives satisfying results since the ink and paper shift will induce an offset of the threshold value. Automatic threshold algorithms should dynamically adapt to this shift, however the threshold strategies deployed in literature were not developed specifically for halftone prints. Thus, a threshold algorithm based on the shift of the ink peak is proposed. It has to be noted that in the case of solid ink and of bare paper the light diffuses into paper however no light trapping can occur since the print surface is homogeneous. The reflectance for the solid ink print can be written:

$$R_{is} = T_i \, R_{ps} \, T_i \qquad [6.7]$$

with $T_i(\lambda)$ the ink transmittance and $R_{ps}(\lambda)$ the bare paper reflectance. This equation can be rewritten to express the ink transmittance (spectral dependency omitted):

$$T_i = \sqrt{\frac{R_{is}}{R_{ps}}} \qquad [6.8]$$

The model of the light diffusion introduced by introduced by Callahan, Yule and Lehmbeck [8–16] is given in equation [6.1]. When considering an infinite point spread function the convolution of the point spread function with the ink transmittance becomes equal to 1 (spectral dependency omitted):

$$[T_i(x,y) \circledast H(x,y)] = 1 \qquad [6.9]$$

This uncover a limit with the halftone reflectance equal to :

$$R_a(x,y) = R_{ps}(x,y)\, T_i(x,y) \qquad [6.10]$$

Thus the ink reflectance cannot be larger than this limit and the paper reflectance cannot be smaller than this limit. With the paper reflectance normalized to 1, the limit of the ink and paper shift becomes equal to T_i. However, this limit cannot be used as a threshold value. On Figure 6.17 for example, the mean ink reflectance of the solid ink patch is measured at a reflectance 3.05×10^{-3}. The theoretical ink reflectance limit is then set at the value of the ink transmittance of 5.52×10^{-2}. The ink peak for the ink coverage of 10.3% is observed at a reflectance 1.25×10^{-1} which is greater than T_i. A variation of the ink thickness deposited for small ink coverages as well as more complex ink, paper and light interactions are responsible for the divergences of measurements and model.

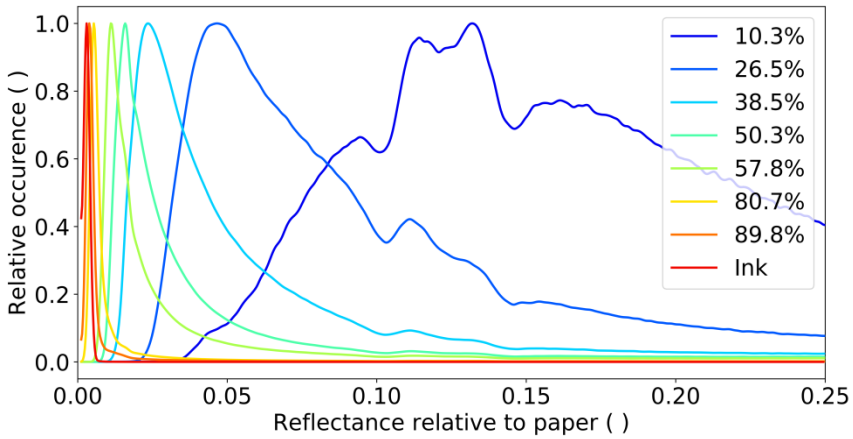

Figure 6.17: Normalized histograms in the reflectance range of 0 to 0.25 of 150 lpi amplitude modulated halftones printed with electrophotography for different ink coverages.

The threshold algorithm strategy proposed relies then on the measurement of the ink reflectance peak on the histogram for the solid ink image and for a corresponding halftone image. The center of the ink peak can be seen as the average of the reflectance distribution over the inked region. Ink reflectance distributions are assumed to follow Gaussian distributions. The center of each ink peak is then obtained by a fitting of the ink reflectance distribution with a Gaussian function. The fitting is performed following the methodology developed in chapter 4. The method is based on a double optimization of two parameters of the Gaussian function: the width of the Gaussian σ and the position of the center of the Gaussian μ. The third parameter of the Gaussian function is fixed: the height of the Gaussian γ is set to be equal to the height of the histogram distribution at a given reflectance. The optimization of the width of the Gaussian σ works through a minimization of the average of the absolute differences between the Gaussian curve and the histogram distribution. The optimization of the position of the center of the Gaussian μ works through the maximization of 3 criteria: the fitted Gaussian function should be closest to the histogram distribution, the width of the Gaussian function should be as small as possible and the height of the Gaussian should be as high as possible. The

Gaussian fitting requires computing first the histogram of the image. The image is smoothened with a Gaussian kernel of size 3. The histogram of the image is then computed with Numpy 1.14.3 function and Python 3.5. To combine accuracy and speed of the Gaussian fitting, the histogram is computed on 15000 bins in the range of reflectances from 0 to 1.5. This gives an effective quantization on 13.88 bits matching the minimum discretization of the source image corresponding to 14 bits. The most critical fitting is for large ink coverages associated with small ink reflectance peak. For electrophotography for example (solid ink reflectance of 0.003) an error of +/- 1 bin corresponds to a relative reflectance error of +/- 3.3%. With the shift of the ink peak to larger reflectance values this relative reflectance measurement error is reduced. For example at an ink reflectance of 0.055 the relative error is reduced to +/- 0.2%. Conversely to the Gaussian fit developed in chapter 4 only the ink peak Gaussian fitting is required. Thus the histogram does not need to be split into two sub histograms and a simple upper bound is specified. This upper bound is set at ¼ of the histogram length after having removed the bins without occurrences.

The Gaussian fitting is then performed for the solid ink image and for a halftone image. The corresponding ink reflectance peak positions are obtained and denoted R_{is} for the solid ink image and R_i for the halftone image. A ratio called the M factor is computed :

$$M = \frac{R_i}{R_{is}} \qquad [6.11]$$

The M factor describes the amount of shift present on the halftone compared to the solid ink. The threshold value used to threshold the solid ink patches is denoted K_{is}. The threshold value for the halftone print denoted K_I can then be computed as:

$$K_i = K_{is}\, M \qquad [6.12]$$

Similarly it was found that by dividing the reflectance values of the halftone image by the M factor, the distribution of the ink reflectances were compressed and shifted to lower reflectance values and superposed with the ink distribution of the solid ink image. An example of this shift and compression obtained from the measured M factor is presented for electrophotography, offset and inkjet in Figure 6.18. It can be observed that when the paper diffuses the light, the interactions with the ink generate a shift and a spread of the ink peak. The position of the ink peak of the electrophotography is found at a reflectance of 0.0264 for the effective 42.04% ink coverage amplitude modulated 150 lpi halftone. The solid ink reflectance peak is measured at 0.0031. The M factor is computed and found at 8.53. The threshold set for the solid ink at the reflectance value of 0.0342 is then shifted to the reflectance value of 0.2920. It can be observed that the computed threshold value is correctly placed in-between the ink and paper peaks. Dividing the halftone image by the M factor aligns the solid ink and halftone ink peaks. Moreover the halftone ink peak reflectance distribution spreading is reduced and can be observed closer to the solid ink reflectance distribution, Figure 6.18. The fitted Gaussian width of the halftone is then decreased from 0.00512 to 0.00060 and can be compared to the fitted Gaussian width of the solid ink peak of 0.00024. For the inkjet halftone of effective ink coverage of 23.54% a similar shift and compression is obtained with a measured ink peak reflectance at 0.1113 and at 0.0067 for the solid ink. With a M factor of 16.71, fitted Gaussian width is decreased from 0.02107 to 0.00126 and can be compared to the fitted Gaussian width of the solid ink peak of 0.00087. The threshold value is obtained ideally in between the ink and paper peaks. For the offset print, the solid ink patch has a heterogeneous ink surface with multiple mis-inked regions. This generates a slight shift of the solid ink peak and a spread of the solid ink distribution. This effect can be accounted for by adjusting the threshold value for the solid ink. The halftone of 23.54% effective ink coverage has an ink peak reflectance at 0.0248 and a solid ink at 0.0043 giving a M factor of 5.75. The fitted Gaussian width is decreased from 0.00425 to 0.00074 and can be compared to the fitted Gaussian width of the solid ink peak of 0.00041.

The strategy of the threshold algorithm proposed is to assess the ink peak based on the histogram of the reflectance distribution of the halftone print. The threshold algorithm can be then classified in the shape category and is named LveShape. Moreover it is interesting to notice that with the reflectance of the bare paper normalized to 1 and the theoretical upper limit for the ink reflectance and lower limit for the paper reflectances set at T_i, the ratio of T_i divided by R_{is} is equal to the ratio of R_{ps} divided by T_i:

$$\frac{T_i}{R_{is}} = \frac{R_{ps}}{T_i} \qquad [6.13]$$

The equality of these two ratios is essential. By considering that the solid ink threshold K_{is} is always placed between R_{is} and T_i and considering that the ink reflectance of the halftone are found between R_{is} and T_i, the maximum value of the computed threshold K_i is equal to 1. Indeed with the ink peak obtained at $R_i = T_i$ and the solid ink threshold at $K_{is} = T_i$:

$$K_i = T_i \frac{T_i}{R_p T_i^2} = 1 \qquad [6.14]$$

The minimum threshold is then obtained at $K_i = R_i$.

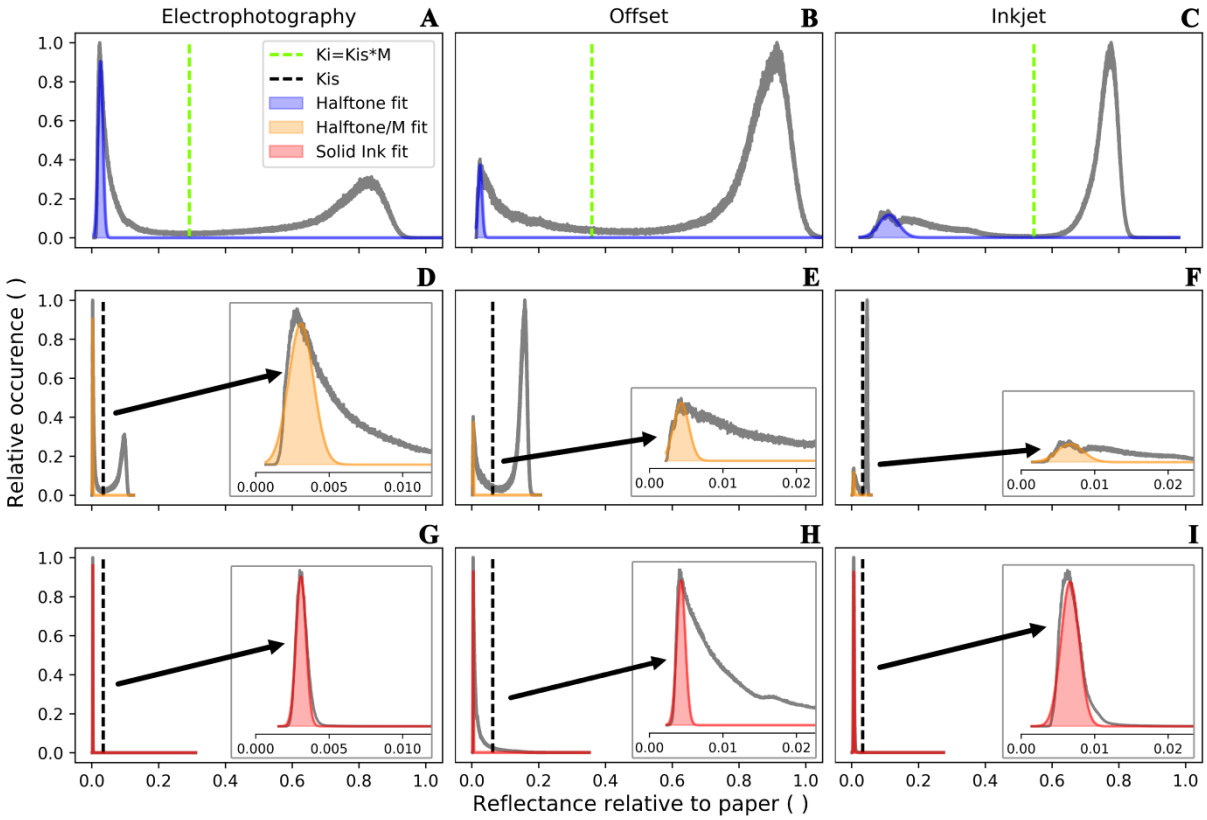

Figure 6.18: Histograms of a halftone (A, B, C), a halftone corrected with the M factor (D, E, F) and of the solid ink (G, H, I). Halftone printed with respectively electrophotography (A, D, G), offset (B, E, H) and inkjet (C, F, I) with effective ink coverages of 42.0%, 22.6% and 23.5%.

In order to fully automate the proposed threshold algorithm, the threhsold value of the solid ink has to be computed. In theory this value could be determined by the user, choosing a level where the solid ink patch is correctly thresholded. Nevertheless it was found that a manual setting of the solid ink threshold level could introduce a bias. Automatic threhsold algorithms such as the Otsu method for example can be used to determine the thredhold value of the solid ink patch. Their performances can

however be altered in the case of a perfect solid ink patch presenting only a narrow Gaussian distribution of the ink reflectances (most threshold algorithms assume a bimodal distribution). Multiple attempts were pursued to define the solid in reflectance threshold level theoretically. Nevertheless, the experiments with different level of ink transmittance showed that a direct "physical" relation could not be easily obtained. Thus, an empirical model, based on a linear regression, was proposed, Figure 6.19. The regression was established on a set of 90 halftone images of various ink coverage, print processes, halftone types, halftone resolutions and ink transmittances. For each different subsets the ink transmittance was determined and an optimization allowed to compute to the best solid ink threshold value K_{is}. It can be observed that the solid ink threshold values as a function of the ink transmittance are linear. A coefficient of determination R^2 of 0.99680 was obtained. A linear model is then established to compute K_{is} as a function of T_i:

$$K_{is}(T_i) = 0.78065\, T_i + 0.02684 \qquad [6.15]$$

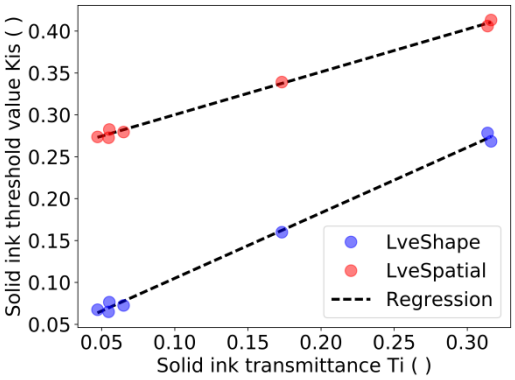

Figure 6.19: Solid ink threshold values as a function of the solid ink transmittances.

6.2.2.2 LveSpatial threshold algorithm

The second threshold algorithm proposed is based on a pre-treatment targeted at removing the mixed regions (mixed ink and paper reflectances). The pre-treatment is applied for each pixel considering a neighborhood of pixels. Thus the pre-treatment strategy is similar to local threshold algorithms adjusting the threshold value as a function of the neighborhood. In the case of the proposed threshold algorithm, a global threshold is applied after the pre-treatment. The threshold algorithm developed can then be attributed to the spatial class of the threshold classification and is called LveSpatial. The threshold algorithm pre-treatment was developed following the measurement framework and convolution strategy to differentiate physical and optical dot gain presented in chapter 5. The pre-treatment principle relies on the light diffusion on halftones model introduced by introduced by Callahan, Yule and Lehmbeck [8–16], equation [6.1]. The ink transmittance can be obtained from the solid ink reflectance (in the following, the reflectances are normalized with the bare paper reflectance in order to have $R_{ps}(x,y) = 1$):

$$T_i(x,y) = \sqrt{R_{is}(x,y)} \qquad [6.16]$$

By adopting the approximation that the ink transmittance can be obtained from the halftone, the effects of the light diffusion can then be obtained and removed from the halftone, giving access to the halftone without light trapping effects:

$$R_{a_{w1}}(x,y) = \left(\frac{R_a(x,y)}{\sqrt{R_a(x,y)} \circledast H(x,y)} \right)^2 \qquad [6.17]$$

Experiments have showed that a double convolution with two different paper point spread functions was describing better the light diffusion on halftones. Following the same principles of the model of the light diffusion on halftones, the double convolution was proposed to obtain the halftone reflectance without light trapping effects, equation [6.18].

LveSpatial pre-treatment

[6.18]

$$R_{a_{w2}}(x,y) = \frac{R_a(x,y)^2}{c_1\, c_2}$$

$$C_1 = \left(\sqrt{R_a(x,y)} \circledast H_1(x,y)\right)$$

$$C_2 = \left(\sqrt{R_a(x,y)} \circledast H_2(x,y)\right)$$

Symbol	Unit	Denomination
$R_{a_{w2}}(x,y)$	1	Halftone reflectance without optical dot gain
$R_a(x,y)$	1	Halftone reflectance
$H_k(x,y)$	1	Paper point spread function k
$\circledast$	-	Convolution operator

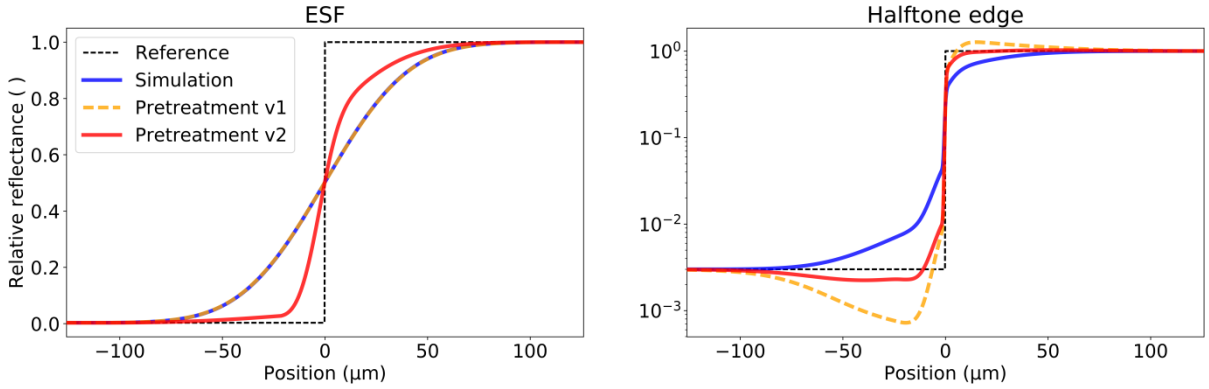

Figure 6.20: Edge spread functions (ESF) and halftone edges as a function of the position for the reference, simulation of the halftones and pre-treatments.

The threshold algorithm proposed requires then to compute $R_{a_{w2}}(x,y)$ from $R_a(x,y)$, $H_1(x,y)$ and $H_2(x,y)$. Both paper point spread function (PSF) are defined empirically. The first PSF used is a Gaussian function of length of 105.3 µm. The second PSF used is a Gaussian function of length of 42.7 µm. The two types and sizes of PSF are similar to the two PSF used to generate the synthetic halftone images. Nevertheless the global ESF for the simulation of the light diffusion on the halftone and the separation of the light diffusion differs. For the halftone simulation, the second convolution is performed on the result of the first convolution. For the separation (pre-treatment), convolving the result of the first convolution overestimates the effects of light trapping near the edges of the halftone dots. This overestimation comes from the approximation adopted to obtain the ink transmittance from the halftone reflectance: $T_{i_{approx}}$. The over estimation generates an over removal of the light trapping effects, clearly visible on Figure 6.20 (labelled "pre-treatment v1"). By experimental trial and error, it was found that improved results were achieved computing the two convolutions independently using the same $T_{i_{approx}}$ for both convolutions, equation [6.18]. The reduction of the light trapping corresponds then better to the ideal edge, as illustrated on Figure 6.20 (curve with label "pre-treatment v2"). The second version of the pre-treatment is then associated with a different ESF than the one used for the halftone simulation. Compared to the simulated edge inducing a shift of the ink reflectances near the edge of the halftone toward higher reflectances values and of the paper reflectances toward lower reflectances, the pre-treated halftone is associated with a sharper edge. The ink reflectances are moved back toward to solid ink reflectance and the paper reflectances are moved back toward 1. The pre-treatment over performs in the ink region, resulting in an estimation of the ink reflectances lower than the solid ink reflectances. Nevertheless this effect is limited to a decrease from the reflectance of 0.0030 to 0.0022, representing an optical density increase from 2.52 to 2.66.

Results of the pre-treatment are proposed for electrophotography, offset and inkjet, Figure 6.21. The edges of the halftone dots are more clearly defined for the three processes. Less mixed region corresponding to the transition from the paper reflectances to the ink reflectances are visible. Heterogeneous regions on the ink surface are more visible after the treatment, especially for the offset process. The effects of the pre-treatment can be also analyzed by comparing the histogram of the halftone image and of the pre-treated halftone image. The ink reflectances are systematically shifted back toward smaller reflectances The paper reflectances are oppositely shifted back toward larger ink reflectances. These ink and paper peaks shifts demonstrate that the effects of the light trapping are partially removed, showing the performance of the pre-treatment. It is interesting to note that for electrophotography and offset the paper reflectance peak is found around the reflectance of 1 after treatment, as if the effects of the light trapping were completely removed. The ink peak although compressed is not totally shifted back, showing that although partially removed, a part of light trapping effects remains. It is interesting to note also that for electrophotography and offset the same paper was used. In the case of inkjet, the paper differed and therefore the paper point spread function differed. However, the PSF of the pre-treatment were not adapted. Even with non-optimized PSF for the inkjet, the pretreatment shows high separation performances.

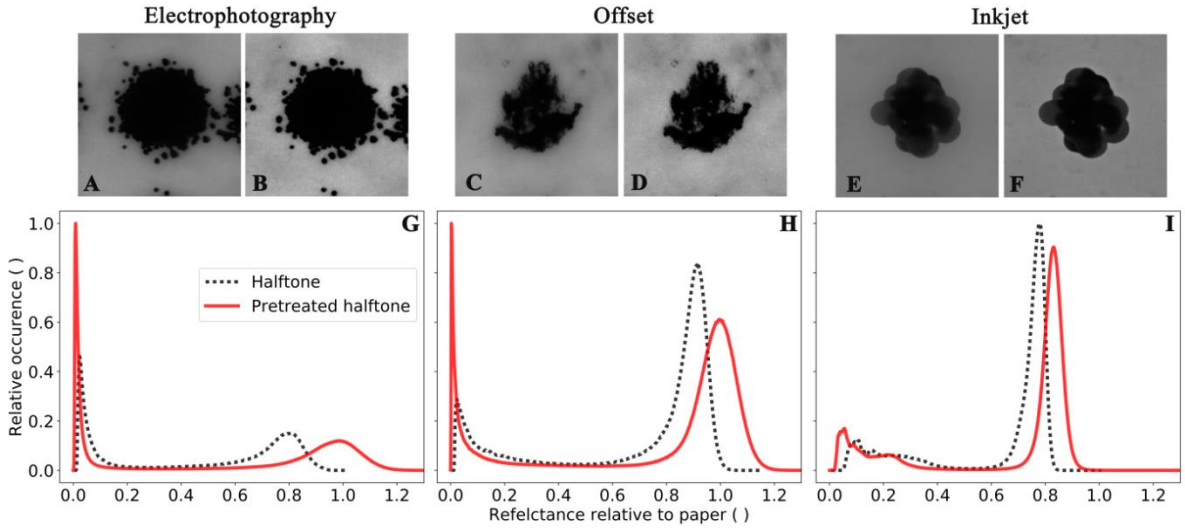

Figure 6.21: 150 lpi amplitude modulated halftone dots printed with: (A) electrophotography, (C) offset and (E) inkjet. Pre-treatment applied to remove the effects of the optical dot gain for dots printed with: (B) electrophotography, (D) offset and (F) inkjet. Histogram of the halftones and of the pre-treated halftones for: (G) electrophotography, (H) offset and (I) inkjet.

After the pre-treatment, the threshold algorithm simply applies a constant threshold for all ink coverages halftones. The threshold value is defined as a function of the solid reflectance. Similarly to the first threshold algorithm proposed, several theoretical definitions of the threshold values as a function of the ink transmittances were analyzed. However, the best results were obtained by performing a linear regression on a set of 90 halftone images printed with multiple print processes and having multiple ink transmittances. An accurate fit of the linear regression was obtained with a coefficient of determination equal to 0.99680. The model linking the ink transmittance to the threhsold value is given by:

$$K_{is}(T_i) = 0.51070\,T_i + 0.24903 \qquad [6.19]$$

A further analysis revealed that the best optimized threshold value was slighly dependent on the ink coverage with a variation in the ink surface range of 22.40% of the solid ink threshold value, Figure 6.22. This dependency appears to be linear and thus could be easily modeleld to improve the performance of the LveSpatial threshold algorithm. However, it was decided to conserve a constant threhsold value for simplicity and to leave this axis of improvments for further developpements.

Finally, it has to be noted that the discretization level does not impact significantely the speed of the threshold algorithm since its processing is not based on the histogram. Thus, a level of discretization equal to the level of the input image is used.

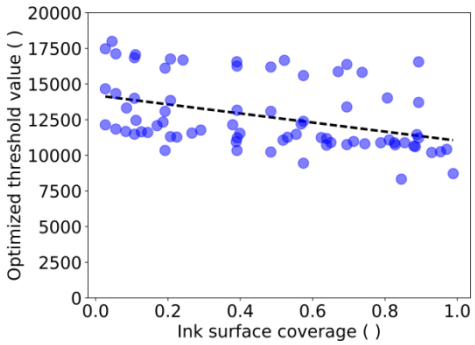

Figure 6.22: Optimized threshold value as a function of the ink coverage for a set of halftones.

6.2.2.3 Threshold algorithms evaluation

The threshold evaluation method developed in section 6.1 is re-employed to evaluate the performances of the two novel threshold algorithms. The evaluation and comparison are performed using the 3920 halftone images and the associated ground truth images. A part of the 3920 SDI corresponds to conventional halftones printed with electrophotography, offset and inkjet (GTI obtained from thresholded MCI). The other part is composed of simulated GTI presenting more exotic configurations potentially associated with larger thresholding errors.

6.2.2.4 Optical and physical dot gain measurements

A direct application of the novel threshold algorithms is the measurement and characterization of optical and physical dot gain. A study of the optical and physical dot gain is then conducted on the 1231 AM and FM halftone images used to evaluate the threshold methods, Table 6.8. Two further experiments are conducted.

The first experiment, called EP1, is composed of a set of 1060 patches where the size of the halftone dot and the spacing between the halftone dots vary. Circle dots, triangle dots with angles of 0° and 45° and square dots with angles of 0° and 90° were generated. Moreover these dots are generated for different dot diameters of 5 pixels, 9 pixels and 17 pixels giving sizes of respectively 50 µm, 90 µm and 170 µm for dots printed with offset, 88 µm, 159 µm and 300 µm for dots printed with inkjet and 106 µm, 191 µm and 360 µm for dots printed with electrophotography. These dots are then placed in patches applying different spaces between the dots. The dots are arranged in a honeycomb halftone configuration. More information on the generation is given in Chapter 3.

The second experiment, called EP2, investigates the effect of the perimeter of the halftone dots having identical area on the optical dot gain. 200000 dot shapes are generated by variating the arguments of the Superformula: a=1, b from 0.5 to 2.5 with a step of 0.5, m from 0 to 6 with a step of 0.25, n_1 from 0.1 to 3.85 with a step of 0.25, n_2 from 0 to 2.25 with a step of 0.25, n_3 from 0 to 2.25 with a step of 0.25. The area and perimeter are computed and the halftone dots are grouped by area. 417 patches are then generated using the selected halftone dots with a constant spacing between the dots of 12 pixels. More information on the generation is given in Chapter 3.

The characterizations of optical and physical dot gains rely on the 3 different ink coverages:

- The apparent ink coverage a_a, obtained by inversing the Murray-Davies model and computed from the mean reflectance of the halftone. The mean reflectance can either be obtained averaging an image captured at the microscale (the images captured are systematically normalized with the bare paper image) or can be obtained with macroscale densitometric measurements. In the case of

densitometric measurements a spectrophotometer Techkon SpectroDens B104052, with polarized filter and Iso E density filter is used.

- The effective ink coverage a_e, obtained by applying the LveSpatial threshold algorithm and by measuring the ink coverage of the thresholded region corresponding to the ink.
- The nominal ink coverage a_n defined on the binary image sent to the printer. The coverage is measured directly on the binary image by counting the number of ink pixels divided by the total number of pixels.

The optical dot gain Δa_{opt} and the physical dot gain Δa_{phy} can then be computed by:

$$\Delta a_{opt} = a_a - a_e \quad [6.20]$$

$$\Delta a_{phy} = a_e - a_n \quad [6.21]$$

Table 6.8: Optical density as a function of the patch series (halftone type, resolution, ink, inking level and paper properties).

Process	Paper (g/m²)	Ink (Black)	Halftone type and resolution	Optical density
Offset: Heidelberg Speedmaster 52, 2540 dpi	Glossy 1: Unknown supplier, coated, 135	Novavit 918 supreme	AM: 150 and 200 lpi FM: 2540, 1270, 847, 635, 318 dpi EP1: discs (0°), triangles (0°, 90°), squares (0°, 45°): 150, 282, 508 dpi EP2: 102 lpi	1.59
			AM: 150 and 200 lpi EP1: discs (0°): 150, 282, 508 dpi	1.89
			AM: 150 and 200 lpi EP1: discs (0°): 150, 282, 508 dpi	2.37
Electrophotography: Xerox Versant 180 Press, 1200 dpi	Glossy 1: Unknown supplier, coated, 135	Xerox Versant 80 Press	AM: 150 and 200 lpi FM: 1200, 600, 400, 300, 150 dpi EP1: discs (0°), triangles (0°, 90°), squares (0°, 45°): 70, 133, 240 dpi EP2: 48 lpi	2.51
	Glossy 2: Mondi, coated, 135		AM: 150 and 200 lpi EP1: Discs (0°): 85, 160, 288 dpi	2.47
	Epson: Epson proofing, coated 205		AM: 150 and 200 lpi EP1: Discs (0°): 85, 160, 288 dpi	2.51
	Uncoated: Inapa, uncoated, 160		AM: 150 and 200 lpi EP1: Discs (0°): 85, 160, 288 dpi	2.51
Inkjet: Epson Stylus Pro 4900, 1440 dpi	Epson: Epson proofing, coated 205	Epson MK T6538	AM: 150 and 200 lpi FM: 1440, 720, 480, 360, 180 dpi EP1: discs (0°), triangles (0°, 90°), squares (0°, 45°): 85, 160, 288 dpi EP2: 58 lpi	2.64
		Epson PK T6531	AM: 150 and 200 lpi EP1: Discs (0°): 85, 160, 288 dpi	2.15

6.2.3 Performances of the threshold algorithms developed

The two proposed threshold algorithms, the LveShape and the LveSpatial are then evaluated and compared to the PalBhandari and Li threshold algorithms, Figure 6.23 and Table 6.9.

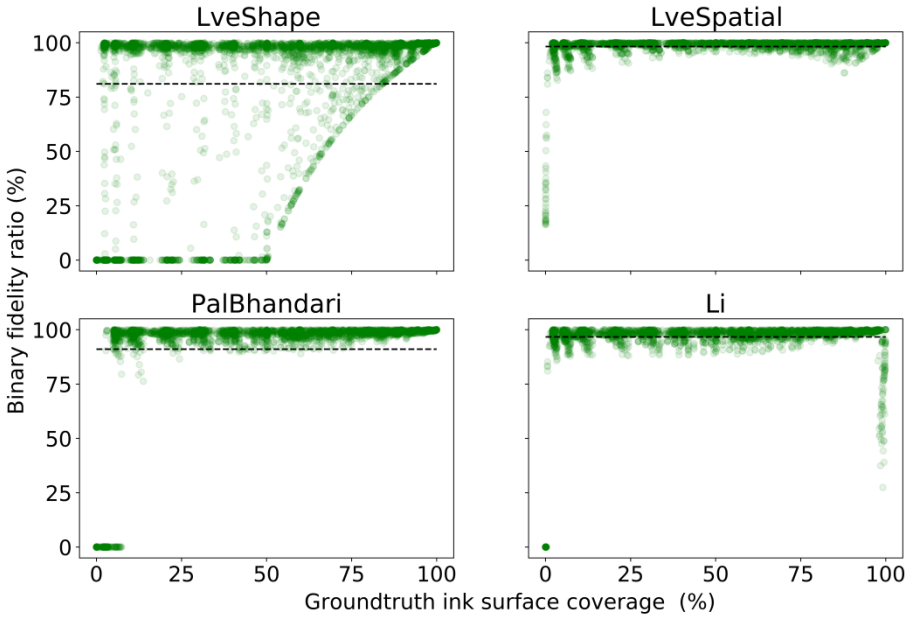

Figure 6.23: Binary fidelity ratio as a function of the ink coverage of the ground truth for the 3920 SDI generated (from real thresholded halftones and from synthetic generated GTI). Black dashed line represents the binary fidelity ratio average over ink coverages.

Table 6.9: Mean binary fidelity ratio and mean ink coverage difference for the GTI obtained from MCI, for the simulated GTI and for all generated GTI. The greenest and the bluest results are associated with the best threshold algorithm performances.

	Mean binary fidelity ratio (%)		**Mean ink coverage absolute difference (%)**			
Ground truth ink coverage:	[0-100%]	[10-90%]	[0-100%]	[10-90%]	<10%	>90%
GTI obtained from MCI (1320 SDI)						
LveSpatial	97.63 +/- 11.39	99.60 +/- 0.61	0.21 +/- 0.33	0.21 +/- 0.37	0.07	0.25
Li	94.26 +/- 17.46	98.52 +/- 1.11	3.70 +/- 11.07	0.79 +/- 0.74	15.74	9.29
LveShape	93.58 +/- 19.60	96.21 +/- 10.21	4.93 +/- 18.18	2.09 +/- 5.75	36.60	0.50
PalBhandari	93.67 +/- 21.74	98.54 +/- 1.28	5.72 +/- 21.59	0.79 +/- 0.79	55.68	0.54
Simulated GTI (2600 SDI)						
LveSpatial	98.61 +/- 2.10	98.81 +/- 1.64	0.61 +/- 1.12	0.64 +/- 1.10	0.11	1.18
Li	97.90 +/- 2.46	97.93 +/- 2.23	0.81 +/- 1.32	0.96 +/- 1.08	0.13	0.75
PalBhandari	89.74 +/- 27.31	97.91 +/- 2.27	8.87 +/- 26.56	0.93 +/- 1.01	51.55	0.54
LveShape	74.81 +/- 38.45	77.15 +/- 35.99	17.22 +/- 29.79	14.47 +/- 24.56	39.67	1.98
GTI obtained from MCI and Simulated GTI (3920 SDI)						
LveSpatial	98.28 +/- 6.83	99.07 +/- 1.44	0.48 +/- 0.96	0.50 +/- 0.94	0.10	0.73
Li	96.68 +/- 10.45	98.12 +/- 1.96	1.78 +/- 6.64	0.90 +/- 0.98	3.65	4.89
PalBhandari	91.06 +/- 25.64	98.12 +/- 2.02	7.81 +/- 25.04	0.88 +/- 0.94	52.48	0.54
LveShape	81.11 +/- 34.49	83.44 +/- 31.35	13.09 +/- 27.09	10.39 +/- 21.19	38.98	1.26

The performances of the LveShape threshold algorithm are more dispersed than the PalBhandari and the Li threshold algorithms with respectively a standard deviation of 10.21% compared to 1.28% and 1.11% in the ink coverage range of 10 to 90%. The ink surface extrema are ignored since it was

shown that the PalBhandari and the Li threshold algorithms were associated with low binary fidelity ratios. Although 10 times superior to the dispersion of the threshold algorithms selected from literature, it can be observed that a large amount of the halftone binary fidelity ratios are associated with high performances, as shown by the green line formed by the superposition of multiple binary fidelity ratios near 100%. Over 3920 tested halftones thresholded with the LveShape threshold algorithm, 966 obtained a binary fidelity ratio below 90%. 46.7% of the mis-performances are found below 25% ink coverage, 20.3% between 25% and 50% ink coverage, 22.3% between 50% and 75% ink coverage and 20.3% above 75% ink coverage. 90.6% of the 966 mis-performances are associated with SDI obtained from simulated GTI, Table 6.10. The GTI obtained from the thresholded MCI represent only 9.4% of the misthresholded halftones. Inkjet and electrophotography are associated with a similar mis-performance level. Offset is found slightly higher and most of the mis-performances are attributed to the offset patches with ink transmittances of 0.01 and 0.1. Studying the halftone obtained from the simulated GTI, almost no differences are observed between amplitude modulated halftones and frequency modulated halftones.

A dependency of the LveShape threshold performance can be observed as a function of the halftone resolution, Table 6.11. The ratio of mis-performances increases with the increase of the resolution for both AM and FM halftones. The highest mis-performances are then found for large halftone resolutions of 605 lpi for AM and a dot size of 4838 dpi for FM halftones. The solid ink reflectance level does not influence the number of mis-performances; however the size of the paper point spread functions is associated with a large influence, Table 6.12. Finally, no tendency could be associated with the mis-inked dots number, the pixel dislocation iterations and the dot aspect ratio, Table 6.13. It can be concluded that aside from extreme cases of large halftone resolutions and paper PSF, the LveShape threshold algorithm performs well. By excluding the 966 halftones associated with a binary performance below 90%, the mean binary fidelity ratio computed over the remaining 2954 halftones reaches 98.14% +/- 1.86%. This performance can be compared to the PalBhandari and Li Threshold algorithm having a binary fidelity ratio of 98.12% +/- 2.02% and 98.12% +/- 1.96%. The performance of the LveShape threshold algorithm is then slightly superior with a slightly inferior dispersion of the measurements

Table 6.10: Ratio of halftones giving a binary fidelity ratio below 90% (Rb90) as a function of the GTI generation strategy, process and halftone type.

GTI generation	**From measured MCI**			**Simulated**	
Process or halftone type	Electrophotography	Offset	Inkjet	AM	FM
Ratio of Rb90	2.6%	5.5%	1.3%	38.9%	51.7%

Table 6.11: Ratio of halftones generated from simulated GTI giving a binary fidelity ratio below 90% (Rb90) as a function of the resolution and halftone type.

AM halftones (lpi)	**101**	**151**	**202**	**302**	**605**
Ratio of Rb90	6.4%	11.7%	16.5%	23.7%	41.8%
FM halftones (dpi)	**403**	**806**	**1210**	**2419**	**4838**
Ratio of Rb90	2.6%	9.2%	17.8%	33.9%	36.5%

Table 6.12: Ratio of halftones generated from simulated GTI giving a binary fidelity ratio below 90% (Rb90) as a function of the ink transmittance and paper point spread function size.

Ink transmittance ( )	**0.003**	**0.03**	**0.1**	**0.003**	**0.003**
PSF sizes (µm)	105+21	105+21	105+21	157+52	52+2
Ratio of Rb90	21.4%	18.4%	17.0%	43.2%	0.0%

Table 6.13: Ratio of halftones generated from simulated GTI giving a binary fidelity ratio below 90% (Rb90) as a function of the mis-inked dot number, the pixel dislocation iteration and the dot aspect ratio.

Mis-inked dots number	**0**	**0**	**200**	**500**
Pixel dislocation iterations	100	100	100000	100
Dot aspect ratio	1.0	0.7	0.7	0.7
Ratio of Rb90	20.0%	21.1%	29.4%	29.5%

The second algorithm developed, the LveSpatial is associated with very high binary fidelity ratios, Figure 6.23. A total dispersion of +/- 6.83% of the fidelity ratio is obtained and can be compared to the PalBhandari and Li threshold algorithms associated with dispersion respectively of 25.64% and 34.49%. Restraining the ink coverage range to the 10% to 90% range (to remove small and large ink coverages where the Li and PalBhandari threshold algorithms performances present large variations), a dispersion of +/- 1.44% of the fidelity ratio is obtained and can be compared to the PalBhandari and Li threshold algorithms associated with dispersion respectively of 2.02% and 1.96%. The mean binary fidelity ratio obtained for the LveSpatial threshold algorithm is superior with 99.07% compared to the PalBhandari and Li threshold algorithms having respectively 98.12% and 98.12%. Small errors however can be observed for both large and small ink coverages for the LveSpatial. The dispersion is smallest for ink coverages around 50%.

The LveSpatial performs the best for the halftones generated from threshold MCI with a binary fidelity ratio of 99.60% +/- 0.61%. This improvement is not as marked as for the PalBhandari and the Li threshold algorithm with respectively 98.54% +/- 1.28% and 98.52% +/- 1.11%. The performances of the LveSpatial are decreased for the halftones generated with simulated GTI. The PalBhandari and the Li threshold algorithms present also decreased performances. It can be concluded that the LveSpatial threshold algorithm performs better than the PalBhandari and the Li threshold algorithms.

An investigation of the ink coverage difference (ICD) is then conducted to analyze the dependency of the two threshold algorithms developed to the ink coverage, Figure 6.24 and Table 6.9. Only halftones and GTI obtained from thresholded MCI are analyzed in order to focus on conventional halftone, resolutions, dot morphologies and ink homogeneities. The LveShape ICD are found between +0.5% and –2.5%. A small number of halftones thresholded with the LveShape resulted to ICD with larger dispersions located in two clusters around 60% ink coverage and 80% ink coverage. These twos clusters have ICD around + 4% demonstrating an over-thresholding and represents 10.7% of the number of halftones analyzed. Most halftone resulting in large ICD are associated with offset (presenting ink heterogeneities). Excepting these two clusters, the LveShape threshold algorithm performance can be compared to the PalBhandari and Li threshold algorithms. A mean absolute ICD of 0.86% +/- 0.71% is obtained by excluding the two clusters for ink coverages above 10% and below 90%. It can be compared to an average absolute difference of respectively 0.79% +/- 0.79% and 0.79% +/- 0.74% for the PalBhandari and Li threshold algorithms. It can be concluded that by thresholding conventional halftones the LveShape threshold algorithm gives slightly lower results than the PalBhandari and Li threshold algorithms. The LveShape follows a similar dependency with the ink coverage compared to the PalBhandari and the Li thresholds with a maximum performance toward the small and large ink coverages (excluding the ink coverages around 0% and 100%). The three threshold algorithms perform less accurately for ink coverage around 50%. The dependency of the LveShape differs slightly from the PalBhandari and the Li threshold, as the absolute ICD progressively increase from 0 to 50% and decreases from 50 to 100% ink coverage. The absolute ICD of the PalBhandari and Li threshold algorithms increase from 0 to 80% and decreases from 80 to 100%. The dependency with the ink coverage is then not symmetrical for these two threshold algorithms. The LveShape, PalBhandari and Li threshold algorithm globally under threshold the halftones resulting to a smaller ink coverage obtained compared to the ground truth.

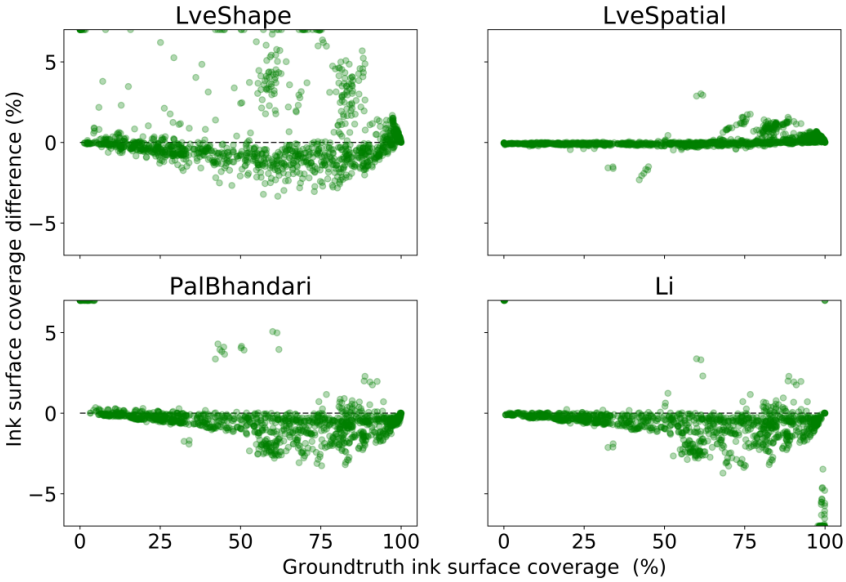

Figure 6.24: Ink coverage difference as a function of the ground truth ink coverage for the 1320 SDI generated from thresholded MCI. Ink coverage differences larger and smaller than 7% and -7% are represented at this limit.

The LveSpatial threshold algorithm performs better than the PalBhandari and the Li algorithms. Only a small dispersion of the ICD is observed for large ink coverages. The ICD obtained with the LveSpatial are globally not dependent on the ink coverage. This property is extremely interesting to test the performance of reflectance models. A cluster of LveSpatial small ICD errors can be observed with an over thresholding of the ink region for large ink coverages. This cluster corresponds to 9.8% of the 1320 halftones and is caused also by the ink heterogeneities of the offset print. A small cluster of under thresholded halftones can also be observed; however it represents only 0.7% of the halftones analyzed and corresponds to offset prints with high ink transmittances of 0.1. The LveSpatial threshold algorithm is the threshold algorithm that performs the best compared to all other tested threshold algorithms. For the halftones obtained from thresholded MCI, a mean absolute ICD of 0.21% +/- 0.33% is obtained for all ink coverages and 0.21% +/- 0.37% is obtained for the halftone of ink coverages above 10% and below 90%. This performance can be compared to an average absolute ICD in the 0% to 90% ink coverage range of respectively 0.79% +/- 0.79% and 0.79% +/- 0.74% for the PalBhandari and Li threshold algorithms. The LveSpatial is then associated with an improvement of the performances by 4 times. The dispersion is small and independent with the ink coverage. An ink coverage measurement error of less than 0.25% can then be expected. The LveSpatial threshold algorithm performs accurately also for small and large ink coverages.

The halftones generated with simulated GTI allow exploring more critical halftone configurations, such as halftones with high halftone resolutions (AM 605 lpi, FM 2419 dpi and FM 4838 dpi), halftones with multiple ink heterogeneities, halftones with large dot edge fuzziness, etc. The threshold performances of all threshold algorithms are then smaller than for the halftones obtained from thresholded MCI. The LveSpatial threshold algorithm remains nevertheless superior to the PalBhandari and Li algorithms with a mean absolute ICD of 0.64% +/- 1.10% compared to respectively 0.93% +/- 1.01% and 0.96% +/- 1.08%. Analyzing the LveSpatial threshold algorithm globally for the 3920 test halftone show an improvement of the effective ink coverage by two times compared to the PalBhandari and Li thresholds, excluding extreme ink coverages. The dispersion obtained for all halftones patches analyzed reach a similar level for the LveSpatial than for the PalBhandari and the Li thresholds. Finally, it can be observed that the LveSpatial threshold algorithm thresholds better the extreme ink coverages than the PalBhandari and the Li thresholds. The performances of the LveShape are more complicated to analyze since, it gives more dispersed results for extreme halftones parameters.

The performances of the four threshold algorithms are analyzed as a function of the halftone resolution, the solid ink reflectance and the paper point spread function, Figure 6.25. To perform this analysis the SDI obtained from simulated GTI were considered. Analyzing the effect of the resolution on the performances of the threshold algorithms shows that globally the increase of the resolution generates a decrease of the thresholding accuracy. This tendency is extremely pronounced for the LveShape algorithm with a strong increase for the 302 and 605 lpi halftones. For these resolutions the LveShape cannot be used accurately since the mean ink coverages obtained differ by respectively 29.6% and 49.6%. For resolutions below 302 lpi, the LveShape threshold algorithm performs more accurately with mean absolute ink coverage difference below 2%. The PalBhandari and Li thresholds algorithm are also impacted by the decrease of the dot size. The increase of the mean absolute ICD is inferior to 1% except for the 605 lpi halftone. The LveSpatial shows also an increase of the mean absolute ICD with the decrease of the dot size; however the results obtained demonstrate small variations. The increase is more significant for the 605 lpi halftone with a mean absolute ICD of 0.99%. The decrease of the printed dot size increases the effects of the optical dot gain. Consequently, the threshold algorithms perform better for halftones associated with small optical dot gain. The LveSpatial threshold algorithm performs well with the increase of optical dot gain and provides accurate measurements with less than 1% error for halftones with high resolution. The PalBhandari and Li threshold algorithms are more impacted with errors exceeding 2%. The LveShape threshold algorithm is extremely sensitive to the amount of optical dot gain producing extremely large errors for small halftone dot sizes.

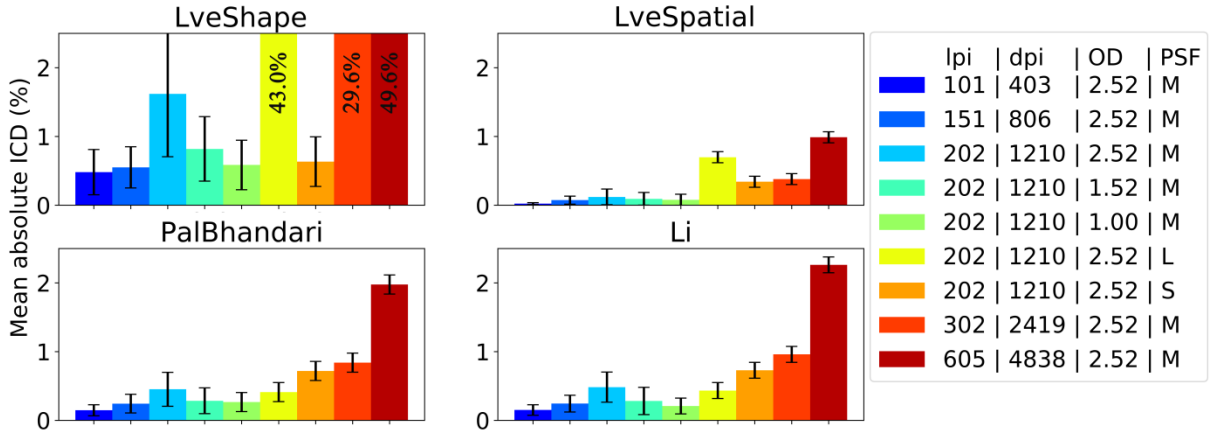

Figure 6.25: Mean absolute ink coverage difference (ICD) as a function of the halftone resolution, the solid ink reflectance (OD: optical density) and the paper point spread function (PSF). The average of AM and FM halftones is computed, associating the halftone resolutions given in lpi for AM and in dpi for FM. The paper PSF M corresponds to 105 µm + 21µm, L to 157 µm + 52 µm and S to 52 µm + 2 µm. Halftones inferior to 10% and superior to 90% ink coverage are excluded.

The effect of the paper point spread function size is also evaluated for the 4 threshold algorithms, Figure 6.25. An increase of the paper point spread function length increases the optical dot gain generated. The sensitivity of the LveShape threshold algorithm with the optical dot gain can be observed. The large paper PSF generates a large mean absolute ICD. The PalBhandari and Li threshold algorithms are associated with an increase of the mean absolute ICD for the large and small PSF sizes compared to the medium size. That behavior illustrates the requirement for the two threshold algorithm to have a specific distributed histogram. In a same manner an over distributed histogram reduces the accuracy of the threshold algorithms. The LveSpatial threshold algorithm behavior is interesting to analyze since the PSF used to separate the ink from the paper was kept constant, matching the paper PSF of the SDI generated with the medium PSF. The thresholding of large and small paper PSF SDI, generates an increase of the mean absolute ICD. The increase remains small with a mean absolute ICD of 0.70% for the large paper PSF and 0.34% for the small paper PSF compared to a mean absolute ICD of 0.12% for the medium paper PSF. Adapting the PSF of the

LveSpatial threshold algorithm to fit the paper PSF can improve the performances of the algorithm. The possibility to adapt the algorithm parameters as a function of the paper used is a tremendous advantage. Moreover testing different paper PSF without adapting the parameters of the LveSpatial threshold algorithm showed its robustness for error tolerance in the input of the PSF.

The effects of the ink transmittance (expressed as the solid ink reflectance) on the performances of the threshold algorithms are studied, Figure 6.25. For the two threshold algorithms developed and the two reference threshold algorithms, the decrease of the solid ink optical density generates an increase of the performances. In the case of the LveShape the threshold, performances are increased from a mean absolute ICD of 1.68% to 0.82% for a decrease of the solid ink optical density from 2.52 to 1.52. A similar improvement is demonstrated for the LveSpatial with respectively an increase from 0.12% to 0.09%. The observed tendency is more difficult to correlate directly to optical dot gain. An inverse tendency with a decrease of the thresholds performances was expected, since the decrease of the solid ink optical density produces halftones with less separated ink and paper regions. Nevertheless, this analysis showed that the LveSpatial algorithm presented only small performances variations with the variations of the solid ink optical density and demonstrated improved performances compared to the PalBhandari and Li threshold algorithms.

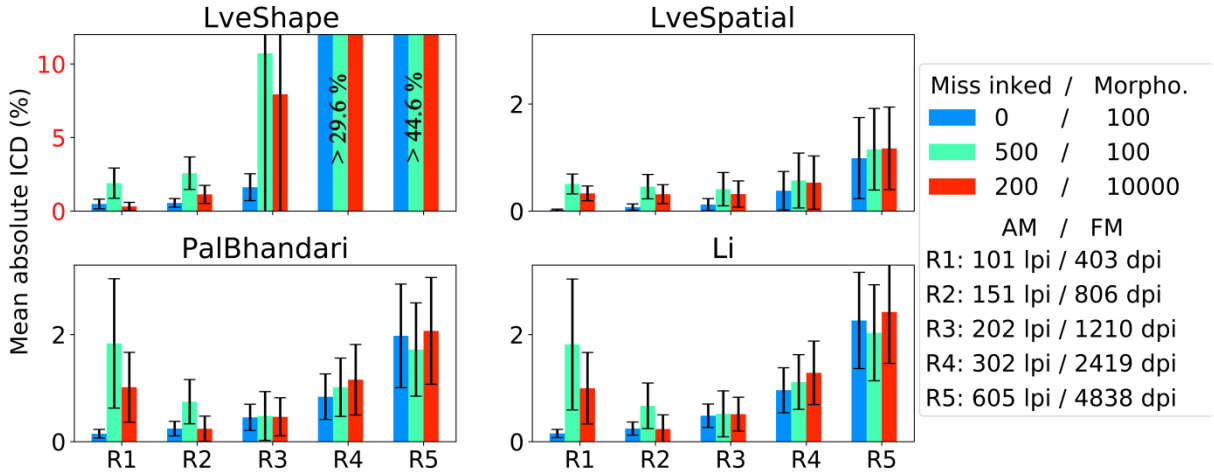

Figure 6.26: Mean absolute ink coverage difference (ICD) as a function of the missed inked (ink homogeneity) and the dot morphology (edges fuzziness) for the 5 halftone resolutions and a solid ink optical density of 2.52. The average of AM and FM halftone is computed, associating the halftone resolutions given in lpi for AM and in dpi for FM. Halftones inferior to 10% and superior to 90% ink coverage are excluded.

The performances of the four threshold algorithms are analyzed as a function of the ink homogeneity and the dot morphology, Figure 6.26. The analysis is performed for the different halftone sizes since the characteristic sizes of ink heterogeneities and dot morphology are fixed. An important dependency of the performances of the threshold algorithms is observed as a function of the resolution for the different homogeneity and morphology configurations. The performances of the two reference threshold algorithms, the PalBhandari and Li algorithms decrease with the decrease of the halftone size for homogeneous ink region with rounded dots. The introduction of ink heterogeneities and a distortion of the edges of the printed dots change this almost linear tendency to an inverse bell shape tendency. The best performances for the two reference algorithms are found around the halftone sizes of 150 to 200 lpi for the AM halftones and around 800 to 1200 dpi for the FM halftones. For smaller and larger halftone sizes, the performances of the two threshold algorithms decrease. The two threshold algorithms developed show a linear dependency of the threshold performances, increasing with the increase of halftone resolution. Less performances variations are introduced between different ink homogeneities and dot morphologies for different halftone resolutions. It has to be noted that a performance limit appears for the LveShape threshold algorithm starting from 202 lpi or 1210 dpi.

6.2.4 Optical and physical dot gain characterizations

6.2.4.1 Measurement method influence

The optical dot gains obtained from the apparent ink coverages measured with densitometry and on microscale images are compared, Figure 6.27 (A) and (B). The optical dot gain tendencies for the three print processes are similar for AM halftones and for FM halftones with high resolution. For FM halftones with smaller resolutions (600 dpi and 300 dpi) the optical dot gains obtained with the densitometry present larger optical dot gain variations. The shapes of the optical dot gain curves are less close to theoretical bell shape curves. The results obtained with microscale images are also associated with larger variations, nevertheless the mean optical dot gains obtained follow smoother bell shape curves. Moreover it can be observed that a shift of the levels of optical dot gain measured with the microscale images and the macroscale images occur. The dot gain levels obtained with microscale images are found to be smaller than with the densitometric images. This tendency is caused by a difference in the measurement of the apparent ink coverage. It should be noted that the two measurement methods present differences in the geometry of the measurements (45°/0° for the densitometry and 0°/0° for the microscale images), in the illuminant (standard illuminant for the densitometry and halogen-tungsten with blue filter for the microscale images) and in the filters used (Iso E for the densitometer and no filters for the microscale images). Complementary measurements are conducted on EP1 halftone images and results demonstrated similar tendencies and differences between the two measurement methods. The results are presented in appendix, Figure A.1, Figure A.2 and Figure A.3. Further dot gain analysis will be conducted using microscale images.

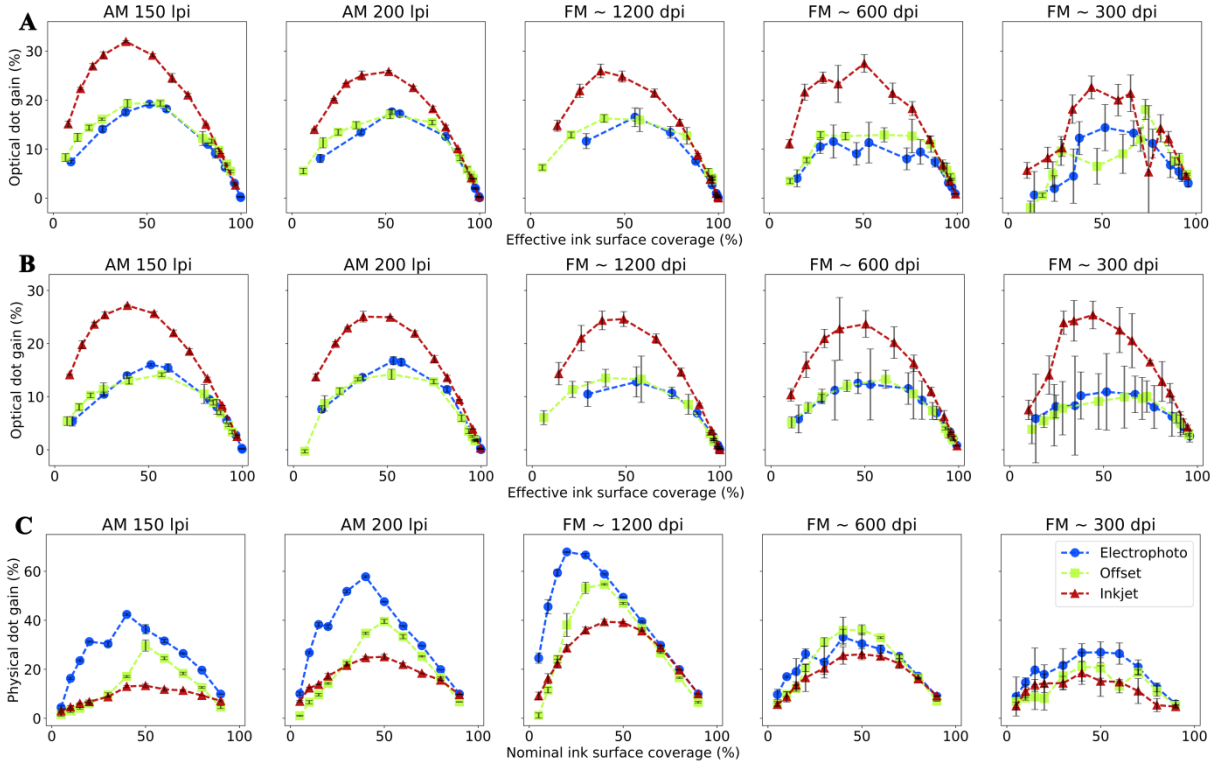

Figure 6.27: Print process, halftone type and halftone size influences on (A) the optical dot gain with apparent ink coverage measured with a densitometer, (B) the optical dot gain with apparent ink coverage measured on microscale images and (C) the physical dot gain.

6.2.4.2 Print process influence

The influence of the print process is analyzed on the optical, Figure 6.27 (B). It can be observed that the halftones printed with inkjet display a larger optical dot gain for all halftone types and sizes. This is mainly caused by the Epson proofing paper used to print the halftones with inkjet. This paper is

associated with larger light diffusion characteristics. However, the difference of paper is not the only reason explaining the differences observed as demonstrated by the characterization of the paper influence with a similar print process, Figure 6.30. The maximum optical dot gain for the inkjet prints is found around 30%. The maximal optical dot gains associated with the electrophotography and inkjet prints are smaller with a maximum obtained around 17%. The electrophotography and inkjet halftones were printed on a similar glossy coated paper. This paper is associated with smaller light diffusion characteristics. The ink coverage at which the maximum optical dot gain is observed differs also from inkjet and offset/electrophotography. Theoretically the maximal dot gain is obtained at the 50% ink coverage. This ink coverage is observed for the offset and electrophotography prints, however the inkjet prints show a maximum of optical dot gain located around 40% ink coverage. The tendencies observed are similar for the halftone types and sizes.

The influence of the print process was also analyzed on the physical dot gain, Figure 6.27 (C). The physical dot gain is mostly influenced by the ink deposition and by the physico-chemical interactions between the ink and the paper. The physical dot gain shows then large differences as a function of the print process. The electrophotography process is associated with the largest physical dot gain, with a maximum obtained around 70%. The inkjet process performs the most accurately, however the physical dot gain remains large with a maximum around 40%. The offset process has a physical dot gain similar to the inkjet process for small ink coverages and then similar to the electrophotography for larger ink coverages. The physical dot gains of the halftones printed with inkjet have smoother variations and are close to a bell shape curve. The maximum physical dot gain occurs near the 50% ink coverage showing a dependency of the physical dot gain with the ratio of ink and paper regions (influenced also by the ink region total perimeter). The electrophotography and offset prints are also associated with an increase of the physical dot gain up to 50% ink coverage and then by a decrease for larger ink coverages. However, the shapes of the physical dot gains are more variating.

Complementary optical and physical dot gain measurements are performed on EP1 halftone images and demonstrated similar tendencies and differences. The results are presented in appendix, Figure A.1, Figure A.2 and Figure A.3. It should be noted that the physical dot gain is expressed as a function of the nominal ink coverage and the optical dot gain is expressed as a function of the effective ink coverage.

6.2.4.3 Halftone type and size influences

The halftones type and sizes influence the optical dot gain. The halftone type influences the shape and the maximum level of optical dot gain. This influence is particularly visible by comparing the halftone printed with AM halftoning with the halftones printed with constant dot sizes and variating dot spacing, Figure 6.27 (B), Figure A.1, Figure A.2 and Figure A.3. The optical dot gain variations induced by the different halftone types do not seem to depend on the print processes. The halftone size has a small effect on the optical dot gain for the inkjet prints. The influence of the halftone size is more important for offset and electrophotography. This effect is highlighted comparing the halftones with the different dot size, Figure A.1, Figure A.2 and Figure A.3. The global tendency observed is then a decrease of the optical dot gain with the increase of the halftone dot size. The influence of the halftone size is however small compared to the influence of the paper.

The halftones types and sizes influence also the physical dot gain, Figure 6.27 (C). The shapes of the physical dot gain curves depend on the halftone type, as observed comparing the AM halftones at 150 lpi and the FM halftones at 300 dpi. Considering a circular halftone dot printed with AM halftones at 200 lpi, the diameter of the dot at 50% ink coverage is equal to 0.8 times the halftone cell size and is then equivalent to a FM dot of 250 dpi. Comparing then the AM halftones at 200 lpi and the FM halftones at 300 dpi, a clear difference of physical dot gain appear. This difference may be triggered by the organization of the halftone dots, where for AM halftones more ink-paper interfaces appear. The physical dot gain would then be dependent on the total length of the perimeter of the ink

region, with an increase with the increase of the perimeter length. This effect is also amplified by the size of the halftone dots with a large increase of the physical dot gain with the decrease of the halftone dot size. The physical dot gain is almost two times larger on the FM halftones at 1200 dpi than on the FM halftones at 600 dpi. The differences between 600 lpi and 300 lpi are less marked. It can be concluded that both the halftone type and halftone size influence the physical dot gain.

6.2.4.1 Inks influence

The optical dot gain and physical dot gain for two different inks printed with similar conditions are analyzed, Figure 6.28. The ink type influences the optical dot gain, especially for AM halftones. The shapes of the optical dot gains are similar for the two inks; however the levels of optical dot gain differ. The photo black ink is associated with a higher ink transmittance and displays more optical dot gain. For the matte black ink the ink is associated with lower transmittance and less optical dot gain occurs. It should be noted that the paper used was the Epson proofing paper, subject to large light diffusion. Internal reflections at the interface between the ink-paper and the air can also occur. A print with an ink less absorbing will be associated with a higher amount of internal reflections before reaching a total attenuation of the light trapped inside the print. Therefore the optical dot gain generated would be larger, as observed experimentally. The two inks tested gives similar physical dot gains. A small difference is observed for the physical dot gain of the AM halftone at 200 lpi, however these variations are not repeated for other halftone types and sizes. Since both inks are supplied by Epson and are of the same type, the influences of the inks on the print process are similar. The physical interactions with the paper substrate can also be considered similar and therefore a similar level of physical dot gain is achieved. The differences between the two inks rely mostly on the difference of dyes used. This difference mostly influence the level of optical dot gain.

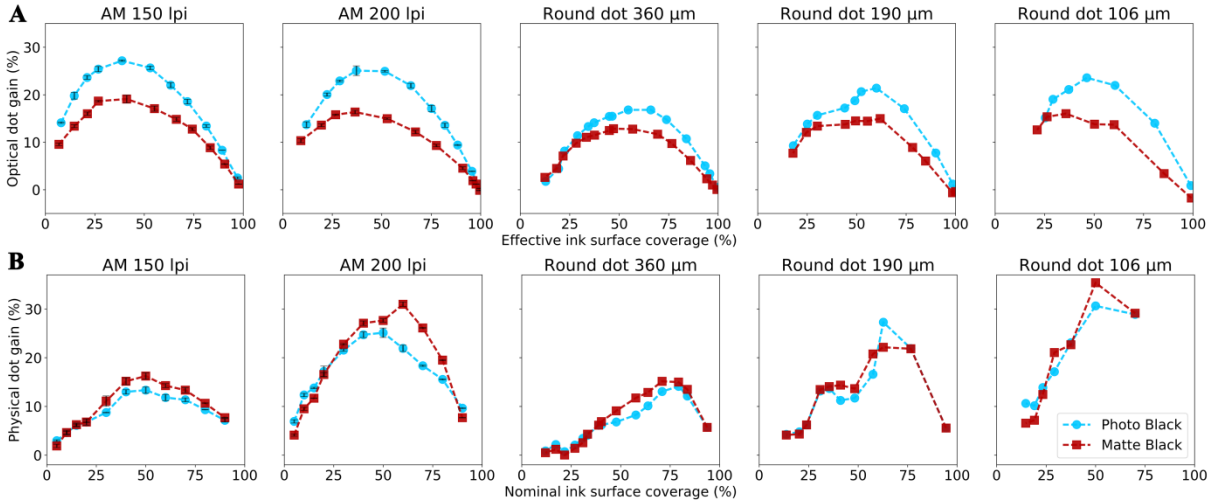

Figure 6.28: Inks, halftone type and halftone size influences on (A) the optical (B) the physical dot gains. The samples are printed with inkjet with two inks: the Epson photo black and matte black.

6.2.4.2 Inking influence

The optical dot gain and physical dot gain for three different inking levels under the exact similar condition are analyzed, Figure 6.29. The optical dot gain shows a small dependency with the inking level. It is interesting to notice that the standard inking is associated with more optical dot gain the medium and the light inking. The decrease of inking also modifies the shape of the halftone dots printed with offset and this can counteract the increase of the ink transmittance. The difference between the inking levels is more important for smaller halftone sizes. The shapes of the optical dot gain curves remain nevertheless similar and only an optical dot gain shift occurs between different inking levels. The physical dot gain is on another side highly influenced by the increase of the inking. More ink produces a larger physical dot gain. This effect can easily be interpreted, as the increase of

the amount of ink will induce more spread during the transfer between the different cylinders of the offset printer and from the offset printer to the paper. The paper partially absorbs the ink and smaller ink levels set on paper more easily contributing to preventing the ink spread. It can be noticed for light inking that the physical dot gain levels become negative, especially for the AM halftones and the FM halftones with large dot sizes. Negative physical dot gain signifies that less ink was transferred onto paper than the ink coverage requested from the printed. In the case of the offset prints, large heterogeneities of the ink layer are observed with mis-inked regions inside the inked regions. These heterogeneities are caused by physico-chemical interactions between the ink, the dampening solution and the paper. Higher inking levels will tend to reduce these defects since the ink spread will tend to fill the heterogeneous regions. The shape of the physical dot gain curves measured depend then on the inking level and have a tendency to be tilted toward large ink coverages (larger impact of the ink heterogeneities for large ink coverages). The effect of the inking level is less marked for small dots, since less ink heterogeneities occur on smaller inked surfaces. It can be concluded that the inking level presents a large influence on the physical dot gain and a small influence of the optical dot gain. The results should nevertheless be interpreted with special care since complementary phenomena impacts the physical dot gain such as inking heterogeneities caused by the offset print process.

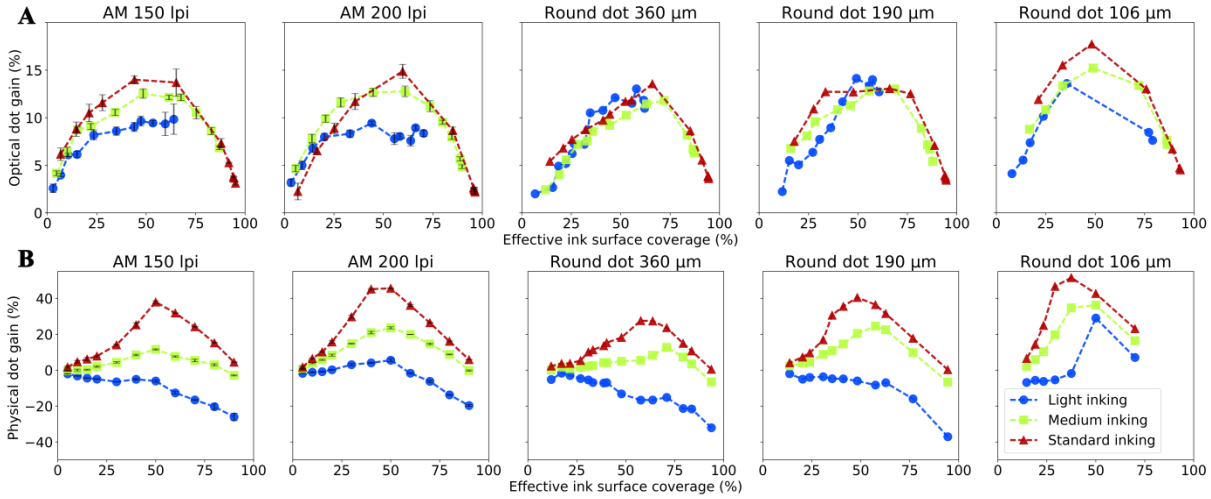

Figure 6.29: Inking, halftone type and halftone size influences on (A) the optical (B) the physical dot gains. The samples are printed with offset applying three level of inking: light inking, medium inking and standard inking.

6.2.4.1 Paper influence

The optical dot gain and physical dot gain for four different papers printed with the exact similar conditions are analyzed, Figure 6.30. This evaluation was performed for halftones printed with electrophotography. It can be observed that the Epson and the uncoated papers are associated with larger optical dot gains that for the glossy coated paper 1 and 2. The optical dot gain is 3/2 smaller for the glossy coated papers. The influence of the optical dot gain on the paper type is visible for all halftone types and sizes. The halftone types and sizes do not appear to influence the optical dot gain shift between the two glossy papers and the Epson and uncoated papers. The ink coverage at which the optical dot gain is maximal also depends on the paper type. The two coated papers have maximum at ink coverages slightly superior to 50%. The Epson and uncoated paper maximum optical dot gains are found around 50% ink coverage. A difference of optical dot gain is visible for the uncoated and the Epson papers for halftones with large dot sizes with the uncoated paper becoming less sensitive to optical dot gain than the Epson paper. The physical dot gain is almost not influenced by the paper type, except for the uncoated paper. The two glossy coated and the Epson papers present smooth surfaces and the ink deposition is less impacted. The uncoated paper is rougher, generating ink deposition defects influencing the physical dot gain levels. It should be noted that this influence is only visible for AM and FM halftones.

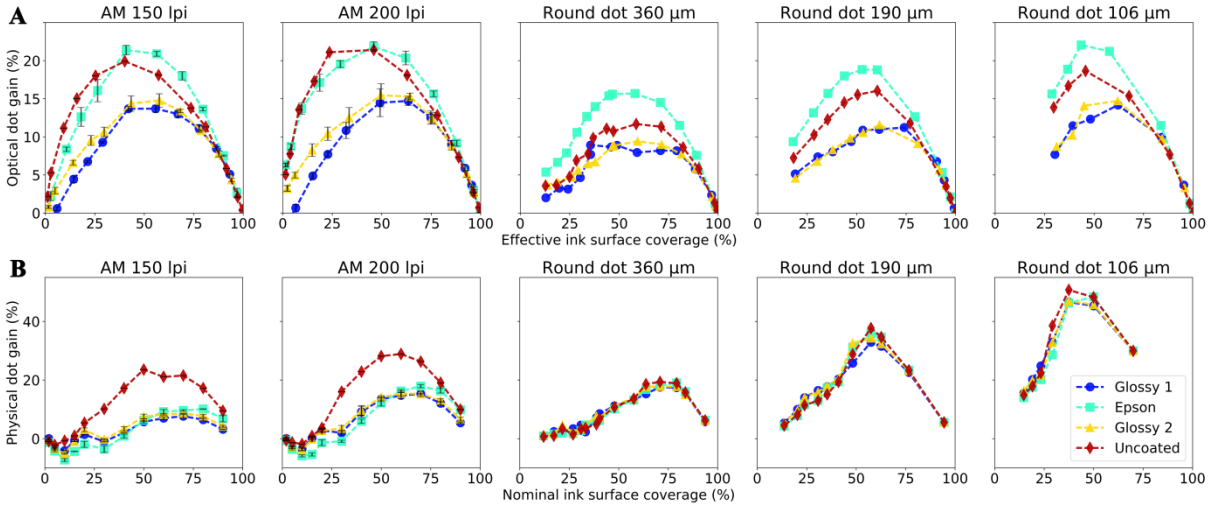

Figure 6.30: Paper, halftone type and halftone size influences on (A) the optical (B) the physical dot gains. The samples are printed with electrophotography on four different papers: a glossy coated paper (Glossy 1 and 2), an Epson proofing paper (Epson) and an uncoated paper (Uncoated).

6.2.4.2 Dot size influence

The dot size influences the optical and physical dot gain, Figure 6.31. The influence is extremely marked for the physical dot gain. This analysis is complementary to the halftone size analysis for which the halftone the dot size depends also on the ink coverage. Halftone dots with constant sizes and variating dot-dot distances are investigated here allowing demonstrating more accurately the impact of the dot size. Smaller dot sizes are impacted with increased optical and physical dot gain. The optical dot gain shape is shifted as a function of the dot size. The physical dot gain shape depends on the size of the dot size with a tendency deforming the shape and pushing the maximum toward larger ink coverages for increasing dot sizes. The dots printed with electrophotography are the most sensitive, especially when the perimeter of the ink – paper interfaces are maximal. Similar tendencies are observed for optical and physical dot gain as a function of the dot size printed with offset and inkjet, presented in appendix, Figure A.4 and Figure A.5.

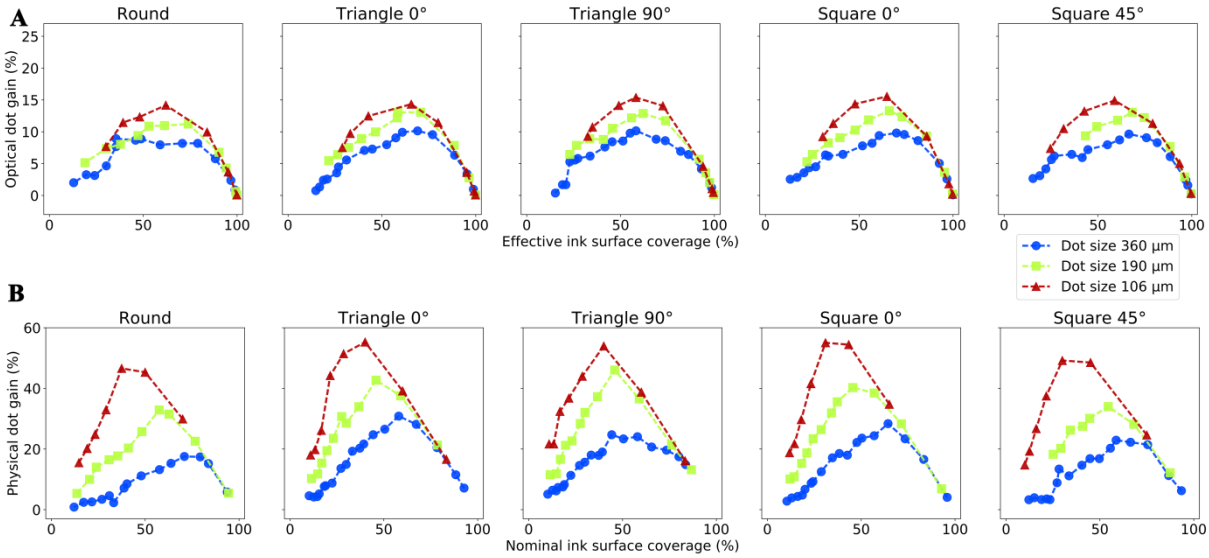

Figure 6.31: Halftone dot size influence on (A) the optical (B) the physical dot gains. The samples are printed with electrophotography. The halftone dot sizes are constant as a function of the ink coverage, the distance between the dots varies.

6.2.4.3 Dot shape influence

Three different dot shapes with different dot orientation angles are analyzed, Figure 6.32. It can be observed that the shape of the dots does not influence the level of optical dot gain. This demonstrates that the effect of the dot perimeter as a function of the dot area does not impact significantly the amount of optical dot gain. This tendency is observed for dots printed with electrophotography, inkjet and offset. With smaller dots similar conclusions are obtained, appendix, Figure A.6 and Figure A.7. The physical dot gain shows a dependency with shape of the dots. This dependency is generated by different levels of ink spreading induced, depending on the shape of the dots. Dots with smaller perimeters as a function of the area are theoretically less sensitive to physical dot gain. This is confirmed experimentally with the small physical dot gains obtained for the circular dots. The square dot with a rotation of 0° presents a medium sensitivity to physical dot gain. Finally the triangle dots at 0° and 90° and the square dots present larger levels of physical dot gain. Similar tendencies are observed for smaller ink dots, appendix, Figure A.6 and Figure A.7.

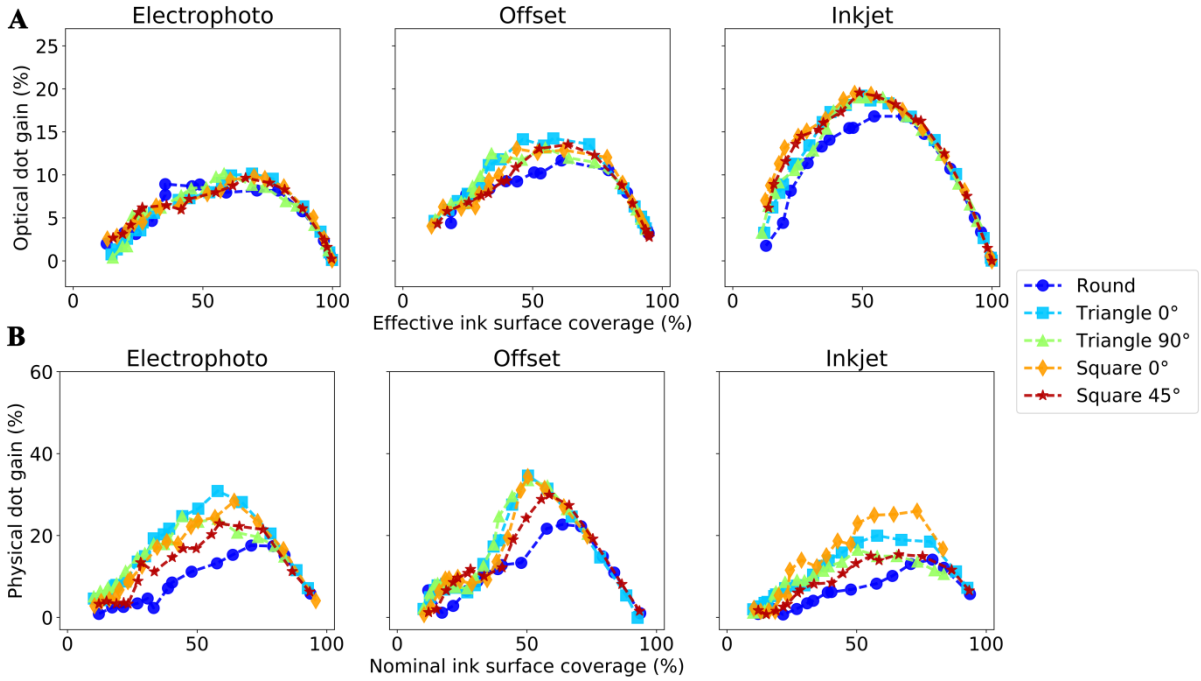

Figure 6.32: Halftone dot shape influence on (A) the optical (B) the physical dot gains. The halftone dot size is fixed at 170 µm for dots printed with offset, 300 µm for dots printed with inkjet and 360 µm for dots printed with electrophotography.

6.2.4.4 Dot-Dot distance influence

The optical dot gain can effect can be studied as a function of the distance between the halftone dots, Figure 6.33. The halftones are then printed with constant halftone sizes and the distance between the dots varies (experiment EP1). The optical and physical dot gains are then plotted as a function of the dot distance, instead of plotting them as a function of the ink coverage. Plotting the optical and physical dot gains as a function of the dot distance provides a novel tool to understand the relation between the dot gains and the ink and paper morphology. The study of the influence of the dot-dot distance is a characterization of the ink morphology as a function of the paper morphology.

For the electrophotography, the offset and the inkjet prints the optical dot gain shows an exponential increase as the effective distance between the dots converges toward 0. Then a more linear decrease is observed with the increase of the effective dot distance. This tendency is caused by the relation of the dot size to the ink region sizes. Around an effective distance of 0 µm numerous small ink and paper regions are generated. The small paper regions present a large light trapping inducing a

strong optical dot gain. It can be observed that the position of the maximal optical dot gain depends also on the halftone dot size with larger optical dot gain obtained for smaller dots. This confirms the influence of the ink and paper morphology on the optical dot gain.

Similar physical dot gain sensitivities are demonstrated with an exponential increase around the 0 µm nominal distance. The maximal physical dot gain depends also on the dot size. The larger dot sizes are associated with smaller maximum physical dot gain levels. This demonstrates that the total perimeter of the printed dots influences the physical dot gain. Near the 0 µm distance, the maximum of ink – paper interfaces appear and therefore a larger interface perimeter appears. Electrophotography generates the largest physical dot gain and a large amount of physical dot gain persists for increasing and decreasing the dot distances. For offset the physical dot gain sensitivity is concentrated around the 0 µm dot distance. For inkjet, the sensitivity of the physical dot gain to the dot distance is smaller and the sensitivity is more spread to small and large dot-dot distances.

Analyzing the influence of the dot-dot distance on the sensitivity of optical and physical dot gain can help produce halftone configurations that are less sensitive to optical and physical dot gain by variating accordingly the dot size and the dot-dot distance. Moreover a different approach can be focused on tuning the halftone dots to induce large optical dot gains and in this way produce print with similar reflectance characteristics while reducing the ink quantity deposited. This could potentially allow producing more cost effective prints and help the deinking. A further application beneficiating from the control of the optical and physical dot gain are the printed anti-counterfeiting applications. Generating a controlled optical dot gain allows improving the level of security; copies reproducing the reflectances measured using more ink than the original. A tuning of the ink spreading can also help to control the amount of physical ink dot spreading and improve the robustness of the security solution.

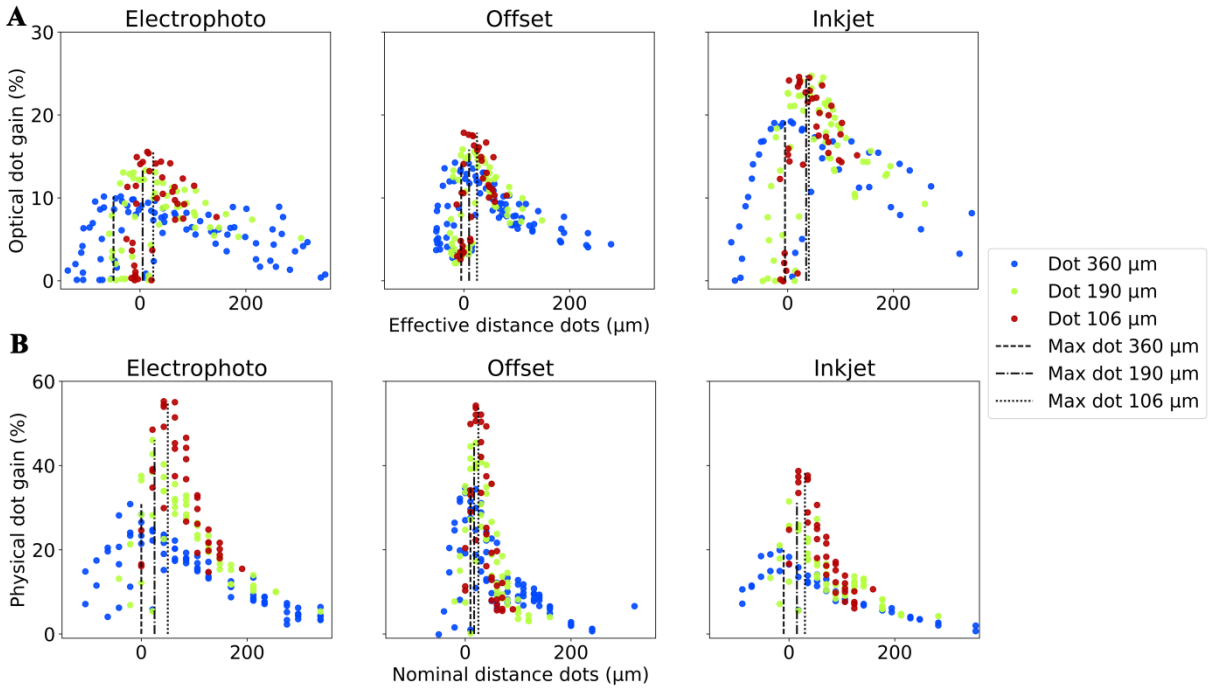

Figure 6.33: Effective and nominal distance between dots influence on (A) the optical (B) the physical dot gains.

6.2.4.5 Dot perimeter influence

By assessing the influence of the dot perimeter on the optical dot gain, it is possible to evaluate if the optical dot gain occurs mostly around the edges of the printed dots. A specific experiment, called EP2, was designed where ink dots with different perimeters and a constant area were generated. Large ink dots were adopted for this generation in order to limit the dots distortion effects due to printing

(altering the dot perimeter and area). The results are plotted as a function of circularity quantifying the length of the perimeter as a function of the area, Figure 6.34. A circularity of 1 corresponds to a minimization of the perimeter compared to the area. Larger circularities are associated with longer perimeter lengths as a function of the area. The optical dot gain is demonstrated to be almost not influenced by the circularity of the dots. No clear tendencies are observed of the optical dot gain variations as a function of the circularity. This shows that the perimeter is not the most influencing parameter on the optical dot gain. The optical dot gain is therefore influenced by other characteristics such as the dot-dot distances. The dispersion of the optical dot gains are larger dot electrophotography and inkjet compared to offset. It should be noted that the circularity was measured on the nominal ink dots. However, a deformation is induced by the printer and the effective circularity of the printed dots differs. Since the printed dots are large this effect should be small. The results could nevertheless be improved by characterizing the effective circularity. This requires to identify each dot and to measure the effective area and perimeters of the dots.

The physical dot gain demonstrates variations associated with the dot circularity. The physical dot gain increases with the increase of circularity. The length of the perimeter as a function of the area influences then the level of ink spreading. This confirms the previous observations that the physical dot gain is impacted by the length of the perimeters of the ink regions. With larger ink paper interfaces, a larger spreading can effectively occur. The increase of physical dot gain is globally linear for the 3 print processes as a function of the circularity. The ratio of physical dot gain increase is found to be dependent on the print process. Electrophotography is associated with the largest dependency of the physical dot gain with the dot circularity. Offset and inkjet ratio are almost similar, however the levels of physical dot gain differ. The offset prints are impacted by more physical dot gain. It can be concluded that the perimeter lengths of the dots as a function of the dot area does not impact significantly the level of optical dot gain. On the contrary a linear dependency of the dot circularity with the level of physical dot gain is observed. This effect can also be used to control and improve the level of security of printed solutions to fight against counterfeits.

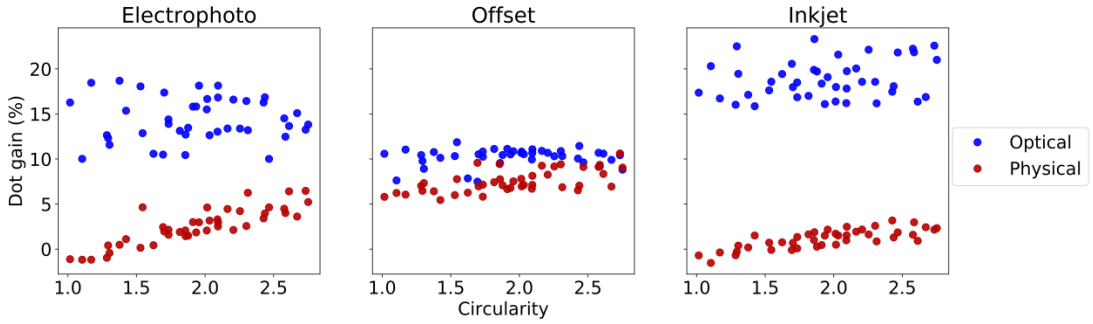

Figure 6.34: Circularity (ratio of dot perimeter and area) influence on (A) the optical (B) the physical dot gains.

6.2.5 Conclusion

Two novel threshold algorithms based on the properties of printed halftones and developed specifically to process halftone dots were proposed. The first threshold algorithm proposed, called the LveShape is based on the position of the ink peak on the histogram of the halftone. A M factor was computed by fitting the halftone and the solid ink peaks with Gaussian functions and by finding the center of the Gaussian curves. The threshold value of the solid ink patch could be stretched with the M factor to define the best threshold position for the halftone patch. The second threshold algorithm proposed is based on the model of the light diffusion on halftones. By adopting the approximation that the square root of the spatial halftone reflectance is equivalent to the spatial ink transmittance, the spatial representation of the optical dot gain effect could be approximated and partially removed from the halftone. Thresholding the pre-treated halftone is then performed by applying a constant threshold level set for the solid ink halftone. For the two threshold algorithms proposed, a theoretical approach

to define the threshold value for the solid ink was explored. Results showed that the best threshold value for the solid ink was dependent on the ink transmittance level. A linear function to link the solid ink threshold value to the ink transmittance was proposed and fitted empirically.

The two threshold algorithms developed were then evaluated and compared to the PalBhandari and the Li threshold algorithms. Results showed that the LveSpatial threshold algorithm was performing better than the PalBhandari and Li threshold algorithms. Excluding the extreme ink coverages (below 10% and above 90%) a mean absolute binary fidelity ratio of 99.07% was reached and could be compared to the 98.12% obtained for the PalBhandari algorithm and 98.12% obtained for the Li algorithm. The dispersion of the absolute binary fidelity ratio is smaller for the LveSpatial with 1.44% compared to respectively 2.02% and 1.96%. Analyzing the performances for the halftones obtained from thresholded MCI showed that the LveSpatial was not dependent on the ink coverage. The PalBhandari and Li Threshold algorithms were associated with larger variations as a function of the ink coverage. For the halftones obtained from thresholded MCI, the LveSpatial reached a mean absolute ICD of 0.21% +/- 0.33% for all ink coverages. This performance can be compared to the PalBhandari and Li thresholds algorithms reaching 0.79% +/- 0.79% and 0.79% +/- 0.74% in the reduced ink coverage range of 10% to 90%.

The LveShape threshold algorithm reached a global performance inferior to the PalBhandari and Li threshold algorithms. 24.6% of the halftones thresholded with the LveShape threshold algorithm obtained a binary fidelity ratio below 90%. Aside from these cases the LveShape threshold algorithm performed well, with a mean binary fidelity ratio of 98.14% +/- 1.86% and could be compared to the PalBhandari and Li Threshold algorithm having a binary fidelity ratio of 98.12% +/- 2.02% and 98.12% +/- 1.96%. The LveShape follows a similar dependency with the ink coverage compared to the PalBhandari and the Li thresholds. The LveShape, PalBhandari and Li threshold algorithms globally under threshold the halftones resulting to smaller ink coverages obtained compared to the ground truth.

The dependency to the halftone resolution, ink reflectance, paper PSF, ink homogeneity and edge fuzziness was analyzed. It was found that an increase of halftone resolution decreased the performances of the two threshold algorithms proposed. An increase of the ink transmittance produced an increase of the performances of the two threshold algorithms proposed. The increase of the paper PSF size, produced a decrease of the performances for the LveShape and produced an increase followed by a decrease for the LveSpatial threshold algorithm. The increase of ink heterogeneities and edges fuzziness decreased the performances of the two threshold algorithms proposed. Globally the LveSpatial threshold algorithm was found to be less sensitive to the halftone resolution, ink reflectance, paper PSF, ink homogeneity and edge fuzziness compared to the PalBhandari and Li threshold algorithms.

An extended analysis of the LveSpatial threshold algorithm revealed that the best optimized threshold value was slighly dependent on the ink coverage. This dependency appears to be linear and thus could be easily modeleld to improve the performance of the LveSpatial threshold algorithm. The LveShape threshold algorithm could be improved by taking into consideration the ink transmittance dependency with the ink coverage.

Finally a study of the optical and physical dot gain was proposed. The print characteristics influencing the most the optical dot gain were then the paper type and the dot-dot distance. The print process, the halftone size, the inks and inking and the dot size influenced only slightly the optical dot gain. The halftone type, the dot shape and the dot perimeter had a very limited effect on optical dot gain. The influence of the print parameters differed on the physical dot gain. The physical dot gain was extremely influenced by the halftone size, the inking quantity, the dot size and the dot-dot distance. The print process, halftone type, dot shape and dot perimeter influenced only slightly the physical dot gain. Finally the ink type and the paper type (with similar surface roughness) were found to have a very limited effect on the physical dot gain.

Chapter 7 Raster to print halftone models

Louis Vallat-Evrard, Lionel Chagas, Raphaël Passas, Nadège Reverdy-Bruas
Univ. Grenoble Alpes, CNRS, Grenoble INP*, LGP2, F-38000 Grenoble, France
Agefpi, LGP2, F-38000 Grenoble, France

With the improvement and automation of the measurement methods of the print at the microscale, it becomes possible to measure a large amount of printed dots [17–19,21,28]. These measurements allow then understanding the relations between the binary image sent to the printer and the effective ink coverages obtained. Models can be developed based on the characterization of the printed dot deformations and of the dot-dot interactions. At the same time, the microscale description of the ink and paper regions of the halftone print leads to a more accurate analysis of the ink, paper and light interactions. A more accurate analysis allows, in fine, obtaining more accurate models yielding to an improved prediction of the reflectance of halftones as a function of the print parameters and as a function of the description of the ink setting on the paper surface. These physical ink coverage and optical dot gain models allow then obtaining models describing the halftone from raster to visual perception. The print parameters can be precisely tuned in order to take advantage of the physical and optical do gains, in order to reduce the ink consumption, to create special visual effects and to improve the performances of the anti-counterfeiting printed solutions (better control and prediction of the print deformations leading to produce more robust micro-barcodes, better measurement through a better understanding of the optical distortions) [26,208,209].

7.1 Single ink dot model and dot-dot interactions

7.1.1 Physical dot gain models

Researches have been conducted to model the halftone dots at the microscale. It is interesting to notice that the development of models to simulate the printed dot shapes were often associated with other purposes than to understand to the printer deformation. Murray-Davies were the first to model the halftone dots at the microscale [2]. They modelled the dot using a perfect disc and used the model to obtain the ink coverage of the dot as a function of the measured dot diameter. Later Pappas proposed to re-employ the perfect disc model, called in their work the circular dot-overlap model, in order to improve the halftoning algorithms [385,386]. The dots were modelled by overlapping discs and accounting then for the printer distortions. The overlapping of the discs resulted in different colorant coverages and positions. Several other studies modelled the halftone dots with perfect discs [191,373,387–392]. Kriss proposed to model halftone dots using a dispersion of ink particles using a Poisson distribution noise on the edges of the dots [393]. Norris and Smith proposed a similar approach where the halftone dots were modelled by the generation of ink particles with a probabilistic distribution taking into account the number of ink particles and their diameters [394]. The ink spreading is a direct consequence of the printed dot deformations induced by the printer. Emmel and Hersch proposed to determine the influence of the halftone dot configuration on the ink spreading [361,395]. Namedanian and Nyström proposed to study the influence of the halftone dot shape in relation with the printer deformation [396]. Nguyen [24,26,27] worked on the development of a statistical model to simulate the shape of the ink dot at microscopic scale. Microdots were analyzed and parameters determined through maximum likelihood estimation and with Bayesian interference. The effect of the dot clustering on the dot shape was

studied by analyzing the average of more than 100 measurements of 14 different dot patterns. More information on Nguyen's work was provided in chapter 2. The dot misplacement was also studied in order to improve the printer models [397]. The influence of the measurement on the captured shape of the halftone dot was also analyzed [398]. Halftone dot deformations were used by researchers in order to obtain the signature of the printer [399,400]. Printed dots were measured and modelled to provide identification and authentication for anti-counterfeiting applications. Wu proposed to authenticate a printer based on the halftone dot arrangement [401]. A difficulty encountered to measure and model halftone dots at the microscale are the random print variations occurring. Therefore, to conduct a reliable analysis, several dots require to be measured and averaged. Measuring several dots for different configurations was proven to be a difficult task [402,403].

In this work the goal is to analyze halftone dots, in order to understand the deformations induced by the printer. The influences of the dot-dot interactions on the physical dot gain can then be characterized. The development of an automated measurement algorithm yielded to the creation of a large database of halftone dots printed at several sizes (several binning) and with several print processes. The database is composed of 43269 codes with up to 10 redundancies per halftone dots. A model simulating the single dots is proposed. Halftone dots composed of multiple simulated single dots are then generated and are compared to the printed halftone dots.

7.1.2 Materials and methods

7.1.2.1 Test form, printed samples and acquisition

To evaluate the dot deformations induced by the printer and the dot-dot interactions, specific test forms are developed. The test forms are composed of large arrays with stitched codes, Figure 7.1. A code is composed of a matrix of 3 pixels by 3 pixels at the center, of a margin of 4 pixels of white pixels around and of an array border of 1 black pixel. By generating all the inking configurations of the 3 by 3 matrix, 512 codes are obtained. The interactions between printed pixels (i.e. ink dots) can then be studied. The shape of the printed dots varies due to a constant and to a random deformation. For this reason the 512 inking configurations are reproduced multiple times. The array allows retrieving the location of each code after printing. These arrays are produced at the native resolution of the printer with different levels of binning. A code designed for the offset print, at the resolution of 2540 dpi with a binning of 1 will have an effective resolution of 2540 lpi and will therefore measure 130 µm. A similar code with a binning of 2 will have an effective resolution of 1270 lpi and will therefore measure 260 µm, Figure 7.1. In the case of a binning of 2, all pixels at the effective resolution will be composed of 4 pixels (2 by 2 pixels) at the native resolution of the printer. The arrays of codes are printed with three different processes: offset, inkjet and electrophotography. The characteristics of the print processes and of the paper used are summarized in Table 7.1.

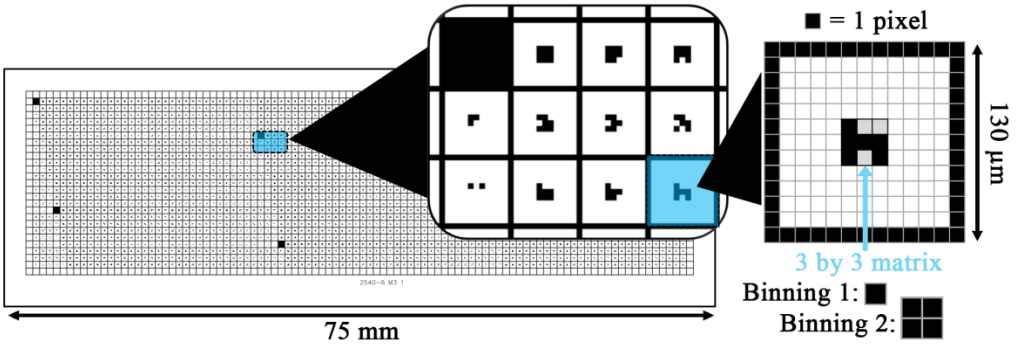

Figure 7.1: Test form with 3 by 3 matrix. Each matrix is placed in a patch having white margins and black borders. Codes are stitched together in a large array corresponding to the size of a microscope slide.

A Zeiss Axio Imager M1m optical microscope mounted with 3 EC Epiplan Neofluar HD DIC objectives (5x/0.13, 10x/0.25 and 20x/0.50) is used to image the codes with a Canon 1200D camera

(RGGB, CMOS, 17.9 megapixels). Total magnification on sensor is 5x, 10x and alternatively 20x with a physical pixel size on sensor of 4.21 µm/pixel. The calibrated system captures images of 0.8404 µm/pixel for the 5x objective, 0.4202 µm/pixel for the 10x objective and 0.2101 µm/pixel for the 20x objective. Crossed analyzer-polarizer (90°) reflected light microscopy with a 0°/0° geometry is chosen to capture images excluding the specular reflections. A halogen lamp Zeiss Hal 100 is used as light source for the microscope with a blue filter giving a spectrum similar to the standard D65 illuminant. The source voltage is regulated and set at 10.0V. The source luminance variations are recorded with a luxmeter placed on the side of the light path and images captured are corrected accordingly. The iso of the camera is set at 800 and exposure times are selected to optimize the dynamic range of the capture. The exposure time is optimized for each objective of the microscope, for each ink and for each paper. The exposure time is nevertheless kept constant for the measurement of each set of codes. Images are saved in raw .CR2 format and processed with Python 3.6 to perform black frame subtraction and to correct the uniformity of the field of view.

Table 7.1: Print processes characteristics, paper and inks. Objectives used on the microscope.

Process	Paper (g/m²)	Ink (Black)	Binning	3 by 3 matrix size (µm)	Microscope objective	Number of codes measured
Offset: Heidelberg Speedmaster 52, 2540 dpi	Glossy 1: Unknown supplier, coated, 135	Novavit 918 supreme	2	60	20x	5274
			3	90	10x	5290
			4	120	10x	5199
			6	180	5x	2136
			8	240	5x	1060
Electrophotography: Xerox Versant 180 Press, 1200 dpi		Xerox Versant 80 Press	2	127	10x	5068
			3	191	5x	2184
			4	254	5x	1067
Inkjet: Epson Stylus Pro 4900, 1440 dpi	Epson: Epson proofing, coated 205	Epson MK T6538	1	53	20x	5971
			2	106	10x	5259
			3	159	5x	3148
			4	212	5x	1613

An automated measurement is developed to facilitate the capture of a large number of printed codes. The automation is based on two algorithms: an autofocus and an image recognition and positioning of the sample.

- The autofocus is used to find the best focus altitude by moving the Z stage of the microscope and at the same time by capturing images. The images are processed to compute a focus index. An optimization by dichotomy is proposed to find the altitude giving the best focus. Verifications were performed to ensure that the focus index as a function of the Z stage position had a bell shape, in such way that the maximum could be accurately determined by dichotomy. The starting step and stopping step defining the initial and final offset movement of the Z stage for the dichotomy are tuned. The focus indicator is calculated from the "LiveView" images by converting them to grayscale and by cropping them to a smaller image called to the region of interest. Restraining to a region of interest allows obtaining a more precise autofocus for images where the surface of the sample is rougher than the optical depth of field. A double convolution is then applied to the image with two modified Laplacian operators, one in the X direction and one in the Y direction, re-implementing the method developed by Nayar and Nakagawa [350]. The focus index is then computed from the result of the convolution and from the standard deviation of the pixel values of the captured image. More information on the focus algorithm is given in Chapter 2.
- The image recognition and positioning of the sample is used to move the microscope stage in the X-Y plane and center the codes on the microscope. It allows measuring, mapping and registering precisely each dot in the array. The function was developed to detect the edges of the array surrounding the halftone dots, Figure 7.1. A median blur filter and a box blur filter were first applied to the "LiveView" image. The detection algorithm computes then the sum of the black

pixels in the X and Y directions after a threshold using the mean method. By plotting the sum of the pixels as a function of the position on the axis, peaks appear around the edges of the array containing the 3 by 3 matrixes. A simple detection of the centers of the peaks yields to a set of coordinates giving the position of the edges of the array. Multiple conditions are checked in order to circumvent potential defects in the image (dust particles, incomplete printing and print margins). Four different centering locations were proposed in relation to the array including the halftone dots: the intersection of a column edge of the array and a line, the center of the array line, the center of the array column and the center of a code. A X-Y displacement can then be computed by subtracting the center of the camera frame with the measured center position. The X-Y displacements are converted into microscope stage displacement quantities as a function of the objective magnification and a displacement commands are sent to the microscope. Usually several codes are captured on a single image. The number of images to capture in the X and Y directions and the steps between the images (number of codes to shift) are specified by the experimenter.

The automation of the measurement allowed measuring 43269 codes in a short period of time (several weeks). The capture speed was measured at 32 seconds per image including the stage movement, centering, the autofocus optimization and the image capture.

7.1.2.2 Dots measurements

From the images captured, the image recognition and positioning algorithm is re-implemented in order to obtain the positions of the edges of the codes. The number of codes per row and columns of the array imaged are specified by the experimenter. The codes can then be registered, split and cropped accurately. Each code is saved independently and identified with the original code sent to the printer (binary image sent to the printer). The printed codes are then thresholded using the Otsu threshold algorithm, [168].

Single dots can designate different quantities depending on the definition adopted. It can either be the smallest controlled ink deposition (one pixel at the printer native resolution), or it can be the smallest dot printed at a defined resolution (one pixel with a binning of n times the native resolution of the printer, or it can also be the size of the unitary ink components (toner, inkjet drop, or offset pigment). For this study, the single dots designate the smallest dot printed at a defined resolution and correspond to 1 or multiple nominal dots (at the nominal resolution of the printer). The single dots correspond for this study to codes with only one location of the 3 by 3 matrix printed. The nominal dots refer to the printing of 1 pixel at the resolution of the printer. The nominal dots are considered to be composed of ink particles. The original and printed codes can then be compared using several indexes:

- The registration of the printed code is given by the variation of the code image size (size between edges of the array). Since the codes are registered and split according to the image recognition and positioning algorithm, positioning and cropping errors generates a variation of the image size of the code. The code dimensions in the X and Y direction are then compared to the original code dimensions. The printed codes are converted in micrometers by multiplying with the imaging resolution (for example 0.2101 µm/pixel for images with the 20x objective). The original codes are given at the printer's resolution and are converted in micrometers by multiplication with the printer nominal dot size (10.0000 µm/pixel for offset, 21.167 µm/pixel for electrophotography and 17.639 µm/pixel for inkjet).
- For codes with a single dot, shape descriptors [185,186] are proposed to quantify the dot shape and the edges roughness, equations [7.1]. The shape descriptors are computed with the OpenCV connected component function, used to individualize the dots and to obtain a measurement of their area. The OpenCV find contours function was used to identify the edges of the dots and to compute their perimeters. The OpenCV convex hull function was used to compute the convex perimeter and the convex area. The OpenCV fit ellipse function was used to find the major and minor axis and angle

of the ellipse fitting the dots. Four shape descriptors based on the ISO 9276-6 were considered. The solidity describes the degree to which the area of the dot is closed (i.e. composed of only convex surfaces). The dot is the most closed when the solidity converges toward 1. The fitted ellipse major and minor axis lengths were called Feret diameters and were used to compute the aspect ratio. Using major and minor axis from the ellipse fit differs from the exact definition of the Feret diameters. Nevertheless the ellipse fitting method was found more effective for printed dots. The aspect ratio describes the shape of the particle. An aspect ratio converging to 1 signifies that the particle is iso-dimensional. The convexity describes the roughness of the edges of the particle. High roughness is associated with a convexity converging toward 0. The circularity describes the degree to which a dot is close to a disc. The circularity is directly linked to the particle roughness and has to be analyzed in conjunction with it. When the circularity is close to 1, the dot shape is close to a disc with smooth edges.

- The OpenCV connected component function outputs also the position of the center of gravity of the particle. The position of this center is used in order to quantify the single dot placement error. The position of the center of the dot on the original code is compared to the position of the center of the dot on the printed code. A vector linking the centers of the original dot and the printed dot is set and the norm of the vector associated with the direction of the vector is computed. The angle is defined with the 0° reference at the 6 O'clock of the code. Clockwise rotation is defined by a positive angle.
- A similarity index to compare dots is proposed based on a modified exclusive disjunction logical operation (XOR). Over and under inking ratios are computed by counting the number of pixels that were respectively added and missing on the printed code compared to the original code. A ratio called the binary fidelity ratio (FD) is then expressed by the modulus of the difference of the over inked pixels and the under inked pixels relatively to the surface coverage of the original code, equations [7.2] and [7.3].

Shape descriptors

		Symbol	Unit	Denomination
[7.1]	$\text{Solidity} = \frac{A}{A_c}$	A	μm^2	Area
	$\text{Aspect ratio} = \frac{D_{min}}{D_{max}}$	A_c	μm^2	Convex area
	$\text{Convexity} = \frac{P_c}{P}$	P	μm	Perimeter
	$\text{Circularity} = \sqrt{\frac{4\pi A}{P^2}}$	P_c	μm	Convex perimeter
		$D_{min,max}$	μm	Feret diameters

Binary fidelity index – Printed & original code

		Symbol	Unit	Denomination
[7.2]	$FD_1 = \begin{cases} FD_1 & \text{if } FD_1 > 0 \\ 0 & \text{else} \end{cases}$	FD_1	1	Binary fidelity index 1
	$FD_1 = \left(1 - \frac{\lvert \sum_x \sum_y O(x,y) - \sum_x \sum_y U(x,y) \rvert}{\sum_x \sum_y IM_{or}(x,y)}\right)$	$IM_{pr}(x,y)$	1	Printed code image
		$IM_{or}(x,y)$	1	Original code image
	$O(x,y)=1$ where $IM_{pr}(x,y)<IM_{or}(x,y)$	$O(x,y)$	1	Over inked region
	$U(x,y)=1$ where $IM_{pr}(x,y)>IM_{or}(x,y)$	$U(x,y)$	1	Under inked region

To compare the shape descriptor indexes and the morphological characteristics of the codes a relative mean index difference is computed, equation [7.4]. The mean index difference allows a dimensionless comparison between different indexes (area and circularity for example). The mean index difference is expressed by a percentage of increase or decrease of an index compared to the

reference index. For example if the area on the printed dots measures 1.5 times the area of the original code, the mean index difference would be equal to +50%.

Binary fidelity index – Simulated & printed code

[7.3]

$$FD_2 = \begin{cases} FD_2 & \text{if} \quad FD_2 > 0 \\ 0 & \text{else} \end{cases}$$

$$FD_2 = \left(1 - \frac{|\sum_x \sum_y O(x,y) - \sum_x \sum_y U(x,y)|}{\sum_x \sum_y IM_{pr}(x,y)}\right)$$

$$O(x,y) = 1 \quad \text{where } IM_{si}(x,y) < IM_{pr}(x,y)$$

$$U(x,y) = 1 \quad \text{where } IM_{si}(x,y) > IM_{pr}(x,y)$$

Symbol	Unit	Denomination
FD_2	1	Binary fidelity index 2
$IM_{si}(x,y)$	1	Simulated code image
$IM_{pr}(x,y)$	1	Printed code image
$O(x,y)$	1	Over inked region
$U(x,y)$	1	Under inked region

Relative mean index differences

[7.4]

$$Q_{r1} = \left(\frac{Q_{pr}}{Q_{or}} - 1\right)$$

$$Q_{r2} = \left(\frac{Q_{is}}{Q_{pr}} - 1\right)$$

Symbol	Unit	Denomination
Q_{r1}, Q_{r2}	1	Relative mean index difference 1 and 2
Q_{pr}	1	Printed code index
Q_{is}	1	Simulated code index
Q_{or}	1	Original code index

7.1.3 Single dot measurements

The inkjet process is the only process tested allowing a reproduction of codes at the native resolution of the printer. For electrophotography and offset the codes printed at the native resolution of the printer cannot be used since the edges of the array are extremely rough and overlap with the printed dots of the 3 by 3 matrix, Figure 7.2. The visual comparison of the three processes at the native resolution of the printer shows the differences of the "ink particles" of the single dots (i.e. toner particles, ink droplet, etc.). For inkjet and electrophotography the ink particles are well defined. Ink particles are not visible for the offset process. In the case of electrophotography the ink particles correspond to the size of the toner particles deposited and melted on the surface of the paper. In the case of inkjet it corresponds to the size of a single droplet. Nevertheless differences appear between electrophotography and inkjet. In the case of electrophotography a single toner particle cannot be addressed by the printer and a single dot is composed of multiple toner particles. In the case of inkjet each droplet can be addressed and a single dot results in a single droplet deposited on paper. For offset, small filaments appear resulting from the ink layer separation during its transfer and from physico-chemical interactions.

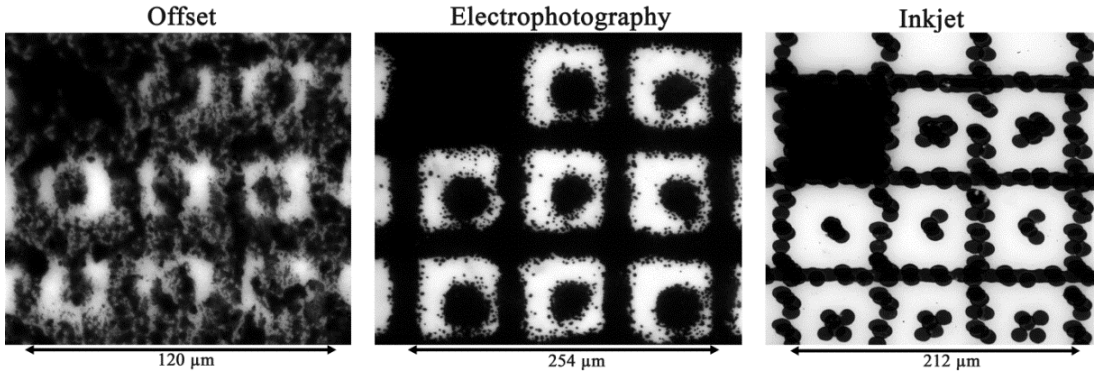

Figure 7.2: Comparison of an array of codes with 3 different processes: offset, electrophotography and inkjet at the nominal resolution of the printer.

7.1.3.1 Effect of the single dot position on the 3 by 3 matrix

84 single dots printed with electrophotography at 600 lpi (printer native resolution of 1200 dpi with a binning of 2) were measured and analyzed. The single dots were printed at different locations in order to investigate effects of the position on the matrix. Five printed dots and the superpositions with the original dots are presented in Figure 7.3.

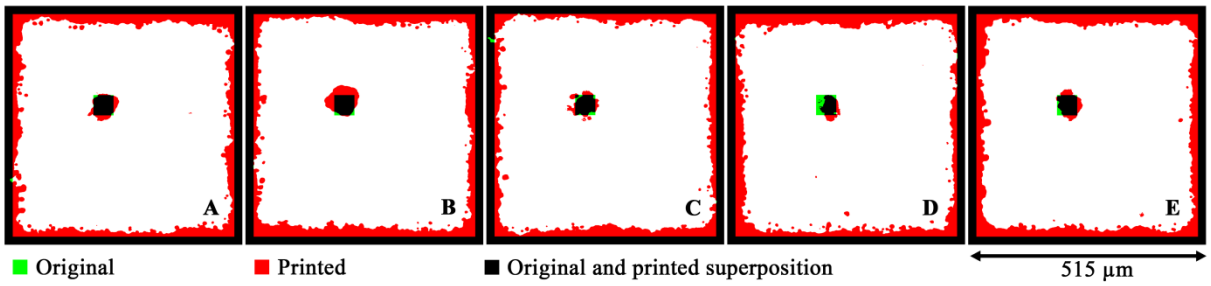

Figure 7.3: Superposition of single dot codes: original and printed with electrophotography, located at [-1, -1] on the [y,x] 3 by 3 matrix with binning of 2. Five measured codes (A, B, C, D, E).

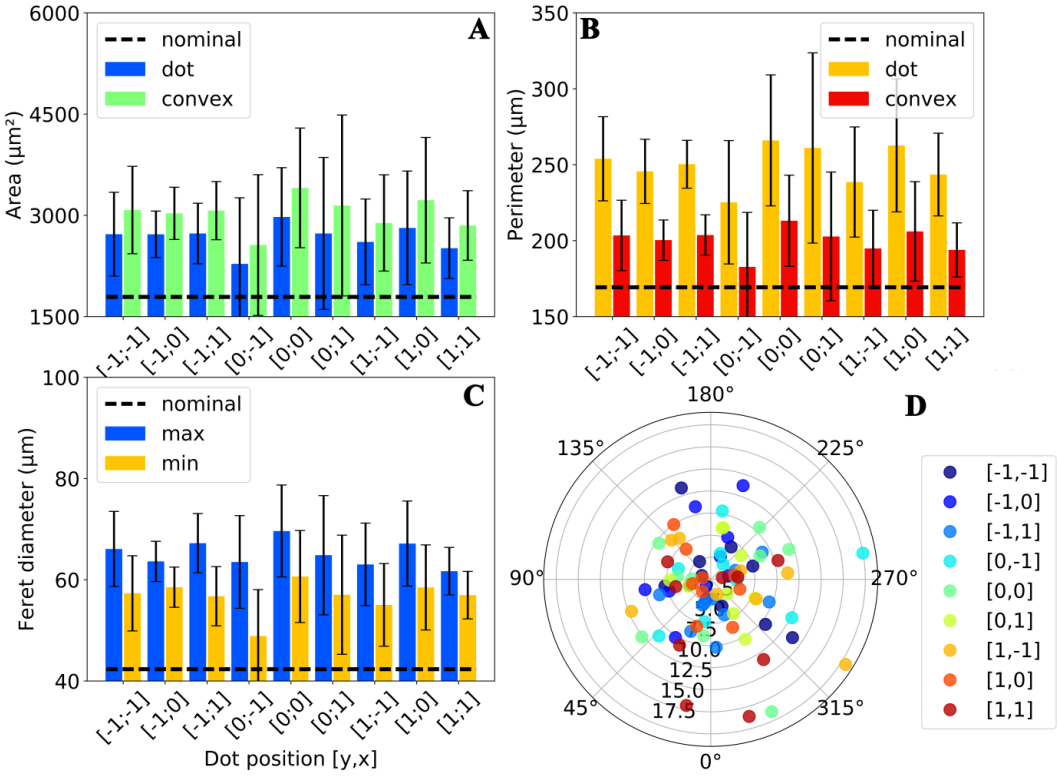

Figure 7.4: Areas (A), perimeters (B), Feret diameters (C) and positioning errors in µm (D) for 84 single dots with a binning of 2 printed in electrophotography at 1200 dpi. Nominal values obtained from original codes. [y,x] corresponds to the single dot position on the 3 by 3 matrix.

The printed dot area measured is larger than the area of the original dots for all positions, Figure 7.4 (A). The average area measured is obtained at 2679 µm² with a coefficient of variation of 26.3% and can be compared to the theoretical area of 1792 µm². There is no significant dot position influence on the 3 by 3 matrix with a variation of the average at each position of 7.3%. This coefficient of variation is smaller than the global coefficient of variation and thus confirms the independency of the dot position on the dot area. Variations observed for all positions show the sensitivity of the print process, Figure 7.3. The convex area follows globally a similar tendency with an average of 3029 µm² and a coefficient of variation of 26.3%. No significant influence from the dot position is observed with a coefficient of variation between the averages at each position of 8.0%. The analysis of the dot perimeter and convex perimeter yields to similar conclusions, Figure 7.4 (B). The average perimeter is

measured at 250 µm with a coefficient of variation of 14.9%. The coefficient of variation dots at different positions reaches 5.2%. For the convex perimeter, the average is found at 200 µm with a global coefficient of variation of 13.5% and a coefficient of variation between the dot positions of 4.3%. It can be concluded that the dot position has almost no influence on the dot perimeter and convex perimeters. Both perimeters are found larger than the perimeter of the original dot reaching 169 µm, Figure 7.3. No dependencies of the Feret diameters with the dot position are observed with a maximum diameter average of 65 µm with a global coefficient of variation of 12.0% and a coefficient of variation between each dot position of 3.9%, Figure 7.4 (C). The minimum diameter average is equal to 57 µm with a global coefficient of variation of 16.9% and a coefficient of variation between each dot position of 5.8%. The Feret diameter of the original dot is found at 42.3 µm and is smaller than the printed dot as expected due to physical dot gain. The dot positioning errors are compared for each position on the 3 by 3 matrix, Figure 7.4 (D). No clear tendencies are observed for position errors distances and angles and show that the printed position does not influence the positioning error of the printed dot. A position error length average of 6.0 µm with a global coefficient of variation of 62.6% and a coefficient of variation between each dot position of 24.8% is obtained. The mean position error length corresponds to $1/10^{th}$ of the printed dot diameter and to $1/4^{th}$ of the original dot diameter and can be considered small. Since the single dot position does not influence the indexes, an averaging over all positions over the 3 by 3 matrix is adopted

7.1.3.2 Electrophotography

The characterization of the single dots morphology for several levels of binning is then proposed. The dimensions of the array containing the printed single dot are similar to the nominal values with a difference of respectively +1.3%, +1.5% and +1.5% for the binning of 2, 3 and 4, for the Y dimension of the code. For the X dimensions differences of +1.3%, +1.7% and +1.7% are respectively found. As a matter of fact, since the center of each code is obtained by taking the middle of the edge of the array, an iso-dimensional increase of the border line width when printing would not affect the position of the center. Small coefficients of variation of 0.3%, 0.2% and 0.2% for the for the binning of 2, 3 and 4, for the Y dimension of the code and 0.6%, 0.5% and 0.4% for the X dimension of the code are found. Thus, it can be concluded that for electrophotography the printed codes are well registered with accurate dimensions and small variations, insuring a valid measurement of the single dots inside the array. It has to be noted that a slight decrease of the coefficient of variation is observed when decreasing the apparent resolution of the code. This effect is coherent with the decrease of magnification used to image the codes. For codes printed with a binning of 2, the 10x objective was used and for the binning of 3 and of 4 the 5x objective was used. A larger magnification results in more accurate measurements and to larger size variations.

Both the area and convex area of the single dots are dependent on the effective resolution of the printer. The area increase compared to the original dots represents +49% for a binning of 2, +174% for a binning of 3 and +218% for a binning of 4. The convex area follows a similar tendency with an increase of respectively +69%, +209% and +261%. These increases are unexpected since larger dot sizes should be reproduced more accurately by the printer (higher number of nominal dots to print the effective dot). By considering a dot size increase of 30%, the nominal dots located on the edge of the single dot increase the single dot area by 32% for a binning of 2, 21% for a binning of 3 and 16% for a binning of 4. The physical dot gain induced by electrophotography depends then on the size of the single dots [4] and can be attributed to the process control characteristics [404]. The mean relative differences of perimeters, convex perimeters and Feret diameters compared to the original dots show also an increase with the decrease of the effective resolution. Increases of 47%, 110% and 150% are found for the perimeters for the binning 2, 3, and 4 respectively. The increases found for the convex perimeters are obtained at respectively 18%, 59% and 72%. The ratios obtained for the Feret maximum diameter are found at respectively 54%, 102% and 113% and respectively 34%, 87% and

102% for the Feret minimum diameter. These results are the direct consequence of the area increases as a function of the effective printer resolution.

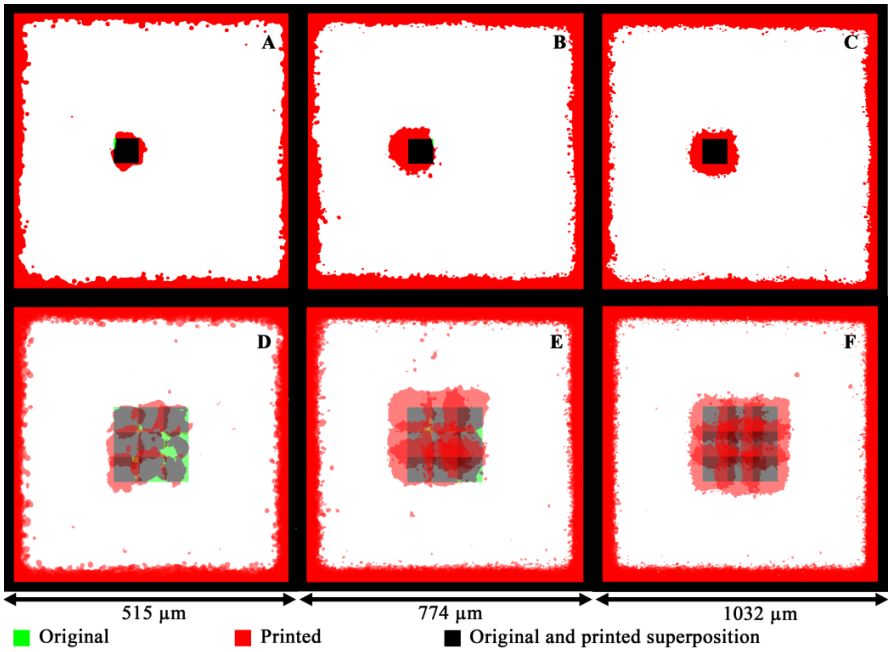

Figure 7.5: Superposition of single dot codes: original and printed with electrophotography, located at [0, 0] on the [y,x] 3 by 3 matrix with binning of 2 (A), 3 (B) and 4 (C). Superposition and stitching of single dot codes at each location on the 3 by 3 matrix with binning of 2 (D), 3 (E) and 4 (F).

The mean aspect ratio increases toward 1 with respectively 0.87, 0.93 and 0.95 for the binning of 2, 3 and 4. This shows that the increase of apparent resolution tends to improve the reproduction of the original dot shape as confirmed on Figure 7.5. With the increase of binning, the single dots are closer to the original squared dot inputted to the printer. With the increase of binning more nominal dots are used to represent the single dot and thus the shape can be more closely reproduced. The solidity index is kept constant as a function of the amount of binning with respectively 0.88, 0.89 and 0.88 for a binning of 2, 3 and 4. On Figure 7.5 the closeness of the shape of the single dots remains similar. The convexity descriptor decreases with the increase of the binning with respectively 0.80, 0.76 and 0.69 for a binning of 2, 3 and 4. Edges become then rougher with the increase of the binning and are a consequence of the larger physical dot gain as observed on Figure 7.5. The edges of the single dot of binning 2 have smoother edges with more fusioned particles on the edges. On the contrary the single dot with binning of four shows a large amount of single toner particles on the edges of the single dot. The circularity index decreases with the increase of the binning with respectively 0.73, 0.70 and 0.64 with the binning of 2, 3 and 4. The nominal circularity value of a square is equal to 0.89. The decrease measured is mostly due to the roughness of the edges. This is demonstrated computing the circularity with the convex perimeter resulting in a circularity of respectively 0.92, 0.92 and 0.92 for the binning 2, 3 and 4.

Another effect of the increase of binning is an increase of the print repeatability as demonstrated by the decrease of the coefficients of variation for the area, convex area, perimeter, convex perimeter and Feret diameters. The coefficient of variation stabilizes for single dots with binning of 3 and 4. For example the coefficient of variation for the area shows a large decrease from the dots with binning 2 to binning 3 going from 26.5% to 6.0% and a smaller decrease going from the dots with binning 3 to binning 4 going from 6.0% to 3.7%.

The error of the dot registration as a function of the amount of binning is stable with a misregistration length average for a binning of 2 of 6.0 µm +/- 3.8 µm and is equivalent to the results found for a binning of 4 with 8.3 µm +/- 4.7 µm. For the binning of 3, a systematic misregistration

error of 24.2 µm +/- 8.8 µm is measured and can be observed on Figure 7.5 and Figure 7.6. This systematic misregistration is close to the size of one dot at the printer nominal resolution: 21.2 µm. This shows that an alteration was introduced during printing, however the exact cause was not determined. The direction of the misregistration is globally in the upper left region of the code, corresponding a positioning error around 135°.

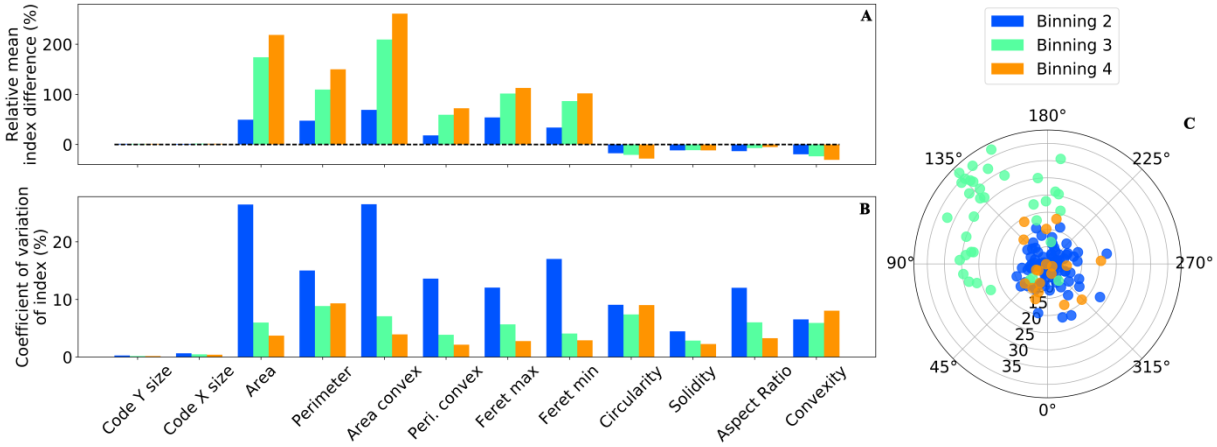

Figure 7.6: (A) Single dots similarity between original and printed with electrophotography. (B) Standard deviation of the indexes of printed single dots. (C) Positioning errors length (µm) and direction.

7.1.3.3 Offset

For offset, the shapes of the printed dots obtained are different than for electrophotography. The area, convex area, the perimeter, convex perimeter, the Feret diameters and the Y and X position errors are not dependent on the position of the single dot on the 3 by 3 matrix, Figure 7.7. The codes are accurately registered for all binnings and both X, Y directions with a global average reaching +1.2% +/- 0.1%. The coefficients of variation associated for each binning are small with respectively 0.9%, 0.6%, 0.4%, 0.2% and 0.2% for the Y dimension and 0.6%, 0.5%, 0.4%, 0.2% and 0.2% for the X dimension for a binning of 2, 3, 4, 6 and 8. Although small, the variations of the dimensions tend to decrease with the increase of binning.

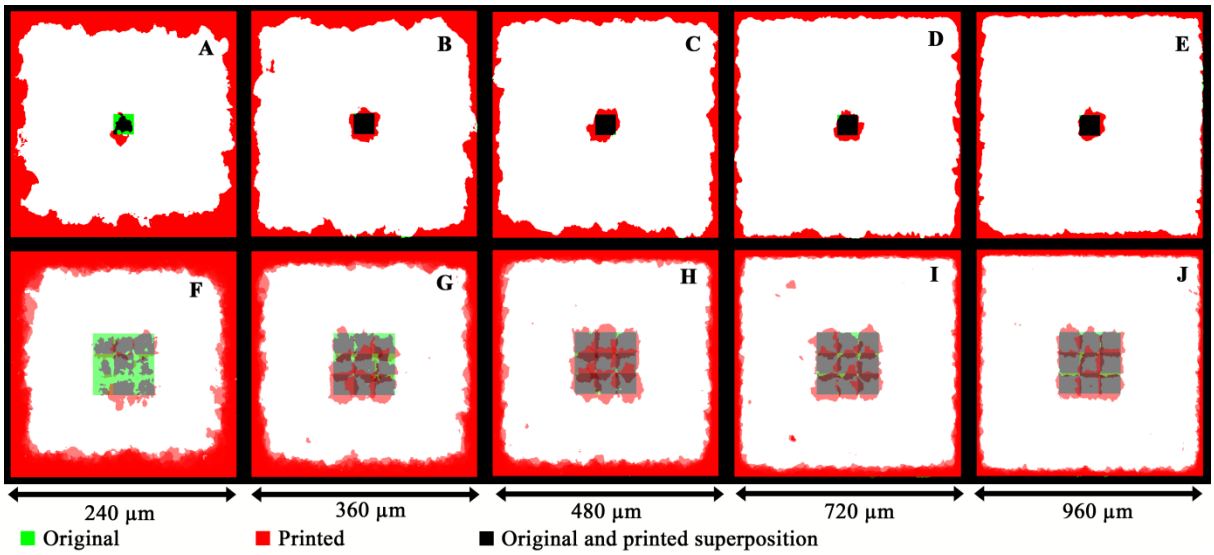

Figure 7.7: Superposition of single dot codes: original and printed with offset, located at [0, 0] on the [y,x] 3 by 3 matrix with binning of 2 (A), 3 (B), 4 (C) 6 (D) and 8 (E). Superposition and stitching of single dot codes at each location on the 3 by 3 matrix with binning of 2 (F), 3 (G), 4 (H), 6 (I) and 8 (J).

The dot indexes such as the area, perimeter, convex area and convex perimeter, Ferret diameters and shape descriptor are then analyzed, Figure 7.8. The average area is first found below the nominal surface for a binning of 2 with a decrease of -28% and a standard deviation of 54.6% compared to the original single dot. This shows that the printing of a single dot with a binning of 2 is extremely sensitive to the process variations. 7 single dots over 90 codes were not printed illustrating the large print variations. These variations in the process can explain that the average obtained is smaller than the nominal surface. With a binning larger than 2, it can be observed that the relative mean area difference becomes positive, demonstrating a physical dot gain increase. The physical dot gain, first increases and then decreases with the increase of binning with a single dot area of respectively +58%, +69%, +53% and +46% for a binning of 3, 4, 6 and 8. This first increase of the physical dot gain indicates that less miss inking appears, Figure 7.7. Then the physical dot gain decreases with the increase of binning, since the ink coverage increase occurs mostly on the edges of the dots. The coefficient of variation of the dot area for the 90 measured codes is also dependent on the amount of binning, decreasing with the increase of binning. The coefficient of variation for the single dot area decreases from 54.6% to 15.1%, 12.4%, 8.0% and 6.9% with the increase of binning from 2 to 3, 4, 6 and 8 respectively. Similar tendencies are observed for the convex area, the convex perimeter and Feret diameters. The coefficients of variations are also reduced with the increase of binning. The perimeter follows also a similar tendency, with the exception for the binning of 2. This is caused by a large roughness of the edges. The shape descriptors circularity, convexity, solidity and aspect ratio increase with the increase of the binning indicating an improved conformity to the single dots. Simultaneously, the coefficients of variation associated with the shape descriptors decrease with the increase of binning.

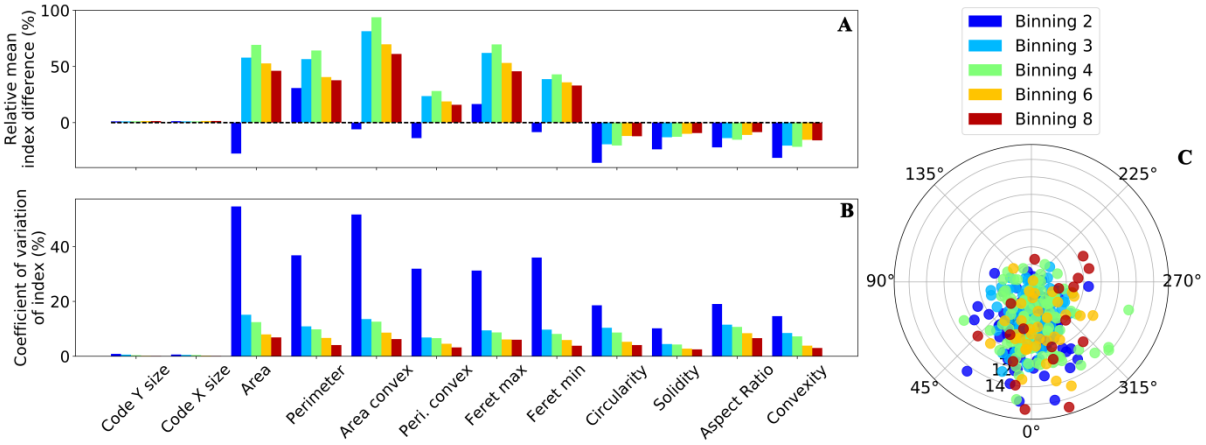

Figure 7.8: Single dots similarity between original and printed with offset. (B) Standard deviation of the indexes of printed single dots. (C) Positioning errors length (µm) and direction.

The positioning errors of the single dots centers are not influenced by the increase of binning with an error length of 6.5 µm, 4.8 µm, 5.5 µm, 5.9 µm and 7.6 µm for the binning of respectively 2, 3, 4, 6 and 8. Nevertheless, the increase of the binning reduced the coefficient of variation with respectively 77.6%, 49.3%, 57.2%, 49.0% and 47.0% for the binning of 2, 3, 4, 6 and 8. It has to be noted that the average of the positioning errors length corresponds to one half of the dot size at the nominal resolution of the printer. The dots are mostly mis-positioned in the bottom center of the codes, around the 0° direction. This direction corresponds to the printing direction and the misplacements occur due to a spreading of the ink in the printing direction. This spreading of the single dots can be observed on Figure 7.7.

7.1.3.4 Inkjet

For inkjet, differences with the offset and electrophotography appeared for small binnings, since only a single droplet was printed for a single dot at the native resolution, Figure 7.9. The elliptical

shapes of the single droplets at the native resolution of the printer differ then from the original square dots. The dimensions of the codes printed with inkjet are investigated and it can be observed that only small variation compared to the original codes are observed, Figure 7.10. A small increase in code dimensions of +1.3%, +1.3%, +1.1% and +1.5% are observed for binnings of respectively 1, 2, 3 and 4 for the Y dimension and respectively +1.6%, +1.1%, +1.2% and +1.4% for the X dimension. The coefficients of variation associated are found inferior to 1% for all binnings. A slight decrease of the coefficient of variation with the increase of binning is observed going from 0.55% to 0.20%, 0.17% and 0.14% for binnings of respectively 1, 2, 3, and 4 for the Y dimension and respectively 0.99%, 0.56%, 0.18% and 0.63% for the X dimensions. The codes are then accurately registered.

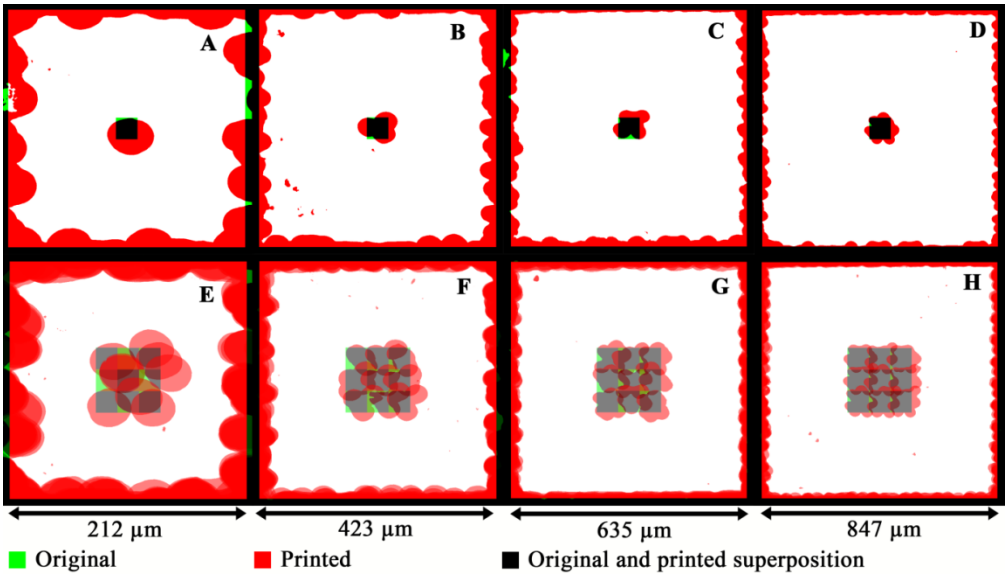

Figure 7.9: Superposition of single dot codes: original and printed with inkjet, located at [0, 0] on the [y,x] 3 by 3 matrix with binning of 1 (A), 2 (B), 3 (C) and 4 (D). Superposition and stitching of single dot codes at each location on the 3 by 3 matrix with binning of 1 (E), 2 (F), 3 (G) and 4 (H).

The area of the single dots is strongly dependent to the binning level. The relative mean area difference reaches +194% for a binning of 1 and is reduced to +104% for a binning of 2, +80% for a binning of 3 and +67% for a binning of 4. The coefficient of variation of the area does not decrease with the increase of binning with 5.4% for a binning of 1, 10.5% for a binning of 2, 8.2% for a binning of 3 and 4.8% for a binning of 4. Single dot area variations originate from the variations of the shape of each droplet, from the error of the droplet registration and from the physical interactions between ink and paper. The relative mean differences of the convex area, the perimeter, the convex perimeter and the Feret diameters decrease with the increase of binning. However, the shape descriptors do not systematically converge toward the nominal value with the increase of binning, Figure 7.10. This is a direct consequence of the large size of the printed droplets yielding to large variations in dot shape depending on the printing configuration. The circularity illustrate this effect: a single dot printed at the native resolution of the printed is composed of a single droplet with an ellipsoid shape. The average circularity index obtained is then large, obtained at 0.93. The single dot of binning 2 is composed of 3 droplets partially superposing having a shape further away from a circle shape with a circularity of 0.84. The circularity index is similarly reduced when the binning is increased reaching respectively 0.82 and 0.78 for binnings of 3 and 4. It has to be noted that the nominal single dot shape is a square with a circularity of 0.89. Starting from a binning of 3 the shape of the single dot is close to a square, however the edges of the dot are rougher inducing a decrease of the circularity ratio. This is also confirmed by computing the circularity with the convex perimeter instead of the perimeter. Resulting "convex" circularities of respectively 0.99, 0.93, 0.92 and 0.92 are obtained for binnings of 1, 2, 3 and 4. The convexity also decreases with the increase of the binning indicating rougher single dot edges. The solidity follows a similar tendency. The aspect ratio differs and is the only shape descriptor

converging toward the nominal value with the increase of binning. This explained by the fact that with the increase of binning the single dot shape becomes closer to the nominal square.

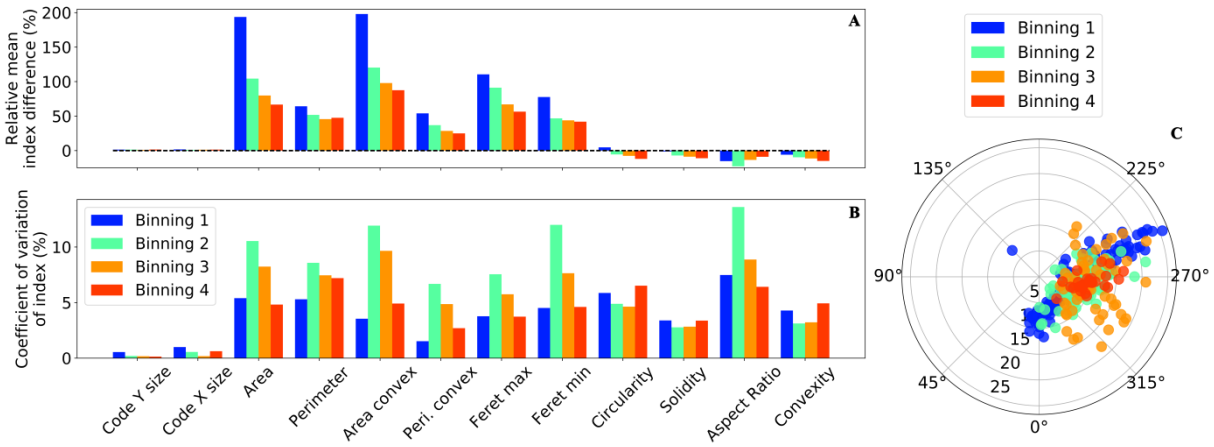

Figure 7.10: Single dots similarity between original and printed with inkjet. (B) Standard deviation of the indexes of printed single dots. (C) Positioning errors length (µm) and direction.

The printed single dot positioning error is constant with the increase of binning with a misregistration length of respectively 10.6 µm, 9.4 µm, 11.9 µm and 10.0 µm for binnings of 1, 2, 3 and 4. The mean registration error corresponds to one half of the nominal dot diameter. It has to be noted that the increase of binning tends to reduce the misregistration length variations with respectively 51.3%, 33.0%, 35.7% and 29.2%. The directions of the misregistrations are mostly found in the lower right quadrant and appear directed on a diagonal axis oriented at 45°. This direction corresponds to the direction of the print (the print head print from left to right and the paper moves from top to bottom).

7.1.4 Single dot model

A model to simulate single dots is proposed based on the assumption that single dots are composed of one or several ink particles located on the surface of the printed dot following a probability distribution. Single dots are then modelled by defining first the spatial probability distribution, then by feeding ink particles to the dot and finally by fusing the particles.

7.1.4.1 Spatial probability distribution generation

The mask is obtained by generating an ellipse, Figure 7.11. The diameter D_{e1} of the first axis of the ellipse is defined by setting the model parameter called D_{mask}. The physical size of a nominal dot depends on the printer resolution. For example with a printer resolution of 1200 dpi the nominal dot size is equal to 21.2 µm. A nominal dot imaged on the microscope will be described by a number of pixels depending on the nominal dot size and on the magnification used. For example a nominal dot of 21.2 µm will be imaged by 50.5 pixels using the 10x objective. In order to facilitate the implementation of the model for different nominal dot sizes and different imaging magnification, the D_{mask} is given relatively, with for example a $D_{mask}=1$ corresponding to 50.5 pixels when modelling a code with nominal dot of 21.2 µm and imaged at 10x.

$$D_{e1}=D_{mask}\ \frac{25400\ (\text{objective magnification})}{4.204\ (\text{printer resolution})} \qquad [7.5]$$

with the objective magnification corresponding to (5x, 10x, 20x, etc.) and the printer resolution in dpi. The diameter of the second axis of the ellipse is calculated using the model parameter called τ_{mask}.

$$D_{e2} = D_{e1}\ \tau_{mask} \qquad [7.6]$$

τ_{mask} defines the aspect ratio of the ellipse. When set to 1 the ellipse is a circle. τ_{mask} is designed range from 1 to infinity. The ellipse is oriented specifying an angle with the model parameter θ_{mask} defined in the range from 0° to 360°. The ellipse is filled with pixel values equal to 0 on a background composed of pixel values equal to 255. The ellipse is then blurred using a Gaussian blur kernel. The size of the Gaussian blur kernel k_n is computed using D_{mask} parameter.

$$k_n = 4\, D_{mask} \frac{25400\ (\text{objective magnification})}{4.204\ (\text{printer resolution})} \qquad [7.7]$$

The result of the Gaussian blurring gives a spatial probability distribution function.

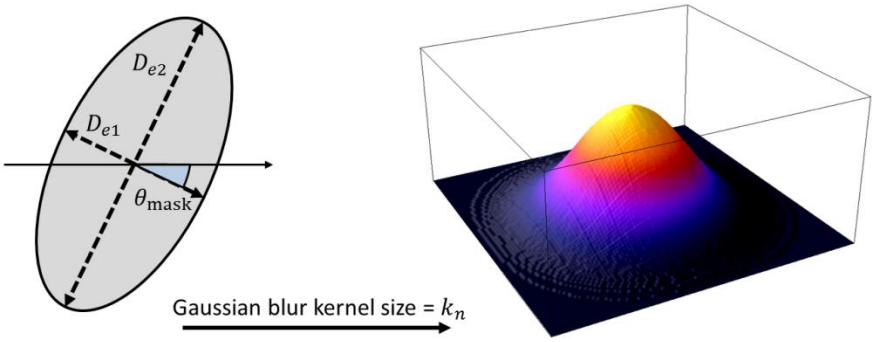

Figure 7.11: Model parameters for the spatial probability distribution (mask) generation.

7.1.4.2 Ink particle feeding

The next step to simulate the single dots is to feed ink particles at the positions where nominal dots should be printed. These positions are given by the original code sent to the printer, Figure 7.12 (A). The original code is composed of pixels and the positions of these pixels are the centers where the mask is anchored and ink particles are fed. For each pixel position, a controlled number N_{pc} of ink particles corresponding to discs of D_{pc} of diameter are generated. For each particle, a position is determined according to the spatial probability distribution mask. The discs are filled with pixel values 0 and the code background is composed of pixel values equal to 255, Figure 7.12 (B). It should be noted that the resolution of the codes generated corresponds to the printer resolution and to the measurement magnification in order to enable a pixel to pixel comparison with the printed codes.

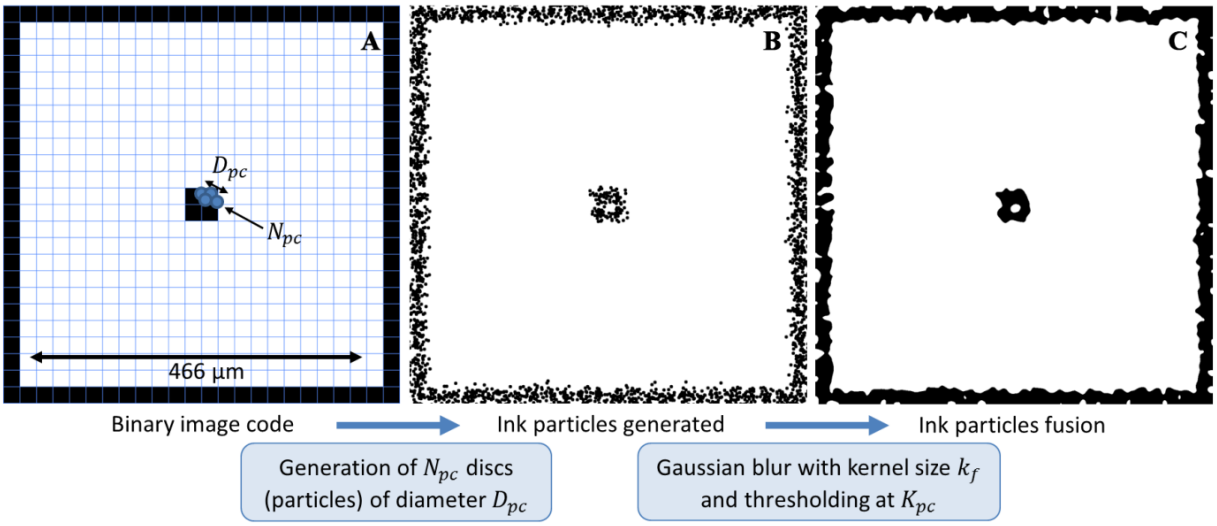

Figure 7.12: Binary image of the original code sent to the printer and ink particles generated around a pixel center following the spatial probability distribution mask.

7.1.4.3 Ink particle fusing

The last step to simulate the single dots is performed by fusioning the particles, Figure 7.12 (C). This fusion is achieved by applying a Gaussian blur filter on image generated. The size of the Gaussian blur kernel is defined by k_f and depends on the parameter D_{fuz}. The size of k_f is relative to the printer resolution and to the measurement magnification.

$$k_f = D_{fuz} \frac{25400\ (\text{objective magnification})}{4.204\ (\text{printer resolution})} \quad [7.8]$$

A grayscale image of the simulated code is then obtained after the Gaussian blurring. However, on the measured code the ink and the paper regions are represented by a constant pixel value. A threshold of the Gaussian blurred code is then required and a threshold value K_{fuz} is set. The pixel values inferior to K_{fuz} are thresholded to constant pixel values corresponding to the ink. The pixel values superior or equal to K_{fuz} are thresholded to constant pixel values corresponding to the paper.

7.1.4.4 Effects of parameters

The effects of the seven parameters of the model allowing simulating the single dots are analyzed by variating a parameter and by fixing the 6 others, Figure 7.13 and Table 7.2. The effect of the spatial probability distribution mask D_{mask} influences the dispersion of the ink particles. A small D_{mask} generates circular aggregations by superposition of the ink particles over an almost constant position located at the center Figure 7.13 (B). On the contrary a large D_{mask} generates ink particles largely dispersed around the original pixel positions. With large D_{mask} the fusion operation cannot spread the ink particles sufficiently and isolated ink particles appear Figure 7.13 (C). It should be noted that the size of the D_{mask} influence the size of the single dots generated.

The aspect ratio of the mask τ_{mask} and the angle of rotation of the mask θ_{mask} influence the shape of the single dot. With the increase of τ_{mask}, the single dot starts to be more elongated, Figure 7.13 (D and E). θ_{mask} impacts directly the direction of the elongation of the single dot, Figure 7.13 (E, F and G). A θ_{mask} of 0° generates a vertical elongation corresponding to an elongation in the machine direction. It should be pointed out that larger aspect ratio will also induce a larger dispersion of the ink particles.

The diameter of the ink particles D_{pc} influences the size, the shape and the homogeneity of the single dots. With the fusion parameter kept constant, small and dispersed ink particles are more sensitive to the fusion than large and grouped ink particles. With a small D_{pc} the single ink dot is composed of an heterogeneous ink region and dot shape, Figure 7.13 (H). With large D_{pc} the single dots are more circular and homogeneous, Figure 7.13 (I).

The number of ink particles N_{pc} influences also the physical dot gain and the shape of the dots. With a small number of ink particles the spatial probability distribution mask is only lightly filled and the ink particles are largely distributed inside the mask, Figure 7.13 (J). With a large number of ink particles the opposite effect is produced and the ink particles follow precisely the shape of the mask generating less fuzzy edges, Figure 7.13 (K).

The fusion parameter D_{fuz} controls the size of the kernel employed to blur the ink particles. A smaller D_{fuz} yields to less fusion between the dots and therefore to more fuzzy edges, heterogeneous inking and to a smaller physical dot gain, Figure 7.13 (L). With lager D_{fuz} the single dots are smoother and the dot shape converge toward a disc, Figure 7.13 (M).

Finally the fusion parameter K_{fuz} controls the physical dot gain as well as the shape and homogeneity of the single dot. A smaller K_{fuz} yields to rougher (sharper) edges and to heterogeneous

ink regions, Figure 7.13 (N). On another hand, a larger K_{fuz} produces more rounded edges, fills the un-inked holes on the ink region and tends to increase the physical dot gain, Figure 7.13 (O).

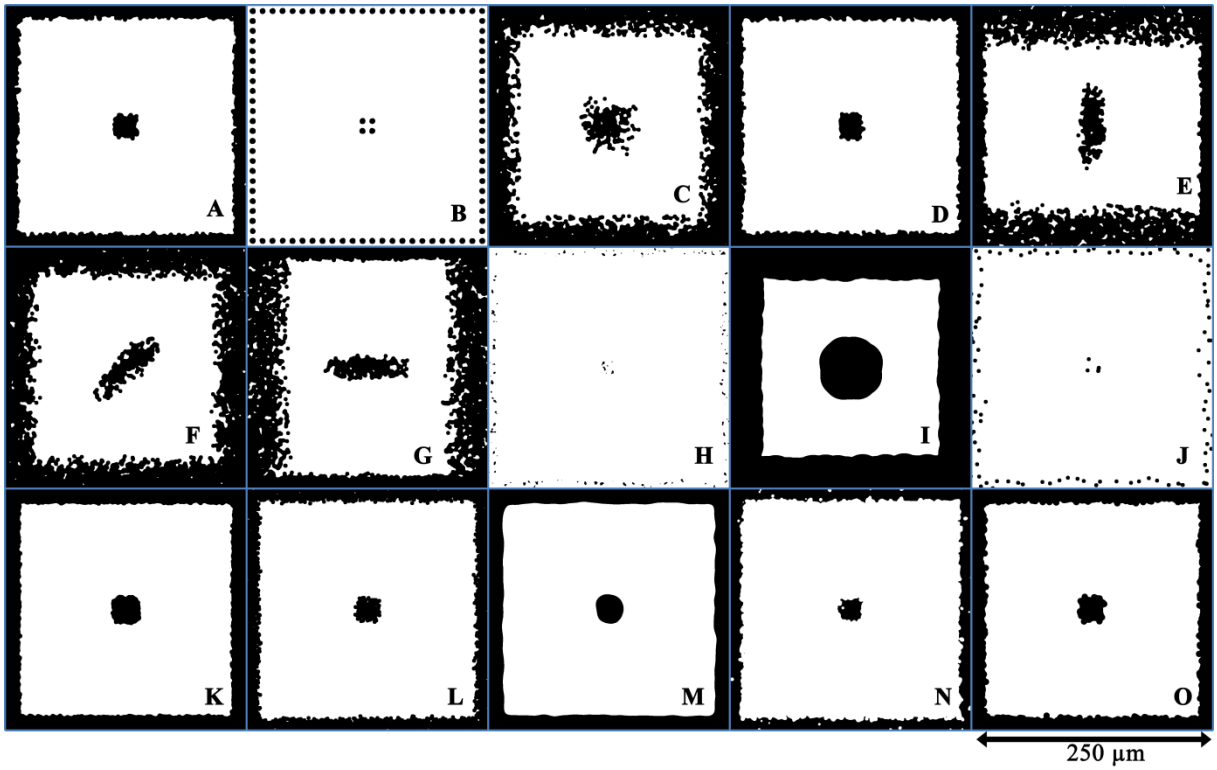

Figure 7.13: Effects of the model parameters on the generated single dots. Nominal code with a single dot and a binning of 2. (A) to (O) model parameters are given in Table 7.2.

Table 7.2: Set of parameters adopted to analyze the effects on the generated codes.

Generation #	D_{mask}	τ_{mask}	θ_{mask}	D_{pc}	N_{pc}	D_{fuz}	K_{fuz}
A	0.8	1.0	0	10	50	0.5	150
B	0.1	1.0	0	10	50	0.5	150
C	2.0	1.0	0	10	50	0.5	150
D	0.8	1.5	0	10	50	0.5	150
E	0.8	9.0	0	10	50	0.5	150
F	0.8	9.0	45	10	50	0.5	150
G	0.8	9.0	90	10	50	0.5	150
H	0.8	1.0	0	2	50	0.5	150
I	0.8	1.0	0	100	50	0.5	150
J	0.8	1.0	0	10	1	0.5	150
K	0.8	1.0	0	10	500	0.5	150
L	0.8	1.0	0	10	50	0.5	150
M	0.8	1.0	0	10	50	3.0	150
N	0.8	1.0	0	10	50	0.5	10
O	0.8	1.0	0	10	50	0.5	240

7.1.1 Single dot model performances

A single dot is generated at the center of the ink pixels on the original image. For codes with binnings larger than 1, the dots are composed of multiple single dots. The set of parameters used for the single dots simulation are given in Table 7.3. The performances of the single dot generation model are analyzed for electrophotography, offset and inkjet by computing the average of the area, perimeter, convex area, convex perimeter, ferret diameters, circularity, solidity, aspect ratio and convexity indexes. Averages are obtained for large number of dots.

Table 7.3: Set of parameters adopted to simulate single dots.

Process	Binning	D_{mask}	τ_{mask}	θ_{mask}	D_{pc}	N_{pc}	D_{fuz}	K_{fuz}
Electrophoto-graphy	2	0.8	1.0	0	10	50	0.50	150
	3	1.5	1.0	0	5	110	0.50	150
	4	2.0	1.0	0	5	200	0.50	150
Offset	2	1.5	1.0	0	4	30	1.80	190
	3	3.0	1.1	0	2	50	1.80	185
	4	3.0	1.1	0	2	50	1.80	200
	6	4.0	1.1	0	1	40	1.80	185
	8	4.0	1.1	0	1	30	3.00	200
Inkjet	1	0.1	5.0	90	65	3	0.01	150
	2	0.6	2.0	90	40	1	0.01	150
	3	0.7	2.0	90	20	1	1.00	150
	4	0.7	2.0	90	20	1	1.20	150

7.1.1.1 Electrophotography

The visual comparison shows that the dots modelled are similar to the printed dots, Figure 7.14. For the code with a binning of 2, the simulated dot has smaller ink coverage. However the shape and the edges roughness are similar. No isolated ink particles are visible with the simulated dot. It has to be noted that the simulation of the single dot with a binning of 2 can be improved by tuning more precisely the parameter of the model. For the code with a binning of 3, the simulated dot and the printed dot are extremely similar, with almost the same ink coverage, the same amount of isolated ink particles, the same shapes and edges roughness. The positioning error of the printed dot, visible on Figure 7.5 is not reproduced by the simulation. The dot modelled presents a physical dot gain similar to the printed dot, making the positioning error less visible. It can however be observed that the simulated dot presents an over-inking compared to the measurement on the right side of the dot and an under-inking on the left side of the dot that are caused by the positioning error of the printed dot. For the code with a binning of 4, the simulated dot and the printed dot are also extremely similar. The edges present a similar roughness level and the shape of the dots are similar. Multiple isolated ink particles appear for both the printed dot and the simulated dot.

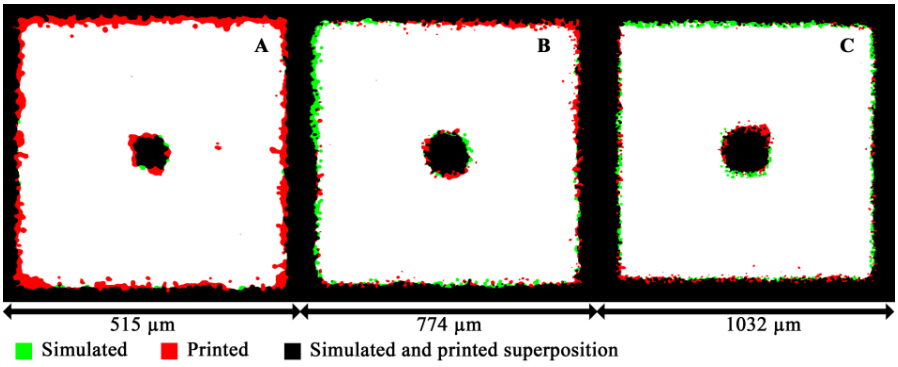

Figure 7.14: Superposition of single dot codes: simulated and printed with electrophotography, located at [0, 0] on the [y,x] 3 by 3 matrix with binning of 2 (A), 3 (B) and 4 (C).

A further analysis is conducted by comparing the shape descriptor indexes, Figure 7.15. For the codes with a binning of 2, the mean area and convex area are similar for the printed and simulated dots with a mean relative difference of respectively -0.8% and -1.0%. The simulated dot has a smaller area and convex area dispersion with a decrease of the standard deviation by respectively 85.1% and 81.9%. The simulated dots are purposely less dispersed with a variation generated only by the feeding of the ink particles onto the mask. More variability can be introduced in the model, however the comparison with the printed codes would become more complicated. The similarity of the area and

convex area with the printed dots induces a similar solidity. A relative mean solidity difference of 0.4% is reached. It can be concluded that the printed and simulated dots have similar degree of closing of the dots. The perimeter is associated with a mean relative difference of -4.9%. The convex perimeter is more similar to the printed dots with a mean relative difference of -0.3%. A smaller perimeter for the simulated dots signifies that the edges simulated dots are slightly less rough. This is demonstrated by the mean relative convexity difference of +4.7%. The circularity shows also a positive mean relative difference of 5.5% demonstrating that the simulated dots are more circular and have less fuzzy edges. The variation for the perimeter, the convex perimeter, the convexity and the circularity are smaller on the simulated dots. Finally the Ferret diameters shows a mean relative difference of respectively -5.6% and +6.7% demonstrating that the simulated dots are slightly more iso-dimensional that the printed dots. The mean relative aspect ratio difference is therefore increased by 13.1%. It should be noted that the mean relative differences obtained between the simulated dots and the printed are small. It can be concluded that the model simulates correctly the printed dots at the binning of 2.

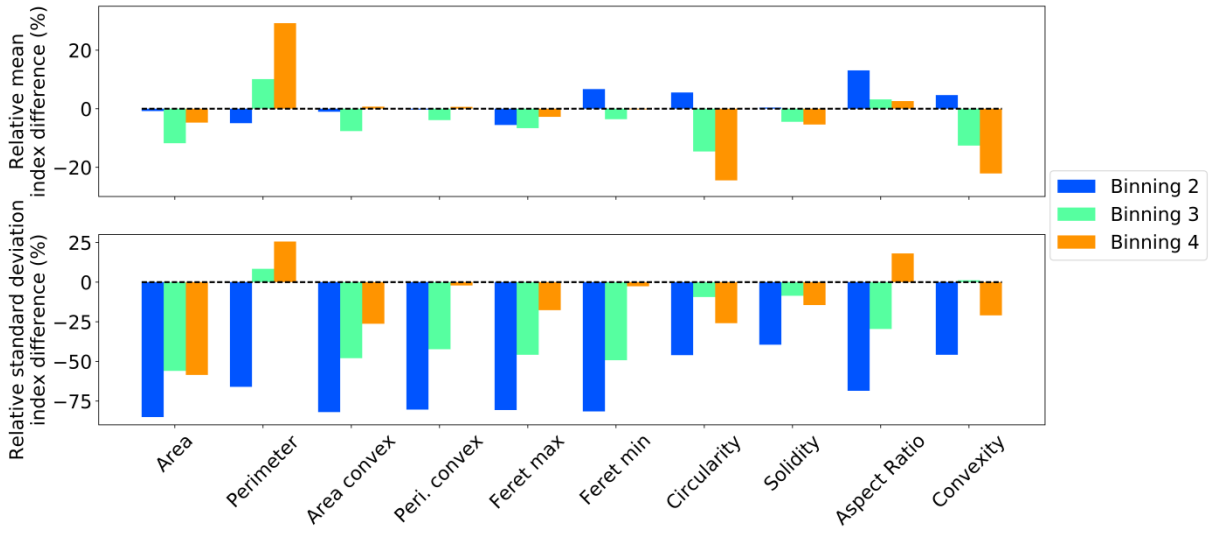

Figure 7.15: Single dots similarity (index average and standard deviation) simulated and printed with electrophotography.

The parameters of the model were optimized for each binning level. Thus, the similarity between the printed dots and the simulated dots differ for each binning level. For a binning level of 3, the mean area of the simulated dots is slightly smaller than the area of the printed dots with a mean relative difference reaching -11.8%. The convex perimeter is also found smaller for the simulated dot with a mean relative difference of -7.7%. The simulated ink dots are found with slightly more closed surface with a mean relative difference of -4.5%. On another hand, the perimeter obtained with the simulated dots is larger and the convex perimeter is smaller. Thus, the simulated dots have rougher edges, as demonstrated by the negative mean relative difference for the convexity and the circularity of respectively -12.6% and -14.6%. The Ferret diameters are both smaller for the simulated dots compared to the printed dots and the aspect ratio demonstrates that the simulated dots are more iso-dimensional. Compared to the binning of 2, the simulated dots with a binning of 3 are associated with smaller relative standard deviation differences. With a larger binning the printed dots presents less variations, the relative standard deviation differences are then smaller. The simulated dots are nevertheless associated with fewer variations. For the simulated dots with a binning of 4, similar tendencies are observed. The area of the simulated dots is slightly smaller than the area of the printed dots with a mean relative difference of -4.8%. The convex perimeter of the simulated dots is similar to the printed dots. Therefore the simulated dots have a surface less closed than the printed dots. The perimeter of the simulated dots is larger than the perimeter of the printed dots with a mean relative difference of +29.2%. The convex perimeter is similar for simulated and printed dots. The simulated

dots are then associated with rougher edges, as demonstrated by the negative convexity and circularity mean relative differences. The Ferret diameters are almost similar, giving simulated dots slightly more iso dimensional. The relative standard deviation differences are further reduced. It can be concluded that for electrophotography the model proposed simulates correctly the printed dots. The fidelity ratio is computed for the 3 levels of binning. The fidelity ratio for the binning of 2 reaches 75.7% +/- 24.3%. For the binning of 3, a fidelity ratio of 87.5% +/- 5.3% is obtained. Finally a fidelity ratio of 95.2% +/- 3.2% is reached for the binning of 4. Dots with larger binnings are less sensitive to variations and have a higher fidelity ratio.

7.1.1.2 Offset

For offset, several small ink particles are generated and a large particle fusion (Gaussian blur and threshold) is applied. This results in single dots with fuzzy edges and slightly elongated particles (aspect ratio of 1.1), Figure 7.16. The single dot generated for the binning of 2 is less fuzzy than the printed dot. The ink surface increase is nevertheless globally similar. It can be observed than the edges of the printed array are impacted with more physical dot gain than for the simulated array. With larger binning, the shapes of the simulated dots and of the edges correspond better to the measurements. Similarly the simulated ink surface increases on the edges of the array correspond better to the measurements. It can be concluded that the simulation reproduces correctly the global shapes of the dots, the fuzziness of the edges and the ink coverage.

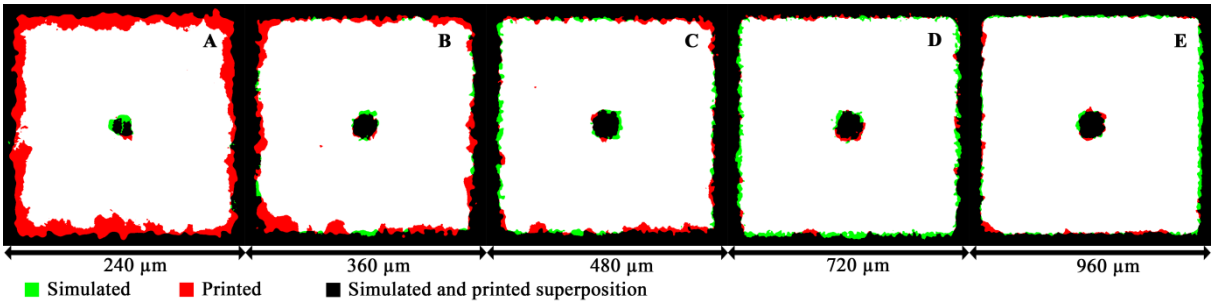

Figure 7.16: Superposition of single dot codes: simulated and printed with offset, located at [0, 0] on the [y,x] 3 by 3 matrix with binning of 2 (A), 3 (B), 4 (C), 6 (D) and 8 (E).

The relative mean performances of the indexes depend strongly on the level of binning, Figure 7.17. Different parameters were adopted for each level of binning and can potentially explain these differences. With a binning of two, a large area increase is obtained with the simulated dots. Similarly the convex area of the simulated dots shows a large increase. These increases result from the large variations of the printed dot (Figure 7.8). The offset process presents large variations for dots with small inked surface. The simulated dots do not follow this tendency. This is confirmed by the reduction of relative standard variation for the simulated dots. For larger single dot sizes (larger binning), this effect is reduced and a more accurate simulation of the area of the single dots is achieved. With a binning of 3 the simulated single dot area is found inferior to the area of the printed dot. The perimeters of the simulated dots are globally inferior to the perimeters of the printed dots, except for a large increase of the simulated single dot perimeter at a binning of 6. This increase is induced by the lower level of fusion of the ink particles generating rougher edges. The increase of the relative standard deviation confirms this hypothesis. The convex perimeter is associated with small relative mean index differences, except for the binning of 2 (caused by a lower roughness of the edges of the dots simulated). The maximum Ferret diameter shows small mean relative differences compared to the printed dots except for the binning of 2. The minimum Ferret diameter shows larger variations, demonstrating that the aspect ratio used to simulate the single dots was not large enough. The relative mean aspect ratio differences confirm this observation. It can be concluded that for offset, the model proposed simulates correctly the printed dots, except for a binning of 2. The fidelity ratio for the

binning of 2 reaches 46.1% +/- 38.6%%. For the binning of 3, 4, 6 and 8, fidelity ratios of respectively 85.2% +/- 9.5%, 85.8% +/- 12.3%, 89.8% +/- 8.4% and 93.5% +/- 6.0% are obtained.

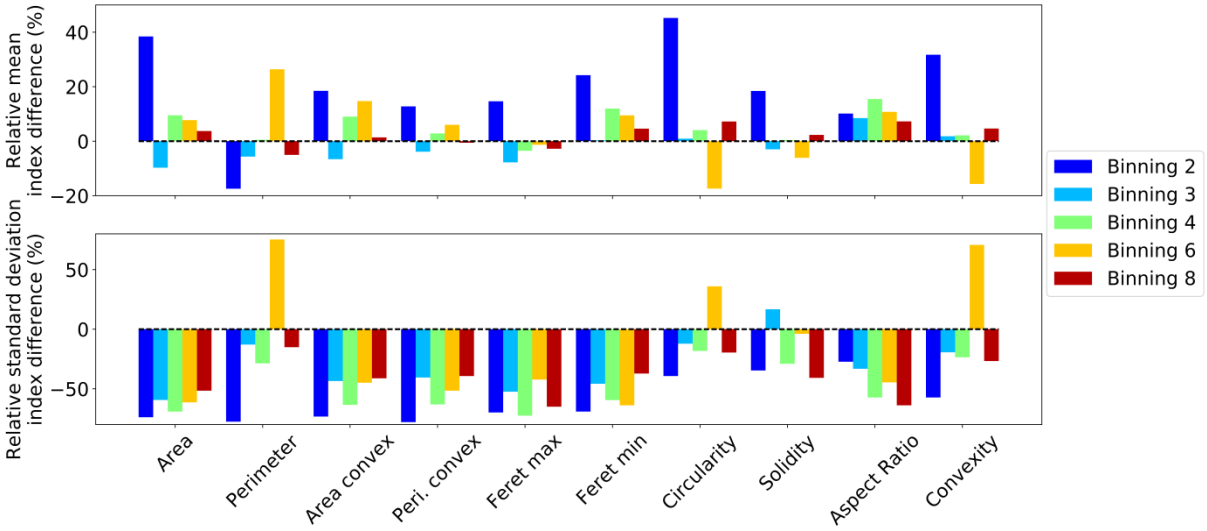

Figure 7.17: Single dots similarity (index average and standard deviation) simulated and printed with offset.

7.1.1.3 Inkjet

For inkjet, the singles dot printed with a binning of 1 are associated with larger positioning variations since the dot is only composed of a single droplet, Figure 7.18. The placement of the simulated single dot differs then from the printed dot. With larger binnings, this effect is reduced since multiple droplets are ejected to form the single dot. The single dot shapes are rounded and the simulated single dots display similar tendencies. Starting from a binning of 2, the edges of the array are well reproduced by the model. It should be noted that a pattern of dot placement could be observed for the printed dots depending on the print direction and the printing steps increments. This positioning discretization was not reproduced by the model implemented with a Gaussian probability positioning mask. This mask can be modified to correspond better to the dot positions observed.

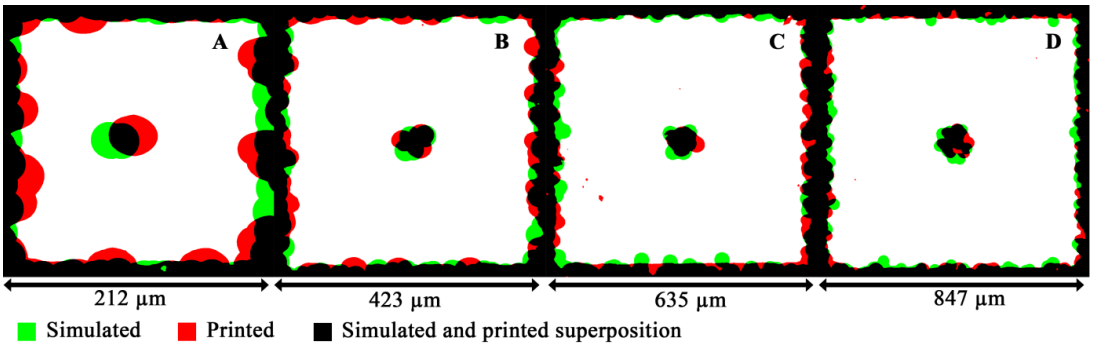

Figure 7.18: Superposition of single dot codes: simulated and printed with inkjet, located at [0, 0] on the [y,x] 3 by 3 matrix with binning of 1 (A), 2 (B), 3 (C) and 4 (D).

The absolute levels of the relative mean differences of the indexes are smaller for inkjet than for offset and electrophotography, Figure 7.19. These observations demonstrate that the model proposed correspond very well for the inkjet dots, however larger dispersions of the dot positioning are observed. The development of a customized probability positioning mask could then improve the model. The standard deviations are larger for the simulated dots compared to the printed dots. The area and the convex area of the simulated dots are smaller than the printed dots. The solidity obtained is equivalent for simulated and printed single dots. The perimeters and convex perimeters of the simulated dots are first inferior compared to the printed dots and are then superior. The convexity obtained is equivalent for simulated and printed single dots, demonstrating similar level of edge

roughness. The aspect ratio follows an inverse tendency compared to the perimeter. It can be concluded that for inkjet, the model proposed simulates correctly the printed dots. The fidelity ratios for the binnings of 1, 2, 3 and 4 reach respectively 81.5% +/- 8.5%%, 87.2% +/- 10.8%, 90.1% +/- 7.5% and 91.7% +/- 5.1%.

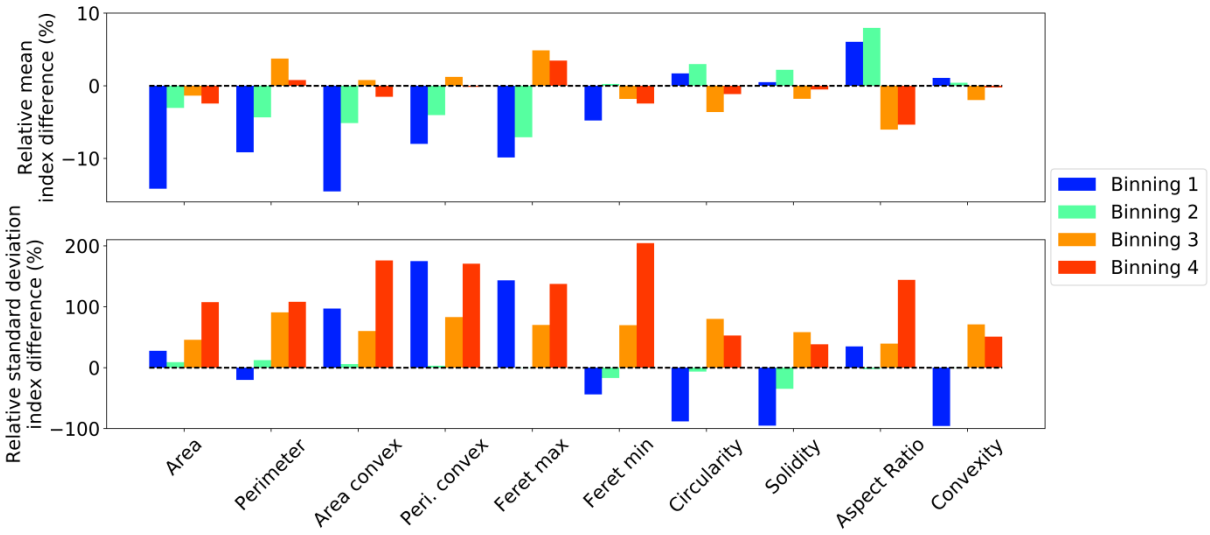

Figure 7.19: Single dots similarity (index average and standard deviation) simulated and printed with inkjet.

7.1.2 Dot-Dot interactions and model

A large amount of codes are measured and a study of the dot-dot interactions for each 3 by 3 matrix of codes is difficult to conduct. A global approach was then proposed to characterize the conditions impacting the dot-dot interactions. The model proposed for the single dots is directly implemented to simulate the different multiple dots configurations. Results are compared to the measurements using the binary fidelity ratio index. The parameters used to simulate the multiple dots codes are presented in Table 7.4.

Table 7.4: Set of parameters adopted to simulate multiple dots codes.

Process	Binning	D_{mask}	τ_{mask}	θ_{mask}	D_{pc}	N_{pc}	D_{fuz}	K_{fuz}
Electrophoto-graphy	2	1.2	1	0	10	50	0.5	150
	3	1.7	1	0	5	120	1	150
	4	2	1	0	5	200	1	150
Offset	2	2.6	1.3	0	4	60	1.8	190
	3	3	1.1	0	2	50	1.8	185
	4	3	1.1	0	2	50	1.8	200
	6	4	1.1	0	1	40	1.8	185
	8	4	1.1	0	1	30	3	200
Inkjet	1	0.5	2	90	80	1	1	150
	2	0.6	2	90	40	1	1	150
	3	0.6	2	90	20	1	1.2	190
	4	0.6	2	90	20	1	1.2	190

7.1.2.1 Electrophotography

The fidelity ratio levels obtained for the multiple codes printed with electrophotography are presented in Figure 7.21. The fidelity ratios are globally independent on the number of single dots in the matrix of the code. The mean fidelity ratio of printed codes compared to the nominal codes reaches 35.7% +/- 8.4%. This low fidelity ratio demonstrates that a large physical dot gain occurs when printing dots with a binning of 2. The mean fidelity ratio of the simulated codes compared to the

printed codes is largely improved, reaching 89.2% +/- 10.6%. The model proposed improves then the spatial description of the ink compared to the nominal codes. For each set of codes, large variations of the physical dot gain can be observed. These variations occur for all number of single dots in the matrix code and are not dependent on the number of single dots. The configurations of the single dots in the matrix code influences then the physical dot gain. The codes with low fidelity ratio were associated with separated printed dots configurations, Figure 7.20. Separated dots presents a larger total dot perimeter and influences the ink spreading. The total physical dot gain appears to be mostly induced by the physical dot gain of single dots and no strong dot-dot interaction tendency is observed. This observation is confirmed by the results showing similar levels of fidelity ratio variations for all number of single dots. The codes presenting the highest fidelity ratios are the full square codes with 9 single dots, appendix Figure A.8. Since no strong dot-dot interactions are observed, the model with the single dots applied to the multiple single dots codes simulates accurately the codes. The improvement brought by the model and compared to the nominal dots can be observed on Figure 7.20. The model generates a similar amount of physical dot gain and the shape of the code is similar. A larger fusion between the ink particles is nevertheless observed for the printed dots. The model can then be improved by optimizing this parameter. Moreover, it can be observed that for higher number of single dots, the performances of the model are improved and present smaller variations as a function of the disposition of the single dots on the code.

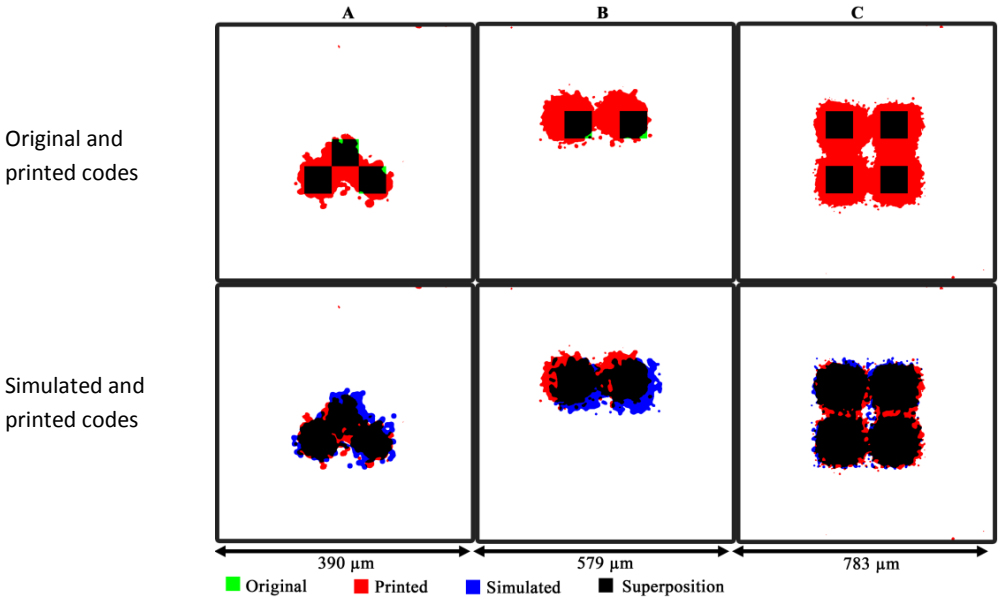

Figure 7.20: Nominal, printed and simulated codes superposition printed with electrophotography. Code configuration selected presenting the lowest fidelity ratio: (A) code #491, binning 2, (B) code #192, binning 3 and (C) code #187, binning 4.

For larger binnings of 3 and 4, the fidelity ratio levels decrease comparing the printed codes with the nominal codes, Figure 7.21. Larger binning sizes decrease the fidelity ratios due to an increase of the physical dot gain, Figure 7.20. This increase of physical dot gain with the increase of bin size is opposed to the tendencies observed for offset and inkjet. Fidelity ratio of 5.2%+/-10.1% and 1.3% +/- 4.4% are respectively obtained for a binning of 3 and 4. On another side, the model proposed simulated accurately the printed dots with fidelity ratio of respectively 88.1%+/-8.7% and 97.8% +/- 1.2% for a binning of 3 and 4. With larger binning the model follows then more accurately the printed dots. As observed for the single dots, the printed codes with a binning of 3 are associated with a positioning error. These positioning errors do not impact the level of fidelity ratio since large physical dot gains are induced. However, since the centers of the nominal single dots were used to generate the ink particles, the constant misregistration was not accounted for in the model. It resulted in superposition errors, as demonstrated on Figure 7.20, yielding to a reduction of the binary fidelity

ratio. For the binning of 3 and 4 the physical dot gain is accurately reproduced with the model. The model could be further improved by increasing the level of particle fusion. For the binning 3 and 4, the codes presenting the largest fidelity ratios are square codes, appendix Figure A.8. The standard deviations are globally reduced by the increase of binning, appendix Figure A.12. It should be noted that since the binary fidelity ratio minimum limit is set at 0, codes configurations can have a misleading standard deviation equal to 0 (the negative variations of the fidelity ratio are not accounted). The standard deviations should then be analyzed in conjunction with the binary fidelity ratios, Figure 7.21.

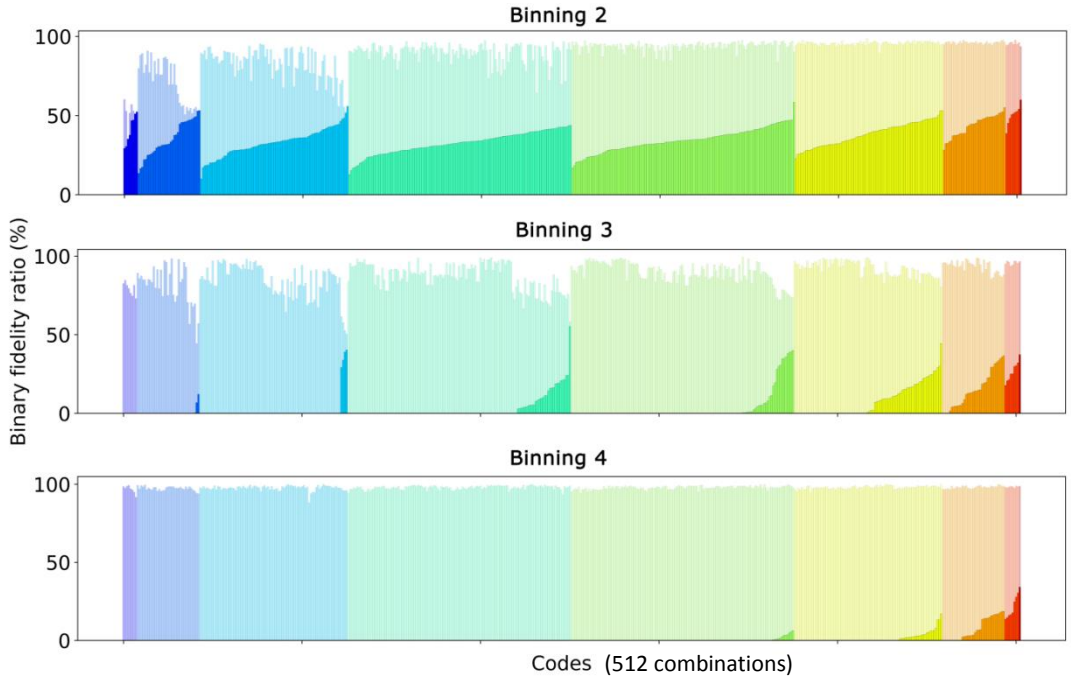

Figure 7.21: Codes corresponding to the 512 combinations of the 3 by 3 matrix and split as a function of the number of dots printed and simulated (refer to Table 7.5) for different level of binnings. Codes printed with electrophotography.

Table 7.5: Color legend identifying the number of single dots printed in a code (independent from the level of binning, the single dots are then composed of one or several nominal dots).

Number of single dots	1	2	3	4	5	6	7	8	9
Printed as a function of nominal dot									
Simulated as a function of printed dot									

7.1.2.1 Offset

For the offset process, similar observations than for electrophotography are made, Figure 7.23. The fidelity ratios are globally independent on the number of single dots in the matrix of the code and display variations that are induced by variations of the dot configuration on the matrix. Conversely to the codes printed with electrophotography, the binary fidelity ratio of the printed dots increases with the increase of binning. For the codes with only one single dot, the maximum levels of fidelity ratio reach similar levels than for codes with multiple single dots. On another side, the minimum levels of fidelity ratio for codes with only one single dot reach higher levels than for the multiple single dots codes. These effects demonstrate the influence of the dot-dot interactions. These differences tend to be reduced with the increase of the binning level. The simulated codes with single dots dot not follows

this tendency and the fidelity ratio levels obtained are larger than the printed dots and have smaller variations for the different codes. A similar influence of the dot-dot interactions can be observed as a function of the binning level. The mean fidelity ratio of printed codes compared to the nominal codes reaches 13.7% +/- 15.4% for a binning of 2, 18.6% +/- 12.7% for a binning of 3, 27.8% +/- 13.4% for a binning of 4, 49.9% +/- 9.8% for a binning of 6 and 59.2% +/- 8.5% for a binning of 8. The mean fidelity ratio of the printed dots increases then with the increase of the binning. This effect can be observed on Figure 7.22, with a decrease of the physical dot gain with the increase of dot gain. Since a large physical dot gain continue to impact the single dots, even with large amount of binning, the codes with multiple single dots present also dot-dot interactions. This phenomenon can be observed on Figure 7.22, with a superposition of the physical dot gain of the single dots generating a global physical dot gain. The model reproduces the global physical dot gain and generates the dot-dot interactions observed with the fusion of the ink particles generated. The model could be further improved by adopting a higher fusion of the ink particles and with slightly larger position probably masks. The codes presenting the largest fidelity ratios are mainly full square codes, appendix Figure A.9. The model simulates accurately the printed dots and large fidelity ratio levels are obtained with 87.5% +/- 12.7% for a binning of 2, 93.1% +/- 3.5% for a binning of 3, 93.5% +/- 2.0% for a binning of 4, 96.0% +/- 2.0% for a binning of 6 and 96.6% +/- 2.0% for a binning of 8. Finally, it should be noted that in Figure 7.23, on the mean binary fidelity ratios were computed averaging several similar codes. The standard deviations are globally reduced by the increase of binning and by the increasing number of single dots in the codes, showing that the influence of the random print variations are significant for single dots and that dot-dot interactions with a larger number single dots are more reproductible, appendix Figure A.12.

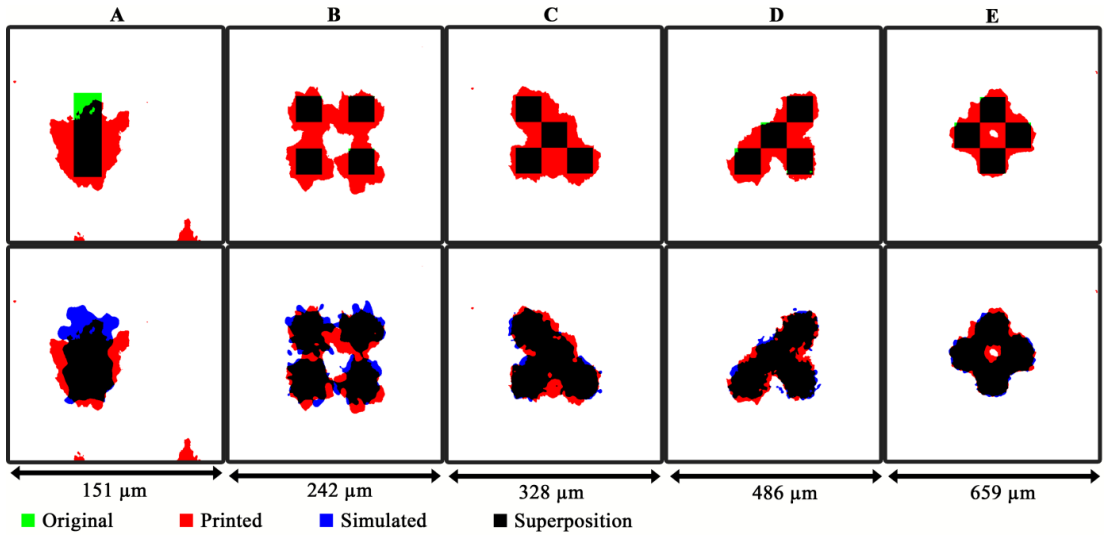

Figure 7.22: Nominal, printed and simulated codes superposition printed with offset. Code configuration selected presenting the lowest fidelity ratio: (A) code #220, binning 2, (B) code #187, binning 3, (C) code #235, binning 4, (D) code #427, binning 6 and (E) code #342, binning 8.

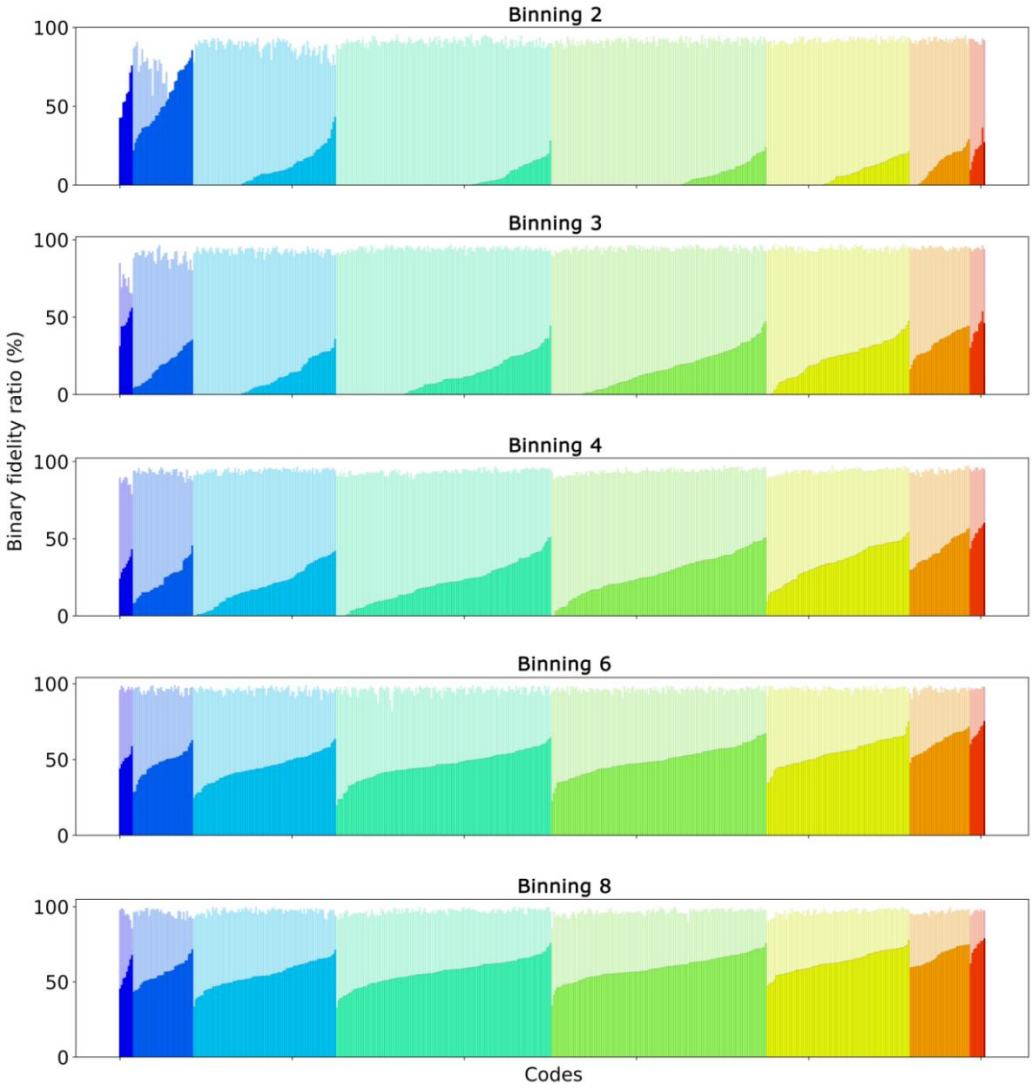

Figure 7.23: Codes corresponding to the 512 combinations of the 3 by 3 matrix and split as a function of the number of dots printed and simulated (refer to Table 7.5) for different level of binnings. Codes printed with offset.

7.1.2.2 Inkjet

For the inkjet process, similar observations than for offset are made, Figure 7.25. The fidelity ratio of the printed dots increases with the increase of binning. The fidelity ratios are globally independent on the number of single dots in the matrix of the code and display variations that are partially induced by variations in the process and partially by the single arrangement on the matrix code. The fidelity ratio variations for codes with a similar amount of single dots present larger variations for small binnings (except for binning of 1 where fidelity ratios are cut at 0%). This shows that for inkjet, the dot-dot interactions depend on the number of single dots printed, Figure 7.24. The codes associated with the smallest binary fidelity ratios are not necessarily associated with dispersed single dots. The physical dot gain of single codes generates then the global physical dot gain. The mean fidelity ratio of printed codes compared to the nominal codes reaches 2.4% +/- 4.7% for a binning of 1, 22.7% +/- 13.0% for a binning of 2, 43.2% +/- 12.3% for a binning of 3 and 54.8% +/- 9.9% for a binning of 4. The model simulates accurately the printed dots and large fidelity ratio levels are obtained with 89.5% +/- 3.8% for a binning of 1, 91.2% +/- 2.1% for a binning of 2, 95.4% +/- 3.8% for a binning of 3 and 95.3% +/- 1.7% for a binning of 4. The codes presenting the largest fidelity ratios are full square codes, appendix Figure A.10. For inkjet, large misplacements of the

single dots can be observed for the single dots and generates a decrease of the fidelity ratio for small binning levels. This effect is not reproduced by the model, since the introduction of misplacements variations would increase the dispersion of the performances of the simulated codes. The standard deviations are globally reduced by the increase of binning and by the increasing number of single dots in the codes, appendix Figure A.13.

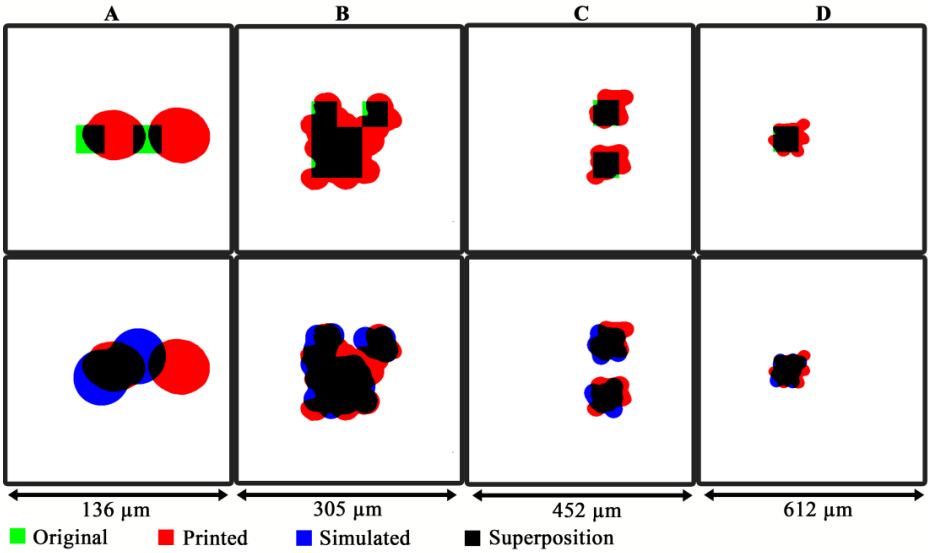

Figure 7.24: Nominal, printed and simulated codes superposition printed with inkjet. Code configuration selected presenting the lowest fidelity ratio: (A) code #472, binning 1, (B) code #138, binning 2, (C) code #447, binning 3 and (D) code #480, binning 4.

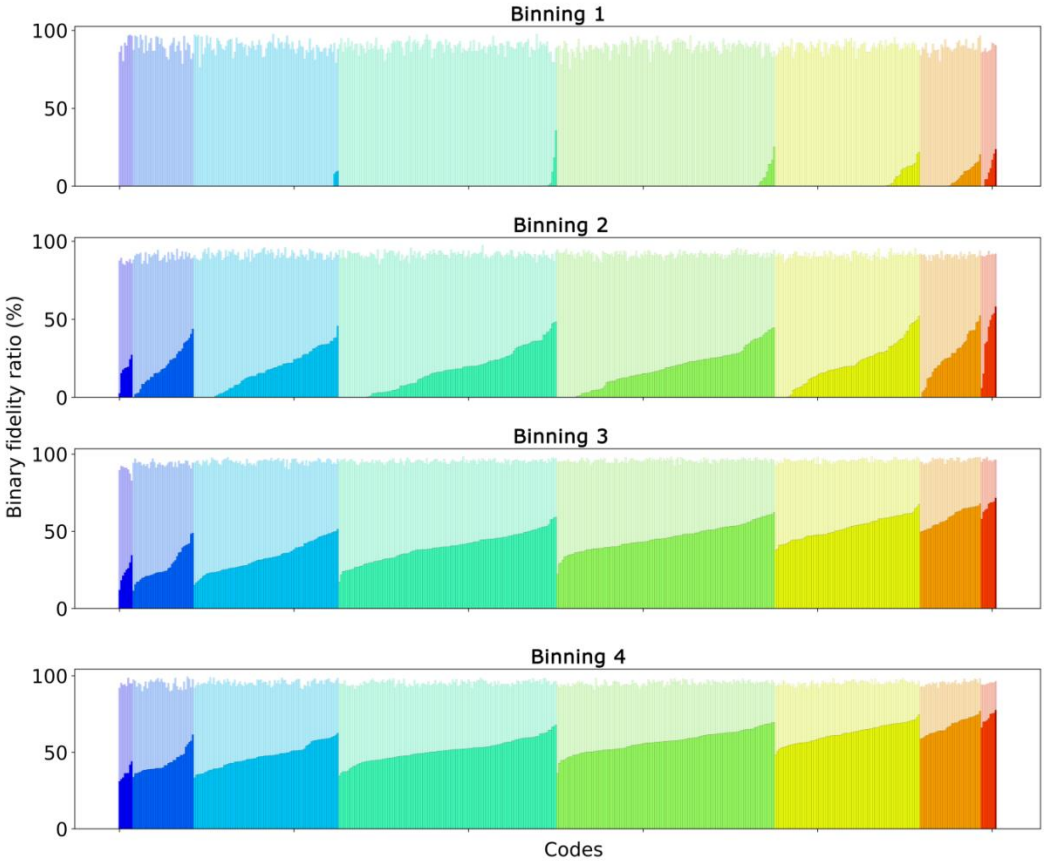

Figure 7.25: Codes corresponding to the 512 combinations of the 3 by 3 matrix and split as a function of the number of dots printed and simulated (refer to Table 7.5) for different level of binnings. Codes printed with inkjet.

7.1.3 Conclusion

The goal was to analyze halftone dots, in order to understand the deformations induced by the printer. The development of an automated measurement algorithm yielded to the creation of a large database of halftone dots printed at several sizes (several binning) and printed with several processes. The database was composed of 43269 codes with up to 10 redundancies per halftone dots. The printed codes were found to be well registered with accurate dimensions and small variations, insuring a valid measurement of the dots inside the code.

The effect of the single dot position on the 3 by 3 matrix was analyzed for 84 single dots printed with electrophotography at 600 lpi. The area, convex area, perimeter, convex perimeter and Ferret diameters were found to be independent from the single dot position on the 3 by 3 matrix. Large variations of the indexes were observed for all positions showing the variability of the print process. Since the position did not influence the indexes, an averaging for the single dots over all positions on the 3 by 3 matrix was adopted, averaging the random print variations.

For electrophotography the printed single dots area and convex area demonstrated increases compared to the original dot sizes with the increase of the original dot sizes (binning). These increases were unexpected since larger dot sizes should be reproduced more accurately by the printer (higher number of nominal dots to print the effective dot). It was concluded that the physical dot gains induced with the electrophotography process were dependent on the size of the single dots. Although showing a larger physical dot gain, the shape of the single dots were found to become more similar to the original dots with the increase of binning. Dot edges became rougher with the increase of the binning and were a consequence of the larger physical dot gain. The printed dot registration error was centered on the center of the original dot with a binning of 2 and 4. For the binning of 3 a systematic misregistration error was observed and the length was found to be close to the size of one dot at the printer nominal resolution. The direction of the misregistration was globally in the upper left region of the code. An alteration was therefore introduced during printing with a binning of 3, however the exact cause was not determined.

For offset, the codes were also accurately registered. The printing of a single dot with a binning of 2 was extremely sensitive to the process variations with a mean single area decrease and a large standard deviation (7 single dots over 90 codes were not printed). With binnings larger than 2, the single dots were then impacted by larger physical dot gains. The physical dot gain levels were found to be dependent on the binning level with an increase and then a decrease with the increase of binning. The maximal physical dot gain was found at a binning of 4 (single dots of 40 µm of diameter). The positioning errors of the single dots centers were not influenced by the increase of binning with a mean positioning errors length corresponding to one half of the dot size at the nominal resolution of the printer. The dots were mostly mis-positioned in the bottom center of the codes, corresponding to an ink spreading in the printing direction.

For inkjet, differences with the offset and electrophotography appeared for small binnings, since only a single droplet was printed for a single dot at the native resolution. Nevertheless the codes were found to be accurately registered. The area of the single dots was strongly dependent to the binning level with a decrease of the mean relative difference with the original dots with the increase of the binning. Single dot edges became rougher with the increase of binning due to the increase of the number of droplets printed. Similarly with the increase of binning, the single dot surfaces became less closed (more convex). With the increase of binning the single dot shapes became closer to the nominal squares. The printed single dot positioning error was constant with the increase of binning and corresponded to one half of the nominal dot diameter. The directions of the misregistrations were mostly found in the lower right quadrant and appeared directed on a diagonal axis corresponding to the print head and paper direction

A model to simulate single dots was proposed based on the assumption that single dots were composed of one or several ink particles located on the surface of the printed dot following a probability distribution. Single dots were then modelled by defining first the spatial probability distribution, then by feeding ink particles to the dot and finally by fusing the particles. The model proposed relied on seven parameters and their effect on the shape of the single dot simulated were evaluated. Different dot shapes could be generated with different levels of edge roughness, ink heterogeneities and physical dot gains. For electrophotography the model globally simulated correctly the printed dots. The fidelity ratio reached 81.6% +/- 19.4% for all binnings. Dots with larger binnings were less sensitive to random variations and were more accurately simulated. For offset, the model globally simulated correctly the printed dots, except for a binning of 2. The fidelity ratio for the binning of 2 reached 46.1% +/- 38.6%%. The offset process presented large variations for printed dots with small inked surface. The simulated dots did not follow this tendency. For the other binning levels a mean fidelity ratio of 86.7% +/- 11.0% was obtained. Moreover, aspect ratio of the simulated dots differed from the printed dots, demonstrating that the τ_{mask} parameter was not large enough. For inkjet, the model globally simulated correctly the printed dots. The mean fidelity ratio for all binnings reached 86.1% +/- 9.6. The singles dot printed with a binning of 1 were associated with large positioning variations and a dot placement pattern for larger binnings could be observed. These positioning variations were not reproduced by the model. The simulated dots were associated with smaller variations. More variability could be introduced in the model, however the comparison with the printed codes would become more complicated.

The model proposed for the single dots was directly implemented to simulate the multiple dots configurations. Results were compared to the measurements using the binary fidelity ratio index. For electrophotography the fidelity ratios were globally independent on the number of single dots in the matrix of the code. The mean fidelity ratio of printed codes compared to the nominal codes for all binnings reached 14.1% +/- 17.3%. These low fidelity ratios demonstrated that large physical dot gains occurred. The mean fidelity ratios of the simulated codes compared to the printed codes for all binnings were largely improved reaching 91.7% +/- 9.0%. The model improved then the spatial description of the ink compared to the nominal codes. For offset, the binary fidelity ratio of the printed dots increased with the increase of binning. The mean fidelity ratio of printed codes compared to the nominal codes for all binnings reached 33.8% +/- 21.5%. The model simulated accurately the printed dots and high fidelity ratio levels for all binnings were obtained with 93.3% +/- 6.9%. The model could be further improved by adopting a higher fusion of the ink particles and with slightly larger position probably masks. For inkjet, the fidelity ratio variations for codes with a similar amount of single dots presented larger variations for small binnings. This showed that for inkjet, the dot-dot interactions were more dependent on the number of single dots printed. The codes associated with the smallest binary fidelity ratios were not necessarily associated with dispersed single dots. The mean fidelity ratio of printed codes compared to the nominal codes for all binnings reached 30.8% +/- 22.6%. The model simulated accurately the printed dots and large fidelity ratio levels for all binnings were obtained with 92.9% +/- 3.6%. For all print processes, the physical dot gain of the singles dots generated dot-dot interactions and induced a global physical dot gain. The configurations of the single dots in the matrix code influenced the physical dot gain. The codes with low fidelity ratio were associated with separated printed dots configurations. Separated dots presented a larger total dot perimeter and influenced the ink spreading.

The model reproduced the global physical dot gains and generated the dot-dot interactions observed with the fusion of the ink particles. Moreover, it was observed that for higher number of single dots, the performances of the model were improved and presented smaller variations as a function of the configurations of the single dots on the code.

7.2 Spatial reflectance prediction model applied to halftones

7.2.1 Spatial reflectance prediction models

Models previously developed and found in literature mostly propose a prediction of the halftone reflectance based on the ink coverage, the solid ink reflectance and the bare paper reflectance [2,244,245]. However, the light diffusion on paper generates a light trapping phenomenon, referred to as optical dot gain [318], impacting the ink and paper reflectances. The ink and paper reflectances become dependent on the ink coverage, the halftone morphology, the ink homogeneity, the halftone dot edge fuzziness, the paper diffusion characteristics, etc. Yule-Nielsen and Arney proposed to adapt the models to account for the optical dot gain. Yule-Nielsen proposed to introduce an empirical parameter, called n, fitted to adapt for the each paper and for each halftone configuration. Arney proposed to introduce a model, called the probability model predicting the ink and paper reflectances as a function of the halftone configuration parameters, however multiple empirical parameters remained required to fit the model to the experiments [5–7]. The requirement to fit the model for each halftone configuration is time consuming, since it requires to print calibration patches, to measure and to compute the parameters.

Moreover the models developed do not take into consideration the spatial description of the ink layer deposited on paper. The light diffusion on paper effect affects the ink and paper reflectances levels as a function of the position on the halftone. For example at the edges of and inked dot, the reflectance will be increased compared to the reflectance at the center of the halftone dot. Similarly on paper, the reflectances will be higher at large distances of the ink regions and will be decreased near the edges of the ink dots. A model taking into account the ink and paper spatial dependency was developed. Interestingly, this model was developed almost at the same time as the Yule-Nielsen model, however due to limitations in the microscale measurements of the ink and paper regions the model was not widely applied. Callahan, Yule and Lehmbeck are the first authors to describe the ink and paper regions as a function of the light diffusion of paper [8–16]. The model, called the light diffusion on halftones can predict the halftone reflectance as a function of the paper PSF, the spatial description of the ink transmittance and the bare paper reflectance, equation [7.9] (spectral dependencies are omitted).

Model of the light diffusion on halftones

		Symbol	Unit	Denomination
[7.9]	$R_a(x,y) = R_{ps}(x,y)\, T_i(x,y) [T_i(x,y) \circledast H(x,y)]$	$R_a(x,y)$	1	Halftone reflectance
		$T_i(x,y)$	1	Ink transmittance
		$R_{ps}(x,y)$	1	Bare paper reflectance
		$H(x,y)$	1	Paper point spread function
		$\circledast$	-	Convolution operator

Experimental investigations conducted by Happel, Ukishima and Kriss revealed that the predicted reflectances obtained with model of the light diffusion on halftones slightly diverge from the experiments [10,17,405]. A reason advanced by researchers is that the paper PSF used is not reproducing accurately the paper diffusion. Multiple studies were then conducted and focused on finding the best PSF for different types of papers [10,12,248,249,339,340]. The research for the best paper PSF is still ongoing nowadays and demonstrate the complexities of the optical phenomena involved [406]. Happel analyzed the paper PSF with a dedicated apparatus and obtained highly accurate paper PSF measurements. The performance of the model was then analyzed using the corresponding paper PSF. Despite the accuracy of the paper PSF measured, this PSF applied to the model of the light diffusion on halftones was found to slightly diverge from the experiments [10]. The author concluded that more effects had to be taken into consideration in the model. Gustavson argued that the model is valid only in the case where the

ink is rigorously at the surface of the paper, without ink penetration in the paper and the paper having no roughness [235]. Moreover the ink should have a constant thickness, thus should have a constant transmittance and should only absorb the light (scattering of the light in the ink is not accounted). The paper PSF is be considered independent from the ink properties. The light is a natural light and is considered non-coherent, non-polarized homogeneous and totally diffuse. Moreover the direct reflections (specular reflections) are not considered by the model of the light diffusion on halftones, as explained by Kruse, Wedin, [208,231,240]. It has to be noted that the effects of internal reflections were found significant for coated paper by Williams and Clapper [322]; however in the model of the light diffusion on halftones no internal reflections are considered; the light enters the halftone diffuses and exits the halftone without reflections at the paper-ink-air interfaces. Roger discussed about the relevance of considering the internal reflections and proposed to introduce a model of the light diffusion on halftones taking into account the multiple reflectances of the halftones due to the several internal reflections. The model proposed by Roger is simply a sum of the model of the light diffusion and of the successive terms corresponding to the internal reflections (the light reflected at the air – ink and paper interface will transmit through the ink layer, diffuse into paper and will be reflected trough the ink layer before reaching the interface again), Figure 7.26, equation [7.10] [201]. At each internal reflection, part of the light exits the halftone and part of the light is reflected back into the halftone. This model is then called by number of total reflections (the first one corresponding to the model of the light diffusion on halftones and followings one corresponding to the internal reflections), in contrast with the conventional model of the light diffusion that will be called alternatively "1 reflection model".

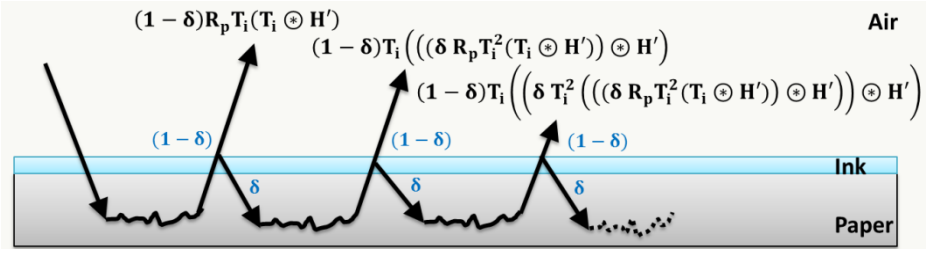

Figure 7.26: Multiple internal reflections on a halftone print.

Model of the light diffusion on halftones extended to internal reflections

$$R_a = (1-\delta)R_{ps}T_i(T_i \circledast H') + (1-\delta)T_i\left((\delta\, R_{ps}T_i^2(T_i \circledast H')) \circledast H'\right) + (1-\delta)T_i\left(\left(\delta\, T_i^2\left((\delta\, R_{ps}T_i^2(T_i \circledast H')) \circledast H'\right)\right) \circledast H'\right) + \cdots \quad [7.10]$$

Symbol	Unit	Denomination
$R_a(x,y)$	1	Halftone reflectance
$T_i(x,y)$	1	Ink transmittance
$R_{ps}(x,y)$	1	Paper reflectance
$H'(x,y)$	1	PSF considering internal reflections
δ	1	ratio reflected back
$\circledast$	-	Convolution operator

The model of the light diffusion on halftones has been employed in this thesis to study multiple halftone properties. The repeated applications of the model lead to several analysis of its performances and helped uncover regions where the model was not following the experiments. In this work, an analysis of the performances of the model of the light diffusion on halftones at the boundary between the ink and the paper regions is proposed considering or excluding the internal reflections. Multiple paper PSF size and shape are analyzed. A discussion over the influences of the model assumptions is proposed in order to identify the phenomena responsible for the divergence of the model with the experiments. A modification of the model of the light diffusion on halftones is then proposed. The new model performances are then evaluated with several halftone configurations, dot morphologies, print

processes and papers. Finally, the novel model is compared to the model of the light diffusion on halftones and with the Yule-Nielsen model.

7.2.2 Material and methods

7.2.2.1 Halftone patches and microscope captured halftone images

The halftones were printed with three different processes: offset, inkjet and electrophotography, Table 7.6. Amplitude modulated (AM) grayscale patches at 150 and 200 lpi and consisting of 14 different ink coverage of (0%, 2%, 5%, 10%, 15%, 20%, 30%, 40%, 50%, 60%, 70%, 80%, 90%, 100%) were printed. Frequency modulated (FM) grayscale patches at the resolutions of 1, ½, 1/3, ¼ and 1/8 the native resolution and consisting of 13 different ink coverage of (0%, 5%, 10%, 15%, 20%, 30%, 40%, 50%, 60%, 70%, 80%, 90%, 100%) were also printed. The halftone patches were printed on four different papers: two glossy coated denoted "Glossy 1" and "Glossy 2", one coated paper with a layer compatible for inkjet prints denoted "Epson" and one uncoated paper denoted "Uncoated", Table 7.6.

A Zeiss Axio Imager M1m optical microscope mounted with two EC Epiplan Neofluar HD DIC 10x/0.25 and 20x/0.50 objectives is used to image the halftones with a modified Canon 1200D camera (monochrome, CMOS, 13.8 megapixels). Total magnification on sensor is 20x with a calibrated system of 0.2101 µm/pixel for the 20x objective. Crossed analyzer-polarizer (90°) reflected light microscopy with a 0°/0° geometry is chosen to capture images excluding the specular reflections. A halogen lamp Zeiss Hal 100 is used as light source for the microscope with a blue filter giving a spectrum similar to the standard D65 illuminant. The source voltage is regulated and set at 10.0V. The source luminance variations are recorded with a luxmeter placed on the side of the light path and images captured are corrected accordingly. The iso of the camera is set at 800 and exposure times are selected to perform high dynamic range captures. Images are saved in raw .CR2 format and processed with Python 3.6 to perform black frame subtraction and to correct the uniformity of the field of view. A high dynamic range capture is performed allowing increasing the measurement accuracy in the ink region. A total of 1231 AM and FM halftone patches were imaged for this study, Figure 3.2.

Table 7.6: Halftone patches configurations: halftone type, resolution, ink and paper properties). (*) the optical density is computed by taking the fitted ink peak center reflectance obtained with the Gaussian fit of the ink peak on the histogram of the corresponding solid print.

Process	**Paper (g/m²)**	**Ink (Black)**	**Halftone type, resolution and (designation)**		**Optical density***
Offset: Heidelberg Speedmaster 52, 2540 dpi	Glossy 1: Unknown supplier, coated, 135	Novavit 918 supreme	O1	AM: 150 lpi (AM1) and 200 lpi (AM2) FM: 2540 dpi (FM1), 1270 dpi (FM2), 847 dpi (FM3), 635 dpi (FM4), 318 dpi (FM8)	2.37
			O2	AM: 150 lpi (AM1) and 200 lpi (AM2)	1.91
			O3	AM: 150 lpi (AM1) and 200 lpi (AM2)	1.01
Electrophotography: Xerox Versant 180 Press, 1200 dpi	Glossy 1: Unknown supplier, coated, 135	Xerox Versant 80 Press	E1	AM: 150 lpi (AM1) and 200 lpi (AM2) FM: 1200 dpi (FM1), 600 dpi (FM2), 400 dpi (FM3), 300 dpi (FM4), 150 dpi (FM8)	2.52
	Glossy 2: Mondi, coated, 135		E3	AM: 150 lpi (AM1) and 200 lpi (AM2)	2.52
	Epson: Epson proofing, 205		E2	AM: 150 lpi (AM1) and 200 lpi (AM2)	2.47
	Uncoated: Inapa, uncoated, 160		E4	AM: 150 lpi (AM1) and 200 lpi (AM2)	2.51
Inkjet: Epson Stylus Pro 4900, 1440 dpi	Epson: Epson proofing, 205	Epson MK T6538	IM	AM: 150 lpi (AM1) and 200 lpi (AM2) FM: 1440 dpi (FM1), 720 dpi (FM2), 480 dpi (FM3), 360 dpi (FM4), 180 dpi (FM8)	2.65
		Epson PK T6531	IG	AM: 150 lpi (AM1) and 200 lpi (AM2)	2.21

7.2.2.2 Simulation of halftone image with the model of the light diffusion on halftones

Halftone images captured on the microscope are considered as the experimental reference and are called the MCI. The spatial description of the ink is obtained by thresholding the MCI with the LveSpatial threshold algorithm developed (chapter 6). A constant ink transmittance is applied to the spatial description of the ink to obtain the spatial transmittance function $T_i(x,y)$. The constant ink transmittance level is computed taking the square root of the corresponding mean solid print reflectance. A Simulated Halftone Image (SHI) is then obtained by applying the model of the light diffusion, equation [7.9].

Several paper point spread function with multiple lengths are used to obtain several SHI: 8 paper PSF are used with parameters defined empirically and 8 different paper PSF lengths. The functions correspond to usual paper PSF described in literature [10] Table 7.7. The paper PSF length is called d_{PSF} and the 1D paper PSF are referred to as $P(x)$. The lengths d_{PSF} are in range going from 5 µm to 199 µm (legend of Figure 7.28) and correspond to a larger range than the paper PSF length range measured conventionally. It has to be noted that multiple studies in literature have found paper PSF lengths around 100 µm for glossy coated papers [332,340]. The shapes of the 8 paper PSF for a length of 55 µm are presented in Figure 7.28 (I). PSF with different shape are then obtained with wide or narrow peaks. The shape of the two sums of Gaussian functions differs: the first one being associated with a large peak and then a convex ring; the second one having a larger peak and a concave ring. The narrowest peaks are obtained with the modified exponential function and the quadratic rational function. The quadratic rational is the steepest peak. 3-dimensionnal descriptions of the paper PSF are generated by rotating the functions on themselves. The 3D descriptions are then normalized with the sums of the functions equal to unity in order to satisfy the law of conservation of energy. The 3D descriptions of the point spread functions are referred to as $H(x,y)$ in equation [7.9].

Table 7.7: Paper PSF profiles functions P and parameters implemented.

Name	Function		Parameters
Pillbox [10]	$P_p(x) = \begin{cases} 1 & \text{for } x \le (\alpha_1\, d_{PSF}) \\ 0 & \text{else} \end{cases}$	[7.11]	$\alpha_1 = 0.50$
Ramp [10]	$P_r(x) = \begin{cases} (\alpha_2 - x) & \text{for } x < (\alpha_2\, d_{PSF}) \\ 0 & \text{else} \end{cases}$	[7.12]	$\alpha_2 = 0.50$
Gaussian [10,261]	$P_g(x) = \exp\left(-\frac{x^2}{(\alpha_3\, d_{PSF})}\right)$	[7.13]	$\alpha_3 = 0.42$
Sum of Gaussian 1 [334,337]	$P_{sg}(x) = \sum_{i=1}^{4} \beta_i \exp\left(-\frac{x^2}{(\gamma_i\, d_{PSF})}\right)$	[7.14]	$\beta_{1;2;3;4} = 1; 0.5; 0.25; 0.031$ $\gamma_{1;2;3;4} = 0.12; 0.48; 1.08; 1.92$
Sum of Gaussian 2 [334,337]			$\beta_{1;2;3;4} = 1; 2; 0.067; 1$ $\gamma_{1;2;3;4} = 0.12; 1.20; 0.60; 1.44$
Exponential [10,236,323]	$P_e(x) = \exp\left(-\frac{x}{(\alpha_4\, d_{PSF})}\right)$	[7.15]	$\alpha_3 = 0.15$
Modified exponential [10,208]	$P_{me}(x) = \frac{\exp\left(-\frac{x}{(\alpha_5\, d_{PSF})}\right)}{x}$	[7.16]	$\alpha_5 = 0.40$
Quadratic rational [10,340]	$P_q(x) = \frac{\sinh^{-1}\left(\frac{\alpha_6}{x}\right)}{1+x^2}$	[7.17]	$\alpha_6 = 1$

7.2.2.3 Models performances evaluations

Reflectance profile evaluation

A halftone patch with dots of 155 µm of diameter, printed with electrophotography on the "glossy 1" coated paper was imaged on the microscope and is used as the experimental reference MCI for the profile evaluation. A profile corresponding to the reflectances along a line going from the paper region toward the center of the ink dot on the printed halftone is measured for the MCI. The profiles are defined manually by selecting a set of coordinates on the halftone. The profiles are chosen systematically in the cross direction relatively to the machine direction. An average of the profile can be obtained by averaging multiple reflectances values adjacent and orthogonal to the profile direction. SHI are then simulated for 8 different paper PSF associated to 8 different paper PSF lengths. The profiles along the same line as for the MCI are measured on the SHI. The aim of this analysis is to demonstrate that even with different paper PSF and lengths, the model diverges from the experiments in the transition region around the edges of the halftone dots and the paper (ink-paper limit). Authors have observed this ink-paper limit region and called it as the mixed ink-paper region [293,407–409]. Results are presented in Figure 7.28.

To compare the MCI halftone profile and the SHI profiles a similarity index inspired from the Pearsons chi-square test is proposed, equation [7.18]. This index characterizes the amount of similarity between two sets of reflectance profiles (the reflectance profiles are function of the position x). The CS_p index is computed for 3 different regions of the halftone: the ink region, the mixed region and the paper region. These regions are defined by setting two reflectance limits dividing the total reflectance range in 3 sub ranges, corresponding to the ink, the mixed and the paper regions. The reflectance limits were defined manually by inspecting the reflectances profile of the MCI and the histogram of the MCI. The upper and lower reflectance limits for the mixed region were defined at respectively 0.5 and 0.05. The ink region corresponds then to the reflectances going from the smallest reflectance to 0.05 and the paper region to reflectances going from 0.5 to the largest reflectance.

Profile similarity index inspired from the Pearsons chi-square test

[7.18]
$$CS_p = \frac{1}{n}\sum_{x=0}^{n}\begin{cases}\dfrac{\left(O_s(x)-O_r(x)\right)^2}{O_r(x)} & \text{if } O_r(x)>0\\ O_s(x)^2 & \text{else}\end{cases}$$

Symbol	Unit	Denomination
CS_p	1	Profile similarity index
$O_r(x)$	1	Reference reflectance profile
$O_s(x)$	1	Tested reflectance profile
n	1	Number of positions
x	1	Position on the profile

Mixed region evaluation

A quantification of the reflectances differences between the MCI and SHI can be computed in term of fitted ink coverage differences, giving a better appreciation of the divergence of the model prediction with the experiments. To compute the fitted ink coverage a specific methodology is proposed:

1- Manual definition of the regions reflectance limits (ImageJ, Threshold function with manually adjusted min and maximum reflectances corresponding to the mixed region), Figure 7.31 (A).

2- Measurement of the mean reflectances for the ink (R_i), mixed (R_m) and paper (R_p) regions of the MCI and of the SHI and measurement of the mean halftone MCI reflectance (R_a).

3- Measurement of the ink coverage of each region (corresponding to the number pixels having the reflectance included in a region divided by the total amount of pixels)

4- R_i and R_p of the SHI are set to be equal to the R_i and R_p of the MCI (in order to compare only the effects of the ink coverage differences generated by differences in the mixed region)

5- The halftone reflectance of the SHI is computed using a linear additive model (similar to Arney's extended Murray-Davies model) with three different colorants (the ink, the mixed and the paper regions). The linear additive model is similar to the Neugebauer model [293,409,410], nevertheless the reflectances of the colorants are defined within each halftones similarly to Arney's model [5,407]. It should be also noted that a continuous Yule-Nielsen model has been proposed by Hébert and Hersch [408]. The linear additive model used is expressed by:

$$R_a = a_i R_i + a_m R_m + a_p R_p \qquad \text{with} \qquad a_i + a_m + a_p = 1 \qquad [7.19]$$

and with a_i the ink coverage, a_m the mixed region coverage and a_p the paper coverage.

6- The effective ink coverage a_e of the MCI is measured by thresholding the halftone image with the LveSpatial threshold algorithm.

7- The Yule-Nielsen n parameter is optimized by solving the Yule-Nielsen model for the MCI taking as input the effective ink coverage a_e, the solid ink reflectance R_{is} (mean reflectance of the corresponding solid ink image) and the bare paper reflectance R_{ps} (the mean reflectance of the corresponding bare paper image), (spectral dependency omitted) [244]:

$$R_a = \left[(1 - a_e)\, R_{ps}^{\frac{1}{n}} + a_e\, R_{is}^{\frac{1}{n}} \right]^n \qquad [7.20]$$

8- The effective ink coverage of the SHI is then determined reversing the Yule-Nielsen model using the R_a computed for the SHI (including the effects of the mixed region), the n fitted and R_{is}, R_{ps} defined for the MCI (spectral dependency omitted).

$$a_e = \frac{R_a^{\frac{1}{n}} - R_{ps}^{\frac{1}{n}}}{R_{is}^{\frac{1}{n}} - R_{ps}^{\frac{1}{n}}} \qquad [7.21]$$

9- The effective ink coverage difference Δa_e can then be obtained by subtraction of the effective ink coverage obtained for the SHI (including the effects of the mixed region) with the effective ink coverage obtained for the MCI.

Novel model performance evaluation

An evaluation of the novel model performances is proposed, by comparing the apparent ink coverage differences obtained with the novel model, with the model of the light diffusion on halftones (1 reflection model) and with the Yule-Nielsen model. The apparent ink coverage differences are obtained by subtracting the apparent ink coverage predicted and the apparent ink coverage measured experimentally. The apparent ink coverages are obtained by fitting the apparent ink coverage in the Murray-Davies model with the halftone reflectance and account for the physical and optical dot gains. The halftone reflectances are obtained either experimentally or are obtained with the models, Figure 7.27. Comparing the apparent ink coverage is interesting because it gives a direct evaluation of the model performances allowing comparing easily different print processes, halftone types and sizes, papers and inks. The Apparent Ink Coverage Difference (AICD) can be compared to the optical or physical dot gain expressed also as an ink coverage difference. Moreover the ink coverage differences can be compared to the ink coverages to assess directly the expected accuracy of the models. In order to compare the performance of the models with different print processes, halftone types and sizes, papers and inks, the average of the absolute AICD is computed for all ink coverages of the set of halftones considered. It should be noted that a drawback of this evaluation method is that only the apparent ink coverages are compared. The ink coverages are obtained from the halftone mean reflectance. Thus differences in the distribution of the reflectances for the different regions of the halftones cannot be analyzed and a compensation phenomenon can occur (similar halftone mean reflectances with different reflectance distributions for the ink, the mixed and the paper regions). The

comparison method has nevertheless the advantage of giving a global assessment of the model performances.

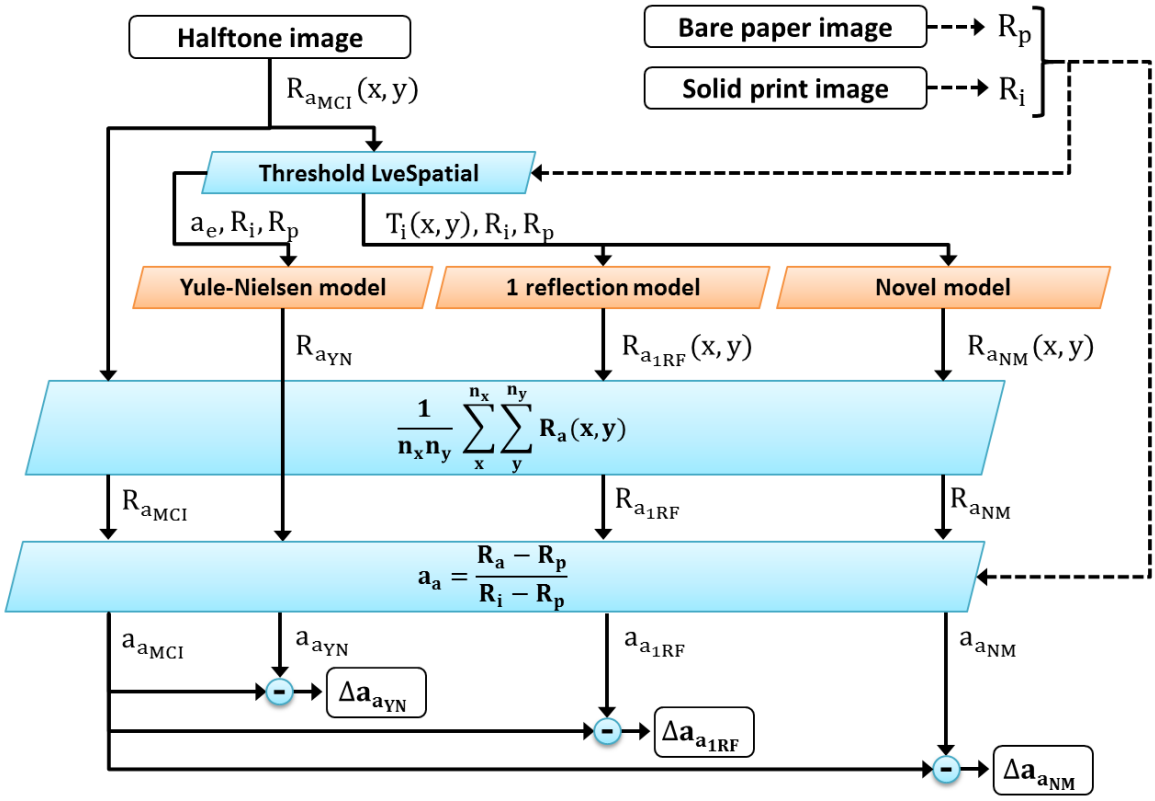

Figure 7.27: Diagram of the method developed to obtain the apparent ink coverage difference for 3 tested models: The Yule-Nielsen model, the model of the light diffusion on halftones (1 reflection model) and the novel model. For the 3 models the parameters are fitted for each set of halftones.

The Yule-Nielsen n parameter is optimized for a halftone set by minimization of the differences of the predicted reflectances and the measured reflectances, using Microsoft Excel generalized reduced gradient nonlinear solver. It should be noted that the Yule-Nielsen n parameter is optimized taking the effective ink coverage in the input of the model. In this way, only the optical dot gain is expressed in the parameter. The paper PSF for the model of the light diffusion on halftones, and the two PSF and the m parameter for the novel model could not directly be fitted using a solver because it required computing the SHI multiple times for each halftone in the set and because long computation times were associated. Instead a manual optimization was proposed finding the best parameters by computing the SHI for selected halftones of a set.

The performances of the novel model are also compared in the mixed regions of the halftones with the performances of the model of the light diffusion on halftones (1 reflection). The comparison requires computing the mean reflectance of the mixed regions. The corresponding apparent ink coverage can then be computed using the Murray-Davies model. The mixed regions reflectance range depends on the halftone characteristics and is not constant. For this reason a definition of the mixed region is proposed with K the threshold value representing the reflectance value separating the ink and the paper reflectances:

$$\text{Mixed region reflectance range} = \left[\frac{K}{2}\,;\left(\frac{R_{ps}+K}{2}\right)\right] \qquad [7.22]$$

7.2.3 Performances of the model of light diffusion on halftones

7.2.3.1 Reflectance profile evaluation

To evaluate the performances of the halftone reflectance models, the predicted reflectance is conventionally compared to the reflectance measured on printed halftones. This approach assesses the global performances of the models; however it does not allow studying the reflectance distributions of the different regions of the halftone. In some cases, a model can have accurate global performances with at the same time poor performances for the different regions: the errors generated for a region are compensated by other regions. Therefore an evaluation for each region allows an improved comparison of the model performances. The reflectances profiles along a line on the halftone are then evaluated.

The profile is obtained measuring the reflectance values along a line on the halftone. A similar line position is used for the MCI and for the several SHI. The profile obtained for the MCI shows a transition from the paper to ink with an "S" shaped curved and differs from a theoretical step function, Figure 7.28. The transition is not clearly defined with the paper reflectance decreasing before the effective limit of the ink dot. Similarly the ink dot reflectance is increased near its effective edge. SHI profiles of the 8 paper PSF associated with the 8 different lengths are presented in Figure 7.28. It can be observed that the similarity of SHI profiles with the MCI profile depends on the type paper PSF used and on the PSF length. Small and large PSF lengths do not follow accurately the profile of the MCI. The simulated profiles shapes obtained with the ramp PSF, the Gaussian PSF, the exponential and modified exponential are reproducing more closely the global shape of the MCI profile. An index comparing the similarity of the SHI profile and the corresponding MCI profile was computed to quantify the performance of the different paper PSF and associated length. The CS_P index proposed is based on the Pearsons chi-square test. The best similarity between the two profiles is associated with the smallest index. The global CS_P index for three regions show that the Exponential is the paper PSF performing the most accurately for the halftone considered printed with electrophotography on glossy coated paper. The best global CS_P index of the exponential PSF is found at 0.0096 with a PSF length of 136 µm. The modified exponential paper PSF is the second best function to simulate the halftone reflectance with a global CS_P index to the exponential PSF of 0.0097. The third best paper PSF is the Gaussian function with a global CS_P of 0.0104. The 1st sum of Gaussians, Quadratic rational, ramp, pillbox and 2nd sum of Gaussians are associated with larger global CS_P of respectively 0.0108, 0.0109, 0.0113, 0.0117 and 0.0130.

Three different regions are considered on the halftone surface: the ink region, the mixed ink-paper region and the paper region. For each region, the best performances are obtained with different length. However the model of the light diffusion on halftones uses only one PSF length. The global CS_P indexes can be compared to the CS_P index for the ink, mixed and paper region. Improved profile similarities are obtained by evaluating only the ink region and the paper. Three different regions are evaluated independently:

- For the paper region, the PSF lengths showing the smallest profiles differences with the MCI are found around 105 µm for the pillbox PSF, 136 µm for the ramp PSF, 105 µm for the Gaussian PSF, 73 µm for the 1st and 2nd sum of Gaussians PSF, 136 µm for the exponential PSF and modified exponential PSF and 73 µm for the quadratic rational PSF. The mean paper region CS_P index for all PSF reaches 0.0051 +/- 0.0018 for the paper region and can be compared to the mean CS_P index of 0.0109 +/- 0.0011 for all regions.
- For the ink region, the PSF lengths required are globally larger with optimal length around 168 µm for the pillbox PSF, 199 µm for the ramp PSF, 136 µm for the Gaussian PSF, 105 µm for the 1st and 2nd sum of Gaussians PSF, 168 µm for the exponential PSF, 136 µm for the modified exponential PSF and 105 µm for the quadratic rational PSF. It has to be noted that the relative difference obtained for the ink region are smaller for the ink region and could explained the shift

of optimized PSF length found. The mean paper region CS_P index for all PSF reaches 0.0025 +/- 0.0011 for the paper region and can be compared to the mean CS_P index of 0.0109 +/- 0.0011 for all regions.

- For the mixed region, larger differences between the MCI and the several SHI obtained appear. These divergences can be observed directly on the profiles with a sharp edge for the several SHI compared to the more rounded "S" shape edge for the MCI, Figure 7.28. The model of the light diffusion on halftones generates SHI with overestimated reflectances near the edge of paper and underestimated the reflectances near the edge of the ink dot. The model does not reproduce accurately the light trapping effects generated at the edge of the ink and the paper region. And thus the ink-paper edge remains visible on the SHI. The PSF length influences only slightly the shape of the SHI profiles in the mixed region. The SHI profiles are less steep near the ink-paper edges for PSF lengths around 100 µm; however the shapes of the SHI edges remain steeper than the MCI. The mixed region is associated with a larger mean CS_P index of 0.0691 +/- 0.0011 compared to the mean CS_P index of 0.0109 +/- 0.0011 for all regions. The dispersion for the mean CS_P index for the mixed region is small showing a marked tendency of the SHI profiles to diverge with the MCI. The divergence of the SHI profiles appears globally independent with the PSF type. Moreover the mean CS_P differences between the ink and paper regions with a mean CS_P index of 0.0038 +/- 0.0023 and the mixed region with mean CS_P index of 0.0691 +/- 0.0011 are large, about 18 times larger, showing the mis-performance of the model of the light diffusion on halftones in the mixed region.

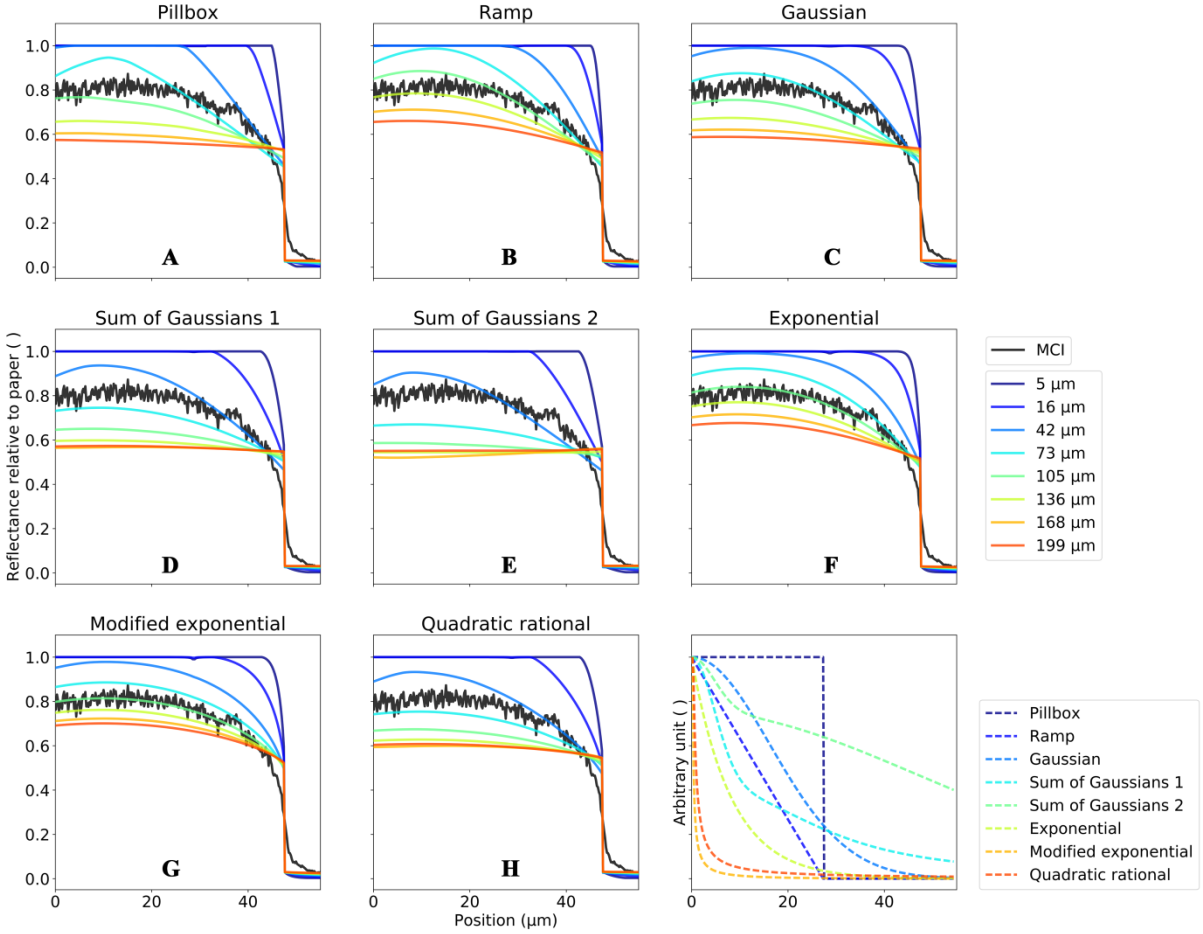

Figure 7.28: (A to H) MCI and SHI reflectance profiles for multiple paper PSF types and lengths. The halftone patch is composed of halftone dots of 155 µm of diameter and is printed in electrophotography on glossy 1 coated paper. (I) the different paper PSF used at a paper PSF length of 55 µm.

It has to be noted that the evaluation performed in this section could be improved by fitting precisely the PSF length for each PSF. Nevertheless the aim of the analysis was to demonstrate the even for different paper PSF types and lengths, the large profiles differences were occurring in the mixed region. This shows that the multiple assumptions adopted in the model of the light diffusion on halftones may oversimplify the physical phenomena impacting the light reflection on printed halftones. Complementary light interactions with the ink and the paper should then to be considered.

7.2.3.2 Non constant ink transmittance and imaging sharpness effects

The influence of the ink layer transmittance homogeneity is analyzed for an exponential PSF with multiple PSF lengths, Figure 7.29. The variable ink transmittance was generated by applying a Gaussian blur followed by a selective threshold, as presented by Hébert and Hersch [408]. The variations of the ink transmittance generated account for an increase of the transmittance near the edges of the dots. Comparing the profiles with a constant ink transmittance and with a variable ink transmittance reveals that the SHI profiles are improved in the mixed region when accounting for the ink transmittance variation. The PSF length that fit best the MCI profile remains around 136 µm. Computing the CS_P index shows that the global performance of the model is increased with a CS_P of 0.0091 for the SHI obtained from variable ink transmittance compared to a CS_P of 0.0096 for the SHI obtained from constant ink transmittance. The ink region profile similarity is improved with a CS_P of 0.0008 for the variable ink transmittance compared to a CS_P of 0.0014. The paper region performs less accurately with a CS_P of 0.0048 for the variable ink transmittance compared to a CS_P of 0.0040. The mixed region is the region where the most improvements should be measured. However the CS_P is only slightly improved with a CS_P of 0.0644 for the variable ink transmittance compared to a CS_P of 0.0672. The mixed region near the ink edges is better reproduced, however the mixed region near the paper edges continues to present large differences with the MCI. This result shows that the variable ink thickness is not the only phenomenon impacting the model performances in the mixed region.

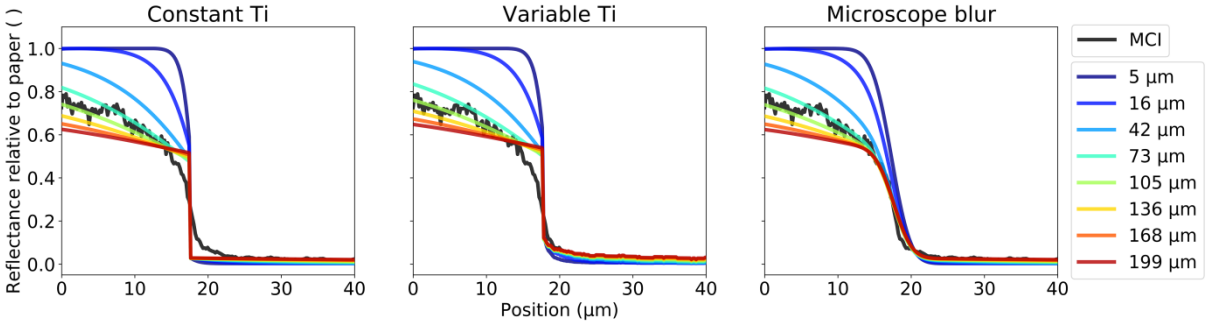

Figure 7.29: MCI and SHI reflectance profiles for the exponential paper PSF with multiple lengths. The ink layer has either a constant transmittance (Constant Ti) or a variable transmittance with less absorption near the edges of the dots (Variable Ti). A Gaussian blur with a kernel size of 12.4 µm is applied to the SHI with the constant ink transmittance simulating potentials out of focus effects (Microscope blur).

The hypothesis of a divergence of the performances caused by an optical blur coming from focusing errors and from diffusion in the imaging system is investigated. A Gaussian blur was applied to the SHI obtained with an exponential PSF. The results show a large improvement of the similarities between the simulated and measured profiles in the mixed region. The transition from the paper to the ink is more accurately reproduced with less steep edges. The PSF length that fit best the MCI profile remains around 136 µm. The global similarity index CS_P is improved for the SHI with Gaussian blur with a CS_P of 0.0047 compared to a CS_P of 0.0096 for the SHI without blur. The ink region is found at a similar CS_P level for SHI with and without Gaussian blur. The SHI with Gaussian blur performs better in the paper region with a CS_P of 0.0031 compared to a CS_P of 0.0040. The largest profile similarity improvement is measured in the mixed region with a CS_P of 0.0268 for the SHI with Gaussian blur compared to a CS_P of 0.0672 for the SHI without Gaussian blur. This improvement is significant and confirms the increased similarities between the MCI profile and the SHI with Gaussian

blur profile. Nevertheless, the CS_P obtained in the mixed region remains large compared to the ink and paper regions.

A Gaussian blur kernel size of 12.4 µm is required to obtain similar MCI and SHI profiles in the mixed region. The MCI is imaged with a 20x objective having a numerical aperture of 0.5. This gives a resolution limit of 0.67 µm, at an average wavelength of 550 nm, according to the Rayleigh criterion. The Gaussian blur required to match the measured and SHI profiles is then 18.5 times larger. The digital camera pixel size is 0.21 µm. Taking into account the Nyquist sampling theorem, a minimum of two pixels are required to image an object. Thus the camera produces an uncertainty of 0.42 µm. The Gaussian blur required to match the measured and SHI profiles is then 29.5 times larger. Error in the focusing of the apparatus can also impact the measurements. Happel conducted an extended characterization of the all of the effects impacting the measurements of a projected edge on paper [10]. The author tested the impact of focus errors on the sharpness of a projected edge response. According to the author's results the edge response at best focus corresponded to a Gaussian blur with a kernel size around 10 µm. Focusing error and microscope diffusion might be partially responsible of the profile response of the MCI in near the effective ink paper edge in the ink region. It should be noted that sharpness error of the projected edge can also be responsible for a part of the length of the edge response recorded. Moreover by analyzing the halftone visual appearance, it appear that a Gaussian blur with a kernel of 12.4 µm produces a blur exaggerated compared to the MCI, Figure 7.30 (A & G). On the halftone image simulated and blurred the satellites ink dots are less sharp than for the MCI satellites dot. The paper surface shadows, generated by the variations of the coated layer, are less visible on the blurred image. It can be concluded that the optical blur is not the only effect affecting the performances of model of the light diffusion on halftones compared to the measurements. Other phenomenon such as the internal reflections, the ink penetration into the paper or the ink scattering properties can induce further light trapping effects.

7.2.3.3 Visual assessment of the paper PSF length effect on the SHI

The relation of the PSF length in relation with the halftone dot size can be observed on Figure 7.30. Small PSF lengths result in bright reflectances in the paper regions and dark reflectances in the ink regions. The ink-paper edges are well defined, Figure 7.30 (B). Comparing the MCI and the SHI shows that with small paper PSF lengths the light trapping effects are not pronounced enough to be similar to the MCI. With the increase of the PSF length, a shadow starts to be visible near the edges of the dots. This shadow is particularly visible for the PSF lengths of 42 µm and 73 µm Figure 7.30 (C & D). A shadow is also visible around the MCI dots. Although the reflectance profile is only associated with small curvatures in the mixed region near the paper and near the ink edges, the shadowing effects are clearly visible around the ink dots. With larger PSF lengths the shadowing effects decrease. This decrease in caused by the relations between the size of the halftone dots and the size of the PSF. With PSF lengths larger than the half of the halftone cell size, the complete light diffusion approximation is adopted. This approximation signifies that the effect of the light diffusion and trapping is not dependent anymore on the position on the halftone dot. The paper reflectance and the ink reflectance decreases become then globally homogeneous [4]. This approximation is roughly verified here with the loss of the dot edge shadowing for the PSF lengths starting from 73 µm. The halftone cell size is measured at 212 µm and thus has a half cell size of 106 µm. It should be noted that the variable ink thickness halftone does not appear visually different from the constant ink transmittance corresponding halftone Figure 7.30 (E & F).

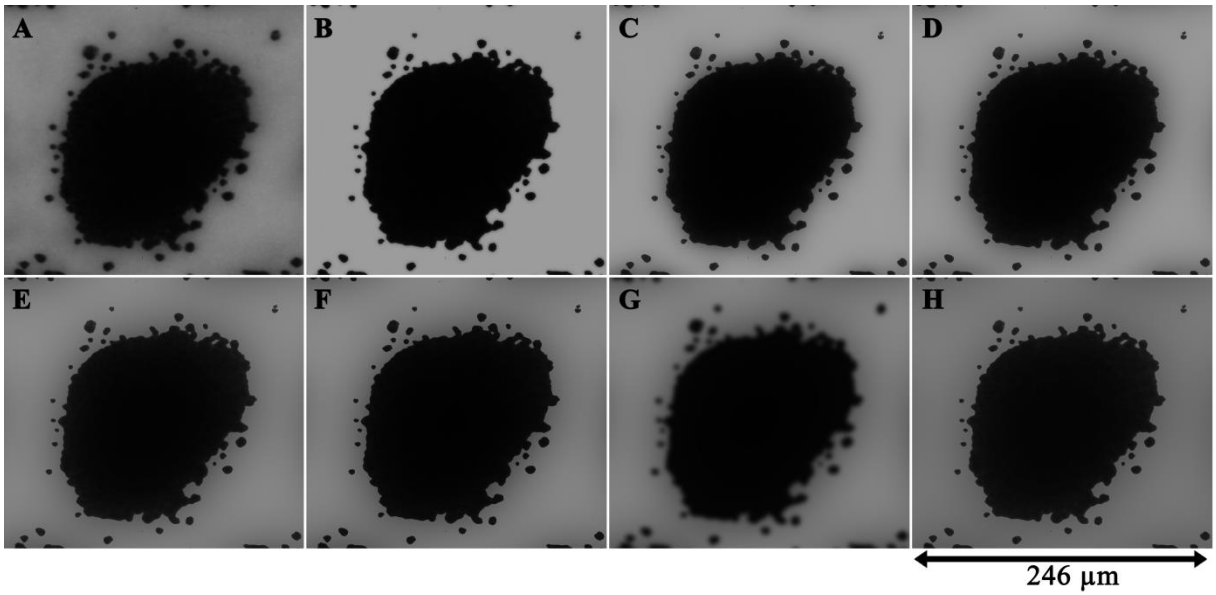

Figure 7.30: Halftone dot of 155 µm diameter printed with electrophotography and (A) imaged on the microscope, (B, C, D, E, H) simulated with an exponential PSF of respectively 5 µm, 42 µm, 73 µm, 136 µm, 199 µm, (F) simulated with an exponential PSF of 136 µm with variable ink transmittance and (G) simulated with an exponential PSF of 136 µm and with a Gaussian blur of 12.4 µm kernel applied.

7.2.3.4 Influence of the mixed region on the halftone apparent ink coverage

It is interesting to investigate the influence of the mixed region SHI and MCI differences on the total halftone reflectance. The regions of the halftone image corresponding to the mixed region (reflectances higher than 0.05 and lower than 0.5) are overlaid in red color, Figure 7.31 (A). It can be observed the mixed region profile length (25 µm) is small compared to the size of the halftone dots (155 µm) and compared to the size of the paper between the dots. Nevertheless the mixed region surface becomes large when considering the surface on the halftone with a coverage of 15% compared to an ink coverage of 50%. The mixed region corresponds then to almost one third of the ink coverage. By assimilating the mixed region to an annulus with an internal diameter equal to the diameter of the ink dot (d_d) subtracted by the mixed region thickness (d_t) and the external diameter equal to the diameter of the ink dot added to the mixed region thickness, the surface of the annulus S_a can be calculated:

$$S_a = \pi\left[\left(\frac{d_d + d_t}{2}\right)^2 - \left(\frac{d_d + d_t}{2}\right)^2\right] = \pi\, d_d\, d_t \qquad [7.23]$$

The ink dot surface S_i is assimilated to a disc and can be easily computed as:

$$S_i = \pi\left(\frac{d_d}{2}\right)^2 \qquad [7.24]$$

The ratio of the annulus surface with the dot surface gives:

$$\frac{S_a}{S_i} = \frac{\pi\, d_d\, d_t}{\pi\left(\frac{d_d}{2}\right)^2} = \frac{4\, d_t}{d_d} \qquad [7.25]$$

By assuming a constant thickness of the annulus, the ratio of the annulus surface with the ink dot surface increases with the decrease of the dot diameter following an $\frac{1}{x}$ law. The importance of the mixed region increases then dramatically as the ink dot size decreases and therefore the effects of the reflectance differences between the MCI and SHI in the mixed region become more important. For ink

dots of 155 µm diameter and a mixed region length fixed at 12.5 µm, the mixed region surface relatively to the ink dot surface is represents 32%. This result is in the same order as the measurement for the MCI halftone with a mixed region representing 30% of the ink dot surface. By decreasing the ink dot size, the relative surface increases representing for example 50% for ink dots of 100 µm diameter, 71% for ink dots of 70 µm, 100% for ink dots of 50 µm, etc. This theoretical study gives then an idea of the importance of the surface of the mixed region as a function of the ink dot diameter.

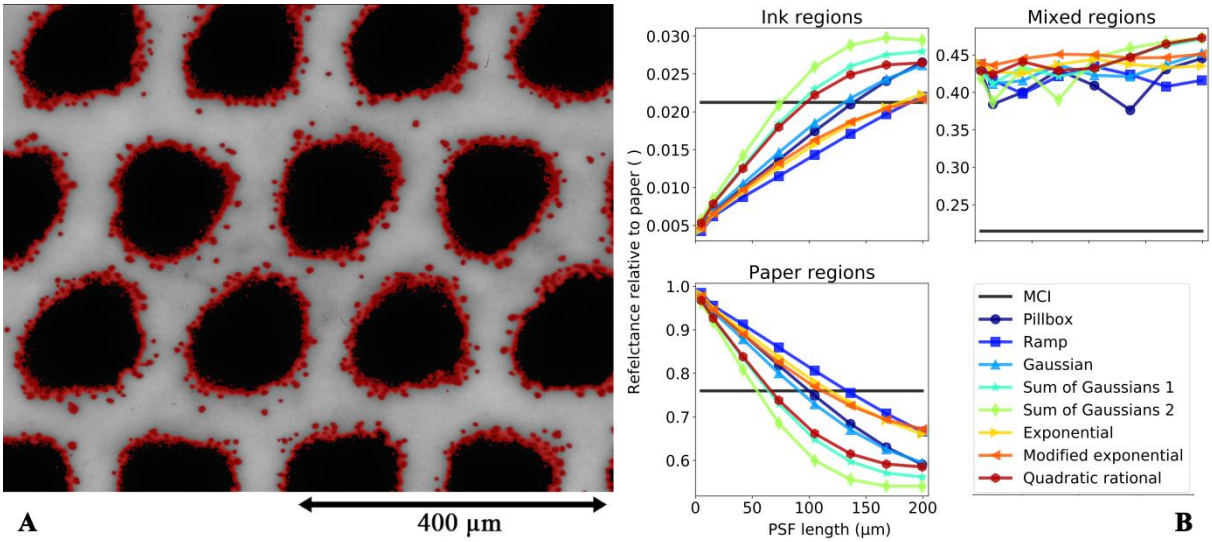

Figure 7.31: (A) Halftone of 155 µm diameter dots printed with electrophotography. (black color): ink regions, (red overlay): mixed regions and (white-grey color): paper regions. (B) Mean reflectances for the ink regions, the mixed regions and the paper regions as a function of the paper PSF lengths.

The mean reflectances of the 3 regions are then computed for the 8 different PSF types associated with the 8 different PSF lengths, Figure 7.31 (B). The PSF type affects the mean reflectances obtained for the ink and paper regions. The mean reflectances of the ink regions increase with the increase of the PSF length. The reflectances of the paper regions decrease with the increase of the PSF length. It should be noted that for large PSF lengths the mean paper and ink region reflectances start to converge toward a constant value. The mean reflectances for the corresponding regions on the MCI are displayed in black color. The optimized PSF lengths as a function of the PSF types can then be obtained by finding the intersection between MCI mean reflectances and the SHI mean reflectances for each region.

For the mixed regions mean reflectances obtained are globally independent from the PSF type and PSF length. The mean reflectances for the mixed region are almost constant and obtained around the reflectance of 0.429. This value suggests that the mixed region is equivalent to a 45%-55% mix of the ink and paper mean reflectances (theoretically, without light trapping effects, the mixed region is composed of 50%-50% mix of the ink and paper reflectance). The mean reflectance of the mixed region can be compared to the MCI mean reflectance of the mixed region reaching 0.215. The MCI mixed region can be considered to be actually equivalent to a 74%-26% mix of the ink and paper mean reflectances. This large difference is caused by the light trapping effects in the mixed region. It can be concluded that none of the PSF types and lengths tested fit correctly the MCI halftone in the mixed region. This result follows the profile differences observed in the mixed region.

A quantification of the halftone mean reflectance difference between the MCI and SHI in the mixed regions can be computed in term of fitted ink coverage differences, giving an improved appreciation of the divergence of the model of the light diffusion on halftones in the mixed regions. An ink coverage difference of -2.99%, accounting for the reflectances differences in the mixed regions, is reached for the SHI with constant ink transmittance obtained from an electrophotography print. Similarly for the inkjet print an ink coverage difference of -2.26% is reached and -1.76% for the

offset print. The model of the light diffusion on halftones tends to produce a mixed region with increase reflectance, generating effective ink coverages smaller than observed on the MCI. This effect is large and may be even increased for smaller halftone dots. Finally the SHI with optical blur is associated with a smaller ink coverage difference of -0.77%. It can be concluded that the model of the light diffusion on halftones may oversimplify the physical interactions between the ink, light and paper. A complementary approach was proposed by taking into account the internal reflections, generated by the difference of refractive indexes at the ink-paper and interfaces.

Table 7.8: Effects of the divergence of the SHI compared to the MCI halftone in the mixed region.

	Electrophotography		Inkjet	Offset
T_i	0.055	0.055 (optical blur after simulation)	0.047	0.112
Mixed region R_m range (min; max)	0.050; 0.500		0.063; 0.500	0.175; 0.625
MCI R_m	0.215		0.160	0.369
SHI R_m	0.429	0.269	0.440	0.539
MCI a_m	14.89%		10.12%	12.65%
MCI measured R_a	0.382		0.418	0.567
SHI calculated R_a	0.414	0.390	0.446	0.589
MCI n Yule-Nielsen parameter	1.42		1.99	1.58
MCI fitted a_e	50.05%		37.20%	32.16%
SHI fitted a_e	47.06%	49.28%	34.94%	30.40%
MCI-SHI difference Δa_e	-2.99%	-0.77	-2.26%	-1.76%

7.2.4 Accounting for the internal reflections

The paper and ink are considered to have roughly the same refractive index. However the refractive index of the air differs generating internal reflections at the print – air interface. The internal reflection effects on halftone light, paper and ink interactions are known. Clapper and Yule proposed a model taking into account the internal reflection already in 1953 [245]. However, the Clapper-Yule model is based on the complete light diffusion approximation and is therefore restricted to small halftone cell sizes or dot sizes. Rogers proposed to extend the Clapper-Yule model, making the model more suitable for halftones larger than the complete light diffusion approximation [201,293]. Nevertheless the extended Clapper-Yule model is a global model and a description of the light diffusion effects on the different regions of the halftone cannot be obtained. Rogers proposed to extend the model of the light diffusion on halftones to include the effects of the multiple internal reflections [201], Figure 7.26, equation [7.10]. It should be noted that the paper PSF $H'(x,y)$ used in Roger extension of the model of the light diffusion on halftones differs from the paper PSF $H(x,y)$ used in the original model. Rogers explained that the PSF usually measured on bare paper $H(x,y)$ contains already the internal reflection effects [201]. $H(x,y)$ is then the result of the multiple $H'(x,y)$ encountered at each internal reflection. However in a halftone the internal reflections interact with the ink layer at each reflection and thus $H'(x,y)$ should be employed. By considering that the light diffusion on solid ink patches is homogeneous the ink transmittance can then be obtained solving:

$$R_{is} = (1-\delta)R_{ps}T_i^2 + (1-\delta)\delta\, R_{ps}T_i^4 + (1-\delta)\delta^2\, R_{ps}T_i^6 + \cdots \qquad [7.26]$$

with R_{is} the reflectance of the solid ink.

By taking a refractive index equal to 1.5 for the ink-paper and 1.0 for the air, δ is equal to 0.596, as proposed in literature [292]. Each consecutive term of the sum represent a smaller and smaller portion of light. Thus, the ink transmittance is found to become constant starting from the third reflection (second internal reflection), converging toward a T_i of 0.0860 for a R_{is} of 0.003. This is due to the

small amount of the light irradiance remaining in the ink-paper after the second internal reflection. In fact with δ=0.596, 40.4% of the light exit at the first reflection, 24.1% of the light exit at the second reflection, and 14.4% at the third reflection. At the same time at each internal reflection, photons are absorbed by the ink layer. Thus at the first reflection, the light absorption due to the ink is equal to T_i^2, at the second reflection to T_i^4 and at the third reflection to T_i^6. Taking the total reflectance for a solid ink patch as reference equal to 100% and a solid print reflectance of 0.003, the first reflection represents then 99.559% of the total reflectance, the second reflection represents 0.439% and the third reflection represents only 0.002%. Even by taking an ink with high reflectance, for example equal to a R_{is} of 0.3, the first reflection would represent 94.635% of the total reflectance, the second reflection represents 5.076% and the third reflection represents only 0.272%. For this reason the ink transmittance obtained converges rapidly to a constant value when increasing the number of internal reflections. Then by taking into account an ink coverage of 50% and considering the complete light diffusion approximation, at the 9th reflection, 99.66% of the light has exited. Similarly for bare paper, 99.05% of the light has exited at the 9th reflection. For this reason a total of 9 reflections are considered to analyze the performances of the model of the light diffusion on halftones extended to internal reflections.

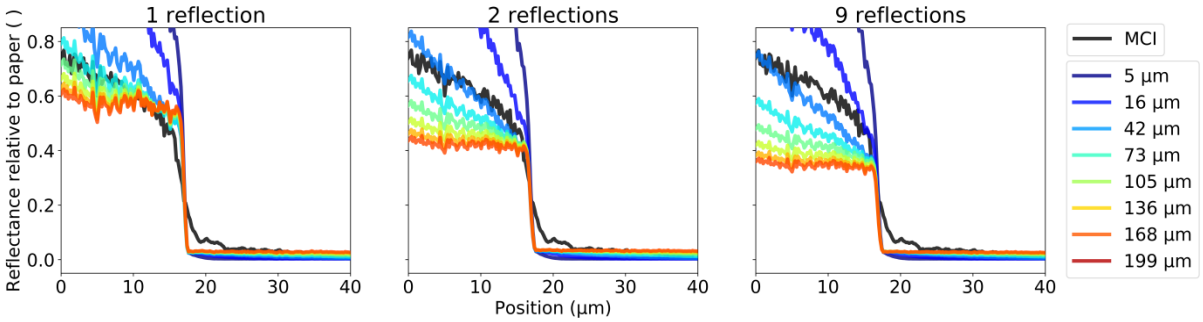

Figure 7.32: Measured (MCI) and simulated reflectance profiles at the limit between ink and paper regions as a function of the PSF length for different number of internal reflections: (1 reflection) model of light diffusion on halftones (2 reflections) Rogers expansion of the model of light diffusion on halftones with 1 internal reflection and (9 reflections) Rogers expansion of the model of light diffusion on halftones with 8 internal reflections. The PSF type is a Gaussian.

7.2.4.1 Reflectance profile evaluation of the extended model of the light diffusion on halftones

The extended model of light diffusion on halftones proposed by Rogers [201] was analyzed for 2 reflections and for 9 reflections and for multiple PSF lengths (with Gaussian PSF), Figure 7.32. Improvements of the similarity between the microscope captured image and the extended model of the light diffusion on halftones can be observed. The model with 2 and 9 reflections reproduces more accurately the reflectances variations observed near the paper edges. The reflectances variations near the ink edges are not improved. The best fits were found for PSF lengths decreasing with the increase of the number of internal reflections. For the 1 reflection model the best fit is found at 105 µm for the paper region and at 136 µm for the ink region. For 2 internal reflections, the best fit is found at 73 µm for the paper region and at 105 µm for the ink region. Finally for 9 internal reflections the best fit is found at 42 µm for the paper region and at 136 µm for the ink region. The PSF length for multiple internal reflections do not require to be as large than for a single PSF to diffuse the photons at a distance since multiple internal reflections can propagate the photons in a series of smaller diffusions [201]. It should be noted that for the ink region, this tendency is not observed for the 9 reflections model, this behavior being attributed to the light absorption by the ink.

The similarity index CS_P is slightly improved for the SHI simulated with the 2 reflections model compared to the 1 reflection model having a global CS_P of 0.0083 compared to 0.0089. For the ink regions and the paper regions, the model with 2 reflections performs less accurately with a CS_P of

respectively of 0.0013 and 0.0065. This can be compared to performances of the 1 reflection model with 0.0012 and 0.0057 for respectively the ink and paper regions. A large improvement is nevertheless observed for the mixed region with a CS_P of 0.0324 compared to 0.0535. For the model with the 9 reflections similar performances are reached for the ink and paper regions. The CS_P reaches 0.0344 for the mixed region, performing about 2 times more accurately than the model of the light diffusion on halftones with 1 reflection. It can be concluded that the extended model of the light diffusion on halftones taking into account internal reflections improve the SHI, especially in the mixed regions, however the SHI profiles dot not show a total similarity with the MCI.

7.2.5 A novel model of the light diffusion on halftones

A novel model is proposed in order to improve the performances of the light diffusion on halftones in the mixed regions. The model proposed gives a spatial description of the halftone reflectance as output and takes the paper bare reflectance, the ink transmittance, two paper PSF and an empirical parameter accounting for the edge effects as inputs, equation [7.28]. The model proposed is empirical, however it is inspired from the physically based model of the light diffusion on halftones including internal reflections. By setting m to 1 and $H_1(x,y) = H_2(x,y)$ in equation [7.28], the following equation is obtained:

$$R_a(x,y) = R_{ps}\, T_i \left(\left((T_i \circledast H_1)\, T_i^2 \right) \circledast H_1 \right) \qquad [7.27]$$

and corresponds to the reflectance of the light exiting the print after the first internal reflection in Roger's extended model of the light diffusion on halftones. Moreover in the model proposed, the two paper PSF, the first one $H_1(x,y)$ and the second one $H_2(x,y)$ differ. The first paper PSF is defined to be larger than the second paper PSF and accounts for the global paper region reflectances decrease and ink region reflectance increase (reproduces the long range diffusion of the light into the paper). The second paper PSF accounts for shadowing effects near the edges of the ink dots (reproduces the short range diffusion of the light into the paper). The results of the first diffusion and absorption of the light into the print is convolved with the second diffusion. The second diffusion includes then both effects and only this term is considered as the halftone reflectance. An additional dependency is introduced in the novel model to account for the ink thickness decrease near the edges of the dots. The ink transmittance is increased by taking the m root of the ink transmittance of the second convolution. The m parameter is comprised between 1 and infinity, the lower bound yielding to an ink transmittance equal to the ink transmittance used for the first diffusion and the higher bound generating a non-absorbing ink layer. The size of the second PSF impacts the size of the region where the ink transmittance is considered thinner.

Novel model of the light diffusion on halftones

[7.28] $$R_a(x,y) = R_{ps}\, T_i^{\frac{1}{m}} \left(\left((T_i \circledast H_1)\, T_i^{\frac{1}{m}+1} \right) \circledast H_2 \right)$$

T_i, R_{ps} and H (x, y)dependencies are omitted

Symbol	Unit	Denomination
$R_a(x,y)$	1	Halftone reflectance
$T_i(x,y)$	1	Ink transmittance
$R_{ps}(x,y)$	1	Bare paper reflectance
$H_1(x,y)$	1	First paper PSF
$H_2(x,y)$	1	Second paper PSF
m	1	Edge effects factor
$\circledast$	-	Convolution operator

The ink transmittance is obtained considering that the effects of the light diffusion on solid print do not affect the total halftone reflectance. Thus, both convolutions are simplified yielding to equation

[7.30]. By considering the paper reflectance equal to 1, the ink transmittance is then the η root of the solid print reflectance. By considering the m factor describing the edge effects on the ink transmittance, the following relation can be obtained:

$$\eta = \frac{2}{m} + 2 \qquad [7.29]$$

with $m = 1$, the ink transmittance is equal to $\sqrt[4]{R_{is}}$, which corresponds to the ink transmittance of the second term of Rogers extended model of the light diffusion on halftones. With $m \to \infty$, the ink transmittance converge to $\sqrt{R_{is}}$, which corresponds to the ink transmittance of the model of the light diffusion on halftones. It should be noted, that although the ink transmittances are similar for $m \to \infty$, the novel model is not similar to the model of the light diffusion on halftones since the second convolution induces further light diffusion effects. The novel model is similar to the model of the light diffusion on halftones only if m is ∞ and $H_2(x,y)$ converges toward 1. The novel model can then be considered as a mix between no internal reflections and a single internal reflection, by adjusting m and $H_2(x,y)$ length.

Ink transmittance determination for the novel model of the light diffusion on halftones

		Symbol	Unit	Denomination
[7.30]	$T_i(x,y) = R_{ps}(x,y)\, R_{is}^{\varphi}(x,y)$	$T_i(x,y)$	1	Ink transmittance
	$\varphi = \frac{1}{\frac{2}{m} + 2}$	$R_{is}(x,y)$	1	Solid ink reflectance
		$R_{ps}(x,y)$	1	Bare paper reflectance
		m	1	Edge effects factor

7.2.5.1 Reflectance profile evaluation of the novel model

The performances of the novel model are then compared to the MCI, the model of the light diffusion on halftones without internal reflections (total of 1 reflection) and with 8 internal reflections (total of 9 reflections) with optimize PSF lengths (with Gaussian PSF), Figure 7.33. On the figure the reflectance profiles at 3 different positions are presented. It has to be noted that the 0 µm does not correspond to the edge of the image but is the starting point of the profile measured on the halftone image. This starting point is located at 115 µm of the nearest edge of the image. On the profile corresponding to the position from 0 µm to 40 µm, an ink-paper edge is presented. The novel model follows accurately the MCI profile on the paper and ink regions near the paper-ink edge. In the paper region near the edge, the reflectances decrease following a bell shape similarly than observed on the MCI. In this region the novel model improves the performances compared to the 1 and 9 reflections models. The 1 reflection model presents reflectances in the paper region near the edge too bright compared to the MCI. On another hand the 9 reflections model presents reflectances in the same region too dark compared to the MCI. The proposed model is found in between the 1 and 9 reflections models and follows the reflectances decreases observed on the MCI. A slight variation of the novel model profile compared to the MCI profile can be observed for the paper region near the edge around the position of 15 µm. This variation might be induced by the paper reflectances dispersion. On the ink regions near the edge the novel model conforms also better to the MCI than the 1 and 9 reflections models with a more progressive decrease of the ink reflectances.

On the ink regions away from the edges, the three models reach similar level of ink reflectances around 0.004 and are found larger than the observed MCI ink reflectance of 0.011. Taking for example a 50% nominal ink coverage, this difference corresponds to a difference of fitted ink coverage of 0.35%. It was found experimentally that by adjusting the ink transmittance, this difference could be removed while conserving the accuracy of the profile simulation for the paper region and for the edge

region. Nevertheless taking a different ink transmittance than the measured one introduces an additional parameter. It was then chosen to not change the ink transmittance and to conserve the ink transmittance measured on the solid print patches according to equation [7.30]. Moreover results for inkjet and offset print showed profiles with reflectance values in the ink region similar to the reflectances of the MCI. The global shape of the profiles on the ink dots differ from the MCI for the 3 models. The MCI profile has fairly constant ink reflectance near the center of the dot and then large reflectance decreases near the edges. The novel model also shows a profile with a plateau near the center of the dot, however the reflectances decreases near the edges of the dot are smaller. The model with 1 reflection follows better the shape of the dot on the ink region.

On the paper region, the 3 models perform accurately compared to the MCI. It should be noted that the profiles variations induced by isolated ink particles are better simulated with the novel model than with the 1 and 9 reflection model. The novel model follows precisely the reflectances increase near the paper edges.

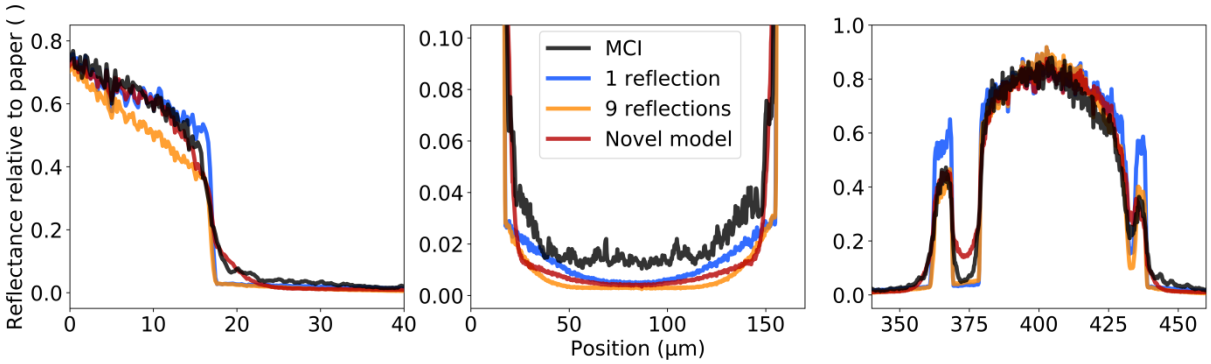

Figure 7.33: Measured (MCI) and simulated reflectance profiles at different position as a function of the model: (1 reflection) model of light diffusion on halftones (9 reflections) Rogers expansion of the model of light diffusion on halftones with 9 internal reflections and novel model. The PSF type is a Gaussian.

The similarity index is computed for the ink, paper and mixed regions for the 3 models. On the ink region the 1 reflection model performs the most accurately with a CS_P of 0.0029. This performance is two times more accurate than for the novel model with a CS_P of 0.0060 and almost 3 times more accurate than for the 9 internal reflections with a CS_P of 0.0083. The performance on the ink region can be improved by setting a different ink transmittance, reaching for the novel model a CS_P of 0.0018. For the paper region, the novel model performs better than the 1 and 9 reflections models with a CS_P of 0.0024 compared to a CS_P of respectively 0.0052 and 0.0050. The largest improvement of the novel model is observed in the mixed region with a CS_P of 0.0172 compared to a CS_P of respectively 0.0539 and 0.0367 the 1 and 9 reflections models. Globally the novel model performs better than the 1 and 9 reflections models with a global CS_P of 0.0063 compared to a global CS_P of respectively 0.0094 and 0.0106. The proposed model performs then around 2 times better than the previous models on the tested profile.

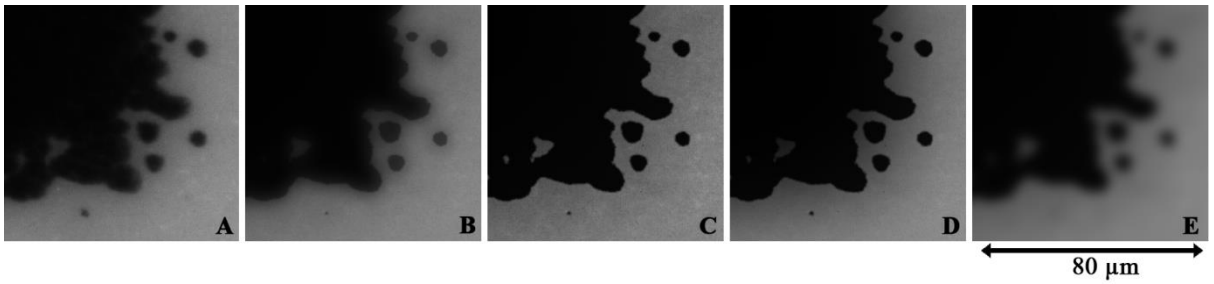

Figure 7.34: Region of an halftone dot of 155µm diameter printed with electrophotography and (A) imaged on the microscope, (B) simulated with the novel model, PSF_1=94 µm, PSF_2=10 µm and m=4, (C) simulated with the 1 reflection model, PSF=94 µm, (D) simulated with the 9 reflections model, PSF=47 µm and (E) simulated with the 1 reflection model, PSF=94 µm with a Gaussian blur of 12 µm kernel. PSF are Gaussian.

7.2.5.2 Visual assessment of the novel model performances

The results of the SHI obtained with the novel model can be compared to the MCI, to the SHI obtained with the 1 and 9 reflections models and to the SHI obtained with the 1 reflection model with a Gaussian blur. Comparing the SHI of the novel model with the MCI shows than similar reflectance decrease can be observed for the toner particles outside the inked dot, Figure 7.34 respectively (B) and (A). Similarly the transparency effect observed with the MCI is reproduced with the novel model. The mis-inked region inside the printed dot appears impacted by optical dot gain similarly for the novel model and the MCI. The shadowing around the edges is also similar on the SHI obtained with the novel model compared to the MCI. The shadowing and optical dot gain effects, on the mis-inked regions, are also accurately reproduced on the SHI obtained with the 9 reflections model. The shadowing is not reproduced on the SHI obtained with the 1 reflection model. The SHI obtained with the 1 reflection model and the Gaussian blur differs from the SHI obtained with the novel model and demonstrate that the model operation on the edges of the halftone is not a simple optical blurring.

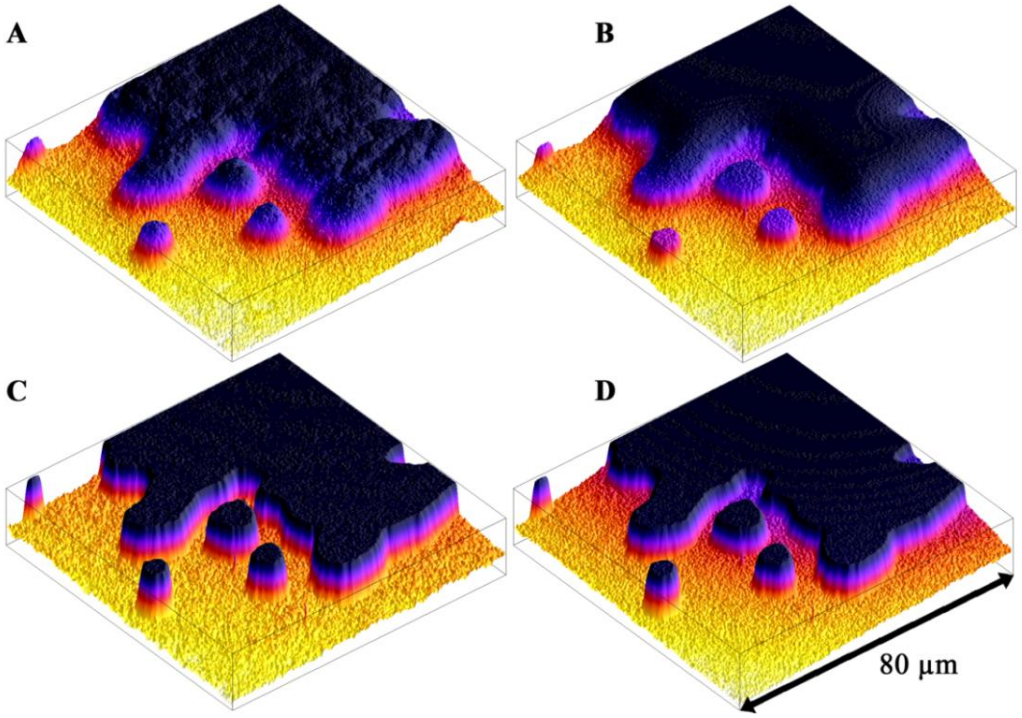

Figure 7.35: Region of an halftone dot of 155µm diameter printed with electrophotography and (A) imaged on the microscope, (B) simulated with the novel model, PSF_1=94 µm, PSF_2=10 µm and m=4, (C) simulated with the 1 reflection model, PSF=94 µm and (D) simulated with the 9 reflections model, PSF=47 µm. PSF are Gaussian. Pixel values represented as the inverse height.

In order to improve the visual comparison of the SHI obtained with the different models and with the MCI, 3D images are plotted with the reflectance represented as the height (inversed) and are colored accordingly, Figure 7.35. For the SHI obtained with the novel model (B) and the SHI obtained with the 9 reflections (D), similar paper height increases are obtained near the edges of the dots and corresponds to the height increases observed for the MCI (A). The increase of the heights corresponds to a decrease of the reflectances. The 1 reflection model (C) does not follow this tendency. On the ink region near the edges, only the novel model reproduces accurately the height variations compared to the MCI. For the 1 and 9 reflections models, the ink heights do not vary significantly in the ink region near the edges. More variations are induced on the ink region of the MCI compared to the SHI obtained with the novel model. These reflectance variations can be induced by variations of the ink layer thickness inducing local ink transmittance variations. It should be noted that the novel model does not reproduce accurately the center of the isolated ink particles, producing almost constant reflectances compared to more variating reflectances for the MCI. This can be attributed to either an over evaluated m parameter inputted on the proposed model.

7.2.5.3 Influence of the novel model parameters

Next, the influence of the parameters of the novel model are explored, Figure 7.36. The influence of the length increase of the first PSF can be observed with an increase of the ink reflectances and a decrease the paper reflectances in respectively the ink and paper regions outside of the edges regions. The effect can be considered as a long distance light diffusion. The shapes of the edges are only slightly impacted by the first PSF size. Optimizing the first PSF length is then extremely important in order to simulate the global light diffusion effects. The optimized PSF size obtained has a similar size than for the 1 reflection model and the tools developed to find the PSF for this model can be re-employed. The second PSF length changes the shape of the reflectance profile near the edges of the dots, in the mixed region. A larger PSF induces softer dot edges with more progressive decrease of the paper reflectances and a more progressive decrease of the ink reflectances going from the paper region to the ink region. The optimized second PSF length differs for the paper and the ink in the mixed region with an optimized fitting with the 7 µm PSF for the paper and 15 µm for the ink. This difference can be explained by the ink transmittance decrease near the edges of the dot (region from the position 20 µm to 35 µm on the profile). It should be noted that the second PSF length, does not affect significantly the long diffusion effects induced by the first PSF. Finally, it can be observed that the m parameter influences the shape of the slope at the edge of the dot. A larger m parameter induces a less steep slope, presenting a smoother transition from the paper region to the ink region. Results show that with m=1, the proposed model already shows accurate results in the paper region; however the reflectance slope at the edges is too steep. m=4 is then adopted.

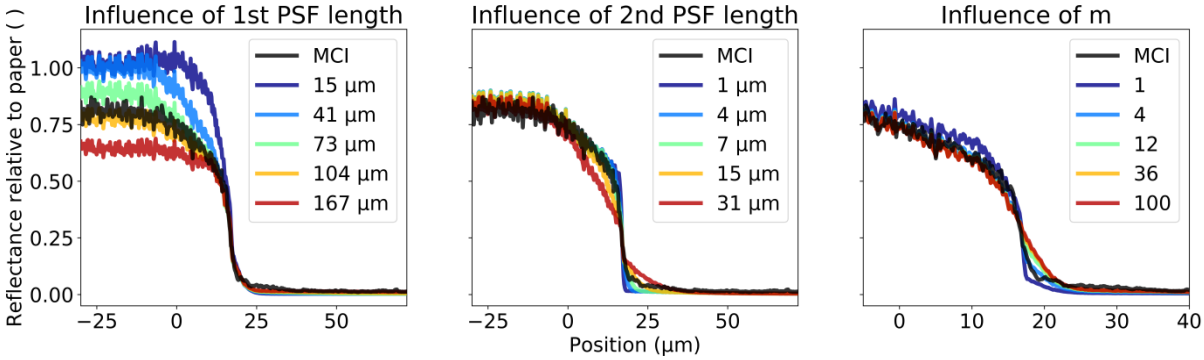

Figure 7.36: Measured (MCI) and simulated reflectance profiles as a function of (A) the first PSF length with PSF_2=10 µm and m=4, (B) the second PSF length with PSF_1=84 µm and m=4 and (C) the m factor with PSF_1=84 µm and PSF_2=10 µm. The PSF type is a Gaussian.

7.2.5.4 Influence of the mixed region on the halftone apparent ink coverage

The performances of the novel model are also evaluated on mixed region for 3 print processes: electrophotography, inkjet and offset, Table 7.9. The fitted ink coverage difference can be computed to represents the effect of the mixed region reflectances differences on the total fitted ink coverage. The novel model reaches an ink coverage difference of -0.41% for electrophotography. This improves the simulation in the mixed region by 4 times compared to the 9 reflections model and by 7 times for the 1 reflection model. For inkjet print the ink coverage difference for the novel model reaches -0.58%. This improves the simulation in the mixed region by 3 times compared to the 9 reflections model and by 4 times for the 1 reflection model. For offset print the ink coverage difference for the novel model reaches -0.35%. This improves the simulation in the mixed region by 4 times compared to the 9 reflections model and by 5 times for the 1 reflection model. The improvements of the halftone simulations in the mixed regions are then significant with the proposed model allowing obtaining more accurate optical dot gain simulations.

Table 7.9: Effect of the divergence of the SHI obtained with the novel model (Novel), the 1 reflection model (1 refl.) and the 9 reflection model (9 refl.) compared to the MCI halftone in the mixed region.

	Electrophotography			Inkjet			Offset		
	1 refl.	**9 refl.**	**Novel**	**1 refl.**	**9 refl.**	**Novel**	**1 refl.**	**9 refl.**	**Novel**
T_i	0.055			0.047			0.112		
Mixed region R_m range (min; max)	0.050; 0.500			0.063; 0.500			0.175; 0.625		
MCI R_m	0.215			0.160			0.369		
SHI R_m	0.429	0.337	0.244	0.440	0.401	0.230	0.539	0.494	0.402
MCI a_m	14.89%			10.12%			12.65%		
MCI measured R_a	0.382			0.418			0.567		
SHI calculated R_a	0.414	0.400	0.387	0.446	0.443	0.425	0.589	0.583	0.572
MCI fitted a_e	50.05%			37.20%			32.16%		
SHI fitted a_e	47.06%	48.34%	49.64%	34.94%	35.26%	36.62%	30.40%	30.85%	31.81%
MCI-SHI difference Δa_e	-2.99%	-1.71%	-0.41%	-2.26%	-1.84%	-0.58%	-1.76%	-1.31%	-0.35%

7.2.6 Novel model performances on multiple halftone types and sizes

An evaluation of the novel model performances is proposed, by comparing the mean absolute Apparent Ink Coverage Difference (AICD) obtained with the novel model, with the model of the light diffusion on halftones (1 reflection model) and with the Yule-Nielsen model. 1231 AM and FM halftone patches are modelled and measured following the process presented in Figure 7.27. The results obtained for different print processes, halftone types, halftone sizes, papers and inks are presented in an ascending order considering the novel model mean absolute AICD, Figure 7.37. The halftone set characteristics and the model parameters used are given in Table 7.6 and Table 7.11. It should be noted that the mean absolute AICD are computed by optimizing the n parameter of the Yule-Nielsen model for each halftone set. The 1 reflection model and novel model parameters optimizations are performed for each combination of print process, paper and inks (for example, the halftone sets EE1-AM1 and EE2-AM2 are optimized with similar parameters). Another global evaluation is proposed by regrouping the different halftone sets into larger sets, Figure 7.38. The models parameters for these larger sets are then fitted on the same sets for all models, allowing an accurate comparison of the models performances. One drawback of choosing a fitting of the parameter on larger sets is that it is not the ideal case, where each halftone type requires being fitted independently.

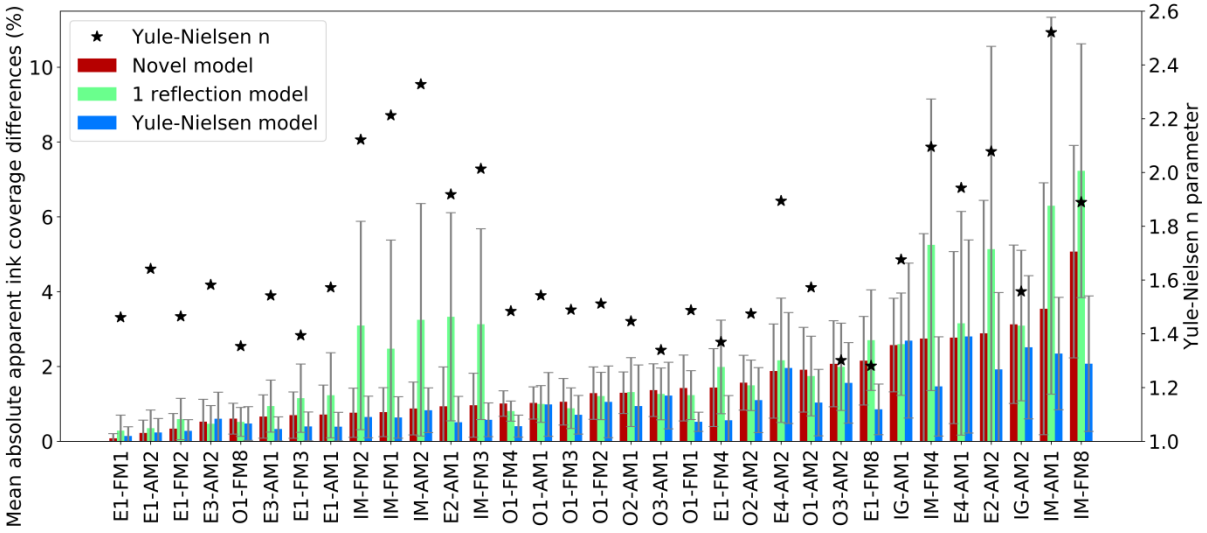

Figure 7.37: Mean absolute apparent ink coverage differences of halftone sets obtained with several print processes, halftone types, halftone sizes, papers and inks. The halftone set characteristics are given in Table 7.6 and Table 7.11.

The best model performances are found with a mean absolute AICD of 0.1% and lowest performances are found at 7.2%. The performance levels of the models are not directly associated with the level of Yule-Nielsen n parameter, however it can be noticed that the lowest performances obtained are mostly found for large n levels. The Yule-Nielsen n parameter can be considered to describe the light diffusion associated with the halftone dot morphologies. A large n parameter will then be attributed to a halftone with large optical dot gain. It can be noted that the large n are associated with the Epson papers "IM", "IG" and with the uncoated papers "EE4". Large mean absolute AICD for the 1 reflection model occur for halftones printed on paper with large light diffusion. The specific coated layer allowing a high quality inkjet print for the Epson paper may induce more internal reflections. It can then explain the differences of the level of performances achieved with the 1 reflection model and the novel model. This hypothesis is reinforced by the optimized Yule-Nielsen n parameters found at levels larger than 2. In the complete light diffusion approximation, the Yule-Nielsen n parameter was demonstrated to be equal to 2, chapter 2. This case considered nevertheless only a single reflection. With internal reflections the light trapping effect becomes larger and thus the Yule-Nielsen n parameter can larger than 2.

The standard deviations are globally large compared to the mean absolute AICD and their sizes are correlated with the sizes of the mean absolute AICD. This can be explained by the fact that the performances of the models vary as a function of the ink coverage. The averages computed include all the ink coverages in the halftone set. Different mean absolute AICD levels are then obtained resulting in large standard deviations. Despite the large standard deviation the comparison between mean absolute AICD are significant as it assesses the global performance of a model.

It can be observed that for all halftone sets the Yule-Nielsen model performs slightly more accurately than the 1 reflection and the novel models. The average of all mean absolute AICD reaches 1.47% for Yule Nielsen model. The novel model is found to have a performance close to the Yule-Nielsen model with an average of all mean absolute AICD of 1.65%. The average standard deviation associated is smaller for the novel model than for the Yule-Nielsen model. The average performance for the model of the light diffusion on halftones with 1 reflection is found slightly larger at 2.23%, Table 7.10.

Table 7.10: Mean absolute apparent ink coverage differences. Models fitted for each halftone set and averaged by print processes.

	halftone			**Mixed region**	
	Novel model	**1 Reflection model**	**Yule-Nielsen**	**Novel model**	**1 Reflection model**
Offset	1.44%	1.36%	1.17%	1.21%	2.35%
Electrophoto-graphy	1.40%	2.18%	1.36%	0.83%	1.92%
Inkjet	2.47%	3.61%	2.15%	3.22%	4.12%
All processes	1.65%	2.23%	1.47%	1.49%	2.55%

An average of the mean absolute AICD of the halftone sets for each print process, inks and papers is computed to compare the three models with a similar parameter optimization definition, Figure 7.38 (A). The comparison of the three model performances shows similar tendencies than for the each halftone set, with a decrease of the performances for large light diffusion papers and with large standard deviations. The performances of the novel model are analyzed as a function of print processes, the halftone type and size, the ink and the paper.

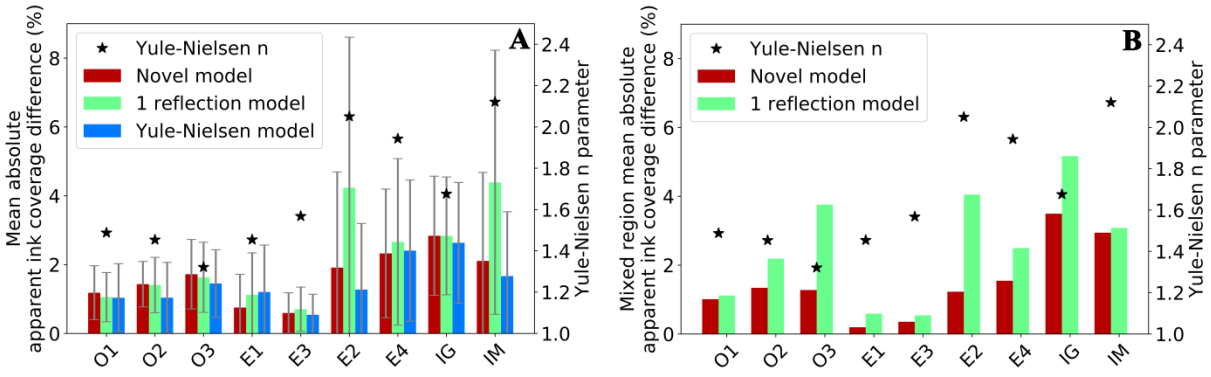

Figure 7.38: Mean absolute apparent ink coverage differences of halftone sets obtained with several print processes, halftone types, halftone sizes, papers and inks. The model parameters optimizations are performed for each set. The halftone sets characteristics are given in Table 7.6 and Table 7.11.

7.2.6.1 Print process

The influences of print processes on the performances of the three models can be analyzed comparing the halftone sets "E1" (electrophotography), "O1" (offset) and "IM" (inkjet). Electrophotography and offset are associated with similar performance level with a mean absolute AICD of respectively 0.75% +/- 0.96% and 1.18% +/- 0.78% for the novel model, 1.12% +/- 1.22% and 1.05% +/- 0.72% for the 1 reflection model and 1.20% +/- 1.36% and 1.04% +/- 0.99% for the Yule-Nielsen model. The novel model performs better than the two other models for electrophotography and is associated with a smaller standard deviation. For offset, the novel model performs slightly less accurately than the two other models; however the novel model presents a smaller standard deviation. These differences can be explained by the inability of the novel model to predict more accurately the reflectances in the mixed region for the offset prints, Figure 7.38 (B). This can come from non-perfectly optimized novel model parameters. For the inkjet print process, the novel model performs similarly than the Yule-Nielsen model and more accurately than the 1 reflection model. The mean absolute AICD reaches 2.11% +/- 2.57% for the novel model, 4.39% +/- 3.84% for the 1 reflection model and 1.66% +/- 1.87% for the Yule-Nielsen model. A limiting factor affecting the performances of the models is the size of the field of view used to capture the halftone image for halftone sets with large ink dots associated with large light diffusion papers. The implementation of the model was designed to account for overlapping of the convolution kernel outside of the field of view using a mirror strategy (extension of the field of view by reflection scheme). Nevertheless in the case of large ink dots, the field of view often does not corresponds to the halftone cell size generating large errors in the spatial ink transmittance description (i.e. effective ink coverage). The performances for the three models given in this section differ slightly from the average performances given in Table 7.10. In the table the average of the performances for all halftone sets printed with electrophotography, offset and inkjet are reported, including for example the halftone sets "E1", "E2", "E3" and "E4" in the electrophotography category.

7.2.6.2 Halftone type and size

The halftone types (AM or FM) and the halftone sizes (respectively cell sizes or dot sizes) influence the performance of the three models. The FM halftone sets with small dot sizes are associated with improved results for the novel model than the FM halftone sets with larger dot sizes or than the AM halftone sets. An average of the mean absolute AICD of 0.72% +/- 0.49% is obtained for the novel model for the FM halftones with dot size around 1200 dpi (exact dot size depends on the print process) and can be compared to 0.61% +/- 0.59% for the Yule-Nielsen and 1.32% +/- 1.32% for the 1 reflection model. Similarly for FM halftones with dot size around 600 dpi an average of the mean absolute AICD of 0.70% +/- 0.47% is obtained for the novel model and can be compared to 0.44% +/- 0.38% for the Yule-Nielsen and 1.50% +/- 1.20% for the 1 reflection model. With larger

FM halftones with dot sizes, around 300 dpi, the performances are reduced with an average of the mean absolute AICD reaching 1.59% +/- 1.42% for the novel model and can be compared to 0.83% +/- 0.81% for the Yule-Nielsen and 2.59% +/- 1.84% for the 1 reflection model. It can be concluded for FM halftones that the novel model performs better with smaller halftone dots. The novel model performs slightly less accurately than the Yule-Nielsen model. However the novel model performs more accurately than the 1 reflection model. For the AM halftones the two tested halftone sizes, 150 lpi and 200 lpi reach similar performances with the novel model, with an average of the mean absolute AICD of respectively 1.61% +/- 1.18% and 1.61% +/- 1.25%. The performance of the novel model is slightly inferior to the Yule-Nielsen model reaching respectively 1.32% +/- 1.11% and 1.28% +/- 1.08% for the two halftones cell sizes. However the novel model performs better than the 1 reflection model reaching respectively 2.23% +/- 1.67% and 2.07% +/- 1.28%. It can be concluded that the novel model is almost as accurate as the Yule-Nielsen model for AM halftones and could be improved optimizing the model parameters for each halftone set resolutions.

7.2.6.3 Inks and Inking

Two different inks, "IM" (matte black ink) and "IG" (photo black ink), having different ink transmittances are compared. The photo black ink has a higher transmittance, associated with a slight decrease of the novel model performances. These performances decreases are also observed for the Yule-Nielsen model. The novel model performs better than the 1 reflection model with average of the mean absolute AICD of respectively 2.21% +/- 2.04% and 2.85% +/- 1.68% for "IM" and "IG" for the novel model and respectively 4.77% +/- 4.07% and 2.86% +/- 1.69% for the 1 reflection model. The Yule-Nielsen model performs more accurately with 1.59% +/- 1.05% and 2.60% +/- 1.99%.

The inking levels can be compared on the offset prints, "O3" (light-light inking), "O2" (light inking) and "O1" (standard inking). A decrease of the performances for the novel model is observed with the increase of the ink transmittance (thinner ink layer deposited). The performances obtained with the novel model are decreased from 1.47% +/- 0.78% for the standard inking to 1.72% +/- 0.93% for the light-light inking. This tendency is also observed on the performances of the Yule-Nielsen model and of the 1 reflection model. The novel model performs better than the 1 reflection model in the mixed region with an average of the mean absolute AICD reaching respectively 1.32% compared to 1.55% for the standard inking and respectively 1.27% compared to 3.76% for the light-light inking. The novel model performs then more accurately in the mixed region than the 1 reflection model, especially for high transmittance ink layers.

7.2.6.4 Paper

Four papers are tested, two coated glossy papers "E1" and "E3" (glossy 1 and glossy 2), an uncoated paper "E4" (uncoated) and a paper with a coating for inkjet "E2" (Epson). It can be observed that similar performances of the novel model are achieved for the two glossy coated papers with 0.47% +/- 0.56% and 0.59% +/- 0.70% respectively for the glossy 1 and the glossy 2. These performances can be compared to the uncoated paper reaching an average of the mean absolute AICD of 2.32% +/- 1.78%. The Epson paper is also associated with lower novel model performances with 1.91% +/- 2.30%. The novel model is then less accurate for large light diffusion halftones. The 1 reflection model and Yule-Nielsen follow a similar tendency with improved performances for the coated glossy papers. The Yule-Nielsen is found to perform more accurately than the novel model. The 1 reflection model is found to perform less accurately than the novel model.

By analyzing the novel model performance on the edges compared to the 1 reflection model, Figure 7.38, it can be observed than the novel model performs systematically more accurately in the mixed region. The performance improvements introduced by the novel model ranges from a 3.30 times improvement to a 1.05 times improvement with an average over all halftone sets 2.02 times improvement. The optimized m parameter of the novel model was found to be correlated to the ink thickness of the halftone sets, Table 7.11.

Table 7.11: Halftone sets designation and associated print process, ink, inking, paper and print resolution characteristics. Model parameters used for each halftone set, n (Yule-Nielsen), PSF 1 (model of the light diffusion on halftones), PSF 1, PSF 2 and m (novel model).

Designation	Process	Ink / Inking	Paper	Printer resolution (dpi)	PSF1 (µm)	PSF2 (µm)	m ( )	n ( )
O1	Offset	Normal inking	Glossy 1	2540	105	7	4	1.49
O2		Light inking	Glossy 1	2540	105	10	16	1.45
O3		Light light inking	Glossy 1	2540	105	10	30	1.32
E1	Electrophotography	-	Glossy 1	1200	84	10	4	1.45
E2		-	Epson	1200	210	58	4	2.05
E3		-	Glossy 1	1200	84	10	4	1.57
E4		-	Uncoated	1200	210	21	4	1.94
IM	Inkjet	Matte Black (MK)	Epson	1440	210	84	3	2.12
IG		Photo Black (PK)	Epson	1440	210	21	16	1.68

7.2.7 Conclusion

The aim of this study was to analyze the performances of the model of the light diffusion and to propose a novel model improving the spatial description of the optical dot gain effects. The model of the light diffusion on halftones requires inputting the spatial description of the ink transmittance and is extremely interesting because it outputs the spatial description of the ink reflectance. Compared to conventional models outputting a reflectance integrated over a surface, a model yielding to a spatial description of the reflectance allows assessing the reflectance distribution for any region of the halftone allowing studying the influences of the optical dot gain on the halftone sizes and shapes. It provides then, theoretically, a prediction model that requires be optimized only as a function of the paper diffusion, the model becoming independent from the halftone size, shape and physical dot gain.

First an analysis of the performances of the model of the light diffusion on halftones was proposed for 8 different paper PSF associated with 8 different paper PSF lengths. The simulated profiles shapes obtained with the ramp PSF, the Gaussian PSF, the exponential and modified exponential were reproducing more accurately the global shape of the MCI profile. The global CS_P index for three regions showed that the Exponential paper PSF was performing the most accurately. In the mixed region, the SHI profiles obtained for all PSF tested were associated with large differences with the MCI profile. The PSF type affected the mean reflectances obtained for the ink and paper regions. The mean reflectances of the ink regions increased with the increase of the PSF length. The reflectances of the paper regions decreased with the increase of the PSF length. For the mixed regions mean reflectances obtained were constant and thus independent from the PSF type and PSF length. An increase of 18 times for the CS_P index was observed in the mixed region compared to the paper and ink regions. The mean reflectance obtained with the SHI suggested that the mixed region was equivalent to a 45%-55% mix of the ink and paper mean reflectances. However the reference MCI was impacted by increased light trapping effects in the mixed region and was found equivalent to a 74%-26% mix of the ink and paper mean reflectances. It was concluded that none of the PSF types and lengths tested fitted correctly the MCI halftone in the mixed region. A quantification of the halftone mean reflectance differences between the MCI and SHI in the mixed regions was computed in term of fitted ink coverage differences. For the SHI from electrophotography print, inkjet print and offset print, an ink coverage difference of respectively -2.99%, -2.26% and -1.76% was reached. It can be concluded that the reflectance differences due to the divergence of the model of the light diffusion on halftones in the mixed region are important.

Comparing the profiles with a constant ink transmittance and with a variable ink transmittance revealed that the model was improved in the mixed region when accounting for the ink transmittance variation. The mixed region near the ink edge was better reproduced however the mixed region near

the paper edge continued to present a large divergence. Applying a Gaussian blur to the SHI improved the results with similar profiles for SHI and MCI in the mixed region. The hypothesis that the differences observed between the MCI and SHI profiles in the mixed region were caused only by an optical blurring during measurements (focusing errors and microscope diffusion) was nevertheless excluded since the visual comparison of the MCI and blurred SHI showed differences. The visual comparison of the MCI and SHI halftone dots at the microscale showed that two effects appeared on the MCI and that only a single effect could be reproduced for a PSF length on the SHI. The first effect consisted in a long range global darkening of the paper regions and a global brightening of the ink regions. The second effect consisted in a short range shadowing around the edges of the dots. This indicated the possibility that multiple reflections were impacting the halftone. An assessment of the influence of the mixed region surface as a function of the dot size was proposed. For round 155 µm dots the mixed region represented 15% of the halftone surface and 30% of the ink dot surface. A theoretical assessment of the mixed region surface as a function of the ink dot diameter demonstrated that the mixed region surface increased dramatically as the dot size decreased.

Rogers's extended model of the light diffusion on halftones was then evaluated to take into account the effects of the internal reflections. The model with 2 and 9 reflections reproduced more accurately the reflectances variations observed near the paper edges. The reflectances variations near the ink edges were not improved. The best fits were found for PSF lengths decreasing with the increase of the number of internal reflections.

A novel model was then proposed in order to take into account the light trapping effects in the mixed region. The novel model gave a spatial description of the halftone reflectance as output and took the paper bare reflectance, the ink transmittance, two paper PSF and an empirical parameter accounting for the edge effects as inputs. An analysis of the influence of the novel model parameters was performed. The first PSF affected globally the ink reflectances increases and paper reflectances decreases. The second PSF length controlled the shape of the reflectance profile near the edges of the dots, in the mixed region. The m parameter influenced the shape of the slope at the edge of the dot. The optimized m parameter was found to be correlated to the ink thickness of the halftone sets. The novel model followed accurately the MCI profile on the paper and ink regions near the paper-ink edge and improved the performances compared to the 1 and 9 reflections models. The novel model was found visually to reproduce accurately the long range light diffusion effects and at the same time the shadowing effects near the edges of the dots, as observed on the MCI. Similarly the "transparency" effect near the edges of the dot observed with the MCI was reproduced with the novel model. 3D images were plotted (the height represented the inverse reflectance). An improvement of the edge modelling was directly visible for the novel model compared to the 1 and 9 reflection models. The fitted ink coverage difference was computed to analyze the effect of the mixed region reflectance differences on the total fitted ink coverage. The novel model reached an ink coverage difference of -0.41% for electrophotography, -0.58% for inkjet and -0.35% for offset. This improved the simulation in the mixed region by around 4 times compared to the 9 reflections model and by 5 times for the 1 reflection model.

An evaluation of the novel model performances was proposed, by comparing the mean absolute apparent ink coverage difference for 1231 halftone patches. The novel model was compared to the 1 reflection model and with the Yule-Nielsen model. It was observed that the Yule-Nielsen model performed slightly more accurately than the 1 reflection and the novel models. The average of all mean absolute AICD reached 1.47% +/- 1.39% for Yule Nielsen model. The novel model was found to have a performance close to the Yule-Nielsen model with an average of all mean absolute AICD of 1.65% +/- 1.44%. The average standard deviation associated was smaller for the novel model than for the Yule-Nielsen model. The average performance for the model of the light diffusion on halftones with 1 reflection was found slightly larger at 2.23% +/- 1.86%. The novel model performed 2 times more accurately than the 1 reflection model in the mixed region. The novel model achieved improved performances for halftone sets printed with electrophotography and offset. Inkjet was associated with

larger mean absolute AICD. The FM halftone sets with small dot sizes were associated with improved results for the novel model than the FM halftone sets with larger dot sizes or than the AM halftone sets. The two different inks (with different ink transmittances) were evaluated with inkjet print and a slight decrease of the novel model performances was observed for the photo black ink having a higher transmittance. Similarly the inking level was evaluated on offset prints with light-light inking, light inking and standard inking. A decrease of the performances for the novel model was observed with the increase of the ink transmittances (thinner ink layer deposited). A study over four different papers demonstrated that the novel model performed better for glossy coated papers (smaller light diffusion) than with uncoated or Epson papers (larger light diffusion).The novel model performed globally more accurately than the 1 reflection model. The novel model was associated with slightly lower performances than the Yule-Nielsen model, however it benefited from a 2D description of the reflectances of the halftone allowing a more accurate characterization of the ink, mixed and paper regions. Moreover a more accurate parameter optimization for the novel model can improve the performances of the novel model.

These physical and optical dot gain models allowed then obtaining models describing the halftone from raster to visual perception. The print parameters could then be tuned to take advantage of the physical and optical do gains, in order to reduce the ink consumption, to create special visual effects or to improve the performances of the anti-counterfeiting printed solutions.

Chapter 8 Conclusion

8.1 Summary

In this work, methods have been developed to measure, characterize and model the print at the microscale, Figure 8.1. An optical dot gain characterization tool was proposed. The optical and physical dot gains were separated and analyzed. Finally, optical and physical dot gains models were proposed.

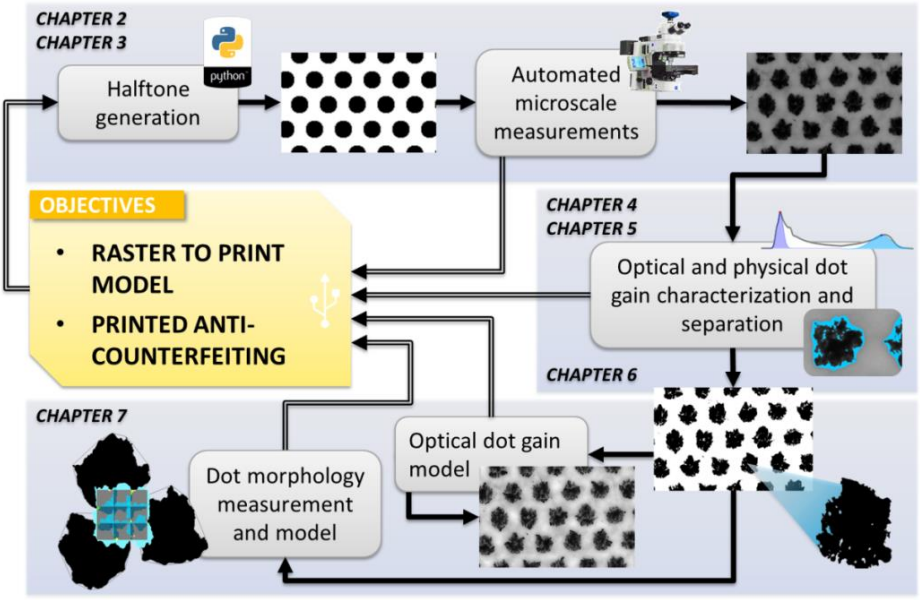

Figure 8.1: Chapters organization, relationships between chapters and objectives.

8.1.1 Print measurement at the microscale and design of test forms

A specific apparatus was designed to measure halftone dots at the microscale automatically (chapter 3). This apparatus was composed of the optical microscope (Zeiss Axio Imager M1m) equipped with a motorized X, Y, Z stage and mounted with a commercial digital camera (Canon 1200D). This allowed capturing images in a raw format without non-controlled processing (pixel interpolation, white balance, exposition compensation and gamma correction). The camera was modified to monochromatic to facilitate the capture of the ink and paper reflectances and to allow a multispectral characterization. The temperature of the camera and the radiant flux of the illuminant were controlled by installing specific sensors. All sensors and actuators of the apparatus were controlled in a graphic user interface developed in Python language. A characterization of the apparatus has been performed and showed a high control and accuracy of the measurements. Functions such as an autofocus and an auto-positioning of the stage were developed to allow an automatic capture of the halftone dots. A comparison of the illumination condition was performed in order to assess the best measurement strategy and analyze the effect of the illuminant geometries on the optical dot gain occurrence. No significant increase of optical dot gain was found between the darkfield reflected light, the 90° analyzer-polarizer reflected light and the brightfield transmitted light. Finally a high dynamic range method was proposed to improve the accuracy of the pixels values measured when imaging simultaneously ink and paper regions. The improvement of the method was demonstrated by studying the pixel values along a line in an inked region of a halftone image and

along a line in the paper region. The measurement dispersion in the ink region was improved from a coefficient of variation of 29.3% for a single exposure time capture to a dispersion with a coefficient of variation of 5.9% for the high dynamic range. On the paper regions only a slight improvement was demonstrated using the high dynamic range method. The HDR method helped also to measure the paper edge spread function.

Test forms were designed and implemented (chapter 3). Nine different test forms were produced in order to study the optical and physical dot gain as a function of the dot shape and organization. Conventional amplitude modulated halftone were obtained with Photoshop. The Superformula was used to produce multiple dot shapes having constant ink surface with multiple edge perimeters. This allowed studying the impact of the ratio of area and perimeter on the optical dot gain. Halftone dots configurations were generated and placed in an array in order to measure the elementary dot-dot interactions on the shape of the halftone dot. The morphology of the ink deposition was also analyzed using scanning electron images. This revealed that the offset ink layer deposited was extremely thin and ink particles were visible on the layer. The inkjet inks penetrated in the first layer of the paper coating. The matte inkjet ink produced cracks at the edges of the superposition of two droplets. The electrophotography produced a thick layer totally covering the paper coating particles. Four papers were used for printing and were analyzed. The two different glossy coated papers showed a layer of mineral particles and bounding agents, covering totally the cellulose fibers. The inkjet paper also had a coating on its surface, however the roughness appears to be much smaller than with the glossy coated paper. Finally the uncoated paper displayed a rough surface (5 times larger than for the coated paper) with apparent cellulose fibers and mineral fillers.

8.1.2 Optical dot gain characterization tools

In previous studies manual measurement methods were used to measure the ink and paper reflectance peaks. An automated method based on a Gaussian fitting of the ink and paper peaks on the histogram was proposed in this work (chapter 4). The Gaussian fitting was performed by optimizing two parameters, the Gaussian width and the Gaussian center position. The Gaussian width was optimized for each given Gaussian center position. The height of the Gaussian curve was fixed to the height of the reflectance distribution at the position corresponding to the center of the Gaussian. Two optimization criteria were developed accordingly. The first optimization criterion only assessed the surface differences between the Gaussian fit peak and the histogram peak. The second criterion took into account the previous difference as well as the height and the width of the Gaussian curve. Both optimization criteria were studied and strategies adopted for the optimization were validated. The reflectance distribution of the paper peak was found very close to the Gaussian fit with 99.2% of the peak covered by the Gaussian fitting. For the solid print, the reflectance distribution was also found close to the Gaussian fit with 85.2% of the ink peak covered by the fitted Gaussian. The Gaussian followed accurately the ink reflectance distribution on the left of the peak. The peak seemed composed of multiple Gaussians. Nevertheless, a small difference of 0.004 optical density was obtained between the center of the fitted Gaussian and average reflectance of the peak and was considered not significant. For the halftone patch, the ink and paper peaks differed from single Gaussian functions. For the ink peak, the left region was fitted with high accuracy by a Gaussian function. For the paper the right region of the peak was fitted also accurately. The ink and paper peaks were extended and spreading respectively to higher reflectance values for the ink and to lower reflectance values, due to light diffusion into paper. Nevertheless it was observed that the position of the peak maximum for both ink and paper appeared near the maximum of the fitted Gaussian, showing that the Gaussian fit method was well appropriated for halftones. The repeatability of the Gaussian fitting was verified and fitted reflectance coefficients of variation for the ink and paper peaks were found respectively at 1.68% and 2.32%. These variations were found to be smaller than the coefficients of variation of the average reflectance of the halftone. Simulations of the dot gain with real halftone dot geometries were investigated in order to evaluate the performance of Gaussian fit measurements compared to manual

measurements with an absolute reference (ground truth). The Gaussian fit measurements were found closer to the ground truth than manual measurements. For the three print processes at 150 lpi, the relative average differences between the Gaussian fit and the ground truth reached 9.0% for the ink reflectances and 3.0% for the paper reflectances. This can be compared to the manual measurements reaching 23.6% for the ink reflectances and 10.0% for the paper reflectances. At 200 lpi relative average differences were smaller with 3.0% for the ink and 4.0% for paper for the Gaussian fit compared to 8.6% and 6.6% for the manual measurements. The method developed was automatic and thus was fast and unbiased compared to manual measurements.

8.1.3 Optical and physical dot gains separation

Two novel methods to separate optical dot gain and physical dot gain were proposed based on de-convolution strategies (chapter 5). Both methods relied on the model of the light diffusion on halftones and assumed that the ink transmittance could be obtained from the reflectance image including the optical dot gain. The main differences between the two methods proposed were the strategies applied to obtain the ink transmittance. For the first strategy the ink transmittance was simply defined as the square root of the halftone reflectance. For the second strategy, the ink transmittance was defined by a thresholding of the halftone. The two methods showed an effective separation and images treated revealed un-inked surface previously masked by optical dot gain. Further analysis of the impact of the two separation strategies were conducted by comparing the reflectance values along a same line on the halftone image. Results of the separation showed sharper reflectance transitions going from the paper to the ink. Images after separations were closer to a bimodal distribution, showing that the optical dot gain mixed regions were partially removed. However, paper reflectance levels were not exactly matching the reflectance levels of bare paper, showing that the removal of optical dot gain was not total. Moreover, quantitative evaluations of the separation strategies were difficult to conduct because a reliable reference of the true ink distribution on paper was shown to be not trivial to obtain.

A method to evaluate objectively the performances of the threshold algorithms on halftone print images was then developed (chapter 6). The method was based on a generation of ground truth images, obtained either by thresholding halftones images captured on the microscope (MCI) or by generating synthetically halftone dots and defects. Then a simulation of the optical dot gain effects and of the microscope distortions was performed to obtain simulated microscope images (SMI) that had similar characteristics than the images measured on the microscope. The simulated images were then processed by the threshold algorithms and the performances were evaluated by comparing the thresholded images with the ground truth. The performances of the proposed evaluation method were analyzed. A frequency analysis showed that the histograms were also similar with maxima and minima located at the same levels. An index to quantify the similarity between the two histograms was proposed and reached 94.3% +/-0.24%. Furthermore, 1320 SMI were generated and were found to be extremely similar to the GTI with a mean grayscale fidelity ratio of 96.06% +/- 2.82%. A dependency of the SMI generation performances with the ink coverages was observed, with a decrease of the performances toward the 50% ink coverage.

Thirty threshold algorithms were then evaluated on 3920 generated SMI, composed of the 1320 synthetic images based on thresholded microscope captured images and of 2600 images based on synthetic ground truth images (chapter 6). Globally, the best suited threshold algorithms with ratios superior to 90%, were the PalBhandari, IsoData, SimpsonGobat, Otsu, Intermodes, Minimum, Li, Huang and Phansalkar algorithms. These algorithms presented a limited dependency with the ink coverage. Threshold algorithms such as the MinError, Triangle, Rosenfeld, Whatmough and Moments were associated with only a small dependency on the ink coverage. However these algorithms presented either a large dispersion of the performances or a large decrease of the performances for small ink coverages. Finally threshold algorithms such as the Mean, Median, Percentile, MaxEntropy, RenyiEntropy, Yen, PalDasgupta, Local mean, Local median, Contrast and Niblack presented a large

dependency of the performances on the ink coverage and were associated with binary fidelity ratio inferior to 90%. The difference of ink coverage (ICD) was compared between the results obtained with the threshold algorithms and the ground truth. Over the 3920 halftone images processed, a mean ICD of 1.78% for was obtained for the Li algorithm, 7.81% for PalBhandari, 2.22% for Huang, 2.87% for Minimum, 2.57% for SimpsonGobat, 1.84% for Otsu, 3.24% for Isodata, 3.30% for Intermodes and 2.44% for Phansalkar. These results were refined considering only the 1320 ground truth images obtained from the microscope images and restricting the ink surface range to exclude the ink coverage below 10% and above 90%. With these conditions the two best threshold algorithms obtained were then the Li and PalBhandari. Finally the dependencies of the 6 selected threshold algorithms on the dot size, solid ink optical density, paper PSF, ink heterogeneities and edges fuzziness were investigated. It was found that for the Li and PalBhandari threshold algorithms, an increase of the dot size increased the threshold performances and a decrease of the ink solid optical density increased also the threshold performances. The paper PSF did not affect the global performances. The ink heterogeneity increase decreased the performances of the two threshold algorithms and edge fuzziness increase presented first an increase of the threshold performances for the large dot sizes and the tendency was then reversed for the small dot sizes.

To improve the threshold performances of the halftone images, two novel threshold algorithms developed specifically to process halftone dots were proposed (chapter 6). The first threshold algorithm, called the LveShape was based on the position of the ink peak on the histogram of the halftone. A factor called the M factor was computed by fitting the halftone and the solid ink peaks with Gaussian functions and by finding the center of the Gaussian curves. The threshold value of the solid ink patch was stretched with the M factor to define the best threshold position for the halftone patch. The second threshold algorithm proposed was based on a pre-treatment of the halftone images applying the method developed to separate the optical dot gain. Thresholding the pre-treated halftones was then performed by applying a constant threshold level determined from the solid ink halftone. Results showed that the LveSpatial threshold algorithm was performing better than the PalBhandari and Li threshold algorithms. Excluding the extreme ink coverages (below 10% and above 90%) a mean absolute binary fidelity ratio of 99.07% was reached and was compared to the 98.12% obtained for the PalBhandari algorithm and 98.12% obtained for the Li algorithm. Analyzing the performances for the halftones obtained from the thresholded MCI, showed that the LveSpatial was independent on the ink coverage and reached a mean absolute ICD of 0.21% +/- 0.33% for all ink coverages. This performance was compared to the PalBhandari and Li thresholds algorithms reaching 0.79% +/- 0.79% and 0.79% +/- 0.74% in the reduced ink coverage range of 10% to 90%. The LveShape threshold algorithm reached a global performance inferior to the PalBhandari and Li threshold algorithms. 24.6% of the halftones thresholded with the LveShape threshold algorithm obtained a binary fidelity ratio below 90%. Aside from these cases the LveShape threshold algorithm performed well, with a mean binary fidelity ratio of 98.14% +/- 1.86%. Globally the LveSpatial threshold algorithm was found to be less sensitive to the halftone resolution, ink reflectance, paper PSF, ink homogeneity and edge fuzziness compared to the PalBhandari and Li threshold algorithms.

A study of the optical and physical dot gain was then proposed (chapter 6). The print characteristics influencing the most the optical dot gain were then the paper type and the dot-dot distance. The print process, the halftone size, the inks and inking and the dot size influenced only slightly the optical dot gain. The halftone type, the dot shape and the dot perimeter had a very limited effect on optical dot gain. The influence of the print parameters differed on the physical dot gain. The physical dot gain was extremely influenced by the halftone size, the inking level, the dot size and the dot-dot distance. The print process, halftone type, dot shape and dot perimeter influenced only slightly the physical dot gain. Finally the ink type and the paper type (with similar surface roughness) were found to have a very limited effect on the physical dot gain.

8.1.4 Raster to print models

A physical dot gain model and an optical dot gain model were proposed based on the dot gain separation developed. First, an analysis of the physical dot gain was proposed based on different dot placement configurations (codes) on a 3 by 3 matrix (chapter 7). Automated measurements allowed obtaining a large database of 43269 codes. For electrophotography the printed single dots area and convex area demonstrated increases compared to the original dot sizes with the increase of the original dot sizes (binning). It was concluded that the physical dot gains induced with the electrophotography process were dependent on the size of the single dots. Although showing a larger physical dot gain, the shape of the single dots were found to become more similar to the original dots with the increase of binning. Dot edges became rougher with the increase of the binning. The printed dot registration error was centered on the center of the original dot with a binning of 2 and 4. For a binning of 3 a systematic misregistration error was observed and the length was found to be close to the size of one dot at the printer nominal resolution. For offset, the printing of a single dot with a binning of 2 was extremely sensitive to the process variations with a mean single area decrease and a large standard deviation. With binnings larger than 2, the single dots were then impacted by larger physical dot gains. The physical dot gain levels were found to be dependent on the binning level with an increase and then a decrease with the rise of binning. The maximal physical dot gain was found at a binning of 4 (single dots of 40 µm of diameter). The positioning errors of the single dots centers were not influenced by the increase of binning with a mean positioning errors length corresponding to one half of the dot size at the nominal resolution of the printer. The dots were mostly mis-positioned in the bottom center of the codes, corresponding to an ink spreading in the printing direction. For inkjet, differences with the offset and electrophotography appeared for small binnings, since only a single droplet was printed for a single dot at the native resolution. With the increase of binning the single dot shapes became closer to the nominal squares. Dots edges became rougher with the increase of binning due to the increase of the number of droplets printed. The printed single dot positioning error was constant with the increase of binning and corresponded to one half of the nominal dot diameter. The directions of the misregistrations were mostly found directed on a diagonal axis corresponding to the print direction.

A model to simulate single dots was proposed based on the assumption that single dots were composed of one or several ink particles located on the surface of the printed dot following a probability distribution (chapter 7). Single dots were modelled by defining first the spatial probability distribution, then by feeding ink particles on the spatial distribution and finally by fusing the particles. The proposed model relied on seven parameters allowing the generation of different dot shapes with different levels of edge roughness, ink heterogeneities and physical dot gains. For electrophotography, offset and inkjet the model globally simulated correctly the printed dots. The model proposed for the single dots was then directly implemented to simulate multiple dots configurations. Results were compared to the printed codes measurements. For electrophotography the mean fidelity ratio of printed codes compared to the nominal codes for all binnings reached 14.1% +/- 17.3%. This low fidelity ratio demonstrated that large physical dot gains occurred. The mean fidelity ratio of the simulated codes compared to the printed codes for all binnings was largely improved reaching 91.7% +/- 9.0%. For offset, the binary fidelity ratio of the printed dots increased with the increase of binning. The mean fidelity ratio of printed codes compared to the nominal codes for all binnings reached 33.8% +/- 21.5%. The model simulated accurately the printed dots and high fidelity ratio levels for all binnings were obtained with 93.3% +/- 6.9%. The model could be further improved by adopting a higher fusion of the ink particles. For inkjet, the mean fidelity ratio of printed codes compared to the nominal codes for all binnings reached 30.8% +/- 22.6%. The model simulated accurately the printed dots and large fidelity ratio levels for all binnings were obtained with 92.9% +/- 3.6%. For all printing processes, the physical dot gain of the singles dots generated dot-dot interactions and induced a global physical dot gain. The configurations of the single dots in the matrix code influenced the physical dot gain. However these variations were found to be globally independent on the number of single dots in the matrix. The codes with low fidelity ratio were mainly associated with separated printed dots

configurations presenting a larger total dot perimeter. The model with the fusion of the ink particles reproduced more accurately the dot-dot interactions observed.

Then in a second part the optical dot gain was analyzed and modelled (chapter 7). The performance of the model of the light diffusion on halftones was analyzed for 8 different PSF associated with 8 different PSF lengths. The profile of reflectances along a line on the halftone was evaluated. Three regions were identified: the ink region, the paper region and the mixed region. The mixed region was the one near the ink dot edges where the reflectances are higher than the ink reflectance and lower than the paper reflectances. The global CS_P index for three regions showed that the Exponential paper PSF was performing the most accurately. In the mixed region, the SHI profiles obtained for all PSF tested were associated with large differences with the MCI profile. The mean reflectances of the ink regions increased with the increase of the PSF length. The mean reflectances of the paper regions decreased with the increase of the PSF length. For the mixed regions mean reflectances obtained were constant and thus independent on the PSF type and PSF length. It was concluded that none of the PSF types and lengths tested fitted correctly the MCI halftone in the mixed region.

A novel model was then proposed in order to take into account the light trapping effects in the mixed region (chapter 7). The novel model gave a spatial description of the halftone reflectance as a function of the paper bare reflectance, the ink transmittance, two paper PSF and an empirical parameter accounting for the edge effects as inputs. The first PSF controlled the global ink reflectance increase and paper reflectance decrease. The second PSF controlled the reflectance profile in the mixed region. The novel model followed accurately the MCI profile on the paper and ink regions near the paper-ink edge and improved the performances compared to the 1 reflection model. The fitted ink coverage difference was computed to analyze the effect of the mixed region reflectance differences on the total fitted ink coverage. The novel model reached an ink coverage difference of -0.41% for electrophotography, -0.35% for offset and -0.58% for inkjet. This improved the simulation in the mixed region by 5 times for the 1 reflection model. A further evaluation of the novel model performances was proposed by comparing the mean absolute apparent ink coverage difference for 1231 halftone patches. It was observed that the Yule-Nielsen model performed slightly more accurately than the 1 reflection and the novel models. The average of all mean absolute ink coverage differences (AICD) reached 1.47% +/- 1.39% for Yule Nielsen model. The novel model was found to have a performance close to the Yule-Nielsen model with an average of all mean AICD of 1.65% +/- 1.44%. The average standard deviation associated was smaller for the novel model than for the Yule-Nielsen model. The average performance for the model of the light diffusion on halftones with 1 reflection was larger at 2.23% +/- 1.86%. The novel model improved performances for halftone sets printed with electrophotography and offset. A decrease of the performances for the novel model was observed with the increase of the ink transmittances. A study over four different papers demonstrated that the novel model performed better for glossy coated papers presenting a smaller light diffusion than with uncoated or Epson papers. The novel model performed globally more accurately than the 1 reflection model. The novel model was associated with slightly lower performances than the Yule-Nielsen model. However it benefited from a 2D description of the reflectances of the halftone allowing a more accurate characterization of the optical dot gain. Moreover a more accurate parameter optimization for the novel model can improve performances.

These physical and optical dot gain models allowed then obtaining models describing the halftone from raster to visual perception. The print parameters could then be tuned to take advantage of the physical and optical do gains, in order to reduce the ink consumption, to create special visual effects or to improve the performances of the anti-counterfeiting printed solutions.

8.2 Perspectives

8.2.1 Apparatus improvement and further experiments

The proposed apparatus allowed improving the measurement of halftone dots at the microscale. The accuracy of the measurements could be further improved by adapting a camera with similar specifications as the Canon 1200D used:

- large sensor surface and large amount of pixels
- raw capture
- USB control
- live stream of images "LiveVew"

and with improved specifications by :

- electronic shuttering of the sensor in order to remove all moving components
- temperature cooling of the sensor and of the electronics to reduce capture variations
- anti-aliasing filter removing to improve the resolution
- increasing the pixel value discretization to 16 bits to obtain more accurate measurements

Moreover the illuminant of the microscope was found to be variating in time. A Led based illuminant could improve the stability of the illuminant and could shorten the warm up time.

A continuation of the analysis of the proposed experiments (chapter 3) could yield to an improved characterization of the optical and physical dot gain. The following experiments could be further analyzed:

- Influence of the distance between halftone dots and of the size of the halftone dots on the optical and physical dot gains. Dots with triangle shapes rotated at 45°, dots with pentagon shapes, dots with hexagon shapes rotated at 0°, 45° and 90°.
- Influence of the perimeter of the halftone dots on the optical and physical dot gains. 417 different configurations were generated and printed with each process and 126 configurations were measured. This experiment could be improved measuring more printed configurations. Moreover the quantification of the circularity was based on the nominal perimeter and area of the dots. The optical dot gain analysis could be improved considering the circularity based on a measurement of the perimeter and of the area of the printed dots (including the physical dot gain). An extension of the characterization of the perimeter effects can also be proposed generating dots with different diameters.
- Several halftoning algorithms could be characterized using the optical and physical dot gain separation method developed. An evaluation and a classification of the halftoning algorithms could then be proposed and would allow optimizing the halftoning as a function of the print process, the resolution and the user input.
- The proposed model of the light diffusion on halftones relies on the two paper point spread functions and on an empirical parameter. The optimization of these variables was performed manually by trial and errors. An automatic optimization of the parameters could then be developed. The automatic optimization algorithm could then also be used to obtain a characterization of the paper PSF of prints (reversing the model).
- The physical dot gain and the dot-dot interactions were studied on the 3 by 3 matrix codes yielding to 512 different configurations. Codes with a 5 by 5 matrix, presenting more complex dot-dot configurations were generated and printed. A continuation of this work could focus on a detailed analysis of these configurations.

8.2.2 Multispectral optical and physical dot gain characterizations

A continuation of this work can focus on extending the experimental methods, treatments and analyses to color printing. The apparatus developed and presented in chapter 3 can capture multispectral images using 17 band pass filters mounted on a custom filter wheel controlled directly in the GUI. An example of the first measurements obtained is presented in Figure 8.2. Extensions of the methods developed in this thesis are then proposed:

- The high dynamic range method can be employed directly. However the reflected irradiances of the halftones are filtered by a bandpass filter. Therefore an automatic detection of the exposure times, required to cover the range of the dynamic range of the halftone, could be developed. This detection would then allow an automated HDR capture for each bandpass filter and for each halftone.
- The Gaussian fit method for automated ink and paper peak measurements can be directly implemented for multispectral images by considering independently each images obtained at a specific wavelength. The method could be re-developed to fit 3D Gaussian functions on 3D histograms with on the X axis the reflectance level, on the Y axis the associated wavelength and on the Z axis the occurrence. The Gaussian fitting would then be performed for multiple peaks; one peak for each colorant (individual inks, paper and superpositions).
- The separation of optical and physical dot gain can be performed directly on each captured image corresponding to the reflectance filtered with a bandpass filter. The developed thresholding method only requires adjusting the two PSF. A dependency of the PSF on the wavelength was observed by Ukishima [17] and an optimization for each bandpass filter may be required.
- The automated measurement method and analysis of the physical dot gain and of the dot-dot interactions could be re-implemented for color print halftones. The influence of the superpositions of several inks on the shape of the dots and on the physical dot gain could then be studied.

Finally, an example of separation of the halftone colorant is proposed using only 1 bandpass filter per ink and allows a faster capture and analysis, Figure 8.3. The methods proposed in this manuscript could then be adapted to process each separated image and to study the influence of ink superpositions.

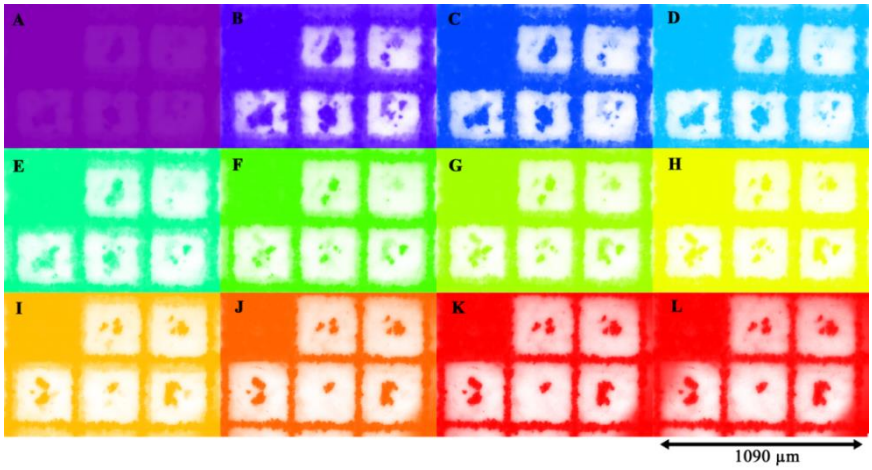

Figure 8.2: Spectral reflectance of color printed codes. Images are colored as a function of the center wavelength of the bandpass filter used for the acquisition – (A) 400 nm, (B) 425 nm, (C) 450 nm, (D) 475 nm, (E) 500 nm, (F) 525 nm, (G) 550 nm, (H) 575 nm, (I) 600 nm, (J) 625 nm, (K) 650 nm, (L) 675 nm.

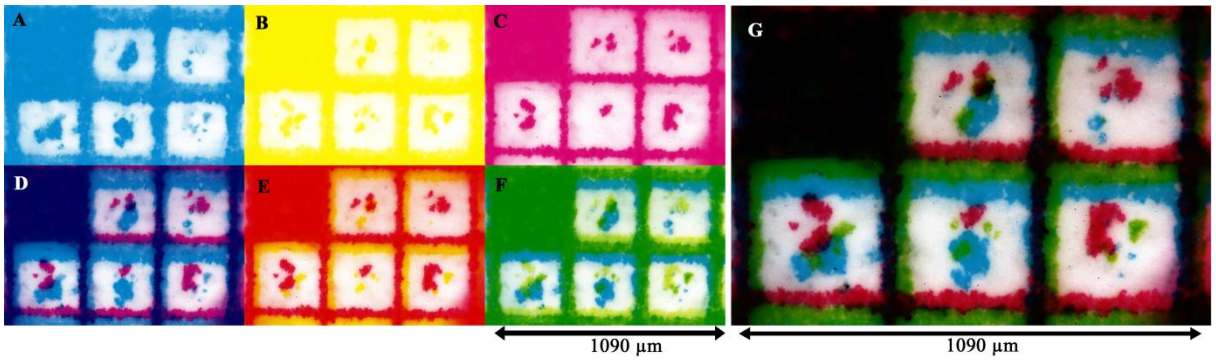

Figure 8.3: Spectral reflectance of color printed codes. Selection of 3 bandpass filters (A) 450 nm, (B) 550 nm, (C) 625 nm and coloration according to the 3 inks - (A) cyan, (B) yellow, (C) magenta. Superpositions of (D) cyan & magenta, (E) magenta & yellow, (F) cyan & yellow and (G) cyan, yellow & magenta.

8.2.3 Applications

Ultimately, a continuation of this work could focus on industrial applications:

- The method developed could then be used to propose more secured anti-counterfeiting solutions by measuring more precisely the dot shapes and characteristics at the microscale and by predicting the dot-dot interactions.
- Halftone methods could be developed using the two models proposed in order to obtain a prediction from raster to print. An inversion of the model could then help achieving improved color reproduction and reduce the ink consumption.

Appendix

Histogram normalized probability mass function and moments

[A.1]

$$p_i = \frac{h(i)}{\sum_{i=1}^{t_{max}} h(i)}$$

$$M_t^m = \sum_{i=1}^{t} i^m p_i$$

$$\bar{M}_t^m = \sum_{i=t+1}^{t_{max}} i^m p_i$$

Symbol	Unit	Denomination
p_i	1	Normalized probability mass function
M_t^n	1	n moment from 0 to t
$\bar{M}_t^n$	1	n moment from $t+1$ to t_{max}
$h(i)$	1	Histogram
i	1	Pixel value
t	1	Pixel value
t_{max}	1	Max pixel value

MinError threshold algorithm

[A.2]

$$CT_k(t) = M_t^0 \ln\left(\frac{\sigma_1}{M_t^0}\right) + \bar{M}_t^0 \ln\left(\frac{\sigma_2}{\bar{M}_t^0}\right)$$

$$\sigma_1 = \sqrt{\frac{M_t^2}{M_t^0} - \left(\frac{M_t^1}{M_t^0}\right)^2} \qquad \sigma_2 = \sqrt{\frac{\bar{M}_t^2}{\bar{M}_t^0} - \left(\frac{\bar{M}_t^1}{\bar{M}_t^0}\right)^2}$$

Symbol	Unit	Denomination
$CT_k(t)$	1	Kittler criterion
t	1	Pixel value
M_t^n	1	n moment from 0 to t
$\bar{M}_t^n$	1	n moment from $t+1$ to t_{max}

Pal & Bhandari threshold algorithm

[A.3]

$$CT_{pb}(t) = \frac{M_{t_{max}}^1}{M_{t_{max}}^0} - M_t^0\left[\ln(M_t^0) + \left(\frac{M_t^1}{M_t^0}\right)\ln\left(\frac{M_t^1}{M_t^0}\right)\right] - \bar{M}_t^0\left[\ln(\bar{M}_t^0) + \left(\frac{\bar{M}_t^1}{\bar{M}_t^0}\right)\ln\left(\frac{\bar{M}_t^1}{\bar{M}_t^0}\right)\right]$$

Symbol	Unit	Denomination
$CT_{pb}(t)$	1	Pal Bhandari criterion
t, t_{max}	1	Pixel value, max pixel value
M_t^n	1	n moment from 0 to t
$\bar{M}_t^n$	1	n moment from $t+1$ to t_{max}

IsoData threshold algorithm

[A.4]

$$CT_r(t) = \frac{1}{2}\left(\frac{M_t^1}{M_t^0} + \frac{\bar{M}_t^1}{\bar{M}_t^0}\right)$$

Symbol	Unit	Denomination
$CT_r(t)$	1	Ridler criterion
t	1	Pixel value
M_t^n	1	n moment from 0 to t
$\bar{M}_t^n$	1	n moment from $t+1$ to t_{max}

Otsu threshold algorithm

[A.5]

$$CT_o(t) = M_t^0 \bar{M}_t^0 \left(\frac{M_t^1}{M_t^0} - \frac{\bar{M}_t^1}{\bar{M}_t^0}\right)^2$$

Symbol	Unit	Denomination
$CT_o(t)$	1	Otsu criterion
t, t_{max}	1	Pixel value, Max pixel value
M_t^n	1	n moment from 0 to t

MaxEntropy threshold algorithm

[A.6]

$$CT_a(t) = -\sum_{i=1}^{t} \frac{p_i}{M_t^0} \ln\left(\frac{p_i}{M_t^0}\right) - \sum_{i=t+1}^{t_{max}} \frac{p_i}{\overline{M}_t^0} \ln\left(\frac{p_i}{\overline{M}_t^0}\right)$$

Symbol	Unit	Denomination
$CT_a(t)$	1	Kapur entropy
p_i	1	Normalized probability mass
$i,\ t, t_{max}$	1	Pixel value, max pixel value
M_t^n	1	n moment from 0 to t
$\overline{M}_t^n$	1	n moment from $t+1$ to t_{max}

RenyiEntropy threshold algorithm

[A.7]

$$CT_y(t,\alpha) = \frac{1}{1-\alpha} \ln\left(\sum_{i=1}^{t} \frac{p_i}{M_t^0}\right)^{\alpha} + \frac{1}{1-\alpha} \ln\left(\sum_{i=t+1}^{t_{max}} \frac{p_i}{\overline{M}_t^0}\right)^{\alpha}$$

[A.8]

$$K = K_{0.5}\left[M_{t_1}^0 + \frac{\beta_1\left(M_{t_3}^0 - M_{t_1}^0\right)}{4}\right] + K_{0.9}\left[\frac{\beta_2\left(M_{t_3}^0 - M_{t_1}^0\right)}{4}\right] + K_2\left[1 - M_{t_3}^0 + \frac{\beta_3\left(M_{t_3}^0 - M_{t_1}^0\right)}{4}\right]$$

$$(\beta_1,\ \beta_2, \beta_3) = \begin{cases} (1,2,1) \text{ if } (|t_1 - t_2| \le 5 \text{ and } |t_2 - t_3| \le 5 \\ (1,2,1) \text{ if } (|t_1 - t_2| > 5 \text{ and } |t_2 - t_3| > 5 \\ (0,1,3) \text{ if } (|t_1 - t_2| \le 5 \text{ and } |t_2 - t_3| > 5 \\ (3,1,0) \text{ if } (|t_1 - t_2| > 5 \text{ and } |t_2 - t_3| \le 5 \end{cases}$$

Symbol	Unit	Denomination
$CT_y(t,\alpha)$	1	Renyi entropy
K	1	Threshold value
α	1	Renyi factor
i, t	1	Pixel value
t_{max}	1	Max pixel value
M_t^n	1	n moment from 0 to t
$\overline{M}_t^n$	1	n moment from $t+1$ to t_{max}
K_α	1	Threshold values obtained for $\alpha = 0.5, 0.9$ and 2

Li threshold algorithm

[A.9]

$$CT_l(t) = \sum_{i=1}^{t} i\, p_i \ln\left(\frac{i}{\frac{M_t^1}{M_t^0}}\right) + \sum_{i=t+1}^{t_{max}} i\, p_i \ln\left(\frac{i}{\frac{\overline{M}_t^1}{\overline{M}_t^0}}\right)$$

Symbol	Unit	Denomination
$CT_l(t)$	1	Li cross-entropy
p_i	1	Normalized probability mass
i, t	1	Pixel value
t_{max}	1	Max pixel value
M_t^n	1	n moment from 0 to t
$\overline{M}_t^n$	1	n moment from $t+1$ to t_{max}

Shanbhag threshold algorithm

[A.10]
$$CT_s(t) = \left| -\frac{1}{2\,M_t^0}\sum_{i=1}^{t} p_i \ln\left(1-\frac{M_i^0}{2\,M_t^0}\right) + \frac{1}{2\bar{M}_t^0}\sum_{i=t+1}^{t_{max}} p_i \ln\left(1-\frac{\bar{M}_i^0}{2\,\bar{M}_t^0}\right)\right|$$

Symbol	Unit	Denomination
$CT_s(t)$	1	Shanbhag fuzzy entropy
p_i	1	Normalized probability mass
$i,\ t$	1	Pixel value
t_{max}	1	Max pixel value
M_t^n	1	n moment from 0 to t
$\bar{M}_t^n$	1	n moment from $t+1$ to t_{max}

Moments threshold algorithm

[A.11]
$$\text{Solve for t}:\ M_t^0 = \frac{(z - M_t^1)}{\sqrt{c_1^2 - 4c_0}}$$
$$z = \frac{1}{2}\left(-c_1 + \sqrt{c_1^2 - 4c_0}\right)$$
$$c_0 = \frac{M_t^1 M_t^3 - (M_t^2)^2}{M_t^2 M_t^0 - (M_t^1)^2}$$
$$c_1 = \frac{M_t^0 M_t^3 - M_t^1 M_t^2}{M_t^2 M_t^0 - (M_t^1)^2}$$

Symbol	Unit	Denomination
$i, t,$	1	Pixel value
t_{max}	1	Max pixel value
M_t^n	1	n moment from 0 to t
$\bar{M}_t^n$	1	n moment from $t+1$ to t_{max}

Huang threshold algorithm

[A.12]
$$CT_h(t) = \sum_{i=1}^{t} p_i\left[-\mu_a(i)\ln(\mu_a(i)) - (1-\mu_a(i))\ln(1-\mu_a(i))\right] + \sum_{i=t+1}^{t_{max}} p_i\left[-\mu_b(i)\ln(\mu_b(i)) - (1-\mu_b(i))\ln(1-\mu_b(i))\right]$$
$$\mu_a(i) = \frac{1}{1+\frac{\left|i - \frac{M_t^1}{M_t^0}\right|}{n}}$$
$$\mu_b(i) = \frac{1}{1+\frac{\left|i - \frac{\bar{M}_t^1}{\bar{M}_t^0}\right|}{n}}$$

Symbol	Unit	Denomination
$CT_h(t)$	1	Huang fuzziness
p_i	1	Normalized probability mass
i, t	1	Pixel value
t_{max}	1	Max pixel value
M_t^n	1	n moment from 0 to t
$\bar{M}_t^n$	1	n moment from $t+1$ to t_{max}

Pal Dasgupta threshold algorithm

[A.13]

$$CT_{pd}(t) = \frac{1}{M_t^0}\sum_{i=1}^{t} p_i \left[\frac{\delta_{12}+\delta_{13}+\delta_{23}}{4} + \frac{\tau_1+\tau_2+\tau_3}{3}\right]$$

$$\tau_m = \min(\mu_m; 1-\mu_m)$$

$$\delta_{mn} = |\mu_m - \mu_n|$$

$$\mu_1 = \begin{cases} 0 & i < a \\ \left(\frac{i-a}{c-a}\right)^2 & a \le i \le c \\ 1 & i > c \end{cases}$$

$$\mu_2 = \begin{cases} 0 & i < a \\ 1-\left(1-\frac{i-a}{c-a}\right)^2 & a \le i \le c \\ 1 & i > c \end{cases}$$

$$\mu_3 = \begin{cases} 0 & i < a \\ 2\left(\frac{i-a}{c-a}\right)^2 & a \le i \le t \\ 1-2\left(\frac{i-c}{c-a}\right)^2 & t < i \le c \\ 1 & i > c \end{cases}$$

Symbol	Unit	Denomination
$CT_{pd}(t)$	1	Pal Dasgupta ambiguity
p_i	1	Normalized probability mass
i, t	1	Pixel value
M_t^n	1	n moment from 0 to t
a, c	1	$c - t = t - a = 200$

2D histogram normalized probability mass functions

[A.14]

$$p_{ij} = \frac{h(i,j)}{\sum_{i=1}^{t_{max}}\sum_{j=1}^{t_{max}} h(i,j)}$$

$$P(i,j|t,s) = \frac{p_{ij}}{\sum_{i=1}^{t}\sum_{j=1}^{s} p_{ij}}$$

$$\overline{P}(i,j|t,s) = \frac{p_{ij}}{\sum_{i=t+1}^{t_{max}}\sum_{j=s+1}^{s_{max}} p_{ij}}$$

Symbol	Unit	Denomination
p_{ij}	1	Normalized probability mass 2D function
$P(i,j\|t,s)$	1	Object probability mass 2D function
$\overline{P}(i,j\|t,s)$	1	Background probability mass 2D function
$h(i,j)$	1	2D histogram
i, j, t, s	1	Pixel value
t_{max}, s_{max}	1	Max pixel value

Abutaleb threshold algorithm

[A.15]

$$CT_u(t,s) = -\sum_{i=1}^{t}\sum_{j=1}^{s} P(i,j|t,s)\log\big(P(i,j|t,s)\big) - \sum_{i=t+1}^{t_{max}}\sum_{j=s+1}^{s_{max}} \overline{P}(i,j|t,s)\log\left(\overline{P}(i,j|t,s)\right)$$

Symbol	Unit	Denomination
$CT_u(t,s)$	1	Abutaleb total entropy
i, j, t, s	1	Pixel value
t_{max}, s_{max}	1	Max pixel value

Brink threshold algorithm

[A.16]

$$CT_{ba}(t,s) = -\sum_{i=1}^{t}\sum_{j=1}^{s} P(i,j|t,s)\log\big(P(i,j|t,s)\big)$$

$$CT_{bb}(t,s) = -\sum_{i=t+1}^{t_{max}}\sum_{j=s+1}^{s_{max}} \overline{P}(i,j|t,s)\log\left(\overline{P}(i,j|t,s)\right)$$

Symbol	Unit	Denomination
$CT_{ba}(t,s)$, $CT_{bb}(t,s)$	1	Brink entropies
i, j, t, s	1	Pixel value
t_{max}, s_{max}	1	Max pixel value

Local Niblack threshold algorithm

[A.17] $$K_n(x,y) = \frac{M^1_{t_{max}}}{M^0_{t_{max}}} + e\sqrt{\frac{M^2_{t_{max}}}{M^0_{t_{max}}} - \left(\frac{M^1_{t_{max}}}{M^0_{t_{max}}}\right)^2}$$

Symbol	Unit	Denomination
$K_n(x,y)$	1	Niblack threshold value
$M^n_{t_{max}}$	1	n moment from 0 to t_{max}
e	1	Parameter

Local Sauvola threshold algorithm

[A.18] $$K_s(x,y) = \frac{M^1_{t_{max}}}{M^0_{t_{max}}}\left(1 + e\left(\frac{1}{r}\sqrt{\frac{M^2_{t_{max}}}{M^0_{t_{max}}} - \left(\frac{M^1_{t_{max}}}{M^0_{t_{max}}}\right)^2} - 1\right)\right)$$

Symbol	Unit	Denomination
$K_s(x,y)$	1	Sauvola threshold value
$M^n_{t_{max}}$	1	n moment from 0 to t_{max}
e, r	1	Parameters

Local Phansalkar threshold algorithm

[A.19] $$K_p(x,y) = \frac{M^1_{t_{max}}}{M^0_{t_{max}}}\left(1 + f\ \exp\left(-g\ \frac{M^1_{t_{max}}}{M^0_{t_{max}}}\right)\right) + e\left(\frac{1}{r}\sqrt{\frac{M^2_{t_{max}}}{M^0_{t_{max}}} - \left(\frac{M^1_{t_{max}}}{M^0_{t_{max}}}\right)^2} - 1\right)\Bigg)$$

Symbol	Unit	Denomination
$K_p(x,y)$	1	Phansalkar threshold value
$M^n_{t_{max}}$	1	n moment from 0 to t_{max}
e, r, f, g	1	Parameters

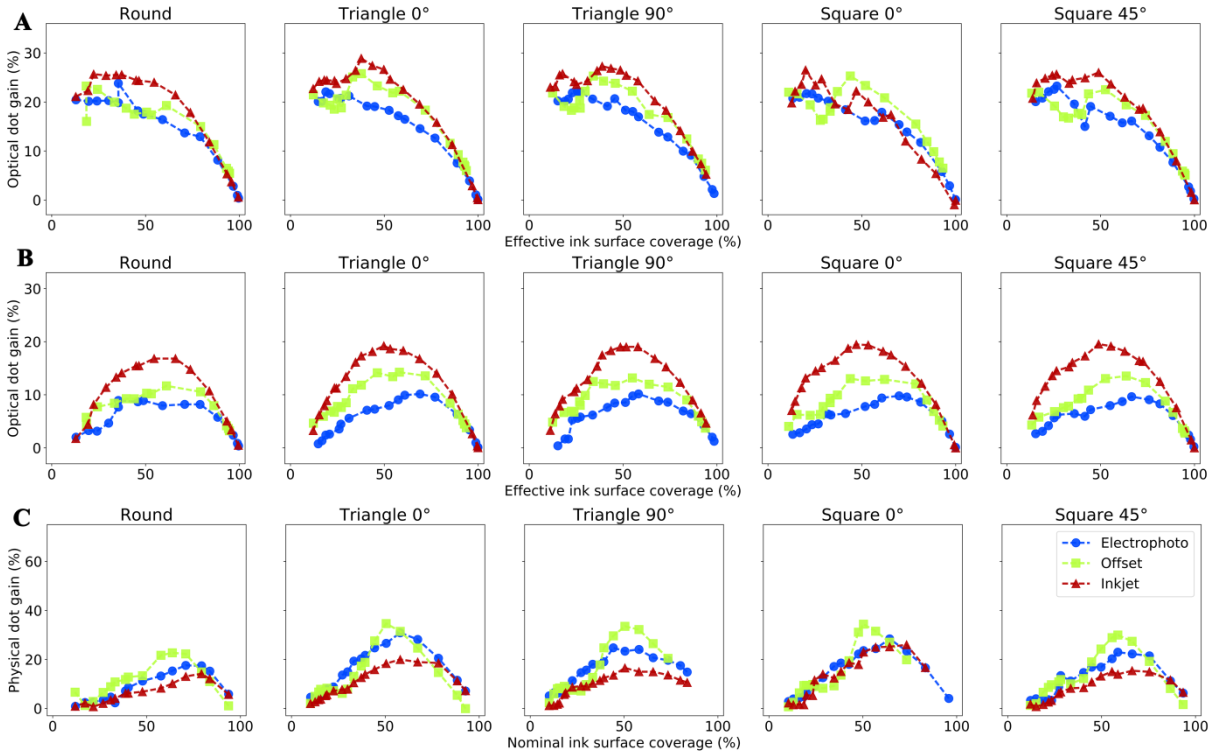

Figure A.1: Print process, halftone type and halftone size influences on (A) the optical dot gain with apparent ink coverage measured with a densitometer, (B) the optical dot gain with apparent ink coverage measured with microscale images and (C) the physical dot gain. EP1 halftones with dot sizes of 17 pixels.

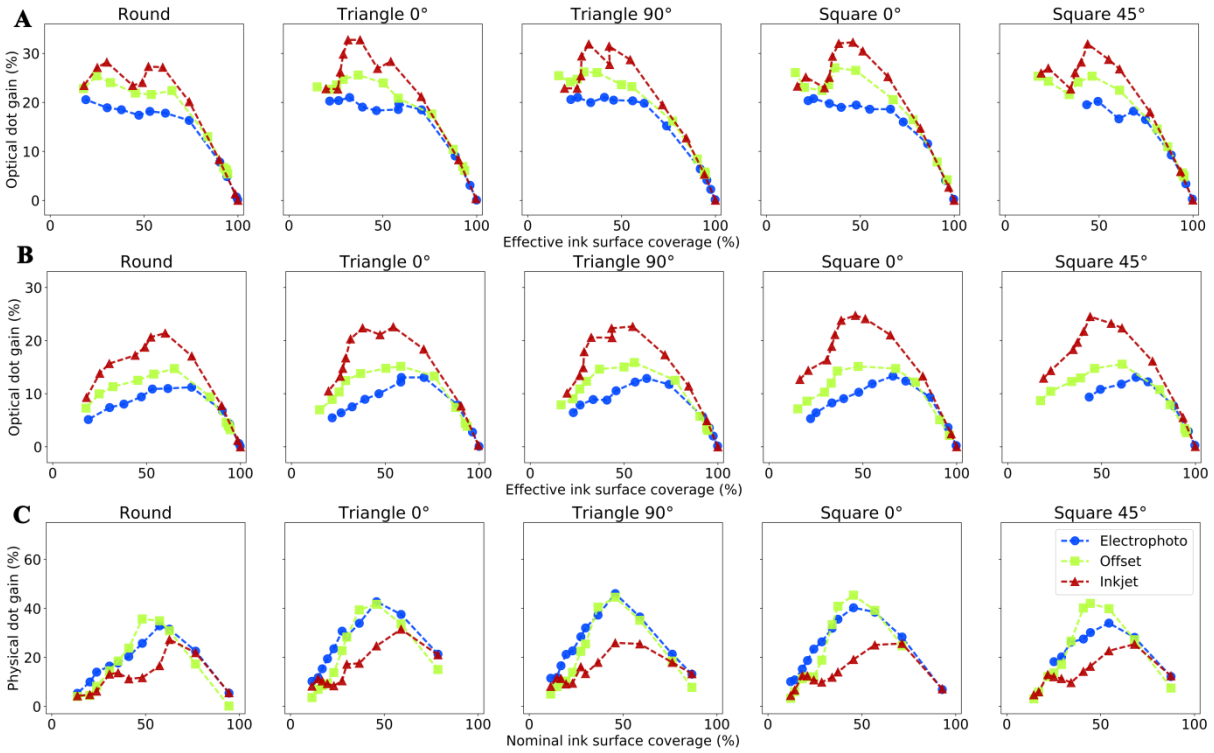

Figure A.2: Print process, halftone type and halftone size influences on (A) the optical dot gain with apparent ink coverage measured with a densitometer, (B) the optical dot gain with apparent ink coverage measured with microscale images and (C) the physical dot gain. EP1 halftones with dot sizes of 9 pixels.

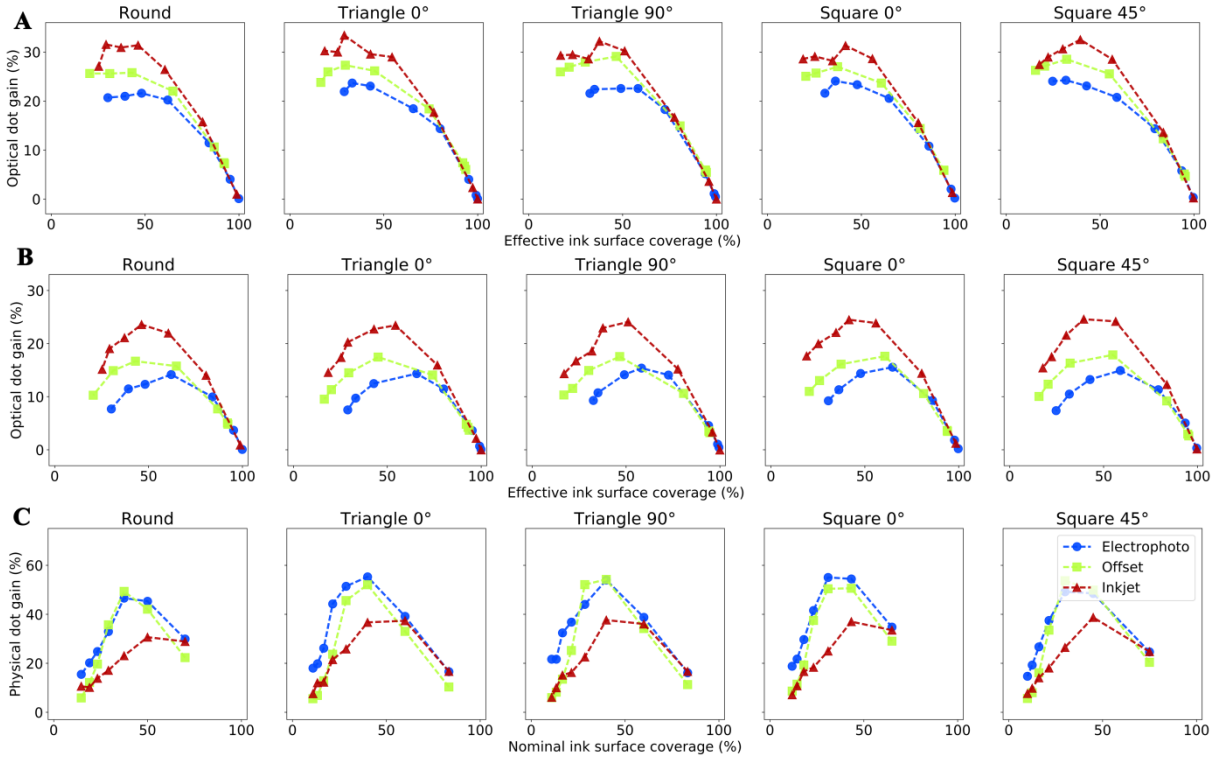

Figure A.3: Print process, halftone type and halftone size influences on (A) the optical dot gain with apparent ink coverage measured with a densitometer, (B) the optical dot gain with apparent ink coverage measured with microscale images and (C) the physical dot gain. EP1 halftones with dot sizes of 5 pixels.

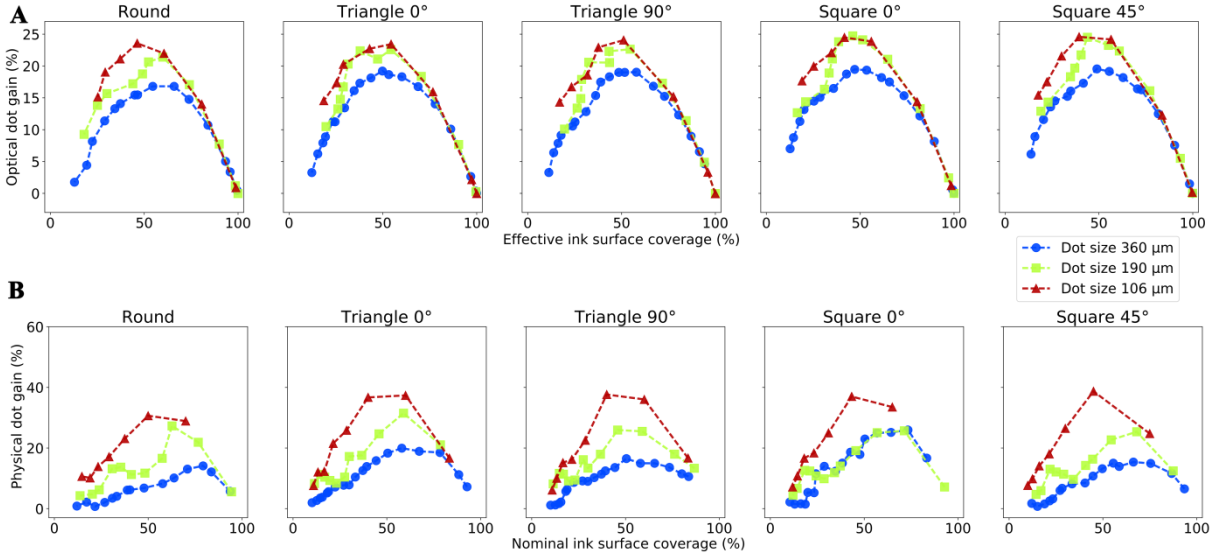

Figure A.4: Halftone dot size influence on (A) the optical (B) the physical dot gains. The samples were printed with inkjet. The halftone dot sizes are constant as a function of the ink coverage, the distance between the dots varies.

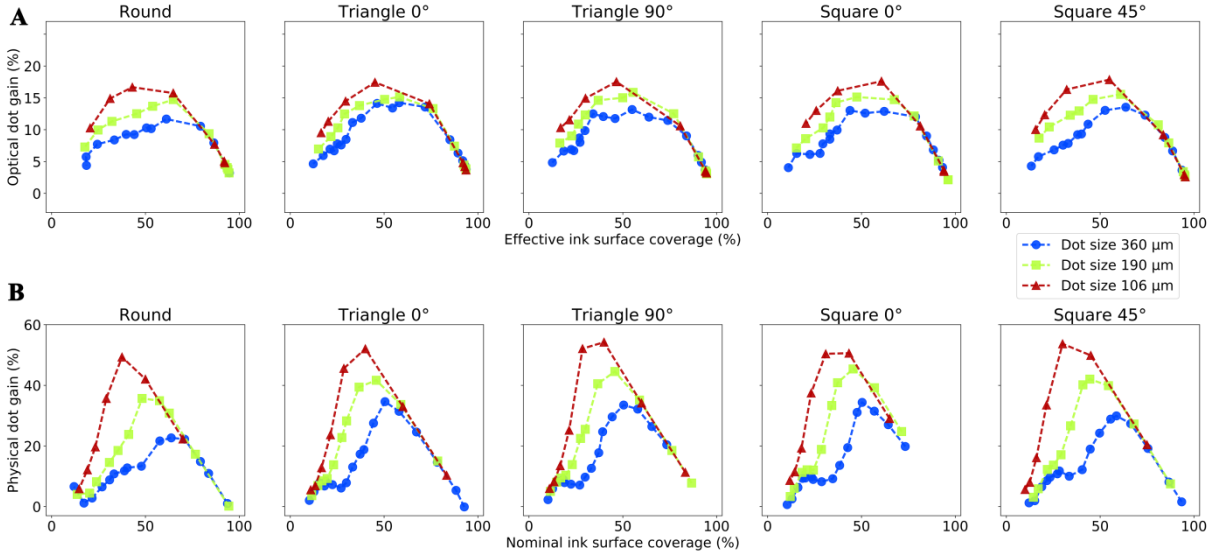

Figure A.5: Halftone dot size influence on (A) the optical (B) the physical dot gains. The samples were printed with offset. The halftone dot sizes are constant as a function of the ink coverage, the distance between the dots varies.

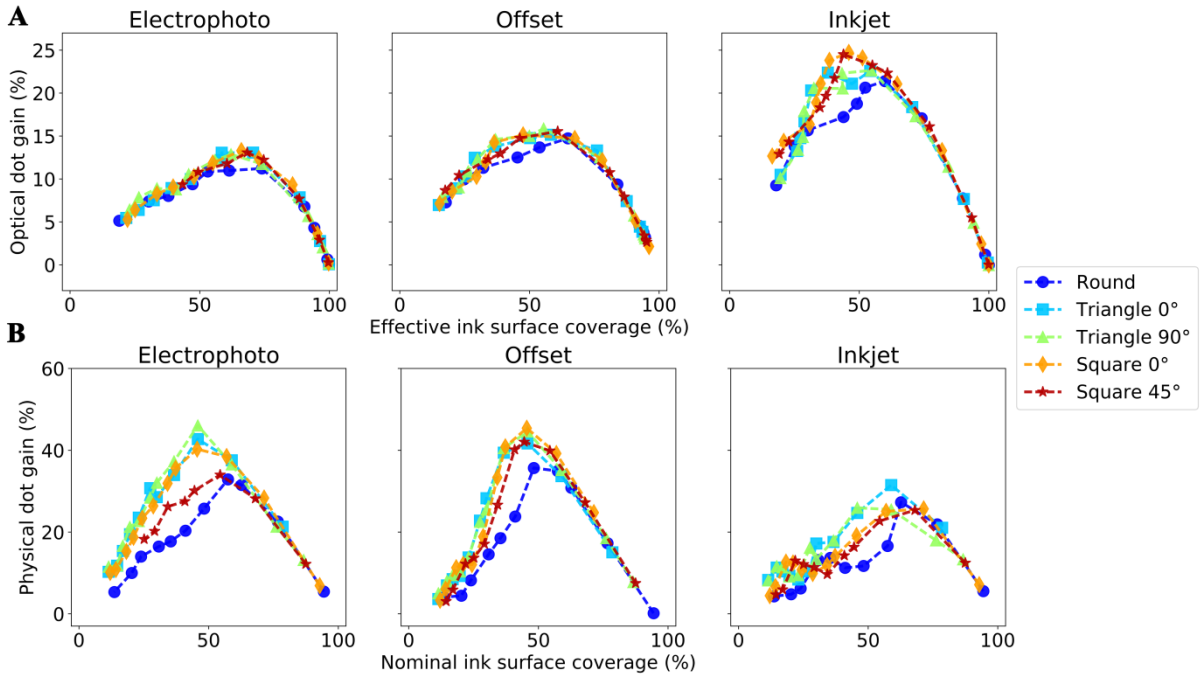

Figure A.6: Halftone dot shape influence on (A) the optical (B) the physical dot gains. The halftone dot size is fixed at 90 µm for dots printed with offset, 159 µm for dots printed with inkjet and 191 µm for dots printed with electrophotography.

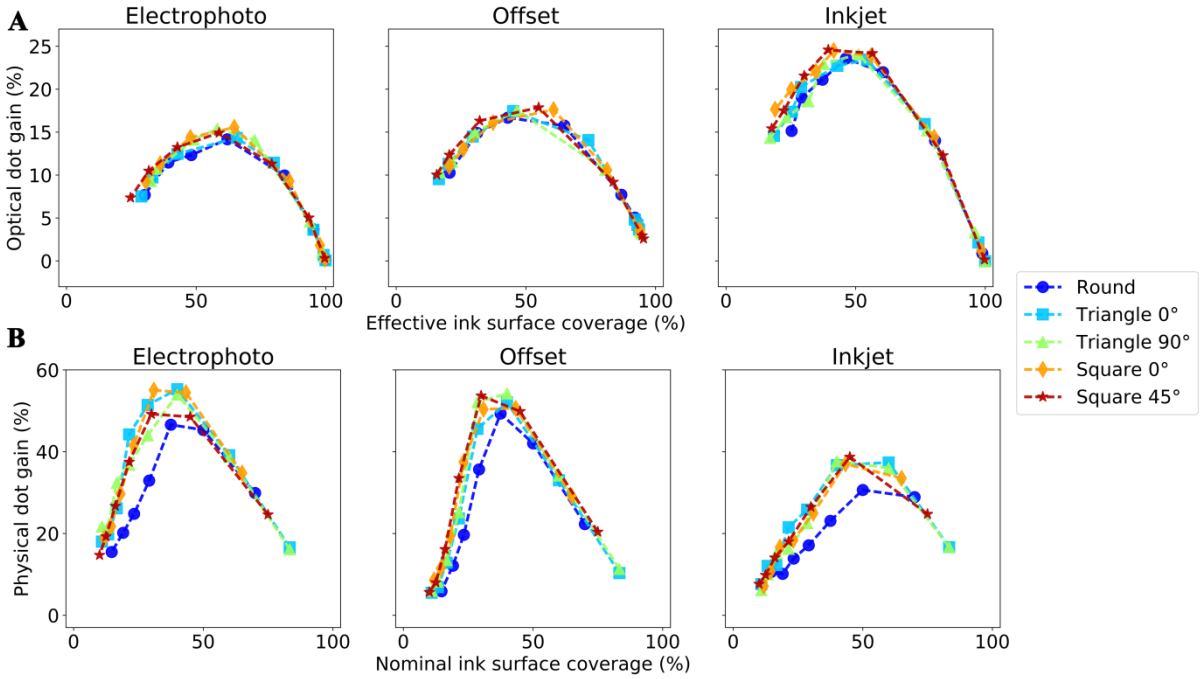

Figure A.7: Halftone dot shape influence on (A) the optical (B) the physical dot gains. The halftone dot size is fixed at 50 µm for dots printed with offset, 88 µm for dots printed with inkjet and 106 µm for dots printed with electrophotography.

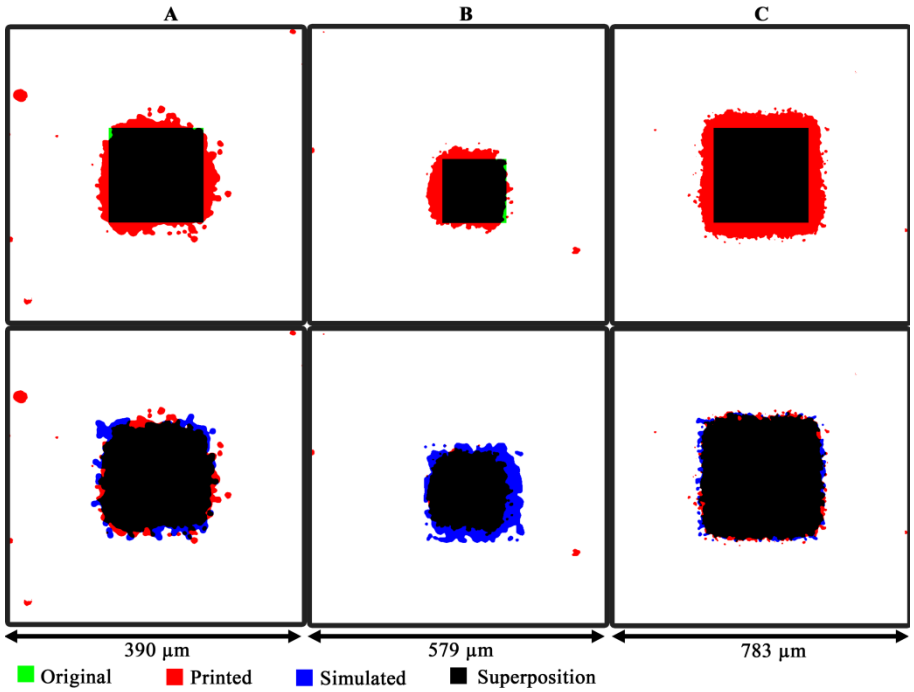

Figure A.8: Nominal, printed and simulated codes superposition printed with electrophotography. Code configuration selected presenting the highest fidelity ratio: (A) code #001, binning 2, (B) code #485, binning 3 and (C) code #001, binning 4.

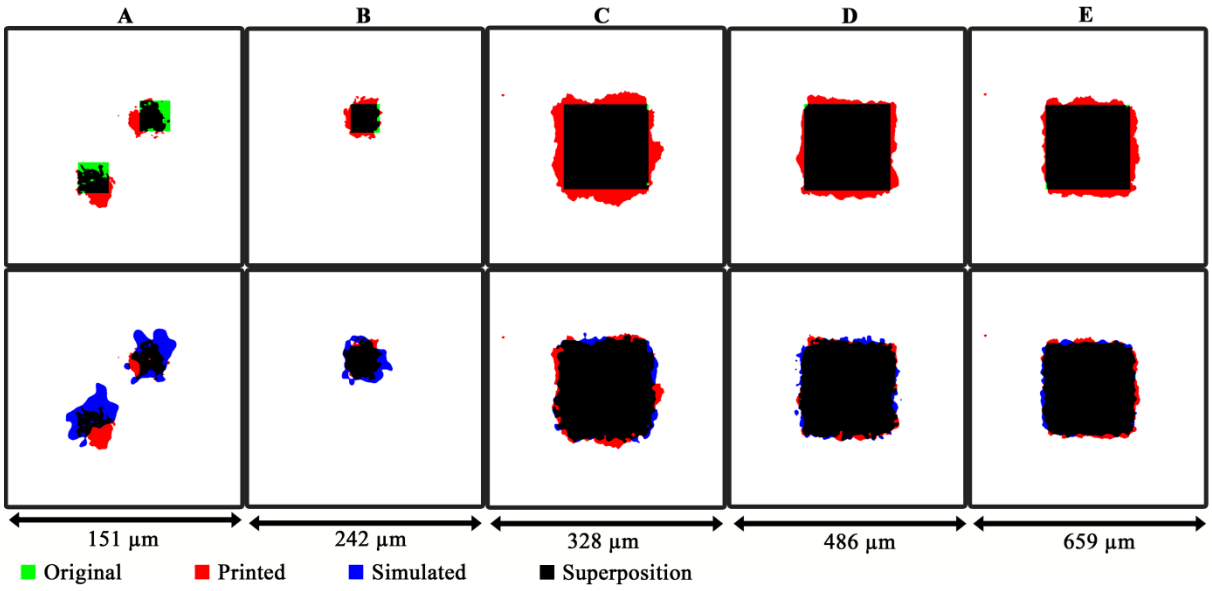

Figure A.9: Nominal, printed and simulated codes superposition printed with offset. Code configuration selected presenting the highest fidelity ratio: (A) code #444, binning 2, (B) code #384, binning 3, (C) code #001, binning 4, (D) code #001, binning 6 and (E) code #001, binning 8.

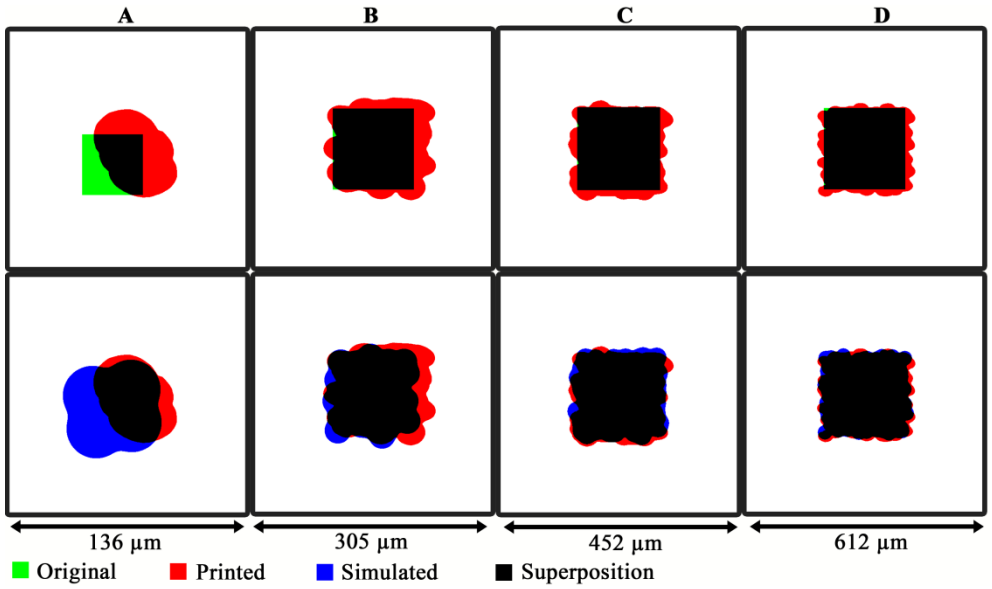

Figure A.10: Nominal, printed and simulated codes superposition printed with inkjet. Code configuration selected presenting the highest fidelity ratio: (A) code #458, binning 1, (B) code #001, binning 2, (C) code #001, binning 3 and (D) code #001, binning 4.

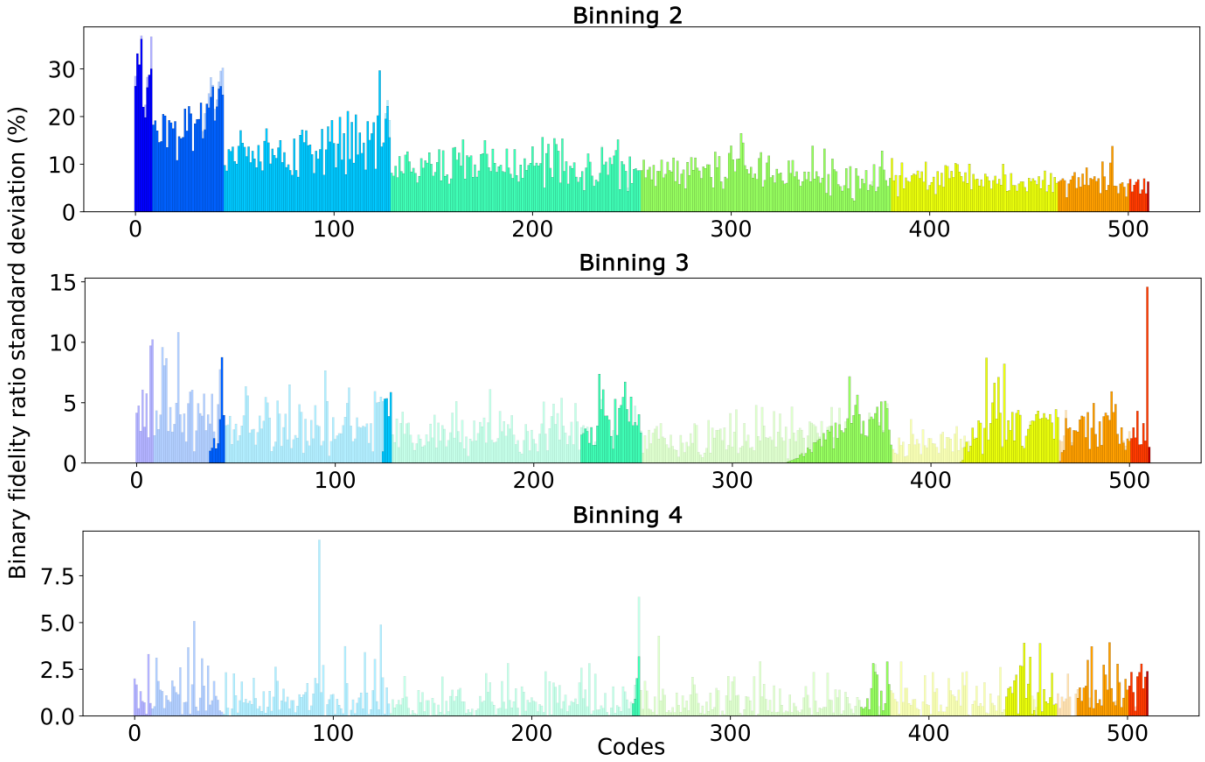

Figure A.11: Codes corresponding to the 512 combinations of the 3 by 3 matrix and split as a function of the number of dots printed and simulated (refer to Table 7.5) for different level of binnings. Codes printed with electrophotography.

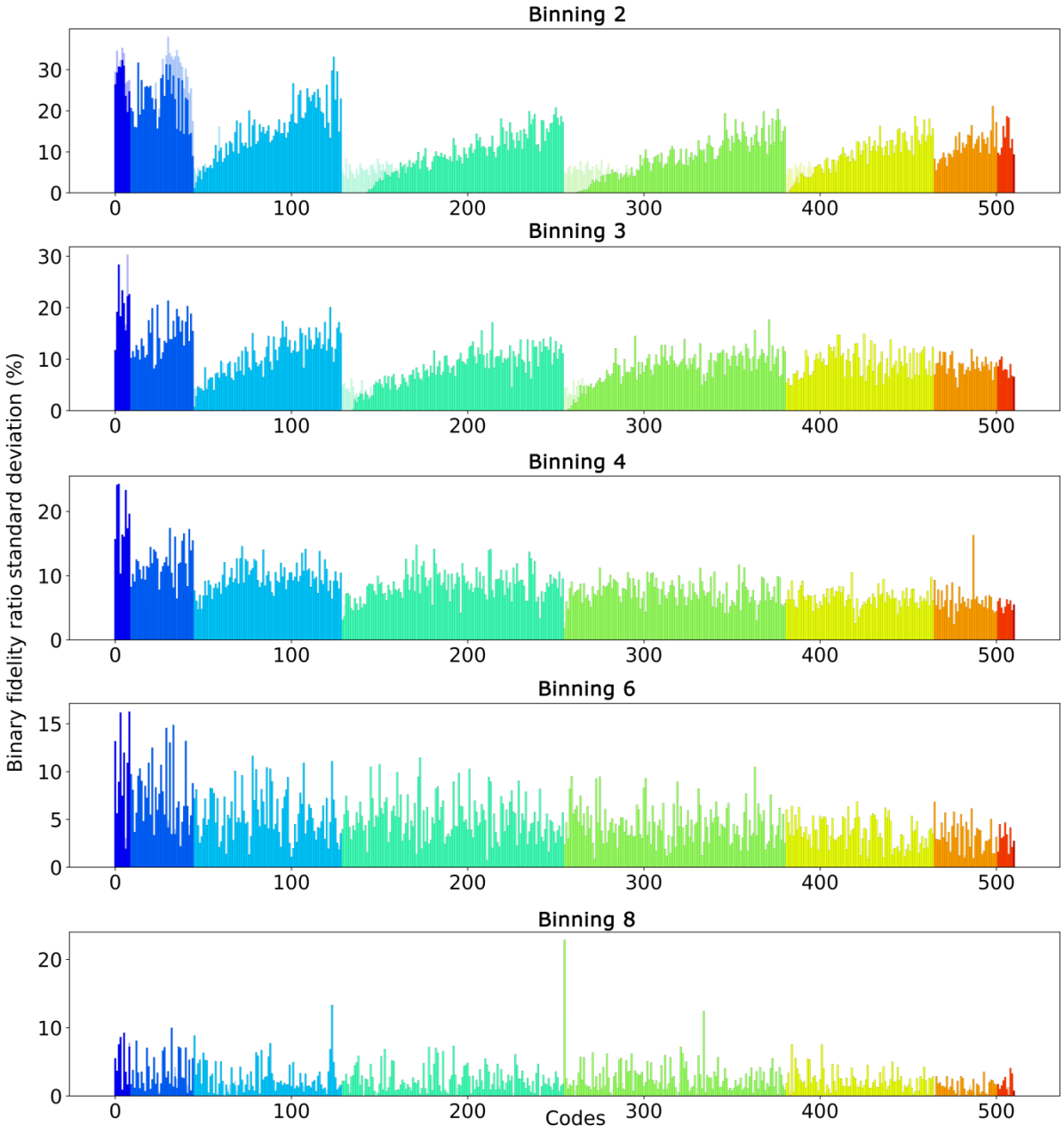

Figure A.12: Codes corresponding to the 512 combinations of the 3 by 3 matrix and split as a function of the number of dots printed and simulated (refer to Table 7.5) for different level of binnings. Codes printed with offset.

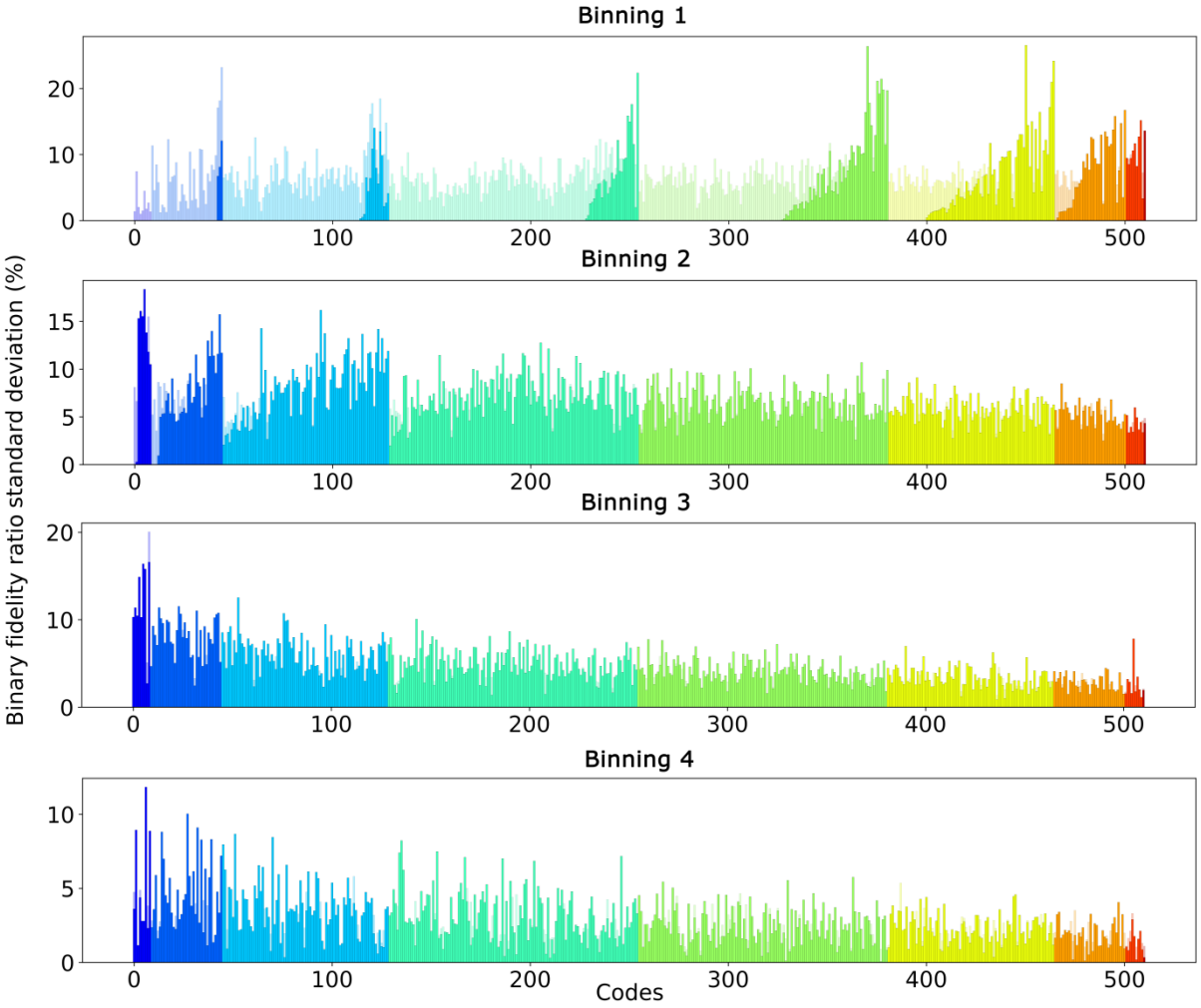

Figure A.13: Codes corresponding to the 512 combinations of the 3 by 3 matrix and split as a function of the number of dots printed and simulated (refer to Table 7.5) for different level of binnings. Codes printed with inkjet.

References

1. Lau, D. L. & Arce, G. R. Modern digital halftoning. (CRC Press, 2001).
2. Murray, A. Monochrome reproduction in photoengraving. J. Frankl. Inst. 221, 721–744 (1936).
3. Wyble, D. R., Berns, R. S. & others. A critical review of spectral models applied to binary color printing. Color Res. Appl. 25, 4–19 (2000).
4. Kriss, M. Handbook of Digital Imaging. (Wiley, 2015).
5. Arney, J. S., Engeldrum, P. G. & Zeng, H. An expanded Murray-Davies model of tone reproduction in halftone imaging. J. Imaging Sci. Technol. 39, 502–508 (1995).
6. Arney, J. S. & Katsube, M. A probability description of the Yule-Nielsen effect II: The impact of halftone geometry. J. Imaging Sci. Technol. 41, 637–642 (1997).
7. Arney, J. S. A probability description of the Yule-Nielsen effect. J. Imaging Sci. Technol. 41, 633–636 (1997).
8. Arney, J., Chauvin, J., Nauman, J. & Anderson, P. G. Kubelka-Munk theory and the MTF of paper. J. Imaging Sci. Technol. 47, 339–345 (2003).
9. Callahan, F. P. Light scattering in halftone prints. JOSA 42, 104–105 (1952).
10. Happel, K. Led-based light scattering measurements of papers for printing applications. (Doctoral dissertation, Darmstadt Technische Universität, 2011).
11. Lehmbeck, D. R. Light scattering model for predicting density relationships in reflection images. Proc. 28th Annu. Conf. SPSE Soc. Photogr. Sci. Eng. Wasington DC 155–156 (1975).
12. Modrić, D., Petric Maretić, K. & Hladnik, A. Determination of point-spread function of paper substrate based on light-scattering simulation. Appl. Opt. 53, 7854 (2014).
13. Ruckdeschel, F. R. & Hauser, O. G. Yule-Nielsen effect in printing: a physical analysis. Appl. Opt. 17, 3376–3383 (1978).
14. Ukishima, M. et al. Spectral Image Prediction of Color Halftone Prints Based on Neugebauer Modified Spectral Reflection Image Model. in Conference on Colour in Graphics, Imaging, and Vision 2010, 444–451 (2010).
15. Yang, L., Gooran, S. & Kruse, B. Simulation of optical dot gain in multichromatic tone production. J. Imaging Sci. Technol. 45, 198–204 (2001).
16. Yule, J. A. C. Effect of the spread-function of paper on halftone reproduction. TAPPI J 50, 337–344 (1967).
17. Ukishima, M. Prediction and evaluation of color halftone print quality based on microscopic measurement. (Doctoral dissertation, University of Eastern Finland, 2010).
18. Namedanian, M. Characterization of Halftone Prints based on Microscale Image Analysis. (Doctoral dissertation, Linköping University, 2013).
19. Nyström, D. High resolution analysis of halftone prints: a colorimetric and multispectral study. (Doctoral dissertation, Linköping University, 2008).
20. Rahaman, G. M. Image analysis approach for modeling color predictions in printing. (Licenciate dissertation, Mid Sweden University, 2014).
21. Lundström, J. & Verikas, A. Detecting halftone dots for offset print quality assessment using soft computing. in International Conference on Fuzzy Systems 1–7 (IEEE, 2010).
22. Yang, L., Lenz, R. & Kruse, B. Light scattering and ink penetration effects on tone reproduction. JOSA A 18, 360–366 (2001).

23. Trade in counterfeit and pirated goods: Mapping the economic impact. Trends Organ. Crime 20, 383–394 (2017).

24. Nguyen, T. Q., Delignon, Y., Chagas, L. & Septier, F. Printer identification from micro-metric scale printing. in Acoustics, Speech and Signal Processing. (2014).

25. Reverdy-Bruas, N., Chagas, L., Poletti, J.-P. & Passas, R. Image analysis as a tool to discriminate counterfeit from true 2D printed codes. J. Print Media Technol. Res. 4, 205–216 (2015).

26. Nguyen, Q.-T., Delignon, Y., Chagas, L. & Septier, F. Printer technology authentication from micrometric scan of a single printed dot. in Media Watermarking, Security, and Forensics. (2014).

27. Nguyen, Q. T. Modélisation probabiliste d'impression à l'échelle micrométrique. (Doctoral dissertation, Lille University, 2015).

28. Rahaman, G. M. A., Norberg, O. & Edström, P. Microscale halftone color image analysis: perspective of spectral color prediction modeling. in Color Imaging XIX: Displaying, Processing, Hardcopy, and Applications 9015, (International Society for Optics and Photonics, 2014).

29. Russ, J. C. The Image Processing Handbook, Seventh Edition. (CRC Press, 2016).

30. Fleming, P. D., Cawthorne, J. E., Mehta, F., Halwawala, S. & Joyce, M. K. Interpretation of dot area and dot shape of inkjet dots based on image analysis. in NIP & Digital Fabrication Conference, 474–477 (Society for Imaging Science and Technology, 2002).

31. Hersch, R. & Yang, L. Kubelka-Munk model for imperfectly diffuse light distribution in paper. J. Imaging Sci. Technol. 52, 30201–1 (2008).

32. Kristiansson, P. et al. Optical dot gain on newsprint determined with the Lund nuclear microprobe. Nucl. Instrum. Methods Phys. Res. Sect. B Beam Interact. Mater. At. 130, 303–307 (1997).

33. Viggiano, J. A. S. Physical Significance of Negative Yule-Nielsen n-value. Proc. IS&T International Congress of Imaging Sciences (2006).

34. Berns, R. S., Bose, A. & Tzeng, D.-Y. The spectral modeling of large-format ink-jet printers. Munsell Color Sci. Lab. Intern. Rep. (1996).

35. Engeldrum, P. G. The color between the dots. J. Imaging Sci. Technol. 38, 545–551 (1994).

36. Happel, K., Walter, M., Urban, P. & Dörsam, E. Measuring anisotropic light scatter within graphic arts papers for modeling optical dot gain. in Color and Imaging Conference, 347–352 (Society for Imaging Science and Technology, 2010).

37. Hsieh, Y.-C. Measuring Dot Gain from Film to Plate: Murray-Davies or Yule-Nielsen Equation? Vis. Commun. J. 24–30 (1998).

38. Nyström, D. Micro-scale properties of color prints. Proc Print. Future Days Chemnitz 154–158 (2005).

39. Land, A. D., Penno, K. L. & Brzezinski, J. L. Identification of Microorganisms Isolated From Counterfeit and Unapproved Decorative Contact Lenses. J. Forensic Sci. (2017).

40. Blackstone, E. A., Fuhr Jr, J. P. & Pociask, S. The health and economic effects of counterfeit drugs. Am. Health Drug Benefits 7, 216 (2014).

41. Veloutsou, C. & Bian, X. A cross-national examination of consumer perceived risk in the context of non-deceptive counterfeit brands. J. Consum. Behav. Int. Res. Rev. 7, 3–20 (2008).

42. Bian, X. & Veloutsou, C. Consumers' attitudes regarding non-deceptive counterfeit brands in the UK and China. J. Brand Manag. 14, 211–222 (2007).

43. Gamble, K. Counterfeit Fashion: A Comprehensive Study Determining The Influence Factors of Fashion Counterfeit Purchase Decisions. (Doctoral Dissertation, University of North Carolina, 2011).

44. Trade in Counterfeit and Pirated Goods. (OECD Publishing, 2016).

45. Anons. Raaque's: Counterfeit Ink for Epson Printer: How Counterfeiters are Getting Better. http://raaque.blogspot.com/2012/12/counterfeit-ink-for-epson-printer-how.html. (2012).

46. Lohweg, V. et al. Banknote authentication with mobile devices. in Media Watermarking, Security, and Forensics 8665, 866507 (International Society for Optics and Photonics, 2013).

47. Lohweg, V. et al. Mobile devices for banknote authentication–is it possible? in Optical Document Security-The Conference on Optical Security and Counterfeit Detection 3, 1–12 (2012).

48. Pfeifer, A. & Lohweg, V. Authentication of Commercial Raster Printing on Cost-Effective Hardware. in Kommunikation und Bildverarbeitung in der Automation 204–217 (Springer, 2018).

49. AL-Gawda, M., Beiji, Z. & Mohammed, N. Yemeni Mobile Counterfeit Detection System Using Support Vector Machines, Fuzzy Logic and Image Processing Techniques. J. Comput. Theor. Nanosci. 13, 2965–2977 (2016).

50. Gillich, E., Hoffmann, J. L., Dorksen, H., Lohweg, V. & Schaede, J. Data Collection Unit – A Platform for Printing Process Authentication. 12 (2016).

51. Prabhu, R., Ambadiyil, S., P.S., K. & Mahadevan, V. P. Banknote authentication using chaotic elements technology. in Counterterrorism, Crime Fighting, Forensics, and Surveillance Technologies. (2017).

52. Berenguel, A., Terrades, O. R., Lladós, J. & Cañero, C. e-Counterfeit: a mobile-server platform for document counterfeit detection. 14th IAPR International Conference on Document Analysis and Recognition. Vol. 9. (2017).

53. Baride, A. & Meruga, J. Upconverting Nanoparticles for Security Applications. Upconverting Nanomater. Perspect. Synth. Appl. 291 (2016).

54. Di Venuto, C., Kutter, M. & Jordan, F. Means for using microstructure of materials surface as a unique identifier. (Google Patents, 2012).

55. Bourrieres, F., Kaiser, C. & Bourrieres, F. Method for certifying and subsequently authenticating original, paper of digital documents for evidences. (Google Patents, 2011).

56. Mohan, A., Woo, G., Hiura, S., Smithwick, Q. & Raskar, R. Bokode: imperceptible visual tags for camera based interaction from a distance. in ACM Transactions on Graphics 28, 98 (ACM, 2009).

57. Massicot, J. P., Foucou, A. & Sagan, Z. Methods and devices for marking and authenticating a product by a consumer. (Google Patents, 2014).

58. Guigan, F. Security barcode. (Google Patents, 2015).

59. Porter, R. & Gotanda, T. High-value document authentication system and method. (Google Patents, 2017).

60. Rodriguez, T. F., Rhoads, G. B. & Sharma, R. K. Authenticating identification and security documents and other objects. (Google Patents, 2015).

61. Lanneau, A., Chagas, L. & Reverdy-Bruas, N. Characterization of the deterioration of a 2D code due to counterfeiting. (Graduate thesis, LGP2 Grenoble INP Pagora, 2012).

62. Pflimlin, M., Chagas, L. & Reverdy-Bruas, N. Characterization of printed 2D codes by image analysis. (Graduate thesis, LGP2 Grenoble INP Pagora, 2013).

63. Poletti, J.-P., Chagas, L. & Reverdy-Bruas, N. Characterization of the deterioration of printing according to the process: application to securing documents via 2D codes. (Graduate thesis, LGP2 Grenoble INP Pagora, 2013).

64. Tkachenko, I. Generation and analysis of graphical codes using textured patterns for printed document authentication. (Doctoral Dissertation, Montpellier University, 2015).

65. Papazian, E. Our rising ad dosage: It's not as oppressive as some think. Media Matters 21, 1–3 (2007).

66. Kang, H. R. Digital color halftoning. (SPIE press, 1999).

67. Waite, J. J. & Oliver, M. G. R. Viewing Distance as a Variable in Discerning Grayscale Halftone Dots at Varying Screen Frequencies. J. Ind. Technol. 22, 1–9 (2006).

68. Gooran, S. Digital halftoning. Dep. Sci. Technol. Linköping Univ. (Report, 2005).

69. Crounse, K. & Levantovsky, V. Automatic generation of supercell halftoning threshold arrays for high addressability devices. (Google Patents, 2006).

70. Bayer, B. E. An optimum method for two-level rendition of continuous tone pictures. in IEEE International Conference on Communications, 26. (1973).

71. Bryngdahl, O. Halftone images: spatial resolution and tone reproduction. JOSA 68, 416–422 (1978).

72. Eschbach, R. & Knox, K. T. Error-diffusion algorithm with edge enhancement. JOSA A 8, 1844–1850 (1991).

73. Ulichney, R. Digital halftoning. (MIT press, 1987).

74. Floyd, R. W. An adaptive algorithm for spatial gray-scale. in Proc. Soc. Inf. Disp. 17, 75–77 (1976).

75. Allebach, J. P. & others. Model-based color halftoning using direct binary search. Image Process. IEEE Trans. On 14, 1945–1959 (2005).

76. Pappas, T. N. Model-based halftoning of color images. Image Process. IEEE Trans. On 6, 1014–1024 (1997).

77. Ostromoukhov, V. Pseudo-random halftone screening for colour and black&white; printing. in 9th International Congress in Non Impact Printing Technologies 579–582 (1993).

78. Velho, L. & Gomes, J. Stochastic screening dithering with adaptive clustering. in Proceedings of the 22nd annual conference on Computer graphics and interactive techniques 273–276 (1995).

79. Scheermesser, T. & Bryngdahl, O. Control of texture in image halftoning. JOSA A 13, 1645–1652 (1996).

80. Wang, S.-G. Stoclustic (stochastic clustered) halftone screen design. in International conference on digital printing technologies 516–521 (IS&T Societe For Imaging Science and Technology, 1997).

81. Aoki, S. New halftoning method using adaptive cell. in NIP & Digital Fabrication Conference, 277–280 (Society for Imaging Science and Technology, 1998).

82. He, Z. AM/FM halftoning: digital halftoning through simultaneous modulation of dot size and dot density. J. Electron. Imaging 13, 286 (2004).

83. Wesner, J. W. Screen Patterns Used in Reproduction of Continuous-Tone Graphics. Appl. Opt. 13, 1703 (1974).

84. Kawaguchi, T., Tsumura, N., Haneishi, H., Miyake, Y. & Kouzaki, M. Vector error diffusion method for spectral color reproduction. in PICS 394–397 (1999).

85. Lee, J.-H. & Allebach, J. P. CMYK Halftoning Algorithm Based on Direct Binary Search. Color Imaging Conf., 199–204 (2001).

86. Gooran, S. Dependent color halftoning: Better quality with less ink. J. Imaging Sci. Technol. 48, 354–362 (2004).

87. Kipphan, H. Handbook of print media: technologies and production methods. (Springer Science & Business Media, 2001).

88. Pineaux, B. Le procédé d'impression offset: effets liés à la dureté de la solution de mouillage. (Doctoral Dissertation, Grenoble INPG, 1997).

89. Chagas, L. & Baudin, G. Characterization of Blankets by their Transfer Properties. Adv. Print. Sci. Technol. 23, 355–374 (1997).

90. Beach, M., Shepro, S. & Russon, K. Getting it printed: how to work with printers and graphic arts services to assure quality, stay on schedule, and control costs. (Coast to Coast Books, 1986).

91. MacPhee, J. Fundamentals of lithographic printing: Mechanics of printing. (GATFPress, 1998).

92. Schein, L. B. Electrophotography and Development Physics. (Springer Science & Business Media, 2013).

93. Kajondecha, P. & Hoshino, Y. Halftone Dot Size Variation in Offset, Electrophotographic, and Flexographic Printing and Its Perception. J. Imaging Sci. Technol. 52, 60503-1-60503–7 (2008).

94. Comizzoli, R. B., Lozier, G. S. & Ross, D. A. Electrophotography—a review. Proc. IEEE 60, 348–369 (1972).

95. Dong, H., Carr, W. W. & Morris, J. F. Visualization of drop-on-demand inkjet: Drop formation and deposition. Rev. Sci. Instrum. 77, 085101 (2006).

96. Beeson, R. & Skip, R. D. Thermal inkjet technology-review and outlook. Adv. Res. Lab. Inkjet Bus. Unit Hewlett-Packard Co. Corvallis Or. US (1998).

97. Yang, Y., Naarani, V. & Thillainayagam, V. Color Repeatability in Inkjet Printing. AATCC Rev. 7, (2007).

98. Raje, P. V. & Murmu, N. C. A Review on Electrohydrodynamic-inkjet Printing Technology. 4, 10 (2014).

99. Vassilev, S. V., Baxter, D., Andersen, L. K. & Vassileva, C. G. An overview of the chemical composition of biomass. Fuel 89, 913–933 (2010).

100. Hämäläinen, T. Modelling of fibre orientation and fibre flocculation phenomena in paper sheet forming. (Doctoral Dissertation, Tampere University of Technology, 2008).

101. Ghosh, A. Fundamentals of Paper Drying – Theory and Application from Industrial Perspective. in Evaporation, Condensation and Heat transfer. (2011).

102. ISO 12647-2:2013(fr), Technologie graphique — Maîtrise des procédés pour la fabrication des séparations de couleur en ton tramé, des épreuves et des tirages en production — Partie 2: Procédés lithographiques offset. Available at: https://www.iso.org/obp/ui/#iso:std:iso:12647:-2:ed-3:v1:fr. (2013).

103. Hubbe, M. A., Venditti, R. A. & Rojas, O. J. What happens to cellulosic fibers during papermaking and recycling? A review. BioResources 2.4: 739-788. (2007).

104. Lundell, F., Söderberg, L. D. & Alfredsson, P. H. Fluid mechanics of papermaking. Annu. Rev. Fluid Mech. 43, 195–217 (2011).

105. Shen, J. & Fatehi, P. A review on the use of lignocellulose-derived chemicals in wet-end application of papermaking. Curr. Org. Chem. 17, 1647–1654 (2013).

106. Biermann, C. J. Essentials of pulping and papermaking. (Academic press, 1993).

107. Vallette, P. & de Choudens, C. Le bois, la pâte, le papier. (Centre Technique de l'Industrie des Papiers, Cartons et Celluloses, 1987).

108. Wu, Q., Merchant, F. A. & Castleman, K. R. Microscope image processing. (Elsevier/Acad. Press, 2008).

109. Olympus Microscopy Resource Center | Digital Imaging in Optical Microscopy. Available at: http://olympus.magnet.fsu.edu/primer/digitalimaging/. (2012).

110. Davidson, M. W. & Abramowitz, M. Optical microscopy. Encycl. Imaging Sci. Technol. (2002).

111. Chinga-Carrasco, G. Complementary microscopy techniques for surface characterisation of uncoated and mineral pigment coated paper. Current Microscopy Contributions to Advances in Science and Technology: 1448-1455.(2012).

112. Posluszny, U., Scott, M. G. & Sattler, R. Revisions in the technique of epi-illumination light microscopy for the study of floral and vegetative apices. Can. J. Bot. 58, 2491–2495 (1980).

113. Vyörykkä, J. & others. Confocal Raman microscopy in chemical and physical characterization of coated and printed papers. (Doctoral Dissertation, Helsinki University of Technology, 2004).

114. Aguet, F. Super-resolution fluorescence microscopy based on physical models. (Doctoral Dissertation, Ecole polytechnique Lausanne, 2009).

115. Juškaitis, R. Measuring the real point spread function of high numerical aperture microscope objective lenses. in Handbook of biological confocal microscopy 239–250 (Springer, 2006).

116. Heintzmann, R. Band-limit and appropriate sampling in microscopy. Cell Biol. Lab. Handb. 3, 29–36 (2006).

117. Murphy, D. B. Fundamentals of light microscopy and electronic imaging. (Wiley-Liss, 2001).

118. Ehret, G., Bodermann, B. & Mirandé, W. Quantitative linewidth measurement down to 100 nm by means of optical dark-field microscopy and rigorous model-based evaluation. Meas. Sci. Technol. 18, 430–438 (2007).

119. McDonald, J. Optical microscopy. Microelectron. Fail. Anal. Desk Ref. 541–559 (2004).

120. Bueno-Ibarra, M. A., Acho, L. & others. Fast autofocus algorithm for automated microscopes. Opt. Eng. 44, 063601–063601 (2005).

121. Firestone, L., Cook, K., Culp, K., Talsania, N. & Preston, K. Comparison of autofocus methods for automated microscopy. Cytometry 12, 195–206 (1991).

122. Langehanenberg, P., Kemper, B. & von Bally, G. Autofocus algorithms for digital-holographic microscopy. in European Conference on Biomedical Optics 66330E–66330E (International Society for Optics and Photonics, 2007).

123. Leong-Hoi, A., Montgomery, P. C., Serio, B., Twardowski, P. & Uhring, W. High-dynamic-range microscope imaging based on exposure bracketing in full-field optical coherence tomography. Opt. Lett. 41, 1313–1316 (2016).

124. Debevec, P. E. & Malik, J. Recovering high dynamic range radiance maps from photographs. in 369–378, Proceedings of the 24th Annual Conference on Computer Graphics and Interactive Techniques. (1997).

125. Mertens, T., Kautz, J. & Van Reeth, F. Exposure Fusion: A Simple and Practical Alternative to High Dynamic Range Photography. Comput. Graph. Forum 28, 161–171 (2009).

126. Chow, S. K. et al. Automated microscopy system for mosaic acquisition and processing. J. Microsc. 222, 76–84 (2006).

127. Abrahamsson, S. et al. Fast multicolor 3D imaging using aberration-corrected multifocus microscopy. Nat. Methods 10, 60–63 (2013).

128. Schroettner, H., Schmied, M. & Scherer, S. Comparison of 3D Surface Reconstruction Data from Certified Depth Standards Obtained by SEM and an Infinite Focus Measurement Machine (IFM). Microchim. Acta 155, 279–284 (2006).

129. Berns, R. S., Cox, B. D. & Abed, F. M. Wavelength-dependent spatial correction and spectral calibration of a liquid crystal tunable filter imaging system. Appl. Opt. 54, 3687 (2015).

130. Gat, N. Imaging spectroscopy using tunable filters: a review. in AeroSense 50–64 (International Society for Optics and Photonics, 2000).

131. Hardeberg, J. Y., Schmitt, F. J. & Brettel, H. Multispectral image capture using a tunable filter. in Electronic Imaging 77–88 (International Society for Optics and Photonics, 1999).

132. Hensley, B. & Wyble, D. Spectral imaging using a liquid crystal tunable filter. Munsell Color Sci. Lab. Tech. Rep. (Report, 2012).

133. Lapray, P.-J., Wang, X., Thomas, J.-B. & Gouton, P. Multispectral Filter Arrays: Recent Advances and Practical Implementation. Sensors 14, 21626–21659 (2014).

134. Nyström, D. Reconstructing Spectral and Colorimetric Data Using Trichromatic and Multi-channel Imaging. in MCS 07-9th International Symposium on Multispectral Color Science and Application,7 45–52 (The Society for Imaging Science and Technology, 2007).

135. Shinoda, K. et al. Multispectral filter array and demosaicking for pathological images. in Asia-Pacific Signal and Information Processing Association Annual Summit and Conference 697–703 (IEEE, 2015).

136. Jahne, B. Practical handbook on image processing for scientific and technical applications. (CRC Press, 2004).

137. Fossum, E. R. & Hondongwa, D. B. A Review of the Pinned Photodiode for CCD and CMOS Image Sensors. IEEE J. Electron Devices Soc. 2, 33–43 (2014).

138. Magnan, P. Detection of visible photons in CCD and CMOS: A comparative view. Nucl. Instrum. Methods Phys. Res. Sect. Accel. Spectrometers Detect. Assoc. Equip. 504, 199–212 (2003).

139. Toyoda, A., Suzuki, Y., Orihara, K. & Hokari, Y. A novel tungsten light-shield structure for high-density CCD image sensors. IEEE Trans. Electron Devices 38, 965–968 (1991).

140. Ishihara, Y. et al. Interline CCD image sensor with an anti blooming structure. in Solid-State Circuits Conference. Digest of Technical Papers. 25, 168–169 (IEEE, 1982).

141. Nakamura, J. Image sensors and signal processing for digital still cameras. (CRC press, 2016).

142. Hamamatsu Learning Center: Digital Camera Readout and Frame Rates. Available at: http://hamamatsu.magnet.fsu.edu/articles/readoutandframerates.html. (2018).

143. El Gamal, A. & Eltoukhy, H. CMOS image sensors. IEEE Circuits Devices Mag. 21, 6–20 (2005).

144. Zhou, Z., Pain, B. & Fossum, E. R. CMOS active pixel sensor with on-chip successive approximation analog-to-digital converter. IEEE Trans. Electron Devices 44, 1759–1763 (1997).

145. El Gamal, A. Trends in CMOS image sensor technology and design. in Digest. International Electron Devices Meeting, 805–808 (IEEE, 2002).

146. Bigas, M., Cabruja, E., Forest, J. & Salvi, J. Review of CMOS image sensors. Microelectron. J. 37, 433–451 (2006).

147. Schanz, M., Nitta, C., Bussmann, A., Hosticka, B. J. & Wertheimer, R. K. A high-dynamic-range CMOS image sensor for automotive applications. IEEE J. Solid-State Circuits 35, 932–938 (2000).

148. Ossi, J. Light Microscopy Digital Imaging. in Current Protocols in Cytometry (John Wiley & Sons, Inc., 2008).

149. Joubert, J., Sabharwal, Y. & Sharma, D. "Digital camera technologies for scientific bio-imaging. Part 3: Noise and signal-to-noise ratios." Microscopy and Analysis (2011).

150. Sabharwal, Y., Joubert, J. & Sharma, D. "Digital camera technologies for scientific bio-imaging. Part 1: The sensors." Microscopy and Analysis (2011).

151. Sabharwal, Y., Joubert, J. & Sharma, D. "Digital camera technologies for scientific bio-imaging. Part 2: Sampling and signal." Microscopy and Analysis (2011).

152. Sabharwal, Y., Joubert, J. & Sharma, D. "Digital camera technologies for scientific bio-imaging. Part 4: Signal-to-noise ratio and image comparison of cameras." Microscopy and Analysis (2011).

153. Lukas, J., Fridrich, J. & Goljan, M. Digital camera identification from sensor pattern noise. IEEE Trans. Inf. Forensics Secur. 1, 205–214 (2006).

154. Kawai, N. & Kawahito, S. Noise analysis of high-gain, low-noise column readout circuits for CMOS image sensors. IEEE Trans. Electron Devices 51, 185–194 (2004).

155. Chen, S. & Ginosar, R. Adaptive sensitivity CCD image sensor. in Electrical and Electronics Engineers (IEEE, 1995).

156. Glasbey, C. A. & Horgan, G. W. Image analysis for the biological sciences. 1, (Wiley Chichester, 1995).

157. Arora, S., Acharya, J., Verma, A. & Panigrahi, P. K. Multilevel thresholding for image segmentation through a fast statistical recursive algorithm. Pattern Recognit. Lett. 29, 119–125 (2008).

158. Ayala, H. V. H., Santos, F. M. dos, Mariani, V. C. & Coelho, L. dos S. Image thresholding segmentation based on a novel beta differential evolution approach. Expert Syst. Appl. 42, 2136–2142 (2015).

159. Glasbey, C. A. An analysis of histogram-based thresholding algorithms. CVGIP Graph. Models Image Process. 55, 532–537 (1993).

160. Gonzales-Barron, U. & Butler, F. A comparison of seven thresholding techniques with the k-means clustering algorithm for measurement of bread-crumb features by digital image analysis. J. Food Eng. 74, 268–278 (2006).

161. Hammouche, K., Diaf, M. & Siarry, P. A multilevel automatic thresholding method based on a genetic algorithm for a fast image segmentation. Comput. Vis. Image Underst. 109, 163–175 (2008).

162. Huang, L.-K. & Wang, M.-J. J. Image thresholding by minimizing the measures of fuzziness. Pattern Recognit. 28, 41–51 (1995).

163. Kapur, J. N., Sahoo, P. K. & Wong, A. K. A new method for gray-level picture thresholding using the entropy of the histogram. Comput. Vis. Graph. Image Process. 29, 273–285 (1985).

164. Kittler, J. & Illingworth, J. Minimum error thresholding. Pattern Recognit. 19, 41–47 (1986).

165. Li, C. H. & Lee, C. K. Minimum cross entropy thresholding. Pattern Recognit. 26, 617–625 (1993).

166. Navon, E., Miller, O. & Averbuch, A. Color image segmentation based on adaptive local thresholds. Image Vis. Comput. 23, 69–85 (2005).

167. Obrist, A. F., Flisch, A. & Hofmann, J. Point cloud reconstruction with sub-pixel accuracy by slice-adaptive thresholding of X-ray computed tomography images. NDT E Int. 37, 373–380 (2004).

168. Otsu, N. A threshold selection method from gray-level histograms. IEEE Trans. Syst. Man Cybern. 9, 62–66 (1979).

169. Raju, P. D. R. & Neelima, G. Image Segmentation by using Histogram Thresholding. International Journal of Computer Science Engineering and Technology 2.1: 776-779. (2012).

170. Ridler, T. W. & Calvard, S. Picture thresholding using an iterative selection method. IEEE Trans Syst Man Cybern 8, 630–632 (1978).

171. Sezgin, M. Survey over image thresholding techniques and quantitative performance evaluation. J. Electron. Imaging 13, 146–168 (2004).

172. Shanbhag, A. G. Utilization of information measure as a means of image thresholding. CVGIP Graph. Models Image Process. 56, 414–419 (1994).

173. Tsai, W.-H. Moment-preserving thresholding-a new approach. Comput. Vis. Graph. Image Process. 29, 377–393 (1985).

174. Whatmough, R. J. Automatic threshold selection from a histogram using the "exponential hull". CVGIP Graph. Models Image Process. 53, 592–600 (1991).

175. Yen JC, Chang FJ, Chang S. A New Criterion for Automatic Multilevel Thresholding. 4, (1995).

176. Zhang, H., Fritts, J. E. & Goldman, S. A. Image segmentation evaluation: A survey of unsupervised methods. Comput. Vis. Image Underst. 110, 260–280 (2008).

177. Polak, M., Zhang, H. & Pi, M. An evaluation metric for image segmentation of multiple objects. Image Vis. Comput. 27, 1223–1227 (2009).

178. Philipp-Foliguet, S. & Guigues, L. Multi-scale criteria for the evaluation of image segmentation algorithms. J. Multimed. 3, 42–56 (2008).

179. Marpu, P. R., Neubert, M., Herold, H. & Niemeyer, I. Enhanced evaluation of image segmentation results. J. Spat. Sci. 55, 55–68 (2010).

180. Cárdenes, R., de Luis-García, R. & Bach-Cuadra, M. A multidimensional segmentation evaluation for medical image data. Comput. Methods Programs Biomed. 96, 108–124 (2009).

181. Mhamda, N., Nacereddine, N. & Hamami, L. Evaluation de la Segmentation d" Images Radiographiques des Joints Soudés. in Conférence Internationale sur le Soudage, le CND et l'Industrie des Matériaux et Alliages (2014).

182. McGuinness, K. & O'Connor, N. E. Toward automated evaluation of interactive segmentation. Comput. Vis. Image Underst. 115, 868–884 (2011).

183. Johnson, B. & Xie, Z. Unsupervised image segmentation evaluation and refinement using a multi-scale approach. ISPRS J. Photogramm. Remote Sens. 66, 473–483 (2011).

184. Chabrier, S., Emile, B., Rosenberger, C. & Laurent, H. Unsupervised Performance Evaluation of Image Segmentation. EURASIP J. Adv. Signal Process. 2006, 1–13 (2006).

185. Olson, E. Particle shape factors and their use in image analysis-Part 1: Theory. J. GXP Compliance 15, 85 (2011).

186. Olson, E. Particle shape factors and their use in image analysis part II: practical applications. J. GXP Compliance 15, 77 (2011).

187. Zhang, D. & Lu, G. Review of shape representation and description techniques. Pattern Recognit. 37, 1–19 (2004).

188. Rosin, P. L. Fitting superellipses. Pattern Anal. Mach. Intell. IEEE Trans. On 22, 726–732 (2000).

189. Hébert, M., Hersch, R. D. & Emmel, P. Fundamentals of optics and radiometry for color reproduction. Handb. Digit. Imaging (2015).

190. Takahashi, Y., Fujita, H. & Sakata, T. Ink transfer and dot gain mechanisms in offset printing process. Graph. Arts Jpn. 28, 22–32 (1986).

191. Yang, L. & Lundstrom, N. Physical dot gain of offset: Understanding and determination. Nord. Pulp Pap. Res. J. 22, 388–393 (2007).

192. Rousu, S. Differential absorption of offset ink constituents on coated paper. (Doctoral Dissertation, Åbo Akademi University, 2000).

193. Yang, L. & Kruse, B. Ink penetration and its effects on printing. in Proc. SPIE 3963, 365–375 (2000).

194. Yang, L., Fogden, A., Pauler, N., Sävborg, Ö. & Kruse, B. A novel method for studying ink penetration of a print. Nord. Pulp Pap. Res. J. 20, 423–429 (2005).

195. Aspler, J. S. Interactions of ink and water with the paper surface in printing. Nord. Pulp Pap. Res. J. 8, 68–74a (1993).

196. Aspler, J. S. & Lepoutre, P. The transfer and setting of ink on coated paper. Prog. Org. Coat. 19, 333–357 (1991).

197. Olsson, R., Yang, L., van Stam, J. & Lestelius, M. Effects on ink setting in flexographic printing: coating polarity and dot gain. Nord. Pulp Pap. Res. J. 21, 569–574 (2006).

198. Kettle, J., Lamminmäki, T. & Gane, P. A review of modified surfaces for high speed inkjet coating. Surf. Coat. Technol. 204, 2103–2109 (2010).

199. Arney, J., Ye, L. & Wible, J. Analysis of paper gloss. Pulp Pap. Tech. Assoc. Can. PAPTAC 32, (2006).

200. Franz, G., Pfeister, W., Arney, J. & Anderson, P. Color properties of specular reflections. J. Imaging Sci. Technol. 50, 228–232 (2006).

201. Rogers, G. A generalized Clapper–Yule model of halftone reflectance. Color Res. Appl. 25, 402–407 (2000).

202. Carlsson, J., Persson, W., Hellentin, P. & Malmqvist, L. The propagation of light in paper: Modelling and monte carlo simulations. in International Paper Physics Conference 83–86 (1995).

203. Modrić, D., Bolanča, S. & Beuc, R. Monte Carlo Modeling of Light Scattering in Paper. J. Imaging Sci. Technol. 53, 020201 (2009).

204. Coppel, L. Effect of fibre length and sheet thickness on light scattering in paper-comparing measurements to Monte Carlo simulations. (Thesis, Umeaa Swed., 2001).

205. de Mul, F. F. M. Monte-Carlo Simulations of Light Scattering in Turbid Media. in Handbook of Coherent-Domain Optical Methods, 593–661 (Springer, 2013).

206. Servant, L., Tinet, E., Avrillier, S. & Carmona, F. Similarity relations in multiple scattering through turbid media: a Monte Carlo evaluation. in Optical Engineering and Photonics in Aerospace Sensing 154–163 (International Society for Optics and Photonics, 1993).

207. Yun, T. et al. Monte Carlo simulation of polarized photon scattering in anisotropic media. Opt. Express 17, 16590–16602 (2009).

208. Gustavson, S. Dot gain in colour halftones. (Doctoral Dissertation, Linköping University, 1997).

209. Yang, L. Ink-paper interaction: a study in ink-jet color reproduction. (Doctoral Dissertation, Linköping University, 2003).

210. ISO 5-3:2009(en), Photography and graphic technology — Density measurements — Part 3: Spectral conditions. Available at: https://www.iso.org/obp/ui/#iso:std:iso:5:-3:ed-3:v1:en. (2009)

211. Nyström, D., Kruse, B. & Yang, L. A Micro-scale study of optical dot gain in color halftone. in The 34: th International Research Conference of iarigai, Grenoble, 171–179, (Acta Graphic Publishers, 2007).

212. Sharma, G. Color fundamentals for digital imaging. Digit. Color Imaging Handb. 20, (2003).

213. Yang, L. Physical Evaluation of the Quality of Color Halftone. Handb. Digit. Imaging (2015).

214. Tegenfeldt, C. A Comparison of Color Computation in RGB versus in spectral Space. (Report, Linköping University, 1991).

215. Mercier, C. Caractérisation de propriétés d'usage des papiers par l'analyse topographique de leurs états de surface. (Doctoral Dissertation, Grenoble, INPG, 2004).

216. Jiang, X. J. & Whitehouse, D. J. Technological shifts in surface metrology. CIRP Ann. 61, 815–836 (2012).

217. Chinga-Carrasco, G. Exploring the multi-scale structure of printing paper–a review of modern technology. J. Microsc. 234, 211–242 (2009).

218. Arney, J. S., Arney, C. D. & Engeldrum, P. G. Modeling the Yule–Nielsen halftone effect. J. Imaging Sci. Technol. 40, 233–238 (1996).

219. Langlais, E., Adudodla, S. & Mehta, P. Using machine vision based system for benchmarking various printing plate surfaces. in NIP & Digital Fabrication Conference, 595–597 (Society for Imaging Science and Technology, 2003).

220. Nyström, D. An Expanded Neugebauer formula, using varying microreflectance of the Neugebauer primaries. in Conference on Colour in Graphics, Imaging, and Vision, 157–162 (Society for Imaging Science and Technology, 2012).

221. Nyström, D. Micro-reflectance Measurements of Multiple Colorants in Halftone Prints. in TAGA 2011-The 36: rd Annual Technical Conference, Pittsburgh, March 6-9, 157–176 (Technical Association of the Graphic Arts, 2011).

222. Nyström, D. Microscopic color measurements of halftone prints. in NIP & Digital Fabrication Conference, 459–462 (Society for Imaging Science and Technology, 2010).

223. Nyström, D. A Close-Up Investigation of Halftone Color Prints. (Technical Association of the Graphic Arts, 2008).

224. Nyström, D. A Micro-Scale View on Color Reproduction. in Conference on Colour in Graphics, Imaging, and Vision, 542–547 (Society for Imaging Science and Technology, 2008).

225. Namedanian, M. et al. Analysis of optical and physical dot gain by microscale image histogram and modulation transfer functions. J. Imaging Sci. Technol. 57, 20504-1-20504–5 (2013).

226. Namedanian, M. & Gooran, S. Characterization of Total Dot Gain by Microscopic Image Analysis. J. Imaging Sci. Technol. 55, 40501-1-40501–7 (2011).

227. Nunes, J-C, Deléchelle E. "Empirical mode decomposition: Applications on signal and image processing." Advances in Adaptive Data Analysis 1.01: 125-175.(2009).

228. Latorre, P., Peris-Fajarnés, G. & Figueiredo, M. A. Image segmentation for the application of the neugebauer colour prediction model on inkjet printed ceramic tiles. in Image Analysis and Recognition 9–16 (Springer, 2005).

229. Tse, M.-K. & Klein, A. H. Automated Print Quality Analysis in Inkjet Printing: Case Study Using Commercially Available Media. NIP & Digital Fabrication Conference. (Society for Imaging Science and Technology, 1998).

230. Saleh, A. G. The analysis of the dot gain problems and its effect on colour reproduction. in TAGA Proceedings (1982).

231. Wedin, M. Modelling of dot gain in halftone colour prints. (Doctoral Dissertation, Linköping University, 1995).

232. Streckel, B., Steuernagel, B., Falkenhagen, E. & Jung, E. Objective print quality measurements using a scanner and a digital camera. in International Conference on Digital Production Printing and Industrial Applications 5, 145–147 (2003).

233. Farnood, R. R., Yan, N., Kortschot, M. T. & Dodson, C. T. J. Modelling flocculation: A gallery of simulated flocculated papers. Nord. Pulp Pap. Res. J. Swed. (1997).

234. Suzuki, T., Taguchi, S. & Uchida, T. The New Method of Evaluating Dot Area. J. Print. Sci. Technol. 25, 98–104 (1988).

235. Gustavson, S. Modelling of light scattering effects in print. (Doctoral Dissertation, Linköping University, 1995).

236. Koopipat, C., Tsumura, N., Miyake, Y. & Fujino, M. Effect of ink spread and opitcal dot gain on the MTF of ink jet image. J. Imaging Sci. Technol. 46, 321–325 (2002).

237. Yamashita, J., Sekine, H., Nakaguchi, T., Tsumura, N. & Miyake, Y. Spectral Based Analysis and Modeling of Dot Gain in Ink-jet Printing. NIP Digit. Fabr. Conf., 769–772 (2003).

238. Ukishima, M. et al. A Method to Separately Model Mechanical and Optical Dot Gain Effects in Color Halftone Prints. in TAGA conference proceeding 16–18 (2010).

239. Wedin, M. & Kruse, B. Modeling of screened color prints through singular value decomposition. in International Symposium on Electronic Imaging: Science and Technology 318–326 (International Society for Optics and Photonics, 1994).

240. Kruse, B. & Wedin, M. A reflection model for translucent media. in Proceedings of the scandinavian conference on image analysis 1, 381–388 (1995).

241. Wedin, M. & Kruse, B. Halftone colour prints: dot gain and modelling of colour distributions. Color Hard Copy Graph. Arts IV 344–355 (1995).

242. Rogers, G. L. Measurement of the modulation transfer function of paper. Appl. Opt. 37, 7235–7240 (1998).

243. Yule, J. A. C. Theory of the halftone process. III. Dot size and halftone density. J. Frankl. Inst. 236, 473–487 (1943).

244. Yule, J. & Nielsen, W. The penetration of light into paper and its effect on halftone reproduction. in 3, 65–76 (1951).

245. Clapper, F. R. & Yule, J. A. C. The effect of multiple internal reflections on the densities of half-tone prints on paper. JOSA 43, 600–603 (1953).

246. Arney, J. S., Pray, E. & Ito, K. Kubelka–Munk theory and the Yule–Nielsen effect on halftones. J. Imaging Sci. Technol. 43, 365–370 (1999).

247. Ukishima, M. et al. A simple method to measure mtf of paper and its application for dot gain analysis. IEICE Trans. Fundam. Electron. Commun. Comput. Sci. 92, 3328–3335 (2009).

248. Happel, K., Dörsam, E. & Urban, P. Measuring isotropic subsurface light transport. Opt. Express 22, 9048 (2014).

249. Happel, K., Urban, P., Dörsam, E. & Ludewig, X. Classifying Papers According to their Light Scatter Properties. in Midterm Meeting of the International Colour Association, 138–141 (2011).

250. Ukishima, M. et al. Dependence analysis of the paper MTF on the geometric condition. Pan-Pac. Imaging Conf. PPIC 298–301 (2008).

251. Miyake, Y., Inoue, S., Inui, M. & Kubo, S. An evaluation of image quality for quantized continuous tone image. J. Imaging Technol. 12, 25–34 (1986).

252. Inoue, S., Tsumura, N. & Miyake, Y. Measuring MTF of paper by sinusoidal test pattern projection. J. Imaging Sci. Technol. 41, 657–661 (1997).

253. Koopipat, C., Tsumura, N., Fujino, M., Miyata, K. & Miyake, Y. Image evaluation and analysis of ink jet printing system (I): MTF measurement and analysis of ink jet images. J. Imaging Sci. Technol. 45, 591–597 (2001).

254. Brunner, F. Method and apparatus for setting up for a given print specification defined by a binary value representing solid color density and dot gain in an autotype printing run. (Google Patents, 1991).

255. Stapleton, R. E. The sharpness of reflected images. J. Photogr. Sci. 12, 289–295 (1964).

256. Preucil, F., Elyjiw, Z., & Reed, R. F. The GATF Dot Gain Scale. GATF Research Progress Report, (6), 9. (Report, 1965).

257. Van Hunsel, J. & Van Cauwenberge, J. Visual control strip for imageable media. (Google Patents, 2000).

258. Brydges, D., Deppner, F., Kunzil, H., Heuberger, K. & Hersch, R. D. Application of a 3-CCD color camera for colorimetric and densitometric measurements. in SPIE Proceedings 3300, Color Imaging: Device Independent Color, Color Hardcopy and Graphics Arts III 292–301 (1998).

259. Allen, R. D. Method and apparatus for display of banding. (Google Patents, 2004).

260. Frisch, J. N. System and method for print screen tonal control and compensation. (Google Patents, 2005).

261. Inoue, S., Tsumura, N. & Miyake, Y. A new model to estimate optical dot gain in printings and its applications. in IS&T conference 353–355, The Society For Imaging Science and Technology, (1996).

262. Barak, I. Method and apparatus for creating a control strip. (Google Patents, 1997).

263. Warner, R. D. Device for indicating a quantitative change in dot area of an image in a printing process and the method of making the same. (Google Patents, 1985).

264. Ukishima, M. et al. A method to analyze preferred MTF for printing medium including paper. in Scandinavian Conference on Image Analysis 607–616 (Springer, 2009).

265. Inoue, S., Yamazaki, S., Tsumura, N. & Miyake, Y. An evaluation of image quality for hardcopy based on the MTF of paper. J. Imaging Sci. Technol. 44, 188–195 (2000).

266. Koopipat, C. Application of Ink Jet Printer Model to Evaluate the Sharpness of Printed Images. NIP Digit. Fabr. Conf. 2003, 773–776 (2003).

267. Mannos, J. & Sakrison, D. The effects of a visual fidelity criterion of the encoding of images. IEEE Trans. Inf. Theory 20, 525–536 (1974).

268. Madsen, M. H. & Hansen, P.-E. Imaging scatterometry for flexible measurements of patterned areas. Opt. Express 24, 1109–1117 (2016).

269. Song, Q., Wu, Y., Li, J. & Gui, J. Surface contour measurement by LC-SLM digital phase-shifting holography, In Holography and Diffractive Optics III (Vol. 6832, p. 68320B). (International Society for Optics and Photonics, 2007).

270. Roth, E. A. et al. Inkjet printing for high-throughput cell patterning. Biomaterials 25, 3707–3715 (2004).

271. Chinga, G., Gregersen, O., Dougherty, B. & Anal, M. Paper surface characterisation by laser profilometry and image analysis. Microsc. Anal. 96, 21–24 (2003).

272. Dou, R., Wang, T., Guo, Y. & Derby, B. Ink-Jet Printing of Zirconia: Coffee Staining and Line Stability. J. Am. Ceram. Soc. 94, 3787–3792 (2011).

273. Vespini, V. et al. Forward electrohydrodynamic inkjet printing of optical microlenses on microfluidic devices. Lab. Chip 16, 326–333 (2016).

274. Optical surface profiling: Profilometer advances benefit surface analysis, film-thickness measurement. Available at: https://www.laserfocusworld.com/articles/print/volume-46/issue-1/features/optical-surface-profiling.html. (2018).

275. Tekin, E., de Gans, B.-J. & Schubert, U. S. Ink-jet printing of polymers ? from single dots to thin film libraries. J. Mater. Chem. 14, 2627 (2004).

276.Li, Y. & He, B. Characterization of ink pigment penetration and distribution related to surface topography of paper using confocal laser scanning microscopy. BioResources 6.3: 2690-2702. (2011).

277. Udriștioiu, E. G., Bunaciu, A. A., Aboul-Enein, H. Y. & Tănase, I. Gh. Forensic Analysis of Color Toners by Raman Spectroscopy. Instrum. Sci. Technol. 37, 23–29 (2009).

278. Vikman, K. & Sipi, K. Applicability of FTIR and Raman Spectroscopic Methods to the Study of Paper–ink Interactions in Digital Prints. Journal of imaging science and technology, 47(2), 139-148. (2003).

279. Lozo, B., Vyörykkä, J., Vuorinen, T. & Muck, T. Nondestructive microscopic and spectroscopic methods for depth profiling of ink jet prints. J. Imaging Sci. Technol. 50, 333–340 (2006).

280. Stubbe, A., Kark, A. & Kalbitz, W. Investigation of the Applicational Properties of Carbon Blacks used in Pigmented Ink Jet Inks. In NIP & Digital Fabrication Conference (Vol. 1998, No. 1, pp. 103-106). Society for Imaging Science and Technology. (1999).

281. Chinga, G. Structural studies of LWC paper coating layers using SEM and image analysis techniques. (Doctoral Dissertation, Norwegian University of Science and Technology, 2002).

282. Heard, P. J., Preston, J. S., Parsons, D. J., Cox, J. & Allen, G. C. Visualisation of the distribution of ink components in printed coated paper using focused ion beam techniques. Colloids Surf. Physicochem. Eng. Asp. 244, 67–71 (2004).

283. Koivula, H., Preston, J. S., Heard, P. J. & Toivakka, M. Visualisation of the distribution of offset ink components printed onto coated paper. Colloids Surf. Physicochem. Eng. Asp. 317, 557–567 (2008).

284. Kristiansson, P., Malmqvist, L., Sjöland, K. A. & Sunnerberg, G. The Lund nuclear microprobe in newsprint research. Nucl. Instrum. Methods Phys. Res. Sect. B Beam Interact. Mater. At. 104, 584–589 (1995).

285. Krasnoshlyk, V. et al. Three-dimensional visualization and quantification of the fracture mechanisms in sparse fibre networks using multiscale X-ray microtomography. Proc R Soc A 474, (2018).

286. Kent, H. J., Climpson, N. A., Coggon, L., Hooper, J. J. & Gane, P. A. C. Novel techniques for quantitative characterization of coating structure. Tappi J. 69, 78–83 (1986).

287. Wagberg, P. & Johansson, P.-A. Surface profilometry: a comparison between optical and mechanical sensing on printing papers. Tappi J. USA (1993).

288. Soltman, D. & Subramanian, V. Inkjet-Printed Line Morphologies and Temperature Control of the Coffee Ring Effect. Langmuir 24, 2224–2231 (2008).

289. Secor, E. B. et al. Gravure printing of graphene for large-area flexible electronics. Adv. Mater. 26, 4533–4538 (2014).

290. Park, J.-U. et al. High-resolution electrohydrodynamic jet printing. Nat. Mater. 6, 782 (2007).

291. Hébert, M. & Hersch, R. D. Review of spectral reflectance models for halftone prints: Principles, Calibration, and prediction accuracy. Color Res. Appl. 40, 383–397 (2015).

292. Hersch, R. D. & Hébert, M. Base Models for Color Halftone Reproduction. in Handbook of Digital Imaging, 1–54, (John Wiley & Sons, Ltd, 2015).

293. Hersch, R. D. & Hébert, M. Interaction between Light, Paper and and Color Halftones: Challenges and Modelization Approaches. in Conference on Colour in Graphics, Imaging, and Vision, 1–7 (Society for Imaging Science and Technology, 2006).

294. Huntsman, J. R. A Simple Alternative to the Neugebauer Equations for Computing Dot Area and Dot Gain Colorimetrically. J. Print. Sci. Technol. 28, 345–357 (1991).

295. Buchdahl, R. Polglase, M.F. and Schwalbe, H.C. Pap. Trade J. 122, 41 (1946).

296. Viggiano, J. S. The color of halftone tints. in Proc. TAGA 37, 647–661 (1985).

297. Arney, J. S. & Yamaguchi, S. The physics behind the Yule-Nielsen equation. in PICS 381–385 (1999).

298. Bala, R. Device Characterization-Digital Color Imaging Handbook, Chapter 5. (CRC Press, 2003).

299. Chang, S. A Dot-gain Analysis of Inkjet Printing. DPP Eye Future 364–368 (2001).

300. Coppel, L. G. Dot gain analysis from probabilistic spectral modelling of colour halftone. Adv. Print. Media Technol. 41, 13–18 (2014).

301. Coppel, L. G., Slavuj, R. & Hardeberg, J. Y. Modeling coverage-dependent ink thickness in ink-jet printing. Appl. Opt. 55, 1138 (2016).

302. Hébert, M. Yule-Nielsen effect in halftone prints: graphical analysis method and improvement of the Yule-Nielsen transform, in Color Imaging XIX: Displaying, Processing, Hardcopy, and Applications (Vol. 9015, p. 90150R). (International Society for Optics and Photonics, 2014).

303. Hébert, M., Nebouy, D. & Mazauric, S. Color and Spectral Mixings in Printed Surfaces. in Computational Color Imaging 9016, 3–15 (Springer International Publishing, 2015).

304. Reem, R. & Hurysz, B. A Method to Separate Ink/Paper Interaction Effects from Halftone Effects in the Study of Inkjet Prints. in NIP & Digital Fabrication Conference, 358–362 (Society for Imaging Science and Technology, 2000).

305. Urban, P. & Grigat, R.-R. Spectral-based color separation using linear regression iteration. Color Res. Appl. 31, 229–238 (2006).

306. Zeng, H. Modeling dot area coverage of halftone printing. SPIE Proceeding Color Imaging Device-Indep. Color Color Hardcopy Graph. Arts V January (2000).

307. Abitan, H., Bohr, H. & Buchhave, P. Correction to the Beer-Lambert-Bouguer law for optical absorption. Appl. Opt. 47, 5354–5357 (2008).

308. Lewandowski, A., Ludl, M., Byrne, G. & Dorffner, G. Applying the Yule-Nielsen equation with negative n. JOSA A 23, 1827–1834 (2006).

309. Viggiano, J. A. Ink Penetration, Isomorphic ColorantMixing, and Negative Values of Yule-Nielsen n. in Color and Imaging Conference, 285–290 (Society for Imaging Science and Technology, 2010).

310. Pearson, M. L. N-value of General Conditions. (Report, Graphic Arts Research Center, Rochester Institute of Technology, 1980).

311. Viggiano, J. S. Modeling the color of multi-colored halftones. in Proc. TAGA 42, 44–62 (1990).

312. Arney, J. S., Arney, C. D., Katsube, M. & Engeldrum, P. G. An MTF analysis of papers. J. Imaging Sci. Technol. 40, 19–25 (1996).

313. Engeldrum, P. G. & Pridham, B. Application of turbid medium theory to paper spread function measurements. in TAGA 339–339 (1995).

314. Oittinen, P. Limits of microscopic print quality. Adv. Print. Sci. Technol. 16, 121–128 (1982).

315. Maltz, M. Light scattering in xerographic images. J. Appl. Photogr. Eng. 9, 83–89 (1983).

316. Kofender, J. L. The optical spread functions and noise characteristics of selected paper substrates measured in typical reflection optical system configurations. (Graduate Thesis, 1987).

317. Iino, K. & Berns, R. S. Building color-management modules using linear optimization I. Desktop color system. J. Imaging Sci. Technol. 42, 79–94 (1998).

318. Wakeshima, H., Kunishi, T. & Kaneko, S. Light scattering in paper and its effect on halftone reproduction. JOSA 58, 272–273 (1968).

319. Nyström, D. & Yang, L. Physical and optical dot gain: separation and relation to print resolution. in The 36: th International research conference of iarigai, 337–344 (2009).

320. Huntsman, J. R. A new model of dot gain and its application to a multilayer color proof. J. Print. Sci. Technol. 24, 189–202 (1987).

321. Rogers, G. L. Optical dot gain in a halftone print. J. Imaging Sci. Technol. 41, 643–656 (1997).

322. Williams, F. C. & Clapper, F. R. Multiple internal reflections in photographic color prints. JOSA 43, 595–599 (1953).

323. Kruse, B. & Wedin, M. A new approach to dot gain modelling. in TAGA 329–329 (1995).

324. Kubelka, V. P. Ein Beintrag zur Optik der Farbanstriche. Zeits Techn Phys. 12, 593–601 (1931).

325. Berg, F. Isotrope Lichtstreuung in Papier-Neue: Uerlegungen zur Kubelka-Munk-Theorie. (Doctoral Dissertation, 1997).

326. Mourad, S. Color Predicting Model for Electrophotographic Prints on Common Office Paper (Graduate thesis, Swiss Federal Institute of Technology, 2003)

327. Gustavson Coppel, L. & Edström, P. Open source Monte Carlo simulation platform for particle level simulation of light scattering from generated paper structures In Papermaking Research Symposium. (2009).

328. Edström, P. & Gustavson Coppel, L. A Monte Carlo Simulation Tool for Simulating Light Scattering in Paper and Print. Open PaperOpt (2010).

329. Green, K., Lamberg, L. & Lumme, K. Stochastic modeling of paper structure and Monte Carlo simulation of light scattering. Appl. Opt. 39, 4669–4683 (2000).

330. Dahlgren, R. Monte carlo simulation of light scattering in paper. (Doctoral Dissertation, Linköping University, 2005).

331. Mitsurou, S., Shiraiwa, Y., Mizuno, T. & Usami, A. Light Propagation inside Paper and Color Analysis by the Monte Carlo Method. Jpn. TAPPI J. 48, 1177–1185 (1994).

332. Linder, T., Löfqvist, T., Coppel, L. G., Neuman, M. & Edström, P. Lateral light scattering in fibrous media. Opt. Express 21, 7835–7840 (2013).

333. Linder, T. & Löfqvist, T. Anisotropic light propagation in paper. Nord. Pulp Pap. Res. J. 27, 500 (2012).

334. Coppel, L. G., Neuman, M. & Edström, P. Lateral light scattering in paper-MTF simulation and measurement. Opt. Express 19, 25181–25187 (2011).

335. Bohren, C. F. & Huffman, D. R. Absorption and scattering of light by small particles. (John Wiley & Sons, 2008).

336. Gustavson, S., Wedin, M. & Kruse, B. 3D modelling of light diffusion in paper. in TAGA 848–855 (1995).

337. Neuman, M., Coppel, L. G. & Edström, P. Point spreading in turbid media with anisotropic single scattering. Opt. Express 19, 1915–1920 (2011).

338. Gustavson, S. & Kruse, B. Modelling optical dot gain by a 3-D model of light diffusion in paper. in 3. European Research Symposium on Image Analysis for Pulp and Paper Research and Production, (1996).

339. Modrić, D., Petric Maretić, K. & Milković, M. Modeling light dispersion in the printing substrate within the Monte Carlo method. Teh. Vjesn. 19, 77–81 (2012).

340. Petric Maretić, K., Milković, M. & Modrić, D. Akaike information criterion in the edge analysis of the screen element. Teh. Vjesn. 20, 441–447 (2013).

341. Hübler, A. C. The optical behaviour of screened images on paper with horizontal light diffusion. in International conference on digital printing technologies 506–509 (IS&T Society for Imaging Science anf Technology, 1997).

342. Yang, L. A Unified Model of Optical and Physical Dot Gain in Print Color Reproduction. J. Imaging Sci. Technol. 48, 347–353 (2004).

343. Gielis, J. A generic geometric transformation that unifies a wide range of natural and abstract shapes. Am. J. Bot. 90, 333–338 (2003).

344. Abbe, E. Beiträge zur Theorie des Mikroskops und der mikroskopischen Wahrnehmung. Arch. Für Mikrosk. Anat. 9, 413–418 (1873).

345. Vos, J. J. Colorimetric and photometric properties of a 2° fundamental observer. Color Res. Appl. 3, 125–128 (1978).

346. Starikov, S. N. & Konnik, M. V. Using commercial photo camera's RAW-based images in optical-digital correlator for pattern recognition. Proc SPIE Opt. Pattern Recognit. XIX 6977, 69770R (2008).

347. Hashimoto, M. & Kishimoto, J. Two-shot type 6-band still image capturing system using commercial digital camera and custom color filter. in Conference on Colour in Graphics, Imaging, and Vision, 538–541 (Society for Imaging Science and Technology, 2008).

348. Akkaynak, D. et al. Use of commercial off-the-shelf digital cameras for scientific data acquisition and scene-specific color calibration. J. Opt. Soc. Am. A 31, 312 (2014).

349. Debayering an 1100D sensor (Removing Colour Filter Array). Stargazers Lounge Available at: https://stargazerslounge.com/topic/194781-debayering-an-1100d-sensor-removing-colour-filter-array/. (2019)

350. Nayar, S. K. & Nakagawa, Y. Shape from focus: an effective approach for rough surfaces. in , IEEE International Conference on Robotics and Automation Proceedings 218–225 vol.2 (1990).

351. Robertson, M. A., Borman, S. & Stevenson, R. L. Estimation-theoretic approach to dynamic range enhancement using multiple exposures. J. Electron. Imaging 12, 219–229 (2003).

352. Mitchell, T. J., Saunter, C. D., O'Nions, W., Girkin, J. M. & Love, G. D. Quantitative high dynamic range beam profiling for fluorescence microscopy. Rev. Sci. Instrum. 85, 103713 (2014).

353. Belloir, J.-M. et al. Dark Current Blooming in Pinned Photodiode CMOS Image Sensors. IEEE Trans. Electron Devices 64, 1161–1166 (2017).

354. Eisenhauer, J. G. Regression through the origin. Teach. Stat. 25, 76–80 (2003).

355. Arney, J. & Stewart, D. Surface-topography of paper from image-analysis of reflectance images. Soc. Imaging Sci. Technol. 37, 504–509 (1993).

356. Abràmoff, M. D., Magalhães, P. J. & Ram, S. J. Image processing with ImageJ. Biophotonics Int. 11, 36–42 (2004).

357. Ferreira, T. & Rasband, W. ImageJ User Guide, (2012).

358. Optiques – Objectifs d'Imagerie - Photonique - Optomécanique - Laser | Edmund Optics. Available at: https://www.edmundoptics.fr/. (2018)

359. Arney, J. S. & Alber, M. L. Optical effects of ink spread and penetration on halftones printed by thermal ink jet. J. Imaging Sci. Technol. 42, 331–334 (1998).

360. Wand, M. P. Data-Based Choice of Histogram Bin Width. Am. Stat. 51, 59–64 (1997).

361. Emmel, P. & Hersch, R. D. Modeling ink spreading for color prediction. J. Imaging Sci. Technol. 46, 237–246 (2002).

362. Zhang, Y. J. A survey on evaluation methods for image segmentation. Pattern Recognit. 29, 1335–1346 (1996).

363. Zhang, Y. J. & Gerbrands, J. J. On the design of test images for segmentation evaluation. Proc EUROSCO 1, 551–554 (1992).

364. Vallat-Evrard, L., Chagas, L., Passas, P. & Reverdy-Bruas, N. Microscale halftone dots analysis: A spatial threshold evaluation method. in Proceedings of the 43rd International Iarigai Conference (2016).

365. Fisher, R., Perkins, S., Walker, A. & Wolfart, E. Hypermedia image processing reference. Engl. John Wiley Sons Ltd (1996).

366. Sun, K.-H. A Study of mechanical dot gain for different dot shapes based on the border zone theory. (1991).

367. Zweng, A., Rittler, T. & Kampel, M. Evaluation of histogram-based similarity functions for different color spaces. in Computer Analysis of Images and Patterns 455–462 (Springer, 2011).

368. Doyle, W. Operation useful for similarity-invariant pattern recognition. 9, (1962).

369. Pal, N. R. & Bhandari, D. Image thresholding: Some new techniques. Signal Process. 33, 139–158 (1993).

370. Simpson, J. Improved cloud detection in GOES scenes over the oceans. Remote Sens. Environ. 52, 79–94 (1995).

371. Prewitt, J. M. & Mendelsohn, M. L. The analysis of cell images. Ann. N. Y. Acad. Sci. 128, 1035–1053 (1966).

372. Zack, G. W., Rogers, W. E. & Latt, S. A. Automatic measurement of sister chromatid exchange frequency. J. Histochem. Cytochem. 25, 741–753 (1977).

373. Rosenberg, C. J. Measurement-based evaluation of a printer dot model for halftone algorithm tone correction. J. Electron. Imaging 2, 205–212 (1993).

374. Sahoo, P., Wilkins, C. & Yeager, J. Threshold selection using Renyi's entropy. Pattern Recognit. 30, 71–84 (1997).

375. Jui-Cheng Yen, Fu-Juay Chang & Shyang Chang. A new criterion for automatic multilevel thresholding. IEEE Trans. Image Process. 4, 370–378 (1995).

376. Li, C. H. & Tam, P. K.-S. An iterative algorithm for minimum cross entropy thresholding. Pattern Recognit. Lett. 19, 771–776 (1998).

377. Pal, S. K. & Dasgupta, A. Spectral fuzzy sets and soft thresholding. Inf. Sci. 65, 65–97 (1992).

378. Abutaleb, A. S. Automatic thresholding of gray-level pictures using two-dimensional entropy. Comput. Vis. Graph. Image Process. 47, 22–32 (1989).

379. Brink, A. D. Thresholding of digital images using two-dimensional entropies. Pattern Recognit. 25, 803–808 (1992).

380. Soille, P. Morphological Image Analysis: Principles and Applications. (Springer Science & Business Media, 2013).

381. Bernsen, J. Dynamic thresholding of gray-level images. Proc Eighth Intl Conf Pattern Recognit. (1986).

382. Niblack, W. An introduction to digital image processing. (Strandberg Publishing Company, 1985).

383. Sauvola, J. & Pietikäinen, M. Adaptive document image binarization. Pattern Recognit. 33, 225–236 (2000).

384. Neerad Phansalkar, Sumit More, Ashish Sabale & Madhuri Joshi. Adaptive local thresholding for detection of nuclei in diversity stained cytology images. in International Conference on Communications and Signal Processing 218–220 (IEEE, 2011).

385. Pappas, T. N. Digital Halftoning Techniques for Printing. in Icps 94, 47th (1994).

386. Pappas, T. N. & Neuhoff, D. L. Model-based halftoning. in Electronic Imaging, 244–255 (International Society for Optics and Photonics, 1991).

387. Baqai, F. A. & Allebach, J. P. Halftoning via direct binary search using analytical and stochastic printer models. IEEE Trans. Image Process. 12, 1–15 (2003).

388. Zhou, Y. & Cao, H. A Variable Printer Model in Tone-Dependent Error Diffusion Halftone. In International Conference on Computer Science and Software Engineering (Vol. 6, pp. 101-104). 101–104 (IEEE, 2008).

389. Guo, J.-M. A Complete Printer Model in Error-Diffused Halftone Images. in Image Processing, IEEE International Conference 1529–1532 (IEEE, 2006).

390. Kim, C.-Y., Kweon, I.-S. & Seo, Y.-S. Color and printer models for color halftoning. J. Electron. Imaging 6, 166–180 (1997).

391. Lai, C.-C. & Tseng, D.-C. Printer Model and Least-Squares Halftoning Using Genetic Algorithms. J. Imaging Sci. Technol. 42, 241–249 (1998).

392. Balasubramanian, R. Colorimetric modeling of binary color printers. in Proceedings., International Conference on Image Processing 2, 327–330 (IEEE Comput. Soc. Press, 1995).

393. Kriss, M. Laser printers simulated by computer model. SPIE Newsroom (2007).

394. Norris, M. & Barney Smith, E. H. Printer modeling for document imaging, CISST. (2004).

395. Emmel, P. & Hersch, R. D. Exploring ink spreading. in Color and Imaging Conference, 335–340 (Society for Imaging Science and Technology, 2000).

396. Namedanian, M., Nyström, D., Zitinski Elias, P. & Gooran, S. Physical and optical dot gain: characterization and relation to dot shape and paper properties. In Color Imaging Xix: Displaying, Processing, Hardcopy, and Applications (Vol. 9015, p. 901509). (International Society for Optics and Photonics, 2014).

397. Je-Ho Lee & Allebach, J. P. Inkjet printer model-based halftoning. IEEE Trans. Image Process. 14, 674–689 (2005).

398. Youn, J. et al. Effect of image capture device on the accuracy of black-box printer models. In Color Imaging XIX: Displaying, Processing, Hardcopy, and Applications (Vol. 9015, p. 90150T). (International Society for Optics and Photonics, 2014).

399. Oliver, J. & Chen, J. Use of signature analysis to discriminate digital printing technologies. in NIP & Digital Fabrication Conference, 218–222 (Society for Imaging Science and Technology, 2002).

400. Suh, S., Allebach, J. P., Chiu, G. T.-C. & Delp, E. J. Printer mechanism-level data hiding for halftone documents. in NIP & Digital Fabrication Conference, 436–440 (Society for Imaging Science and Technology, 2006).

401. Wu, H., Kong, X. & Shang, S. A printer forensics method using halftone dot arrangement model. in IEEE China Summit and International Conference on Signal and Information Processing, 861–865 (IEEE, 2015).

402. Ulichney, R., Gaubatz, M. & Simske, S. Encoding information in clustered-dot halftones. in NIP & Digital Fabrication Conference, 602–605 (Society for Imaging Science and Technology, 2010).

403. Crounse, K. R. Measurement-based printer models with reduced number of parameters. in Electronic Imaging 121–129 (International Society for Optics and Photonics, 2001).

404. Kacker, D., Camis, T. & Allebach, J. P. Electrophotographic process embedded in direct binary search. IEEE Trans. Image Process. 11, 243–257 (2002).

405. Kriss, M. A. Spectral model of an electro-photographic printing system. In Color Imaging XVI: Displaying, Processing, Hardcopy, and Applications (Vol. 7866, p. 786611). (International Society for Optics and Photonics, 2011).

406. Itrić, K., Modrić, D. & Milković, M. Edge spread function for the paper-ink system. Nord. Pulp Pap. Res. J. 33, 542–547 (2018).

407. Arney, J. S., Mehta, P. & Anderson, P. G. A Continuous Tone Model of Halftones. J. Imaging Sci. Technol. 48, 45–49 (2004).

408. Hébert, M. & Hersch, R. D. Analyzing halftone dot blurring by extended spectral prediction models. J. Opt. Soc. Am. A 27, 6 (2010).

409. Rahaman, G. M. A., Norberg, O. & Edström, P. Extension of Murray-Davies tone reproduction model by adding edge effect of halftone dots. In Measuring, Modeling, and Reproducing Material Appearance (Vol. 9018, p. 90180F). (International Society for Optics and Photonics, 2014).

410. Neugebauer, H. Die Theoretischen grundlagen Des Mehrfarbendruckes. Z. Für Wiss. Photogr. Photophys. Photochem. translated and commented by Wyble, D., Kraushaar, A., 2005. The theoretical basis of multicolor letterpress printing, Hans E. J. Neugebauer. Color Res. Appl. 30, 322–331. (1937).

Abstract - Applications in the field of product security and authentication to prevent counterfeiting rely on abilities of microscale measurements of printed dots. Thus, researches described in this manuscript have been directed toward the development of measurement methods and apparatus to characterize halftone dot at the microscale. A polarized reflection optical microscope has been adapted with a commercial digital camera. The Bayer matrix was removed from the surface of the camera and raw images were retrieved. The microscope stage, the camera, the photometer and the thermometer were controlled directly in a Python graphic user interface specifically developed. A high dynamic range capture method was proposed and tuned specifically to obtain richer information on the ink and paper regions. The measurement apparatus and methods helped improve the accuracy and automate the measurements of the halftone dots at the microscale. The physical and optical dot gains were then separated and analyzed. A Gaussian fitting of the ink and paper histogram peaks was proposed to measure automatically the ink and paper region reflectance as a function of the ink coverage. Thresholding algorithms were applied to separate optical and physical dot gain. An objective threshold evaluation method was developed in order to define the best threshold algorithms for halftone images. The method was based on a simulation of the optical dot gain effects and of the microscope distortions to obtain test images and ground truth images. 30 threshold algorithms from literature were evaluated and demonstrated dependency on the ink coverage of the halftones. Two novel threshold algorithms were then developed specifically to process halftones. The first threshold algorithm was based on the determination of the amount of ink peak shift. The second threshold algorithm proposed a pretreatment of the images by applying a pseudo-deconvolution strategy, removing the optical dot gain from the halftones. Characterizations of the optical and physical dot gains were then conducted analyzing 2708 different halftones. Finally, a physical dot gain model and an optical dot gain model were proposed in order to predict the halftone reflectances from raster to print. The physical dot gain model was based on the generation of single ink particles placed according to a probability mask and on a fusion of the ink particles. The model was evaluated with 43269 dot morphologies that were captured automatically on the microscope. A novel halftone reflectance model was proposed based on a double convolution with two different paper point spread functions. It allowed an accurate reproduction of the main effects of the light diffusion with, at the same time, an accurate reproduction of the light entrapment near the edges of the dots.

Résumé – Les solutions pour lutter contre la contrefaçon permettant une sécurisation des produits dépendent des capacités de mesure à l'échelle microscopique de points imprimés. Les recherches explicitées dans ce manuscrit ont donc été consacrées au développement d'un équipement et de méthodes permettant de mesurer les imprimés à l'échelle microscopique. Un microscope en réflexion avec lumière polarisée a été associé avec un appareil photographique numérique. La matrice de Bayer a été retirée de la surface du capteur photographique et des images raw ont été enregistrées. La platine du microscope, l'appareil photographique, un photomètre et un thermomètre ont été contrôlés directement dans une interface logicielle développée en Python. Une méthode de mesure permettant d'élargir la gamme dynamique de reflectances mesurées a été proposée. L'appareil et les méthodes de mesures ont permis d'améliorer la précision et d'automatiser la mesure des points de trame à l'échelle microscopique. Les élargissements physique et optique des points de trame ont alors été séparés et analysés. Une méthode d'ajustement des pics de l'histogramme, correspondant à l'encre et au papier, avec une fonction Gaussienne a été proposée. Des algorithmes de seuillage ont été employés pour séparer l'élargissement optique et physique des points de trame. Une méthode objective d'évaluation des algorithmes de seuillage a été développée pour déterminer leurs performances sur les images de tramés. Cette méthode d'évaluation procède à une simulation des effets de la diffusion de la lumière et des défauts générés par l'imagerie afin de générer des images tests et images de référence. 30 algorithmes de seuillage de la littérature ont été évalués et ont présenté une dépendance avec le pourcentage de couverture de l'encre. Deux nouveaux algorithmes de seuillage ont alors été développés spécialement pour traiter les imprimés tramés. Le premier algorithme détermine le déplacement du pic correspondant à l'encre sur l'histogramme. Le deuxième algorithme proposé se base sur une pseudo-déconvolution permettant de prétraiter les images et se basant sur une séparation des effets de l'élargissement optique. Une caractérisation de l'élargissement optique et physique a alors été menée sur 2708 images d'imprimés tramés. Enfin, un modèle de l'élargissement physique et un modèle de l'élargissement optique des points de trame ont été proposés. Le modèle physique se base sur une génération de particules d'encre placées selon une fonction de probabilité et sur une fusion des particules d'encre. Le modèle a été évalué en considérant 43269 points de trame différents, mesurés automatiquement sur le microscope. Un nouveau modèle prédisant la réflectance des tramés a été développé, basé sur une double convolution avec deux fonctions différentes d'étalement du point. Ce modèle a permis de simuler de manière précise les effets principaux de la diffusion de la lumière dans le tramé, tout en simulant les effets de piégeage de la lumière à proximité des bords des points de trame.